Materials Chemistry
Principal Investigators' Meeting–2018

July 9-11, 2018

Gaithersburg Marriott Washingtonian Center

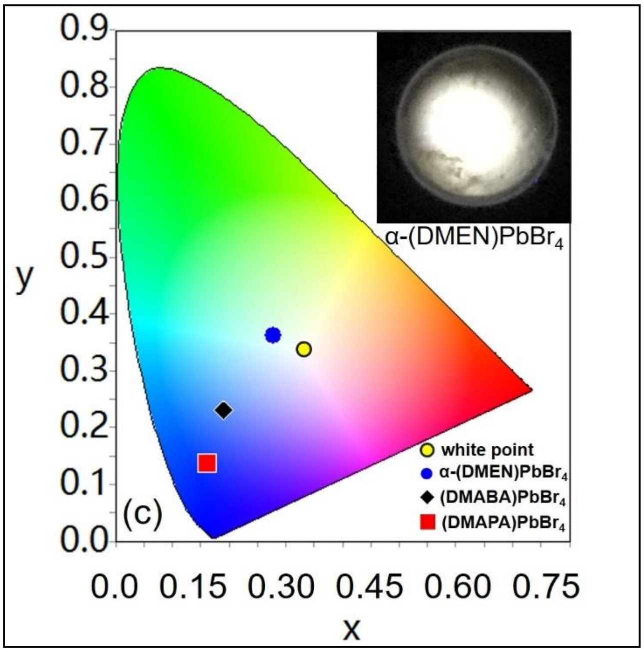

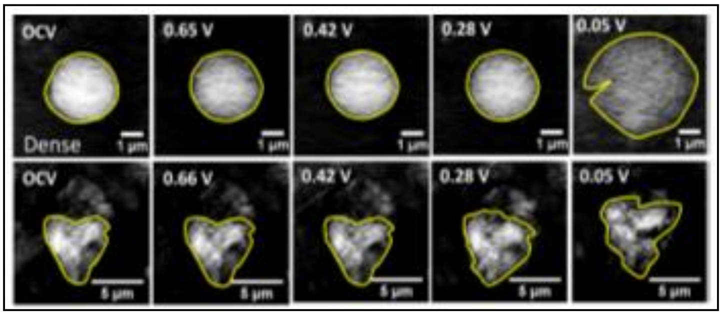

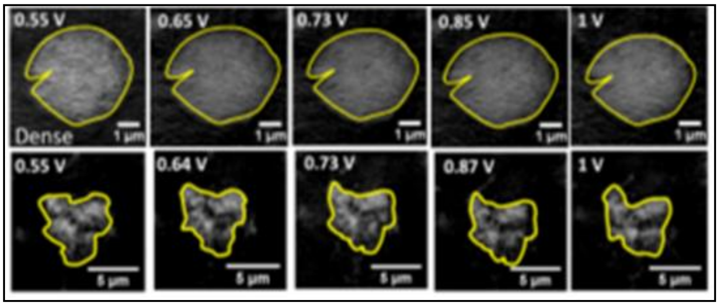

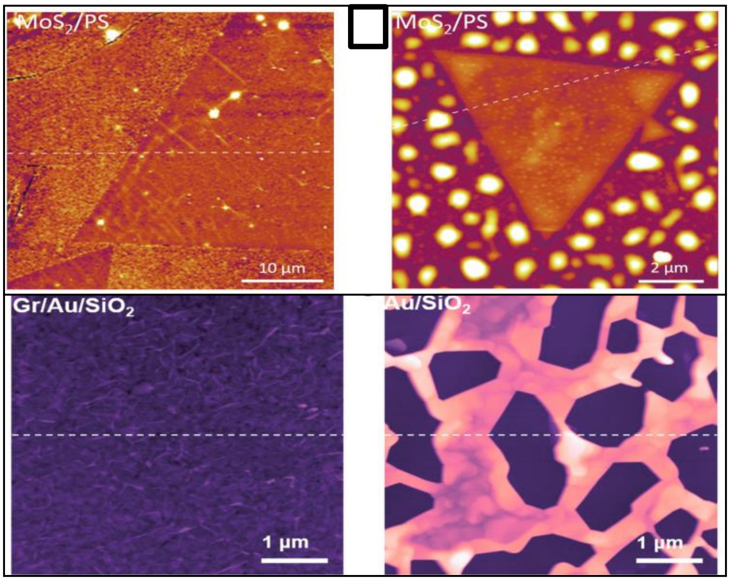

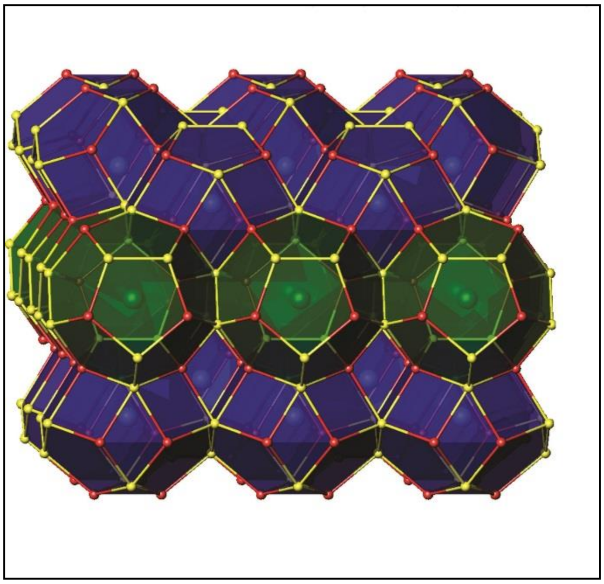

U.S. DEPARTMENT OF ENERGY

Office of Basic Energy Sciences
Materials Sciences and Engineering Division

On the Cover

Top Left: Color coordinate map illustrating the photoluminescent emission colors of different hybrid perovskite halide materials relative to pure white (yellow circle). The insert (upper right) is a photo of the light emitted by a sample of α-(DMEN)$PbBr_4$ after stimulation by 365 nm (UV) radiation.
Mercouri Kanatzidis, Northwestern University

Top Right: ***Upper****:* Transmission x-ray microscopy (TXM) images of bulk and nanoporous tin upon lithiation. Dense tin (top) shows burst-expansion occurring predominantly at the end of the insertion process. This process leads to tremendous strain in the material, followed by crack formation observed at 0.05 V. The nanoporous tin (bottom) expands less than dense tin and evolves to the final lithiated state more homogeneously. ***Lower****:* TXM images of bulk and nanoporous tin during delithiation. Dense tin (top) was found to be irreversibly deformed and does not return to its original shape or size. Cracks formed during lithiation remain in the material. By contrast, the nanoporous tin (bottom) contracts back nearly to its original size, leading to the long cycle lifetimes observed for this material.
Sarah Tolbert, UCLA

Bottom Left: ***Top***: Dewetting suppression of a polystyrene (PS) thin film by an MoS_2 capping layer. AFM height images before (left) and after (right) annealing at 180°C for 300 s. ***Bottom***: Dewetting suppression of thin gold films by graphene capping layer. AFM height images with (left) and without (right) graphene (Gr) coverage.
Ting Xu, LBNL

Bottom Right: Crystal structure depiction of a new clathrate compound $Ba_8M_{24}P_{28+\delta}$ (M = Cu/Zn) that breaks the tetra-coordinate framework rule for clathrates.
Kirill Kovnir, Iowa State University

This document was produced under contract number DE-SC0014664 between the U.S. Department of Energy and Oak Ridge Associated Universities.

The research grants and contracts described in this document are supported by the U.S. DOE Office of Science, Office of Basic Energy Sciences, Materials Sciences and Engineering Division.

Table of Contents

Laboratory Projects

University Grant Projects

Foreword

This document is a collection of abstracts of the presentations made at the Principal Investigators' Meeting of the Materials Chemistry program, sponsored by the Materials Sciences and Engineering (MSE) division in the Office of Basic Energy Sciences (BES) of the U.S. Department of Energy (DOE). The meeting was held on July 9–11, 2018, at the Marriott Washingtonian Center in Gaithersburg, Maryland, and is one of a series of principal investigators' meetings organized by BES. The purpose of the meeting is to bring together all the principal investigators with currently active projects in the Materials Chemistry program for the multiple purposes of raising awareness among PIs of the overall program content and of each other's research, encouraging exchange of ideas, promoting collaboration, and stimulating innovation. The meeting also provides an opportunity for the program managers and MSE/BES management to get a comprehensive overview of the program on a periodic basis, which provides opportunities to identify program needs and potential new research directions. The meeting agenda is organized in five sessions around topical areas in materials research that encompass many of the projects in the current Materials Chemistry portfolio. These include Energy Storage, Transport; Novel Materials, Physical Properties; Energy Materials I – Organic and Hybrid; Energy Materials II, Inorganic – Organometallic – Organic; New Materials Synthesis, Catalysis.

Recent BES workshops and other reports have identified as a Grand Challenge goal the ability to design and synthesize new materials having specific properties tailored for use in next-generation technologies. In support of this objective, the Materials Chemistry program supports basic research in the discovery, design and synthesis of materials with an emphasis on elucidating the complex relationships between a material's functional properties and its composition, atomic and molecular structure, and higher-order morphology. Major focus areas of the program include the discovery, synthesis, and characterization of new materials and the manipulation of materials' structure across a range of length scales using chemistry.

We thank all of the meeting attendees, for their active participation and for sharing their ideas and new research results. The assistance of the meeting chairs, Arthi Jayaraman and Miquel Salmeron, in organizing this meeting is greatly appreciated. Sincere thanks also go to Teresa Crockett of BES/MSE and Linda Severs and her colleagues at the Oak Ridge Institute for Science and Education (ORISE) for their excellent work providing all the logistical support for the meeting.

Michael Sennett
Craig Henderson
Program Managers, Materials Chemistry
Materials Sciences and Engineering Division
Office of Basic Energy Sciences
U.S. Department of Energy

AGENDA

2018 DOE BES Materials Chemistry PI Meeting

Meeting Chairs: **Arthi Jayaraman**, University of Delaware, and
Miquel Salmeron, Lawrence Berkeley National Laboratory

Day 1 (Monday, July 9, 2018)

7:30 – 8:30 am	Breakfast
8:30 – 9:00 am	*Welcome Message* **Linda Horton**, Director, Materials Sciences and Engineering Division, Office of Basic Energy Sciences
9:00 – 9:10 am	Introductory Remarks from **Michael Sennett and Craig Henderson**, Program Managers, Materials Chemistry
9:10 – 9:40 am	Invited talk by **John Mitchell**, Argonne National Laboratory *High Pressure Floating-Zone Crystal Growth of Correlated Electron Oxides*
Session I	***Topic: Energy Storage, Transport*** <u>Discussion Chairs</u>***:*** **Felix Fischer**, University of California, Berkeley and **Richard L. Brutchey**, University of Southern California
9:40 – 10:00 am	**David Mitlin,** Clarkson University *High Rate Sodium Storage Mechanisms in Non-Graphitic Carbons*
10:00 – 10:20 am	**Xiaowei Teng**, University of New Hampshire *Transition Metal Oxides Nanomaterials for Aqueous Electrochemical Energy Storage*
10:20 – 10:40 am	**May Nyman**, Oregon State University *Counterions for Controlled Dissolution, Precipitation and Stabilization of Molecular Clusters and Extended Lattices*
10:40 – 11:00 am	---Break---
11:00 – 11:20 am	**Vojislav R. Stamenkovic**, Argonne National Laboratory *Energy and Fuels from Multifunctional Electrochemical Interfaces*
11:20 – 11:40 am	**Gary Rubloff**, University of Maryland *Molecular Design and Vapor Phase Synthesis of Hybrid Ion-Conducting Materials Based on Crown Ethers*
11:40 – 12:00 pm	**Mircea Dincă**, Massachusetts Institute of Technology *Fundamental Studies of Thermal and Electrical Transport in Microporous Metal-Organic Frameworks*
12:00 – 12:20 pm	PANEL DISCUSSION
12:20 – 1:25 pm	**Working Lunch and Informal Discussions**

Session II *Topic: Novel Materials, Physical Properties*

Discussion Chairs*:* **Miquel Salmeron,** Lawrence Berkeley National Laboratory and **Arumugam Manthiram**, University of Texas at Austin

1:30 – 1:50 pm	**Robert Cava**, Princeton University *New Superconducting Materials*
1:50 – 2:10 pm	**Danna E. Freedman**, Northwestern University *High Pressure Synthesis of New Magnets Featuring Diamagnetic Sources of Anisotropy*
2:10 – 2:30 pm	**Mauricio Terrones**, Penn State University *2D Electrically Functional Carbon-Chalcogenide Alloys by Design (2D-EFICACY)*
2:30 – 2:50 pm	---Break---
2:50 – 3:10 pm	**Yi Cui**, SLAC National Accelerator Laboratory *Two-Dimensional Chalcogenide Nanomaterials*
3:10 – 3:30 pm	**Yury Gogotsi,** Drexel University *Compositional Control of Fundamental Electronic and Magnetic Properties of Ordered Layered Multi-element MXenes*
3:30 – 3:50 pm	**Hans-Conrad zur Loye**, University of South Carolina *Directed Synthesis of New Actinide Containing Oxides, Fluorides and Chalcogenides*
3:50 – 4:10 pm	PANEL DISCUSSION
4:20 – 6:00 pm	**Poster Session 1 (ODD numbered posters)** Chaired by **Arthi Jayaraman**, University of Delaware and **Rachel Segalman**, University of California, Santa Barbara *1-minute poster synopsis from each presenter*
6:00 – 8:00 pm	**Working Dinner**

Day 2 (Tuesday, July 10, 2018)

7:30 – 8:30 am	Breakfast

Session III *Topic: Energy Materials I – Organic and Hybrid*

Discussion Chairs: **Greg Grason**, University of Massachusetts at Amherst and **Thomas Epps**, University of Delaware

8:30 – 8:50 am	**Kenneth R. Graham**, University of Kentucky *Surface Ligand Effects on Energetics, Charge Transfer, and Stability at Interfaces between Metal Halide Perovskites and Organic Semiconductors*
8:50 – 9:10 am	**James R. Neilson**, Colorado State University *Informed Materials Design Principles from Local Structures and Dynamics in Hybrid Inorganic-Organic Perovskite Halides*

9:10 – 9:30 am	**Marc Baldo**, Massachusetts Institute of Technology *Bimolecular Interactions in Organic Semiconductors: Hot Charge, Hot Excitons, Efficiency Droop, and Instability*
9:30 – 9:50 am	--- Break---
9:50 – 10:10 am	**Thuc-Quyen Nguyen**, University of California, Santa Barbara *Understanding Novel Lewis Acid Doping Mechanisms in Organic Semiconductors*
10:10 – 10:30 am	**Samuel W. Thomas III**, Tufts University *Controlling Solid-State Conjugated Materials with Aromatic Interactions of Side Chains*
10:30 – 10:50 am	**Rachel Segalman**, University of California, Santa Barbara *Energy Flow in Polymers with Mixed Conduction Pathways: New Routes to Improving Thermopower and Thermoelectric Power Factor*
10:50 – 11:10 am	**Ryan Hayward,** University of Massachusetts at Amherst *Targeted Design of Co-continuous Nanostructures in Randomly End-Linked Copolymer Networks*
11:10 – 11:30 am	PANEL DISCUSSION
11:45 – 1:10 pm	**Working Lunch and Informal Discussions**
	Craig Henderson and Michael Sennett *BES Presentation on Programmatic Issues*

Session IV *Topic: Energy Materials II, Inorganic – Organometallic – Organic*

Discussion Chairs: **Vladimir Tsukruk**, Georgia Institute of Technology and **Ram Seshadri**, University of California, Santa Barbara

1:20 – 1:40 pm	**Kirill Kovnir**, Iowa State University *Structure-Properties Relationship in Transition Metal-Phosphorus Clathrate Thermoelectrics*
1:40 – 2:00 pm	**Vinayak Dravid**, Northwestern University *Design of Next Generation Thermoelectrics*
2:00 – 2:20 pm	**Aaron Rossini,** AMES Laboratory *Materials Characterization with Sensitivity-Enhanced Solid-State NMR Spectroscopy*
2:20 – 2:40 pm	--- Break---
2:40 – 3:00 pm	**Thomas Gray**, Case Western Reserve University *Late-Metal Phosphorescent Lumophores*
3:00 – 3:20 pm	**Jeramy Zimmerman,** Colorado School of Mines *Understanding and Controlling Aggregation Processes in Mixed-Molecular Solids*

3:20 – 3:40 pm	**Abraham Clearfield**, Texas A&M University *Studies of Reactive Amorphous Compounds and Surfaces: Their Pathways to Crystallinity and Surface Functionality*
3:40 – 4:00 pm	**Lei Zhu**, Case Western Reserve University *An Integrated Theoretical and Experimental Approach to Achieve Highly Polarizable Relaxor Ferroelectric Liquid Crystalline Polymers*
4:00 – 4:20 pm	PANEL DISCUSSION
4:30 – 6:00 pm	**Poster Session 2 (EVEN numbered posters)** Chaired by **Ting Xu,** Lawrence Berkeley National Laboratory and **Lisa Hall,** Ohio State University *1-minute poster synopsis from each presenter*
6:00 – 8:00 pm	**Working Dinner**

Day 3 (Wednesday, July 11, 2018)

7:30 – 8:30 am	Breakfast
Session V	***Topic: New Materials Synthesis, Catalysis*** Discussion Chairs: **Rebekka Klausen**, Johns Hopkins University and **Timo Thonhauser**, Wake Forest University
8:40 – 9:00 am	**Adam Veige**, University of Florida *iClick Synthesis of Metallopolymers and Highly Emissive Materials*
9:00 – 9:20 am	**Philip Power,** University of California at Davis *Activation of Hydrogen under Ambient Conditions by Main Group Molecules*
9:20 – 9:40 am	**Nicholas Melosh,** SLAC National Accelerator Laboratory *Diamondoid Science and Applications*
9:40 – 10:00 am	---Break---
10:00 – 10:20 am	**Siddhartha Das**, University of Maryland *Polyelectrolyte-grafted nanochannels for enhanced electro-chemo-mechanical energy conversion*
10:20 – 10:40 am	**Kai Landskron**, Lehigh University *Anionic Porous Organic Frameworks as Advanced Functional Adsorbents for CO2 and Organic Micropollutants in Water*
10:40 – 11:00 am	**Alexei Sokolov**, Oak Ridge National Laboratory *Dynamics in Multicomponent Polymeric Materials*
11:00 – 11:20 am	**Hong Wang**, University of North Texas *Linearly- and Cross-Conjugated Porphyrin Oligomers*
11:20 – 11:40 am	PANEL DISCUSSION

11:40 – 12:00 pm	Concluding remarks
12:00 – 12:30 pm	Program Managers and Meeting Chairs Wrap-up, debriefing, evaluation
12:30 pm	Departure

LABORATORY PROJECTS

Physical Chemistry of Inorganic Nanostructures

A. Paul Alivisatos, Department of Chemistry, UC Berkeley; Materials Sciences Division, Lawrence Berkeley National Laboratory

Stephen R. Leone, Department of Chemistry, UC Berkeley; Materials Sciences Division, Lawrence Berkeley National Laboratory

Eran Rabani, Department of Chemistry, UC Berkeley; Materials Sciences Division, Lawrence Berkeley National Laboratory

Peidong Yang, Department of Chemistry, UC Berkeley; Materials Sciences Division, Lawrence Berkeley National Laboratory

Program Scope

This program emphasizes the fundamental science of synthesis and preparation of the basic building blocks of nanomaterials, as well as the characterization and theoretical understanding of their physical properties. The program consists of three subtasks: Physical Chemistry of Semiconductor Nanocrystals, Fundamentals of Semiconductor Nanowires, and Microscopy, Optical and X-ray Investigations of Nanostructured Materials. The first subtask develops the science of colloidal inorganic nanocrystals, and reliable and robust methods to prepare uniform nanocrystals of different materials, including semiconductors, metals, and magnetic materials and investigates fundamental optical, electrical, structural, and thermodynamic properties. The second subtask develops the science and technology of a broad spectrum of 1-dimensional inorganic semiconducting nanostructures or nanowires. The final subtask develops state-of-the-art optical, electron and x-ray characterization microscopies and ultrafast dynamics measurements that provide higher spatial, spectroscopic, and time resolutions than are afforded by conventional techniques. Theoretical and computational tools adequate for low-dimensional nanostructures will be developed and used to provide insights to the aforementioned physical processes.

Recent Progress

I. Auger recombination in Nanocrystals: The fast, nonradiative decay of multiexcitonic states via Auger recombination (AR) in nanocrystals (NCs) is an important process affecting a variety of applications based on semiconductor NCs. From a theoretical perspective, the description of AR in confined semiconductor NCs is a challenging task due to the large number of valence electrons and the need to couple single- and bi-excitonic states. These challenges have restricted the treatment of AR to simple non-interacting electron-hole models (the Non-interacting Formalism in Figure 1). We recently developed a novel approach (the Interacting Formalism in Figure 1) for calculating AR lifetimes in confined NCs with thousands to tens of thousands of electrons, explicitly including electron-hole interactions. We then demonstrated why the inclusion of electron-hole correlations are imperative for an accurate calculation of the AR lifetime in NCs, even for sizes below the exciton Bohr radius. Our method calculates the correlated electron-hole states (i.e., excitonic states) by solving the Bethe-Salpeter equation and uses the resulting correlated excitonic states together with Fermi's golden rule to calculate AR lifetimes. We applied the new approach to CdSe quantum dots of varying sizes and for one-dimensional (1D) CdSe nanorods of varying diameters and lengths to establish the utility of this method. Our calculations correctly predict the experimentally known "universal volume scaling law" (1) for CdSe quantum dots (Figure 1) and make novel predictions for 1D CdSe nanorods. This method is the first atomistic electronic structure method for calculating AR lifetimes to be generally applicable to realistically sized 0D, 1D, 2D and heterostructured NCs.

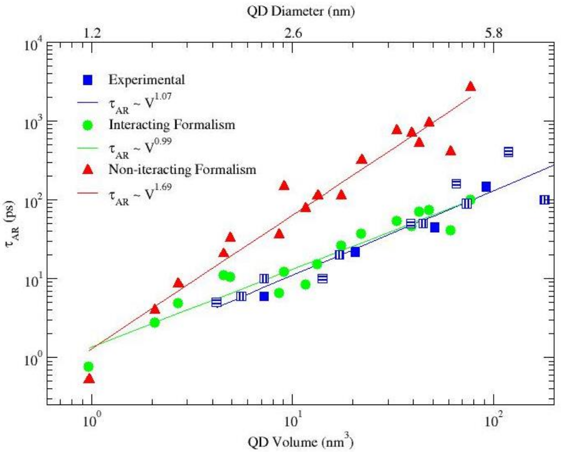

Figure 1. Comparison of AR lifetimes from experiments, our new interacting formalism and non-interacting formalism.

II. Ultra-High, Hot Carrier Transient Photocurrent in Nanocrystal Arrays: Solution-processed colloidal semiconductor NCs are promising building blocks for developing next generation electronics and optoelectronics devices, yet transport studies of NC quantum dot arrays fall short of idealizations because of the difficulties associated with bringing these NCs close enough together for strong electronic coupling. One established approach improving carrier transport is to replace the native ligands during wet chemistry synthesis with shorter organic or inorganic ligands, thereby enhancing inter-NC coupling. However, such surface treatments typically introduce defect states or mid-gap states and results in a significant reduction of the modulation ratio in transistors (with gate bias/ without gate bias < 10^5) and photoconductivity (photocurrent/dark-current < 10), due to carrier transport at high density mid-gap states. Here, we show that at high excitation intensity and on ultrafast time scales, there is a new mechanism for carrier transport that allows for facile intrinsic transport as prepared NC over long distances. By combining high speed photoconductive switch (2) and ultrafast laser excitation in a photoconductor with sub- 40 ps response time, we observed a peak photocurrent

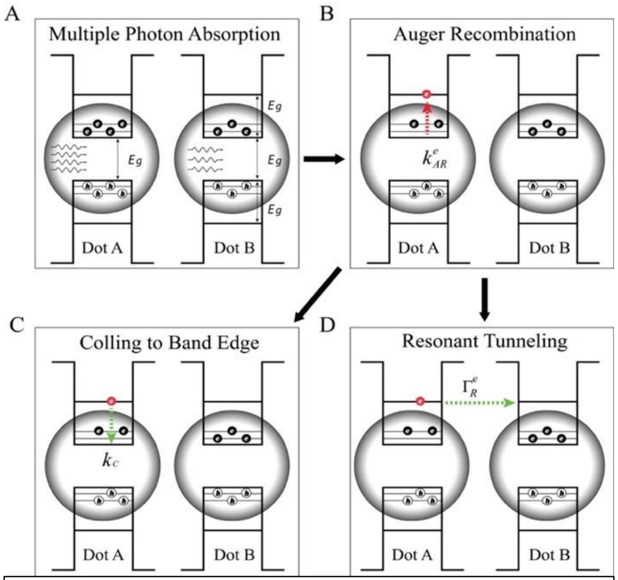

Figure 2. (A) Each NC has band-edge excitons distributed according to the Poisson distribution. (B) AR promotes charge carriers to higher energies. (C) Excited charge carriers can cool to the band edge or (D) tunnel to a neighboring NC.

density of more than 10^6 mA/cm^2 in arrays of PbSe NCs capped with native oleic acid ligands. The ratio between peak photocurrent and dark current is ten orders of magnitude. The effective mobility is in the order of ~10 cm^2/Vs, which is more than eight orders of magnitude higher than previous results in PbSe, CdSe, and CdTe NCs capped with native ligands. By analyzing the results using a kinetic model (shown pictorially in Figure 2), we attributed the ultra-high photocurrent to multiple photo-generated excitons undergoing Auger recombination, followed by resonant, rapid tunneling at high energies. This mechanism is demonstrated for a wide range of PbSe NCs sizes (diameter from 2.7 nm to 7.1 nm) and device dimensions. Our observations indicate that native ligand capped NC arrays are promising for optoelectronics applications wherein multiple carriers are photo-injected to inter-band states.

III. Investigations into Lead Halide Perovskite Surface Chemistry: During the previous funding cycle, we leveraged our expertise on colloidal syntheses to develop a complete family of perovskite nanomaterials, including 2D nanoplates (3,4), 1D nanowires (5,6), and 0D nanocrystals (7). More recently, our focus has shifted to understanding and controlling the surface chemistry of these materials, which is critical for improving optoelectronic properties, controlling self-assembly, and expanding the versatility of these materials. Halide perovskite nanocrystals have demonstrated remarkably high photoluminescence quantum yields (PLQYs) without the need for a passivating shell, which is often attributed to the defect tolerance that arises in ionic semiconductors (8). However, PLQYs do not yet regularly approach unity, indicating that undesirable charge trapping and nonradiative recombination are both present. Through multiple combined experimental and theoretical study, we have determined that halide vacancies on the surface of perovskite nanocrystals are the origin of charge trapping and nonradiative recombination. These halide vacancies leave underlying Pb atoms with a dangling bond, and these nonbonding states are relatively close in energy to the conduction band minimum (CBM). The CBM energy changes with halide composition, resulting in a deep trap in CsPbCl3, a shallow trap in CsPbBr3, and a band-edge resonance in CsPbI3, consistent with the significantly different PLQYs for different compositions (Figure 3). With these surface defects identified, we selected new passivating ligands that bond to undercoordinated Pb, namely softer Lewis bases like phosphonates, sulfonates, and fluorinated carboxylates. These ligands clear the bandgap of undesirable trap states, resulting in near-unity PLQY emitters. We have also tested these findings on nanoplates and

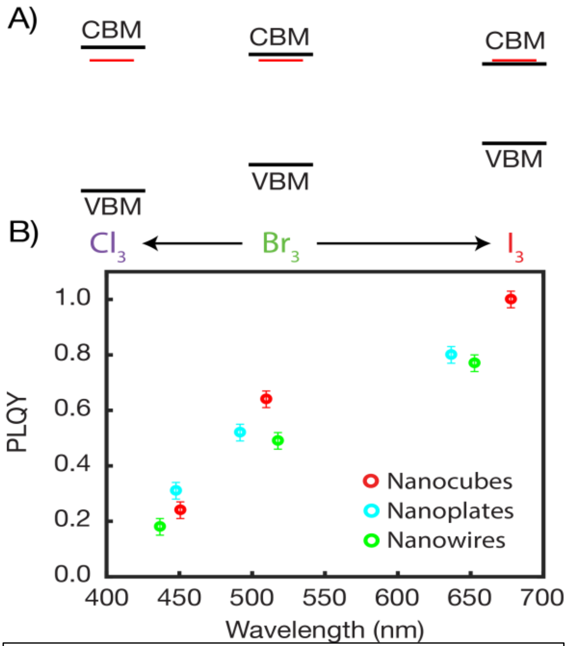

Figure 3. (A) Trap state (red) moving from a deep trap (Cl3) to a band-edge resonance (I3). (B) PLQY for the differing shapes and halides.

nanowires, demonstrating that our surface model is applicable to the entire family of perovskite nanomaterials.

Additionally, we developed a versatile ligand exchange method that greatly enhances the functionality of these materials. This newfound control over the surface is being used to coat CsPbBr3 nanowires with functional polymers, to increase packing density of thin films of CsPbBr3 in optoelectronic devices, and to modulate self-assembly of 2D CsPbBr3 nanosheets into layered Ruddlesden-Popper materials. Additionally, we recently showed that a significant improvement in the quantum efficiency in lead halide perovskites can be obtained by oxygen gas exposure, achieving close to three order-of-magnitude efficiency enhancement and about a fourfold increase in the spontaneous carrier recombination lifetime as the dimension of perovskites shrinks to nanoscale. We also performed density functional theory calculations to prove that oxygen absorption on the Pb-rich surface is an effective method for removing the mid-gap surface trapped states.

Future Plans

In the future, we plan to continue with our enhanced synthetic and post-synthetic control of surfaces, heterostructure interfaces and device design via nanocrystal arrays. For example, we would like to apply our newly developed formalism for calculating Auger recombination lifetimes in NCs for the rational design of heterostructured NCs with application specific Auger recombination lifetimes. Additionally, we would like to continue developing computational methods to handle perovskite NCs with experimentally relevant sizes – similar to have used to study for type II-VI NCs. This joint focus on the synthesis and characterization of the physical properties of perovskite NCs along with developing a theoretical understanding of their unique properties will allow for a virtuous cycle of design, synthesis, measurement, computation and application.

References

1. Klimov, V. I.; Mikhailovksy, A. A.; McBranch, D. W.; Leatherdale, C.A.; Bawendi, M.G. Science 2000, 287, 1011-1013.
2. Fidler, A. F.; Gao, J. B.; Klimov, V. I. Nat Phys **2017,** 13, (6), 604-610.
3. L. Dou, A. B. Wong, Y. Yu, M. Lai, N. Kornienko, S. W. Eaton, A. Fu, C. G. Bischak, J. Ma, T. Ding, N. S. Ginsberg, L.-W. Wang, A. P. Alivisatos, P. Yang; Science 2015, 349, 1518–1521.
4. Y. Bekenstein, B. A. Koscher, S. W. Eaton, P. Yang, A. P. Alivisatos; JACS 2015, 137, 16008–16011.
5. D. Zhang, S. W. Eaton, Y. Yu, L. Dou, P. Yang; JACS 2015, 137, 9230–9233.
6. D. Zhang, Y. Yu, Y. Bekenstein, A. B. Wong, A. P. Alivisatos, P. Yang; JACS 2016, 138, 13155–13158.
7. Q. A. Akkerman, V. D'Innocenzo, S. Accornero, A. Scarpellini, A. Petrozza, M. Prato, L. Manna; JACS 2015, 137, 10276–10281.
8. J. Kang, L.-W. Wang; J Phys. Chem. Lett. 2017, 8, 489-493.

2-Year Publication List

1. B. A. Koscher, N. D. Bronstein, J. H. Olshansky, Y. Bekenstein, A. P. Alivisatos; JACS 2016, 138, 12065–12068.

2. S.N. Raja, Y. Bekenstein, M.A. Koc, S. Fisher, D. Zhang, L. Lin, R. Ritchie, P. Yang, A. P. Alivisatos; ACS Appl. Mater. Interfaces 2016, 8, 35523–35533.

3. Y. Yu, D. Zhang, C. Kisielowski, L. Dou, N. Kornienko, Y. Bekenstein, A. P. Alivisatos, P. Yang; Atomic Resolution Imaging of Halide Perovskites. Nano Letters 2016, 16,7530–7535.

4. M. Lai, Q. Kong, C. G. Bischak, Y. Yu, L. Dou, S. W. Eaton, N. S. Ginsberg, P. Yang; Structural, optical, and electrical study of phase controlled cesium lead iodide nanowires. Nano Research 2016, doi:10.1007/s12274-016-1415-0.

5. Q. Kong, D. Kim, C. Liu, Y. Yu, Y. Su, Y. Li, P. Yang; Directed assembly of nanoparticle catalysts on nanowire photoelectrodes for photoelectrochemical CO_2 reduction. Nano Letters 2016, 16, 5675–5680.

6. D. Zhang, Y. Yang, Y. Bekenstein, Y. Yu, N. A. Gibson, A. B. Wong, S. W. Eaton, N. Kornienko, Q. Kong, M. Lai, A. P. Alivisatos, S. R. Leone, P. Yang; Synthesis of Composition Tunable Cesium Lead Halide Nanowires through Anion-Exchange Reactions. JACS 2016, 138, 7236–7239.

7. S. W. Eaton, A. Fu, A. B. Wong, C. Z. Ning, P. Yang; Semiconductor Nanowire Lasers. Nature Rev. Mater. 2016, 1, 16028.

8. Y. Su, C. Liu, S. Brittman, J. Tang, A. Fu, P. Yang; Single nanowire photoelectrochemistry. Nature Nano. 2016, 11, 609.

9. L Dou, M Lai, CS Kley, Y Yang, CG Bischak, D Zhang, SW Eaton, NS Ginsberg, and P Yang. "Spatially Resolved Multi-Color CsPbX3 Nanowire Heterojunctions via Anion Exchange," Proc. Natl. Acad. Sci. U.S.A. 114 (28), pp 7216-7221 (2017).

10. Balan AD, Eshet H, Olshansky JH, Lee YV, Rabani E, Alivisatos AP. Effect of Thermal Fluctuations on the Radiative Rate in Core/Shell Quantum Dots. Nano Lett. 2017 Mar 8;17(3):1629-1636. DOI: 10.1021/acs.nanolett.6b04816.

11. Z Liu, Y Bekenstein, X Ye, SC Nguyen, J Swabeck, D Zhang, S-T Lee, P Yang, W Ma, and AP Alivisatos. “Ligand Mediated Transformation of Cesium Lead Bromide Perovskite Nanocrystals to Lead Depleted Cs4PbBr6 Nanocrystals,” J. Am. Chem. Soc. 139 (15), pp 5309–5312 (2017).

12. BA Koscher, JK Swabeck, ND Bronstein, and AP Alivisatos. “Essentially Trap-Free CsPbBr3 Colloidal Nanocrystals by Postsynthetic Thiocyanate Surface Treatment,” J. Am. Chem. Soc. 139 (19), pp 6566–6569 (2017).

13. LM Carneiro, SK Cushing, C Liu, Y Su, P Yang, AP Alivisatos, and SR Leone. “Excitation-wavelength-dependent small polaron trapping of photoexcited carriers in α-Fe2O3,” Nat. Mater. 16, pp 819–825 (2017).

14. JH Olshansky, AD Balan, TX Ding, X Fu, YV Lee, and AP Alivisatos. “Temperature-Dependent Hole Transfer from Photoexcited Quantum Dots to Molecular Species: Evidence for Trap-Mediated Transfer,” ACS Nano 11 (8), pp 8346–8355 (2017).

15. W. Lee, H Li, AB Wong, D Zhang, M Lai, Y Yu, Q Kong, E Lin, JJ Urban, JC Grossman, and P Yang. "Ultralow thermal conductivity in all-inorganic halide perovskites," Proc. Natl. Acad. Sci. U.S.A. 114 (33), pp 8693-8697 (2017).

16. Yu Y, Zhang D, Yang P. “Ruddlesden-Popper Phase in Two-Dimensional Inorganic Halide Perovskites: A Plausible Model and the Supporting Observations.” Nano Lett. 2017 Sep 13;17(9):5489-5494. DOI: 10.1021/acs.nanolett.7b02146.

17. Lin J, Lai M, Dou L, Kley CS, Chen H, Peng F, Sun J, Lu D, Hawks SA, Xie C, Cui F, Alivisatos AP, Limmer DT, Yang P. Thermochromic halide perovskite solar cells. Nat Mater. 2018 Mar;17(3):261-267. DOI: 10.1038/s41563-017-0006-0.

18. Ondry JC, Hauwiller MR, Alivisatos AP. Dynamics and Removal Pathway of Edge Dislocations in Imperfectly Attached PbTe Nanocrystal Pairs: Toward Design Rules for Oriented Attachment. ACS Nano. 2018 Feb 26. DOI: 10.1021/acsnano.8b00638.

19. Wong AB, Bekenstein Y, Kang J, Kley CS, Kim D, Gibson NA, Zhang D, Yu Y, Leone SR, Wang L-W, Alivisatos AP, Yang P. Strongly quantum confined colloidal cesium tin iodide perovskite nanoplates: lessons for reducing defect density and improving stability. Nano Lett. 2018 Mar. DOI: 10.1021/acs.nanolett.8b00077.

20. I Hadar, JP Philbin, YE Panfil, S Neishdtadt, I Liberman, H Eshet, S Lazar, E Rabani and U Banin. “Semiconductor Seeded Nanorods with Graded Composition Exhibiting High Quantum-Yield, High Polarization, and Minimal Blinking,” Nano Lett. 17, pp 2524-2531 (2017).

21. E Arnon, E Rabani, D Neuhauser, and R Baer. “Equilibrium Configurations of Large Nanostructures Using Embedded-Fragment Stochastic Density Functional Theory,” J. Chem. Phys. 146, 224111 (2017).

22. M Park, N Kornienko, SE Reyes-Lillo, M Lai, JB Neaton, P Yang, and RA Mathies. “Critical Role of Methylammonium Librational Motion in Methylammonium Lead Iodide ($CH_3NH_3PbI_3$) Perovskite Photochemistry,” Nano Lett. 17 (7), 4151−4157 (2017).

23. DM Monahan, L Guo, J Lin, L Dou, P Yang and GR Fleming. “Room-Temperature Coherent Optical Phonon in 2D Electronic Spectra of $CH_3NH_3PbI_3$ Perovskite as a Possible Cooling Bottleneck,” J. Phys. Chem. Lett. 8 (14), 3211−3215 (2017).

24. McCaffrey DL, Nguyen SC, Cox SJ, Weller H, Alivisatos AP, Geissler PL, Saykally RJ. Mechanism of ion adsorption to aqueous interfaces: Graphene/water vs. air/water. Proc. Natl. Acad. Sci. USA. 2017 Dec 19;114(51):13369-13373. DOI:10.1073/pnas.1702760114.

Materials and Interfacial Chemistry for Next Generation Electrical Energy Storage

S. Dai, C. A. Bridges, M. P. Paranthaman, X. G. Sun, G. M. Veith
Oak Ridge National Laboratory, Oak Ridge, TN 37831

Program Scope

The overarching goal is t*o investigate fundamental principles governing energy storage through integrated synthesis and advanced characterization.* Our current research is focused on fundamental investigation of electrolytes based on ionic liquids and rational synthesis of novel electrode architectures through Fermi level engineering of anode and cathode redox levels by employing porous structures and surface modifications as well as advanced operando characterization techniques including neutron diffraction and scattering. The key scientific question concerns the relationship between chemical structures and their energy-storage efficacies.

Recent Progress

- While the high operation voltage (>4.3 V vs Li/Li^+) of promising cathode materials such as $LiNi_{0.5}Mn_{1.5}O_4$ (LNMO) increases power and energy density, it also causes extensive oxidation of the conventional carbonate electrolytes, resulting in large irreversible capacity loss, low coulombic efficiency, and considerable thickening of the SEI layer. One approach to mitigate this is to develop additives that promote the formation of a passivating layer in the initial discharge cycle, which then protects the cell from parasitic electrolyte reactions at the electrode surface. We hypothesized that by substituting functional groups (e.g., a C-2 methyl group) into a malonatoborate anion, we could form a more stable, highly conducting salt with good SEI formation capability. Therefore, we synthesized a new lithium salt by replacing the acidic hydrogen with a methyl group, forming lithium bis(2-methyl-2-fluoromalonato)borate (LiBMFMB), which demonstrates utility as an additive in conventional carbonate electrolyte for LNMO based lithium ion batteries, taking advantage of its good SEI formation ability.
- Our goal has been to develop a strategy to combine the benefits of liquid electrolytes with the rigidity of a solid electrolyte. In principle, it is easy to combine the advantages both from solid electrolytes and liquid electrolytes in one material that has a solid-like mechanical modulus for dendrites blocking and liquid-like room-temperature ionic conductivities for Li^+ transport. We identified two different types of quasi-solid liquid electrolytes (QSLE) that demonstrate the utility of this approach. In one case, a novel class of graphene-analogues boron nitride (g-BN) nanosheets confine an ultrahigh concentration of ionic liquids (ILs) in an interlayer and out-of-layer chamber to give rise to a quasi-liquid solid electrolyte (QSLE). The electron-insulated g-BN nanosheet host with a large specific surface area can confine ILs as much as 10 times of the host’s weight to afford high ionic conductivity (3.85×10^{-3} S cm^{-1} at 25 °C, even 2.32×10^{-4} S cm^{-1} at −20 °C), which is close to that of the corresponding bulk IL electrolytes. The high ionic conductivity of QSLE is attributed to the enormous absorption for ILs and the confining effect of g-BN to form the ordered lithium ion transport channels in an interlayer and out-of-layer of g-BN.
- We have focused on the development of new electrode materials that demonstrate functionality beyond that of common electrodes. In one example we have prepared a nanostructured graphite that tests the relationship between electrochemical performance and graphitic domain size. The synthesis involves a simple electrochemical route for the graphitization of amorphous carbons through cathodic polarization in molten $CaCl_2$ at

temperatures of about 1100 K, which generates petaloid nanoflakes that agglomerate to form a porous graphite. While graphite is typically only considered as an anode, the nanostructured graphite instead allows fast and reversible intercalation/deintercalation of anions as a cathode material for batteries. In a $Pyr_{14}TFSI$ (1-butyl-1-methylpyrrolidinium TFSI) ionic liquid, it exhibits a specific discharge capacity of 65 and 116 mAh g^{-1} at a rate of 1800 mA g^{-1} when charged to 5.0 and 5.25 V vs. Li/Li^+, respectively. The relatively weaker total force of the van der Waals interactions between the smaller graphitic domains allows the cation to intercalate at high voltages.

- The team has further gained insight into the solid-electrolyte interface using advanced surface characterization methods, such as small-angle neutron scattering (SANS – EQSANS at the SNS) and neutron reflectometry (NR- the liquid reflectometer at the SNS). In particular, we have utilized in situ small-angle neutron scattering of ordered mesoporous hard carbon (OMC) to understand the interfacial chemistry of electrolytes at low voltages. OMC is a useful model anode material with a high surface area and is relevant to various storage technologies in which interfacial reactions, morphology, and stress can all affect performance.

Future Plans

- Further understand what chemical functionality is needed to design ionic liquids with intrinsically stable SEI formation
- Investigate what is the relationship between conducting salt and additive structure and SEI composition for Li-ion and Na-ion batteries
- Further explore what influence does salt concentration have on the formation of the SEI layer
- Investigate how confinement of ionic liquids in nanocomposite solid electrolytes influences the ion transport
- Explore how sodium/lithium ions conduct through a single ion polymer and how this affects the interfacial passivation

Publications (2017-2018)

(1) Yang, Q. W.; Zhang, Z. Q.; Sun, X. G.; Hu, Y. S.; Xing, H. B.; Dai, S. Ionic liquids and derived materials for lithium and sodium batteries. *Chem. Soc. Rev.* **2018**, *47*, 2020-2064. 10.1039/c7cs00464h

(2) Lyu, H. L.; Li, P. P.; Liu, J. R.; Mahurin, S.; Chen, J. H.; Hensley, D. K.; Veith, G. M.; Guo, Z. H.; Dai, S.; Sun, X. G. Aromatic Polyimide/Graphene Composite Organic Cathodes for Fast and Sustainable Lithium-Ion Batteries. *ChemSusChem* **2018**, *11*, 763-772. 10.1002/cssc.201702001

(3) Banerjee, A.; Lampen-Kelley, P.; Knolle, J.; Balz, C.; Aczel, A. A.; Winn, B.; Liu, Y. H.; Pajerowski, D.; Yan, J. Q.; Bridges, C. A.; Savici, A. T.; Chakoumakos, B. C.; Lumsden, M. D.; Tennant, D. A.; Moessner, R.; Mandrus, D. G.; Nagler, S. E. Excitations in the field-induced quantum spin liquid state of alpha-RuCl3. *npj Quantum Mater.* **2018**, *3*. 10.1038/s41535-018-0079-2

(4) Zhu, X.; Jin, T.; Tian, C. C.; Lu, C. B.; Liu, X. M.; Zeng, M.; Zhuang, X. D.; Yang, S. Z.; He, L.; Liu, H. L.; Dai, S. 1 In Situ Coupling Strategy for the Preparation of FeCo Alloys and Co4N Hybrid for Highly Efficient Oxygen Evolution. *Adv. Mater.* **2017**, *29*. 10.1002/adma.201704091

(5) Zhang, Q.; Kercher, A. K.; Veith, G. M.; Sarbada, V.; Brady, A. B.; Li, J.; Stach, E. A.; Hull, R.; Takeuchi, K. J.; Takeuchi, E. S.; Dudney, N. J.; Marschilok, A. C. Lithium Vanadium Oxide (Li1.1V3O8) Coated with Amorphous Lithium Phosphorous Oxynitride (LiPON): Role of Material Morphology and Interfacial Structure on Resulting Electrochemistry. *J. Electrochem. Soc.* **2017**, *164*, A1503-A1513. 10.1149/2.0881707jes

(6) Zhang, M. H.; Yin, K. B.; Hood, Z. D.; Bi, Z. H.; Bridges, C. A.; Dai, S.; Meng, Y. S.; Paranthaman, M. P.; Chi, M. F. In situ TEM observation of the electrochemical lithiation of N-doped anatase TiO2 nanotubes as anodes for lithium-ion batteries. *J. Mater. Chem. A* **2017**, *5*, 20651-20657. 10.1039/c7ta05877b

(7) Wong, A. T.; Noh, J. H.; Pudasaini, P. R.; Wolf, B.; Balke, N.; Herklotz, A.; Sharma, Y.; Haglund, A. V.; Dai, S.; Mandrus, D.; Rack, P. D.; Ward, T. Z. Impact of gate geometry on ionic liquid gated ionotronic systems. *APL Mater.* **2017**, *5*. 10.1063/1.4974485

(8) Sun, X. G.; Zhang, Z. Z.; Guan, H. Y.; Bridges, C. A.; Fang, Y. X.; Hu, Y. S.; Veith, G. M.; Dai, S. A sodium-aluminum hybrid battery. *J. Mater. Chem. A* **2017**, *5*, 6589-6596. 10.1039/c7ta00191f

(9) Sun, X. G.; Wan, S.; Guang, H. Y.; Fang, Y. X.; Reeves, K. S.; Chi, M. F.; Dai, S. New promising lithium malonatoborate salts for high voltage lithium ion batteries. *J. Mater. Chem. A* **2017**, *5*, 1233-1241. 10.1039/c6ta07757a

(10) Shen, B. H.; Veith, G. M.; Armstrong, B. L.; Tenhaeff, W. E.; Sacci, R. L. Predictive Design of Shear-Thickening Electrolytes for Safety Considerations. *J. Electrochem. Soc.* **2017**, *164*, A2547-A2551. 10.1149/2.1171712jes

(11) Sacci, R. L.; Lehmann, M. L.; Diallo, S. O.; Cheng, Y. Q. Q.; Daemen, L. L.; Browning, J. F.; Doucet, M.; Dudney, N. J.; Veith, G. M. Lithium Transport in an Amorphous LixSi Anode Investigated by Quasi-elastic Neutron Scattering. *J. Phys. Chem. C* **2017**, *121*, 11083-11088. 10.1021/acs.jpcc.7b01133

(12) Ponomaryov, A. N.; Schulze, E.; Wosnitza, J.; Lampen-Kelley, P.; Banerjee, A.; Yan, J. Q.; Bridges, C. A.; Mandrus, D. G.; Nagler, S. E.; Kolezhuk, A. K.; Zvyagin, S. A. Unconventional spin dynamics in the honeycomb-lattice material alpha-RuCl3: High-field electron spin resonance studies. *Phys. Rev. B* **2017**, *96*. 10.1103/PhysRevB.96.241107

(13) Peng, J. J.; Chen, N. Q.; He, R.; Wang, Z. Y.; Dai, S.; Jin, X. B. Electrochemically Driven Transformation of Amorphous Carbons to Crystalline Graphite Nanoflakes: A Facile and Mild Graphitization Method. *Angew. Chem.-Int. Edit.* **2017**, *56*, 1751-1755. 10.1002/anie.201609565

(14) Little, A.; Wu, L.; Lampen-Kelley, P.; Banerjee, A.; Patankar, S.; Rees, D.; Bridges, C. A.; Yan, J. Q.; Mandrus, D.; Nagler, S. E.; Orenstein, J. Antiferromagnetic Resonance and Terahertz Continuum in alpha-RuCl3. *Phys. Rev. Lett.* **2017**, *119*. 10.1103/PhysRevLett.119.227201

(15) Li, Y. C.; Wan, S.; Veith, G. M.; Unocic, R. R.; Paranthaman, M. P.; Dai, S.; Sun, X. G. A Novel Electrolyte Salt Additive for Lithium-Ion Batteries with Voltages Greater than 4.7 V. *Adv. Energy Mater.* **2017**, *7*. 10.1002/aenm.201601397

(16) Li, Y. C.; Veith, G. M.; Browning, K. L.; Chen, J. H.; Hensley, D. K.; Paranthaman, M. P.; Dai, S.; Sun, X. G. Lithium malonatoborate additives enabled stable cycling of 5 V lithium metal and lithium ion batteries. *Nano Energy* **2017**, *40*, 9-19. 10.1016/j.nanoen.2017.07.051

(17) Li, Y. C.; Cheng, Y. Q.; Daemen, L. L.; Veith, G. M.; Levine, A. M.; Lee, R. J.; Mahurin, S. M.; Dai, S.; Naskar, A. K.; Paranthaman, M. P. Neutron vibrational spectroscopic

studies of novel tire-derived carbon materials. *Phys. Chem. Chem. Phys.* **2017**, *19*, 22256-22262. 10.1039/c7cp03750c

(18) Lee, S.; Sun, X. G.; Lubimtsev, A. A.; Gao, X.; Ganesh, P.; Ward, T. Z.; Eres, G.; Chisholm, M. F.; Dai, S.; Lee, H. N. Persistent Electrochemical Performance in Epitaxial VO2(B). *Nano Lett.* **2017**, *17*, 2229-2233. 10.1021/acs.nanolett.6b04831

(19) Lampen-Kelley, P.; Banerjee, A.; Aczel, A. A.; Cao, H. B.; Stone, M. B.; Bridges, C. A.; Yan, J. Q.; Nagler, S. E.; Mandrus, D. Destabilization of Magnetic Order in a Dilute Kitaev Spin Liquid Candidate. *Phys. Rev. Lett.* **2017**, *119*. 10.1103/PhysRevLett.119.237203

(20) Klein, M. J.; Veith, G. M.; Manthiram, A. Rational Design of Lithium-Sulfur Battery Cathodes Based on Experimentally Determined Maximum Active Material Thickness. *J. Am. Chem. Soc.* **2017**, *139*, 9229-9237. 10.1021/jacs.7b03380

(21) Klein, M. J.; Veith, G. M.; Manthiram, A. Chemistry of Sputter-Deposited Lithium Sulfide Films. *J. Am. Chem. Soc.* **2017**, *139*, 10669-10676. 10.1021/jacs.7b03379

(22) Herklotz, A.; Guo, E. J.; Wong, A. T.; Meyer, T. L.; Dai, S.; Ward, T. Z.; Lee, H. N.; Fitzsimmons, M. R. Reversible Control of Interfacial Magnetism through Ionic-Liquid Assisted Polarization Switching. *Nano Lett.* **2017**, *17*, 1665-1669. 10.1021/acs.nanolett.6b04949

(23) Cheng, Y. Q.; Balachandran, J.; Bi, Z. H.; Bridges, C. A.; Paranthaman, M. P.; Daemen, L. L.; Ganesh, P.; Jalarvo, N. The influence of the local structure on proton transport in a solid oxide proton conductor La0.8Ba1.2GaO3.9. *J. Mater. Chem. A* **2017**, *5*, 15507-15511. 10.1039/c7ta01396e

(24) Browning, K. L.; Sacci, R. L.; Veith, G. M. Energetics of Na+ Transport through the Electrode/Cathode Interface in Single Solvent Electrolytes. *J. Electrochem. Soc.* **2017**, *164*, A580-A586. 10.1149/2.0311704jes

(25) Bridges, C. A.; Sun, X. G.; Guo, B. K.; Heller, W. T.; He, L. L.; Paranthaman, M. P.; Dai, S. Observing Framework Expansion of Ordered Mesoporous Hard Carbon Anodes with Ionic Liquid Electrolytes via in Situ Small-Angle Neutron Scattering. *ACS Energy Lett.* **2017**, *2*, 1698-1704. 10.1021/acsenergylett.7b00472

(26) Banerjee, A.; Yan, J. Q.; Knolle, J.; Bridges, C. A.; Stone, M. B.; Lumsden, M. D.; Mandrus, D. G.; Tennant, D. A.; Moessner, R.; Nagler, S. E. Neutron scattering in the proximate quantum spin liquid alpha-RuCl3. *Science* **2017**, *356*, 1055-1058. 10.1126/science.aah6015

(27) al-Wahish, A.; al-Binni, U.; Tetard, L.; Bridges, C. A.; Kharel, K.; Gunaydin-Sen, O.; Huq, A.; Musfeldt, J. L.; Paranthaman, M. P.; Mandrus, D. Structure and Dynamics Investigations of Sr/Ca-Doped LaPO4 Proton Conductors. *J. Phys. Chem. C* **2017**, *121*, 11991-12002. 10.1021/acs.jpcc.7b02254

Precision synthesis and assembly of ionic and liquid crystalline polymers

Juan J. de Pablo(1) (PI)

Wei Chen(1), Seth Darling(2), Paul Nealey(1), Matthew Tirrell(1) (co-PIs)

Institute for Molecular Engineering, Materials Sciences Division(1), and Nanoscale Science and Technology Division(2), Argonne National Laboratory

Program Scope

Past efforts to understand charged polymeric and liquid crystalline materials have largely focused on homopolymers and their properties in the bulk. In this FWP, entitled Precision Synthesis and Assembly of Ionic and Liquid Crystalline Polymers, we are investigating (1) the role of charge sequence on the behavior of polymeric molecules, (2) the role of patterned surfaces in directing the assembly of charged block polymer electrolytes, and the concomitant transport properties, and (3) the use of polymer-brush patterned substrates in controlling the 3D assembly of chiral liquid crystalline materials. Brushes (end-tethered polymer chains) composed of charged macromolecules are a frequently used model system and tool in this work. The program relies on the synergistic use of synthesis, characterization, theory and computation to make progress on these three fronts. The overall aim of the research is to elucidate fundamental principles that will impact a wide array of energy technologies, ranging from antifouling coatings for separation membranes, to solid electrolytes for energy storage applications.

Recent Progress

Building on our previous work, which was focused on homo-charged polyelectrolytes, and multi-valent interactions among them, we have recently started to explore new ground in macromolecules bearing both positive and negative charges. Though special cases of hetero-charged polymers have been explored in the past, there is actually a continuum of possible charge distributions that constitutes a progression from randomness to increasing degrees and scales of order in charge sequences. The diverse possibilities suggested by Figure 1, and our ability in the Argonne Polymer Foundry to synthesize many such structures with precision by living anionic polymerization, controlled free radical polymerization and, with amino acid monomers, solid phase peptide synthesis, highlights the bio-inspired character of this work, bringing to synthetic polymers a similar diversity of interactions as in biological macromolecules and, in some cases, going beyond. We know that in biology such a diversity of primary sequences in proteins dictates larger scale structures ranging from highly ordered to intrinsically disordered, each evolved to carry out particular functions. This abstract focuses on some recent discoveries in the realm of charged polymer brushes underpinning work in the entire FWP.

An example of our efforts is illustrated in Figure 2, where coarse-grained molecular dynamics enhanced by free-energy sampling methods was used to examine the roles of solvophobicity and multivalent salts on polyelectrolyte brush collapse. Specifically, we demonstrated that while ostensibly similar, solvophobic collapsed brushes and multivalent-ion collapsed brushes exhibit distinct mechanistic and structural features (1). Notably, we found that multivalent-induced heterogeneous brush collapse is observed under good solvent polymer backbone conditions, demonstrating that the mechanism of multivalent collapse is not contingent upon a solvophobic backbone (2). The potential of mean-force (PMF) between two individual brush strands confirms this analysis, revealing starkly different PMFs under solvophobic and multivalent conditions, suggesting the role of multivalent "bridging" as the discriminating feature in trivalent collapse (3). Structurally, multivalent ions show a propensity for nucleating order within collapsed brushes, whereas poor-solvent collapsed brushes are more disordered; this difference is traced to the existence of a metastable PMF minimum for poor solvent conditions, and a global PMF minimum for trivalent systems, under experimentally relevant conditions.

The most recent results for this FWP are on the frictional forces between brushed in the presence of multi-valent ions. In contrast to results in no added salt or in low concentrations of mono-valent salt (4), we find that very small proportions of multi-valent salt, even at low total ionic strength, greatly enhance friction (5). In Figure 3, it is seen that even 10 *micromolar* tri-valent ion produces enhanced friction.

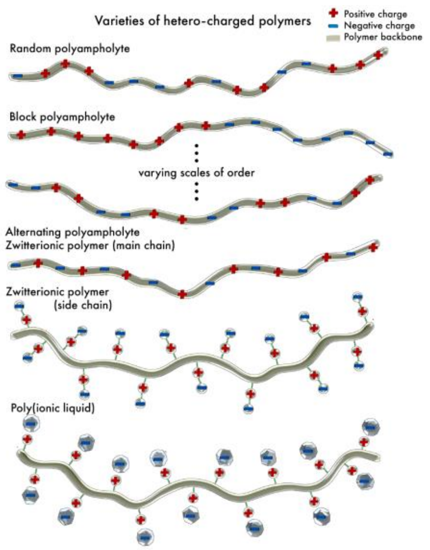

Figure 1 - Varieties of hetero-charged polymers shown schematically with differing degrees and arrangements of positive and negative charges. In addition to the specific structures illustrated here, one can envision (a) block copolymers with either neutral or homo- or hetero-charged blocks, (b) incorporation of additional types of interactions (hydrophobic, hydrogen bonding, mesogenic, for example) and, of course, (c) poly(ionic liquids) with the positive and negative charges positionally exchanged.

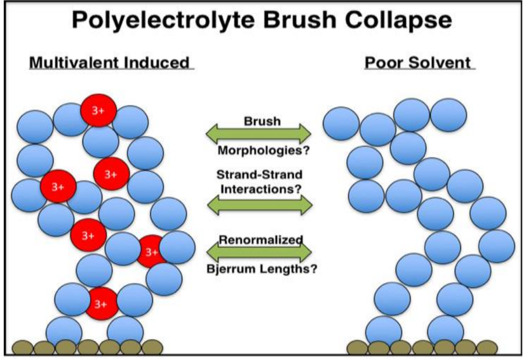

Figure 2 – Schematic representation of hetero-charged polymer brushes undergoing collapse as a result of (a) multivalent cations and (b) poor solvent conditions.

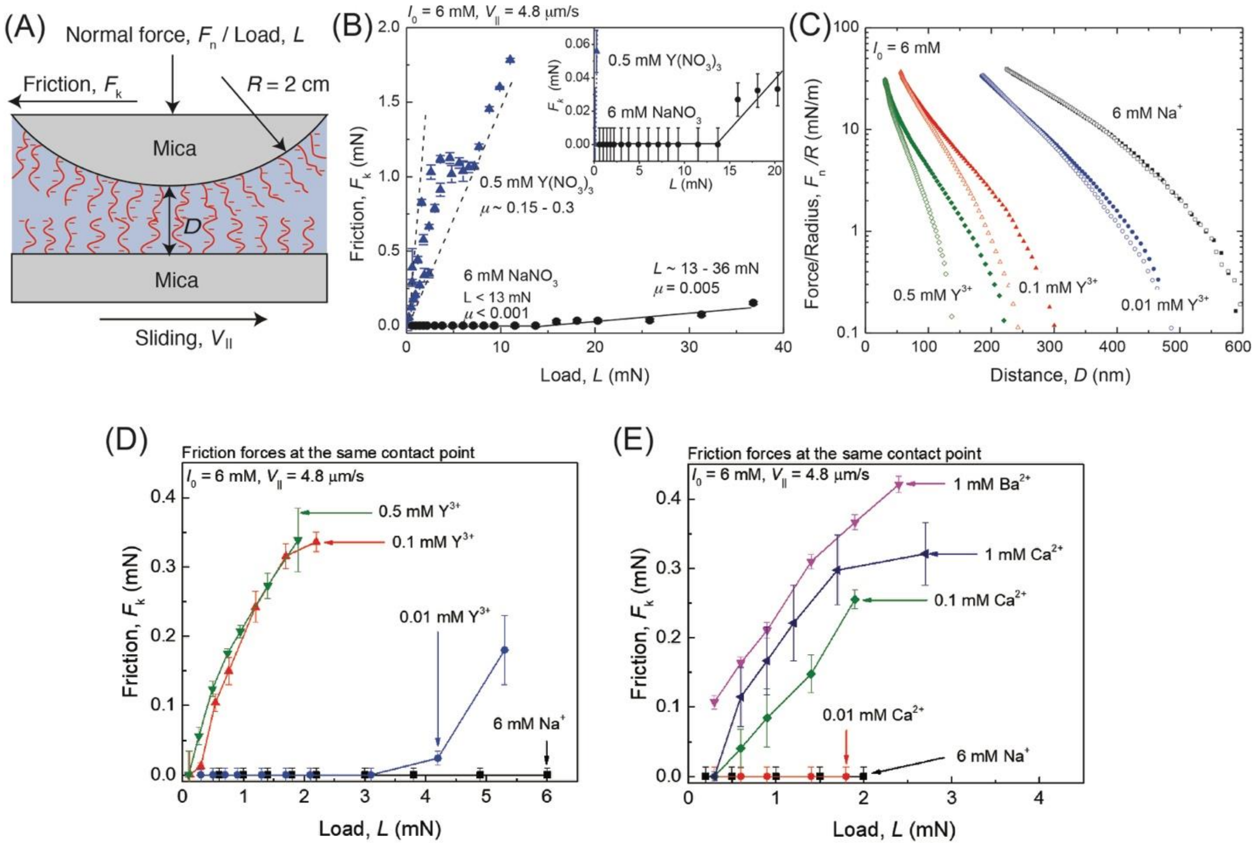

Figure 3. Forces between apposing PSS brush layers in solution. (A) The geometry of normal force, F_n (also called load, L) and friction force measurements with the SFA. (B) The friction forces between two PSS brush layers in 6 mM $NaNO_3$ (circles), 0.5 mM $Y(NO_3)_3$, and 3 mM $NaNO_3$ (triangles) solutions. (C) Normal force–distance curves and (D) friction forces of apposing PSS brushes measured at constant contact point and ionic strength (6 mM) in 6 mM $NaNO_3$, 0.01 mM, 0.1 mM, and 0.5 mM $Y(NO_3)_3$ and (E) 0.01 mM, 0.1 mM, 1 mM $Ca(NO_3)_2$, and 1 mM $Ba(NO_3)_2$. No damage was detected during the friction measurements. Error bars represent +/- SD, averaged over six to ten repeat measurements.

The presence of multivalent ions (Y^{3+}, Ca^{2+}, Ba^{2+}), even at minute concentrations, dramatically increases the friction forces between brush layers due to electrostatic bridging and brush collapse. Our results suggest the lubricating properties of polyelectrolyte brushes in multivalent solution are hindered relative to those in monovalent solution. Simulations have helped us understand two regimes of this frictional behavior. At weak overlap, friction is enhanced by tri-valent attractions between weakly interpenetrating chains. At higher loads and degrees of overlap, brush friction is high due to surface texture arising from brush collapse.

Future Plans

Plans on polyelectrolyte brushes are to begin to explore the effect of oppositely charged polymers in solution on adhesion and friction between polyelectrolyte brushes and to explore zwitterionic polymer brush structure and properties. In the directed self-assembly aspects of this project, recent and future work is aimed at understanding of (a) ion conduction in microphase-separated block copolymer electrolytes, (b) the distribution of ions in microphase-separated copolymers with periodic dielectric permittivity, and (c) directed self-assembly of liquid crystalline materials. We are also exploring various uses of ionic liquids to achieve voltage control and gating in magnetic materials.

References

(1) "Lateral structure formation in polyelectrolyte brushes induced by multivalent ions," B. Brettmann, P. Pincus, M. Tirrell, *Macromolecules*, **50**, 1225 (2017).

(2) "Comparing solvophobic and multivalent induced collapse in polyelectrolyte brushes," N. E. Jackson, B. K. Brettmann, V. Vishwanath, M. Tirrell, J. J. de Pablo, *ACS Macro Letters*, **6**, 155 (2017).

(3) "Sweet, hairy, soft and slippery," S. Lee, N. D. Spencer, *Science* **319**, 575-576 (2008).

(4) "Multivalent ions induce lateral structural inhomogeneities in polyelectrolyte brushes," J. Yu, N.E. Jackson, X. Xu, B.K. Brettmann, M. Ruths, J.J. de Pablo, M. Tirrell, *Science Advances*, **3**, eaao1497 (2017).

(5) J. Yu, N.E. Jackson, X. Xu, Y. Morgenstern, Y. Kaufman, M. Ruths, J.J. de Pablo, M. Tirrell, *unpublished* (2018).

Publications (2-year list of publications SUPPORTED BY BES)

(1) Brettmann, B.K.; Hoffman, P.; Pincus, P.; Tirrell, M., Bridging Contributions to Polyelectrolyte Brush Collapse in Multivalent Salt Solutions, *J. Polymer Sci., Part A, Polymer Chemistry*, **54**, 184 (2016).

(2) Qin, J.; de Pablo, J. J., Criticality and Connectivity in Macromolecular Charge Complexation. *Macromolecules* **49**, 8789 (2016).

(3) Zhang, R.; Roberts, T.; Aranson, I. S.; de Pablo, J. J., Lattice Boltzmann simulation of asymmetric flow in nematic liquid crystals with finite anchoring. *Journal of Chemical Physics*, **144** (8) (2016).

(4) Qin, J.; de Pablo, J. J., Ordering Transition in Salt-Doped Diblock Copolymers. *Macromolecules*, **49**, 3630 (2016).

(5) Arges, C. G.; Kambe, Y.; Suh, H. S.; Ocola, L. E.; Nealey, P. F. "Perpendicularly Aligned, Anion Conducting Nanochannels in Block Copolymer Electrolyte Films." *Chem. Mater.,* **28**, 1377 (2016).

(6) Li, X.; Armas-Perez, J. C.; Martinez Gonzalez, J.A.; Liu, X.; Xie, H.-L.; Bishop, C. E.; Zhang, R.; Hernandez-Ortiz, J. P.; de Pablo, J.J.; Nealey, P.F. Directed Self-Assembly of Nematic Liquid Crystals on Chemically Patterned Surfaces: Morphological States and Transitions." *Soft Matter*, **12**, 8595 (2016).

(7) Xiong, S.; Chapuis, Y. A.; Wan, L.; Gao, H.; Li, X.; Ruiz, R.; Nealey, P. F. Directed self-assembly of high-chi block copolymer for nano fabrication of bit patterned media via solvent annealing. *Nanotechnology*, **27**, 415601 (2016).

(8) Xiong, S.; Wan, L.; Ishida, Y.; Chapuis, Y.-A.; Craig, G. S. W.; Ruiz, R.; Nealey, P. F. Directed Self-Assembly of Triblock Copolymer on Chemical Patterns for Sub-10-nm Nanofabrication via Solvent Annealing. *ACS Nano*, **10**, 7855 (2016).

(9) Ren, J.; Ocola, L.E.; Divan, R.; Czaplewski, D.A.; Segal-Peretz, T.; Xiong, S.; Kline, R.J.; Arges, C.G.; Nealey, P.F. Post-Directed-Self-Assembly Membrane Fabrication for *in Situ* Analysis of Block Copolymer Structures. *Nanotechnology*, ***27***, 435303 (2016) .

(10) Li, X.; Armas-Perez, J. C.; Hernandez-Ortiz, J. P.; Arges, C. G.; Liu, X. Y.; Martinez-Gonzalez, J. A.; Ocola, L. E.; Bishop, C.; Xi, H. L.; de Pablo, J. J.; Nealey, P. F., Directed Self-Assembly of Colloidal Particles onto Nematic Liquid Crystalline Defects Engineered by Chemically Patterned Surfaces. *ACS Nano*, **11**, 6492 (2017).

(11) Martinez-Gonzalez, J. A.; Li, X.; Sadati, M.; Zhou, Y.; Zhang, R.; Nealey, P.F.; de Pablo, J.J., Directed self-assembly of liquid crystalline blue-phases into ideal single-crystals. *Nature Communications*, **8**, 15854 (2017).

(12) Li, X.; Martinez-Gonzalez, J. A.; Hernandez-Ortiza, J. P.; Ramirez-Hernandez, A.; Zhou, Y.; Sadati, M.; Zhang, R.; Nealey, P.F.; de Pablo, J.J., Mesoscale martensitic transformation in single crystals of topological defects. *Proceedings of the National Academy of Sciences of the United States of America*, **114**, 10011 (2017).

(13) Khaira, G.; Doxastakis, M.; Bowen, A.; Ren, J.X.; Suh, H.S.; Segal-Peretz, T.; Chen, X.X.; Zhou, C.; Hannon, A.F.; Ferrier, N.J.; Vishwanath, V.; Sunday, D.F.; Gronheid, R.; Kline, R. J.; de Pablo, J.J.; Nealey, P.F., Derivation of Multiple Covarying Material and Process Parameters Using Physics-Based Modeling of X-ray Data. *Macromolecules*, **50**, 7783 (2017).

(14) Zhou,C.; Segal-Peretz, T.; Oruç, M.E.; Suh, H.S.; Wu, G.; Nealey, P.F., Fabrication of Nanoporous Alumina Ultra-filtration Membrane with Tunable Pore Size Using Block Copolymer Templates. *Adv. Funct. Mater.*, **27,** 1701756 (2017).

(15) Segal-Peretz, T.; Ren, J.; Xiong, S.; Khaira, G. S.; Bowen, A.; Ocola, L. E.; Divan, R.; Doxastakis, M.; Ferrier, N. J.; Pablo, J.J.; Nealey, P.F., Quantitative Three-Dimensional Characterization of Block Copolymer Directed Self-Assembly on Combined Chemical and Topographical Pre-Patterned Templates. *ACS Nano*, **11**, 1307 (2017).

(16) Arges, C. G.; Kambe, Y.; Dolejsi, M.; Wu, G.; Segal-Pertz, T.; Ren, J.; Cao, C.; Kline, R. J.; Nealey, P. F. Interconnected Ionic Domains Enhance Conductivity in Microphase Separated Block Copolymer Electrolytes. *Journal of Materials Chemistry A*, **11**, 5619 (2017).

(17) Kambe, Y.; Arges, C.G.; Patel, S.; Stoykovich, M.; Nealey, P.F., Ion Conduction in Microphase-Separated Block Copolymer Electrolytes. *The Electrochemical Society Interface,* **26**, 61 (2017).

(18) Armas-Pérez, J.C.; Li, X.; Martínez-González, J.A.; Smith, C.; Hernández-Ortiz, J.P.; Nealey, P.F.; de Pablo, J.J. Sharp Morphological Transitions from Nanoscale Mixed–anchoring Patterns in Confined Nematic Liquid Crystals. *Langmuir*, **33,** 12516 (2017)

(19) Li, X.; Armas-Perez, J. C.; Hernandez-Ortiz, J. P.; Arges, C. G.; Liu, X. Y.; Martinez-Gonzalez, J. A.; Ocola, L. E.; Bishop, C.; Xi, H. L.; de Pablo, J. J.; Nealey, P. F., Directed Self-Assembly of Colloidal Particles onto Nematic Liquid Crystalline Defects Engineered by Chemically Patterned Surfaces. *ACS Nano*, **11**, 6492 (2017).

(20) Xue, X.; Dong, G.; Zhou, Z.; Xian, D.; Hu, Z.; Ren, W.; Ye, Z.-G.; Chen, W.; Jiang, Z.-D.; Liu, M., Voltage Control of Two-Magnon Scattering and Induced Anomalous Magnetoelectric Coupling in Ni–Zn Ferrite, *ACS Appl. Mater. Interfaces*, **9**, 43188 (2017).

(21) Jiang, Z.; Chen, W., Generalized skew-symmetric interfacial probability distribution in reflectivity and small-angle scattering analysis, *J. Appl. Crystallogr.*, **50**, 1653 (2017).

(22) Mao, J.; Zaborin, A.; Poroyko, V.; Goldfeld, D.; Lynd, N. A.; Chen, W.; Tirrell, M. V. Zaborina, O.; Alverdy, J. C., *De novo* synthesis of phosphorylated tri-block copolymers with pathogen virulence suppressing properties that prevent infection-related mortality, *ACS Biomater. Sci. Eng.*, **3**, 2076 (2017).

(23) Brettmann, B.; Pincus, P.; Tirrell M, Lateral structure formation in polyelectrolyte brushes induced by multivalent ions, *Macromolecules*, **50**, 1225 (2017).

(24) Jackson, N.E.; Brettmann, B.K. Vishwanath, V.; Tirrell, M.; de Pablo, J.J., Comparing solvophobic and multivalent induced collapse in polyelectrolyte brushes, *ACS Macro Letters*, **6**, 155 (2017).

(25) Yu, J.; Jackson, N.E.; Xu, X.; Brettmann, B.K.; Ruths, M.; de Pablo, J.J.; Tirrell, M., Multivalent ions induce lateral structural inhomogeneities in polyelectrolyte brushes, *Science Advances*, **3**, eaao1497 (2017).

(26) Ramirez-Hernandez, A.; Peters, B. L.; Schneider, L.; Andreev, M.; Schieber, J. D.; Muller, M.; Kroger, M.; de Pablo, J. J., A Detailed Examination of the Topological Constraints of Lamellae-Forming Block Copolymers. *Macromolecules*, **51**, 2110 (2018).

(27) Langenberg, M.; Jackson, N. E.; de Pablo, J. J.; Muller, M., Role of translational entropy in spatially inhomogeneous, coarse-grained models. *Journal of Chemical* Physics, **148** (9) (2018).

(28) Chu, W.W.; Qin, J.; de Pablo, J.J., Ion Distribution in Microphase-Separated Copolymers with Periodic Dielectric Permittivity. *Macromolecules*, **51**, 1986 (2018).

(29) Ramirez-Hernandez, A.; Peters, B. L.; Schneider, L.; Andreev, M.; Schieber, J. D.; Muller, M.; de Pablo, J. J., A multi-chain polymer slip-spring model with fluctuating number of entanglements: Density fluctuations, confinement, and phase separation. *Journal of Chemical Physics*, **146** (1) (2018).

(30) Yang, Q.; Wang, L.; Zhou, Z.; Wang, L.; Zhang, Y.; Zhao, S.; Dong, G.; Cheng, Y.; Min, T.; Hu, Z.; Chen, W.; Xia, K.; Liu M., Ionic Liquid Gating Control of RKKY Interaction in FeCoB/Ru/FeCoB and (Pt/Co)2/Ru/(Co/Pt)2 Multilayers, *Nat. Commun.*, **9**, 991 (2018).

(31) Han, L.; Wang, M.; Jia, X.; Chen, W.; Qian, H.; He, F., Uniform Two-Dimensional Square Assemblies from Conjugated Block Copolymers Driven by π–π Interactions with Controllable Sizes, *Nat. Commun.*, **9**, 865 (2018).

(32) Ziemba, C.; Khavkin, M.; Priftis, D.; Acar, D.; Mao, J.; Benami, M.; Gottlieb, M.; Tirrell, M.; Kaufman, Y.; Herzberg, M., Antifouling Properties of a Self-Assembling Glutamic Acid-Lysine Zwitterionic Polymer Surface Coating, *Langmuir*, ASAP, DOI: 10.1021/acs.langmuir.8b00181, Publication Date (Web): April 11 (2018).

(33) Piatkovsky, M.; Acar, H.; Marciel, A.B.; Tirrell, M.; Herzberg, M., A zwitterionic block-copolymer, based on glutamic acid and lysine, reduces the biofouling of UF and RO membranes, *J. Membrane Sci.*, **549**, 507 (2018).

Rational Synthesis of Superconductors

Mercouri G. Kanatzidis, Materials Science Division, Argonne National Laboratory
Duck Young Chung, Materials Science Division, Argonne National Laboratory

Program Scope

This is a materials synthesis and discovery program aimed at identifying new superconductors. The project seeks to generate deeper understanding and new insights in synthesis as well as control of structural/electronic instabilities in complex materials to move the state of the art closer to the rational design of superconductors. The goals of this program are: a) to design, synthesize and tune the electronic and magnetic properties of new low-dimensional materials that display density-wave instabilities and b) to induce superconductivity in these materials through external doping. These studies will yield important insights into the design and synthesis of novel compositions and through our collaborations provide the basis for fundamental insights into the physical behavior of electron systems over a wide range of electron correlation strengths. Our strategies focus on designing a diverse set of two-dimensional materials with well-defined characteristics such as square sheets and complex heterostructures with intergrown layers. We investigate Fermi surface tuning by doping with a wide variety of controlled chemical replacements which may drive the phases from a normal to superconducting state. Our roadmap includes the study of selected pnictide and intermetallic compounds possessing desired physical attributes such as homoatomic square lattices alternating with other types of stacked layers, atomic sites readily amenable to alloying and doping for property tuning.

Recent Progress

We discovered several novel metal chalcogenides, pnictides, and germanides with unusual structures and electronic and magnetic features.

Exploratory Synthesis of New Phases Targeting New Superconductors:

– Quasi-one-dimensional materials containing transition metal elements bonded with main group elements can exhibit various interesting phenomena such as charge density wave and superconductivity. We synthesized the new compound KMn_6Bi_5 with a new quasi-one-dimensional structure featured by unique $[Mn_6Bi_5]^-$ nanowires which consist of a Bi nanotube acting as the cladding and a Mn-cluster core column as a squeezed Mn-centered icosahedra Mn_{13} sharing their vertices, Figure 1(a). Magnetization and specific heat

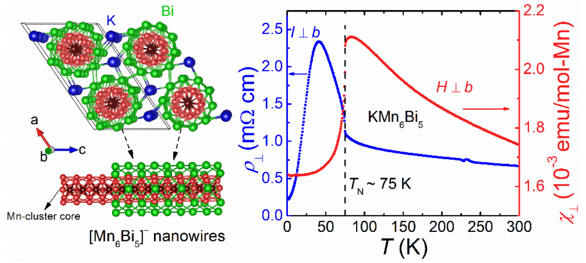

Figure 1 (a) Crystal structure of KMn_6Bi_5 viewed along the column direction and $[Mn_6Bi_5]^-$ nanowires and (b) Temperature dependence of resistivity (blue) and magnetic susceptibility (red) perpendicular to the column direction $\rho_\perp$ under magnetic fields $\mu_0 H = 0$ and 8 T.

measurements prove an antiferromagnetic order at ~75 K with short range magnetic correlations above the ordering temperature, Figure 1(b). Anisotropic resistivity measurements reveal a quasi-one-dimensional transport property with an incoherent-to-coherent crossover at ~ 40 K for conductivity perpendicular to the $[Mn_6Bi_5]^-$ nanowires. KMn_6Bi_5 also provides a good platform to study the link between magnetism, carrier and dimensionality in quasi-1D materials.

– Novel compounds exhibiting CDW order therefore serve as starting point to search for new superconductors. We have discovered a new polymorph of the $R_2Ru_3Ge_5$ (R=rare earth) compounds that harbor a unique type of transition that has many signatures of CDW behavior, Figure 2. These compounds crystallize in the tetragonal $Sc_2Fe_3Si_5$-type structure and exhibit a structural transition at low temperature, which is attributed to a CDW formation. The CDW is manifested in an incommensurate superstructure observed with synchrotron x-ray diffraction, as well as in electrical transport and heat capacity measurements.. The discovery of a CDW in these materials with the $Sc_2Fe_3Si_5$ structure type implies that similar CDWs may also exist in analogous germanides, silicides, and gallides. These materials are further of interest as candidate superconductors, since a number of other isostructural compounds, including the series $R_2Fe_3Si_5$ (R = rare earth), display superconductivity upon suppression of CDW order.

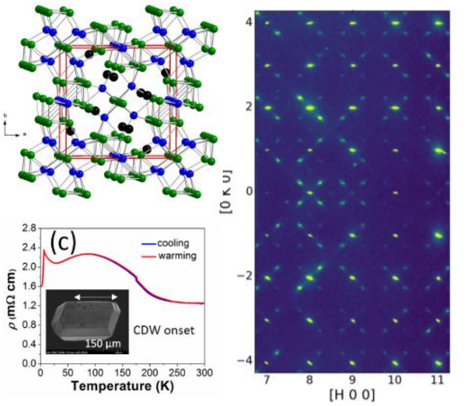

Figure 2. Crystal structure of $Sm_2Ru_3Ge_5$ (top left). The incommensurate CDW order observed from the synchrotron x-ray data (right) as well as from the electric resistivity (bottom left).

– The new two-dimensional compound $Pb_{3-x}Sb_{1+x}S_4Te_{2-\delta}$ possessing CDW at room temperature was synthesized. The CDW is incommensurate by a positional and occupational long range ordering of Te atoms in the sheets. The resistivity increases with decreasing temperature, indicating a semiconductor. The transition temperature (T_{CDW}) of the CDW is ~ 350 K above which the Te square sheets become ideal and the energy gap closes. First-principles density functional theory calculations on the undistorted structure show Fermi surface nesting in the Te sheets which drives the CDW due to the distortion in the Te monoatomic sheets. Calculations on an approximate commensurate supercell reveal the CDW gap formation.

Superconductivity found by doping narrow gap semiconductors:

– A 2D homologous series of alkali metal bismuth chalcogenides, intrinsically the valence precise intrinsic narrow gap semiconductors were investigated. We discovered superconductivity near 3 K in the semimetallic $RbBi_{11/3}Te_6$ and $AM_mBi_3Q_{5+m}$ (m = 1,2), (A = Cs, Rb; M = Pb, Sn; Q = Se, Te) by doping alkali metal or chalcogens.

- The narrow gap semiconductor $CsBi_4Te_6$ doped with Na and K leads to structural change to the $RbBi_{11/3}Te_6$–type orthorhombic phases with superconductivity at 5 K which is the currently highest transition temperature (Figure 3) observed among the superconductors originated from the doped semiconductors.

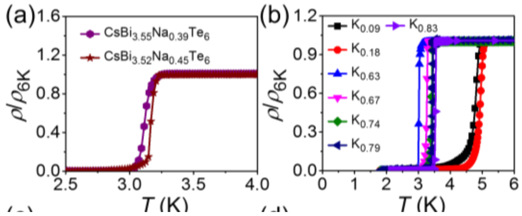

Figure 3. Temperature dependence of normalized resistance (ρ/ρ_{6K}) for (a) Na-doped $CsBi_4Te_6$ and (b) K-dope $CsBi_4Te_6$.

–

***Crystal growth of high quality iron pnictide superconductors*:**

- For the iron arsenide superconducting systems, we continued the effort to refine the conditions for synthesis and crystal growth to produce high quality samples with precise compositions in both polycrystalline and single crystal. We synthesized the single crystals of $Ca_{1-x}Na_xFe_2As_2$ ($0.20 \le x \le 0.50$) and studied the magnetic C4 dome ($0.40 \le x \le 0.42$) with a reentrance at 52 K below which a second reentrance where the antiferromagnetic *C*2 phase is recovered was also observed.
- Using a KAs flux we produced very high purity single crystals of KFe_2As_2 and studied on ^{75}As nuclear magnetic resonance (NMR), nuclear quadrupole resonance (NQR), and resistivity measurements in KFe_2As_2 under pressure (*p*) that showed an increase of the coherence/incoherence crossover temperature $T*$ by the increase in hybridization between localized and conducting bands caused by pressure application. Also, AFM spin fluctuations in the paramagnetic state is found to correlate with *T*c, evidencing clearly that the AFM spin fluctuations play an important role for the appearance of superconductivity in KFe_2As_2.
- Optimizing crystal growth conditions by RbAs flux enabled to achieve high quality single crystals of $RbEuFe_4As_4$ superconductor (Tc = 36.8 K) that had been challenging to study its structure and physical properties at a higher accuracy and reliability, Figure 4(a). We fully characterized the crystal structure and confirmed that the ab plane lattice match between AFe_2As_2 (A = alkali metal) and $AeFe_2As_2$ (Ae = alkaline earth metal) as well as the large ionic radius difference between A^+ and Ae^{2+} are required for the formation of the ordered $AAeFe_4As_4$. We also observed a magnetic transition at ∼15 K that is associated with the ordering of the Eu^{2+} sublattice, Figure 4(b).

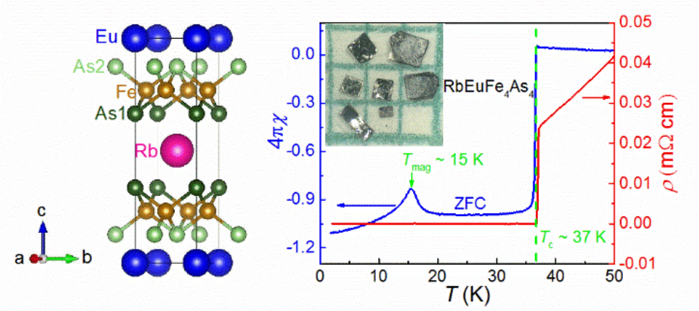

Figure 4. (a) Crystal structure of holed doped superconductors *RbEu*Fe_4As_4. (b) Temperature dependence of *ab*-planar resistivity and magnetic susceptibility of $RbEuFe_4As_4$ single crystal (Inset).

Future Plans

The science-driver underpinning this project is the study and understanding of electronic and phonon interactions in new and exotic classes of complex pnictides (i.e. phosphides, arsenides, antimonides) and chalcogenides (i.e. sulfides, selenides, tellurides). We will continue to address several key overarching scientific questions: a) do competing states such as CDW/ SDW/superconductivity really exist in the proposed systems, b) can they co-exist, in a noncompeting fashion, c) in what kinds of structures are competing states likely to be manifested, d) how can they be controlled and manipulated so that selectivity for a given state can be achieved, and e) how do they couple to one another? Our approach to answer these questions will focus on Fermi surface tuning accompanied by doping with a wide variety of controlled chemical substitutions which may drive the phases from a normal state to a superconducting state, which will fuel new synergies with several condensed matter physics groups at ANL/MSD. This ambitious collaborative research will generate better understanding of rational design of superconductors and new insights in controlling structural/electronic instabilities in complex materials. Our roadmap includes the study of approximately 10-15 metallic compounds selected because of the physical attributes described above i.e. homoatomic square lattices alternating with other types of stacked layers, and the synthesis of entirely new low-dimensional structures.

Here we will investigate these possibilities with new CDW systems which offer fresh opportunities for discovery.

1. Systems with Group 16 square sheets such as $Pb_3SbS_4Te_{2-\delta}$ system further in detail because it defines a good platform to investigate CDW behavior by itself and upon chemical perturbation.
2. Systems with Group 15 square sheets such as La_2O_2Pn (Pn=As, Sb, Bi), GdSP, LaSeSb, and $RETe_3$ (RE = rare-earth element) show CDW phenomena
3. Pnictide-cuprate heterostructures such **as** $Ba_2CuO_2Fe_2As_2$ and $K_2CuO_2Fe_2Se_2$, predicted by theory to be high temperature superconductors. These compounds consist of square CuO_2 layers and antifluorite-type Fe_2Pn_2 (Pn = As, Se) layers separated by Ba/K. The calculations of binding energies and phonon spectra indicate that they are stable, which motivates us to experimentally synthesize them. The Fermi surfaces and electronic structures of the two compounds seem to inherit the characteristics of both cuprates and iron-based superconductors. If successful, these compounds will not only provide us with an opportunity to explore exotic properties in cuprates and ferropnictides simultaneously but provide new opportunities to better understand the mechanism of unconventional superconductivity.
4. Synthesis of mixed chalcopnictide materials featured by mixed anion systems with O/As, S/Sb, S/As etc.

Publications

1. "*Single crystal growth and study of the ferromagnetic superconductor* $RbEuFe_4As_4$" Jin-Ke Bao, Kristin Willa, Matthew P. Smylie, Haijie Chen, Ulrich Welp, Duck Young Chung, and Mercouri G. Kanatzidis *Cryst. Growth Des.* **2018**, Article ASAP.
2. *"Superconductivity in the 2-Dimensional Homologous Series* $AM_mBi_3Q_{5+m}$ *(m = 1, 2) (A = Cs, Rb; M = Pb, Sn; Q = Se, Te)"* Malliakas C. D., Chung D. Y., Claus H., Kanatzidis M. G. *Chem. Eur. J.* **2018**, 24, 1-6.
3. *"Unique* $[Mn_6Bi_5]^-$ *nanowires in* KMn_6Bi_5*: a quasi-one-dimensional antiferromagnetic metal"* Jin-Ke Bao, Zhang-Tu Tang, Hee Joon Jung, Ji-Yong Liu, Yi Liu, Lin Li, Yu-Ke Li, Zhu-An Xu, Chun-Mu Feng, Haijie Chen, Duck Young Chung, Vinayak P. Dravid, Guang-Han Cao, and Mercouri G. Kanatzidis *J. Am. Chem. Soc.* **2018**, *140*, 4391-4400.
4. *"Pressure dependence of coherence-incoherence crossover behavior in* KFe_2As_2 *observed by resistivity and* ^{75}As*-NMR/NQR"* P. Wiecki, V. Taufour, D. Y. Chung, M. G. Kanatzidis, S. L. Bud'ko, P. C. Canfield, and Y. Furukawa *Phys. Rev. B* **2018**, *97*, 064509-1-10.
5. *"Spin Quenching Assisted by a Strongly Anisotropic Compression Behavior in MnP"* Fei Han, Yonggang Wang, Nana Li, Jin-Ke Bao, Duck Young Chung, Yuming Xiao, Paul Chou, Jiuhua Chen, Mercouri G. Kanatzidis, Wenge Yang, and Ho-Kwang Mao *New J. Phys.* **2018**, 20, 023012-1-9.
6. *"Polycrystalline* $ZrTe_5$ *Described as a Small Band Gap Semiconductor to Optimize Thermoelectric Performance"* Samuel A. Miller, Ian Witting, Umut Aydemir, Lintao Peng, Alex Rettie, Prashun Gorai, Duck Young Chung, Mercouri Kanatzidis, Matthew Grayson, Vladan Stevanovic, Eric S. Toberer, and G. Jeffrey Snyder *Phys. Rev. Appl.* **2018,** *9*, 014025-1-11.
7. "*Flux Crystal Growth of the* $RE_2Ru_3Ge_5$ *(RE = La, Ce, Nd, Gd, Tb) Series and Their Magnetic and Metamagnetic Transitions*" Daniel E. Bugaris, Christos D. Malliakas, Sergey L. Bud'ko, Nicholas P. Calta, Duck Young Chung, Mercouri G. Kanatzidis *Inorg. Chem.* **2017**, *56*, 14584–14595.
8. *"Semiconducting* $Ba_3Sn_3Sb_4$ *and Metallic* $Ba_{7-x}Sn_{11}Sb_{15-y}$ *(x = 0.4, y = 0.6) Zintl Phases"* Chen, Haijie; Narayan, Awadhesh; Stoumpos, Constantinos; Zhao, Jing; Han, Fei; Chung, Duck Young; Wagner, Lucas; Kwok, Wai-Kwong; Kanatzidis, Mercouri *Inorg. Chem.* **2017,** *56*, 14251–14259.
9. "*Spectroscopic signature of the moment-dependent electron-phonon coupling in* $2H\text{-}TaS_2$" Kapila Wijayaratne, Junjing Zhao, Christos Malliakas, Duck Young Chung, Mercouri G. Kanatzidis, and Utpal Chatterjee *J. Mater. Chem. C* **2017**, 5, 11310-11316.
10. *"Reentrant Metallic Behavior in the Weyl Semimetal NbP"* J. Xu, D. E. Bugaris, Z. L. Xiao, Y. L. Wang, D. Y. Chung, M. G. Kanatzidis, W. K. Kwok *Phys. Rev. B* **2017**, 96, 115152-1-6.
11. *"Separation of Electron and Hole Dynamics in the Semimetal LaSb"* F. Han, J. Xu, A. S. Botana, Z. Xiao, Y. Wang, W. G. Yang, D. Y. Chung, M. G. Kanatzidis, M. Norman, G. Crabtree, W.-K Kwok *Phys. Rev. B* **2017**, *96*, 125112-1-12.
12. *"Orbital selectivity causing anisotropy and particle-hole asymmetry in the charge density wave gap of* $2H-TaS_2$*"* J. Zhao, K. Wijayaratne, A. Butler, J. Yang, C. D. Malliakas, D. Y. Chung, D. Louca, M. G. Kanatzidis, J. van Wezel, and U. Chatterjee *Phys. Rev. B* **2017**, *96*, 125103.

13. *"Charge Density Wave and Narrow Energy Gap at Room Temperature in 2D $Pb_{3-x}Sb_{1+x}S_4Te_{2-\delta}$ with Square Te Sheets"* Haijie Chen, Christos D. Malliakas, Awadhesh Narayan, Lei Fang, Duck Young Chung, Lucas K. Wagner, Wai-Kwong Kwok, and Mercouri G. Kanatzidis *J. Am. Chem. Soc.* **2017**, *139*, 11271-11276.
14. "*Copper vacancies and heavy holes in the two-dimensional semiconductor $KCu_{3-x}Se_2$*" Rettie, Alexander; Sturza, Mihai; Malliakas, Christos; Botana, Antia; Chung, Duck Young; Kanatzidis, Mercouri *Chem. Mater.* **2017,** *29*, 6114−6121.
15. *"Spectroscopic evidence for temperature-dependent the convergence of light- and heavy-hole valence bands of PbQ (Q = Te, Se, S)"* J. Zhao, C. D. Malliakas, K. Wijayaratne, V. Karlapati, N. Appathurai, D. Y. Chung, S. Rosenkranz, M. G. Kanatzidis, and U. Chatterjee *Euro. Phys. Lett.* **2017,** 27006-1-6.
16. *"Charge Density Wave in the New Polymorphs of $RE_2Ru_3Ge_5$ (RE = Pr, Sm, Dy)"* Bugaris, D. E.; Malliakas, C. D.; Han, F.; Calta, N. P.; Sturza, M.; Krogstad, M.; Osborn, R.; Rosenkranz, S.; Ruff, J.; Trimarchi, G.; Bud'ko, S. L.; Balasubramanian, M.; Chung, D. Y.; Kanatzidis, M. G. *J. Amer. Chem. Soc.*, **2017**, 139, 4130-4143.
17. *"Observation of the magnetic C4 phase in $Ca_{1-x}Na_xFe_2As_2$ and the Universality of in the hole-doped 122 Superconductors"* K.M. Taddei, J.M. Allred, D.E. Bugaris, S. Lapidus, M. Krogstad, H. Claus, D.Y. Chung, M. Kanatzidis, R. Osborn, S. Rosenkranz, and O. Chmaissem *Phys. Rev. B,* **2017**, *95*, 064508-1-9.
18. *"Hybridization gap in the semiconducting compound $SrIr_4In_2Ge_4$"* Nicholas P. Calta, Jino Im, Lei Fang, Thomas C. Chasapis, Daniel E. Bugaris, Duck Young Chung, Wai-Kwong Kwok, Mercouri G. Kanatzidis *Inorg. Chem.* **2016**, *55*, 12477−12481.
19. *"Superconductivity in the narrow gap semiconductor $RbBi_{11/3}Te_6$"* Malliakas C. D., Chung D. Y., Claus H., Kanatzidis M. G. *J. Am. Chem. Soc.* **2016**,*138*, 14694-14698.

Energy and Fuels from Multifunctional Electrochemical Interfaces

Nenad M. Markovic (lead-PI) and Vojislav R. Stamenkovic (PI)
Materials Science Division
Argonne National Laboratory

Program Scope

Developing and deploying renewable energy technologies require the application of knowledge, concepts, and tools from a variety of fields including chemistry, materials science, physics and, in particular, electrochemistry. A science-based strategy is applied to develop highly active, stable, selective and conductive solid-aqueous, solid-organic and solid-solid electrochemical interfaces that are capable to resolve many of the challenging problems related to clean energy production, conversion and storage.

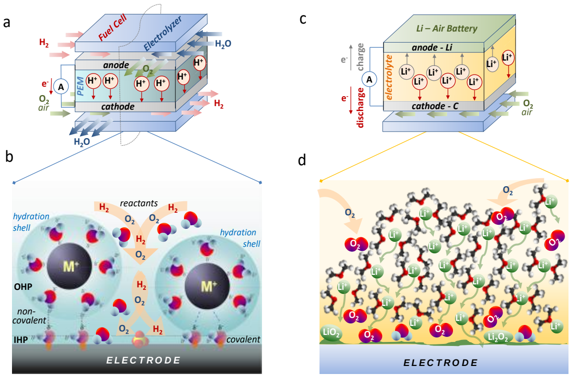

Illustration of EC interfaces in aqueous and organic environments in energy conversion and storage systems

The research effort is directed towards discovering common physicochemical parameters that can unify the complexities of (electro)chemistry at these three types of interfaces. Along the way we develop the needed fundamental framework that will merge synthesis, characterization, understanding and application of knowledge into a program that goes beyond discrete interfacial properties.

Recent Progress

Research activities from the last two years resulted in total of 16 published articles. The unique strength of this program is particularly reflected in articles published in high impact journals such as Nature Publishing Group. Research highlights from some of these articles are summarized below.

Materials-by-design strategy for development of active materials for the ORR: [1] Traditionally, two different strategies have been used to improve the activity of electrochemical interfaces for the ORR: (i) the materials-by-design strategy and (ii) the double-layer-by-design strategy. The first strategy, materials-by-design, has centered on developing materials that optimize the interactions between reaction intermediates and spectator species. The especially relevant adsorbate is OH$_{ad}$, a species that can be produced from supporting electrolytes (H2O in acid solutions or OH$^-$ in alkaline solutions) or from O$_2$ as an intermediate (OH$_{ad}$*). Even though

OH_{ad} can be produced from different sources, the substrate OH_{ad}/OH_{ad}* binding energy is sufficient to describe all volcano relationships established on metal cathode materials in acidic media.

The success of this approach has been demonstrated in the development of catalysts for PEMFCs, mostly by alloying Pt with transition metals or by de-alloying some alloys of Pt, as well as by synthesizing Pt core-shell or octahedral-shaped catalysts.

Among all of these catalysts, alloying Pt with transition metals such as Ni or Co has been most successful in enhancing the catalytic activity. The catalyst design relies on the results obtained on well-defined surfaces and segregation-induced formation of the so-called 'Pt-skin' with unique electronic structure, adsorption properties and catalytic activity, which was discovered by this project.

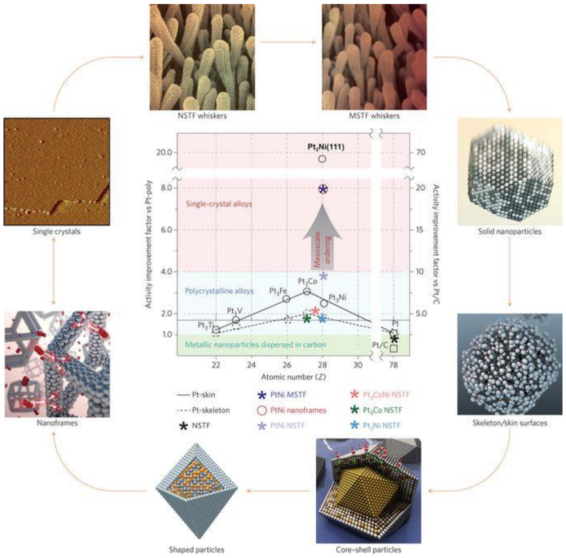

Extended single-crystalline well-defined surfaces, thin-film-based catalysts with nano- and mesostructured surface morphology.

Balancing activity, stability and conductivity for the OER catalysts: [2] The selection of oxide materials for catalyzing the oxygen evolution reaction in acid-based electrolyzers must be guided by the proper balance between activity, stability and conductivity-a challenging mission of great importance for delivering affordable and environmentally friendly hydrogen. It was found that the highly conductive nanoporous architecture of an iridium oxide shell on a metallic iridium core, formed through the fast dealloying of osmium from an $Ir_{25}Os_{75}$ alloy, exhibits an exceptional balance between oxygen evolution activity and stability as quantified by the activity-stability factor.

On the basis of this metric, the nanoporous Ir/IrO_2 morphology of dealloyed $Ir_{25}Os_{75}$ shows a factor of ~30 improvement in activity-stability factor relative to conventional iridium-based oxide materials, and an ~8 times improvement over dealloyed $Ir_{25}Os_{75}$ nanoparticles due to optimized stability and conductivity, respectively. It was proposed that the activity-stability factor is a key metric for determining the technological relevance of oxide-based anodic water electrolyzer catalysts.

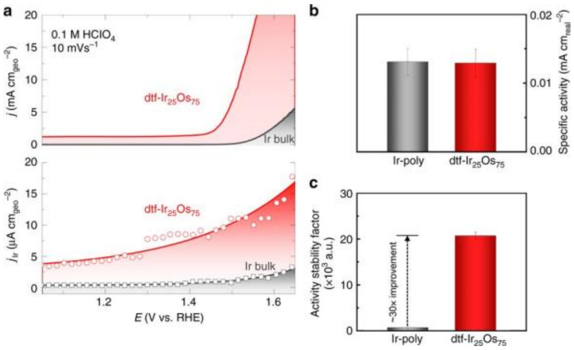

Activity-stability relationships for dtf-$Ir_xOs_{(1-x)}$ catalysts.

Electrocatalytic transformation of HF impurity: [3] The formation of solid electrolyte interphase on graphite anodes plays a key role in the efficiency of Li-ion batteries. However, to date, fundamental understanding of the formation of LiF as one of the main solid electrolyte interphase components in hexafluorophosphate-based electrolytes remains elusive. It is found from experimental and theoretical efforts that LiF formation is an electrocatalytic process that is controlled by the electrochemical transformation of HF impurity to LiF and H_2. Although the kinetics of HF dissociation and the concomitant production of LiF and H_2 is dependent on the structure and nature of surface atoms, the underlying electrochemistry is the same. The morphology, and thus the role, of the LiF formed is strongly dependent on the nature of the substrate and HF inventory, leading to either complete or partial passivation of the interface.

Our finding is of general importance and may lead to new opportunities for the improvement of existing, and design of new, Li-ion technologies.

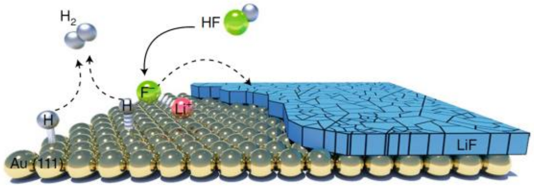

Schematic of the proposed reaction mechanism for the electrocatalytic conversion of HF to H2 and LiF.

Future Plans

Ability to define, at atomic/molecular levels, even more precisely the potential-controlled bond-making and breaking events that are simultaneously controlled by a synergy between electron and ion mobility across electrochemical interfaces, the structure and nature of surface atoms, and organization of the electrolyte components that operates in the double layer[1]. The range of materials and electrolytes that will be explored is broad; involving metals, metal/metal-oxides, pure oxides, S-/N-/C-based materials as well as aqueous electrolytes with a wide pH range, impurity-free organic solvents, and model solid electrolytes. In addition, it is of paramount importance to overcome the gap between surface electrochemistry in aqueous and organic environments. The links between the two artificially divided interfaces will define a new landscape of parameters that govern interfacial versus bulk properties, synthesis, metal deposition, corrosion, formation of SEI, intercalation, diffusion of ions, degradation of organics, oxygen surface and bulk redox processes, and many other physicochemical properties of materials and electrolytes. The development of in situ methods for exploring interfaces in organic environments will quickly be followed by exploring new chemistries that will ultimately determine the future of energy storage systems. Therefore, rather than focusing on engineering particular types of batteries, research should be directed towards new chemistries that await discovery.

References

1. Stamenkovic, V. R.; Strmcnik, D.; Lopes, P. P.; Markovic, N. M. "Energy and Fuels from Electrochemical Interfaces" , ***Nature Materials***, 16 **(2017)** 57–69.

2. Y.-T. Kim, P. P. Lopes, S.-A. Park, A-Y. Lee, J. Limc, H. Lee, S. Back, Y. Jung, N. Danilovic, V. R. Stamenkovic, J. Erlebacher, J. Snyder, and N. M. Markovic; "Balancing activity, stability and conductivity of nonporous core-shell Ir/IrO2 oxygen evolution catalysts", ***Nature Communications***; 8, 1449 (2017).

3. D. Strmcnik, I. A. Castelli, J. G. Connell, D. Haering, M. Zorko, P. Martins, P. P. Lopes, B. Genorio, T. Ostergaard, H. A. Gasteiger, F. Maglia, B. K. Antonopoulos, V. R. Stamenkovic, Jan Rossmeisl, and N. M. Markovic; "Electrocatalytic transformation of HF impurity to H_2 and LiF in lithium-ion batteries", ***Nature Catalysis***, 1 (2018) 255–262.

Publications

16. D. Strmcnik, I. A. Castelli, J. G. Connell, D. Haering, M. Zorko, P. Martins, P. P. Lopes, B. Genorio, T. Ostergaard, H. A. Gasteiger, F. Maglia, B. K. Antonopoulos, V. R. Stamenkovic, Jan Rossmeisl, and N. M. Markovic;
"Electrocatalytic transformation of HF impurity to H_2 and LiF in lithium-ion batteries", ***Nature Catalysis***, 1 (2018) 255–262.

15. Y.-T. Kim, P. P. Lopes, S.-A. Park, A-Y. Lee, J. Limc, H. Lee, S. Back, Y. Jung, N. Danilovic, V. R. Stamenkovic, J. Erlebacher, J. Snyder, and N. M. Markovic
"Balancing activity, stability and conductivity of nonporous core-shell Ir/IrO2 oxygen evolution catalysts", ***Nature Communications***; 8, 1449 (2017).

14. P. P. Lopes, D. Tripkovic, P.F.B.D. Martins, D. Strmcnik, A. Ticianelli, V.R. Stamenkovic and N. M. Markovic, "Dynamics of electrochemical Pt dissolution at atomic and molecular levels", ***J. Electroan.Chemistry***, 819, (2018) 123-129.

13. J. G. Chen, C. W. Jones, S. Linic, and V. R. Stamenkovic, Best Practices in Pursuit of Topics in Heterogeneous Electrocatalysis, ***ACS Catalysis***, 7, 9 (2017) 6392-6393.

12. Z. Zeng, Kee-Cul Chang, J. Kubal, N.M. Markovic and J. Greeley; "Stabilization of ultrathin (hydroxyl)oxide films on transition metal substrates for electrochemical energy conversion", ***Nature Energy***, 2 (2017) 17070.

11. V. R. Stamenkovic, D. Strmcnik, P. P. Lopes, and N. M. Markovic;
"Energy and fuels from electrochemical interfaces", ***Nature Materials***, 16 (2017) 57-69.

10. Y. Kang, P. Yang, N. M. Markovic, and V. R. Stamenkovic;
"Shaping Electrocatalysis through tailored nanomaterials", ***Nano Today***, 11 (2016) 587-600.

9. Y. Shao and N.M. Markovic; "The renaissance of electrocatalysis", ***Nano Energy***, 29(2016)1-3.

8. D. Li, H. Lv, Y. Kang, N. M. Markovic, and V. R. Stamenkovic;
"Progress in the development of the ORR catalysts for low-temperature fuel cells",
Annual Review of Chemical and Biochemical Engineering, 7 (2016) 509-532.

7. H. Lv, D. Li, D. Strmcnik, A. Paulikas, N. M. Markovic, and V. R. Stamenkovic;
"Recent advances in the design of tailored nanomaterials for efficient oxygen reduction reaction", ***Nano Energy***, 29 (2016) 149-165.

6. D. Strmcnik, P.P. Lopes, B. Genorio, V.R. Stamenkovic, and N. M. Markovic;
"Design principles for hydrogen evolution reaction catalyst materials", ***Nano Energy***, 29 (2016) 29-36.

5. P. P. Lopes, D. Strmcnik, D. Tripkovic, J. G. Connell, V. R. Stamenkovic, and N. M. Markovic; "Relationships between atomic level surface structure and stability/activity of platinum surface atoms in aqueous environments", ***ACS Catalysis***, 6 (2016) 2536-2544.

4. J. S. Jirkovsky, C. D. Malliakas, P. P. Lopes, N. Danilovic, S. S. Kota, K-C Chang, B. Genorio, D. Strmcnik, V. R. Stamenkovic, M. G. Kanatzidis, N. M. Markovic; "Design of Active and Stable Co-Mo-S_x Chalcogels as pH-universal Catalyst for the HER"; ***Nature Materials***, 15 (2016) 197-203.

3. B. Genorio, J. Staszak-Jirkovský, R. S. Assary, J. G. Connell, D. Strmcnik, C. E. Diesendruck, P. P. Lopes, V. R. Stamenkovic, J. S. Moore, L. A. Curtiss, and N. M. Markovic; "Superoxide (Electro)Chemistry on Well-Defined Surfaces in Organic Environments" ***Journal of Physical Chemistry C***, 120 (2016) 15909-15914.

2. I. Katsounaros, T. Chen, A. A. Gewirth, N. M. Markovic, and M. T.M Koper; " Evidence for decoupled electron and proton transfer in the electrochemical oxidation of ammonia on Pt(100)", ***Journal of Physical Chemistry Letters***, 7 (2016) 387-392.

1. P. P. Lopes, D. Strmcnik, J. S.-Jirkovisky, J. G. Connell, V. Stamenkovic, N. M. Markovic; "Double Layer Effects in Electrocatalysis: the Oxygen Reduction Reaction and Ethanol Oxidation Reaction on Au(111), Pt(111) and Ir(111) in Alkaline Media Containing Na and Li Cations"; ***Catalysis Today***, 262 (2016) 41-47.

Diamondoid Science and Applications

Nicholas A. Melosh, Stanford University and SLAC National Accelerator Laboratory

Program Scope

Diamondoids are unique new carbon-based nanomaterials consisting of 1–2 nanometer, fully hydrogen-terminated diamond particles. Unlike their conjugated counterparts, graphene or carbon nanotubes, the carbon atoms in diamondoids are exclusively sp^3-hybridized, leading to unique electronic and mechanical properties. Diamondoids behave much like small molecules, with atomic-level uniformity, flexible chemical functionalization, and systematic series of sizes, shapes and chiralities. At the same time, diamondoids offer mechanical and chemical stability akin to those of diamond, and vastly superior size and shape control compared to inorganic nanoparticles. This new family of carbon nanomaterials is thus an ideal platform for approaching the grand challenges of energy flow at the nanoscale and synthesis of atomically perfect new forms of matter with better precision than any other nanomaterials system.

This program explores and develops diamondoids as a new class of nanomaterials based upon their unique electronic, mechanical, and structural properties. This includes all phases of investigation, from diamondoid isolation from petroleum, chemical functionalization, and molecular assembly, as well as electronic, optical, and theoretical characterization. We have currently focused on three areas of research: synthesis, electronic properties, and thin film growth. This requires broad expertise and collaboration between multiple investigators to successfully approach tackle these problems. This approach has yielded fruit, enabling synthesis of important new compounds, and exploration of their structural and electronic properties. In particular, the ability of these materials to control the flow of electrons and emitted electron energy at the molecular level is an exciting direction for mastering energy flow at the nanoscale.

Recent Progress

Mechanochemistry

Chemical reactions driven by mechanical stress have been known for centuries, yet an atomistic understanding of the mechanism and a control of the reactivity through molecular design are missing. We exploited the mechanical rigidity of diamondoids to drive chemical reactions by pressure. Using our expertise in diamondoid assembly, we synthesized ‘molecular anvils’ combining rigid diamondoids with compressible mechanophores, and demonstrated that anisotropic relative motions of diamondoids can deform a mechanophore to drive redox reactions under hydrostatic pressure (*Nature, 2018*). The bulkiness of the diamondoids allowed us to tailor the reactivity of the mechanophore. These results unveil a previously unknown mechanochemical mechanism and opens new routes towards high-specificity mechanosynthesis.

Electron emission

Harnessing the unique interactions between electrons and diamondoids, we constructed a monochromatic electron beam source. We demonstrated that graphene serves as effective diffusion barrier that substantially stabilizes the photoemission from diamondoid monolayers without compromising brightness and monochromaticity of the photoelectrons (*Nanoletters*, 2017), making much more robust emitters.

Diamondoid-guided assembly

We assembled organic-inorganic hybrid materials, using the unique interactions between diamondoids to make transition metal selenides and sulfide-selenide heterostructures with atomically precise structural control and tunable optoelectronic properties (*Nature Mater.*, 2017). We also studied diamondoid molecular interactions to relate size, shape, and symmetry to assembly. This work reveals the molecular basis for diamondoid assembly to enable the design of novel diamondoid-containing functional materials and surfaces with complex properties.

Catalysis

We synthesized diamondoid phosphine, diamine, and dihydroxy derivatives to test for catalytic activity. The latter two ligands are the sp^3 analogs of the ubiquitously used bindentate BINOL-based sp^2-ligands, and we will apply these materials in a variety of catalyzed reactions, starting with Jacobsen-Katsuki-type epoxidations of olefins. We expect the extraordinary bulk rigidity will positively affect stereoinduction leading to higher yields and enantioselectivities. However, this may be specific to tailor-made subsets of substrates, thereby exhibiting high chemoselectivities. This may enable the use of 1,2-disubstituted *trans*-olefins that are notoriously difficult to epoxidize with the typical salen (1,2-diaminocyclohexane) based catalysts.

Diamond Seeding

We used diamondoids to measure the diamond nucleation landscape during plasma-enhanced chemical vapor deposition (PECVD) to enable synthesis of diamond nanoparticles and films for quantum sensing and bio-labeling. By linking molecular interactions in diamondoids to phase transitions, we are determining why some diamondoids volatilize at low temperatures, to lay the groundwork for using diamondoids to seed diamond growth in the bulk plasma phase. This will address low nucleation densities obtained when diamondoids seed PECVD growth on solid surfaces, and we aim to develop new continuous throughput diamond growth processes to synthesize large quantities of high quality diamond nanomaterials.

Diamondoid interactions and reactions inside carbon nanotubes

With our colleagues at Nagoya University in Japan, we explored diamondoid interactions and reactions inside carbon nanotubes. This work, published in *Chem. Commun*. 2018, 54, 3823, describes how hydroxylated diamantanes achieve a highly dense packing within the nanotubes as a result of hydrogen bonding between the diamondoids creating novel 1D-materials.

Diamondoids as seeds for High Pressure-High Temperature Diamond Growth

We demonstrated that diamondoids are the best seeding materials for making diamonds at high pressure and temperature. Using laser-heated diamond anvil cells, diamondoids are found to directly transform into diamond single crystals with a wide range of size distribution from tens of nanometers to micro-sized crystals. Diamondoids, especially lower diamondoids such as triamantane, can be transformed into the diamond phase at significantly lower temperatures (~ 2000 K less) compared with any other carbon-based materials at a comparable pressure.

Future Plans

Mechanochemistry

We will explore using this methodology for other reactions, including mechanochemical CO_2 reduction, C-H bond activation, and enantiomer separation. After understanding the possibilities of diamondoid mechanochemistry, we aim to design systems to drive the improvement, both in expense and environmental impact, of important chemical reactions.

Electron emission

The ultimate goal is to harness the unique electron emission properties of diamondoids. The limitation at this time is stability. We will progress a prototype diamondoid photoemitter and explore additional means in which the stability problem might be overcome.

Diamondoid-guided assembly

We will expand the scope of our synthetic capability to (i) diamondoid pnictides such as phosphines, and (ii) systems with strong electron correlation effects such as 4d and 5d transition metals. Special emphasis will be placed on creating systems with exotic electronic properties, including superconductivity and topologically non-trivial surface or end-states.

Catalysis

We will synthesize diamondoid phosphine, diamine, and dihydroxy derivatives to test as catalysts and explore increasing enantioselectivities of key reactions, which is especially important in pharmacueticals where only one of the enantiomers may be biologically active.

Diamond Seeding

We aim to seed larger diamondoids/diamonds in bulk CVD plasma using diamondoids to enable new families of materials, namely diamondoids ranging from tens of diamond crystal cages to thousands of cages. Currently, we only have access to smaller diamondoids from petroleum extracts, where even obtaining milligrams of material is challenging for diamondoids, like six cage hexamantane. Larger diamondoids would allow us to study how key properties vary with size and such approaches to mass production could lead to commercial production.

Diamondoid Doping

We aim to incorporate heteroatoms in the methylene positions of diamondoids using our recently developed cage opening Barton-type fragmentation (used to prepare the 1,2-

disubstituted diamondoids) for the incorporation of heteroatoms, in particular, oxygen. This would lead to the selective doping of diamond-like materials that has never been accomplished before. These new materials are expected to have exciting semiconductor properties that can be tuned by the choice of the hetereoatom and its state (free, protonated, ionized).

Publications

Sterically-controlled mechanochemistry under hydrostatic pressure. Hao Yan, Fan Yang, Ding Pan, Yu Lin, J. Nathan Hohman, Diego Solis-Ibarra, Fei Hua Li, Jeremy E. P. Dahl, Robert M. K. Carlson, Boryslav A. Tkachenko, Andrey A. Fokin, Peter R. Schreiner, Giulia Galli, Wendy L. Mao, Zhi-Xun Shen, and Nicholas A. Melosh *Nature* **2018**, *554*, 505–510. DOI: 10.1038/nature25765. **Highlights:** a) "Pressure squeezes reduction reactions out of crystals." *Chem. Eng. News* **2018**, *96(9)*, p. 6 ("News of the Week); b) "In a first, tiny diamond anvils trigger chemical reactions by squeezing" *phys.org*, Feb 21, 2018.

One-dimensional hydrogen bonding network of bis-hydroxylated diamantane formed inside double-wall carbon nanotubes. Y. Nakanishi, H. Omachi, N. A. Fokina, P. R. Schreiner, J. Becker, J. E. P. Dahl, R. M. K. Carlson, and H. Shinohara *Chem. Commun.* **2018**, *54*, in press. DOI: 10.1039/c7cc09832d. **Highlight:** *Back cover* of corresponding issue.

Nanodiamond-Palladium Core–Shell Organohybrid Synthesis: A Mild Vapor-Phase Procedure Enabling Nanolayering Metal onto Functionalized sp3-Carbon. Gunawan, M.A., Moncea O, Poinsot D., Keskes M., Domenichini B., Heintz O., Chassagnon R., Herbst F., Carlson R.M.K., Dahl J.E.P, Fokin A.A., Schreiner P.R., and Hierso J.C. *Adv. Funct. Mater.* **2018**, 1705786.

Palladium catalysed *C2*–H arylation of unprotected (*N*–H)-indoles in water using primary diamantyl phosphine oxides as a new class of PPO ligands. Oana Moncea, Didier Poinsot, Andrey A. Fokin, Peter. R. Schreiner, and Jean-Cyrille Hierso *ChemCatChem* **2018**, *yy*, in press. DOI: 10.1002/cctc.201800187.

Monochromatic photocathodes from graphene-stabilized diamondoids. Hao Yan, Karthik T. Narashimha, Jonathan Denlinger, Fei Hua Li, Sung-Kwan Mo, J. Nathan Hohman, Jeremy E. P. Dahl, Robert M. K. Carlson, Boryslav A. Tkachenko, Andrey A. Fokin, Peter R. Schreiner, Zahid Hussain, Zhi-Xun Shen, and Nicholas A. Melosh *Nano Lett.* **2018**, *18*, in press. DOI: 10.1021/acs.nanolett.7b04645.

Nanolayering Metals onto (sp^3)-Carbon Based Materials: Pd@diamondoid Organohybrid Synthesis through Mild Vapor Deposition Processes. Maria A. Gunawan, Oana Moncea, Didier Poinsot, Mariem Keskes, Bruno Domenichini, Olivier Heintz, Rémi Chassagnon, Frédéric Herbst, Jeremy E. P. Dahl, Andrey A. Fokin, Peter R. Schreiner, and Jean-Cyrille Hierso *Adv. Funct. Mat.* **2018**, 1705786/1–15. DOI: 10.1002/adfm.201705786.

Host-guest complexes of cyclodextrins and nanodiamonds as strong non-covalent binding motif for self-assembly. Schibilla F., Voskuhl J., Fokina N.A., Dahl J.E.P., Schreiner P.R. and Ravoo B.J. *Chem. Eur. J.* **2017**, 10.1002/chem.201703392.

London dispersion directs on-surface self-assembly of [121]tetramantane molecules. Daniel Ebeling, Marina Šekutor, Marvin Stiefermann, Jalmar Tschakert, Jeremy E. P. Dahl, Robert M. K. Carlson, André Schirmeisen, and Peter R. Schreiner *ACS Nano* **2017**, *11,* 9459–9466. DOI: 10.1021/acsnano.7b05204.

Chiral Building Blocks Based on 1,2-Disubstituted Diamantane. Andrey A. Fokin, Alexander E. Pashenko, Vladyslav V. Bakhonsky, Tatyana S. Zhuk, Lesya V. Chernish, Pavel A. Gunchenko, Andrey O. Kushko, Jonathan Becker, Raffael C. Wende, and Peter R. Schreiner *Synthesis* **2017**, *49*, 2003–2008. DOI: 10.1055/s-0036-1588694.

Complex magnetic interactions in novel rare earth-rich polar intermetallic systems

Gordon J. Miller,[1,2] Anja Mudring,[1,3] Gerd Meyer,[1] Qisheng Lin,[1,2] Srinivasa Thimmaiah[1]

1) Division of Materials Science & Engineering, Ames Laboratory, US DOE, Ames, IA, 50011
2) Department of Chemistry, Iowa State University, Ames, IA, 50011
3) Department of Materials Science & Engineering, Iowa State University, Ames, IA, 50011

Program Scope

This program endeavors to extend current knowledge and understanding of metal-rich chemistry by combining experiment with theory to uncover and ultimately design new families of solids that are especially rich in various metallic elements. These families include valence networks (Zintl-type), densely packed and cluster-based (Hume-Rothery-type) structures, as well as the emerging "polar intermetallics," which involve both clusters and networks. Besides material discovery, this FWP make efforts to (1) understand the factors that stabilize both new and known metal-rich phases by combining exploratory and/or target syntheses and temperature-dependent structure determinations with electronic structure theory, and to (2) establish structure-property relationships for complex metal-rich materials as related to both practical as well as fundamental issues, e.g., thermoelectric, magnetocaloric, catalytic, and magnetic behavior. The overarching goal is to establish relationships between chemical and electronic structures in complex metal-rich compounds so as to understand the factors that stabilize existing phases and provide insights for finding new materials.

Significant focus includes compounds involving reduced environments for elements of the late 5th and 6th period transition elements (Pd, Pt, Ag, Au), which offer filled d-bands and relativistic enhancements of chemical bonding; Li-rich intermetallics, taking advantage of Li's dual role of both an active as well as an electronegative metal in chemically reduced environments; and 3d metal systems grown in reactive and eutectic fluxes. Techniques employed encompass high-temperature syntheses, novel low-temperature approaches and variable-temperature X-ray or neutron diffraction that elucidates atomic-scale structural details. Theoretical efforts span first-principles to semi-empirical calculations.

Recent Progress

Recent research effort of this FWP continues the design of new polar intermetallic materials with desired chemical and physical characteristics. Polar intermetallics including quasicrystals and approximants, with rich precious metals (Au, Ag, Pt, Pd etc.), have been one of our fertile fields for over a decade. Our recent discovery of novel materials demonstrates that polar intermetallic materials remain rich area with extensive structural versatility and bonding motifs [1-9]. Noteworthy is that considerable effort has also been shifted to the research of structure-property relationship during this funding period [10-13]. In particular, we have extended our current knowledge and understanding of metal-rich chemistry to the development of magnetic materials and their property tuning. Herein we will not detail on the fruitful results of novel gold-rich polar intermetallics with unprecedented structure and bonding motifs. Below is a brief summary of our basic research with potential for the applied science, in collaboration with other fellow physicists and theorists.

Rare earth-rich polar intermetallic featuring planar hydrocarbon-like moieties and complex 3d-4f magnetic interactions

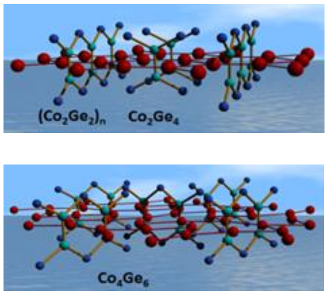

Fig. 1 Featured structural motifs of (top) ethylene- like (Co_2Ge_4) clusters and polyacene-like $(Co_2Ge_2)_n$ ribbons in $Pr_5Co_2Ge_3$ and (bottom) the 1,2,4,5-tetramethylbenzene-like (Co_4Ge_6) clusters in $Pr_7Co_2Ge_4$.

One of the major advances in structural-property relationship stems from the long-term quest of novel ferromagnetic materials, in the collaboration with physicists.[14] We are amazed at the unprecedented planar hydrocarbon-like fragments in $Pr_5Co_2Ge_3$ we first characterized.[10] Unlike other rare-earth rich intermetallics that commonly feature condensed, face-sharing R_6 trigonal prisms or octahedra, together with minor components sitting in the center of polyhedra, this structure contains two different planar hydrocarbon-like moieties mimicking the geometries of ethylene (C_2H_4) and its concatenated form, the polyacene $(C_4H_2)_n$, defined by Co and Ge atoms, as shown in top panel of Figure 1. We speculate that planar hydrocarbon-like metals clusters may foster new insights linking organic molecules with conjugated π-π bonding interactions and inorganic structures in terms of their bonding characters.[11] Although such clusters have been relatively commonly seen in Zintl type phases, however, they are very unusual for polar intermetallics with increased covalent bonding interactions. Therefore, we have extensively explored phase spaces of parallel systems and found that, with slightly increased percentage of rare earth, another new structural motif exists in $R_7T_2Ge_4$ (R = La, Ce, Pr, Nd; T = Co, Ni),[10-11,15] which contain 1,2,4,5-tetramethylbenzene-like clusters, as show in bottom panel of

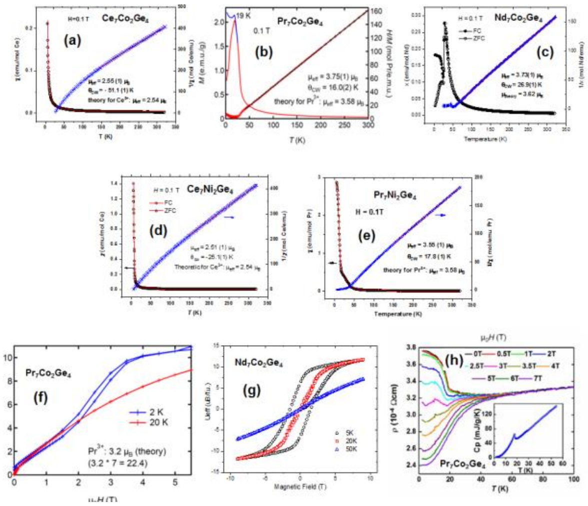

Figure 2. Temperature-dependent susceptibility for (a) Ce_7Co_2Ge (b) $Pr_7Co_2Ge_4$ (c) Nd_7Co_2Ge (d) Ce_7Ni_2Ge (e) Pr_7Ni_2Ge and field-dependent magnetization for (f) Pr_7Co_2Ge (g) Nd_7Co_2Ge, and (h) temperature-dependent magnetoresistance of Pr_7Co_2Ge (inset: hall effect data).

Figure 1. Occurrence of these planar clusters may stimulate further interest to examine whether they exhibit all-metal aromaticity and to explore the existence of similar clusters consisting of other transition metals/metalloid combinations.

$R_7T_2Ge_4$ compounds exhibit complex magnetic and resistivity properties arising from 3*d*-4*f* magnetic interactions, Figure 2. While $Ce_7Co_2Ge_4$ is a heavy frustrated aniferromagnetic (AFM) system, the magnetic interaction progresses to ferrimagnetic or canted-ferromagnetic order in nature for Pr- and $Nd_7Co_2Ge_4$, supported also by hysteresis loops and hall resistivity data. The peculiar magnetoresistance is related to magnetic ordering, which results in the formation of superzone gap effect. Noteworthy is that the experimental μ_{eff} values for all $R_7Co_2Ge_4$ phases are consistently larger than that of respective trivalent rare earth ions, in contrast to that for $R_7Ni_2Ge_4$ (within three standard deviations to expected values). This appears that Co 3*d* states contribute considerable amount of low spin moments to interact with 4*f* states of rare earth ions, whereas Ni 3*d* states are likely fully filled. Spin polarized electronic structure calculations confirm the magnetic contribution from Co. Neutron diffraction is expected to reveal the detailed magnetic structures.

Phase transition on magnetocaloric effect in $GdMn_{1-x}Fe_xAl$ system

Ferromagnetic intermetallics are potential candidates of magnetocaloric (MC) materials, which utilize the entropy change during reversible phase transitions. Both GdMnAl (Fd-3m) and GdFeAl ($P6_3$/mmc) system have been reported to be ferromagnetic around room temperatures.[16] We are interested in $GdMn_{1-x}Fe_xAl$ system to explore whether new phase exists between them and to examine the effect of concurrent structure/magnetic structure transitions on MC effect.

According to structural analyses [15], two phase mixtures were found at x > 0.7 in $GdMn_{1-x}Fe_xAl$, as shown by the refined lattice parameters in Figure 3(a). The temperature-dependent susceptibility data reveal all compositions ($x = 0 - 1$) remain ferromagnetic. The magnetization data for x = 0.7 and 0.75 with clean magnetic responses were carefully characterized and their entropy change (ΔS) calculated by means of $\Delta S = \int_{H1}^{H2} \left(\frac{\partial M}{\partial T}\right)_H dH$. The maximum ΔS for both compositions are ~ 2.6 $J/K^{-1}kg^{-1}$ under magnetic field of 0.1 T, Figure 3(b), much larger than that for the two end members (1.22 and 0.31 $J/K^{-1}kg^{-1}$ at 2T) [16], demonstrating an effective way to improve MC effect by exploring systems with concurrent magnetic/structure transitions.

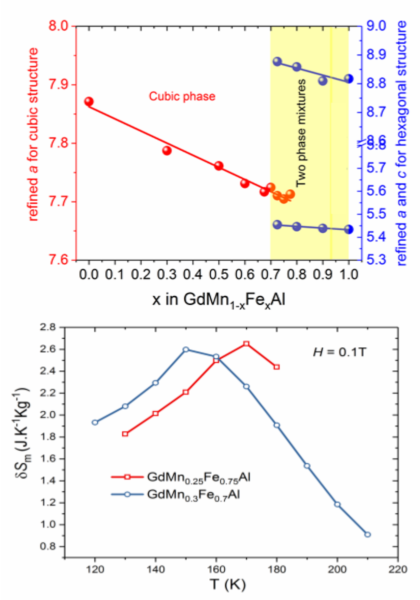

Figure 3. (top) Refined lattice parameters for $GdMn_{1-x}Fe_xAl$ and (bottom) the entropy change for x = 0.7 and 0.75 under a field of 0.1 T.

Future Plans

The overarching goal for this FWP is to establish relationships between chemical and electronic structures in complex metal-rich compounds so as to understand the factors that stabilize existing phases and provide insights for finding new materials. We recognize the DOE BES research needs of functional materials and quantum materials, and will continue to make efforts to take advantage of our experience in discovery, structural analyses, and theoretical background for material synthesis of emergent functional and quantum materials, together with the understanding of structure-property relationships related to both practical as well as fundamental issues, e.g., thermoelectric, magnetocaloric, catalytic, and magnetic behavior, which in turn feed back to new material design.

References

1) Pham, Joyce; Miller, Gordon J., *Inorganic Chemistry* (2018), 57(7), 4039-4049.
2) Pham, Joyce; Meng, Fanqiang; Lynn, Matthew J.; Ma, Tao; Kreyssig, Andreas; Kramer, Matthew J.; Goldman, Alan I.; Miller, Gordon J. *Journal of the American Chemical Society* (2018), 140(4), 1337-1347.
3) Celania C.; Smetana V.; Mudring A.V. *Crystengcomm* **2018** *20*, 348-355.
4) Smetana V.; Mudryk Y.; Pecharsky V.K.; Mudring A.V. *Journal of Materials Chemistry C* **2018** *6*, 1353-1362.
5) Celania C.; Smetana V.; Provino A.; Manfrinetti P.; Mudring A.V. *Design***2018** *18*, 993-1001.
6) Smetana V.; Steinberg S.; Mudring A.V. *Design* **2017** *17*, 693-700.
7) Celania C.; Smetana V.; Provino A.; Pecharsky V.; Manfrinetti P.; Mudring A.V. *Inorganic Chemistry* **2017** *56*, 7247-7256.
8) Thimmaiah S.; Tener Z.; Lamichhane T.N.; Canfield P.C.; Miller G.J. *Zeitschrift Fur Kristallographie-Crystalline Materials* **2017***232*, 601-610.
9) Celania C.; Smetana V.; Mudring A.V. *Acta Crystallographica Section C-Structural Chemistry* **2017** *73*, 692-+.
10) Lin Q.S.; Aguirre K.; Saunders S.M.; Hackett T.A.; Liu Y.; Taufour V.; Paudyal D.; Budko S.; Canfield P.C.; Miller G.J. *Chemistry-a European Journal* **2017** *23*, 10516-10521.
11) Lin, Q.; Miller, G. J. *Accounts of Chemical Research* **2018**, *51*, 49-58.
12) Yuan, Fang; Toombs, Asa; Miller, Gordon J.; Mozharivskyj, Yurij, *Journal of Solid State Chemistry* (2018), 264, 68-76.
13) Lamichhane, T. N.; Taufour, V.; Palasyuk, A.; Lin, Q.; Bud'ko, S. L.; Canfield, P. C. *Physical Review Applied* **2018**, *9*, 024023.
14) Lin, Q.; Taufour, V.; Zhang, Y.; Wood, M.; Drtina, T.; Bud'ko, S. L.; Canfield, P. C.; Miller, G. J. *J. Solid State Chem.* **2015**, *229*, 41-48.
15) Lin, Q. etc. unpublished results.
16) Klimczak, M.; Talik, E. *J. Phys.: Con. Ser.* **2010**, *200*, 092009.

Publication List

1. Pham, Joyce; Miller, Gordon J., *AAuAl (A = Ca, Sc, and Ti): Peierls Distortion, Atomic Coloring, and Structural Competition,* Inorganic Chemistry **2018**, 57(7), 4039-4049.
2. Yuan, Fang; Toombs, Asa; Miller, Gordon J.; Mozharivskyj, Yurij, *Gd(Co1-xGax)2: Synthesis, crystal structures, and investigation of structural transformations and magnetic properties*, Journal of Solid State Chemistry **2018**, 264, 68-76.
3. Fredrickson, Daniel C.; Miller, Gordon J. *Intermetallic Chemistry: New Advances in Humanity's Age-Old Exploration of Metals and Alloys*, Accounts of Chemical Research **2018**, 51(2), 213.
4. Pham, Joyce; Meng, Fanqiang; Lynn, Matthew J.; Ma, Tao; Kreyssig, Andreas; Kramer, Matthew J.; Goldman, Alan I.; Miller, Gordon J. *From Quasicrystals to Crystals with Interpenetrating Icosahedra in Ca-Au-Al: In Situ Variable-Temperature Transformation*, Journal of the American Chemical Society **2018**, 140(4), 1337-1347.
5. Lin, Q.; Miller, G. J. *Electron-Poor Polar Intermetallics: Complex Structures, Novel Clusters, and Intriguing Bonding with Pronounced Electron Delocalization*. Accounts of Chemical Research **2018**, *51*, 49-58.
6. Sangeetha N.S.; Smetana V.; Mudring A.V.; Johnston D.C. *Antiferromagnetism in semiconducting $SrMn_2Sb_2$ and $BaMn_2Sb_2$ single crystals*. Physical Review B **2018** *97*, 014402.
7. Celania C.; Smetana V.; Mudring A.V. *Bringing order to large-scale disordered complex metal alloys: Gd2Au15-xSbx and $BaAu_xGa_{12-x}$*. Crystengcomm **2018** *20*, 348-355.
8. Smetana V.; Mudryk Y.; Pecharsky V.K.; Mudring A.V. *Controlling magnetism via transition metal exchange in the series of intermetallics $Eu(T1, T2)_5In$ (T = Cu, Ag, Au)*. Journal of Materials Chemistry C **2018** *6*, 1353-1362.
9. Celania C.; Smetana V.; Provino A.; Manfrinetti P.; Mudring A.V. *$R_{14}(Au, M)_{51}$ (R = Y, La-Nd, Sm-Tb, Ho, Er, Yb, Lu; M = Al, Ga, Ge, In, Sn, Sb, Bi): Stability Ranges and Site Preference in the $Gd_{14}Ag_{51}$ Structure Type*. Design **2018** *18*, 993-1001.
10. Lamichhane T.N.; Taufour V.; Palasyuk A.; Lin Q.S.; Bud'ko S.L.; Canfield P.C. *Ce3-xMgxCo9: Transformation of a Pauli Paramagnet into a Strong Permanent Magnet*. Physical Review Applied **2018** *9*, 024023.
11. Miller, Gordon J., *Intermetallics: Structure, Properties, and Statistics, by Walter Steurer and Julia Dshemuchadse*, Zeitschrift fuer Anorganische und Allgemeine Chemie (**2017**), 643(17), 1143-1144.
12. Xie, Weiwei; Cava, Robert J.; Miller, Gordon J. *Packing of Russian doll clusters to form a nanometer-scale CsCl-type compound in a Cr-Zn-Sn complex metallic alloy*, Journal of Materials Chemistry C: Materials for Optical and Electronic Devices (**2017**), 5(29), 7215-7221.
13. Zhang, Yuemei; Miller, Gordon J.; Fokwa, Boniface P. T. *Computational Design of Rare-Earth-Free Magnets with the $Ti_3Co_5B_2$-Type Structure*, Chemistry of Materials (**2017**), 29(6), 2535-2541.

14. Jo, N. H.; Lin, Q.; Nguyen, M. C.; Kaluarachchi, U. S.; Meier, W. R.; Manni, S.; Downing, S. S.; Böhmer, A. E.; Kong, T.; Sun, Y.; Taufour, V.; Wang, C.-Z.; Ho, K.-M.; Bud’ko, S. L.; Canfield, P. C. *Growth and characterization of BaZnGa*. Philos Mag **2017**, 1-8.
15. Smetana V.; Steinberg S.; Mudring A.V. *Layered Structures and Disordered Polyanionic Nets in the Cation Poor Polar Intermetallics CsAu1.4Ga2.8 and CsAu2Ga2.6.* Design **2017** *17*, 693-700.
16. Bigun I.; Steinberg S.; Smetana V.; Mudryk Y.; Kalychak Y.; Havela L.; Pecharsky V.; Mudring A.V. *Magnetocaloric Behavior in Ternary Europium Indides EuT5In: Probing the Design Capability of First-Principles-Based Methods on the Multifaceted Magnetic Materials*. Chemistry of Materials **2017** *29*, 2599-2614.
17. Bigun I.; Smetana V.; Mudryk Y.; Hlova I.; Dzevenko M.; Havela L.; Kalychak Y.; Pecharsky V.; Mudring A.V. *EuNi5InH1.5-x (x=0-1.5): hydrogen induced structural and magnetic transitions*. Journal of Materials Chemistry C **2017** *5*, 2994-3006.
18. Cao G.H.; Oertel C.G.; Schaarschuch R.; Skrotzki W.; Russell A.M. *TEM study of the martensitic phases in the ductile DyCu and YCu intermetallic compounds*. Acta Materialia **2017** *132*, 345-353.
19. Celania C.; Smetana V.; Provino A.; Pecharsky V.; Manfrinetti P.; Mudring A.V. *R_3Au_9Pn (R = Y, Gd-Tm; Pn = Sb, Bi): A Link between $Cu_{10}Sn_3$ and $Gd_{14}Ag_{51}$*. Inorganic Chemistry **2017** *56*, 7247-7256.
20. Thimmaiah S.; Tener Z.; Lamichhane T.N.; Canfield P.C.; Miller G.J. *Crystal structure, homogeneity range and electronic structure of rhombohedral gamma-Mn_5Al_8*. Zeitschrift Fur Kristallographie-Crystalline Materials **2017***232*, 601-610.
21. Lin Q.S.; Aguirre K.; Saunders S.M.; Hackett T.A.; Liu Y.; Taufour V.; Paudyal D.; Budko S.; Canfield P.C.; Miller G.J. *Polar Intermetallics $Pr_5Co_2Ge_3$ and $Pr_7Co_2Ge_4$ with Planar Hydrocarbon-Like Metal Clusters*. Chemistry-a European Journal **2017** *23*, 10516-10521.
22. Celania C.; Smetana V.; Mudring A.V. *Crystal structures and new perspectives on Y_3Au_4 and $Y_{14}Au_{51}$*. Acta Crystallographica Section C-Structural Chemistry **2017** *73*, 692-+.
23. Li M.; Smetana V.; Wilk-Kozubek M.; Mudryk Y.; Alammar T.; Pecharsky V.K.; Mudring A.V. *Open-Framework Manganese(II) and Cobalt(II) Borophosphates with Helical Chains: Structures, Magnetic, and Luminescent Properties*. Inorganic Chemistry **2017** *56*, 11104-11112.
24. Smetana V.; Rhodehouse M.; Meyer G.; Mudring A.V. *Gold Polar Intermetallics: Structural Versatility through Exclusive Bonding Motifs*. Accounts of Chemical Research **2017** *50*, 2633-2641.
25. Sangeetha N.S.; Smetana V.; Mudring A.V.; Johnston D.C. *Anomalous Composition-Induced Crossover in the Magnetic Properties of the Itinerant-Electron Antiferromagnet $Ca_{1-x}Sr_xCo_{2-y}As_2$*. Physical Review Letters **2017** *119*, 6.

“High Pressure Floating-Zone Crystal Growth of Correlated Electron Oxides”

J.F. Mitchell, J. Zhang, H. Zheng, M. Norman, D. Phelan, A. Botana
Argonne National Laboratory

H. Li, D. Dessau
University of Colorado, Boulder

The optical floating zone (FZ) technique has been established for more than three decades as a powerful and effective way to grow complex oxide crystals of high purity and sufficient size for condensed matter physics, and in particular neutron scattering. Thus, it has been a tool for the physics community to advance. The recent innovation of adding high pressure of either inert or reactive gases adds a new level of versatility to this technique, allowing the crystal grower (a) to move phase lines to allow growth of 'impossible to grow' crystals, (b) to uncover new compounds, or (c) to extend doping ranges into high metal formal oxidation states. In this talk, I will describe the underlying advantages of this approach, illustrated by examples of each of these capabilities in the area of correlated electron transition metal oxides. Specifically, I will discuss discovery of the previously unknown brownmillerite phase Ca2Co2O5, competing metallic or charge and spin stripes in layered nickelates, the appearance of magnetism in highly doped 2D manganese oxides, and the first FZ crystals of well-known PrNiO3.

Structure and Dynamics of Materials Interfaces

PIs: Miquel Salmeron, Hendrik Bluhm, David Prendergast, Gabor Somorjai
Materials Science Division of the Lawrence Berkeley National Laboratory

Program Scope: The objective of this program is to obtain a fundamental understanding of the structure and dynamics of materials interfaces in gas at ambient pressures and in liquid environments. Interfaces include regions extending nanometers to micrometers away from the ideal sharp interface. Our findings provide the basis for future applications in electronic /semiconductor industry, catalysis, water utilization, energy storage, and atmospheric and geochemical chemistry. We focus on three areas:

a) Interfaces with gases at ambient pressures: How weakly adsorbed species, which at RT are stable only in the presence of the gas phase, can create new equilibrium structures unknown from traditional surface science studies in vacuum.

b) Solid-Liquid Interfaces are investigated microscopically and spectroscopically to determine their structure and dynamics as a function of solution pH, and electrical potential (electrical double layer, EDL).

c) Structure and evolution of nano-crystalline materials, particularly multi-metallics, where the interface includes all the atoms in the material.

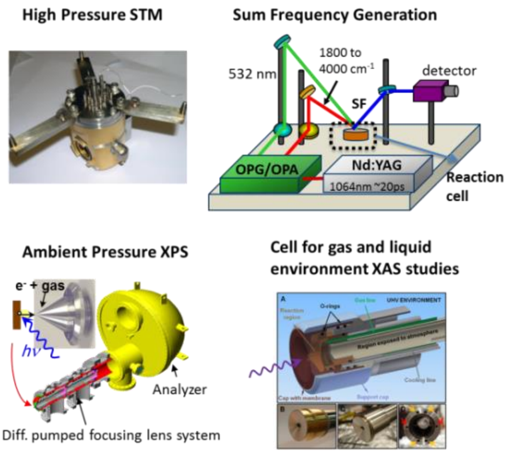

Fig.1. Microscopy and Spectroscopy tools for *in situ* interface studies. Clockwise from top: 1) Ambient pressure STM cell housed inside a UHV chamber; 2) Sum Frequency Generation set-up; 3) Small cell and conduits for fluid circulation, with the front sealed by x-ray transparent membranes; 4) Ambient Pressure XPS.

To accomplish our program we develop new experimental tools when needed (Fig. 1), and we incorporate the full power of theoretical methods to guide the design and interpretation of experimental data.

Recent progress:

1) The solid-gas interface: Copper-Cobalt Alloys. We studied the structure of the copper-cobalt (CuCo) alloy formed by Co deposition on Cu(110) in equilibrium with gas phase CO. Using scanning tunneling microscopy (STM), we found that at room temperature clusters of few Co atoms form at the surface (Fig. 2). In the presence of CO in the Torr pressure range, up to 2.5 CO molecules can bind per Co atom in a carbonyl-like configuration [1]. Together with density function theory calculations, we determined the most stable CuCo cluster structures formed with CO (Fig. 3). The cobalt carbonyl-like formation manifests in shifts in binding energy of the Co core-levels in x-ray photoelectron spectra, as well as shifts in the vibrational modes of adsorbed CO in infrared reflection absorption

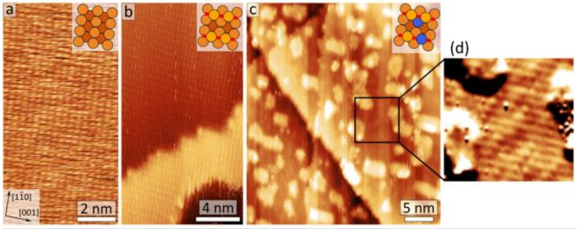

Fig. 2 STM of images of Cu-Co alloy on Cu(110): (a) Clean Cu(110) surface. (b) Cu(110)-(2×1)-O surface. (c) After 0.2 ML of Co deposition. Co atoms and Cu atoms displaced from the initial surface form 2D islands.

spectra. The multiple CO adsorption on Co sites weakens the Co-CO bond and reduces C-O bond scission probability. Our results may explain the higher selectivity of CoCu Fischer-Tropsch catalysts towards alcohol formation, compared to pure Co.

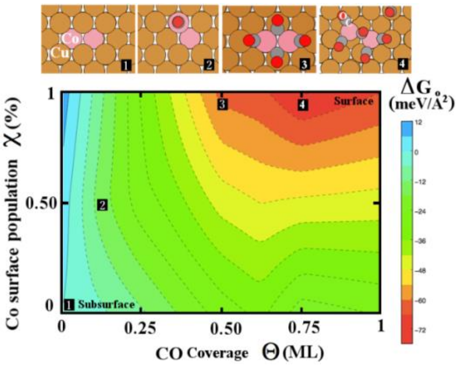

Fig. 3 Gibbs free energy ΔG vs surface Co population and CO coverage in equilibrium with 1 Torr of CO at RT. The amount of Co is fixed at 20% in the surface alloy. Co atoms occupy sites in the first or second layer. The most stable configurations occur in the phase diagram (red area). Selected structures at points 1 to 4 are shown, with Cu atoms in brown, Co pink, and O from CO in red.

2) The solid-liquid interface: 1- Pt-H_2SO_4 (aq.).

Using x-ray absorption spectroscopy in the interface-sensitive electron yield mode (EY-XAS) (Fig. 4), first-principles electronic structure calculations, and multiscale simulations, we determined the chemical composition of the interfacial region of a polycrystalline platinum electrode in sulfuric acid solution at potentials between the hydrogen and oxygen evolution reactions. We found that, in equilibrium between 0.7 and 1.3V vs Ag/AgCl the electric double layer (EDL) region comprises adsorbed sulfate ions (SO_4^{2-}) with hydrated hydronium ions (H_3O^+) in the next layer. No evidence was found for bisulfate (HSO_4^-) or Pt-O/Pt-OH species, which have very distinctive spectral signatures (Fig. 5) [2]. In addition to resolving the long-standing issue of the EDL structure, our work establishes interface- and element-sensitive EY-XAS as a powerful spectroscopic tool for studying condensed phase, buried functional solid-liquid interfaces relevant to batteries, fuel cells, corrosion, and others.

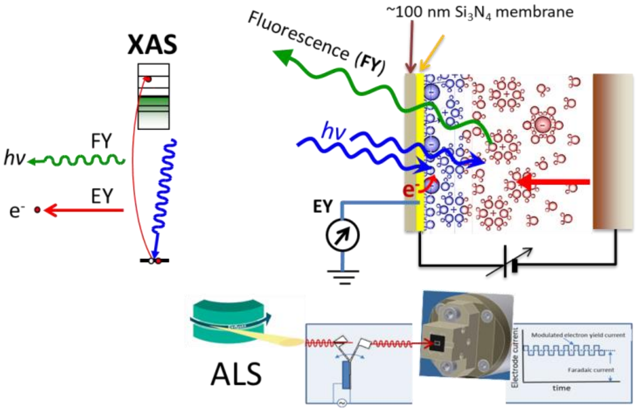

Fig. 4. Schematic of the experiment using x-ray transparent SiN membranes to separate liquid from vacuum. The metal electrode is a film (~20 nm, yellow in the schematic) evaporated on the back of the membrane. Fluorescence X-ray emission (mean free path ~1 μm) probes the bulk liquid, while electron emission (mean free path ~1 nm) captured at the electrode reports the interfacial structure. The small EY current is separated from the background and larger Faradaic current by modulation of the incoming x-ray beam (bottom).

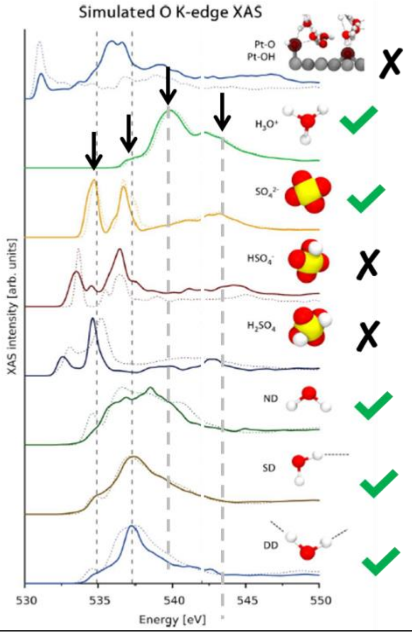

Fig. 5. O K-edge XAS spectra of O-containing species at the Pt-H_2SO_4 (50 mM aq.) interface calculated from first principles. Dashed vertical lines represent the energy of the main XAS features of bulk water.

3) Pt-Ni alloy nanoframes. Pt-based alloys have shown great promise as outstanding catalysts for cathodic oxygen reduction reaction (ORR) in cost-effective proton exchange membrane fuel cells (PEMFCs). Although the controlled synthesis plays an important role in the development of advanced ORR catalysts, post-synthesis treatment has been recognized as an important step to further improve their catalytic behavior by tailoring near-surface structure and composition. We recently developed Pt-Ni nanoframe electrocatalysts with exceptional performance [3]. However, in the practice of ORR measurement, we noticed that the activity and durability of the Pt-Ni nanoframe catalysts fluctuated in a wide range depending on how the catalysts were processed. To understand and alleviate this problem we compared three different processing procedures of our rhombic dodecahedral particles: electrochemical corrosion, mild acetic acid corrosion and strong nitric acid corrosion. Electrochemical corrosion led to the highest initial specific activity (1.35 mA cm-2 at 0.95 VRHE) by retaining more Ni in the nanoframes. However, the activity gradually went down due to continuous Ni loss and concomitant surface reconstruction. The best stability was achieved by nitric acid corrosion. Although the initial activity was compromised, this procedure imparted a less-defective surface and thus the specific activity dropped by only 7% over 30,000 cycles. These results indicate a delicate trade-off between the activity and stability of Pt-Ni nanoframe electrocatalysts. We consider the initial Ni content as a predictor for the activity and long-term durability of Pt-Ni nanoframes. The understanding obtained on how to balance the activity-stability trade-off via catalyst processing can be generalized to other Pt-based alloys.

Future work: Graphene-membranes for S-L interfaces studies. Thanks to its superior strength, graphene mono- and bi-layers can be used to separate gases at atmospheric pressure and liquids from the external environment: air, or high vacuum, where surface science analytical instrumentation is located, for example in Synchrotron beamlines. The atomically thin membranes allows for spectroscopic probes to determine the structure of the liquid film in contact with the graphene. For example photoelectrons from atoms in the phase inside the cell can exit through the electron transparent graphene. Because graphene is conductive we use it as an electrode by itself or supporting nanoparticles [4]. We can then study the electrical double layer with electrolytes, its cations and anions, and the solvation and orientation of water molecules, similar as in the previous example of H_2SO_4 (aq). The graphene is deposited on Au-covered SiN membranes (~200 nm thick) perforated with holes of micrometer diameter, as shown schematically in Fig. 6. The cell contains also counter and reference electrodes. With Kelvin Probe Microscopy we measured and mapped the contact potential of graphene in a cell filled with a NaCl solution as a function of bias. As expected

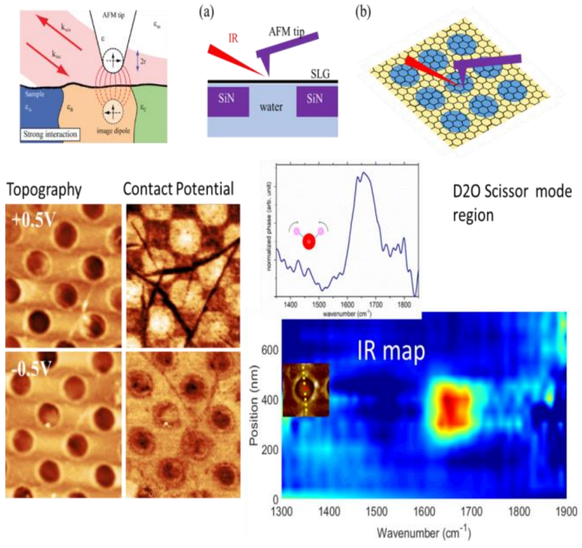

Fig. 6. (a, b): Schematic of the graphene membrane system. A graphene layer is transferred onto a holy (~1 um diameter holes) SiN membrane coated with Au which closes a cell for gases (up to 2.5 atm), or filled with liquid. In addition to holding the pressure differential with the outside, graphene can serves as an electrode. The non-contact AFM images at the bottom show the topography (left) and contact potential measured with KPFM from the outside. The liquid in this case is a NaCl solution. Application of + or – bias bring ions in contact with the membrane, which becomes doped. The doping is detected by KPFM as a change in potential. At the IR beamline of the ALS we obtained near field IR spectra with ~20 nm resolution. A map of the IR intensity of the water scissor mode is shown at the bottom right.

we found that Na^+ cations or Cl^- anions accumulate on the graphene electrode when applying negative of positive bias, sensed by measuring the changes they cause in the contact potential of graphene due to the electronic doping. The same cell was used to the ALS (Berkeley Synchrotron) for XPS studies of composition inside within a depth of ~1 nm from the graphene, as determined by the mean free of the photoelectrons. More recently we used near field tip-plasmonic enhancement to perform vibrational spectroscopy with a spatial resolution of 10 nm (~tip radius). The first result are very promising as shown in Fig. 6, where a map of the water scissor mode intensity shows how water in the cell is sensed through the graphene-covered holes. In the near future we expect to determine the orientation of water and its changes due to solvation of ions as a function of electric field by comparing the intensities of the scissor and O-H stretch modes. We are also studying formation of EDL in various electrolytes (first tests in progress using ammonium sulfate in D_2O), and gas segregation at the interface in gas-saturated solutions.

Future work: Surface sensitive Sum Frequency Generation. An important tool to help determine the molecular structure of S-L interfaces is Sum Frequency Generation (Fig. 1). Currently an electrochemical cell is used to study the surface of Cu electrodes during cyclic voltammetry (Fig. 7). With it we study the structure and passivation properties of Cu by benzotriazole (BTA, $C_6H_5N_3$), an excellent corrosion inhibitor for copper and copper alloy surfaces. In the figure we show the first SFG spectra of the BTA-Cu interface with peaks from the CH and NH stretch regions. The electrochemical cell for in situ studies is shown at the bottom right.

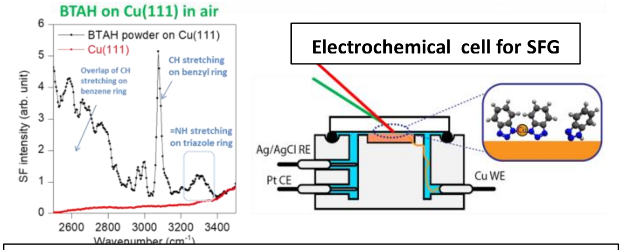

Fig. 7. Left: SFG spectrum of the Cu(111)-BTA interface in air, showing CH and NH peaks and a weak background from Cu (red) before BTA adsorption. A schematic of the new electrochemical cell for in situ SFG at the S-L interface is shown.

References:

[1] Baran Eren, Hendrik Bluhm, Gabor A. Somorjai, Miquel Salmeron, et al. *Structure of Copper−Cobalt Surface Alloys in Equilibrium with Carbon Monoxide Gas*. J. Am. Chem. Soc. **2018**, DOI: 10.1021/jacs.7b13621

[2] Cheng Hao Wu, Tod A. Pascal, Artem Baskin, Huixin Wang, Hai-Tao Fang, Yi-Sheng Liu, Yi-Hsien Lu, Jinghua Guo, David Prendergast, and Miquel B. Salmeron. *The molecular scale structure of electrode-electrolyte interfaces: the case of platinum in aqueous sulfuric acid*. J. Am. Chem. Soc. **2018.** Under review.

[3] C. Chen, Y. Kang, Z. Huo, Z. Zhu, W. Huang, H. L. Xin, J. D. Snyder, D. Li, J. A. Herron, M. Mavrikakis, M. Chi, K.L. More, Y. Li, N.M. Markovic, G. A. Somorjai, P. Yang, and V. R. Stamenkovic. *Highly crystalline multimetallic nanoframes with three-dimensional electrocatalytic surfaces*. Science **2014,** 343, 1339-1343.

[4] Cheng Hao Wu, Robert S. Weatherup, and M. B. Salmeron. *Probing the Solid/Liquid Interface in situ with X-rays: Old Methods, New Tricks.* Phys. Chem. Chem. Phys. **2015**, 17, 30229.

Publications of the Program "Structure and Dynamics of Materials Interfaces"
FWP: MSD KC31SM
Oct. 2017- May 2018

1) Lechner, Barbara; Feng, Xiaofeng; Feibelman, Peter; Cerda, Jorge; Salmeron, Miquel, Scanning Tunneling Microscopy Study of the Structure and Interaction Between Carbon Monoxide and Hydrogen on the Ru(0001) Surface. *J. Phys. Chem. B*, **2017**, *122*, 649–656. DOI: 10.1021/acs.jpcb.7b05657

2) Weatherup, Robert; Wu, Chenghao; Escudero, Carlos; Perez-Dieste, Virginia; Salmeron, Miquel., Environment-Dependent Radiation Damage in Atmospheric Pressure X-ray Spectroscopy. *J. Phys. Chem. B*, **2017,** *122*, 737–744. DOI: 10.1021/acs.jpcb.7b06397

3) Wang, Huixin; Wu, Cheng Hao; Weatherup, Robert S.; Feng, Bingmei; Ye, Yifan; Liu, Yi-Sheng ; Glans, Per-Anders; Guo, Jinghua; Fang, Hai-Tao; Salmeron, Miquel B. X-ray-Induced Fragmentation of Imidazolium-Based Ionic Liquids Studied by Soft X-ray Absorption Spectroscopy. *J. Phys. Chem. Letters.* **2018**, 9, 785–790. DOI: 10.1021/acs.jpclett.8b00057

4) Dürrbeck, Stefan; Shi, Xue-Rong; Samadashvili, Markus; Redinger, Josef; Bertel, Erminald; Salmeron, Miquel. Complex Reactions on a Convertible Catalyst Surface: A Study of the S-O-Cu System. *Surface Science*. **2018.** DOI: 10.1016/j.susc.2018.03.010

5) Miquel Salmeron. The Structure of Surfaces in Equilibrium with Gases and Liquids. Wandelt, K., (Ed.) *Encyclopedia of Interfacial Chemistry: Surface Science and Electrochemistry*, **2018**, 5, 292–298. ISBN: 9780128097397

6) Miquel Salmeron. Liquid-vapor and Liquid-solid Interfaces. Accepted. *Topics in Catalysis*. **2018**

7) Cheng Hao Wu, Tod A. Pascal, Artem Baskin, Huixin Wang, Hai-Tao Fang, Yi-Sheng Liu, Jinghua Guo, David Prendergast, and Miquel B. Salmeron. The molecular scale structure of electrode-electrolyte interfaces: the case of platinum in aqueous sulfuric acid. *J. Am. Chem. Soc.* Accepted. **2018**.

8) Baran Eren, Daniel Torres, Osman Karslıoglu, Zongyuan Liu, Cheng Hao Wu, Dario Stacchiola, Hendrik Bluhm, Gabor A. Somorjai, and Miquel Salmeron. Structure of Copper-Cobalt Surface Alloys in Equilibrium with Carbon Monoxide Gas. J. Am. Chem. Soc. **2018**, DOI: 10.1021/jacs.7b13621

Dynamics in Multicomponent Polymeric Materials

A.P. Sokolov, T. Saito, V. Bocharova, B. Sumpter, A. Kisliuk, M. Dadmun, K. Schweizer*

Oak Ridge National Laboratory, Oak Ridge, TN

***University of Illinois Urbana-Champaign, Illinois**

Program Scope

Polymers present a broad class of materials that are increasingly utilized in energy generation and conversion, energy storage and lightweight materials, chemical separations and gas purification. Yet a fundamental understanding of the interactions that control macroscopic properties remains limited, especially in multicomponent systems. The overarching goal of our research is to develop a fundamental and predictive understanding of dynamics in multicomponent polymeric materials. The pervasive presence of interfaces between different phases or species in multicomponent systems, and their effect on bulk properties, is the unifying aspect of our research. We address the following fundamental issues: How do the nanoparticle-polymer interactions and polymer rigidity affect the structure, dynamics and mechanical properties in the interfacial region? How do confinement and interactions affect polymer and nanoparticles diffusion? How are bulk viscoelastic properties of nanocomposites affected by nanoparticle size, surface chemistry, softness and shape fluctuations? How does molecular architecture affect superelastic properties? We pursue a comprehensive interdisciplinary approach led by advanced theory and simulations, precise synthesis, and state-of-the-art characterization with special emphasis on neutron scattering. The fundamental knowledge developed in this program contributes to the scientific foundation for the rational design of multicomponent polymer based materials with superior properties and function that will have broad applications in energy technologies.

Recent Progress

Polymer nanocomposites (PNC) play important role in many current technologies due to their light weight, high tunability of properties, and relatively low costs. It is now well recognized that interfacial layer controls macroscopic properties in PNCs. Polymer structure and dynamics in the interfacial layer are strongly affected by nanoparticles surface and polymer-nanoparticle interactions. We use broad array of experimental techniques, theory and MD-simulations to provide detailed characterization of the interfacial layer at the nanometer scale. Dielectric relaxation studies and MD-simulations revealed a gradient in the interfacial layer dynamics, but no “glassy” or “dead“ layer [1-3]. Small angle X-ray scattering, dielectric spectroscopy and differential scanning calorimetry provide consistent estimates of the interfacial layer thickness in various PNCs [2-4]. The thickness of the layer increases upon cooling to Tg [2,5], and depends strongly on polymer rigidity [1,5], increasing from ~2nm in flexible polymers to ~5 nm in more rigid ones. At the same time, the increase in strength of the polymer-nanoparticle interactions does not affect the thickness of the interfacial layer, but increases the slowing down of its dynamics [1]. Detailed studies revealed unexpected molecular weight dependence of PNCs properties ascribed to frustration in packing of long polymer chains in the interfacial region [3]. Analysis of mechanical properties using Brillouin light scattering and advanced scanning probe microscopy [4] revealed more than 2 times increase in polymer mechanical modulus in the interfacial layer. This huge increase was ascribed to stretching of the chain in the interfacial region. All these results clearly demonstrate the existence of the interfacial layer with much slower dynamics that propagates a few nm (~2-5 nm) into the polymer matrix, but no signs of any long range (larger than ~10nm) effects. Recent studies [6] also revealed unexpectedly large effects in nanocomposite properties caused by very small (~2nm) nanoparticles. In particular, these small nanoparticles lead to a very sharp temperature variations of viscosity. This effect has been ascribed to mobility of nanoparticles and relatively short chain-nanoparticle association time [6]. At the end, we present a general picture how microscopic parameters control the interfacial layer, and how by tuning the interfacial layer we can tune macroscopic properties of polymer nanocomposites.

Future Plans

To develop deeper fundamental understanding of PNC properties, the project will focus on three interrelated aims: (i) Unravel the interplay between chain adsorption, stretching and packing on the structure and dynamics of the interfacial region in PNCs and its impact on bulk properties; (ii) Shift the PNC paradigm by using small (of the order of the polymer segment) ‘sticky’ nanoparticles; and (iii) Reveal the role of nanoparticle softness and fuzziness as a new route to create PNCs with novel macroscopic properties. To address these aims, we will pursue a comprehensive approach led by advanced theory and simulations, precise synthesis, and state-of-the-art characterization with emphasis on neutron scattering and polymer deuteration, dielectric spectroscopy and rheology.

References

1. J.M.Y. Carrillo, et al., **Macromolecules 48**, 4207 (2015)

2. S. Cheng, et al., **J. Chem. Phys. 143**, 194704 (2015)

3. S. Cheng, et al., **Phys. Rev. Lett 116**, 038302 (2016)

4. S. Cheng, et al., **Nano Letters 16**, 3630 (2016)

5. S. Cheng, et al., **Macromolecules 50**, 2397 (2017).

6. S. Cheng, et al., **ACS Nano 11**, 752 (2017).

Publications

1. S. Cheng, A. P. Holt, H. Wang, F. Fan, V. Bocharova, H. Martin, T. Etampawala, B. T. White, T. Saito, N. G. Kang, M. D. Dadmun, J. W. Mays, A. P. Sokolov, Unexpected molecular weight effect in polymer nanocomposites, *Phys. Rev. Lett.* **116**, 038302 (2016).
2. D. Voylov, T. Saito, B. Lokitz, D. Uhrig, Y. Wang, A. Agapov, A. Holt, V. Bocharova, A. Kisliuk, A.P. Sokolov, Graphene oxide as a radical initiator: free radical and controlled radical polymerization of sodium 4-vinylbenzenesulfonate with graphene oxide, *ACS Macroletters* **5**, 199 (2016).
3. S. Cheng, V. Bocharova, A. Belianinov, S. Xiong, A. Kisliuk, S. Somnath, A. P. Holt, O. S. Ovchinnikova, S. Jesse, H. Martin, T. Etampawala, M. Dadmun, A. P. Sokolov, Unraveling the mechanism of nanoscale mechanical reinforcement in glassy polymer nanocomposites, *Nano Lett*. **16**, 3630 (2016).
4. A. P. Holt, V. Bocharova, S. Cheng, A. M. Kisliuk, B. T. White, T. Saito, D. Uhrig, J. P. Mahalik, R. Kumar, A. E. Imel, T. Etampawala, H. Martin, N. Sikes, B. G. Sumpter, M. D. Dadmun, A. P. Sokolov, Controlling interfacial dynamics: covalent bonding versus physical adsorption in polymer nanocomposites, *ACS Nano* **10**, 6843 (2016).
5. D. N. Voylov, I. N. Ivanov, V. I. Bykov, S. B. Tsybenova, I. A. Merkulov, S. A. Kurochkin, A. P. Holt, A. M. Kisliuk, and A. P. Sokolov, Oscillatory behavior of surface reduction process of multilayer graphene oxide at room temperature, *RSC Advances* **6**, 78194 (2016).
6. S.-J. Xie and K.S. Schweizer, Nonuniversal coupling of local cage hopping and long range elasticity as the origin of dynamic fragility diversity in glass-forming polymer liquids, *Macromolecules* **49**, 9655 (2016).
7. W. Lu, C. Huang, K. Hong, N.G. Kang, J. W. Mays, Poly(1-adamantyl acrylate): living anionic polymerization, block copolymerization, and thermal properties, *Macromolecules* **49**, 9406 (2016).
8. S. Mirigian and K. S. Schweizer, Influence of chemistry, interfacial width, and non-isothermal conditions on spatially heterogeneous activated relaxation and elasticity in glass-forming free standing films, *J. Chemical Physics* **146,** 203301 (2017).
9. D. N. Voylov, A. P. Holt, B. Doughty, V. Bocharova, H. M. Meyer , S. Cheng, H. Martin, M. Dadmun, A. Kisliuk, A. P. Sokolov, Unraveling the molecular weight dependence of interfacial interactions in poly(2-vinylpyridine)/silica nanocomposites, *ACS Macro Letters* **6**, 68 (2017).
10. S. Cheng, S.-J. Xie, J.-M. Y. Carrillo, B. Carroll, H. Martin, P.-F. Cao, M. D. Dadmun, B. G. Sumpter, V. N. Novikov, K. S. Schweizer, A. P Sokolov, Big effect of small nanoparticles: a shift in paradigm for polymer nanocomposites, *ACS Nano* **11**, 752 (2017).
11. S. Cheng, B. Carroll, W. Lu, F. Fan, J.-M. Y. Carrillo, H. Martin, A. P. Holt, N.-G. Kang, V. Bocharova, J. W. Mays, B. G. Sumpter, M. Dadmun, A. P. Sokolov, Interfacial properties of

polymer nanocomposites: role of chain rigidity and dynamic heterogeneity length scale, *Macromolecules* **50,** 2397 (2017).

12. S. Cheng, B. Carroll, V. Bocharova, J.-M. Y. Carrillo, B. G. Sumpter, A. P. Sokolov, Focus: structure and dynamics of the interfacial layer in polymer nanocomposites with attractive interactions, *J. Chem. Phys.* **146**, 203201 (2017).
13. H. Feng, M. Changez, K. Hong, J. W. Mays, and N. Kang, 2-Isopropenyl-2-Oxazoline: Well-defined homopolymers and block copolymers via living anionic polymerization, *Macromolecules* **50**, 54 (2017).
14. K. Misichronis, J. Chen, A. Imel, R. Kumar, J. Thostenson, K. Hong, M. Dadmun, B. G. Sumpter, J. G. Kennemur, N. Hadjichristidis, J. W. Mays, and A. Avgeropoulos, Investigations on the phase diagram and interaction parameter of poly(styrene-b-1,3-cyclohexadiene) copolymers, *Macromolecules* **50**, 2354 (2017).
15. A. Imel, S. Rostom, D. W. Holley, D. Baskaran, J. Mays, and M. Dadmun, The tracer diffusion coefficient of soft nanoparticles in a linear polymer matrix, *RSC Advances* **7**, 15574 (2017).
16. E.R. Duranty, J. Baschnagel, M.D. Dadmun, Diffusion of copolymers composed of monomers with drastically different friction factors in copolymer/homopolymer blends, *J. Chem. Phys.* **146**, 054905 (2017).
17. W. Lu, M. Osa, K. Hong, and J. W. Mays, Solution properties, unperturbed dimensions and chain flexibility of poly(1-adamantyl acrylate), *J. Polym. Sci. Part B: Polym. Phys.* **55**, 1526 (2017).
18. W. Lu, Y. Wang, W. Wang, S. Cheng, J. Zhu, Y. Xu, K. Hong, N.-G. Kang, and J. Mays, All acrylic-based thermoplastic elastomers with high upper service temperature and superior mechanical properties, *Polymer Chemistry* **8**, 5741 (2017).
19. P. Cao, Z. Wojnarowska, T. Hong, B. Carroll, B. Li, H. Feng, L. Parsons, W. Wang, B.S. Lokitz, S. Cheng, V. Bocharova, A. P. Sokolov, T. Saito, A star-shaped single lithium-ion conducting copolymer by grafting a POSS nanoparticle, *Polymer* **124**, 117 (2017).
20. B. Carroll, S. Cheng, and A. P. Sokolov, Analyzing the interfacial layer properties in polymer nanocomposites by broadband dielectric spectroscopy, *Macromolecules* **50**, 6149 (2017).
21. A. Holt, V. Bocharova, S. Cheng, A. Kisliuk, G. Ehler, E. Mamontov, V. Novikov, A. P. Sokolov, Surprising interplay between local dynamics and mechanical reinforcement in glassy polymer nanocomposites. *Phys. Rev. Mat.* **1**, 062601(R) (2017).
22. Y. H. Hur, S. Song, J. Mays, Y.J. Kim, B.-G. Kang, and Y. S. Jung, Synthesis of poly(styrene-b-4-(tert-butyldimethylsiloxy)styrene) block copolymers and characterization of their self-assembled patterns, *Mol. Sys. Des. Eng.* **2**, 589 (2017).
23. H. Feng, X. Lu, W. Wang, N.-G. Kang, and J. W. Mays, Block copolymers: synthesis, self-assembly, and applications, *Polymers* **9**, 494 (2017).
24. H. J. Martin, B.T. White, C. J. Scanlon, T. Saito, M. D. Dadmun, Tunable synthetic control of soft polymeric nanoparticles morphology, *Soft Matter* **13**, 8849 (2017).

25. E. Sheremet, R. D. Rodriguez, A. L. Agapov, A. P. Sokolov, M. Hietschold, D. R. T. Zahn, Nanoscale imaging and identification of four-component carbon sample, *Carbon* **96**, 588 (2016).

26. T. Tai, O. Karácsony, V. Bocharova, G. J. Van Berkel, and V. Kertesz, Topographical and chemical imaging of a phase separated polymer using a combined atomic force microscopy/infrared spectroscopy/ mass spectrometry platform, *Anal. Chem.* **88**, 2864 (2016).

27. F. Fan, W. Wang, A. Holt, H. Feng, D. Uhrig, X. Lu, T. Hong, N.-G. Kang, Y. Wang, J. W. Mays, and A. Sokolov, Effect of molecular weight on the ion transport mechanism in polymerized ionic liquids, *Macromolecules* **49**, 4557 (2016).

28. P. J. Griffin, V. Bocharova, L. R. Middleton, R. J. Composto, N. Clarke, K. S. Schweizer, and K. I. Winey, Influence of the bound polymer layer on nanoparticle diffusion in polymer melts, *ACS Macro Lett.* **5**, 1141 (2016).

29. A. E. Imel, A. Naskar, M. D. Dadmun, Understanding the impact of polyethylene oxide on the assembly of lignin in solution towards improved carbon fiber production, *ACS Appl. Mater. Interfaces* **8**, 3200 (2016).

30. T. Etampawala, D. L. Mull, J. K. Keum, D. M. Jenkins, M. D. Dadmun, Insights into the morphology and kinetics of growth of silver metal-organic nanotubes, *Cryst. Growth & Design* **16**, 1395 (2016).

31. Y. Li, M. P. Paranthaman, L. W. Gill, E. W. Hagaman, Y. Wang, A. P. Sokolov, S. Dai, C. Ma, M. Chi, G. M. Veith, A. Manthiram, J. B. Goodenough, Conductivity below 100C in nominal $Li_6ZnNb_4O_{14}$, *J. Materials Sci.* **51**, 854 (2016).

32. M. Naguib, T. Saito, S. Lai, M. S. Rager, T. Aytug, M. P. Paranthaman, M.-Q. Zhao, Y. Gogotsi, $Ti_3C_2T_x$ (MXene)–polyacrylamide nanocomposite films, *RSC Advances* **6**, 72069 (2016).

33. A. Goodwin, K. Nelson, W. Wang, Y.-G. Yu, J.-S. Lee, S. Mahurin, S. Dai, J. W. Mays, and N.-G. Kang, Anionic polymerization of oxadiazole-containing 2-vinylpyridine by precisely tuning nucleophilicity and the polyelectrolyte characteristics of the resulting polymers, *Macromolecules* **49**, 6213 (2016).

34. G. Dhindsa, D. Bhowmik, M. Goswami, H. O'Neill, E. Mamontov, B. G. Sumpter, L. Hong, P. Ganesh, X-Q. Chu, Enhanced dynamics of hydrated tRNA on nanodiamond surfaces: a combined neutron scattering and MD simulation study, *J. Phys. Chem. B* **120**, 10059 (2016).

35. R. E. Ruther, C.-N. Sun, A. Holliday, S. Cheng, F. M. Delnick, T. A. Zawodzinski, J. Nanda, Stable electrolyte for high voltage electrochemical double-layer capacitors, *J. Electrochem. Soc.* **164**, A277 (2017).

36. P. Lin, Q. Xu, S. Cheng, X. Li, Z. Zhao, S. Sun, C. Peng, A. Joy, S.-Q. Wang, Effects of molecular weight reduction on brittle–ductile transition and elastic yielding due to noninvasive γ irradiation on polymer glasses, *Macromolecules* **50**, 2447 (2017).

37. Y.Y. Stehle, D. Voylov, I.V. Vlassiouk, M.G. Lassiter, J. Park, J.K. Sharma, A.P. Sokolov, G. Polizos, Effect of polymer residues on the electrical properties of large-area graphene-hexagonal boron nitride planar heterostructures, *Nanotechnology* **28**, 285601 (2017).

38. M. Adams, V. Richmond, D. Smith, Y. Wang, F. Fan, A. P. Sokolov, D. A. Waldow, Decoupling of ion conductivity from segmental dynamics in oligomeric ethylene oxide functionalized oxanorbornene dicarboximide homopolymer, *Polymer* **116**, 218 (2017).
39. C. Bilchack, E. Buenning, M. Asai, K. Zhang, C. J. Durning, S. K. Kumar, Y. Huang, B. C. Benicewicz, D.W. Gidley, S. Cheng, A.P. Sokolov, M. Mindelli, F. Doghieri, Polymer-grafted nanoparticle membrane with controllable Free-Volume, *Macromolecules* **50**, 7111 (2017).
40. P.-F. Cao**,** L.-H. Rong, J. D. Mangadlao, and R. Advincula, Synthesizing a trefoil knotted block copolymer *via* ring-expansion strategy, *Macromolecules* **50**, 1473 (2017).
41. T. Hong, S. Chatterjee, S. M. Mahurin, F. Fan, Z. Tian, D. Jiang, B. K. Long, J. W. Mays, A. P. Sokolov, T. Saito, Impact of tuning CO$_2$-philicity in polydimethylsiloxane-based membranes for carbon dioxide separation, *Journal of Membrane Science* **530**, 213 (2017).
42. R. Kumar, J. Mahalik, V. Bocharova, E. Stacy, C. Gainaru, T. Saito, M. Gobet, S. Greenbaum, B. Sumpter, A. P. Sokolov, A Rayleighian approach for modeling kinetics of ionic transport in polymeric media, *J. Chem. Phys*. **146,** 064902 (2017).
43. H. Feng, T. Hong, S. M. Mahurin, K. D. Vogiatzis, K. R. Gmernicki, B. K. Long, J. W. Mays, A.P. Sokolov, N.-G. Kang, T. Saito, Gas separation mechanism of CO$_2$ selective amidoxime poly(1-trimethylsilyl-1-propyne) membranes, *Polymer Chemistry* **8,** 3341 (2017).
44. Z. Wojnarowska, H. Feng , Y. Fu, S. Cheng , B.Carroll, R. Kumar, V.N. Novikov, A. M. Kisliuk, T. Saito, N.-G. Kang, J. W. Mays, A. P. Sokolov, V.Bocharova, Effect of chain rigidity on the decoupling of ion motion from segmental relaxation in polymerized ionic liquids: ambient and elevated pressure studies, *Macromolecules* **50**, 6710 (2017).
45. P. Ye, P.-F.Cao, Z. Su, R. Advincula, Highly efficient reversible addition-fragmentation chain-transfer polymerization in ethanol/water via flow chemistry, *Polymer International* **66**, 1252 (2017).
46. P. Cao, B. Li. T. Hong, K. Xing, D.N. Voylov, S. Cheng, P. Yin, A. Kisliuk, S. M. Mahurin, A.P. Sokolov, T. Saito, Robust and elastic polymer membranes with tunable properties for gas separation, *ACS Appl. Materials & Interfaces* **9**, 26483 (2017).
47. J. M. Borreguero, P. A. Pincus, B. G. Sumpter, M. Goswami, Unraveling the agglomeration mechanism in charged block copolymer and surfactant complexes, *Macromolecules* **50**, 1193 (2017).
48. J. M. Borreguero, P. A. Pincus, B. G. Sumpter, M. Goswami, Dynamics of charged species in ionic-neutral block copolymer and surfactant complexes, *J. Phys. Chem. B.* **121**, 6958 (2017).
49. Y. Fu, V. Bocharova, M. Ma, A. P. Sokolov, B. G. Sumpter, R. Kumar, Effects of counterion size and backbone rigidity on dynamics of ionic polymer melts and glasses, *Phys. Chem. Chem. Phys* **19**, 27442 (2017).
50. Z. Wojnarowska, H. Feng, M. Diaz, A. Ortiz, I. Ortiz, J. Knapik-Kowalczuk, M. Vilas, P. Verdia, E. Tojo, T. Saito, E. Stacy, N. Kang, J. W. Mays, D. Kruk, P. Wlodarczyk, A. Sokolov, V. Bocharova, M. Paluch, Revealing the charge transport mechanism in polymerized ionic liquids: insight from high pressure conductivity studies, *Chem. of Mat.* **29**, 8082 (2017).
51. V. Bocharova, Z. Wojnarowska, Peng-Fei Cao, Y. Fu, R. Kumar, Bingrui Li, V.N Novikov, S. Zhao, A. Kisliuk, T. Saito, Jimmy W. Mays, B.G. Sumpter, A. P. Sokolov, Influence of chain

rigidity and dielectric constant on the glass transition temperature in polymerized ionic liquids, *J. Phys. Chem. B.* **121**, 11511 (2017).

52. Tao Hong, Sophia Lai, Shannon M. Mahurin, Peng-Fei Cao, Dmitry N. Voylov, Harry M. Meyer, III, Christopher B. Jacobs, Jan-Michael Y. Carrillo, Alexander Kisliuk, Ilia N. Ivanov, De-en Jiang, Brian K. Long, Jimmy W. Mays, Alexei P. Sokolov, Tomonori Saito; Highly-permeable Oligo (ethylene oxide)-co-Poly(dimethylsiloxane) Membranes for Carbon Dioxide Separation. *Adv. Sust. Systems* **2**, 1700113 (2018).
53. W. Lu, A. Goodwin, Y. Wang, P. Yin, W. Wang, J. Zhu, T. Wu, X. Lu, B. Hu, K. Hong, N.-G. Kang, and J.Mays, All-acrylic multigraft copolymer superelastomers: facile route to elastomers with exceptional mechanical behavior, *Polymer Chemistry* **9**, 160 (2018).
54. H. Wang, W. Lu, W. Wang, P. N. Shah, K. Misichronis, N.-G. Kang, and J. W. Mays, Design and synthesis of multigraft copolymer thermoplastic elastomers: superelastomers, *Macromol. Chem. Phys*. **219**, 1700254 (2018).
55. Derya Vura, Catalin Gainaru, Hugh O’Neill, Yunquiao Pu, Micholas Dean Smith, Jerry M. Parks, Sai Venkatesh Pongali, Eugene Mamontov, Brian H. Davison, Alexei P. Sokolov, Arthur J. Ragauskas, Jeremy C. Smith, Loukas Petridis. Impact of hydration and temperature history on the structure and dynamics of lignin**,** *Green Chemistry* **20**, 1602 (2018).
56. Carroll, Bobby; Bocharova, Vera; Carrillo, Jan-Michael; Kisliuk, Alexander; Cheng, Shiwang; Yamamoto, Umi; Schweizer, Kenneth; Sumpter, Bobby; Sokolov, Alexei; Diffusion of Sticky Nanoparticles in a Polymer Melt: Crossover from Suppressed to Enhanced Transport. *Macromolecules* **51**, 2268 (2018).
57. Yamamoto, Umi; Carrillo, Jan-Michael; Bocharova, Vera; Sokolov, Alexei; Sumpter, Bobby; Schweizer, Kenneth, Theory and Simulation of Attractive Nanoparticle Transport in Polymer Melts, *Macromolecules* **51**, 2258 (2018).
58. Peng-Fei Cao, Michael Naguib, Zhijia Du, Eric Stacy, Bingrui Li, Tao Hong, Kunyue Xing, Dmitry N. Voylov, Jianlin Li, David L. Wood, III, Alexei P. Sokolov, Jagjit Nanda Tomonori Saito, Effect of Binder Architecture on the Performance of Silicon/Graphite Composite Anodes for Lithium-ion Batteries, ***ACS Appl. Mater. Interfaces*** **10**, 3470 (2018).
59. Kunyue Xing, Martin Tress, Pengfei Cao, Shiwang Cheng, Tomonori Saito, Vladimir N. Novikov, Alexei P. Sokolov, Hydrogen-bond strength changes network dynamic in associating telechelic PDMS, *Soft Matter* **14**, 1235 (2018).

Access Non-equilibrium Assemblies Toward Functional Nanocomposites

Ting Xu, Materials Sciences Division, Lawrence Berkeley National Laboratory, University of California, Berkeley, Berkeley, CA 94720

Program Scope

This project is directed towards organic/inorganic nanocomposite materials. The goal is to design functional materials and make them by parallel and hierarchical self-assembly. In particular, we seek to develop wet chemical processes by which organic/inorganic composites can be created with a high degree of control on many length scales simultaneously. By developing a comprehensive ability to design, assemble, and pattern organic/inorganic composites and control their interfaces, it will be possible to prepare complex materials in which several microscopic processes are independently and simultaneously optimized. A range of functional materials can be created in this manner, with applications in energy conversion and storage, mechanical composites, and optical/electrical devices.

Recent Progress

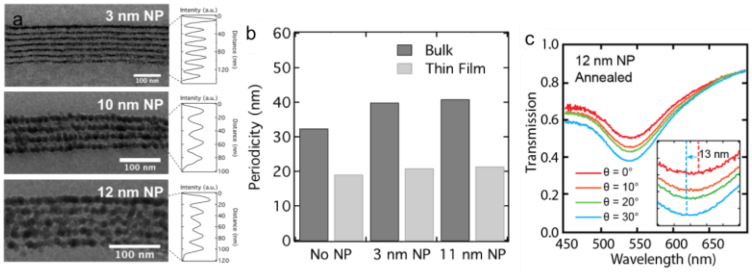

Fig. 1. Toward designer nanocomposites. ~50% reduction in lamellae periodicity was successfully achieved by controlling the kinetic pathway of assembly process. This leads to macroscopic coating with angular- and wavelength dependent optical property.

Access Non-Equilibrium Structures By Understanding Kinetic Pathway: Metamaterials exploit the synergetic responses among nanoscale building blocks to offer new freedoms in manipulating macroscopic property. While the lithography and ion milling generate fine features, they are extremely limited in controlling composition, 3D architecture, and much-needed scalability in fabricating metamaterials. Similar limitations exist in many directed assembly processes, such as DNA, evaporation, and layer-by-layer deposition. In contrast, thin films of polymer/nanoparticle (NP) blends offer the highly desirable capabilities for scalable processing and device integration. However, the NP spatial arrangement is governed by the nanocomposite's phase diagram constraint by thermodynamic equilibrium, which leaves rather limited freedom in metamaterials design. Our recent studies showed that, controlling the kinetic pathway in nanocomposite thin films provides a viable path to reproducibly access NP assemblies far away from the equilibrium state with high precision. ~50% reduction in the lamellar periodicity (Figure 1) is achieved for the first time to enable NP plasmonic coupling in multi-directions that led to rapid fabrication of a wavelength- and angular- dependent metamaterial coating.

Nanocomposite As Low-Cost, Sprayable Conductive Coating: For the last two funding cycles, our team has accumulated significant knowledge on how to manipulate nanostructures in polymer/filler blends and built solid foundation to fabricate technological relevant nanocomposites. Conductive paint has been widely applied in flexible electronics for sensing, energy harvesting, or actuator applications. However, commercially available conductive paints have drawbacks such as poor mechanical properties, high resistances and costly. With the team expertise, we developed block copolymer-based nanocomposite not only possessing excellent mechanical flexibility and electrical conductivity sufficient for LED operation but also compatibility with various scalable processing such as press molding, spraying, 3-D printing etc. Its mechanical and electrical properties can be readily tailored by varying nanostructures. A variety of substrates have been coated and became conductive such as cardboard, wood, plastic etc. Furthermore, the conductive composites can be recycled via disassembly and degradation (Figure 2). Therefore, the composite could be applicable to design wearable electronics, soft robotics, and strain sensors, which require high flexibility and conductivity and low cost for large-scale manufacturing.

Fig. 2 Spray of BCP-based nanocomposites led to conductive cardboard to operate LEDs. Similar results were seen using different materials/surfaces such as glass, wood and plastic.

Optomechano-sensing In Branched Nanoparticle-Containing Nanocomposites. Nanoscale stress sensing is of crucial importance to biomechanics and other fields. An ideal stress sensor would have a large dynamic range to function in a variety of materials spanning orders of magnitude of local stresses (Figure 3). Here we show that tetrapod quantum dots (tQDs) exhibit excellent sensing versatility with stress-correlated signatures in a multitude of polymers. We further show that tQDs exhibit pressure coefficients, which increase with decreasing polymer stiffness, and vary >3 orders of magnitude. This high dynamic range allows tQDs to sense in matrices spanning >4 orders of magnitude in Young's modulus, ranging from compliant biological levels (~100 kPa) to stiffer structural polymers (~5 GPa). We use ligand exchange to tune filler-matrix interfaces, revealing that inverse sensor response scaling is maintained upon significant changes to polymer-tQD interface chemistry. We quantify and explore mechanisms of

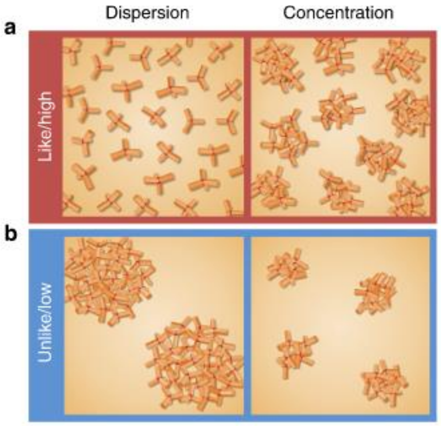

Fig. 3. Branched nanoparticles are effectively in sensing local stress in a polymeric matrix, depending on particle dispersion and interfacial ligand/polymer interactions.

polymer-tQD strain transfer. An analytical model based on Mori-Tanaka theory presents agreement with observed trends.

Future Plans

Develop structure-property relationship in nanocomposites: With the capability to manipulate hierarchical structures in nanocomposites, especially to access non-equilibrium structures by understanding the kinetic pathway, we are in the best position ever to develop design rules toward next generation of functional nanocomposite. Going forward, we will focus on nanocomposites with assemblies far away from the equilibrium rather than that studied previously. Specifically, our team will create a feedback loop among predictive nanocomposite design toward targeted properties, non-equilibrium via controlled kinetic pathway, and property measurements. To this end, we will focus on several properties including dielectric nanocomposites with optimized energy storage density, optical coating, and directed energy flow via nanostructured conductive matrix.

Publications

1. J. Huang, Y. Xiao, and T. Xu, Achieving 3-D Nanoparticle Assembly in Nanocomposite Thin Films via Kinetic Control, *Macromolecules*, **2017**, 50, 2183.

2. Cao, P.; Bai, P.; Omrani, A. A.; Xiao, Y.; Meaker, K. L.; Tsai, H.-Z.; Yan, A.; Jung, H.-S.; Khajeh, R.; Rodgers, G. F.; Kim, Y.; Aikawa, A. S.; Kolaczkowski, M. A.; Liu, Y.; Zettl, A.; Xu, K.; Crommie, M. F.; Xu, T. "Preventing Thin Film Dewetting via Graphene Capping", *Adv. Mater.* **2017**, *29*, 1701536.

3. P. Bai, S. Yang, W. Bao, J. Kao, K. Thorkelsson, M. Salmeron, X. Zhang, T. Xu, Diversifying Nanoparticle Assemblies in Supramolecule Nanocomposites Via Cylindrical Confinement, *Nano Lett.*, **2017,** DOI: 10.1021/acs.nanolett.7b03131

4. X.W. Gu, X. Ye, D.M. Koshy, S. Vachhani, P. Hosemann, A.P. Alivisatos. "Tolerance to structural disorder and tunable mechanical behavior in self-assembled superlattices of polymer-grafted nanocrystals". *PNAS*, **2017**, 114(11), 2836-2841.

5. M.J. Jurow, T. Lampe, E. Penzo, J. Kang, M.A. Koc, T. Zechel, Z. Nett, M. Brady, L.W. Wang, A.P. Alivisatos, S. Cabrini, W. Brutting, Y. Liu. "Tunable Anisotropic Photon Emission from Self-Organized $CsPbBr_3$ Perovskite Nanocrystals". *Nano Lett.*, **2017**, 17(7), 4534-4540

6. M.A. Koc, S.N. Raja, L.A. Hanson, S.C. Nguyen, N.J. Borys, K. Takano, A. Powers, S. Wu, J. Swabeck, J.H. Olshansky, L. Lin, R.O. Ritchie, A.P. Alivisatos. "Characterizing Photon Reabsorption in Quantum Dot-Polymer Composites for Use as Displacement Sensors". *ACS Nano*, **2017**, 11 (2), 2075-2084.

7. A. Pan, B. He, X. Fan, Z. Liu, J.J. Urban, A.P. Alivisatos, L. He, Y. Liu. "Insight into the Ligand-Mediated Synthesis of Coloidal $CsPbBr_3$ Perovskite Nanocrystals: The Role of Organic Acid, Base, and Cesium Precursors". *ACS Nano.* **2016**, 10(8), 7943-7954.

8. Pan, A.; Jurow, M.; Qiu, F.; Yang, J.; Ren, B.; Urban, J. J.; He, L.; Liu, Y. "Nanorod Suprastructures from a Ternary Graphene Oxide-Polymer-$CsPbX_3$ Perovskite Nanocrystal Composite that Display High Environmental Stability", *Nano Lett.* (2017) DOI: 10.1021/acs.nanolett.7b02959

9. Liu, X.; He, B.; Anderson, C.; Kang, J.; Chen, T.; Chen, J.; Feng, S.; Zhang, L.; Kolaczkowski, M.; Teat, S.; Brady, M.; Zhu, C.; Wang, L.; Chen, J.; Liu, Y. "*para*-Azaquinodimethane: a Compact Quinodimethane Variant as an Ambient Stable Building Block for High Performance Low Band Gap Polymers", *J. Am. Chem. Soc.* **2017**, *139*, 8355-8363.

10. Kolaczkowski, M.; He, B.; Liu, Y. "Stepwise Bay Annulation of Indigo for the Synthesis of Desymmetrized Electron Acceptors and Donor-Acceptor Constructs", *Org. Lett.* **2016**, *18*, 5524-5527. DOI: 10.1021/acs.orglett.6b02504

11. S. N. Raja, Y. Bekenstein, M. A. Koc, S. Fischer, D. Zhang, L. Lin, R. O. Ritchie, P. Yang, and A. P. Alivisatos, "Encapsulation of Perovskite Nanocrystals into Macroscale Polymer Matricies: Enhanced Stability and Polarization", *ACS Applied Materials & Interfaces*, **2016,** 8, 35523.

12. S. N. Raja, X. Ye, M. R. Jones, L. Lin, S. Govindjee and R. O. Ritchie, "Microscopic Mechanisms of Deformation Transfer in High Dynamic Range Branched Nanoparticle Deformation Sensors" *Nature Communications*, **2018**, 9, 1155.

UNIVERSITY GRANT PROJECTS

Bimolecular Interactions in Organic Semiconductors: Hot charge, Hot excitons, Efficiency Droop, and Instability

M.A. Baldo, ***Dept. of Electrical Engineering and Computer Science, MIT***
T. Van Voorhis, ***Dept. of Chemistry, MIT***

Program Scope

The poor stability of blue OLEDs is arguably the most important problem in modern organic semiconductor technologies. It is also a mortal threat to the viability of OLED-based solid state lighting. Perhaps the most serious consequence is its impact on efficiency. Indeed, if blue stability was solved, the application of state-of-the-art phosphorescent materials[1] would increase[2] the quantum efficiency for blue emission by a factor of 4, doubling the power efficiency of white OLEDs, and allowing this technology to reach the DOE 2025 target of 150 lm/W.

The absence of stable blue emitters comes after more than 10 years of intensive materials development in industry. This work was remarkably successful in green and red, and the creation of an entirely new market based on organic semiconductors is testament to the power of repeated iterations of material synthesis and commercial stability tests. On the other hand, the failure of this approach in blue suggests that there may be fundamental challenges underlying the performance of blue light emitters; see Figure 1.

Color	CIE	Efficiency (cd/A)	T95 (hours)
Red	(0.64,0.36)	30	50,000
Green	(0.31,0.63)	85	18,000
Light Blue	(0.18,0.42)	50	700

Figure 1. *A comparison of commercial performance and lifetime data for phosphorescent OLEDs operating at 1000 cd/m^2. From Universal Display Corporation (2012).*

Recent Progress

We present a simple model of exciton degradation in organic thin films and test the model by studying the degradation of an optically-pumped film of the archetype green phosphorescent material Iridium tris(phenylpyridine) ($Ir(ppy)_3$). For both simplicity and practical relevance to OLEDs, the model is only accurate for the initial decay. Degradation beyond 90% of initial luminescence can usually not be tolerated in applications.

We define: $[T]$ = the triplet exciton density, $[D]$ = the defect density, G = the optical pumping rate, k_R = the radiative rate, τ = the non-radiative lifetime, k_D = the degradation rate, $k_{ET}[D]$ = the rate of energy transfer to defects, and η = the luminescent efficiency.

As summarized in Figure 2, we assume three outcomes for triplet excitons: radiative emission, non-radiative loss, and energy transfer to defects. The triplet exciton kinetics are then:

$$\frac{d[T]}{dt} = G - k_R[T] - \frac{1}{\tau}[T] - k_{ET}[D][T]$$

The defect kinetics are taken from the measured intensity dependence. In our initial experiments on the archetype phosphorescent molecule $Ir(ppy)_3$, we found a quadratic dependence, consistent with damage due to exciton annihilation:

$$\frac{d[D]}{dt} = k_D [T]^2$$

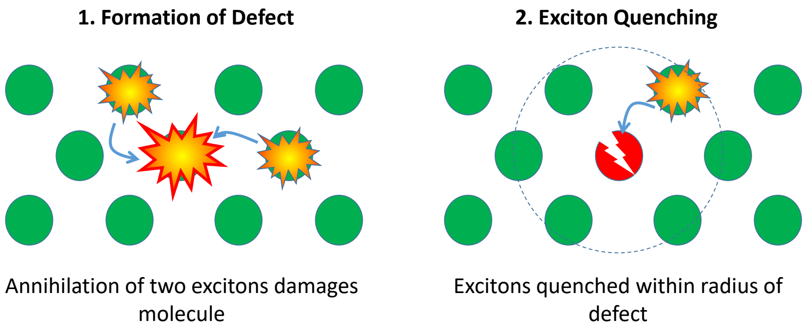

Figure 2. *A two step model for OLED degradation. In step 1, a molecule breaks. Possible causes include a collision between two excitons. In step 2, that defective molecule quenches neighboring excitons.*

The initial degradation rate is

$$\frac{d\eta}{dt} = -k_R k_{ET} k_D G^2 \tau^4$$

Note that the prediction is quadratic in pumping power, but *quartic* in exciton transient lifetime.

Next, we test the prediction experimentally. To vary the non-radiative lifetime we control the spacing, *d*, between a neat layer of Ir(ppy)$_3$ and a silver film. This alters the coupling to the surface plasmon in the silver film. The structures prepared in the experiment, and the measurements of the transient lifetime are shown in Figure 3.

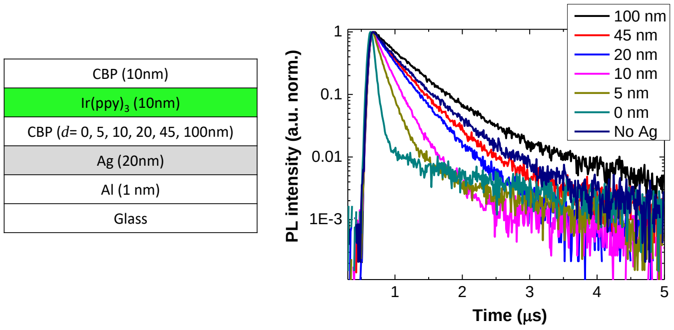

d	Exciton lifetime (ns)
100 nm	415
45 nm	285
20 nm	262
10 nm	168
5 nm	125
0 nm	59
No Ag	757

Figure 3. *We position thin films of Ir(ppy)$_3$ at varying distances from a silver layer and measure the resulting transient lifetime. The resulting exciton lifetime varies between 59ns and 757ns.*

After fabricating multiple structures with different transient lifetimes, we next measure the stability of Ir(ppy)$_3$ as a function of its transient lifetime. Great care is taken to ensure that the degradation results are compared at constant optical pumping rates. We calculate and measure the absorption in each structure. The films are then exposed to the optical pump and allowed to degrade under an inert atmosphere. For each film we extract the exposure time required for the film to fall to 90% of its initial luminance (T90). Representative data is shown in Figure 4.

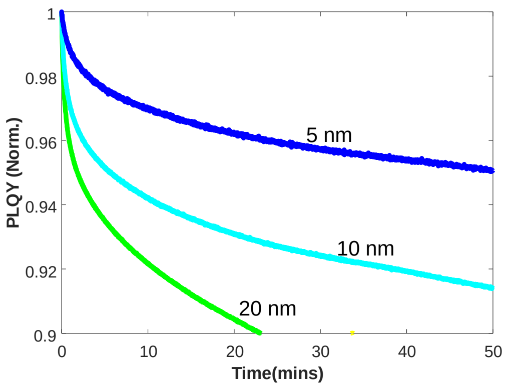

Figure 4. *Degradation data for the structures described in Fig. 3, above.*

To compare the impact of the exciton transient lifetime to the pump intensity, we also measure T90 for the films under varying pump power. These results are shown in

Figure 5. Note that the power law dependence on exciton lifetime is -3.5, approximately consistent with expectations. Although not shown here, the power law dependence on pump power is -2, also consistent with expectations.

Future plans: Bimolecular Interactions in Organic Semiconductors: Hot charge, Hot excitons, Efficiency Droop, and Instability

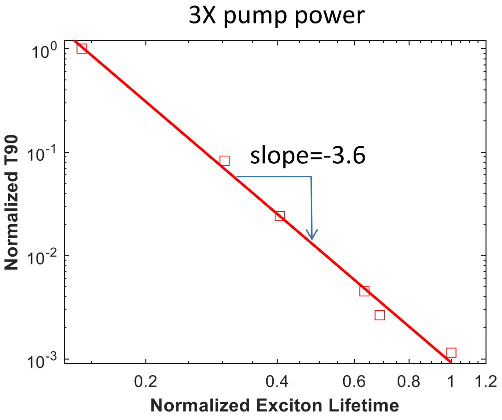

Figure 5. *The stability of Ir(ppy)$_3$ thin films as a function of exciton lifetime (bottom axis).*

Our conclusion is that exciton lifetime is indeed crucial in determining the stability of OLEDs. Physically, this can be understood as minimizing the *energy densit*y stored within an OLED while it is operating. The longer the exciton lifetime, the greater the energy density stored inside the OLED and the poorer its stability. This result builds the foundation for our future efforts to demonstrate OLEDs with accelerated radiative rates, where we expect dramatic improvements in OLED stability.

Efficiency droop is a related and potentially second important application. Efficiency droop in OLEDs is the major source of efficiency losses at high bias. It is particularly important in solid state lighting, and effectively increases the cost of OLED-based solutions because larger device areas are required to achieve the same number of lumens. Like stability, droop is caused by exciton-exciton interactions. Thus, reducing the lifetime of excitons is perhaps the best general approach to alleviating droop.

The two major causes of droop are triplet-triplet annihilation and triplet-charge annihilation, although which mechanism dominates depends on the device and is a source of much debate[3]. We propose a two part protocol for determining the origin of droop. Experimentally, reductions in triplet lifetime are expected to show a quadratic or linear improvement given triplet-triplet or triplet-charge annihilation, respectively. Theoretically, we have demonstrated that Mean Field Steady-State (MFSS) kinetic models has been shown to reproduce KMC results for disordered systems at a fraction of the computational cost. We have extended this method to look at exciton kinetics in OLEDs, with the aim of elucidating the roll-off mechanism in a given device and allowing the extraction of microscopic rate constants from photoluminescence and electroluminescence data.

Our preliminary results suggest that the roll-off mechanism is device dependent. This reinforces the usefulness of a simple model like mean field steady state, as it is computationally efficient enough to be used to screen many different OLEDs, and determine which mechanism dominates on each individual device, guiding rational design. Looking forward, we intend to complete this work by determining an experimental protocol that identifies the origin of droop in a particular OLED. Finally, we intend to demonstrate improvements in efficiency at high bias by decreasing the lifetimes of excitons within OLEDs.

References

1. M. A. Baldo, D. F. O'Brien, Y. You, A. Shoustikov, S. Sibley, M. E. Thompson, S. R. Forrest, High efficiency phosphorescent emission from organic electroluminescent devices. *Nature* **395**, 151-154 (1998).
2. M. A. Baldo, D. F. O'Brien, M. E. Thompson, S. R. Forrest, The excitonic singlet-triplet ratio in a semiconducting organic thin film. *Physical Review B* **60**, 14422-14428 (1999).
3. C. Murawski, P. Liehm, K. Leo, M. C. Gather, Influence of Cavity Thickness and Emitter Orientation on the Efficiency Roll-Off of Phosphorescent Organic Light-Emitting Diodes. *Advanced Functional Materials* **24**, 1117-1124 (2014).

Publications supported under this program

1. “Design of efficient molecular organic light-emitting diodes by a high-throughput virtual screening and experimental approach”, Rafael Gómez-Bombarelli, Jorge Aguilera-Iparraguirre, Timothy D Hirzel, David Duvenaud, Dougal Maclaurin, Martin A Blood-Forsythe, Hyun Sik Chae, Markus Einzinger, Dong-Gwang Ha, Tony Wu, Georgios Markopoulos, Soonok Jeon, Hosuk Kang, Hiroshi Miyazaki, Masaki Numata, Sunghan Kim, Wenliang Huang, Seong Ik Hong, Marc Baldo, Ryan P Adams, Alán Aspuru-Guzik, Nature Materials, 15, 1120 (2016).
2. "Turbocharged molecular discovery of OLED emitters: from high-throughput quantum simulation to highly efficient TADF devices ", Rafael Gómez-Bombarelli ; Jorge Aguilera-Iparraguirre ; Timothy D. Hirzel ; Dong-Gwang Ha ; Markus Einzinger ; Tony Wu ; Marc A. Baldo and Alán Aspuru-Guzik, Proc. SPIE 9941, Organic Light Emitting Materials and Devices XX, 99410A (September 23, 2016); doi:10.1117/12.2236966; http://dx.doi.org/10.1117/12.2236966
3. "Red Phosphorescence from Benzo [2, 1, 3] thiadiazoles at Room Temperature", GD Gutierrez, GT Sazama, T Wu, MA Baldo, TM Swager, The Journal of organic chemistry 81, 4789–4796 (2016)
4. “Charge Recombination in Phosphorescent Organic Light-Emitting Diode Host-Guest Systems through QM/MM Simulations”, TY Zhu and T Van Voorhis J Phys Chem C 120, 19987-19994 (2016)
5. “Study of Static and Dynamic Energetic Disorder in the Emission Layer of an Organic Light-Emitting Diode” de Silva, P.; Van Voorhis, T. QM/MM. J. Phys. Chem. Lett. 2018, 1329–1334.
6. “Mean Field Treatment of Heterogeneous Steady State Kinetics “ Geva, N.; Vaissier, V.; Shepherd, J.; Van Voorhis, T. Chem. Phys. Lett. 2017, 685, 185–190.
7. “Shorter Exciton Lifetimes via an External Heavy-Atom Effect: Alleviating the Effects of Bimolecular Processes in Organic Light-Emitting Diodes.” Einzinger, M.; Zhu, T.; de Silva, P.; Belger, C.; Swager, T. M.; Van Voorhis, T.; Baldo, M. A. Adv. Mater. 2017, 29 (40).
8. “Molecular Design of Deep Blue Thermally Activated Delayed Fluorescence Materials Employing a Homoconjugative Triptycene Scaffold and Dihedral Angle Tuning” Wenliang Huang, Markus Einzinger, Tianyu Zhu, Hyun Sik Chae, Soonok Jeon, Soo-Ghang Ihn, Myungsun Sim, Sunghan Kim, Mingjuan Su, Georgiy Teverovskiy, Tony Wu, Troy Van Voorhis, Timothy M. Swager, Marc A. Baldo, and Stephen L. Buchwald. Chem. Mater., 2018, 30 (5), pp 1462–1466

Novel Pnictides with *d*- and *f*-Metals as Prospective Materials for Thermal Energy Conversion

Svilen Bobev
Department of Chemistry and Biochemistry, University of Delaware, Newark DE 19716

Program Scope

Our research program is focused on the synthetic and structural work on novel materials, stepping up the research efforts in the creation of new crystalline forms of matter for energy production and conversion. The discoveries from our research are expected to be an important part in the development of new materials/technologies for thermoelectric waste heat recovery. From a more fundamental point of view, the structure-property relationships derived from our work can be used for developing a rationale for the synthesis of new compounds, as well as for tuning of properties of existing ones. The 'final product' of our research, naturally, is ascertaining the connection among the synthesis, crystal structure, and properties, and by doing so, building up the predictive power of solid-state chemistry (still in its infancy compared to the other chemical disciplines), establishing new ideas of why and how Nature allows atoms to assemble and form new compounds and structures.

Recent Progress

Transition metal pnictides adopt a large variety of crystal structures, where extended metal-metal bonding and polyatomic pnictogen species, such as isolated olygomers, chains, and/or two-dimensional nets are recurring motifs (the terms pnictogen and pnictides refer to the heavier nitrogen congeners—P, As, Sb, Bi—and their compounds with other metals). Such diverse bonding patterns often come together with complex atomic arrangements. From the properties standpoint, semiconducting behavior is common, and such small-gap pnictides have been actively studied in thermoelectrics—due to the low thermal conductivity resulting from the structural complexity, such semiconductors are regarded as promising thermoelectric materials.

Reviewing the vast literature on transition metal pnictides,[1] we noticed that while pnictides of the late 3*d*-elements appear well-studied, the knowledge on pnictides of the early 1st-row transition metals is relatively scarce. Recent investigations show unusual ferromagnetism in the vanadium antimonide $CeVSb_3$. Several complex crystal structures have been reported in the *RE*–Ti–Sb system, where *RE* stands for a rare-earth metal. The ternary compounds RE_3TiSb_5 (*RE* = La, Ce, Pr, Nd, Sm), $RE_2Ti_7Sb_{12}$ (*RE* = La, Ce, Pr, Nd), and $RE_2Ti_{11-x}Sb_{14+x}$ (*RE* = Sm, Gd, Tb, Yb) display sophisticated crystal chemistry involving Ti–Ti and Sb–Sb bonding interactions. Much less is known about the ternary phases existing in the *RE*–Ti–Bi systems, where only La_3TiBi_5 has been recently described.[2] The only ternary compounds reported in the

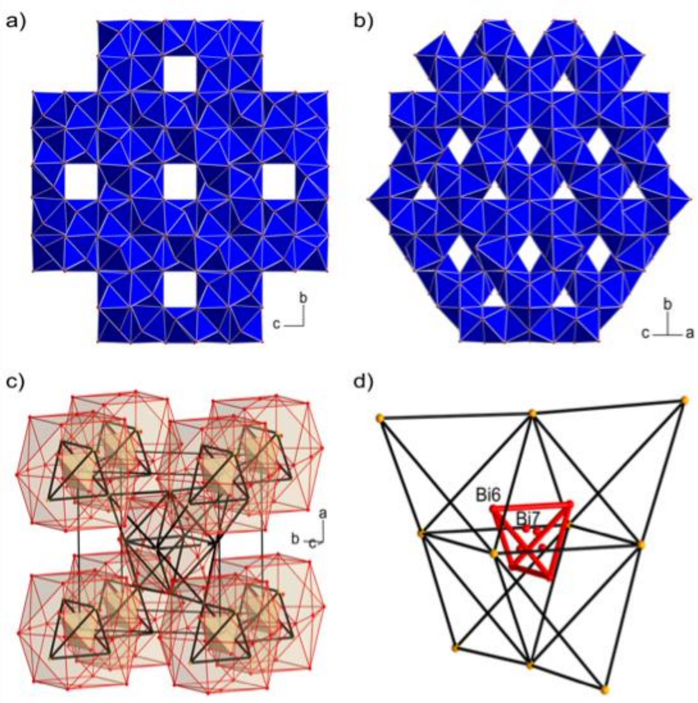

Figure 1. Crystal structure of $AE_5\mathrm{Ti}_{12}\mathrm{Bi}_{19+x}$. *AE* and Bi atoms are shown in orange and red, respectively. (a, b) Ti–Bi framework with one-dimensional channels. Ti atoms are located in the centers of the blue octahedra. (c) γ-brass-type intermetallic clusters in $AE_5\mathrm{Ti}_{12}\mathrm{Bi}_{19+x}$. (d) Disordered Bi sites at the center of the unit cell.

AE–Ti–*Pn* systems (*Pn* = P, As, Sb), where *AE* is an alkaline-earth metal, are the Zintl phases $AE_4\mathrm{Ti}Pn_4$ (*AE* = Sr, Ba; *Pn* = P, As) as well as $\mathrm{Ba}_5\mathrm{Ti}_{12}\mathrm{Sb}_{19+x}$.[3] No ternary phases in the *AE*–Ti–Bi systems are known to date.

Motivated in part by the lack of structural information on titanium bismuthides, we set out to conduct an exploratory work in the *AE*–Ti–Bi systems using the Bi-flux technique. The initial results from this study, namely, the synthesis, crystal and electronic structure, and physical properties of the new ternary compounds $AE_5\mathrm{Ti}_{12}\mathrm{Bi}_{19+x}$ (*AE* = Sr, Ba), as well as $\mathrm{Sr}_{5-\delta}\mathrm{Eu}_{\delta}\mathrm{Ti}_{12}\mathrm{Bi}_{19+x}$ ($\delta \leq 4.0$, $x \leq 1.0$), are summarized in this report.

Preliminary analysis of the powder X-ray diffraction data indicated that $AE_5\mathrm{Ti}_{12}\mathrm{Bi}_{19+x}$ crystallize in cubic syngony, and are isotypic to the antimonides $\mathrm{Ba}_5M_{12}\mathrm{Sb}_{19+x}$ (*M* = Ti, V, Nb). The subsequent single-crystal X-ray diffraction study revealed notable differences between the studied bismuthides and the previously reported antimonides with respect to the details in the disordered part of the crystal structure (*vide infra*).

The titanium atoms in the crystal structure are six-fold coordinated by Bi atoms, and the resulting octahedra are joined by face- and corner-sharing in a complex three-dimensional framework. This framework possesses infinite channels running along the principal axes and face diagonals of the unit cell (Figure 1a, b). These channels accommodate the *AE* cations and additional Bi species. Taking into account the mode of the polyhedral interconnection, the structural formula can be given as $AE_5[\mathrm{TiBi}_{3/3}\mathrm{Bi}_{2/4}\mathrm{Bi}_{1/6}]_6[\mathrm{TiBi}_{2/3}\mathrm{Bi}_{2/4}\mathrm{Bi}_{2/6}]_6\mathrm{Bi}_x$. Disregarding the partially occupied Bi positions, the shortest Bi–Bi contact in the structure is Bi1–Bi5 with a length of about 3.4 Å. Similar to the analogous Sb–Sb interaction in $\mathrm{Ba}_5\mathrm{Ti}_{12}\mathrm{Sb}_{19+x}$, this contact does not show any significant bonding interaction, as evidenced by our first-principle calculations. Following the original description of $\mathrm{Ba}_5\mathrm{Ti}_{12}\mathrm{Sb}_{19+x}$, the alkaline-earth-metal–pnictogen substructure of $AE_5\mathrm{Ti}_{12}\mathrm{Bi}_{19+x}$ can be formally described in terms of complex metal clusters (Figure 1c). The two types of clusters occupy the corners and the center of the unit cell, respectively, and bear resemblance to the intermetallic building blocks in the crystal structure of γ-brass. The cuboctahedral Bi_{18} clusters in the corners of the unit cell accommodate Bi_4 and AE_4

tetrahedra. The latter tetrahedra share common corners with the AE_{10} super-tetrahedra centered around the (½, ½, ½) position.

The AE_{10} super-tetrahedron represents a four-capped AE_6 octahedron and overlaps with the Bi_{16} cuboctahedral cluster in the center of the unit cell. Within this description, the Bi clusters are isolated, giving rise to 18 + 4 + 16 = 38 Bi atoms per unit cell, or 19 Bi atoms per formula unit. Additional Bi in the composition stems from the two partially occupied sites Bi6 and Bi7 around the center of the unit cell (Figure 1d). The arrangement of the Bi6 atoms represents a regular tetrahedron with an edge of about 3.0–3.1 Å. The occupation of this site increases gradually with decreasing unit cell size, reaching a maximum value of about 0.5 for $SrEu_4Ti_{12}Bi_{19+x}$. Such a high occupancy means that locally, more than one Bi atom can reside in the corners of the Bi6 tetrahedron. The distance between the adjacent Bi6 atoms falls in the range typical for single Bi–Bi bonds. A possible model for this partially occupied Bi species is a disordered Bi_2 dumbbell. The occupancy of 0.5 corresponds to exactly one Bi_2 unit in the center of the unit cell. The increased occupation of the Bi6 site seems to counteract the shrinking of the unit cell, to maintain the stability of the rigid covalent Ti–Bi framework. This consideration can explain why the ternary $Eu_5Ti_{12}Bi_{19+x}$ could not be prepared—the further decrease of the unit cell volume, governed by the small size of the Eu^{2+} cation, would call for a higher occupation of the Bi6 position. However, a single Bi_2 unit already occupies the available volume at the composition Eu/Sr = 4 : 1, i.e., no additional Bi can be inserted in the structure. The idealized composition of the end member of such solid solution is $SrEu_4Ti_{12}Bi_{20}$.

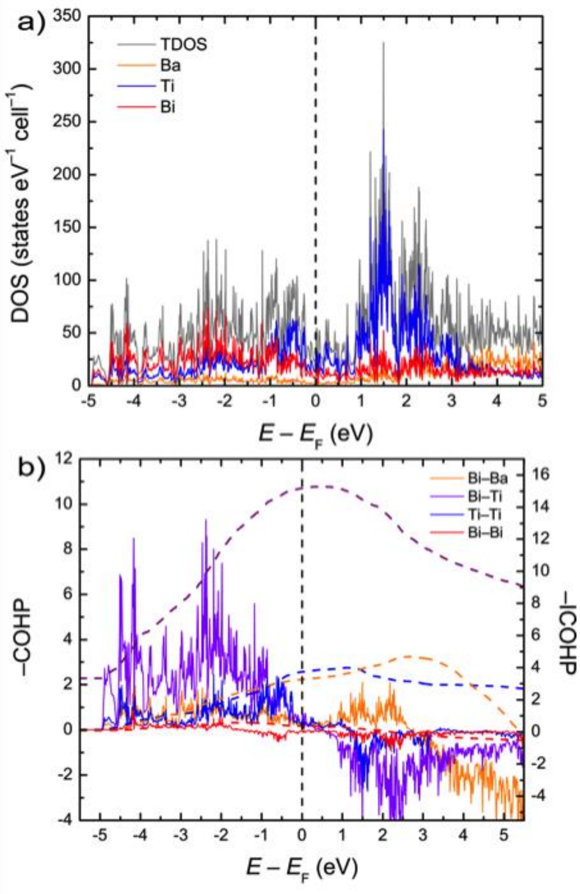

Figure 2. (a) Total and projected electronic densities of states (DOS) for $Ba_5Ti_{12}Bi_{19}$. (b) COHP curves for the selected interactions.

Another important feature of the $AE_5Ti_{12}Bi_{19+x}$ structure is the emergence of regular octahedra and tetrahedra in the AE sub-lattice (Figure 1c). As mentioned above, the introduction of Eu in the AE sites was motivated by the possibility of geometric magnetic frustration, which could arise from competing exchange interactions of Eu^{2+} ions (electronic configuration [Xe]4f^7). Preliminary magnetization measurements support the notion of magnetic frustration in the Eu-substituted member.

Electronic density of states for $Ba_5Ti_{12}Bi_{19}$ is shown in Figure 2a. Below the Fermi level, the DOS is mainly composed of the Ti(3d) and Bi(6p) states. These states are strongly hybridized, especially below $E - E_F = -1.0$ eV. Similarly to other alkaline-earth-metal bismuthides, the bonding between the bismuth and alkaline-earth metal atoms is far from being ionic, which is reflected in a large fraction of the Ba states spread out below E_F. Above the Fermi level, the DOS is dominated by the empty Ti(3*d*) states, suggesting that the electronic configuration of Ti is close to d^0. Spin-polarized calculations showed no localized magnetic moments on any of the atoms.

Crystal orbital Hamilton population (COHP) curves for the symmetrically independent contacts are shown in Figure 2b. Below the Fermi level, the shortest Bi–Bi contact shows a combination of bonding and antibonding interactions that effectively cancel each other. The Bi–Ba contacts expectedly show bonding interactions below the Fermi level with some additional bonding states available above E_F. The –iCOHP values for the Bi–Ba bonds lie in the range 0.33–0.54 eV/bond. The Ti–Ti bonds appear to be much stronger with –iCOHP from 0.84 to 1.47 eV/bond, though these interactions are also slightly underoptimized at E_F. The strongest interactions, as indicated by the COHP analysis, are observed for the Bi–Ti bonds, with the –iCOHP values ranging from 1.62 to 2.23 eV/bond. This, and the fact that the crystal structure is dominated by the Bi–Ti contacts makes these interactions pivotal for the stability of the structure. The Bi–Ti interactions are almost optimized at E_F. Since the hybridization of the Ti(3*d*) and Bi(6*p*) states occurs predominantly below $E - E_F = -1.0$ eV, this energy window contains most bonding states for the Bi–Ti contacts, whereas only a small number of bonding states are available in the vicinity of the Fermi level.

Future Plans

From the electronic structure, it follows that shifting the Fermi level within the energy window $-1.0 \text{ eV} < E - E_F < 1.0$ eV, e.g., by doping, will not have a strong impact on the Bi–Ti bonding. It is reasonable to expect that the introduction of the partially occupied Bi sites confers some Ba–Bi and Bi–Bi bonding interactions, at the same time retaining the stability of the Ti–Bi framework. Therefore, additional synthetic/structural work, coupled with property measurement experiment will be needed in order to understand how varied electron count will modify the heat and charge transport properties. In addition to the electronic factors and the packing considerations, the optimization of the $AE_5Ti_{12}Bi_{19+x}$ structure may also be favored by the entropy gain resulting from the disorder. Entropy factors are neglected in the first-principle calculations, done at the absolute zero temperature, but are important in real materials.

References

[1] Villars, P.; Calvert, L. D. (Eds.), Pearson’s Handbook of Crystallographic Data for Intermetallic Compounds, 2nd Ed., American Society for Metals, Materials Park, OH, USA 1991.

[2] Murakami, T.; Yamamoto, T.; Takeiri, F.; Nakano, K.; Kageyama, H. *Inorg. Chem.* **2017**, *56*, 5041–5045.

[3] Bie, H.; Mar, A. *J. Solid State Chem.* **2009**, *182*, 3131–3137.

Publications (since 2016)

(in reverse order; *the names of the contributing undergraduate researchers are underlined*)

"Rare-earth Metal Substitutions in $\mathrm{Ca}_{9-x}\mathit{RE}_x\mathrm{Mn}_4\mathrm{Sb}_4$ (RE = La–Nd, Sm; $x \approx 1$). Synthesis and Characterization of a New Series of Narrow-Gap Semiconductors"
Wang, Y.; **Bobev, S.** *Chem. Mater.* **2018**, *30*, in print.
doi: 10.1021/acs.chemmater.8b01316 – available online 05/04/2018.

"Niobium-bearing Arsenides and Germanides from Elemental Mixtures not Involving Niobium: A New Twist to an Old Problem in Solid-state Synthesis"
Baranets, S.; He, H.; **Bobev, S.** *Acta Cryst. C* **2018**, *74*, 623.
doi: 10.1107/S2053229618005739

"Crystal Structure of $\mathrm{La}_3\mathrm{TiBi}_5$ from Single-crystal X-ray Diffraction"
Ovchinnikov, A.; **Bobev, S.** *Acta Cryst. C* **2018**, *74*, 618.
doi: 10.1107/S205322961800565X

"On the Effect of Ga and In substitutions in the $\mathrm{Ca}_{11}\mathrm{Bi}_{10}$ and $\mathrm{Yb}_{11}\mathrm{Bi}_{10}$ Bismuthides Crystallizing in the Tetragonal $\mathrm{Ho}_{11}\mathrm{Ge}_{10}$ Structure Type"
Ovchinnikov, A.; **Bobev, S.** *Acta Cryst. C* **2018**, *74*, 269.
doi: 10.1107/S2053229618001596

"Synthesis, Crystal and Electronic Structure of the Novel Titanium Bismuthides $\mathrm{Sr}_5\mathrm{Ti}_{12}\mathrm{Bi}_{19+x}$,$\mathrm{Ba}_5\mathrm{Ti}_{12}\mathrm{Bi}_{19+x}$, and $\mathrm{Sr}_{5-\delta}\mathrm{Eu}_\delta\mathrm{Ti}_{12}\mathrm{Bi}_{19+x}$ ($x \approx 0.5$–1.0; $\delta \approx 2.4, 4.0$)"
Ovchinnikov, A.; **Bobev, S.** *Eur. J. Inorg. Chem.* **2018**, 1266.
doi:10.1002/ejic.201701426

"Crystal Chemistry and Magnetic Properties of the Solid Solutions $\mathrm{Ca}_{14-x}\mathit{RE}_x\mathrm{MnBi}_{11}$ (RE = La–Nd, Sm, Gd–Ho; $x \approx 0.6$–0.8)"
Ovchinnikov, A.; Prakash, J.; **Bobev, S.** *Dalton Trans.* **2017**, *46*, 16041.
doi: 10.1039/c7dt03715e
INSIDE COVER PAGE FOR: *Dalton Trans.* **2017**, vol. 46, number 46, December 14th issue.

"The Ternary Alkaline-earth Metal Manganese Bismuthides $\mathrm{Sr}_2\mathrm{MnBi}_2$ and $\mathrm{Ba}_2\mathrm{Mn}_{1-x}\mathrm{Bi}_2$ ($x \approx 0.1$)"
Ovchinnikov, A.; Saparov, B.; Xia, S.-Q.; **Bobev, S.** *Inorg. Chem.* **2017**, *56*, 12369.
doi: 10.1021/acs.inorgchem.7b01851

"Cu and Zn Substituted Silicon Clathrates with the Cubic Type-II Structure. Synthesis and Characterization of $\mathrm{Cs}_8\mathrm{Na}_{16}\mathrm{Cu}_{3.8}\mathrm{Si}_{132.2}$ and $\mathrm{Cs}_8\mathrm{Na}_{16}\mathrm{Zn}_{6.9}\mathrm{Si}_{129.1}$"
Schäfer, M. C.; **Bobev, S.** *Z. Anorg. Allg. Chem.* **2017**, *643*, 1874.
doi: 10.1002/zaac.201700236
(by invitation; special issue *dedicated to the 60th birthday of Prof. Thomas Schleid*)

"Synthesis and Structural Determination of $Ce_6Cd_{23}Te$. A New Chalcogen-Containing Member of the $RE_6Cd_{23}T$ Family (RE = rare-earth metal; T = late group 14, 15, 16 elements)"
Desrosches, G.; **Bobev, S.** *Acta Cryst.* **2017**, *C73*, 121.
doi: 10.1107/S2053229617001243

"Synthesis and Structural Characterization of the Zintl Phases $Na_3Ca_3TrPn_4$, $Na_3Sr_3TrPn_4$, and $Na_3Eu_3TrPn_4$ (Tr = Al, Ga, In; Pn = P, As, Sb)"
Wang, Y.; Suen, N.-T.; Kunene, T.; Stoyko, S.; **Bobev, S.** *J. Solid State Chem.* **2017**, *249*, 160.
doi: 10.1016/j.jssc.2017.02.026

"Synthesis and Structural Characterization of $RE_6Cd_{23}T$ (RE = La–Gd; T = Sn, Sb, Pb, and Bi)"
Desrosches, G.; **Bobev, S.** *J. Solid State Chem.* **2017**, *246*, 203.
doi: 10.1016/j.jssc.2016.11.015

"$Cu_3Ru_6Sb_8$—a New Ternary Antimonide with a New Structure Type"
Prakash, J.; Suen, N.-T.; Lee, M.; Choi, E.-S.; Ibers, J. A.; **Bobev, S.** *Inorg. Chem. Front.* **2016**, *3*, 1616.
doi: 10.1039/c6qi00418k
(by invitation; special issue *dedicated to the 60th birthday of Prof. Mercouri G. Kanatzidis*)

"Crystal Structures of the Four New Quaternary Copper(I) Selenides $A_{0.5}CuZrSe_3$ and $ACuYSe_3$ (A = Sr, Ba)"
Maier, S.; Prakash, J.; Berthebaud, D.; Perez, O.; **Bobev, S.**; Gascoin, F. *J. Solid State Chem.* **2016**, *242*, 1.
doi: 10.1016/j.jssc.2016.06.023

"Synthesis and Structural Characterization of $Ca_{14}Nb_xIn_{1-x}As_{11}$ ($x \approx 0.85$)"
Wang, Y.; **Bobev, S.** *Solid State Phenom.* **2016**, *257*, 147.
doi: 10.4028/www.scientific.net/SSP.257.147

Programming Function via Soft Materials

Paul Braun, Qian Chen, Randy Ewoldt, Xiuling Li, Jeff Moore, Ralph Nuzzo, John Rogers, Ken Schweizer, Frederick Seitz Materials Research Laboratory, University of Illinois at Urbana-Champaign, Urbana, IL 61801

Program Scope

The cluster has established a unique enabling vision for materials that embraces the dynamically reconfigurable 3-dimensional organization of building blocks into architectures that facilitate ion and electron transport, provide unique mechanical responsivities, and underpin advanced energy harvesting and storage concepts as well as other applications. To achieve this goal we are utilizing materials of diverse chemistry in a broad range of organizations (amorphous/crystalline, soft/hard, static/dynamic, particulate/fibrous/membrane) designed to program equilibrium and nonequilibrium structures with powerful properties. As elementary units we are employing function-encoded colloids, nanoparticles, large mesh fibrillar gels, deterministically fabricated networks and hybrid objects. They are being employed as building blocks for diverse model systems that allow fundamental soft matter principles of wide relevance to be established. Their assembly into materials with useful functional behavior is providing new approaches to challenging problems in basic energy science including energy harvesting, transport and storage. The cluster is organized into two Thrusts. Thrust 1: Reconfigurable and Dynamic Assemblies, and Thrust 2: Dynamic and Driven Mesoscale Structures.

Recent Progress

Thrust 1: Reconfigurable & Dynamic Assemblies:

Selected progress is described with a common theme use of external fields or stimulus to realize functional properties and behavior.

Novel Colloidal Assembly & Dynamics: Low-dose liquid-phase TEM was employed to collect a series of previously inaccessible movies of space-time self-assembly in nanoparticle suspensions (Chen). The consequences of changing nanoparticle size, shape and surface chemistry [1-2] enabled a mechanistic understanding of the connection between particle properties and collective nanoscale organization. Polymerization-like kinetics [3] and non-classical nucleation paths of gold nanoplate superlattice

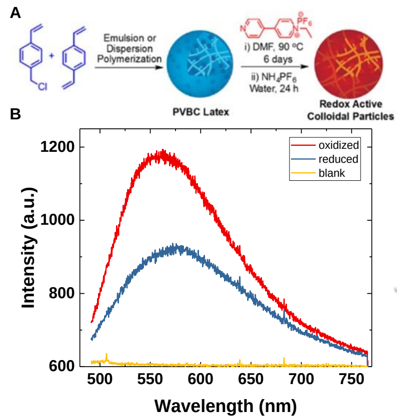

Fig. 1. (A) Synthesis of RAC colloids. (B) Fluorescence spectra of RAC monolayer as a function of oxidation state.

formation were discovered [4]. A unified framework was constructed by integrating in-situ TEM movies, single particle tracking, statistical mechanical analysis and computer simulation.

Building on Moore's foundational studies of viologen-based redox-active colloids (RACs) [5], major new insights concerning electrochemical energy transfer has been achieved this year (Braun, Chen, Moore) (Fig. 1). The oxidation state of the RAC can now be directly optically determined (fluorescence ON coupled with oxidation and OFF with reduction), which allows optical interrogation of charge transport within and between colloidal particles. It is now possible to directly observe lateral colloid-colloid energy transfer, and to measure, for the first time, the intra- and inter-colloid charge-transfer diffusion coefficients.

Dynamic Polymer Networks: Braun, Ewoldt, Moore, and Schweizer have synthesized and characterized spiropyran-containing polymers in the liquid state that form light and temperature triggerable non-covalent reversible crosslinks [6]. In a complementary effort, Ewoldt and Schweizer have more deeply tested our model formulated last year [7] for weakly nonlinear viscoelastic properties as probed in medium-amplitude oscillatory shear in new parameter regimes [8] for strain-stiffening reversible hydrogel networks of poly(vinyl alcohol) (PVA) transiently-crosslinked by sodium tetraborate (Borax) [9]. For additional information see presentation by Jeff Moore.

Responsive Hybrid Composites: Braun, Ewoldt, and Schweizer have demonstrated unprecedented 1-2 orders of magnitude of mechanical stiffness in two different hybrid composite materials based on micron-sized responsive-colloids in semi-flexible large mesh biopolymer gels (fibrin). For iron-fibrin composites (Fig. 2), the sensitivity of the shear moduli to an applied magnetic field far surpasses that of typical magnetoelastomers or magnetohydrogels. We propose a strong interaction between the magnetic particles induces local stress in the fibrin mesh which inherently stiffens due to its semi-flexible nature.

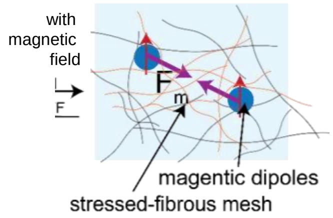

Fig. 2. Schematic of a composite of a large mesh fibrin network containing a low volume fraction (4%) of magnetically-responsive colloids and the forces acting on it that result in it exhibiting a huge strain stiffening driven by magnetic dipolar forces.

Thrust 2: Dynamic and Driven Mesoscale Structures: Selected progress is described in fundamental progress in understanding 3D materials assembly and mesostructure formation.

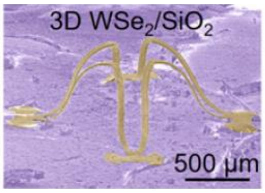

Fig. 3. SEM of WSe$_2$ grown on a 3D structure formed via buckling-induced assembly.

Buckling-Induced Assembly: Via schemes that include photopolymerization, non-linear mechanics and physical transfer, coupled with controlled mechanical compressive buckling, Braun, Nuzzo and Rogers formed 3D structures suitable for integration onto nearly any class of substrate, from planar, hard inorganic materials to textured, soft biological tissues [13]. Fig. 3 illustrates use of a 3D structure as a growth scaffold for WS$_2$. In our (Ewoldt, Rogers) most advanced 3D assembly schemes we realized systems with capabilities in active, dynamic mechanical control through incorporation of multiple, high-performance, piezoelectric thin film actuators for applications in microscale rheological studies of viscosity and density of surrounding complex fluids.

3D and 4D Functional Soft Materials: Ewoldt and Nuzzo reported on a significant advance made in the materials suitable use as inks for the 3D printing of soft material structures and functional devices. Printing particle-free silicone oil-in-water emulsions with a polymer additive, poly(ethylene oxide) allows heretofore unrealized capabilities and design rules for functional soft material structures [14].

Future Plans

Novel Colloidal Assemblies (Thrust 1): We will perform additional detailed experimental studies of redox active colloids in the pursuit of a deeper understanding of the charge-transfer dynamics under concurrent electrochemical biasing (Chen, Braun, Moore). Such experiments will provide foundational information to begin to construct a quantitative model for how charge transfer dynamics is coupled with colloid motion in the liquid state (Schweizer).

Dynamic Polymer Networks (Thrust 1): We aim to understand how to increase the degree of transient crosslinking and optimize the design of reversible, stimuli-responsive polymers based on triggerable mechanophores (See Jeff Moore presentation for additional information).

Responsive Hybrid Composites (Thrust 1): Two new directions will be pursued. First, the possibility of using synthetic semi-flexible polymers (e.g. polyisocyanopeptides) with known and controllable chemistry for programming composites (Ewoldt, Moore, Nuzzo, Schweizer) to exhibit dramatic stimuli-responsiveness such as strain-stiffening. Second, as an alternative route to achieve stimuli responsiveness we (Braun, Ewoldt, Schweizer) will explore using core-shell structured colloidal particles that go beyond the present microgel design. Such particles hold the potential to be tuned over a wider range of reversible sticking/unsticking from the polymer mesh and thus expand the change of composite bulk properties induced by the particles.

Buckling-Induced Assembly (Thrust 2): Ewoldt and Rogers plan the development of 3D mesostructures that can capture full non-linear rheological responses of microliter volumes of complex fluids, with an emphasis on systems that have time-dependent behaviors and address the core scientific questions of broader interest to the collaborating team. Nuzzo and Rogers plan in the addition of microfluidic capabilities into 3D mesostructures and to explore the use of this functionality in delivering and/or removing fluids locally from a complex system to locally modulate its properties. Braun and Rogers plan in exploring the foundational aspects of scaling our 3D assembly approaches into size regimes, i.e. tens of nanometers or less, where mechanical instabilities, Brownian fluctuations, surface forces and other effects may set fundamental limits.

3D and 4D Functional Soft Materials (Thrust 2): Nuzzo, Braun, and Ewoldt will develop new soft functional materials that provide capabilities for autonomous sensing and reporting. Our designs will seek to provide capabilities for deducing the physicochemical attributes of the environments present in a material's use environment. This team will further develop, based on the advances made in the past year, new materials for printing-based methods of grayscale 3D fabrication. The effort will specifically target the development of materials that can be patterned to embed gradient mechanical properties and coupled chemical systems within their 3D structural form. Primary goals are to develop a deeper understanding of the broad range of rheological properties that enable performance new types of structures to be printed, and the post-printing chemical transformations required to obtain useful and durable material properties.

References

1. Kim, J.; Song, X.; Ji, F.; Luo, B.; Ice, N. F.; Liu, Q.; Zhang, Q.; Chen, Q. *Nano Letters* **2017,** *17* (5), 3270.
2. Luo, B.; Smith, J. W.; Wu, Z.; Kim, J.; Ou, Z.; Chen, Q. *ACS Nano* **2017,** *11* (8), 7626.
3. Kim, J.; Ou, Z.; Jones, M. R.; Song, X.; Chen, Q. *Nature Comm.* **2017,** *8* (1), 761.
4. Ou, Z.; Wang, Z.; Luijten, E.; Chen, Q. Under review.
5. Montoto, E. C.; Nagarjuna, G.; Hui, J.; Burgess, M.; Sekerak, N. M.; Hernández-Burgos, K.; Wei, T.-S.; Kneer, M.; Grolman, J.; Cheng, K. J.; Lewis, J. A.; Moore, J. S.; Rodríguez-López, J. *J. Am. Chem. Soc.* **2016,** *138* (40), 13230.
6. Epstein, E. S.; Martinetti, L.; Carey-De La Torre, O.; Moore, J. S.; Ewoldt, R. H.; Braun, P. V. Under review.
7. Bharadwaj, N. A.; Schweizer, K. S.; Ewoldt, R. H. *J. Rheology* **2017,** *61* (4), 643.
8. Carey-De La Torre, O.; Ewoldt, R. H. *Korea-Australia Rheology J.* **2018,** *30* (1), 1.
9. Carey-De La Torre, O.; Martinetti, L.; Schweizer, K. S.; Ewoldt, R. H.Under review.
10. Mirigian, S.; Schweizer, K. S. *J. Chem. Phys.* **2014,** *140* (19), 194506.
11. Yang, J.; Schweizer, K. S. *J. Chem. Phys.* **2011,** *134* (20), 204908.
12. Yang, J.; Schweizer, K. S. *J. Chem. Phys.* **2011,** *134* (20), 204909.
13. Braun, P. V.; Nuzzo, R. G.; Rogers, J. A., et al. *Proc. Nat. Acad. Sci.* **2017,** *114* (45), E9455.
14. Rauzan, B. M.; Nelson, A. Z.; Lehman, S. E.; Ewoldt, R. H.; Nuzzo, R. G. *Adv. Funct. Mater.* **2018,** *0* (0), 1707032.
15. Rogers, J. A.; Nuzzo, R. G. et al. *Adv. Biosys.* **2017,** *1* (9), 1700068.

Publications

1. J. Pikul, J. Liu, P.V. Braun and W.P. King, Integration of High Capacity Materials into Interdigitated Mesostructured Electrodes for High Energy and High Power Density Primary Microbatteries, Journal of Power Sources, 315, 308-315 (2016).
2. A. M. Abdullah, P.V. Braun and J. Hsia, Programmable Shape Transformation of Spherical Domes, Soft Matter, 12, 6184-6195 (2016).
3. J. Liu, X. Chen, J. Kim, Q. Zheng, H. Ning, P. Sun, X. Huang, J. Liu, J. Niu and P.V. Braun, High volumetric capacity three-dimensionally sphere-caged secondary battery anodes, Nano Letters, 16, 4501-4507 (2016).
4. J. Liu, Q. Zheng, M.D. Goodman, H. Zhu, J. Kim, N.A. Krueger, H. Ning, X. Huang, J. Liu, M. Terrones and P.V. Braun, Graphene Sandwiched Mesostructured Li-Ion Battery Electrodes, Advanced Materials, 28, 7696-7702 (2016).
5. N.A.K. Bharadwaj, J.G. Kang, M.C. Hatzell, K.S. Schweizer, P.V. Braun and R. Ewoldt, Integration of colloids into a semi-flexible network of fibrin, Soft Matter, 13, 1430-1443 (2017).
6. H. Zhang, H. Ning, J. Busbee, Z. Shen, C. Kiggins, Y. Huang, J. Eaves, J. Davis, T. Shi, Y.-T. Shao, J.-M. Zuo, X. Hong, Y. Chen, S. Wang, P. Wang, P. Sun, S. Xu, J. Liu, and P.V. Braun, Electroplating Lithium Transition Metal Oxides, Science Advances, 3 e1602427 (2017).
7. Juyeong Kim, Matthew R. Jones, Zihao Ou, Qian Chen, In Situ Electron Microscopy Imaging and Quantitative Structural Modulation of Nanoparticle Superlattices, ACS Nano (2016) 10 (11), 9801–9808 (2016).
8. Kristin M. Hutchins, Chih-Yi Lee, Binbin Luo, Qian Chen, and Jeffrey S. Moore, “Effects of Crosslinking Density on Interfacial Polymerization and Scaffold Formation in Functionalized Polymer Beads,” Industrial & Engineering Chemistry Research, 56, 4883-4886 (2017).
9. Binbin Luo, John W. Smith, Zihao Ou, and Qian Chen, Quantifying the Self-Assembly Behavior of Anisotropic Nanoparticles Using Liquid-Phase Transmission Electron Microscopy, Accounts of Chemical Research, 50, 1125-1133 (2017).
10. Juyeong Kim, Xiaohui Song, Fei Ji, Binbin Luo, Nicole F. Ice, Qipeng Liu, Qiao Zhang and Qian Chen, Polymorphic Assembly from Beveled Gold Triangular Nanoprisms, Nano Letters, 17, 3270-3275 (2017).
11. Juyeong Kim, Zihao Ou, Matthew R. Jones, Xiaohui Song & Qian Chen, Imaging the “Polymerization” of Multivalent Nanoparticles in Solution, Nature Communications, 8, 761 (2017).
12. Bharadwaj, N. A., J. G. Kang, M. C. Hatzell, K. S. Schweizer, P. V. Braun, and R. H. Ewoldt, Integration of hard sphere colloids into a semi-flexible network of fibrin, Soft Matter, 13 1430-1443 (2017).
13. Kumar, M. A., R. H. Ewoldt, C. F. Zukoski, "Intrinsic Nonlinearities in the mechanics of hard sphere suspensions," Soft Matter, 23, 35102 (2016).
14. Y. Zhang, F. Zhang, Z. Yan, Q. Ma, X. Li, Y. Huang, and J. A. Rogers, Printing, Folding and Assembly Methods for 3D Mesostructures in Advanced Materials, Nature Rev. Mater. 2, 17019 (2017).
15. K. Nan, H. Luan, Z. Yan, X. Ning, Y. Wang, A. Wang, J. Wang, M. Han, M. Chang, K. Li, Y. Zhang, W. Huang, Y. Xue, Y. Huang, Y. Zhang, and J.A. Rogers, Engineered Elastomer Substrates for Guided Assembly of Complex 3D Mesostructures by Spatially Nonuniform Compressive Buckling, Adv. Funct. Mater. 27, 1604545 (2017).

16. H. Fu, K. Nan, P. Froeter, W. Huang, Y. Liu, Y. Wang, J. Wang, Z. Yan, H. Luan, X. Guo, Y. Zhang, C. Jiang, L. Li, A. C. Dunn, X. Li, Y. Huang, Y. Zhang, J. A. Rogers, Mechanically-guided deterministic assembly of 3D mesostructures assisted by residual stresses, Small, 3 1700151 (2017).
17. X. Yu, L. L. Goddard, X. Li and X. Chen, Enhanced axial confinement in a monolithically integrated self-rolled-up SiNx vertical microring photonic coupler, Appl. Phys. Lett. 109, 111104 (2016).
18. Z. Yan, F. Zhang, J. Wang, F. Liu, X. Guo, K. Nan, Q. Lin, M. Gao, D. Xiao, Y. Shi, Y. Qiu, H. Luan, J.H. Kim, Y. Wang, H. Luo, M. Han, Y. Huang, Y. Zhang, and J.A. Rogers, Controlled Mechanical Buckling for Origami-Inspired Construction of 3D Microstructures in Advanced Materials, Adv. Funct. Mater. 26, 2629-2639 (2016).
19. Y. Liu, Z. Yan, Q. Lin, X. Guo, M. Han, K. Nan, K.-C. Hwang, Y. Huang, Y. Zhang, and J.A. Rogers, Guided Formation of Three-Dimensional Helical Mesostructures by Mechanical Buckling: Analytical Modeling and Experimental Validation, Adv. Funct. Mater. 26, 2609-2618 (2016).
20. Z. Yan, F. Zhang, F. Liu, M. Han, D. Ou, Y. Liu, Q. Lin, X. Guo, H. Fu, Z. Xie, M. Gao, Y. Huang, J.H. Kim, Y. Qiu, K. Nan, J. Kim, P. Gutruf, H. Luo, A. Zhao, K.-C. Hwang, Y. Huang, Y. Zhang, and J.A. Rogers, Mechanical Assembly of Complex, 3D Mesostructures from Releasable Multilayers of Advanced Materials, Science Advances 2, e1601014 (2016).
21. K. Nan, H. Luan, Z. Yan, X. Ning, Y. Wang, A. Wang, J. Wang, M. Han, M. Chang, K. Li, Y. Zhang, W. Huang, Y. Xue, Y. Huang, Y. Zhang, and J.A. Rogers, Engineered Elastomer Substrates for Guided Assembly of Complex 3D Mesostructures by Spatially Non-Uniform Compressive Buckling, Adv. Funct. Mater. 27 1604281 (2017).
22. X. Ning, H. Wang, X. Yu, J.A.N.T. Soares, Z. Yan, K. Nan, G. Velarde, Y. Xue, R. Sun, Q. Dong, H. Luan, C.M. Lee, A. Chempakasseril, M. Han, Y. Wang, L. Li, Y. Huang, Y. Zhang, and J.A. Rogers, 3D Tunable, Multiscale, and Multistable Vibrational Micro-Platforms Assembled by Compressive Buckling, Adv. Funct. Mater. 27 1605914 (2017).
23. Hutchins, K. M.; Sekerak, N. M.; Moore, J. S. Polymerization Initiated by Particle Contact: A Quiescent State Trigger for Materials Synthesis, J. Am. Chem. Soc. 2016, 138, 12336-12339.
24. Song, Y.; Moore, E. G.; Guo, Y.; Moore, J. S. Polymer–Peptide Conjugates Disassemble Amyloid β Fibrils in a Molecular-Weight Dependent Manner, J. Am. Chem. Soc., 2017, 139, 4298-4301.
25. Z. E. Dell and K. S. Schweizer, Segment-Scale, Force-Level Theory of Mesoscopic Dynamic Localization and Entropic Elasticity in Entangled Chain Polymer Liquids, J. Chemical Physics, 146, 134901 (2017).
26. B. Tsang, Z. E. Dell, L. Zhao, K. S. Schweizer and S. Granick, Cooperative Interchain Displacements in Entangled F-Actin Networks, Proceedings National Academy Sciences, 114, 3322 (2017).
27. N.A. Bharadwaj, K.S. Schweizer and R.H. Ewoldt, A Strain Stiffening Theory for Transient Polymer Networks Under Asymptotically-Nonlinear Oscillatory Shear, Journal of Rheology, 61, 643 (2017).
28. J.M. McCracken, S. Xu, A. Badea, K.-I. Jang, Z. Yan, D.J. Wetzel, K. Nan, Q. Lin, M. Han, M.A. Anderson, J.W. Lee, Z. Wei, M. Pharr, R. Wang, J. Su, S.S. Rubakhin, J.V. Sweedler, J.A. Rogers and R.G. Nuzzo, "Deterministic Integration of Biological and Soft Materials onto 3D Microscale Cellular Frameworks," Advanced Biosystems 1, 1700068 (2017).

29. Z. Yan, M. Han, Y. Shi, A. Badea, Y. Yan, A. Kulkarni, E. Hanson, M.E. Kandel, X. Wen, F. Zhang, Y. Luo, Q. Lin, H. Zhang, X. Guo, Y. Huang, K. Nan, S. Jia, A.W. Oraham, M.B. Mevis, J. Lim, X. Guo, M. Gao, W. Ryu, K.J. Yu, B.G. Nicolau, A. Petronico, S.S. Rubakhin, J. Lou, P.M. Ajayan, K. Thornton, G. Popescu, D. Fang, J.V. Sweedler, P.V. Braun, H. Zhang, R.G. Nuzzo, Y. Huang, Y. Zhang and J.A. Rogers, "Three-dimensional Mesostructures as High-Temperature Growth Templates, Electronic Cellular Scaffolds, and Self-propelled Microrobots," Proceedings of the National Academy of Sciences USA E9455–E9464 (2017).
30. H. Fu, K. Nan, W. Bai, W. Huang, K. Bai, L. Lu, C. Zhou, Y. Liu, F. Liu, J. Wang, M. Han, Z. Yan, H. Luan, Y. Zhang, Y. Zhang, J. Zhao, X. Cheng, M. Li, J.W. Lee, Y. Liu, D. Fang, X. Li, Y. Huang, Y. Zhang and J.A. Rogers, "Morphable 3D Mesostructures and Microelectronic Devices by Multistable Buckling Mechanics," Nature Materials 17, 268-276 (2018).
31. Nina M. Sekerak, Kristin M. Hutchins, Binbin Luo, Jin Gu Kang, Paul V. Braun, Qian Chen, Jeffrey S. Moore, Size control of cross-linked carboxy-functionalized polystyrene particles: Four orders of magnitude of dimensional versatility, European Polymer Journal, Volume 101, 2018, Pages 202-210.
32. Jinyun Liu, Ping Zhou, Tianli Han, Jiarui Huang, Jinhuai Liu, Jinjin Li, Paul V. Braun, Ni-encapsulated TiO_2 nanotube array prepared using atomic layer deposition as a high-performance Li-ion battery anode, Materials Letters, Volume 219, 2018, Pages 12-15.
33. Sanghyeon Kim, Sung-Kon Kim, Pengcheng Sun, Nuri Oh, and Paul V. Braun, Reduced Graphene Oxide/LiI Composite Lithium Ion Battery Cathodes, Nano Letters 2017 17 (11), 6893-6899.
34. P. Yuan, J. M. McCracken, D. E. Gross, P. V. Braun, J. S. Moore a and R. G. Nuzzo, A programmable soft chemo-mechanical actuator exploiting a catalyzed photochemical wateroxidation reaction, Soft Matter, 2017, 13, 7312.
35. Arif M. Abdullah, Paul V. Braun, and K. Jimmy Hsia, Bifurcation of self-folded polygonal bilayers, Appl. Phys. Lett. 111, 104101 (2017).
36. A.D. Phan and K.S. Schweizer, Theory of Activated Dynamics in Randomly Pinned Fluids, J.Chemical Physics, 148, 054502 (2018).
37. Juyeong Kim, Zihao Ou, Matthew R. Jones, Xiaohui Song, and Qian Chen, "Imaging the polymerization of multivalent nanoparticles in solution", Nature Communications 17, 3270–3275 (2017).
38. Carey-De La Torre, O., R. H. Ewoldt, "First-harmonic nonlinearities can predict unseen third-harmonics in medium-amplitude oscillatory shear (MAOS)," Korea-Australia Rheology Journal, 30(1), 1-10 (2018).
39. Rauzan, B. M., A. Z. Nelson, R. H. Ewoldt, and R. G. Nuzzo, "Particle-Free Emulsions for 3D Printing Elastomers," Advanced Functional Materials, 1707032 (2018).
40. Badea, A.; McCracken, J. M.; Tillmaand, E. G.; Kandel, M. E.; Rubakhin, S. S.; Popescu, G.; Sweedler, J. V.; Nuzzo, R. G., 3D-Printed pHEMA Materials for Topographical and Biochemical Modulation of Dorsal Root Ganglion Cell Response, ACS Applied Materials and Interfaces 2017, 9, 30318–30328.
41. X. Yu, L. L. Goddard, J. Zhu, X. Li, and X. Chen, Passive wavelength tuning and multichannel photonic coupling using monolithically integrated vertical micro resonators on ridge waveguides, Appl. Phys. Lett., 112, 021108 (2018).

Quantifying the Phase Behavior and Surface Chemistry of $CsPbBr_3$ Quantum Dots

Richard L. Brutchey
Department of Chemistry, University of Southern California, Los Angeles, CA 90089, USA

Program Scope

A 2015 report from the BESAC on *Challenges at the Frontiers of Matter and Energy* states that next-generation energy technologies will require the design and synthesis of materials trapped in states away from equilibrium. Such *metastable phases* – that is, kinetically trapped phases with positive free energies above the equilibrium state – are pervasive in Nature, but much of our current understanding of synthetic design is based on materials operating at the condition of thermodynamic equilibrium. This provides a new target of opportunity for functional materials by potentially controlling the synthesis of matter not at thermodynamic equilibrium. In order to seize this target of opportunity, better control over arriving at a desired structure (or polymorph) is needed. This will require the development of new molecular routes in order to navigate kinetic pathways in systems away from equilibrium. Using a materials chemistry approach, we will execute basic research with the following specific and deliverable objectives:

1. Leverage kinetically controlled solution methods to synthesize nanocrystals in metastable phases.
2. Perform high-level structural characterization of the resulting nanocrystals to probe the time, temperature, and/or length scales at which the structure persists.

Good progress has been achieved on these objectives since September 2017 as applied to lead halide perovskite quantum dots.

Recent Progress

Following the publication of a facile hot-injection synthesis for producing monodisperse lead halide perovskite quantum dots (QDs) of $CsPbX_3$ (where X = Cl, Br, I),[1] these nanocrystals have been the subject of intense interest. Lead halide perovskite QDs feature high photoluminescence (PL) quantum yields and narrow emission line widths, suppressed photoluminescence blinking, long carrier lifetimes, and band gaps that are tunable over a wide color gamut, making them particularly attractive for next-generation optoelectronic applications such as LEDs and solar cells.[2] The attractive optoelectronic properties that these materials possess are strongly dependent on variations in their crystal structure and their surface composition. For example, results show large changes in the PL intensity and lifetime of $CsPbBr_3$ QDs over a broad temperature window that contains the symmetry-lowering phase transitions in bulk $CsPbBr_3$, suggesting that local distortions play an important role in determining these properties.[3] Moreover, surface treatments have been used to stabilize the metastable black perovskite phase of $CsPbI_3$.[4] While a great deal of effort has gone into exploring the synthesis and properties of these 0-D QDs, almost no accompanying work has gone into developing a quantitative understanding of their structure and surface chemistry.

Colloidal $CsPbBr_3$ QDs were originally reported to possess a metastable cubic, α-perovskite structure at room temperature based on laboratory X-ray diffraction. It was posited that this was the origin of their bright PL emission since the orthorhombic phase of the bulk material at room temperature is non-emissive. We clarified that the QDs actually possess the same orthorhombic, γ-perovskite structure at room temperature as the bulk material using synchrotron X-ray total scattering;[5] this structural information is essential for drawing structure-property relationships and for accurate electronic structure calculations. Herein, we describe our recent efforts in quantifying the phase behavior of $CsPbBr_3$ QDs as a function of temperature, and the thermodynamics of ligand binding to the as-prepared QDs.

Depressed Phase Transitions and Thermally Persistent Local Distortions in $CsPbBr_3$ QDs. Synchrotron X-ray diffraction data were collected on the $CsPbBr_3$ QDs at temperatures spanning the phase transitions of the bulk analog using the 11-BM instrument at the Advanced Photon Source (APS) at Argonne National Laboratory. The refinements to the T = 22 °C data (**Fig. 1a**) show that the $CsPbBr_3$ QDs contain orthorhombic domains that are coherent over sufficiently long scales to generate the observed orthorhombic-only reflections. The reflection at $2\theta = 7.45°$ is absent from the diffraction pattern collected at T = 70 °C (**Fig. 1b**). All existing peaks in this pattern are satisfactorily fit by tetragonal structure, with $\chi^2 = 1.723$ compared to $\chi^2 = 3.127$ for the cubic structure. The absence of the (031), (211), and (112) reflections from the T = 70 °C data suggests that the average structure has become tetragonal at this temperature. The remaining diffraction peaks that are not indexed by the cubic structure are absent from the diffraction pattern at T = 120 °C (**Fig. 1c**). At this temperature, the cubic structure gives a qualitatively satisfactory fit with $\chi^2 = 2.945$. Evolution of the Bragg diffraction in the $6.9° < 2\theta < 8.9°$ range suggests that the temperatures for the orthorhombic-to-tetragonal and tetragonal-to-cubic phase transitions are substantially depressed compared to values for bulk $CsPbBr_3$. The orthorhombic-to-tetragonal phase transition occurs at $50\ °C < T_{\gamma\text{-}\beta} < 59\ °C$, compared $T_{\gamma\text{-}\beta} = 88$ °C for bulk $CsPbBr_3$. The tetragonal-to-cubic phase transition occurs at $108\ °C < T_{\beta\text{-}\alpha} < 117\ °C$, compared with $T_{\beta\text{-}\alpha} = 130$ °C for the bulk material.

To investigate the atomistic nature of changes occurring in the vicinity of the phase transitions observed in the average structure, synchrotron X-ray total scattering data were collected at a series of temperatures using 11-ID-B at the APS. Fits to the pair distribution functions (PDFs) extracted from data collected at T = 22 and 160 °C are given in **Figs. 2a and b**, respectively. At both 22 and 160 °C, the orthorhombic structure provides a qualitatively and

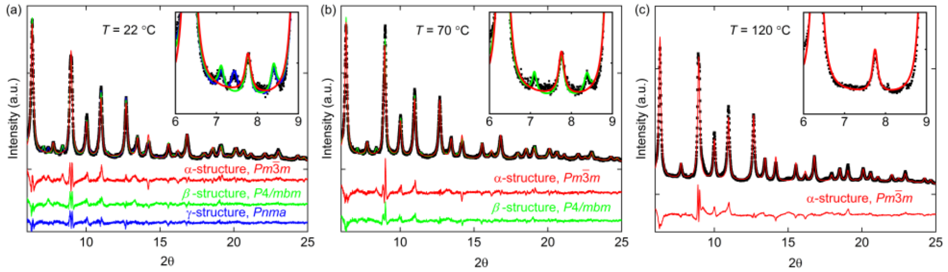

Fig. 1 Synchrotron X-ray diffraction patterns and Rietveld refinements to the cubic $Pm\bar{3}m$ (red), tetragonal $P4/mbm$ (green), and orthorhombic $Pnma$ (blue) structures collected at (a) T = 22 °C, (b) T = 70 °C, and (c) T =120 °C, and the residuals of those fits. $\lambda = 0.457$ Å for all experiments.

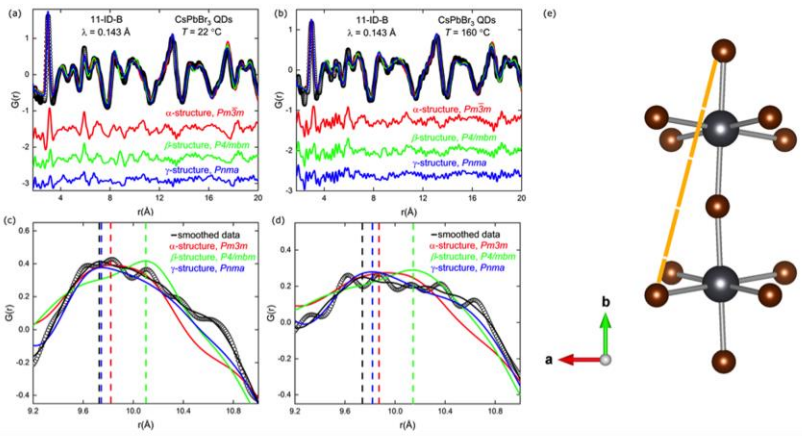

Fig. 2 PDFs extracted from data collected at (a) T = 22 °C and (b) 160 °C along with fits to the cubic, tetragonal, and orthorhombic models using $r_{\max}$ = 20 Å. The lines provided in the magnification of the data at (c) T = 22 °C and (d) 160 °C show the center of the feature generated by the Br-Br pair distance highlighted in (e).

statistically superior fit. The difference is most pronounced for features in the PDF that are generated by the Br-Br and Br-Pb pair distances that are affected by the axial tilting of $PbBr_6$ octahedra, which gives the orthorhombic distortion. **Figs. 2c and d** show the feature in the PDF that corresponds to the Br-Br interatomic distance depicted in **Fig. 2e**, at T = 22 and 160 °C, respectively. At both temperatures, the orthorhombic model provides a superior fit to both the maximum and shape of the feature. The coherence length of the orthorhombic structure is at least r = 40 Å (or roughly 1/2 of the nanocrystal edge length) up to at least 160 °C. This indicates that that the orthorhombic distortion persists at the local scale above the temperature at which the tetragonal-to-cubic phase transition in the average structure has occurred. Furthermore, the magnitude of the local distortion is weakly dependent on temperature for temperatures less than 160 °C; this weak dependence suggests that the phase transitions that occur in $CsPbBr_3$ QDs possess an order-disorder, rather than displacive character.

Quantifying the Thermodynamics of Ligand Binding to $CsPbBr_3$ QDs. We quantified the thermodynamics of ligand binding to $CsPbBr_3$ QDs through the use of carboxylic acid and amine-based ligands possessing a terminal vinyl group that is spectroscopically distinct from the internal alkenyl protons of the native oleylamine and oleic acid ligands. This allows the free and bound fractions of both ligands to be simultaneously tracked, thereby providing valuable thermodynamic data on ligand binding for these QDs.[6] The bound oleate surface density was calculated to be 1.5–1.8 oleate nm^{-2}; because the ligands bind in a $NC(X)_2$ motif,[7] we can assume that for every oleate there is a alkylammonium ion pair, therefore leading to an overall ligand density of 3.0–3.6 ligands nm^{-2}.

Exchange reactions were performed with a long-chain carboxylic acid ligand that possess a terminal vinyl group. Free and bound fractions of both the native and incoming ligands can be quantified, allowing the surface equilibrium and associated thermodynamic parameters to be calculated. For example, upon titration of 10-undecenoic acid into a suspension of $CsPbBr_3$ QDs at room temperature, the bound and free states of oleic acid (δ = 5.73 ppm bound, 5.54 ppm free) and 10-undecenoic acid (δ = 5.32 and 6.12 ppm bound, 5.13 and 5.90 ppm free) are all well resolved in the solution ^{1}H NMR spectra. As increasing amounts of 10-undecenoic acid are titrated into the QD suspension, the amount of bound oleate decreases as the amount of bound 10-undecenoate increases (**Fig. 3a**). In addition, there is a middle alkenyl peak that is attributed to physisorbed oleic acid, which sharpens and shifts upfield toward the free oleic acid peak with increasing concentrations of 10-undecenoic acid. Quantification of the bound and free fractions of oleic acid and the incoming ligand over the titration series gives an average equilibrium constant K_{eq} of 1.97 ± 0.10. The equilibrium constant for exchange with 10-undecenoic acid equates to a ΔG of -1700 ± 100 J mol^{-1}, signifying the reaction is exergonic at room temperature. A van't Hoff plot of variable temperature measurements (**Fig. 3b**) revealed an endothermic reaction (ΔH = 14.3 kJ mol^{-1}) and a positive ΔS, indicating that ligand exchange is spontaneous at elevated temperatures. A gradual decrease in band-edge PL intensity is observed upon exchange with 10-undecenoic acid; because the 10-undecenoic acid-for-oleate exchange is 1:1, the Cs:Pb ratio does not change during exchange, and the PL emission energy is likewise invariant, this suggests that stoichiometric surface reconstruction occurs during exchange that reduces PL intensity.

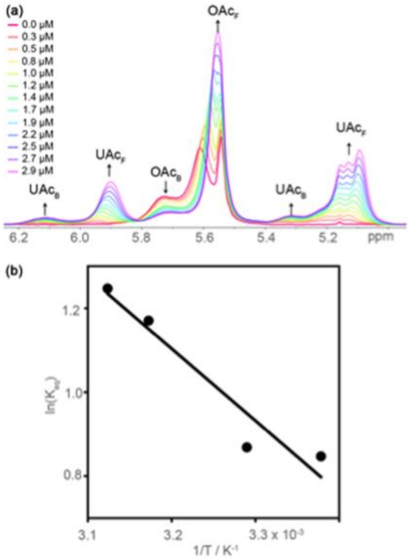

Fig. 3 (a) ^{1}H NMR spectra of $CsPbBr_3$ QD suspension possessing oleic acid (OAc) and dodecylamine native ligands, titrated with increasing amounts of 10-undecenoic acid (UAc), showing both free (F) and bound (B) fractions. (b) Van't Hoff plot of $CsPbBr_3$ QD suspension with 10-undecenoic acid at temperatures ranging from 298 to 320 K.

Future Plans

We will explore the average and local structures of $BaTiO_3$ nanocrystals as a function of temperature using synchrotron X-ray diffraction and total scattering measurements to draw structural parallels between these traditional perovskite oxide nanocrystals and the all-inorganic $CsPbBr_3$ QDs. The ligand binding information will be used to understand why and how certain ligands, such as phosphonic acids, stabilize metastable phases of $CsPbI_3$ QDs in the solid state.

References

(1) Protesescu, L.; et al. *Nano Lett.* **2015**, *15*, 3692; (2) Huang, H.; et al. *NPG Asia Mater.* **2016**, *8*, 328; (3) Diroll, B. T.; et al. *Adv. Funct. Mater.* **2017**, *27*, 1606750; (4) Swarnkar, A.; et al. *Science* **2016**, *354*, 92; (5) Cottingham, P.; et al. *Chem. Commun.* **2016**, *52*, 5246; (6) Knauf, R. R.; et al. *Chem. Mater.* **2016**, *28*, 4762; (7) De Roo, J.; et al. *ACS Nano* **2016**, *10*, 2071.

Publications

(1) Grabowski, C. A.; Fillery, S. P.; Koerner, H.; Tchoul, M.; Drummy, L.; Beier, C. W.; **Brutchey, R. L.**; Durstock, M. F.; Vaia, R. A. Dielectric Performance of High Permittivity Nanocomposites: Impact of Polystyrene Grafting on $BaTiO_3$ and TiO_2. *Nanocomposites* **2016**, *2*, 117-124.

(2) Cottingham, P.; **Brutchey, R. L.** Compositionally Dependent Phase Identity of Colloidal $CsPbBr_{3-x}I_x$ Quantum Dots. *Chemistry of Materials* **2016**, *28*, 7574-7577.

(3) Culver, S. P.; **Brutchey, R. L.** Lanthanide-Activated Scheelite Nanocrystal Phosphors Prepared by the Low-Temperature Vapor Diffusion Sol-Gel Method. *Dalton Transactions* **2016**, *45*, 18069-18073.

(4) Margossian, T.; Culver, S. P.; Larmier, K.; Zhu, F.; **Brutchey, R. L.**; Copérert, C. Composition-Dependent Surface Chemistry of Colloidal $Ba_xSr_{1-x}TiO_3$ Perovskite Nanocrystals. *Chemical Communications* **2016**, *52*, 13791-13794.

(5) Lu, H.; **Brutchey, R. L.** Tunable Room-Temperature Synthesis of Coinage Metal Chalcogenide Nanocrystals from *N*-Heterocyclic Carbene Synthons. *Chemistry of Materials* **2017**, *29*, 1396-1403.

(6) Barim, G.; Cottingham, P.; Zhou, S.; Melot, B. C.; **Brutchey, R. L.** Investigating the Mechanism of Reversible Lithium Insertion into Anti-NASICON $Fe_2(WO_4)_3$. *ACS Applied Materials & Interfaces* **2017**, *9*, 10813-10819.

(7) Cottingham, P.; **Brutchey, R. L.** Depressed Phase Transitions and Thermally Persistent Local Distortions in $CsPbBr_3$ Quantum Dots. **2018**, manuscript submitted.

New Superconducting Materials

R.J. Cava
Department of Chemistry and Materials Institute Princeton University, Princeton NJ 08544, USA

i. Program Scope: The Solid State/Materials Chemistry of new superconducting materials; with the goal of finding new superconducting compounds based on a “bonding + structure = properties” view, a materials chemistry perspective, rather than the “fermi surface geometry + *k* space coupling = properties” view, a materials physics perspective. Both views are critically important in electronic and magnetic materials such as superconductors, in the opinion of the PI, however, and so, finally, our goal is to use this joint view to find new superconducting compounds and to chemically-manipulate previously known superconductors to change their properties, through the structural and synthetic tools of solid state materials chemistry.

ii. Recent Progress. Project I – Chemical manipulation of the superconductivity in $NbSe_2$

Transition metal dichalcogenides (TMDCs) have been studied for decades due to the rich electronic properties that arise due to their low structural dimensionality. (*1-4*); 2H-$NbSe_2$ was one of the earliest layered TMDC materials known to superconduct, with a critical temperature T_c ~7.3 K. This T_c is significantly higher than is encountered for the many other TMDC superconductors known, where Tc is commonly in the 2-4 K range. It is the most studied of the layered transition metal dichalcogenide superconductors, with almost countless experimental and theoretical papers focusing on its behavior over the past 50 years. (see, e.g.*5-14*) The relation between Fermi surface nesting and its superconductivity is still under debate (*12*), for example, even though 2H-$NbSe_2$ has been considered a conventional superconductor for decades (*13*). In addition, due to recent new concepts, such as *d*-wave pairing in cuprates *(14)* and two-gap superconductivity in MgB_2 (*15-17*), studies of the superconductivity in 2H-$NbSe_2$ have recently increased in number (*18-29*).

In our DOE-supported work, we reported a study of the intercalation of Cu into 2H-$NbSe_2$ to form 2H Cu_xNbSe_2. The T_c decreases with increasing Cu content, as is commonly found when introducing “impurities” into optimal superconductors, but the way that superconductivity is suppressed is quite unexpected: An S-shaped character is observed in T_c vs. x, with an inflection point near x = 0.03 and a leveling off, at higher x, of the abnormally high 7 K T_c in the pure phase to a T_c value near 4 K – back down to where it is commonly observed for a layered TMDC. (Figure 1). Our temperature-dependent electron diffraction study (Figure 2) revealed a minor change in the q-vector of $NbSe_2$’s CDW on Cu intercalation - degradation but not destruction of the coherence of the CDW, especially in the direction perpendicular to the layers, and also the extension of CDW fluctuations, evidenced by diffuse scattering, to room temperature. Comparison of the superconducting phase diagram for Cu_xNbSe_2 to those for the other doped 2H-$NbSe_2$ materials Fe_xNbSe_2 and $NbSe_{2-x}S_x$ shows its unexpected character (Figure 1). The underlying reason for this usual S-shape behavior of T_c and the electronic characteristics that give rise to it have not been determined. However, based on the fact that the Tc is unusually high for pure $NbSe_2$ and then settles in to the usual value for TMDCs for Cu_xNbSe_2, it is not unreasonable to speculate that Cu doping destroys the higher energy paring channel that makes $NbSe_2$ unusual among the layered TMDCs. Future detailed characterization experiments and theoretical treatments will be required to determine whether this speculation is indeed the case.

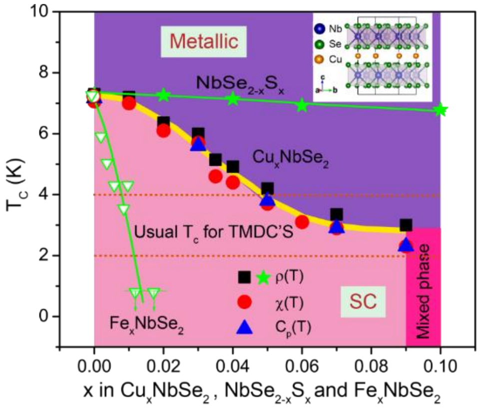

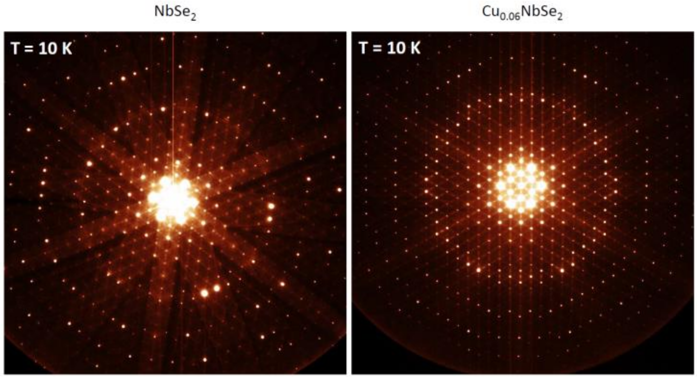

Fig. 1. (Left) The superconducting phase diagram for 2H-Cu_xNbSe_2 compared to those of 2H $NbSe_{2-x}S_x$ and 2H-Fe_xNbSe_2. The usual range of Tc's for transition metal dichalcogenides is illustrated by the dashed lines. "SC" and "metallic" label the superconducting and metallic regions T_cs determined for the materials in the current study from resistivity, magnetic susceptibility and specific heat characterization, $\rho(T)$, $\chi(T)$ and $C_p(T)$ respectively. The limit of the Cu_xNbSe_2 solubility is x = 0.09; Upper right inset – schematic of the crystal structure of Cu_xNbSe_2. **Fig. 2. (Right) The 10 K electron diffraction patterns over a wide volume of reciprocal space in $NbSe_2$ and $Cu_{0.06}NbSe_2$** The intensity distributions of the CDW reflections strongly suggest: 1) The atomic displacements associated with the CDW modulation are longitudinal; and 2) The CDW modulation is relatively weakly correlated between layers (along the *c*-axis) for both materials. For $Cu_{0.06}NbSe_2$, the correlation of the CDW along the c-axis is weaker.

Project II – A new superconductor based on Ta@Ir_7Ge_4 endohedral clusters

Heavy elements such as iridium often form compounds with interesting physical properties due to the presence of the strong spin orbit coupling of Ir; as such, Ir-based compounds have been of particular recent interest *(30-31)*. Our interest is in superconductivity in new Ir-containing compounds where the presence of strong spin orbit coupling may affect the superconducting properties. In ternary intermetallic compounds based on combinations of three elements with different chemical characteristics, "1:2:2" phases are extremely common. Remarkably, despite the great structural similarities and known structural phase transitions between the $CaBe_2Ge_2$ structure type and the $ThCr_2Si_2$-type structures *(32-33)*, which are related through the inversion of the order of one of the constituent layers, almost all of the superconducting 1:2:2 phases based on Ir exist in the $CaBe_2Ge_2$ structure type only *(34-35)*. The starting point of this work was to find one such phase with unusual chemical constituents.

In our DOE-supported program on superconductivity we found a new, superconducting 1:2:2 Ir-based material with a non-archetypical previously unreported crystal structure type, $TaIr_2Ge_2$. Instead of hosting layered features like are found in $CaBe_2Ge_2$ and $ThCr_2Si_2$-type structures, cluster-type structural fragments are found, as in many metallic alloys *(36)*. The previously unreported structure type displayed by this new ternary compound, determined by single crystal X-Ray diffraction *(37)* is understood as consisting of corner and face -sharing Ta@Ir_7Ge_4 clusters. (Figure 3.) The relationship of this material to other germanides was established *(38-40)*. Further, in order to gain a better understanding of the cluster formation in $TaIr_2Ge_2$, the calculated band structure and the density of states based on the VASP results was considered. The resulting diagrams can be found in Figure 4, with the band structure located in the right-most panel. Below values of 1.5 eV below the Fermi energy, primarily Ir and Ge bulk metallic states are observed. However, around the Fermi level, a few bands split off from the main set of states. These consist mostly of contributions from partially hybridized Ta 5*d* and 6*s* states, indicating a weak interaction between valence electrons from Ta in these states and those from Ir/Ge. Considering the total density of states near the Fermi level shown in the left panel of the figure, another significant feature is revealed - the deep pseudogap below the Fermi level. The pseudogap corresponds to 28 valence electrons per $TaIr_2Ge_2$, which is associated with the chemical stability of the compound.

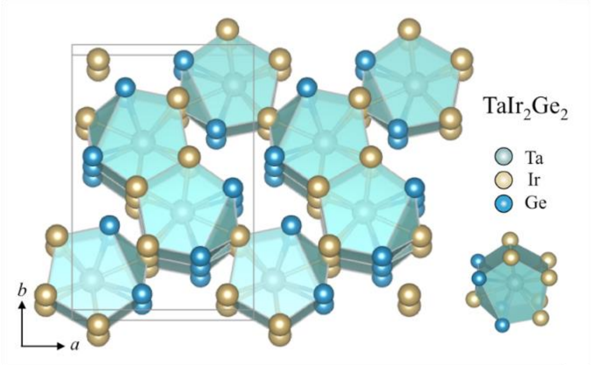

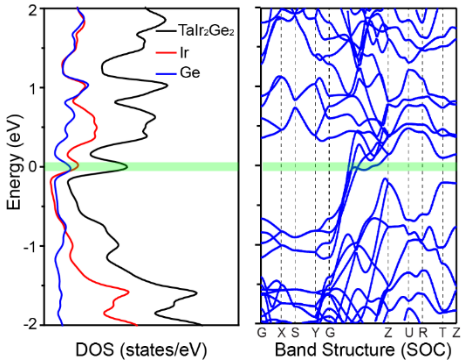

Figure 3: (Left) Crystal structure of $TaIr_2Ge_2$, emphasizing the $Ta@Ir_7Ge_4$ clusters. The tantalum is shown in pale green, iridium in gold, and germanium in blue. Inset: A single 11-coordinate cluster. **Figure 4: (Right)** Calculated electronic structure for $TaIr_2Ge_2$. Left: density of states (DOS) in the vicinity of the Fermi level, right: band structure calculations. Total band structure and density of states curves were calculated with spin-orbit coupling included.

Our measurements showed that the material becomes superconducting below 3.5 K, and specific heat and critical field measurements indicated that it is a weak coupling type II BCS superconductor. There is no obvious indication, in our simple characterization, of anomalous properties that might arise due to the strong spin orbit coupling of Ir, but analogies of the superconducting parameters of $TaIr_2Ge_2$ to those of $PbTaSe_2$ suggest that more detailed electronic characterization may be of future interest.

iii. Future Plans 1. To continue our work in the use of the principles of materials chemistry, in connection with our experimental expertise and knowledge of materials physics, to discover new superconductors. **2**. To continue our work focused on correlations between superconductivity and materials chemistry in layered compounds of the early transition elements. 3. To continue our work on superconductivity in the intergrowth tungsten bronze family, Sb_xWO_{3+x} for example. 3. To continue our work to search for superconductivity and new compounds in ternary oxides based on early transition metals such as Mo in its oxides.

iv. References

1. R. L Withers, L. A Bursil, *Philos. Mag.* **B43**, 635-672 (1981).
2. C. J., Arguello, et. al, *Phys. Rev. B* **89**, 235115 (2014).
3. A. Soumyanarayanana, et. al., *Proc. Natl. Acad. Sci. USA* **110**, 1623-1627 (2013)
4. B. T. Matthias, T. H. Geballe, and V. B. Compton, *Rev. Mod. Phys*. 35, 1 1963.
5. E. Revolinsky, E. P. Lautenschlager, C. H. Armitage. *Solid State Common.* **1**, 59-61 (1963)
6. J. A. Wilson, F. J. Di Salvo, S. Mahajan, *Phys. Rev. Lett*. **32**, 882 (1974).
7. E. Boaknin, et. al., *Phys. Rev. Lett.* **90**, 117003 (2003).

8. H. Suderow, V. G. Tissen, J. P. Brison, J. L. Martínez, and S. Vieira, *Phys. Rev. Lett.* **95**, 117006 (2005).
9. C. H. Du, et. al., *J. Phys.: Condens. Matter* **12,** 5361–5370 (2000).
10. X. X. Xi, L. Zhao, Z. F. Wang, H. Berger, L. F., J. Shan, K. F. Mak, *Nat. Nanotechnol.* **10**, 765-770 (2015).
11. I. Naik, A. K. Rastogi, *Pramana* **76**, 957-963 (2011).
12. T. Kiss, T. Yokoya, A. Chainani, S. Shin, T. Hanaguri, M. Nohara, H. Takagi, https://arxiv.org/vc/cond-mat/papers/0310/0310326v1.pdf.
13. M. D. Johannes, I. I. Mazin, C. A. Howells, *Phys. Rev. B* **73**, 205102 (2006).
14. R. C. Corcoran, et. al., *J. Phys. Condens. Matter*. **6**, 4479-4492 (1994).
15. C. C. Tsuei, J. R. Kirtley, *Physica C: Superconductivity*, **367**, 1-8 (2002).
16. S. Souma, et. al., *Nature* **423**, 65-67 (2003).
17. T. Örda, N. Kristoffel, *Physica C: Superconductivity* **370**, 17-20 (2002).
18. N. Kristoffel, T. Örd, K. Rägo, *EPL* **61**, 109–115 (2003).
19. C. L. Huang, et. al., *Phys. Rev. B* **76**, 212504 (2007).
20. E. Boaknin, et. al. *Phys. Rev. Lett.* **90**, 117003 (2003).
21. M. Zehetmayer, H. W. Weber *Phys. Rev. B* **82**, 014524 (2010).
22. R. Prozorov, T. Olheiser, R. W. Giannetta, *Phys. Rev. Lett*. **98**, 057003 (2007).
23. J. G. Rodrigo, S. Vieira, *Physica C: Superconductivity*. **404**, 306-310 (2004).
24. I. Guillamon, H. Suderow, F. Guinea, S. Vieira. *Phys. Rev. B* **77**, 134505 (2008).
25. Y. Noat, T. Cren, F. Debontridder, D. Roditchev, W. Sacks, P. Toulemonde, and A. San Miguel, *Phys. Rev. B* **82**, 014531 (2010).
26. D. J. Rahn, S. Hellmann, M. Kalläne, C. Short, T. K. Kim, L. Kipp, and K. Rossnagel, *Phys. Rev. B* **85** 224532 (2012).
27. T. Yokoya, T. Kiss, A. Chainani, S. Shin, M. Nohara, H. Takagi, Fermi Surface Sheet-Dependent Superconductivity in 2H-NbSe$_2$, *Science* **294** 2518-2520 (2001).
28. T. Kiss, T. Yokoya, A. Chainani, S. Shin, T. Hanaguri, M. Nohara, H. Takagi, *Nature Phys.* **3**, 720 - 725 (2007).
29. J. Rodríguez-Carvajal, *Comm. Powder Diffr.* **26**, 12-19 (2001).
30. Y. Okamoto, M. Nohara, H. Aruga-Katori, and H. Takagi, Phys. Rev. Lett. **99**, 4 (2007).
31. N. Haldolaarachchige, Q. Gibson, L.M. Schoop, H. Luo, and R.J. Cava, J. Phys. Condens. Matter **27**, 185701 (2015).
32. W.B. Pearson, P. Villars, and L.D. Calvert, *Pearson's Handbook of Crystallographic Data for Intermetallic Phases* (American Society for Metals, Metals Park, OH, 1985).
33. C. Zheng and R. Hoffmann, J. Am. Chem. Soc. **108**, 3078 (1986).
34. R.N. Shelton, H.F. Braun, and E. Musick, Solid State Commun. **52**, 1 (1984).
35. M. Vališka, J. Pospišil, J. Prokleška, M. Diviš, A. Rudajevová, and V. Sechovský, J. Phys. Soc. Japan **81**, 1 (2012).
36. J.-M. Dubois, Nat. Mater. **9**, 287 (2010).
37. G.M. Sheldrick, Acta Crystallogr. Sect. C Struct. Chem. **71**, 3 (2015).
38. A.E. Dwight and P.A. Beck, Trans. Am. Inst. Min. Metall. Eng. **215**, 976 (1959).
39. R. Kubiak, R. Horyn, H. Broda, and K. Lukaszewicz, Bull. l'Academie Pol. Des Sci. Ser. Des Sci. Chim. **20**, 429 (1972).
40. G. Venturini, M. Kamta, E. McRae, J.F. Mareche, B. Malaman, and B. Roques, Mater. Res. Bull. **21**, 1203 (1986).

Publications as a result of this DOE-supported research program late 2016 to mid 2018

1. “Superconductivity in $CaBi_2$”, M.J. Winiarski, B. Wiendlocha, S. Golab, S.K. Kushwaha, P. Wisniewski, D. Kaczorowski, J.D. Thompson, R.J. Cava, and T. Klimczuk, *Physical Chemistry Chemical Physics*, **18** 21737 (2016).
2. “Growth, Crystal Structure and Magnetic Characterization of Zn-Stabilized $CePtIn_4$”, E.M. Carnicom, T. Klimczuk, F. von Rohr, M.J. Winiarski, T. Kong, K. Stolze, W.W. Xie, S.K. Kushwaha, R.J. Cava, *J. Phys. Soc. Jpn.* **86** 084710 (2017).
3. “Characterization of Primary Carrier Transport Properties of the Light-Harvesting Chalcopyrite Semiconductors $CuIn(S_{1-x}Se_x)_2$”, Jessica J. Frick, Satya K. Kushwaha, Robert J. Cava, and Andrew B. Bocarsly, *J. Phys. Chem. C*, **121** 17046 (2017).
4. “Monoclinic 122-Type $BaIr_2Ge_2$ with a Channel Framework: A Structural Connection between Clathrate and Layered Compounds”, X. Gui, T.R. Chang, T. Kong, M.T. Pan, R.J. Cava, and W.W. Xie, *Materials* **10**, 818(2017).
5. “Superconductivity in a new intermetallic structure type based on endohedral $Ta@Ir_7Ge_4$ clusters”, L.C. Srivichitranond, E.M. Seibel, W.W. Xie, Z. Sobczak, T. Klimczuk, R.J. Cava, *Phys. Rev. B* **95** 174521 (2017).
6. “S-Shaped Suppression of the Superconducting Transition Temperature in Cu-Intercalated $NbSe_2$”, H. Luo, J.Strychalska-Nowak, J. Li, J. Tao, T. Klimczuk, and R.J. Cava, *Chemistry of Materials* **29** 3704 (2017).
7. “The $LaPdIn_4$ indide and elementary properties of the $LaTIn_4$ (T = Ni, Pd, Pt) materials family”, E.M. Carnicom, W.W. Xie, E.M. Seibel, T. Klimczuk, and R.J. Cava, *Journal of Alloys and Compounds* **694** 682 (2017).
8. “The effect of Mg-doping and Cu nonstoichiometry on the photoelectrochemical response of $CuFeO_2$”, A. Wuttig, J. W. Krizan, J. Gu, J.J. Frick, R.J. Cava, and A.B. Bocarsly, *Journal of Materials Chemistry A* **5** 165 (2017).
9. “New sigma-phases in the Nb-X-Ga and Nb-X-Al systems (X = Ru, Rh, Pd, Ir, Pt, and Au)”, E.M. Carnicom, W.W. Xie, T. Klimczuk, and R.J. Cava, *Dalton Trans.* **46** 14158 (2017).
10. “Superconductivity in the Nb-Ru-Ge sigma phase”, E.M. Carnicom; W.W. Xie; Z. Sobczak; T. Kong; T. Klimczuk; and R.J. Cava, *Phys. Rev. Materials* **1** 074802 (2017).
11. “Bursting at the seams: Rippled monolayer bismuth on $NbSe_2$”, A. Fang; C. Adamo; S. Jia; R.J. Cava; S.C. Wu; C. Felser; and A. Kapitulnik, *Sci. Advances.* **4** 0330 (2018).
12. “$RE_3Mo_{14}O_{30}$ and $RE_2Mo_9O_{19}$, Two Reduced Rare-Earth Molybdates with Honeycomb-Related Structures (RE = La-Pr)”, S. Forbes; T. Kong; and R.J. Cava, *Inorg. Chem.* **57** 3873 (2018).
13. “Stable Hydrogen Evolution from an $AgRhO_2$ Photocathode under Visible Light”, J.E. Park; Y. Hu; J.W. Krizan; Q.D. Gibson; U.T. Tayvah; A. Selloni; R.J. Cava; and A.B. Bocarsly, *Chem. Mater.* **30** 2574 (2018).
14. “$TaRh_2B_2$ and $NbRh_2B_2$: Superconductors with a chiral noncentrosymmetric crystal structure”, E.M. Carnicom; W.W. Xie; T. Klimczuk; J.J. Lin; K. Gornicka; Z. Sobczak; N.P. Ong; and R.J. Cava, *Sci. Advances* **4** 7969 (2018).

Synthesizing New Metal Organic Frameworks with Tailored Physical and Chemical Properties

Yves J. Chabal, University of Texas at Dallas
Jing Li, Rutgers University
Timo Thonhauser, Wake Forest University

Program Scope

The aim of this program is to develop a fundamental understanding of the interaction of guest molecules in porous metal organic framework (MOF) materials, using a combination of novel synthesis, *ab initio* modeling, and characterization. In particular, we combine high-pressure/low-temperature *in-situ* infrared (IR) absorption and Raman measurements with gas adsorption-desorption experiments and calculations based on density functional theory. Our goal is to study molecular adsorption, diffusion, and reactions in different MOF materials, with a particular emphasis on their effect on the physical and chemical properties of the MOF host materials. The short-term impact of the proposed work is the control and understanding of common MOF systems, with important impact on applications and industrial processes from gas storage and sequestration to catalysis and sensors. The long-term impacts are the development of (i) theoretical and experimental methods to gain a fundamental understanding of molecular interactions within MOFs, and (ii) new guidelines to synthesize microporous MOFs with tailored physical and chemical properties.

Recent Progress

a) *Ligand-free, isolated gold nanoparticles in metal-organic framework materials [1]* – Gold nanoparticles (NPs) exhibit optical, catalytic, and physical properties that are scientifically fascinating and essential for many applications. However, the challenge is to synthesize and disperse ligand-free NPs. We demonstrate that isolated, ligand-free Au NPs (<2nm) can be synthesized by photo-reduction of $HAuCl_4$ inside a novel class of thiol-functionalized MOFs, i.e. MOF-808-SH. A combination of physical, imaging, and spectroscopic measurements, together with *ab initio* calculations, confirm that the Au NPs are dispersed inside the bulk of the MOFs and demonstrate that the thiol group is critical to stabilize the Au NPs inside individual pores. The thiol-functionalized MOF thus fulfills a dual purpose: it fosters the nucleation of the Au NP and also provides confinement and a framework that keeps the NPs separate. In a series of photocatalytic water reduction and TEM studies we show that the Au NPs are remarkably stable (<1.5% diameter change/hour), even under harsh aqueous and irradiation environments necessary for catalytic applications.

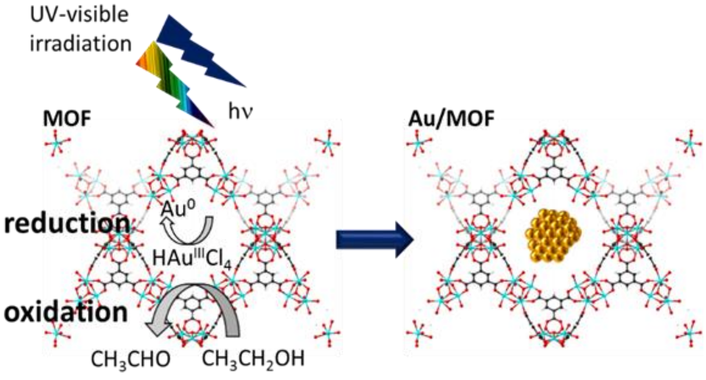

Figure 1. MOFs as nano-reactors for the growth of Au NPs via photo-reduction.

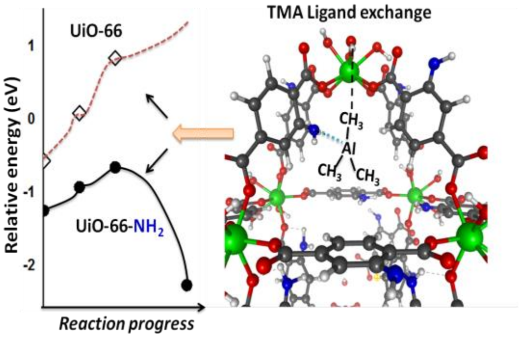

Figure 2. Calculated energy profile for the reaction of TMA with μ_3-OH in UiO-66.

b) *Reactivity of atomic layer deposition precursors with OH/H_2O-containing metal organic framework materials [2]* – The ability of atomic layer deposition (ALD) to incorporate metal atoms or chemical groups into MOFs offers an interesting alternative to chemically modify MOFs for applications such as catalysis and gas separation, for which transport, adsorption, and the reaction of gases is critical. Optimization of these deposition processes requires an understanding of the underlying reaction mechanisms that is best derived from *in situ* characterization. We have therefore combined *in situ* infrared spectroscopy and X-ray photoelectron spectroscopy with *in situ* sputtering and *ab initio* calculations to elucidate the reaction mechanisms of the common ALD precursors trimethylaluminium (TMA), diethylzinc (DEZ), and titanium tetrachloride ($TiCl_4$) with several Zr-MOFs containing hydroxyl (OH) and water (H_2O) groups. We find that the reactivity of OH groups in the $Zr_6(\mu_3\text{-}OH)_4(\mu_3\text{-}O)_4(OH)_x(OH_2)_y$ cluster node is highly dependent on their location, accessibility, and chemical environment. For instance, the activation temperatures of the OH groups of Zr_6 clusters with TMA decrease with the node connectivity: 250, 150, and 24°C for UiO-66-NH_2, Zr-abtc, and MOF-808, respectively. Interestingly, and in contrast to un-functionalized UiO-66, the hydroxyl groups in UiO-66-NH_2 are found to react with TMA molecules. *Ab initio* calculations reveal that the NH_2 group is directly responsible for catalyzing this reaction by anchoring the TMA in close proximity to the target OH. Finally, we show that TMA easily reacts with water adsorbed on the external surfaces of wet MOFs crystals at room temperature, forming a thick Al_2O_3 blocking layer on the periphery of the MOF crystals. These findings provide a basis for the design and modification of MOFs by ALD processes.

c) *Topology-directed tuning of Zr-MOF pore structures for the separation of C6 alkane isomers [3]* – Applying a topology-directed design strategy, we synthesized a series of highly robust Zr-based metal-organic frameworks with optimized pore structure for efficient separation of C6 alkane isomers, a critical step in the petroleum refining process to produce gasoline with high octane rating. A **ftw** Zr-MOF, i.e. $Zr_6O_4(OH)_4(bptc)_3$, selectively adsorbs a large amount of *n*-hexane while excluding all branched isomers. The *n*-hexane uptake is ~70% higher than that of a benchmark adsorbent, zeolite-5A. A derivative structure with **scu** topology, $Zr_6O_4(OH)_8(H_2O)_4(abtc)_2$, is capable of discriminating all three C6 isomers and yielding a high separation factor for 3-methylpentane over 2,3-dimethylbutane. This property is critical for producing gasoline with further improved quality. Multicomponent breakthrough experiments confirm the separation capability of these two materials. This work provides an excellent example of the effectiveness of a topology-directed approach for the development of MOFs with optimal pore size for industrially relevant separations.

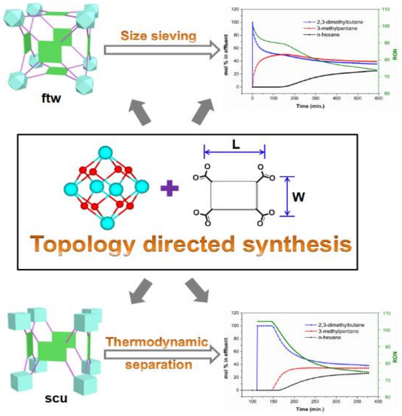

Figure 3. Topology-directed synthesis leads to structures with targeted pore size.

d) *Role of hydrogen bonding on transport of coadsorbed gases in metal-organic framework materials [4]* – We report a novel synergistic effect involving co-adsorption in a prototypical MOF, i.e. MOF-74. We find that addition of NH_3 or H_2O to MOF-74 previously loaded with a variety of small gases (e.g., CO, CO_2, SO_2) prevents the removal of these small gases upon evacuation. We further show, with support of *ab initio* modeling, that this phenomenon is not due to guest-guest binding but instead to an increase in diffusion barrier for these small molecules by H_2O or NH_3 molecules located in the near surface region. Combining *in situ* infrared spectroscopic measurements and DFT calculations, we demonstrate that hydrogen bonding is primarily responsible for the large increase of the diffusion barrier (by a factor of 7 and 8 for CO and CO_2, respectively) along the transport pathway. These relevant findings contribute to the fundamental understanding of co-adsorption in porous materials and dispel common assumptions. For instance, H_2O and NH_3 are usually regarded as impurities that prevent gas adsorption and capture by poisoning active sorption sites. This is clearly not the case here. The mechanism derived from this work also provides a new paradigm to stabilize and trap weakly adsorbed molecules inside MOFs by tuning the diffusion barrier instead of enhancing binding affinity or introducing active adsorption centers.

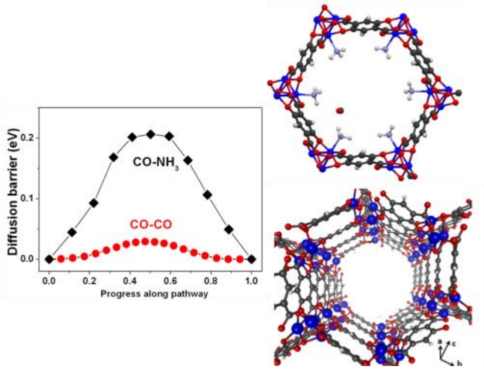

Figure 4. Enhanced diffusion barrier induced by H-bonding interaction during molecular transport in the MOF-74 channel.

e) *Capture of organic iodides from nuclear waste by metal-organic framework-based molecular traps, [5]* – We developed radioactive organic iodide molecular traps by functionalizing water/moisture stable MOF materials to create tertiary amine-binding sites. The molecular trap exhibits a high CH_3I saturation uptake capacity of 71 wt% at 150 °C, more than 340% higher than the industrial adsorbent Ag^0@MOR under identical conditions. The high uptake is attributed to both chemisorption and physisorption. These functionalized MOFs also serve as good adsorbents at low temperatures. Furthermore, the MOF adsorbents can be recycled multiple times without loss of capacity, making recyclability a reality. In combination with their chemical and thermal stability, high capture efficiency and low cost, the MOF adsorbents show strong promise for use as alternative waste capture materials for the nuclear power industry.

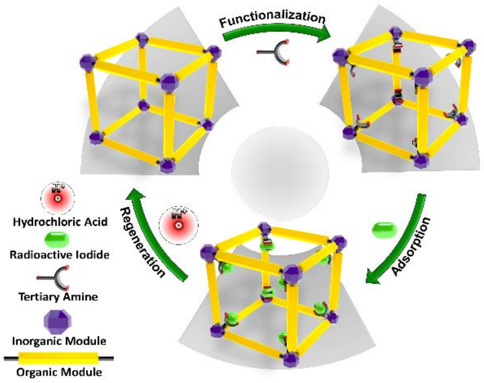

Figure 5. Design of recyclable molecular traps by functionalization of open metal sites.

f) *Interaction of acid gases SO_2 and NO_2 with coordinately unsaturated metal organic frameworks: M-MOF-74 (M = Zn, Mg, Ni, Co) [6] – In situ* infrared spectroscopy and *ab initio* calculations are combined in this work to study the interaction of two corrosive gases, SO_2 and NO_2, with metal organic frameworks M-MOF-74 (M = Zn, Mg, Ni, Co). We find that NO_2 dissociatively adsorbs into MOF-74 compounds, forming NO and NO_3^-. The mechanism is unraveled by considering the Zn-MOF-74 system, for which DFT calculations show that a strong NO_2–Zn bonding interaction induces a significant weakening of the N–O bond, facilitating the decomposition of the NO_2 molecules. In contrast, SO_2 is only molecularly adsorbed into MOF-74 with high binding energy (>90 kJ/mol for Mg-MOF-74 and >70 kJ/mol for Zn-MOF-74). This work gives insight into poisoning issues by minor components of flue gases in metal organic framework materials.

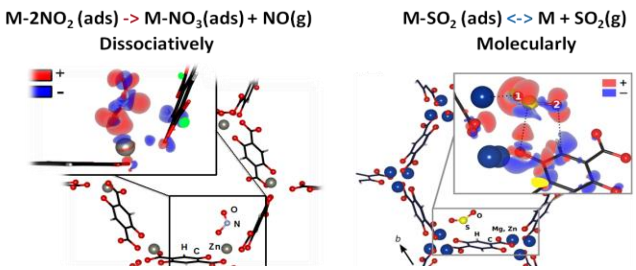

Figure 6. Valence charge density upon adsorption of NO_2 (left) and SO_2 (right) in Zn-MOF-74.

Future Plans

We plan to design new MOFs with targeted functionality, structures, and stability using a precursor approach in which secondary building units are preformed as soluble metal carboxylate clusters, and to (a) elucidate the diffusion and co-adsorption of various molecules inside these MOFs, (b) investigate the diffusion process of metal salts in solution with the ultimate motivation to provide a platform for nanoparticle synthesis, and (c) determine which aspects of the MOF and/or adsorbed guest molecules govern a MOF’s optical, electrical, and mechanical properties, which in turn will guide directed and optimized synthesis.

References

[1] J. Cure, E. Mattson, H. Assi, K. Cocq, S. Jensen, J. F. Veyan, K. Tan, M. Catalano, S. Kwon, S. Yuan, L. Feng, P. Zhang, H. Wang, J. Li, M. Kim, H. C. Zhou, T. Thonhauser, and Y. J. Chabal, *Ligand-free, isolated gold nanoparticles in metal organic framework materials*, Nature Materials, 2018, under revision.

[2] K. Tan, S. Jensen, L. Feng, H. Wang, S. Yuan, M. Ferreri, J. P. Klesko, R. Rahman, J. Cure, J. Li, H. C. Zhou, T. Thonhauser, and Y. J. Chabal, *Reactivity of atomic layer deposition precursors with OH/H_2O-containing metal organic framework materials*, Chemistry of Materials, 2018, under review.

[3] H. Wang, X. Dong, J. Lin, S. J. Teat, S. Jensen, J. Cure, E. V. Alexandrov, Q. Xia, K. Tan, Q. Wang, D. H. Olson, D. M. Proserpio, Y. J. Chabal, T. Thonhauser, J. Sun, Y. Han, and J. Li, *Topologically Guided tuning of Zr-MOF pore structures for highly selective separation of C6 alkane isomers*, Nature Communications, 2018, 9 (1), 1745.

[4] K. Tan, S. Jensen, S. Zuluaga, E. K. Chapman, H. Wang, R. Rahman, J. Cure, T.-H. Kim, J. Li, T. Thonhauser, and Y. J. Chabal, *Role of hydrogen bonding on transport of coadsorbed gases in metal–organic frameworks materials*, Journal of the American Chemical Society 2018, 140 (3), 856-859.

[5] B. Li, X. Dong, H. Wang, D. Ma, K. Tan, S. Jensen, B. J. Deibert, J. Butler, J. Cure, Z. Shi, T. Thonhauser, Y. J. Chabal, Y. Han, and J. Li. *Capture of organic iodides from nuclear waste by metal-organic framework-based molecular traps*, Nature Communications 2017, 8 (1), 485.

[6] K. Tan, S. Zuluaga, H. Wang, P. Canepa, K. Soliman, J. Cure, J. Li, T. Thonhauser, and Y. J. Chabal, *Interaction of acid gases SO_2 and NO_2 with coordinatively unsaturated metal organic frameworks: M-MOF-74 (M = Zn, Mg, Ni, Co)*, Chemistry of Materials 2017, 29 (10), 4227-4235.

DOE Sponsored Publications in the Last Two Years (5/2016 – 5/2018)

1. K. Tan, S. Jensen, S. Zuluaga, E. K. Chapman, H. Wang, R. Rahman, J. Cure, T.-H. Kim, J. Li, T. Thonhauser, and Y. J. Chabal. *Role of hydrogen bonding on transport of coadsorbed gases in metal–organic framework materials,* Journal of the American Chemical Society 2018, 140 (3), 856-859.
2. L. Feng, S. Yuan, L. L. Zhang, K. Tan, J. L. Li, A. Kirchon, L. M. Liu, P. Zhang, Y. Han, Y. J. Chabal, and H. C. Zhou, *Creating hierarchical pores by controlled linker thermolysis in multivariate metal-organic frameworks*, Journal of the American Chemical Society, 2018, 140 (6), 2363-2372.
3. E. Fuentes-Fernandez, S. Jensen, K. Tan, S. Zuluaga, H. Wang, J. Li, T. Thonhauser, and Y. J. Chabal, *Controlling chemical reactions in confined environments: Water dissociation in MOF-74*, Applied Sciences 2018, 8 (2), 270.
4. H. Wang, X. Dong, J. Lin, S. J. Teat, S. Jensen, J. Cure, E. V. Alexandrov, Q. Xia, K. Tan, Q. Wang, D. H. Olson, D. M. Proserpio, Y. J. Chabal, T. Thonhauser, J. Sun, Y. Han, and J. Li, *Topologically guided tuning of Zr-MOF pore structures for highly selective separation of C6 alkane isomers*, Nature Communications, 2018, 9 (1), 1745.
5. N. D. Rudd, H. Wang, S. J. Teat, and J. Li, *A dual linker metal-organic framework demonstrating ligand-based emission for the selective detection of carbon tetrachloride*, Inorganica Chimica Acta, 2018, 470, 312-317 [invited article].
6. D. Lv, H. Wang, Y. Chen, F. Xu, R. Shi, Z. Liu, X. Wang, S. J. Teat, Q. Xia, Z. Li, and J. Li, *Iron-based metal-organic framework with hydrophobic quadrilateral channels for highly selective separation of hexane isomers,* ACS Applied Materials & Interfaces, 2018, 10 (6) 6031-6038.
7. H. Wang and J. Li, *General strategies for effective capture and separation of noble gases by metal-organic frameworks*, Dalton Transactions, 2018, 47 (12) 4027-4031.
8. H. Wang, W. P. Lustig, and J. Li, *Sensing and capture of toxic and hazardous gases and vapors by metal–organic frameworks*, Chemical Society Reviews, 2018, DOI: 10.1039/c7cs00885f.
9. H. Wang, X. Dong, E. Velasco, D. H. Olson, Y. Han, and J. Li. *One-of-a-kind: a microporous metal-organic framework capable of adsorptive separation of linear, mono- and di-branched alkane isomers via temperature- and adsorbate-dependent molecular sieving*, Energy & Environmental Science, 2018, 11 (5) 1226-1231.
10. J. Cure, E. Mattson, H. Assi, K. Cocq, S. Jensen, J. F. Veyan, K. Tan, M. Catalano, S. Kwon, S. Yuan, L. Feng, P. Zhang, H. Wang, J. Li, M. Kim, H. C. Zhou, T. Thonhauser, and Y. J. Chabal, *Ligand-free, isolated gold nanoparticles in metal organic framework materials*, Nature Materials, 2018, under revision.
11. K. Tan, S. Jensen, L. Feng, H. Wang, S. Yuan, M. Ferreri, J. P. Klesko, R. Rahman, J. Cure, J. Li, H. C. Zhou, T. Thonhauser, and Y. J. Chabal, *Reactivity of atomic layer deposition precursors with OH/H_2O-containing metal Organic framework Materials*, Chemistry of Materials, 2018, under review.

12. S. Y. Zhang, S. Jensen, K.Tan, L. Wojtas, M. Roveto, J. Cure, T. Thonhauser, Y. J. Chabal, and M. J. Zaworotko, *Manipulation of water uptake by replacement of single atom in narrow pore metal-organic materials*, Journal of the American Chemical Society, 2018, under review.

13. S. Lo, L. Feng, B. Li, S.Yuan, K. Tan, W. Liu, G. S. Day, C. Yang, T. Luo, J. Li, C. Lin, S. Wang, K. Lu, Y. J. Chabal, and H. C. Zhou. *Ultrafast reversible lattice rearrangement upon solvent adsorption and desorption in an aluminum porous coordination polymer*, Nature Chemistry, 2018, under review.

14. K. Tan, S. Zuluaga, H. Wang, P. Canepa, K. Soliman, J. Cure, J. Li, T. Thonhauser, and Y. J. Chabal, *Interaction of acid gases* SO_2 *and* NO_2 *with coordinatively unsaturated metal organic frameworks: M-MOF-74 (M = Zn, Mg, Ni, Co)*, Chemistry of Materials 2017, 29 (10), 4227-4235.

15. B. Li, X. Dong, H. Wang, D. Ma, K. Tan, S. Jensen, B. J. Deibert, J. Butler, J. Cure, Z. Shi, T. Thonhauser, Y. J. Chabal, Y. Han, and J. Li, *Capture of organic iodides from nuclear waste by metal-organic framework-based molecular traps*, Nature Communications 2017, 8 (1), 485.

16. B. Li, X. Dong, H. Wang, D. Ma, K. Tan, Z. Shi, Y. J. Chabal, Y. Han, and J. Li, *Functionalized metal organic frameworks for effective capture of radioactive organic iodides*, Faraday Discussions, 2017, 201 (0), 47-61.

17. H. Wang, Q. Wang, S. J. Teat, D. H. Olson, and J. Li, *Synthesis, structure, and selective gas adsorption of a single-crystalline zirconium based microporous metal-organic framework*, Crystal Growth & Design, 2017, 17, 2034-2040 [invited article].

18. W. P. Lustig, S. Mukherjee, N. D. Rudd, A. V. Desai, J. Li, and S. K. Ghosh. *Metal-organic frameworks: Functional luminescent and photonic materials for sensing applications*, Chemical Society Reviews, 2017, 46, 3242-3285 [invited review].

19. E. Lashkari, H. Wang, L. Liu, J. Li, and K. Yam, *Innovative application of metal-organic frameworks for encapsulation and controlled release of allyl isothiocyanate*, Food Chemistry, 2017, 221, 926-935.

20. J. Peng, H. Wang, D. H. Olson, Z. Li, and J. Li, *Efficient kinetic separation of propene and propane using two microporous metal organic frameworks*, Chemical Communications, 2017, 53 (67) 9332-9335.

21. K. Tan, S. Zuluaga, E. Fuentes, E. C. Mattson, J.-F. Veyan, H. Wang, J. Li, T. Thonhauser, and Y. J. Chabal, *Trapping gases in metal organic frameworks with a selective surface molecular barrier layer*, Nature Communications 2016, 7, 13871.

22. Y. Zheng, D.-S. Yang, J. M. Kweun, C. Li, K. Tan, F. Kong, C. Liang, Y. J. Chabal, Y. Y. Kim, M. Cho, J.-S. Yu, and K. Cho, *Rational design of common transition metal-nitrogen-carbon catalysts for oxygen reduction reaction in fuel cells*, Nano Energy 2016, 30, 443-449.

23. S. Zuluaga, E. M. A. Fuentes-Fernandez, K. Tan, C. A. Arter, J. Li, Y. J. Chabal, and T. Thonhauser, *Chemistry in confined spaces: reactivity of the Zn-MOF-74 channels*, Journal of Materials Chemistry A 2016, 4 (34), 13176-13182.

24. S. Zuluaga, E. M. A. Fuentes-Fernandez, K. Tan, J. Li, Y. J. Chabal, and T. Thonhauser, *Cluster assisted water dissociation mechanism in MOF-74 and controlling it using helium*, Journal of Materials Chemistry A 2016, 4 (29), 11524-11530.
25. K. Tan and Y. J. Chabal, *Interaction of small molecules within metal organic frameworks studied by in situ vibrational spectroscopy,* in *Metal-Organic Framework,* et. Fahmina Zafar, IntechOpen, 2016.
26. D. Banerjee, H. Wang, A. M. Plonka, T. J. Emge, J. B. Parise, and J. Li, *Direct structural identification of gas induced gate-opening coupled with commensurate adsorption in a microporous metal–organic framework,* Chemistry – A European Journal, 2016, 22 (33) 11816-11825.
27. H. Wang, X.-L. Wang, and J. Li, *Separation of light hydrocarbons through selective molecular exclusion by a microporous metal–organic framework*, ChemPlusChem, 2016, 81 (8) 872-876.
28. N. D. Rudd, H. Wang, E. M. A. Fuentes-Fernandez, S. J. Teat, F. Chen, G. Hall, Y. J. Chabal, and J. Li, *Highly efficient luminescent metal-organic framework for the simultaneous detection and removal of heavy metals from water*, ACS Applied Materials & Interfaces, 2016, 8 (44) 30294-30303.
29. L. An, H. Wang, F. Xu, X.-L. Wang, F. Wang, and J. Li, *Selective carbon dioxide adsorption by two robust microporous coordination polymers*, Inorganic Chemistry, 2016, 55 (24) 12923-12929.

Studies of Reactive Amorphous Compounds and Surfaces: Their Pathways to Crystallinity and Surface Functionality

Prof. Abraham Clearfield, Texas A&M University

Program Scope

It is well known that many inorganic compounds are amorphous as prepared. Many of these compounds may be crystalized by further treatment. This is the case for the four valent phosphates Zr^{4+} and Sn^{4+}. However, the changes that occur between the amorphous and crystallin states of the plus 4 phosphates and phosphonates are not well known.

We have undertaken the task of determining the paths taken from the amorphous to the crystallin states if the latter are attainable. We start with the preparation of $Zr(HPO_4)_2 \cdot H_2O$ and the $Sn(HPO_4)_2 \cdot H_2O$. Our procedure is the reflux method. [1] 200 mL of 0.5M of $ZrOCl_2 \cdot 8H_2O$ is added dropwise to 200 mL of 6M H_3PO_4 and refluxed for 48 h at 94 °C. The product was rinsed with water, centrifugated several times at 3000 rpm and dried in an oven at 65 °C overnight.[1]

This method was first reported by Sun and Clearfield et al.[2] Additional information on early studies was proved by J. R. Garcia [3]. The paper by Garcia *et al*. lists a host of different phases including X-ray patterns of several of the phases. Additional early efforts provided zirconium phosphate gels [4, 5] and that zirconium phosphate could be prepared in crystalline form [6]. However, our interest now is to determine the change in structure that occur when the amorphous zirconium or tin phosphate phases are through its various changes and finally reverts to the crystalline form.

Recent Progress

An example of Zr, zirconium phosphate, was prepared using a small amount of phosphoric acid represented by the 2 using R, the reflux method and dried at 90 °C. Furthermore H stands for hydrothermal and S for stirring. A chart is proved on the right, Figure 1.

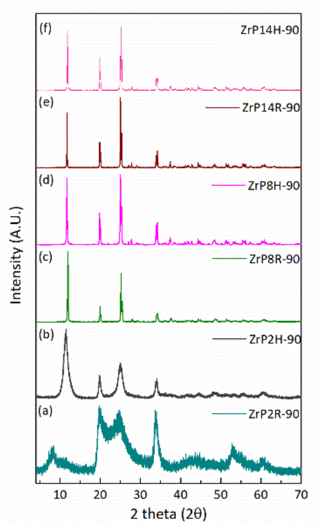

Figure1.PXRD of ZrP, 90 °C set: (a) ZrP2R-90, (b). ZrP2H-90, (c) ZrP8R-90, (d) ZrP8H-90, (e) ZrP14R-90, (f) ZrP14H-90.

We note that just by changing from R, the reflux method to H the hydrothermal method we obtain a more crystalline product.

Increasing the amount of phosphoric acid in the preparation 8 and 14 increases the crystallinity tremendously.

We have carried out many similar reactions as indicated in Table 1. We now have sufficient samples of zirconium phosphate as indicated in Table 1. We now also have data on potentiometric titrations.

Table 1. Summary of the ZrP samples, total of 15

Sample	**H_3PO_4 Molarity**			**Method Synthesis**			**Temperature**			
	2	**8**	**14**	**Hydrothermal**	**Reflux**	**Stirring**	**25**	**90**	**145**	**200**
ZrP2S-25	X					X	X			
ZrP2R-90	X				X			X		
ZrP2H-90	X			X				X		
ZrP2H-145	X			X					X	
ZrP2H-200	X			X						X
ZrP8S-25		X				X	X			
ZrP8R-90		X			X			X		
ZrP8H-90		X		X				X		
ZrP8H-145		X		X					X	
ZrP8H-200		X		X						X
ZrP14S-25			X			X	X			
ZrP14R-90			X		X			X		
ZrP14H-90			X	X				X		
ZrP14H-145			X	X					X	
ZrP214H-200			X	X						X

Figure 2a shows the morphology of the ZP14H-200, hexagonal plates with diameter from 1 to 3 μm. Figure 2b shows the side of the plates with 400 nm of thickness.

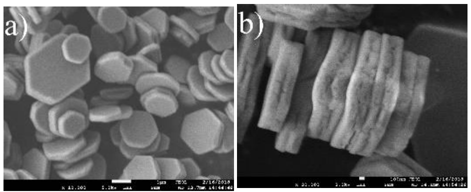

Figure 2. FE-SEM images of ZP14H-200.

Figure 3 a and b compares the difference between ZrP synthesized at 90°C, by the hydrothermal and reflux method. The hydrothermal method gives well-formed plates of 700 nm to 200 nm, with 100 nm of thickness, while the reflux method gives particles between 100 and 200 nm of longitude.

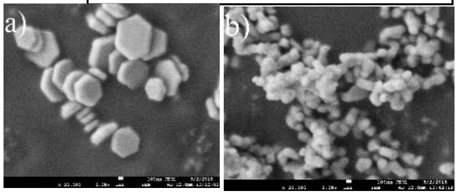

Figure 3. FE-SEM images of: a) ZP14H-90 b) ZP14R-90.

Future Plans

Of time importance is to determine the structure of the samples starting from the amorphous one to the several in between phases. For this propose we have joined with Simon Billinge of Columbia University. We have to have some structural data for the conference. Also, we have begun to examine Tin phosphate and have prepare several Zr and Sn Compounds.

References

1. Wang, Z.K., J.M. Heising, and A. Clearfield, *Sulfonated microporous organic-inorganic hybrids as strong bronsted acids.* Journal of the American Chemical Society, 2003. **125**(34): p. 10375-10383.
2. Sun, L.Y., et al., *Preparation of alpha-zirconium phosphate nanoplatelets with wide variations in aspect ratios.* New Journal of Chemistry, 2007. **31**(1): p. 39-43.
3. Trobajo, C., et al., *On the synthesis of alpha-zirconium phosphate.* Chemistry of Materials, 2000. **12**(6): p. 1787-1790.
4. Amphelett C.B, M.L.A.R.M.J., Chem. Ind. (London) 1956: p. 1314.
5. Kurt A. Kraus, H.O.P., *Adsorption os Inorganic Materials. I. Cation Exchanhe Properties of Zirconium Phosphate.* J. Am. Chem. Soc., 1956. **78**(3): p. 694–694.
6. Clearfield, A. and J.A. Stynes, *The Preparation of Crystalline Zirconium Phosphate and Some Observations on Its Ion Exchange Behaviour.* Journal of Inorganic & Nuclear Chemistry, 1964. **26**(1): p. 117-129.

Transforming Metal-Organic Frameworks into Polymer Hybrids and Biomimetic MetalloMOFzymes

Seth M. Cohen
Department of Chemistry and Biochemistry, University of California, San Diego

Program Scope

Metal-organic frameworks (MOFs) are porous solids that have generated interest for use in several technologies, including many for advanced energy initiatives. The objective of this continuing (renewal) proposal is to develop cutting edge synthetic methods to modify MOFs to obtain unprecedented polymer-MOF hybrid materials and MOF-based catalysts. Our prior accomplishments demonstrate that we can develop new synthetic methods and materials that have had a significant impact on the MOF research community. The achievements of this research program has helped advance the field of MOF research beyond the limits of solvothermal synthesis and in this next phase will move MOFs beyond their ‘form factor’ limitations as microcrystalline solids.

Our ongoing studies will continue to explore MOF-based catalysts, but will add an important dimension with the development of new, unprecedented polymer-MOF hybrids discovered near the end of the last funding period. Studies in catalysis will continue to be focused on energy relevant transformations. The Specific Aims of this continuing research program are:

Specific Aim 1. Development of polyMOFs. Polymers ligands, which are polymers containing metal coordinating units such as 1,4-benzenedicarboxylic acid monomers (H_2bdc), have been shown to self-assemble into a new class of polymer-MOF hybrids termed ‘polyMOFs’. The scope and structural diversity of polyMOFs is in its infancy, and this aim we will seek to further explore polyMOF materials and some proof-of-concept studies for their use in molecular separations.

Specific Aim 2. MOF Hybrids from Postsynthetic Polymerization. Postsynthetic polymerization (PSP) has been introduced as a strategy for combining MOF particles with polymeric binders. In this aim, a variety of PSP reactions will be explored to prepare new forms of porous MOF hybrids in the form of nylon fibers and epoxy composites.

Specific Aim 3. Biomimetic ‘MetalloMOFzyme’ Catalysts. Biomimetic ‘metalloMOFzymes’ for reducing protons or carbon dioxide will be optimized upon integration into functionalized and conducting MOFs. We seek to develop highly active and robust catalysts for these important, energy relevant chemical reactions.

Recent Progress

Progress on this project has been made on all three specific aims, but for purposes of this abstract, advancements made primarily made on Specific Aim 1 will be described. Specific Aim 1 focuses on the synthesis and investigation of a new class of porous materials referred to as polyMOFs (1, 2). polyMOFs are hybrid materials of polymers and metal-organic frameworks (MOFs), where the organic linker component of the MOF is comprised of a special class of metal-coordinating organic polymers. In the last 2 years, several advancements in this area have been made. In one study, the first UiO-type (UiO = University of Oslo) polyMOFs were obtained. Prior work on polyMOFs was largely limited to Zn(II)-derived frameworks, which while interesting, have limited utility due to their generally fragile nature. Zr(IV)-based UiO-type MOFs are far more chemically robust and have progressed much more rapidly toward technological applications of MOFs. After screen a variety of parameters, suitable reactions conditions were identified for generation UiO-66 style polyMOFs (3). These polyMOFs were extremely stable and displayed an unusual, mesoporous morphology (Figure 1).

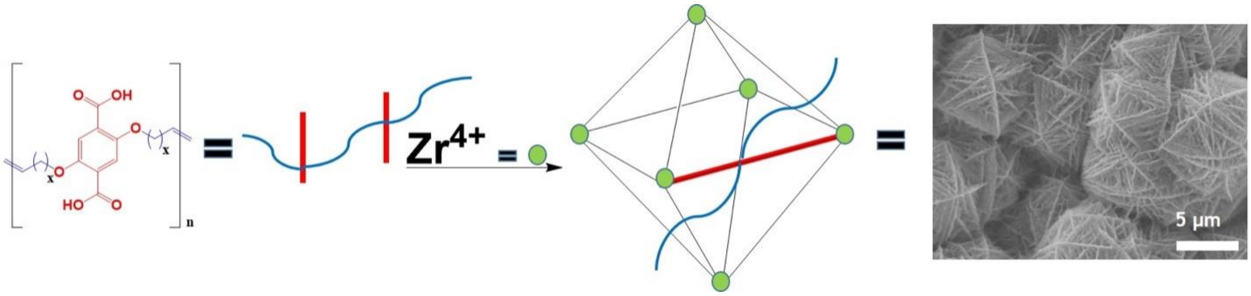

Figure 1. polyMOFs were prepared with Zr(IV) to obtain the first polymer-based, UiO-type frameworks.

In a follow up study, the principle of isoreticular chemistry was demonstrated in polyMOFs. Isoreticularity in MOFs is a largely conserved principle, whereby extension of the MOF ligand results in identical lattice topologies, but with increased dimensions of the framework lattice (4). This core principle in MOF chemistry is incredibly important, as it has been a primary strategy for increasing the pore size and surface area of MOFs. By synthesizing a series of ‘laterally extended’ polymer ligands (Figure 2), we demonstrated that polyMOFs also follow the principle of isoreticular chemistry and that these polyMOFs possessed substantially greater surface areas then previously synthesized systems (5). This was demonstrated with both Zn(II)- and Zr(IV)-based polyMOFs.

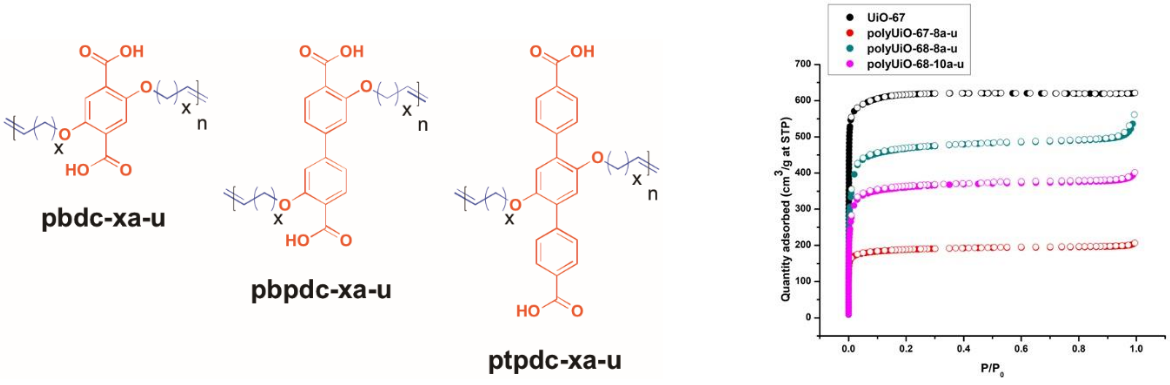

Figure 2. ‘Laterally extended’ polymer ligands (*left*) were used to generate a series of isoreticular polyMOFs. The surface area of these polyMOFs were dramatically enhanced (*right*), relative to earlier reported polyMOFs, showing that some polyMOFs also adhere to the principle of isoreticular chemistry.

Future Plans

The future plans for each of the specific aims on this project are:

Specific Aim 1. Development of polyMOFs. We will explore new polymer architectures, including block copolymers, to develop polyMOFs with improved (polymer-like) processability. polyMOFs that can form films, membranes, and fibers will be pursued. These studied will also reveal fundamental design rules about which organic polymers can and cannot form polyMOFs.

Specific Aim 2. MOF Hybrids from Postsynthetic Polymerization. We will continue our efforts to form nylon fibers and epoxy composites that incorporate MOF materials. Our present effort on nylon fibers are extremely encouraging, using UiO-66-NH_2 particles that can covalently integrate into nylon during a conventional, interfacial synthesis. These results should be forthcoming in a publication soon, which will then be followed up by work on epoxy resins.

Specific Aim 3. Biomimetic ‘MetalloMOFzyme’ Catalysts. Our efforts on biomimetic ‘metalloMOFzymes’ have been highly productive, in large part due to a very fruitful collaboration with Prof. Sascha Ott (U. Uppsala, Sweden). We have reported on the first conducting, electrochemically active UiO-69 type framework and are now using incorporating carbon dioxide reduction catalysts into this structure for electrocatalytic studies. Similar efforts on proton reduction catalysts are ongoing and will be reported in due course.

References

(1) Zhenjie Zhang, Ha Thi Hoang Nguyen, Stephen A. Miller, and Seth M. Cohen, "polyMOFs: A New Class of Interconvertible Polymer-MOF Hybrid Materials" *Angew. Chem. Int. Ed*. **2015**, *54*, 6152-6157. DOI: 10.1002/ANIE.201502733.

(2) Zhenjie Zhang, Ha Thi Hoang Nguyen, Stephen A. Miller, Ann Ploskonka, Jared DeCoste, and Seth M. Cohen, “polyMOFs as Water Tolerant Materials for Selective Carbon Dioxide Separations” *J. Am. Chem. Soc*. **2016**, *138*, 920-925. DOI: 10.1021/JACS.5B11034.

(3) Sergio Ayala, Jr., Zhenjie Zhang, and Seth M. Cohen, “Hierarchical Structure and Porosity in UiO-66 polyMOFs” *Chem. Commun*. **2017**, *53*, 3058-3061. DOI: 10.1039/C6CC10225E

(4) Mohamed Eddaoudi, Jaheon Kim, Nathaniel Rosi, David Vodak, Joseph Wachter, Michael O'Keeffe, Omar M. Yaghi, “Systematic Design of Pore Size and Functionality in Isoreticular MOFs and Their Application in Methane Storage” *Science* **2002**, *295*, 469-472. DOI: 10.1126/science.1067208.

(5) Giulia E. M. Schukraft, Sergio Ayala, Jr., Benjamin L. Dick, and Seth M. Cohen, “Isoreticular Expansion of polyMOFs Achieves High Surface Area Materials” *Chem. Commun*. **2017**, *53*, 10684-10687. DOI: 10.1039/C7CC04222A.

Publications

Ben A. Johnson, Asamanjoy Bhunia, Honghan Fei, Seth M. Cohen, and Sascha Ott*, "Development of a UiO-type Thin Film Electrocatalysis Platform with Redox Active Linkers" *J. Am. Chem. Soc*. **2018**, *140*, 2985-2994. DOI: 10.1021/JACS.7B13077.

Giulia E. M. Schukraft, Sergio Ayala, Jr., Benjamin L. Dick, and Seth M. Cohen*, “Isoreticular Expansion of polyMOFs Achieves High Surface Area Materials” *Chem. Commun*. **2017**, *53*, 10684-10687. DOI: 10.1039/C7CC04222A.

Sergio Ayala, Jr., Zhenjie Zhang, and Seth M. Cohen*, “Hierarchical Structure and Porosity in UiO-66 polyMOFs” *Chem. Commun*. **2017**, *53*, 3058-3061. DOI: 10.1039/C6CC10225E.

Seth M. Cohen*, “The Postsynthetic Renaissance in Porous Solids” *J. Am. Chem. Soc*. **2017**, *139*, 2855-2863 (invited Perspectives article, selected for J. Am. Chem. Soc. Spotlight). DOI: 10.1021/JACS.6B11259.

Two-Dimensional Chalcogenide Nanomaterials

Yi Cui, Harold Y. Hwang, Shoucheng Zhang

Stanford Institute for Materials and Energy Sciences, SLAC National Accelerator Laboratory

Program Scope

Our vision is to build a cutting-edge research program on an exciting class of two-dimensional (2D) chalcogenide (O, S, Se, Te) nanomaterials. We focus on the understanding and manipulation of their physical and chemical properties by the heterogeneous ionic environment, which is realized through electric double layer gating, electrochemical intercalation and chemical tuning. We envision that our research can lead to the rational design and dynamic control of “2D Artificial Materials”, which will lay the foundation for new materials approaches to charge storage for batteries, catalysis, and novel electronics and optoelectronics.

Recent Progress

Highly efficient solar disinfection of drinking water with few-layered vertically(FLV) aligned MoS_2

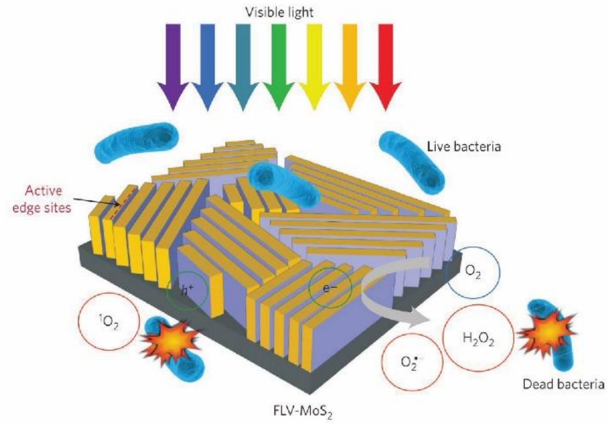

Figure 1. Schematic of the FLV-MoS_2 inactivating bacteria in water through visible-light photocatalytic ROS generation.

Solar energy has been widely employed for water purification to address the challenge of water scarcity. However, current technology mainly relies on ultraviolet light, which represents only 4% of the total solar spectrum, resulting in a slow treatment speed. We show that using FLV-MoS_2 films can harvest the whole spectrum of visible light (~50% of solar energy) and achieve highly efficient water disinfection. By decreasing the domain size, the bandgap of MoS_2 increases from 1.3 to 1.55 eV, allowing FLV-MoS_2 to generate reactive oxygen species (ROS) for bacterial inactivation in the water. The log inactivation efficiency of the indicator bacteria of the FLV-MoS_2 is found to be ~15 times better than that of bulk MoS_2, and a much faster inactivation of bacteria than the widely used TiO_2 was achieved under both visible light and sunlight illumination.

Anionic solid-state electric-double-layer gating with superionic conductor LaF_3

Electric-double-layer gating with liquid electrolyte has been widely used to explore emerging interfacial electronic phenomena due to the large capacitance and a high carrier density up to 10^{14} cm^{-2} that can be induced. However, the liquid nature of the electrolyte has created technical issues including side electrochemical reactions or intercalation, huge strain during cooling, and difficulty in surface characterizations. Herein, we develop an all solid state anionic gating platform with a superionic conductor LaF_3, which can serve as both the substrate and the fluorine ionic gate dielectric. A wide tunability of carrier density can be achieved without the issues of strain or electrochemical reactions, directly leading to the observation of the metal–insulator transition in MoS_2. Interestingly, the well-defined crystal lattice provides a more uniform potential distribution in the substrate, resulting in less interface electron scattering and therefore a higher mobility in MoS_2 transistors.

SnS_2-based seamless lateral heterostructures through rational chemical intercalation

The success of silicon-based integrated circuits lies in the facile and controllable integration of components with different doping levels and electronic properties without introducing a high resistance interface. As a promising candidate beyond Moore's law, the family of atomically thin two-dimensional materials consists of p-type, n-type semiconductors and metals, and their electrical properties can be controlled via chemical doping and electrostatic gating. However, seamless integration of these components in the same parent material remains elusive. Through solvent-based transition metal intercalation, we can tune the doping level in n-type bilayer SnS_2, realizing p-type semiconducting and metallic behavior in this material by the intercalation of Cu and Co, respectively. Combining this intercalation method with lithography, seamless p/n/m junction based on SnS_2 could be realized with precise spatial control.

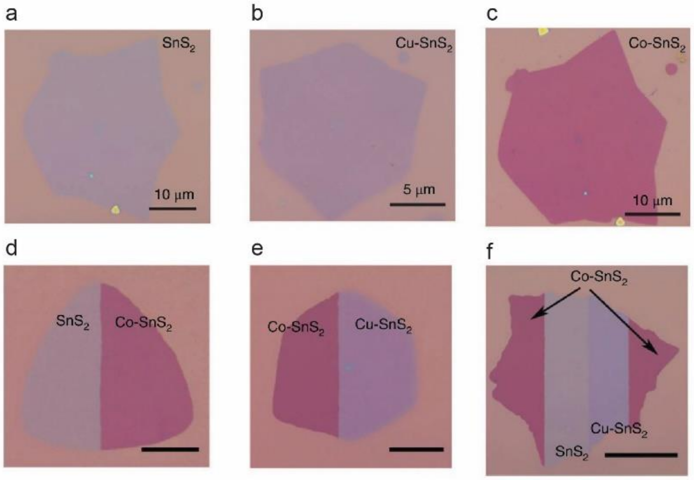

Figure 2. Optical images of (a) pristine, (b) Cu-intercalated, (c) Co-intercalated SnS_2, and (d-f) seamless heterostructures created through the combination of intercalation and lithography.

Accurately-controllable electrochemical intercalation of zero valent copper into nanoscale Bi_2Se_3

Intercalation of exotic species into the van der Waals gap of layered materials has been intensively studied for the rational design and manipulation of material properties. However, strategies such as traditional melt-growth and chemical intercalation are limited by either insufficient intercalant concentration or the lack of controllability. Inspired by the battery cell configuration, we develop a general electrochemical intercalation method that can effectively regulate the concentration of zero valent copper atoms in layered Bi_2Se_3. With this approach, up to 57% of copper atoms ($Cu_{6.7}Bi_2Se_3$) could be intercalated without disrupting the host lattice. Low-temperature transport measurement reveals an unconventional resistance dip accompanied by a hysteresis loop below 40 K in $Cu_xBi_2Se_3$ ($x = 0.5 \sim 1.9$). In addition, the emergence of a new Raman peak in Cu-intercalated Bi_2Se_3 manifests the interplay between the copper atoms with the Bi_2Se_3 host.

Reversible alkali ion intercalation in MoS_2 through basal plane in a sealed-edge geometry

It is widely believed that ions prefer intercalation into the van der Waals gap through the edges of the 2D flake, which generally causes wrinkling and distortion of the flake. In a sealed-edge configuration, we show that intercalation may also take place through the top surface, which is enabled by the existence of natural defects in exfoliated MoS_2 flakes. In addition, fully reversible changes in the optical properties of MoS_2 and a drastic reduction in the resistivity upon intercalation of Na^+ ions are realized. These findings pave the way for designing more stable and reliable energy storage devices, as well as highly tunable 2D-material-based optoelectronic and electronic devices.

Future Plans

In our future research, we will continue the exploration and manipulation of the physical and chemical properties of 2D chalcogenide nanomaterials, with the emphasis on the following directions.

1. Studying the evolution of electronic structure and physical properties with the combination of solid state ionic gating and spectroscopic techniques such as ARPES.
2. Tuning catalyst performance through solid electrolyte gating, focusing on the systems of 2D layered chalcogenides and their single-atom catalyst-decorated counterparts.
3. Understanding the electrical, photonic properties of the chemically/electrochemically intercalated layered materials and their rational design for applications.

References

1. C. Liu, D. Kong, P.-C. Hsu, H. Yuan, H.-W. Lee, Y. Liu, H. Wang, S. Wang, K. Yan, D. Lin, P. A. Maraccini, K. M. Parker, A. B. Boehm, and Yi Cui, "*Rapid water disinfection using vertically aligned MoS2 nanofilms and visible light", Nature Nanotech.* **11**, 1098-1104 (2016)
2. Y. J. Gong, H. T. Yuan, C.-L. Wu, P. Z. Tang, S. Z. Yang, A. K. Yang, J. van de Groep, M. Brongersma, M. F. Chisholm, S.-C. Zhang, W. Zhou, Y. Cui, *"Spatially Controlled Doping of Two-Dimensional SnS_2 through Intercalation for Electronics," Nature Nanotech*. **13**, 294-299 (2018).
3. C.-L. Wu, H. T. Yuan, Y. Li, Y. J. Gong, H. Y. Hwang, Y. Cui, "*Gate-Induced Metal-Insulator Transition in MoS_2 by Solid Superionic Conductor LaF_3*," *Nano Lett.* **18**, 2387-2392 (2018).

4. J. S. Zhang, J. Sun, Y. B. Li, F. F. Shi, and Y. Cui**,** "*Electrochemical Control of Copper Intercalation into Nanoscale* Bi_2Se_3*", Nano Lett.*, **17**, 1741–1747 (2017).
5. J. Zhang, A. Yang, X. Wu, J. van de Groep, P. Tang, B. Liu, F. Shi, J. Wan, Q. Li, Y. Sun, Z. Lu, G. Zhou, J. Li, S.-C. Zhang, M. L. Brongersma, Y. Cui, "*Reversible and Selective Ion Intercalation through Top Surface of Few-Layer* MoS_2", Manuscript under review in Nature Communications.

Publications

References above and the following.

1. J. Sun, Y. Sun, M. Pasta, G. Zhou, Y. Li, W. Liu, F. Xiong, and Y. Cui, "*Entrapment of Polysulfides by a Black-Phosphorus-Modified Separator for Lithium-Sulfur Batteries*", *Advanced Materials* **28**, 9797–9803 (2016).
2. Z. Y. Chen, H. T. Yuan, Y. W. Xie, D. Lu, H. Inoue, Y. Hikita, C. Bell, H. Y. Hwang, "*Dual-Gate Modulation of Carrier Density and Disorder in an Oxide Two-Dimensional Electron System*", *Nano Lett.*, **16**, 6130 (2016).
3. J. X. Wu, H. T. Yuan, M. M. Meng, C. Chen, Y. Sun, Z. Y. Chen, W. H. Dang, C. W. Tan, Y. J. Liu, Y. B. Zhou, S. Y. Huang, H. Q. Xu, Y. Cui, H. Y. Hwang,Z. F. Liu,Y. L. Chen, B. H. Yan, and H. L. Peng, "*High Electron Mobility and Quantum Oscillations in Non-encapsulated Ultrathin Semiconducting* Bi_2O_2Se," *Nature Nanotechnology* **12**, 530 (2017).
4. D. J. Baek, Di Lu, Y. Hikita, H. Y. Hwang, and L. F. Kourkoutis, "*Mapping cation diffusion through lattice defects in epitaxial oxide thin films on the water-soluble buffer layer* $Sr_3Al_2O_6$ *using atomic resolution electron microscopy*," *APL Materials* **5**, 096108 (2017).
5. J. Zhang, J. Sun, Y. Li, F. Shi, and Y. Cui**,** "*Electrochemical Control of Copper Intercalation into Nanoscale* Bi_2Se_3*," Nano Lett.* **17**, 1741–1747 (2017).
6. Z. Zhang, X. Feng, J. Wang, B. Lian, J. Zhang, C. Chang, M. Guo, Y. Ou, Y. Feng, S.-C. Zhang, K. He, X. Ma, Q.-K. Xue, Y. Wang, "*Magnetic Quantum Phase Transition in Cr-doped* $Bi_2(Se_xTe_{1-x})_3$ *Driven by the Stark Effect*," *Nature Nanotech.* **12**, 953-957 (2017).
7. X. G. Liu, J. Kang, H. T. Yuan, J. H. Park, Y. Cui, H. Y. Hwang, and M. L. Brongersma, "*Electrical Tuning of a Quantum Plasmonic Resonance*," *Nature Nanotech*. **12**, 866-870 (2017).
8. Y. Fu, E. Liu, H. Yuan, P. Tang, B. Lian, G. Xu, J. Zeng, Z. Chen, Y. Wang, W. Zhou, K. Xu, A. Gao, C. Pan, M. Wang, B. Wang, S.-C. Zhang, Y. Cui, H. Y. Hwang, F. Miao, "*Gated Tuned Superconductivity and Phonon Softening in Mono- and Bilayer* MoS_2," *npj Quantum Materials* **2**, Article Number 52 (2017)
9. Q. L. He, L. Pan, A. L. Stern, E. C. Burks, X. Che, G. Yin, J. Wang, B. Lian, Q. Zhou, E. S. Choi, K. Murata, X. Kou, Z. Chen, T. Nie, Q. Shao, Y. Fan, S.-C. Zhang, K. Liu, J. Xia, K. L. Wang, "*Chiral Majorana Edge State in a Quantum Anomalous Hall Insulator Superconductor Structure*," *Science* **357**, 294 (2017).
10. J. W. Zeng, E. F. Liu, Y. J. Fu, S. H. Cai, X. X. Yan, Z. Y. Chen, C. Pan, C. Y. Wang, M. Wang, Y. J. Wang, K. Xu, P. Wang, B. G. Wang, Y. Cui, H. Y. Hwang, H. T. Yuan, and F. Miao, "*Discovery of Gate-Induced Interfacial Superconductivity in 1T-*$SnSe_2$," *Nano Lett.* **18**, 1410 (2018).

11. H. T. Yuan, H. Inoue, C. Bell, Y. Hikita, S. S. Hong, D. S. Kong, Y. Cui**,** H. Y. Hwang, "*Dimensionality of Quantum Insulator-Superconductor Transition in Liquid Gating* MoS_2 *Transistors*". Manuscript in preparation.
12. H. T. Yuan, A. G. Curto, B. Lian, G. Xu, L. Yang, Z. Bo, Z. Liu, P. Tang, J. Sun, X. Liu, S. A. Crooker, Z. X. Shen, Y. Chen, M. Brongersma, S.-C. Zhang, H. Y. Hwang, Y. Cui, "*Robust Surface Excitonic States with Linear Polarization in bulk* ReS_2", Manuscript in preparation.

POLYELECTROLYTE-GRAFTED NANOCHANNELS FOR ENHANCED ELECTROCHEMOMECHNICAL ENERGY CONVERSION

Siddhartha Das (PI, Department of Mechanical Engineering, University of Maryland)
Peter W. Chung (co-I, Department of Mechanical Engineering, University of Maryland)

Program Scope

The purpose of the project is to develop both continuum calculations and molecular dynamics (MD) simulations to study the electrokinetic transport and the resulting electrochemomechanical energy conversion (ECMEC) (in presence of an axial pressure-driven flow) in nanochannels grafted with pH-responsive polyelectrolyte (PE) brushes.

The continuum framework would first focus on developing a thermodynamically consistent model for the pH-responsive PE brushes that appropriately accounts for the different energy components associated with the PE brushes and the energy of the induced electric double layer. Subsequently, this brush model will be employed to investigate the electrohydrodynamic transport in presence of an applied pressure gradient and quantify the induced electrokinetic transport and the resulting ECMEC.

The MD simulations would first simulate the pH-responsive PE brushes in explicit water with the PE brushes being grafted on the inner walls of a nanochannel. Subsequently, a pressure-driven transport in such a PE-brush-grafted nanochannel will be studied employing the MD simulations. Finally, the ionic transport induced by this pressure-driven transport and the resulting induced electric field and electrokinetic transport will be quantified.

The MD simulations will provide several key parameters dictating the system. Some of them are the dependence of the net drag coefficient on the monomer distribution of the PE brushes, possible tilt of the PE brushes as a response to the different driving forces, etc. This information obtained through the MD simulations will be eventually used to improve the continuum model and the solutions obtained from the resulting continuum model will be compared with the MD simulation output.

In summary, this project, driven by an appropriate combination of continuum calculations and atomistic simulations, plans to develop for the first time a complete theory of electrokinetic transport and ECMEC in nanochannels grafted with pH-responsive PE brushes.

Recent Progress

Continuum Calculations:

We have been able to employ the Strong Stretching Theory (SST) to obtain the self-consistent thermodynamic description of the pH-responsive PE brushes. Zhulina and Borisov had earlier proposed such a SST for describing the thermodynamics, electrostatics, and the configuration of

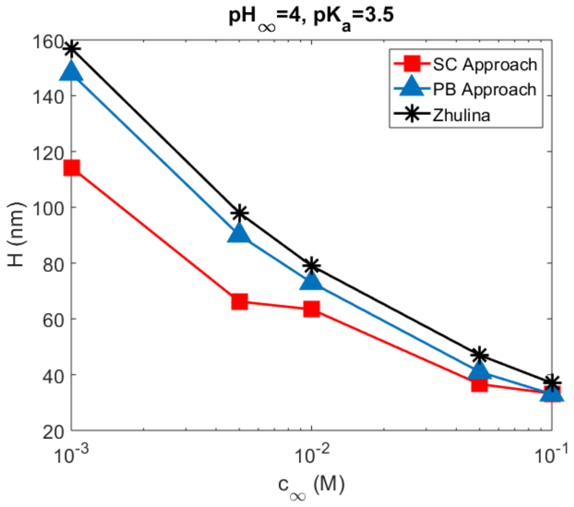

Figure 1: Variation of the brush height with salt concentration for bulk pH (or pH_∞) equal to 4 and pK_a=3.5 (K_a is the ionization constant of the acidic group whose pH-dependent ionization produces the negative charge of the PE brushes). The results from our self-consistent theory is denoted as *SC*, the results obtained by using Poisson-Boltzmann description of the hydrogen ions is denoted as *PB*, while the results from Zulina and Borisov's paper [1] is denoted as "Zhulina".

the pH-responsive PE brushes [1]. However, they had made one critical mistake. They had employed the Boltzmann distribution to describe the hydrogen ion concentration everywhere in the system. This is incorrect – appropriate description of the equilibrium hydrogen ion concentration distribution quantified through the energy minimization route must account for the chemical energy changes associated with pH-responsive ionization of the PE brush (such ionization process generates the hydrogen ions and therefore should contribute to the overall hydrogen ion concentration description). Our SST model explicitly accounts for such ionization contribution in the hydrogen ion concentration description. In the process, all the other variables (such as the brush height, the monomer distribution, distribution of the ends of the PE brushes, and the overall electric double layer electrostatic potential) that are

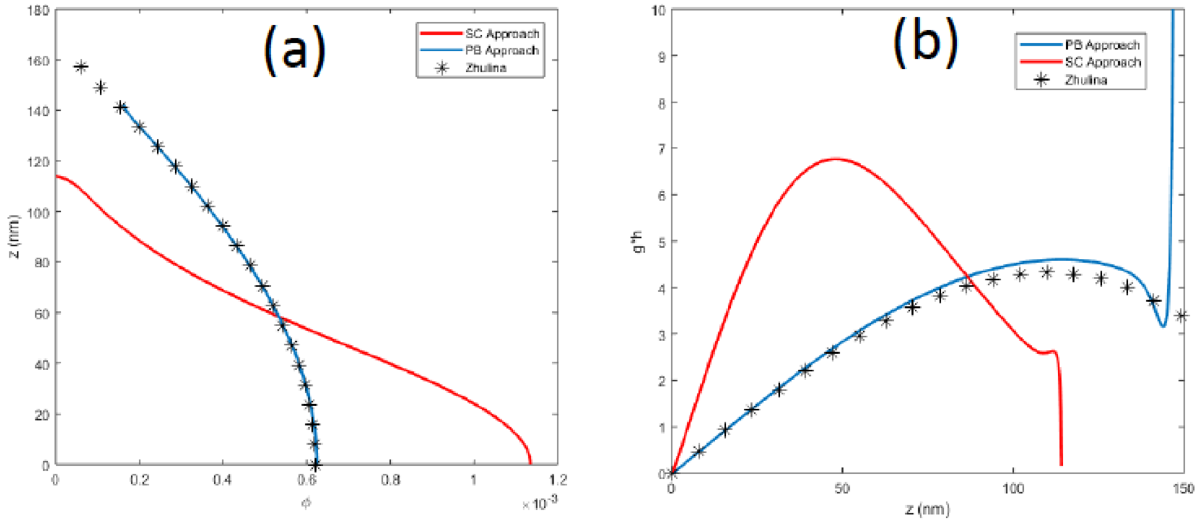

Figure 2: (a) Variation of the dimensionless monomer distribution ϕ along the length of the brush (z). **(b)** Variation of the dimensionless end distribution ($g{*}h$) along the length of the brush (z). Here h represents the half height of the nanochannel on whose two walls the PE brush layers are grafted. In both (a) and (b) the results from our self-consistent theory is denoted as *SC*, the results obtained by using Poisson-Boltzmann description of the hydrogen ions is denoted as *PB*, while the results from Zulina and Borisov's paper [1] is denoted as "Zhulina". The results are shown for pH_∞=4, c_∞=10^{-3} M, and pK_a=3.5.

obtained self consistently also get affected. The results are shown below (please see Figs. 1-3), indicating how our self-consistent theory vastly differs from the theory based on the simple Poisson-Boltzmann (PB) description (which is also approximately the method of Zhulina and Borisov) of the hydrogen ion concentration.

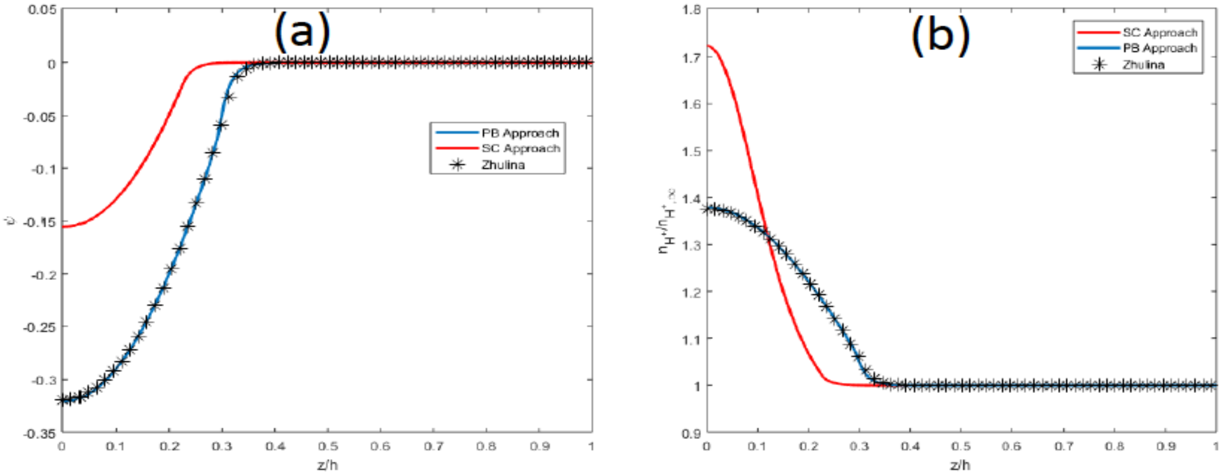

Figure 3: (a) Variation of the dimensionless electric double layer electrostatic potential ($\psi = e\Psi/k_BT$) across the nanochannel cross section for the nanochannel bottom half (*z/h=0* is the nanochannel bottom wall and *z/h*=1 is the nanochannel centreline) **(b)** Variation of the dimensionless hydrogen ion number density across the nanochannel cross section for the nanochannel bottom half. In both (a) and (b) the results from our self-consistent theory is denoted as *SC*, the results obtained by using Poisson-Boltzmann description of the hydrogen ions is denoted as *PB*, while the results from Zulina and Borisov's paper [1] is denoted as "Zhulina". The results are shown for $pH_\infty=4$, $c_\infty=10^{-3}$ M, and $pK_a=3.5$.

Molecular Dynamics Simulations:

Our ultimate aim is to simulate the pressure-driven water transport (with atomistic water modeled using the SPC/E model) in nanochannels grafted with pH-responsive PE brushes and quantify the induced electrokinetic flow and the resulting ECMEC. In order to make a step-by-step progress towards achieving this goal, we have first successfully simulated the pressure driven transport of water (modeled using the SPC/E water model) in a nanochannel grafted with uncharged, hydrophobic polymer brushes using the LAMMPS software package. We model the polymer as a Polyethylene molecule of 20 monomers each. The polymer is grafted to the nanochannel by fixing the last monomer of each polymer chain to the nanochannel wall. To ensure that the polymers and water do not cross the boundary of the nanochannel we add a repulsive potential at the location of grafted monomers. We simulate the system using an NVT ensemble at 300K. To ensure that the thermostat does not affect the flow, we apply a Langevin thermostat to only the polymer molecules. To simulate pressure-driven flow we apply a body force to the oxygen molecules of water in the x–direction. We equilibrate the system for 1 ns and save data for the next 2 ns to analyze the flow profile. We also quantify the overall flow rate and the slip length as a function of the applied force. These results, along with a simulation snapshot, are provided in Fig. 4.

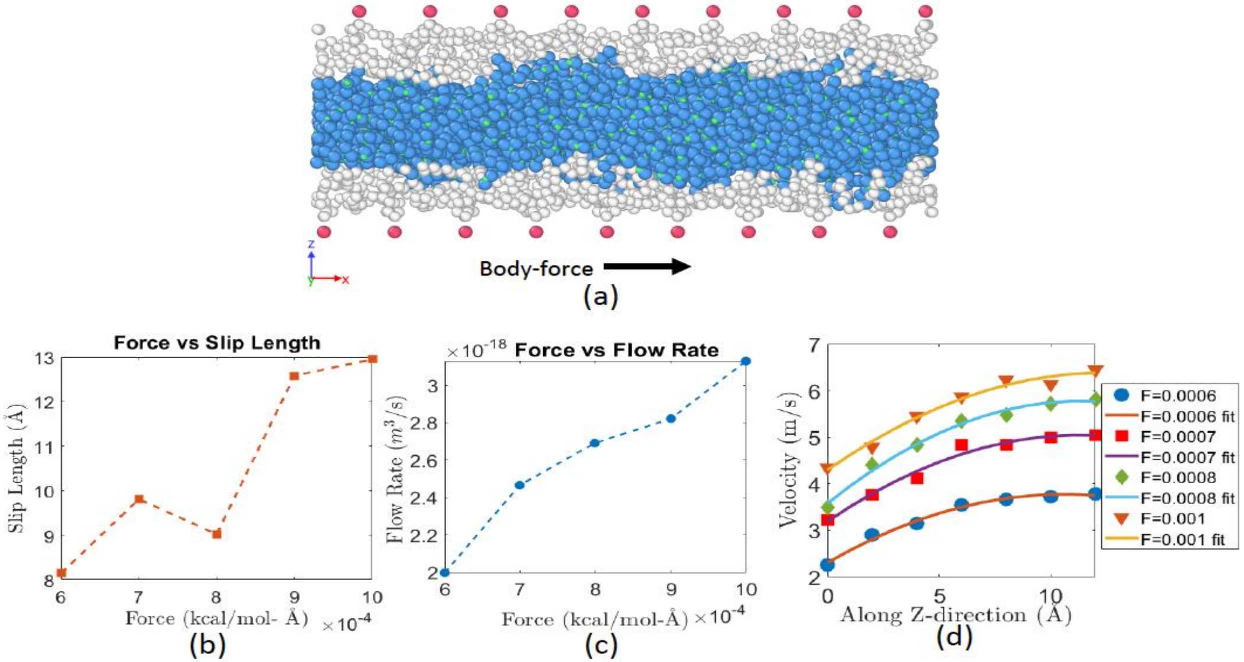

Figure 4: (a) Simulation snapshot showing the pressure-driven transport of SPC/E water in a nanochannel grafted with hydrophobic polymer brushes. **(b)** MD simulation results for the variation of the slip length as a function of the applied force. **(c)** MD simulation results for the variation of the flow rate as a function of the applied force. **(d)** MD simulation results for the flow profile across the channel bottom half for different force values (in kcal/mol-Å) and the corresponding fit.

Future Plans

1. Use the thermodynamically self-consistent model for the pH-responsive PE brush electrostatics to obtain the continuum description of the induced electrokinetics and ECMEC in nanochannels grafted with pH-responsive PE brushes.
2. Employ MD simulations to obtain (a) pressure-driven induced electrokinetic transport in nanochannels grafted with PE brushes with constant (pH-independent) charge density and (b) pressure-driven induced electrokinetic transport in nanochannels grafted with *pH-responsive* PE brushes (i.e., PE brushes having pH-dependent charge density).
3. Use the MD simulation results to pinpoint (a) the dependence of the net drag coefficient on the monomer distribution of the PE brushes and (b) possible alteration of the brush configuration as a response to the driving forces.
4. Use the above information to improve the continuum model and compare the results of the continuum model with the MD simulation results.

References

[1] E. B. Zhulina and O. V. Borisov, "Poisson-Boltzmann theory of pH-sensitive (annealing) polyelectrolyte brush", *Langmuir*, Vol. 27, pp. 10615–10633, 2011.

Publications

No publication yet for this project supported by BES.

Fundamental studies of thermal and electrical transport in microporous metal-organic frameworks

Mircea Dincă, Massachusetts Institute of Technology

Program Scope

More traditionally used for gas storage, separation, or catalysis, porous metal-organic frameworks (MOFs) also offer untapped potential as designer electronic materials. Here, we propose systematic approaches to understanding and manipulating the electronic and phononic structure of MOFs for controlling electrical and thermal transport phenomena. A fundamental understanding of electrical and thermal transport in these porous structures is still lacking; the development of such an understanding will tap a largely unexplored space in this area. The work proposed here will produce new materials whose investigation will also require adapting electrical and thermal transport measurement techniques to porous MOFs, which will benefit the very large communities of chemists, materials scientists, physicists, and engineers now engaged in research with these materials. The fundamental knowledge gained from the work proposed here could herald a new generation of highly porous materials whose unique electrical properties will impact a number of fields including electrical energy storage, chemiresistive sensing, and optoelectronics.

Recent Progress

We have engaged to explore the electrical conductivity of MOFs as enabled by two different charge transport formalisms: through-bond and through-space. These two formalisms, seen extensively in molecular conductors, have been embraced by the MOF community in elaborating numerous other examples of conductive MOFs, following our initial work funded by the DOE. During this existing project, since September 2017, we have extended our knowledge in both fields, with two important published results. First, on the front of through-bond conductivity, we have discovered that mixed-valence, especially in Fe-containing MOFs is a very effective means to increase conductivity in a controlled fashion. In a material known as FeBDT (see Figure 1), we showed that the conductivity varies over 5 orders of magnitude and reaches *record values for any three-dimensionally connected MOF (above 1 S/cm).*[1] The large conductivity is due to the insertion of mid-gap states

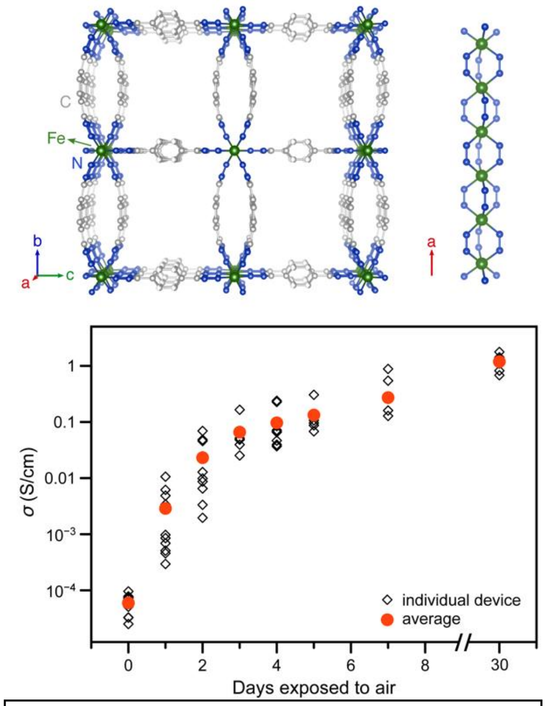

Figure 1. Top: structure of FeBDT. Bottom: electrical conductivity as a function of doping (upon exposure to air).

by Fe^{3+} dopants that are connected to otherwise majority Fe^{2+} in infinite nitrogen-bridged Fe chains.

In the through-space conductivity formalism, we are beginning to uncover a totally new type of topological control for the entire MOF field. In prior work, we have seen signs that pi-stacking interactions can disrupt the coordinative/covalent lattice made by metal-ligand bonds when the pi-stacking stabilization energy equals or exceeds the energy of the metal-ligand bonds. The result of this is that the underlying mathematical topology (and thus structure) of the MOF does not depend on the geometry or structure of the ligand and of the (metallic) secondary building unit (SBU), but rather on the structure of the pi-stacked organic constructs, which can thus be termed *the organic secondary building units (oSBU).* The immediate result, as far as electronic properties are concerned and as relevant to this project, is that the pi-stacking is not disrupted by the covalent lattice anymore, which ideally results in unencumbered transport of charges along the pi-stacking sequence or ladder. Using these principles, we have shown that MOFs that have topologies dictated by these oSBUs can behave as good ion conductors.[2] In one example, we showed that a Mg MOF made from tetrathiafulvalene tetracarboxylate is a rare example of a mesoporous MOF that also exhibits good proton conductivity, with two distinguishable regimes of vehicular and Grotthus transport (see Figure 2).

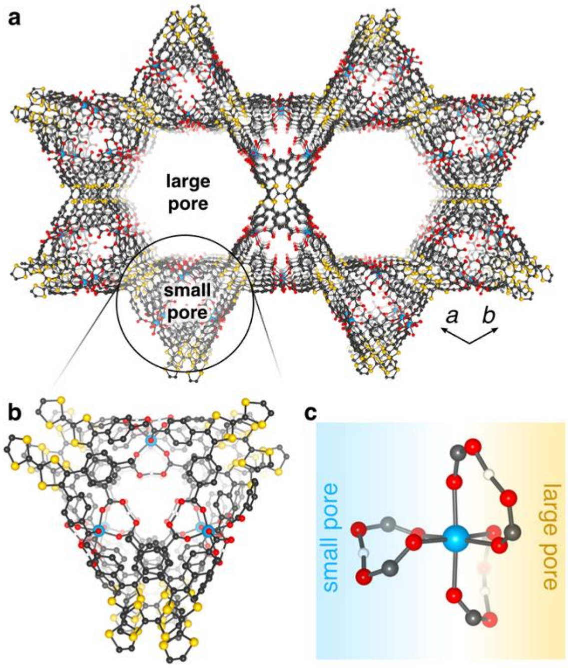

Figure 2. Crystal structure of $Mg_2H_6(H_3O)(\text{tetrathiafulvalenetetrabenzoate})_3$

Future Plans

We are currently working on exploring the extent and scope of the pi-stacking influence on topology, as well as understanding how this unexpectedly disrupting structural element can be used rationally to produce materials with improved electronic or ionic transport properties. We are also developing small sample pucks that allow us to investigate the thermal properties of MOFs with our newly installed PPMS system (Figure 3), which this award helped us purchase, and which is now fully functional in dedicated space in our laboratory.

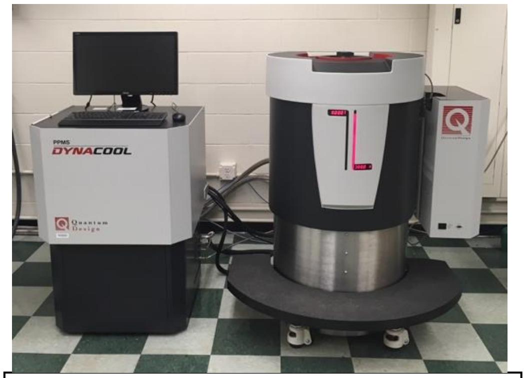

Figure 3. PPMS system with thermal transport capabilities installed recently in the Dincă lab, with support from this award.

References

1) Tunable Mixed-Valence Doping towards Record Electrical Conductivity in a Three-Dimensional Metal–Organic Framework
   Xie, L. S.; Sun, L.; Wan, R.; Park, S. S.; DeGayner, J.; Hendon, C. H.; Dincă, M.
   Journal of the American Chemical Society **2018**, *140*, in press (DOI: 10.1021/jacs.8b03604).
2) Selective Vapor Pressure Dependent Proton Transport in a Metal-Organic Framework with Two Distinct Hydrophilic Pores
   Park, S. S.; Hendon, C. H.; Rieth, A. J.; Dincă, M.
   Journal of the American Chemical Society **2018**, *140*, 2016-2019.

Publications (since Sept 1, 2017 – start date of project)

1) Tunable Mixed-Valence Doping towards Record Electrical Conductivity in a Three-Dimensional Metal–Organic Framework
   Xie, L. S.; Sun, L.; Wan, R.; Park, S. S.; DeGayner, J.; Hendon, C. H.; Dincă, M.
   Journal of the American Chemical Society **2018**, *140*, in press (DOI: 10.1021/jacs.8b03604).
2) Selective Vapor Pressure Dependent Proton Transport in a Metal-Organic Framework with Two Distinct Hydrophilic Pores
   Park, S. S.; Hendon, C. H.; Rieth, A. J.; Dincă, M.
   Journal of the American Chemical Society **2018**, *140*, 2016-2019.

Design of Next Generation Thermoelectrics

Vinayak P. Dravid, PI, Mercouri Kanatzidis; co-PI, Christopher Wolverton, co-PI
Northwestern University, Evanston, IL 60208

Project Scope: Almost 60% of the energy produced annually around the globe is wasted, primarily in the form of heat losses. Thermoelectricity provides an opportunity to recapture even a small portion of this wasted energy by reversibly converting temperature gradients into electricity through the Seebeck effect[1-2]. Advancing thermoelectric materials and their performance require unveiling the fundamental science governing the unique and complex interplay between lattice vibrations (phonons) and charge carriers; all mediated by the microstructure of the materials.

The thermoelectric figure-of-merit, ZT, is one of the most commonly referred to values when evaluating the effectiveness of thermoelectrics. This dimensionless figure of merit ZT is defined by $(\sigma \cdot S^2/\kappa)T$, where σ is the electrical conductivity, S is the Seebeck coefficient, κ the thermal conductivity, and T the absolute temperature. This value is directly related to the efficiency of thermoelectric devices, and therefore thermoelectric devices are optimized through increasing the power factor $(\sigma \cdot S^2)$ or decreasing the total thermal conductivity (κ) or both. Yet, the contraindicating behavior of thermoelectric properties has until recently stagnated the growth of the overall efficiency[2-3]. This project therefore has focused on methodologies for decoupling these material properties through a variety of innovative approaches, invoking multipronged approach to study the origin of the complex thermoelectric material parameters.

In the past, our collaborative efforts have resulted in dramatic reduction in lattice thermal conductivity through all-scale architecturing[4-5]. In recent years, we have focused on investigating the role of point defects on the reduction of lattice thermal conductivity. However as thermal conductivity approaches its lower (amorphous) limit, the importance of dopants and defects in the alteration of electronic properties has proven to be of growing interest. We argue that to continue to push the limits of thermoelectric performance, development of innovative strategies to enhance the power factor are needed. Subsequently our group has been at the forefront of understanding the fundamental factors governing the power factor.

We are leveraging a combination of experimental and data driven strategies to both discover new ideal thermoelectric materials candidates and optimize power factor and reduce thermal conductivity in well-known thermoelectric systems. Several key scientific challenges governing this synergistic and collaborative approach include: a) insights into the collective mechanisms of charge and phonon transport across the atomic, nano- and mesoscale levels, b) understanding microstructural evolution of thermoelectric material systems, and c) potential integration of all the ZT-enhancing mechanisms simultaneously and synergistically into a single material system.

We have also been investigating power factor parameters and strategies such as: valence band convergence, minimizing band offset between multiple phases, and increasing the number of bands contributing to the transport. In addition, we are searching for new candidate materials with intrinsically favorable properties by leveraging data-driven approaches to design and discover new thermoelectric chemistries, explore new chalcogenide and oxide single-phase systems with potential for high-performance thermoelectrics with chemical and thermal stability at high temperature.

The past year progress included tangible advances along all fronts; with peer reviewed publications comprising multiple members of the project team in high-impact journals and other relevant metrics for evaluation of progress. Some examples of these advances are outlined below.

Recent Progress: The full account of our accomplishments during the project period are listed as archival publications. Some of the representative examples of our combined experiment-theory approach to probe the intricate interplay between thermal conductivity and charge transport are outlined below.

One part of our work has primarily focused on p-type lead chalcogenides: alloying on the Pb site to strategically modify the valence band structure and boost the power factor and introducing all-length-scale hierarchical defects into the crystals to suppress phonon transport and lower the thermal conductivity. Through this work, we have developed deeper understanding of the complex interplay between electronic and phonon transport culminating in an outstanding ZT ~ 2.5 in Na-doped PbTe-SrTe.[1] While these results represent notable progress, a remaining challenge was improving ZT over low and intermediate temperatures, as many of the potential applications of thermoelectricity require more moderate temperatures under 600 K. For this purpose, we have leveraged data driven approaches to design and discover new promising thermoelectric materials with favorable intrinsic power factors and thermal conductivities.

For the p-type materials, we have investigated the $NaSbTe_2$–PbTe solid solution ($NaPb_mSbTe_{m+2}$).[6] We studied the full solid solution in detail (m = 1–20), and found that in $NaPb_mSbTe_{m+2}$, the heavy alloying of Na^+ and Sb^{3+} cations onto the Pb^{2+} sites results in ultra-low thermal conductivities of 1.1–0.5 $W{\cdot}m^{-1}{\cdot}K^{-1}$ over 300–650 K, up to 35% lower than PbTe-SrTe over this temperature regime. Furthermore, the introduction of Na and Sb increases the hole effective mass, raising the Seebeck coefficient and shifting the maximum power factor to lower temperature for more $NaSbTe_2$ rich compositions. Together, these factors give excellent *ZT*s of 0.6–1.6 over 323–673 K in $NaPb_mSbTe_{m+2}$ when m = 10–20. These *ZT*s are up to 3 times higher than other state-of-the-art PbTe based thermoelectrics at room temperature and result in an outstanding average *ZT* of 1.1 between 323–67K K, making $NaPb_mSbTe_{m+2}$ competitive with Bi_2Te_3 over this temperature regime and among the most promising candidate thermoelectric materials under 700 K.

While excellent *ZT*s have been achieved for many alloys of p-type lead chalcogenides, the n-type counterparts have lagged behind. This is primarily because the energy difference between L and Σ (light and heavy) conduction bands is too large to achieve band convergence. Therefore, alternative strategies are needed to improve the *ZT* of n-type materials. Recently, we have demonstrated excellent n-type thermoelectric performance in Ga-doped PbTe[7] and Sb-doped PbTe-GeTe,[8] both of which have maximum *ZT*s of ~ 1.3 and record high average *ZT*s of ~ 1 over 300–800 K. Interestingly, the high performance in each system is achieved through entirely different means. In Ga-doped PbTe, the Ga introduces both shallow and deep level donor states. The deep states ionize at high temperatures, boosting the conductivity and increasing *ZT*.[7] Further, the Ga alloying weakens the electron phonon coupling, facilitating high carrier mobility in excess of 1200 $cm^2{\cdot}V^{-1}{\cdot}s^{-1}$. In contrast, in Sb-doped PbTe-GeTe, the GeTe alloy forms a supersaturated solid solution, which facilitates high point-defect scattering, low thermal conductivity, and high *ZT*.[8] These studies represent new routes towards future improvement in n-type PbTe.

We have also demonstrated record high *ZT* ~ 2.6 at 923 K and excellent device *ZT* of 1.3 over 300–800 K in single crystalline SnSe.[11-12] The single crystalline nature of these materials is unfavorable for device applications, which require more robust polycrystalline samples for commercial module fabrication. Unfortunately, the performance of polycrystalline SnSe currently lags significantly behind the single crystals as a result of the severe anisotropy and challenges to properly dope. We theoretically and experimentally investigated a range of dopants for polycrystalline SnSe, including Pb, Li, Na, and K, and found that Na and Pb doped samples show *ZT*s ~ 0.85 at 800 K.[13-14]

While optimizing existing thermoelectric systems is a primary objective for pushing device efficiency, an additional goal in the field is to discover the next generation of high-performance thermoelectric materials. Ternary and quaternary chalcogenide compounds are ideal systems for probing fundamental phonon-blocking mechanisms, and in many cases, also deliver outstanding thermoelectric performance.[2, 16] For example, we found that the $CsAg_5Te_3$ ternary chalcogenide system has a maximum figure of merit *ZT* of 1.5 at 727 K, which is attributed to ultralow thermal conductivity below 0.2 W/mK.[17] Importantly, using DFT, we determined that the remarkably low thermal transport was due to concerted rattling of Ag atoms, a previously unrecognized phonon scattering mechanism. Similarly, we demonstrated that the narrow-gap semiconductor $AgBi_3S_5$ could be electron-doped, yielding an n-type material with a figure of merit of approximately 1.0 at 800 K.[18] DFT-calculated phonon dispersions for these structures revealed low-frequency double rattling modes related to both Ag and Bi, which lowered the thermal conductivity below 0.5 W/mK at 300 K. Additionally, the $K_2Bi_8Se_{13}$ ternary system gave exceptional performance due to a combination of an increase in power factor coupled with a decrease in thermal conductivity.[19] The DFT-calculated electronic structure showed that the n-type material has multiple conduction bands lying near the Fermi level, which lead to a significant enhancement in the Seebeck coefficient. HREM revealed the presence of a secondary $K_{2.5}Bi_{8.5}Se_{14}$ phase at the grain boundaries, which contributed to the low thermal conductivity ranging from 0.42 to 0.2 W/mK, ultimately giving a *ZT* maximum of 1.3 at 873 K.

Motivated by our recent prediction of desirable thermoelectric band structure in the square planar oxide Bi_2PdO_4[20], we devised a new approach to inverse band structure design and applied it to search for similar thermoelectric materials. We screened the Open Quantum Materials Database for compounds analogous to Bi_2PdO_4 in terms of local coordination environment, nominal electron count, thermodynamic stability, electronic band gap, and structural anisotropy. The candidate compounds that were found exhibit many different chemistries, though Pd oxides are dominant. Two such Pd oxides (Bi_2PdO_3 and La_4PdO_7) were found to successfully achieve the desired flat-and-dispersive band structure leading to high power factor.[21] Looking beyond the oxides, we also identified one transition metal sulfide material similarly capturing such a band structure in addition to ultralow lattice thermal conductivity.

Future Plans: The ongoing and future plans will continue to pursue strategies for understanding the origins of Seebeck effect towards power factor enhancement, to further explore novel mechanisms for thermal conductivity reduction, and in search for new anisotropic materials with ultralow intrinsic lattice thermal conductivity. Embedded in all this is the need to understand the structural, chemical and electronic structural parameters that control doping behavior in these materials as well as phonon scattering.

Our ongoing research revolves around tailoring the structural, electronic defects and the role of multiple electronic bands in charge and phonon transport. The future activities will focus on addressing the following three fundamental underpinnings, towards the design of next generation thermoelectrics:

1) **The Discordant Atom Phenomena:** A discordant atom is the doped atomic species in the host crystal that is energetically-reluctant to occupy the host atomic site due to a combination of constraints; size, coordination, for example. We hypothesize that point defects created by discordant atoms in a crystalline matrix may affect phonon scattering across a range of mean free paths. We also propose to investigate the presence, stability, and concentration of point defects created by discordant atoms in a crystalline matrix, and determine their effect on both thermal transport and carrier mobilities in n- and p- type materials.

2) **Ultralow Thermal Conductivity in Layered Systems**: We have experimentally demonstrated and theoretically rationalized ultralow thermal conductivity materials such as SnSe. However, many more details and characteristics of such ultralow conductivity materials remain experimentally elusive and theoretically unexplained. We propose to probe the defining chemical characteristics of ultralow thermal conductivity, and its origin in the complex layered semiconductors.

3) **Multiband Semiconductors:** It is known that the multiple Fermi surface pocket electron/hole states accessible through doping may collectively contribute to the overall Seebeck coefficient and the power factor. The recent examples of doped SnSe and PbTe suggests that a strategy focusing on complex electronic structure materials will unveil new multi-band environments in chalcogenides. We will undertake a synergistic theory-experiment combined approach to identify electronic structural characteristics to leverage multiband semiconductors for high power factor.

Collectively, the future research aims to unravel some of the key scientific questions and fundamental crystal chemical basis for both power factor enhancement and reduction in thermal conductivity in thermoelectric materials. We are excited by the prospects for contributing to the basic energy science concepts related to design of next generation thermoelectric materials.

References:

1. DOE, U., Quadrennial Technology Review: An Assessment of Energy Technologies and Research Opportunities. *no. September* **2015**, 1-505.
2. Snyder, G. J.; Toberer, E. S., Complex thermoelectric materials. *Nat Mater* **2008,** *7* (2), 105-14.
3. Zeier, W. G.; Zevalkink, A.; Gibbs, Z. M.; Hautier, G.; Kanatzidis, M. G.; Snyder, G. J., Thinking like a chemist: intuition in thermoelectric materials. *Angewandte Chemie International Edition* **2016,** *55* (24), 6826-6841.
4. Zhao, L.-D.; Dravid, V. P.; Kanatzidis, M. G., The panoscopic approach to high performance thermoelectrics. *Energy & Environmental Science* **2014,** *7* (1), 251-268.

5. Biswas, K.; He, J.; Blum, I. D.; Wu, C. I.; Hogan, T. P.; Seidman, D. N.; Dravid, V. P.; Kanatzidis, M. G., High-performance bulk thermoelectrics with all-scale hierarchical architectures. *Nature* **2012,** *489* (7416), 414-8.
6. Slade, T. J.; Grovogui, J. A.; Hao, S.; Bailey, T. P.; Ma, R.; Hua, X.; Guéguen, A. l.; Uher, C.; Wolverton, C.; Dravid, V. P., Absence of Nanostructuring in NaPb m SbTe m+ 2: Solid Solutions with High Thermoelectric Performance in the Intermediate Temperature Regime. *Journal of the American Chemical Society* **2018**.
7. Su, X.; Hao, S.; Bailey, T. P.; Wang, S.; Hadar, I.; Tan, G.; Song, T. B.; Zhang, Q.; Uher, C.; Wolverton, C., Weak Electron Phonon Coupling and Deep Level Impurity for High Thermoelectric Performance Pb1− xGaxTe. *Advanced Energy Materials* **2018**, 1800659.
8. Zhong-Zhen, L.; Xiaomi, Z.; Xia, H.; Gangjian, T.; P., B. T.; Jianwei, X.; Ctirad, U.; Chris, W.; P., D. V.; Qingyu, Y.; G., K. M., High Thermoelectric Performance in Supersaturated Solid Solutions and Nanostructured n-Type PbTe–GeTe. *Advanced Functional Materials 0* (0), 1801617.
9. Tan, G.; Shi, F.; Doak, J. W.; Sun, H.; Zhao, L.-D.; Wang, P.; Uher, C.; Wolverton, C.; Dravid, V. P.; Kanatzidis, M. G., Extraordinary role of Hg in enhancing the thermoelectric performance of p-type SnTe. *Energy & Environmental Science* **2015,** *8* (1), 267-277.
10. Tan, G.; Hao, S.; Hanus, R. C.; Zhang, X.; Anand, S.; Bailey, T. P.; Rettie, A. J.; Su, X.; Uher, C.; Dravid, V. P., High Thermoelectric Performance in SnTe–AgSbTe2 Alloys from Lattice Softening, Giant Phonon–Vacancy Scattering, and Valence Band Convergence. *ACS Energy Letters* **2018,** *3* (3), 705-712.
11. Zhao, L. D.; Lo, S. H.; Zhang, Y.; Sun, H.; Tan, G.; Uher, C.; Wolverton, C.; Dravid, V. P.; Kanatzidis, M. G., Ultralow thermal conductivity and high thermoelectric figure of merit in SnSe crystals. *Nature* **2014,** *508* (7496), 373-7.
12. Zhao, L.-D.; Tan, G.; Hao, S.; He, J.; Pei, Y.; Chi, H.; Wang, H.; Gong, S.; Xu, H.; Dravid, V. P., Ultrahigh power factor and thermoelectric performance in hole-doped single-crystal SnSe. *Science* **2015**, aad3749.
13. Wei, T.-R.; Tan, G.; Zhang, X.; Wu, C.-F.; Li, J.-F.; Dravid, V. P.; Snyder, G. J.; Kanatzidis, M. G., Distinct impact of alkali-ion doping on electrical transport properties of thermoelectric p-type polycrystalline SnSe. *Journal of the American Chemical Society* **2016,** *138* (28), 8875-8882.
14. Wei, T.-R.; Tan, G.; Wu, C.-F.; Chang, C.; Zhao, L.-D.; Li, J.-F.; Snyder, G. J.; Kanatzidis, M. G., Thermoelectric transport properties of polycrystalline SnSe alloyed with PbSe. *Applied Physics Letters* **2017,** *110* (5), 053901.
15. Hao, S.; Dravid, V. P.; Kanatzidis, M. G.; Wolverton, C., Research Update: Prediction of high figure of merit plateau in SnS and solid solution of (Pb, Sn) S. *Apl Materials* **2016,** *4* (10), 104505.
16. Sootsman, J. R.; Chung, D. Y.; Kanatzidis, M. G., New and old concepts in thermoelectric materials. *Angewandte Chemie International Edition* **2009,** *48* (46), 8616-8639.
17. Lin, H.; Tan, G.; Shen, J. N.; Hao, S.; Wu, L. M.; Calta, N.; Malliakas, C.; Wang, S.; Uher, C.; Wolverton, C., Concerted rattling in CsAg5Te3 leading to ultralow thermal conductivity and high thermoelectric performance. *Angewandte Chemie International Edition* **2016,** *55* (38), 11431-11436.
18. Tan, G.; Hao, S.; Zhao, J.; Wolverton, C.; Kanatzidis, M. G., High thermoelectric performance in electron-doped AgBi3S5 with ultralow thermal conductivity. *Journal of the American Chemical Society* **2017,** *139* (18), 6467-6473.
19. Pei, Y.; Chang, C.; Wang, Z.; Yin, M.; Wu, M.; Tan, G.; Wu, H.; Chen, Y.; Zheng, L.; Gong, S., Multiple converged conduction bands in K2Bi8Se13: A promising thermoelectric material with extremely low thermal conductivity. *Journal of the American Chemical Society* **2016,** *138* (50), 16364-16371.
20. He, J.; Hao, S.; Xia, Y.; Naghavi, S. S.; Ozoliņš, V.; Wolverton, C., Bi2PdO4: A Promising Thermoelectric Oxide with High Power Factor and Low Lattice Thermal Conductivity. *Chemistry of Materials* **2017,** *29* (6), 2529-2534.
21. Isaacs, E. B.; Wolverton, C., Inverse Band Structure Design via Materials Database Screening: Application to Square Planar Thermoelectrics. *Chemistry of Materials* **2018,** *30* (5), 1540-1546.

Publications resulting from work supported by the DOE grant over the previous two years

1. K. Ahn, H. Kong, C. Uher, and M. G. Kanatzidis, Thermoelectric properties of p-type $Ag_{1-x}(Pb_{1-y}Sn_{y})_{m}Sb_{1-z}Te_{m+2}$, *J. Solid State Chem.* **242**, 34-42 (2016). DOI: https://doi.org/10.1016/j.jssc.2016.03.018

2. I. M. Dayton, N. Sedlmayr, V. Ramirez, T. C. Chasapis, R. Loloee, M. G. Kanatzidis, A. Levchenko, and S. H. Tessmer, Scanning tunneling microscopy of superconducting topological surface states in Bi_2Se_3, *Phys. Rev. B* **93**, 220506 (2016). DOI: https://doi.org/10.1103/PhysRevB.93.220506

3. E. D. Hanson, F. Shi, T. C. Chasapis, M. G. Kanatzidis, and V. P. Dravid, Two-dimensional bismuth-rich nanosheets through the evaporative thinning of Se-doped Bi_2Te_3, *J. Cryst. Growth* **436**, 138-144 (2016). DOI: https://doi.org/10.1016/j.jcrysgro.2015.11.033

4. S. Hao, V. P. Dravid, M. G. Kanatzidis, and C. Wolverton, Research Update: Prediction of high figure of merit plateau in SnS and solid solution of (Pb,Sn)S, *APL Materials* **4**, 104505 (2016). 10.1063/1.4964491

5. S. Hao, F. Shi, V. P. Dravid, M. G. Kanatzidis, and C. Wolverton, Computational Prediction of High Thermoelectric Performance in Hole Doped Layered GeSe, *Chem. Mater.* **28**, 3218-3226 (2016). DOI: 10.1021/acs.chemmater.6b01164

6. J. He, M. Amsler, Y. Xia, S. S. Naghavi, V. I. Hegde, S. Hao, S. Goedecker, V. Ozoliņš, and C. Wolverton, Ultralow Thermal Conductivity in Full Heusler Semiconductors, *Phys. Rev. Lett.* **117**, 046602 (2016). DOI:

7. M. Hong, T. C. Chasapis, Z.-G. Chen, L. Yang, M. G. Kanatzidis, G. J. Snyder, and J. Zou, n-Type $Bi_2Te_{3-x}Se_x$ Nanoplates with Enhanced Thermoelectric Efficiency Driven by Wide-Frequency Phonon Scatterings and Synergistic Carrier Scatterings, *ACS Nano* **10**, 4719-4727 (2016). DOI: 10.1021/acsnano.6b01156

8. X. Hu, P. Jood, M. Ohta, M. Kunii, K. Nagase, H. Nishiate, M. G. Kanatzidis, and A. Yamamoto, Power generation from nanostructured PbTe-based thermoelectrics: comprehensive development from materials to modules, *Energy Environ. Sci.* **9**, 517-529 (2016). DOI: 10.1039/C5EE02979A

9. C. Ioannidou, C. B. Lioutas, N. Frangis, S. N. Girard, and M. G. Kanatzidis, Analysis and Implications of Structural Complexity in Low Lattice Thermal Conductivity High Thermoelectric Performance PbTe–PbSnS2 Composites, *Chem. Mater.* **28**, 3771-3777 (2016). DOI: 10.1021/acs.chemmater.6b00710

10. H. Lin, G. Tan, J. N. Shen, S. Hao, L. M. Wu, N. Calta, C. Malliakas, S. Wang, C. Uher, C. Wolverton, and M. G. Kanatzidis, Concerted Rattling in $CsAg_5Te_3$ Leading to Ultralow Thermal Conductivity and High Thermoelectric Performance, *Angew. Chem. Int. Ed.* **55**, 11431-11436 (2016). DOI: 10.1002/anie.201605015

11. Y. Pei, C. Chang, Z. Wang, M. Yin, M. Wu, G. Tan, H. Wu, Y. Chen, L. Zheng, S. Gong, T. Zhu, X. Zhao, L. Huang, J. He, M. G. Kanatzidis, and L.-D. Zhao, Multiple Converged Conduction Bands in

$K_2Bi_8Se_{13}$: A Promising Thermoelectric Material with Extremely Low Thermal Conductivity, *J. Am. Chem. Soc.* **138**, 16364-16371 (2016). DOI: 10.1021/jacs.6b09568

12. G. J. Snyder, C. Wolverton, and Y. Tang, in Materials Aspect of Thermoelectricity (CRC Press, 2016), p. 365-398.

13. G. Tan and M. G. Kanatzidis, All-Scale Hierarchical PbTe: From Nanostructuring to a Panoscopic Material, Materials Aspect of Thermoelectricity, 125 (2016).

14. G. Tan, L.-D. Zhao, and M. G. Kanatzidis, Rationally Designing High-Performance Bulk Thermoelectric Materials, *Chem. Rev.* **116**, 12123-12149 (2016). DOI: 10.1021/acs.chemrev.6b00255

15. T.-R. Wei, G. Tan, X. Zhang, C.-F. Wu, J.-F. Li, V. P. Dravid, G. J. Snyder, and M. G. Kanatzidis, Distinct Impact of Alkali-Ion Doping on Electrical Transport Properties of Thermoelectric p-Type Polycrystalline SnSe, *J. Am. Chem. Soc.* **138**, 8875-8882 (2016). DOI: 10.1021/jacs.6b04181

16. D. Wu, L. D. Zhao, F. Zheng, L. Jin, M. G. Kanatzidis, and J. He, Understanding Nanostructuring Processes in Thermoelectrics and Their Effects on Lattice Thermal Conductivity, *Adv. Mater.* **28**, 2737-2743 (2016). DOI: 10.1002/adma.201505638

17. W. G. Zeier, A. Zevalkink, Z. M. Gibbs, G. Hautier, M. G. Kanatzidis, and G. J. Snyder, Thinking Like a Chemist: Intuition in Thermoelectric Materials, *Angew. Chem. Int. Ed.* **55**, 6826-6841 (2016). DOI: 10.1002/anie.201508381

18. X. Zhang, G. Tan, S. Hao, C. Wolverton, M. G. Kanatzidis, and V. P. Dravid, Microstructure Evolution in Nanostructured High-Performance Thermoelectrics: The case of p-type $Pb_{1-x}Na_xTe$-SrTe, *Microsc. Microanal.* **22**, 1268-1269 (2016). DOI: 10.1017/S1431927616007182

19. Y. Zhang, S. Hao, L.-D. Zhao, C. Wolverton, and Z. Zeng, Pressure induced thermoelectric enhancement in SnSe crystals, *J. Mater. Chem. A* **4**, 12073-12079 (2016). DOI: 10.1039/C6TA03625B

20. L.-D. Zhao, G. Tan, S. Hao, J. He, Y. Pei, H. Chi, H. Wang, S. Gong, H. Xu, V. P. Dravid, C. Uher, G. J. Snyder, C. Wolverton, and M. G. Kanatzidis, Ultrahigh power factor and thermoelectric performance in hole-doped single-crystal SnSe, *Science* **351**, 141-144 (2016). DOI: 10.1126/science.aad3749

21. L.-D. Zhao, X. Zhang, H. Wu, G. Tan, Y. Pei, Y. Xiao, C. Chang, D. Wu, H. Chi, L. Zheng, S. Gong, C. Uher, J. He, and M. G. Kanatzidis, Enhanced Thermoelectric Properties in the Counter-Doped SnTe System with Strained Endotaxial SrTe, *J. Am. Chem. Soc.* **138**, 2366-2373 (2016). DOI: 10.1021/jacs.5b13276

22. G. Zheng, X. Su, X. Li, T. Liang, H. Xie, X. She, Y. Yan, C. Uher, M. G. Kanatzidis, and X. Tang, Toward High‐Thermoelectric‐Performance Large‐Size Nanostructured BiSbTe Alloys via Optimization of Sintering‐Temperature Distribution, *Adv. Energy Mater.* **6**, 1600595 (2016). DOI: 10.1002/aenm.201600595

23. E. D. Hanson, S. Mayekar, and V. P. Dravid, Applying insights from the pharma innovation model to battery commercialization—pros, cons, and pitfalls, *MRS Energy & Sustainability* **4**, E10 (2017). DOI: 10.1557/mre.2017.12

24. J. He, S. Hao, Y. Xia, S. S. Naghavi, V. Ozoliņš, and C. Wolverton, Bi_2PdO_4: A Promising Thermoelectric Oxide with High Power Factor and Low Lattice Thermal Conductivity, *Chem. Mater.* **29**, 2529-2534 (2017). DOI: 10.1021/acs.chemmater.6b04230

25. S. D. Kang, J.-H. Pöhls, U. Aydemir, P. Qiu, C. C. Stoumpos, R. Hanus, M. A. White, X. Shi, L. Chen, M. G. Kanatzidis, and G. J. Snyder, Enhanced stability and thermoelectric figure-of-merit in copper selenide by lithium doping, *Materials Today Physics* **1**, 7-13 (2017). DOI: https://doi.org/10.1016/j.mtphys.2017.04.002

26. V. Kocevski and C. Wolverton, Designing High-Efficiency Nanostructured Two-Phase Heusler Thermoelectrics, *Chem. Mater.* **29**, 9386-9398 (2017). DOI: 10.1021/acs.chemmater.7b03379

27. G. Tan, S. Hao, J. Zhao, C. Wolverton, and M. G. Kanatzidis, High Thermoelectric Performance in Electron-Doped $AgBi_3S_5$ with Ultralow Thermal Conductivity, *J. Am. Chem. Soc.* **139**, 6467-6473 (2017). DOI: 10.1021/jacs.7b02399

28. T.-R. Wei, G. Tan, C.-F. Wu, C. Chang, L.-D. Zhao, J.-F. Li, G. J. Snyder, and M. G. Kanatzidis, Thermoelectric transport properties of polycrystalline SnSe alloyed with PbSe, *Appl. Phys. Lett.* **110**, 053901 (2017). DOI: 10.1063/1.4975603

29. D. Wu, L. Wu, D. He, L.-D. Zhao, W. Li, M. Wu, M. Jin, J. Xu, J. Jiang, L. Huang, Y. Zhu, M. G. Kanatzidis, and J. He, Direct observation of vast off-stoichiometric defects in single crystalline SnSe, *Nano Energy* **35**, 321-330 (2017). DOI: https://doi.org/10.1016/j.nanoen.2017.04.004

30. B. Xu, M. T. Agne, T. Feng, T. C. Chasapis, X. Ruan, Y. Zhou, H. Zheng, J. H. Bahk, M. G. Kanatzidis, G. J. Snyder, and Y. Wu, Nanocomposites from Solution‐Synthesized PbTe‐BiSbTe Nanoheterostructure with Unity Figure of Merit at Low‐Medium Temperatures (500–600 K), *Adv. Mater.* **29**, 1605140 (2017). DOI: 10.1002/adma.201605140

31. W. G. Zeier, S. Anand, L. Huang, R. He, H. Zhang, Z. Ren, C. Wolverton, and G. J. Snyder, Using the 18-Electron Rule To Understand the Nominal 19-Electron Half-Heusler NbCoSb with Nb Vacancies, *Chem. Mater.* **29**, 1210-1217 (2017). DOI: 10.1021/acs.chemmater.6b04583

32. J. Zhao, S. M. Islam, S. Hao, G. Tan, C. C. Stoumpos, C. Wolverton, H. Chen, Z. Luo, R. Li, and M. G. Kanatzidis, Homologous Series of 2D Chalcogenides Cs–Ag–Bi–Q (Q = S, Se) with Ion-Exchange Properties, *J. Am. Chem. Soc.* **139**, 12601-12609 (2017). DOI: 10.1021/jacs.7b06373

33. J. Zhao, S. M. Islam, S. Hao, G. Tan, X. Su, H. Chen, W. Lin, R. Li, C. Wolverton, and M. G. Kanatzidis, Semiconducting Pavonites $CdMBi_4Se_8$ (M = Sn and Pb) and Their Thermoelectric Properties, *Chem. Mater.* **29**, 8494-8503 (2017). DOI: 10.1021/acs.chemmater.7b03328

34. J. Zhao, S. M. Islam, O. Y. Kontsevoi, G. Tan, C. C. Stoumpos, H. Chen, R. K. Li, and M. G. Kanatzidis, The Two-Dimensional $A_xCd_xBi_{4-x}Q_6$ (A = K, Rb, Cs; Q = S, Se): Direct Bandgap

Semiconductors and Ion-Exchange Materials, *J. Am. Chem. Soc.* **139**, 6978-6987 (2017). DOI: 10.1021/jacs.7b02243

35. J. Zhao, S. M. Islam, G. Tan, S. Hao, C. Wolverton, R. K. Li, and M. G. Kanatzidis, The New Semiconductor $Cs_4Cu_3Bi_9S_{17}$, *Chem. Mater.* **29**, 1744-1751 (2017). DOI: 10.1021/acs.chemmater.6b05298

36. S. Anand, K. Xia, V. I. Hegde, U. Aydemir, V. Kocevski, T. Zhu, C. Wolverton, and G. J. Snyder, A valence balanced rule for discovery of 18-electron half-Heuslers with defects, *Energy Environ. Sci.* (2018). DOI: 10.1039/C8EE00306H

37. R. Deng, X. Su, S. Hao, Z. Zheng, M. Zhang, H. Xie, W. Liu, Y. Yan, C. Wolverton, C. Uher, M. G. Kanatzidis, and X. Tang, High thermoelectric performance in $Bi_{0.46}Sb_{1.54}Te_3$ nanostructured with ZnTe, *Energy Environ. Sci.* (2018). DOI: 10.1039/C8EE00290H

38. E. B. Isaacs and C. Wolverton, Inverse Band Structure Design via Materials Database Screening: Application to Square Planar Thermoelectrics, *Chem. Mater.* **30**, 1540-1546 (2018). DOI: 10.1021/acs.chemmater.7b04496

39. J. F. Khoury, S. Hao, C. C. Stoumpos, Z. Yao, C. D. Malliakas, U. Aydemir, T. J. Slade, G. J. Snyder, C. Wolverton, and M. G. Kanatzidis, Quaternary Pavonites $A_{1+x}Sn_{2-x}Bi_{5+x}S_{10}$ (A+ = Li+, Na+): Site Occupancy Disorder Defines Electronic Structure, *Inorg. Chem.* **57**, 2260-2268 (2018). DOI: 10.1021/acs.inorgchem.7b03091

40. Y. Luo, Y. Zheng, Z. Luo, S. Hao, C. Du, Q. Liang, Z. Li, K. A. Khor, K. Hippalgaonkar, J. Xu, Q. Yan, C. Wolverton, and M. G. Kanatzidis, n ‐ Type $SnSe_2$ Oriented ‐ Nanoplate ‐ Based Pellets for High Thermoelectric Performance, *Adv. Energy Mater.* **8**, 1702167 (2018). DOI: 10.1002/aenm.201702167

41. M. Maeda, K. Yamamoto, T. Mizokawa, N. L. Saini, M. Arita, H. Namatame, M. Taniguchi, G. Tan, L. D. Zhao, and M. G. Kanatzidis, Unusually large chemical potential shift in a degenerate semiconductor: Angle-resolved photoemission study of SnSe and Na-doped SnSe, *Phys. Rev. B* **97**, 121110 (2018). DOI: https://doi.org/10.1103/PhysRevB.97.121110

42. S. Maier, S. Ohno, G. Yu, S. D. Kang, T. C. Chasapis, V. A. Ha, S. A. Miller, D. Berthebaud, M. G. Kanatzidis, G. M. Rignanese, G. Hautier, G. J. Snyder, and F. Gascoin, Resonant Bonding, Multiband Thermoelectric Transport, and Native Defects in n-Type $BaBiTe_{3-x}Se_x$ (x = 0, 0.05, and 0.1), *Chem. Mater.* **30**, 174-184 (2018). DOI: 10.1021/acs.chemmater.7b04123

43. G. Tan, S. Hao, R. C. Hanus, X. Zhang, S. Anand, T. P. Bailey, A. J. E. Rettie, X. Su, C. Uher, V. P. Dravid, G. J. Snyder, C. Wolverton, and M. G. Kanatzidis, High Thermoelectric Performance in SnTe–$AgSbTe_2$ Alloys from Lattice Softening, Giant Phonon–Vacancy Scattering, and Valence Band Convergence, *ACS Energy Letters* **3**, 705-712 (2018). DOI: 10.1021/acsenergylett.8b00137

44. Z. Zheng, X. Su, R. Deng, C. Stoumpos, H. Xie, W. Liu, Y. Yan, S. Hao, C. Uher, C. Wolverton, M. G. Kanatzidis, and X. Tang, Rhombohedral to Cubic Conversion of GeTe via MnTe Alloying Leads to Ultralow Thermal Conductivity, Electronic Band Convergence, and High Thermoelectric Performance, *J. Am. Chem. Soc.* **140**, 2673-2686 (2018). DOI: 10.1021/jacs.7b13611

45. R. Deng, X. Su, Z. Zheng, W. Liu, Y. Yan, Q. Zhang, V. P Dravid, C. Uher, M. G Kanatzidis, and X. Tang, Thermal conductivity in $Bi_{0.5}Sb_{1.5}Te_{3+x}$ and the role of dense dislocation arrays at grain boundaries, *Science Advances* 4, 6, eaar5606(2018). DOI: 10.1126/sciadv.aar5606

46. X. Su, S. Hao, T. P Bailey, S. Wang, I. Hadar, G. Tan, T. ‐ B. Song, Q. Zhang, C. Uher, C. Wolverton, X. Tang, and M. G Kanatzidis, Weak Electron Phonon Coupling and Deep Level Impurity for High Thermoelectric Performance $Pb_{1-x}Ga_xTe$, *Adv. Energy Mater.* 1800659(2018). DOI: 10.1002/aenm.201800659

47. Z. Luo, X. Zhang, X. Hua, G. Tan, T. P. Bailey, J. Xu, C. Uher, C. Wolverton, V. P. Dravid, Q. Yan,* M. G. Kanatzidis, High Thermoelectric Performance in Supersaturated Solid Solutions and Nanostructured n-type PbTe-GeTe, *Adv. Funct. Mater.* 2018, 1801617

Nanostructured Polymer Electrolytes: Tuning Interfaces to Manipulate Transport

Thomas H. Epps, III (University of Delaware; Department of Chemical & Biomolecular Engineering and Department of Materials Science & Engineering)

Lisa M. Hall (The Ohio State University; Department of Chemical & Biomolecular Engineering)

Program Scope

We are developing new interfacially-modified (tapered) block polymers [TBPs] (see Figure 1) through a joint experimental and theoretical effort, with a specific focus on nanoscale network formation and lithium ion transport in salt-doped electrolytes.

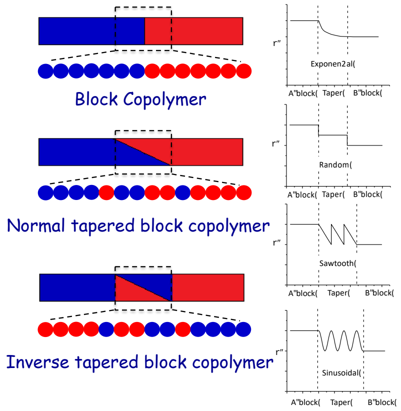

Figure 1: Illustration of the simplest composition profiles in tapered block polymers, and other complex profiles that can lead to unique behavior.

Theory and Simulation Innovations

- Ability to smoothly transition between theory and simulation to combine equilibrium phase information with key system dynamics
    - fDFT: freely-jointed bead-based polymer chains; includes density fluctuations, ions with hard cores plus short-ranged attractions and full Coulomb interactions (in contrast to simpler theories); used to obtain equilibrium density profiles
    - MD: bead-spring chains with ions and Coulomb interactions; used to obtain polymer dynamics and ion transport
- Use of fDFT to determine the lowest free energy phase and create an initial structure for the MD: this strategy has been developed in the **Hall** group and ensures the correct microphase–separated state is obtained in the simulations and also significantly reduces equilibration time
- Validation of models by comparing to multiple types of experimental data; we are closely validating the form of the fDFT-calculated interfacial density profiles through corresponding experiments probing TBP interfacial density profiles

Experimental Innovations

- Innovative tapered BP design to mitigate unfavorable interactions (lower effective interaction parameter), control chain stretching that promotes coordinated lithium ion/polymer backbone motion, and significantly reduce order-disorder transition temperatures in doped systems

- Significantly improved ion-conductivity by using tapered interfaces to reduce conducting-block glass transition temperatures and increase chain motion, thereby retaining the complete advantages of traditional block polymer electrolytes plus increased conductivity
- Unique tapered polymer design that significantly improves on PEO-based polymer electrolytes; use of poly(styrene-*b*-*oligo*-oxyethylene methacrylate) [PS-POEM] TBPs (see also Figure 2)
- Detailed characterization of lithium salt distributions in polymer domains using a cluster ion etching in X-ray Photoelectron Spectroscopy (XPS) combined with X-ray and neutron reflectivity (XRR and NR)

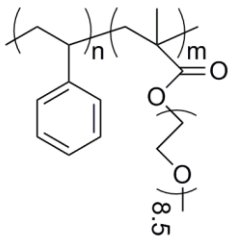

Figure 2: Molecular structure of PS-POEM BP with PEO-like side chains (branches).

Recent Progress

To date, we have completed several impactful studies. For example, Figure 3 shows the results from a combined **Epps**/**Hall** analysis of the interfacial profiles in non-tapered, normal-tapered, and inverse-tapered poly(styrene-*b*-isoprene)-based BPs.[1] A major outcome of that work was the quantitative agreement in segment density distributions obtained from XRR and fDFT. This accomplishment represents a significant advance because it demonstrated that we can map modeling results directly onto experimental data, which enables the prediction and validation of experimental findings through detailed theory and simulation insights. The above system was not salt-doped, and we have expanded those efforts to better understand copolymer behavior in cases where a small molecule salt is added, as described below.

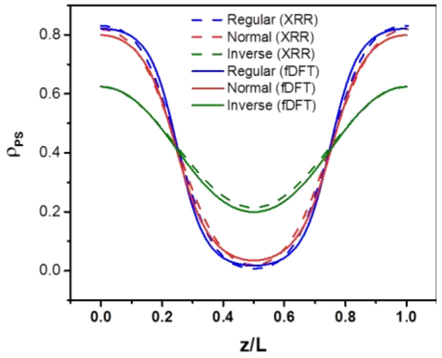

Figure 3: Experimental (XRR, dashed lines) and computational (fDFT, solid lines) density profile data generated by Epps and Hall for a set of poly(isoprene-*b*-styrene) tapered BPs, showing the level of agreement obtained from combined experimental/theoretical studies of actual systems.[1]

To date, we (**Epps**/**Hall**) have probed the interfacial profiles in PS-POEM BPs of various architectures (linear *vs.* cyclic), again using a joint experimental/modeling approach. In this case, we leveraged salt doping of BPs in thin film geometries to demonstrate how BP architecture influenced self-assembly and interfacial widths as a function of effective segregation strength (see Figure 4).[2] The domain spacing and interfacial widths were measured with XRR and compared to MD results; we were able to semi-quantitatively capture the major trends. This unique BP system allows us to directly probe the interplay between chain architecture and segregation strength, which is especially critical for ion-doped polymer systems, in which spatial distributions of salt can change during charge/discharge cycles leading to local differences in BP energetics. Finally, we found that the cyclic BPs had ~20% smaller domain spacings than the linear BPs at all $\chi_{eff}N$s and lower absolute sensitivities to changes in χ_{eff} at identical molecular weights.[2]

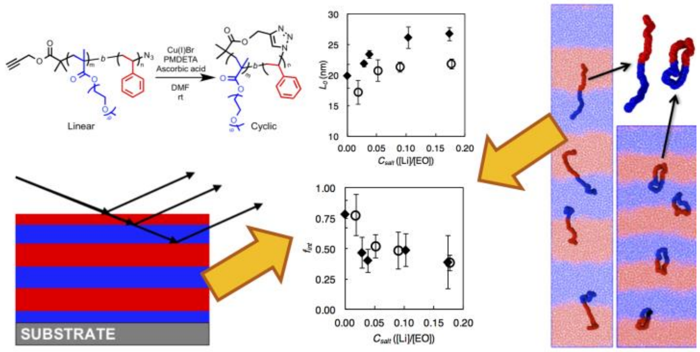

Figure 4: Synthesis, domain spacing, and interfacial width characterization of linear and cyclic PS-POEM BPs. MD simulations were coupled to this effort to demonstrate the effect of architecture on domain spacing.[2]

With respect to the identification of salt distributions in BP domains, we recently reported a quantitative analysis of the lithium salt and polymer distributions in lithium salt-doped PS- POEM thin films, and we explored how the presence of salt affects BP chain conformations and thermodynamics.[3] For the lithium salt distribution, analysis of NR data indicated that all salt-doped BP specimens exhibited lithium salt distributions that were directly proportional with the local POEM concentration, a conclusion supported by the lack of even-order Bragg peaks that would result from scattering from salt-rich (centrally-localized) layers (Figure 5). Then, we used strong-segregation theory to extract both the effective Flory-Huggins interaction parameters and the POEM statistical segment lengths as a function of salt concentration from XRR data. Overall, this report demonstrated that the segregation strength increased at low salt concentrations before plateauing at higher concentrations, while the statistical segment length increased linearly.[3] Taken together, these insights can be harnessed to design new BP materials such as the TBPs and enhanced dielectric constant nanomaterials.

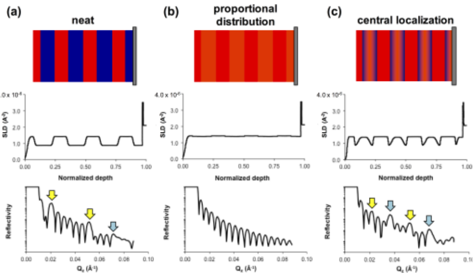

Figure 5: Representations of neutron contrast between PS (red) and POEM (blue) domains (top row) (a) in a neat PS-b-POEM film and if lithium salt distributed (b) proportionally through the POEM domains or (c) preferentially in the center of POEM domains at the contrast match point. Key differences between the three conditions are indicated in modeled SLD (middle row) and reflectivity (bottom row) profiles.[3]

Finally, we recently proposed a new coarse-grained model to capture the overall effects of having different polymer microphases with different dielectric constants (which impacts the ion interactions).[4] When modeling at the atomistic level, the effects of having local partial charges on all atoms allows for natural variation in local dielectric behavior. However, to include explicit partial charges or dipoles at the coarse-grained level would significantly increase complexity and take away the advantages of the coarse-grained approach. While some groups have modeled related systems with a locally varying dielectric strength with success,[5-6] we attempt to simplify the system further and use a model that can be easily implemented in both fDFT and standard MD simulations: we restrict ourselves to spherically symmetric pairwise interactions that do not change based on location. To account for the strong solvation of ions in the higher dielectric microphase, we implement an attraction of the form $-S_{ij}/r^4$, where S is set phenomenologically, between ions and the monomers of the solvating microphase and between ions and other ions (this form can be derived from classical or quantum electrostatics of the interaction between an ion and a induced dipole).[4] We then consider that the ions are predominantly in such a phase and use it to set a single background dielectric constant. In contrast to some prior work without strong solvation, we find (for high enough S) that the microphase domain spacing increases monotonically as a function of salt concentration as is seen in experiments. This potential form is easily added in theoretical calculations. In our initial work, ion and monomer size is the same, and this length scale represents the average size of both charges (ion-ion contact distance), though this assumption can be relaxed. This model also is able to reproduce the experimental trend where the fraction of interface plateaus and increases for large ion concentrations (or the χ_{eff} increases then decreases).

Future Plans

Our future plans include the experimental evaluation of TBP interfacial profiles (polymer and salt) in salt-doped thin films using XRR. These profiles will be compared to the molecular distributions predicted by the **Hall** group with the new salt potentials.

References

1. Luo, M.; Brown, J. R.; Remy, R. A.; Scott, D. M.; Mackay, M. E.; Hall, L. M.; Epps, T. H., III, Determination of Interfacial Mixing in Tapered Block Polymer Thin Films: Experimental and Theoretical Investigations. *Macromolecules* **2016,** *49* (14), 5213-5222.
2. Gartner, T. E.; Kubo, T.; Seo, Y.; Tansky, M.; Hall, L. M.; Sumerlin, B. S.; Epps, T. H., III, Domain Spacing and Composition Profile Behavior in Salt-Doped Cyclic vs Linear Block Polymer Thin Films: A Joint Experimental and Simulation Study. *Macromolecules* **2017,** *50* (18), 7169-7176.
3. Gartner, T. E.; Morris, M. A.; Shelton, C. K.; Dura, J.; Epps, T. H., III, Quantifying Lithium Salt and Polymer Density Distributions in Nanostructured Ion-Conducting Block Polymers. *Macromolecules* **2018,** *(in press)*.
4. Brown, J. R.; Seo, Y.; Hall, L. M., Ion Correlation Effects in Salt-Doped Block Copolymers. *Physical Review Letters* **2018**, *120*, 127801.
5. Wang, Z.-G., Fluctuation in electrolyte solutions: The self energy. *Physical Review E* **2010,** *81* (2), 021501-021501.
6. Nakamura, I.; Balsara, N. P.; Wang, Z.-G., Thermodynamics of Ion-Containing Polymer Blends and Block Copolymers. *Physical Review Letters* **2011,** *107* (19), 198301-198301.

Publications

1. Luo, M.; Brown, J. R.; Remy, R. A.; Scott, D. M.; Mackay, M. E.; Hall, L. M.; Epps, T. H., III *Macromolecules* **2016** *49*(14), 5213-5222. “Determination of Interfacial Mixing in Tapered Block Polymer Thin Films: Experimental and Theoretical Investigations”

2. Levine, W. G.; Seo, Y.; Brown, J. R.; Hall, L. M. *Journal of Chemical Physics* **2016** 145, 234907. “Effect of Sequence Dispersity on Morphology of Tapered Diblock Copolymers from Molecular Dynamics Simulations”

3. Seo, Y.; Brown, J. R.; Hall, L. M. “*ACS Macro Letters* **2017** 6, 375–380. “Diffusion of Selective Penetrants in Interfacially Modified Block Copolymers from Molecular Dynamics Simulations”

4. Morris, M. A.; Gartner, T. E.; Epps, T. H., III *Macromolecular Chemistry and Physics* **2017** *218*, 1600513. (invited talent article) “TALENT: Tuning Block Polymer Structure, Properties, and Processability for the Design of Efficient Nanostructured Materials Systems”

5. Brown, J. R.; Seo, Y.; Sides, S. W.; Hall, L. M. *Macromolecules* **2017** *50*, 5619–5626 “Unique Phase Behavior of Inverse Tapered Block Copolymers: Self-Consistent Field Theory and Molecular Dynamics Simulations”

6. Morris, M. A.; An, H.; Lutkenhaus, J. L.; Epps, T. H., III *ACS Energy Letters* **2017** *2*(8), 1919-1936. “Harnessing the Power of Plastics: Nanostructured Polymer Systems in Lithium-ion Batteries”

7. Gartner, T. E., III; Morris, M. A.; Shelton, C. K.; Dura, J. A.; Epps, T. H., III *Macromolecules* **2018** *51*(5), 1917-1926. “Quantifying Lithium Salt and Polymer Density Distributions in Nanostructured Ion-Conducting Block Polymers”

8. Brown, J. R.; Seo, Y.; Hall, L. M. *Physical Review Letters* **2018**, *120*, 127801. “Ion Correlation Effects in Salt-Doped Block Copolymers”

Pore Space Engineering and Functionalization in Porous Metal-Organic Framework Materials

PI: Pingyun Feng
Department of Chemistry, Materials Science and Engineering Program,
University of California, Riverside, CA 92521

Program Scope

The overall research goal of this project is to develop innovative and transformative synthetic-structural concepts and paradigms to create new crystalline porous materials with unprecedented chemical-structural features and architectural design for high-performance gas-sorption-based applications such as fuel storage, separation and sequestration of gases. Sorption properties of various gases on these new materials are studied to establish composition-structure-property correlation which is then utilized to further refine synthetic strategy to optimize porous materials for efficient energy-related applications.

Specific aims are:

(a) Heterometallic systems: to design synthetic strategies that allow creation of novel heterometallic systems with greatly enhanced stability and gas sorption properties such as tunable binding affinity and high gas-uptake capacity.

(b) Chemical control with functional binding sites: to design synthetic strategies that permit methodological introduction of functional active sites onto the porous frameworks as well as within channels or cages. This strategy allows the tuning of chemical functionality, which affects a number of key properties such as chemical stability and the strength of the host-guest interactions.

(c) Geometrical control with pore space partition: to design synthetic strategies for architectural pore space engineering including pore space partition to create multiple domains of pore space with pore size commensurate with the size of gas molecules for enhanced solid-gas interactions. The pore space partition strategy can dramatically increase the density of binding sites.

(d) Composition-structure-property correlation: to fully characterize thermal and chemical stability, and gas sorption properties for energy-related gases such as CH_4, H_2, and CO_2. Crystal structures of new porous materials will be determined. Crystal structure analysis is an important part in the development of new materials because it allows the understanding of compositional and structural features that correlate with materials' properties. Crystal structure analysis can also reveal previously unknown compositional and structural patterns that may lead to new or improved design strategies and more advanced materials.

Recent Progress

With the support from Materials Chemistry, Materials Sciences and Engineering Division, Office of Basic Energy Sciences, A significant progress on the proposed project has been made. The following summarizes several important contributions in the past two years.

(a) The development of an ultra-tunable platform for molecular engineering of high-performance crystalline porous materials

The development of high-performance materials is important for efficient and cost-effective carbon capture, gas storage and separation. Towards this goal, many materials have been studied. Among them, crystalline porous materials (**CPM**), have risen to a prominent position, because their compositional and structural variety lends them a great potential for property engineering. Currently, the best-performing materials, in terms of CO_2 uptake capacity, belong to the MOF-74 family made from 2,5-dihydroxy-1,4-benzenedicarboxylic acid and various metal ions such as Mg, Co, Ni, and Zn. Specifically, MOF-74-Mg has the highest CO_2 uptake capacity (≈ 230 cm^3 g^{-1} at 273 K and 1 bar) among all solids.[1]

While the MOF-74 structure type has highly desirable features such as high-density open-metal sites, as a platform for property engineering, it has significant limitations with respect to its compositional tunability. For example, the bonding mode between metal ions (M^{2+}) and the ligand in MOF-74 is unique and is inaccessible by other ligands. It is desirable to develop an alternative platform with greater tunability for engineering materials' properties.

In this study, a multi-step and dramatic development of a powerful platform has been achieved, leading to a family of CPMs with exceptional CO_2 uptake properties. This platform, based on the structure type invented at the PI's lab (the *pacs* type, **pacs** = partitioned acs, acs is a symbol for a particular topology), is far more tunable than the MOF-74 type in both metal and ligand types. The PI's materials are fundamentally different from MOF-74, because the pacs-type materials do not have open metal sites and exhibit a totally different mechanism for high CO_2 uptake. It is because of its unique mechanism, the pacs family of materials could accomplish extraordinarily high levels of CO_2 uptake capacity, with a low heat of adsorption (Q_{st}) that is only about half of that for MOF-74 and is among the lowest for MOFs. Such exceptional combination of low-Q_{st} and high-capacity uptake could bring an economic advantage because of the significantly reduced energy consumption for low-temperature activation (≈ 60 ºC) and regeneration of adsorbents. Also due to the low Q_{st}, the process of activation, adsorption, and regeneration induces no strain on the host frameworks, and therefore these pacs materials suffer no loss in crystallinity through these processes. In fact, better crystallinity is often seen after gas sorption measurements, which indicates excellent recyclability of these adsorbents. This work has been published in *Nat. Commun.* 2016, 7, 13645 (DOI: 10.1038/ncomms13645).

(b) Multivariable modular design of pore space partition

As described above, a pore-space-partition strategy involving the insertion of triangular-shaped (denoted as **C3** for 3-fold rotation axis) 2,4,6-tri(4-pyridyl)-1,3,5-triazine (abbreviated as tpt) ligand has been developed. This strategy partitions the MIL-88-type structure (called the **acs** net) to give a new framework type, denoted pacs (partitioned acs).[2] The key to achieve pacs structures is the use of a pore-partition agent whose symmetry and size match well with those of the parent framework. It was further found that the symmetry matching is a more important design parameter than the size matching because the softness of MIL-88 type structures relaxes the size-matching requirement between its channel size and the size of pore-partition agent.

In this study, the PI's group further demonstrate the power of the pacs platform by revealing new members of the pacs family prepared through synthesis routes that are distinctly different from that used for making members of the pacs family from the organic tpt ligand (denoted as **tpt-pacs** materials). Here, a symmetry-guided strategy to develop new pacs members has been developed that uses a variety of in-situ-formed, C3-symmetric di- or tri-nuclear 1,2,4-triazolate clusters as pore-partition agent. Compared to tpt-pacs, this new strategy has the following new features introduced by pore-partition agent: i) it uses much cheaper and readily available azolate ligands that are more diverse than tpt-type ligands, ii) it introduces two extra types of metal clusters (i.e., di- and tri-nuclear triazolate clusters) that permits greater property engineering (including optical or magnetic properties), and iii) it introduces a novel method of controlling the type, location, and orientation of open metal sites through pore-partition agent (triazolate clusters in this work).

While the PI's new design concept is simple and modular, the actual synthesis entails a complex multi-component system. The full assembly involves simultaneous formation of two separate coordination architectures (i.e., the 3-D acs-type metal-organic framework and 0-D di- or tri-nuclear metal-organic clusters) in a dual-metal and dual-ligand mixture and the eventual welding between them. To achieve the desired goal, all the components have to work cooperatively. In this work, a large variety of chemical combinations were explored, leading to a new generation of pacs family of materials with highly tunable properties. This work has been published in a high-impact journal *J. Am. Chem. Soc.* 2016, 138, 15102-15105 (DOI: 10.1021/jacs.6b07901).

(c) Toward the highest density of guest-binding metal sites in metal–organic frameworks

In perspective, this work represents the other extreme in the spectrum of the PI's design strategy, because it is in distinct contrast with the earlier developed pore-space partition method discussed above. The PI's pore space partition method features capabilities from total annihilation of guest-binding metal sites to the relocation of binding sites from the framework to the pore center. In contrast, the new strategy in this work is capable of maximizing the density of guest binding sites. Such broad synthetic capability to control the density and location of guest-binding sites developed in this DOE-supported project makes it possible to develop a suite of materials to realize tunable properties targeting various applications. This work demonstrates new chemical and structural possibilities in developing a record-setting high density of guest-binding metal sites in inorganic–organic porous materials.

Also in contrast with our work on multi-component systems that assign structural roles to each chemical component or even each functional group, this work examines a simpler one-metal-one-ligand system and focuses on features such as metal-to-ligand charge ratio and the ratio between different functional groups. The feasibility of this strategy has been demonstrated here by the synthesis of lithium-organic frameworks using linkers combining phenolate and carboxylate functionality. In porous materials, metal sites with coordinate solvents offer opportunities for many applications, especially those promoted by host–guest chemistry, but such sites are especially hard to create for lithium-based materials, because unlike transition metals, lithium does not usually possess a high enough coordination number for both framework construction and guest binding. In this work, this challenge is addressed by mimicking the functional-group ratio and metal-to-ligand charge ratio in high-performance MOF-74 family of materials. A family of rod-packing lithium–organic frameworks (denoted as CPM-47, CPM-48, and CPM-49) were obtained. These materials exhibit an extremely high density of guest-binding lithium sites, exceeding those in MOF-74. Also unusual is the homo-helical rod-packing in this series of materials, as compared to the hetero-helical rod packing by helices of opposite handedness in MOF-74. This work has been published in *Angew. Chem. Int. Ed.* 2018, 57, 6208-6211 (DOI: 10.1002/anie.201802267).

Future Plans

(a) To extend our success in the pacs-type platform to other chemical systems to further improve their gas adsorption and separation properties and selectivity. The adsorption and separation properties of different gas molecules will be systematically investigated.

(b) To further develop new heterometallic materials with dissimilar metal types. In addition to achieve new M^{3+}/M^{2+} combinations, materials with different M^{3+}/M^{2+} ratios will be developed. Their properties and ligands effects will be systematically studied.

(c) To develop new pore space partitioning strategies with diverse new chemistry approaches for gas separation and storage.

References

(1) Caskey, S. R., Wong-Foy, A. G. & Matzger, A. J. Dramatic tuning of carbon dioxide uptake via metal substitution in a coordination polymer with cylindrical pores, *J. Am. Chem. Soc.* 2008, 130, 10870-10871.

(2) Serre, C.; Mellot-Draznieks, C.; Surble, S.; Audebrand, N.; Filinchuk, Y.; Ferey, G. Role of Solvent-Host Interactions That Lead to Very Large Swelling of Hybrid Frameworks. *Science* 2007, 315, 1828-1831.

Publications

Publications wholly supported by DOE-BES under award no. DE-SC0010596 since 2016

1 Zhao, X.; Wang, Y., Li, D.; Bu, X.; Feng, P. Metal-Organic Frameworks for Separation. Adv. Mater. 2018, 30, 1705189. DOI: 10.1002/adma.201705189

2 Zhao, X.; Shimazu, M. S.; Chen, X.; Bu, X.; Feng, P. Homo-Helical Rod Packing as a Path Toward the Highest Density of Guest-Binding Metal Sites in Metal-Organic Frameworks. Angew. Chem. Int. Ed. 2018, DOI: 10.1002/anie.201802267

3 Lin, Q.; Mao, C.; Kong, A.; Bu, X.; Zhao, X.; Feng, P. Porphyrinic coordination lattices with fluoropillars, J. Mater. Chem. A 2017,5, 21189-21195. DOI:10.1039/C7TA06658A

4 Wang, Y.; Chen, X.; Lin, Q.; Kong, A.; Zhai, Q.; Xie, S.; Feng, P. Nanoporous carbon derived from a functionalized metal-organic framework as a highly efficient oxygen reduction electrocatalyst, Nanoscale 2017, 9, 862-868.

5 Zhai, Quan-Guo; Bu, Xianhui; Zhao, Xiang; Li, Dong-Sheng; Feng, Pingyun, Pore Space Partition in Metal-Organic Frameworks, Acc. Chem. Res. 2017, 50, 407-417.

6 Zhai, Q-G; Bu, X.; Mao, C.; Zhao, X.; Daemen, L.; Cheng, Y.; Ramirez-Cuesta, A. J.; Feng, P., An Ultra-Tunable Platform for Molecular Engineering of High-Performance Crystalline Porous Materials, Nat. Commun. 2016, 7, 13645. DOI: 10.1038/ncomms13645.

7 Zhao, Xiang; Bu, Xianhui; Nguyen, Edward; Zhai, Quan-Guo; Mao, Chengyu; Feng, Pingyun, Multivariable Modular Design of Pore Space Partition, J. Am. Chem. Soc. 2016, 138, 15102-15105.

8 Chen, Xitong; Bu, Xianhui; Lin, Qipu; Zhai, Quan-Guo; Zhao, Xiang; Wang, Yuan; Feng, Pingyun, Organization of Lithium Cubane Clusters into Three-Dimensional Porous Frameworks by Self-Penetration and Self-Polymerization, Cryst. Growth Des. 2016, 16, 6531-6536.

Publications supported partially by DOE-BES , under award no. DE-SC0010596.

1 Zhao, X.; Feng, J.; Li, J.; Lu, J.; Shi, W.; Yang, G.; Wang, G.; Feng, P.; Cheng, P. Metal-Organic Framework-Derived ZnO/ZnS Heteronanostructures for Efficient Visible-Light-Driven Photocatalytic Hydrogen Production. Adv. Sci. 2018, 1700590. DOI: 10.1002/advs.201700590

2 Kong, Aiguo; Mao, Chengyu; Wang, Yuan; Lin, Qipu; Bu, Xianhui; Feng; Pingyun, Hierarchically Porous Few-layer Porphyrinic Carbon Nanosheets Formed by VOx-Templating Method for High-Efficiency Oxygen Electroreduction, J. Mater. Chem. A **2016**, 4, 7305-7312. DOI: 10.1039/c6ta00154h.

Atomically Defined Doping of Graphene Nanoribbons for Mesoscale Electronics

Prof. Dr. Felix R. Fischer

Department of Chemistry University of California Berkeley

Program Scope

The outstanding transformative potential of graphene, an infinite two-dimensional sheet of carbon atoms tightly packed into a honeycomb lattice, has been recognized mostly due to its exceptionally high electric conductivity, thermal conductivity, and tensile strength. These undeniably very desirable properties, however, represent only a very small facet of the true potential of all-sp^2 carbon materials and its promise to revolutionize the field of molecular electronics. Graphene's most unusual characteristics emerge when the infinite macroscopic sheet is scaled down to nanometer dimensions. The exploration, realization, and implementation of these truly exotic magnetic and electronic properties rely on the development of innovative synthetic strategies that provide atomically precise control over the self-assembly of mesoscale objects. The central objective of this research is to develop the crucial chemical tools required to synthesize and to fine-tune the physical properties of graphene nanoribbons (GNR) with atomic precision. The innovative techniques and the expanded knowledge will be used to rationally tailor desired physical properties and function into nanometer-scale molecular electronic devices; e.g. transistors as logic gates in computing, data storage media based on electrically gated spin valves, or molecular amplifiers, all fabricated from readily available molecular building blocks into atomically defined GNRs.

Recent Progress

(1) *Heterostructures Through Divergent Edge Reconstruction in Nitrogen-Doped Segmented Graphene Nanoribbons*[1] Here we introduce a novel bottom-up synthetic strategy founded on the intrinsic reactivity of a single molecular precursor, which allows for a late-stage functionalization of segments along a GNR. We designed a molecular building block bearing a 9-methyl-9*H*-carbazole substituent as an internal reactive moiety. Once incorporated into the edges of a fully fused GNR the electron-rich 9-methyl-9*H*-carbazole can be converted into an electron-deficient phenanthridine substituent via a thermally induced ring-expansion/dehydrogenation reaction. This transformation allows for a versatile and reliable strategy toward the incorporation of heterocycles with diametrically opposite inductive effects at defined positions along the GNR backbone. Bond-resolved imaging of the cyclization/dehydrogenation product using non-contact atomic force microscopy (nc-AFM) indicates that the resulting GNRs feature atomically defined heterojunctions between segments lined by carbazole and phenanthridine substituents.

(2) *Synergistic Enhancement of Electrocatalytic CO_2 Reduction with Gold Nanoparticles Embedded in Functional Graphene Nanoribbon Composite Electrodes*[3] Here we demonstrate the intrinsic performance enhancement of a composite material comprised of gold nanoparticles

(AuNPs) embedded in a bottom-up synthesized GNR matrix for the electrocatalytic reduction of CO_2. Electrochemical studies reveal that the structural and electronic properties of the GNR composite matrix increase the AuNP electrochemically active surface area (ECSA), lower the requisite CO_2 reduction overpotential by hundreds of mV (catalytic onset > –0.2 V vs. reversible hydrogen electrode (RHE)), increase the Faraday efficiency (> 90%), markedly improve stability (catalytic performance sustained over > 24 h), and increase the total catalytic output (>100-fold improvement over traditional amorphous carbon AuNP supports). The inherent structural and electronic tunability of bottom-up synthesized GNR-AuNP composites affords an unrivaled degree of control over the catalytic environment, providing a means for such profound effects as shifting the rate determining step in the electrocatalytic reduction of CO_2 to CO, and thereby altering the electrocatalytic mechanism at the nanoparticle surface.

(3) *Atomically Precise Graphene Nanoribbon Heterojunctions from a Single Molecular Precursor*[4] We report a new technique for fabricating bottom-up GNR heterojunctions through post-growth manipulation that results in atomically perfect heterojunction structures from a single precursor. Such post-growth modification of GNR electronic properties offers a more flexible route for heterojunction fabrication, thus enabling additional bottom-up control that could lead to more complex future molecular device architectures. For this purpose, we designed a new type of GNR precursor molecule that incorporates sacrificial carbonyl groups and results in carbonyl-decorated fluorenone GNRs. While the carbonyl groups survive the GNR synthesis process, they can be removed later by exciting the fluorenone GNR (e.g., temperature, electric field). Fluorenone GNRs are found to have a different band gap and energy alignment than unfunctionalized chevron GNRs, thus enabling fabrication of Type II heterojunctions between carbonyl-decorated and carbonyl-free GNR segments that exhibit atomically precise interfaces. Bond-resolved STM imaging technique (BRSTM) in combination with scanning tunneling spectroscopy (STS) reveals that the electronic structure of atomically-precise bottom-up GNR heterojunctions fully transitions between different band gaps over a length scale of less than 1 nm across a heterojunction interface.

(4) *Inserting Porphyrin Quantum Dots in Bottom-Up Synthesized Graphene Nanoribbons*[8] We report the solution-based bottom-up synthesis and characterization of a GNR heterostructure comprised of two segments of solubilized cove GNRs (cGNRs) linked by a substituted tetraphenylporphyrin core acting as a highly tunable molecular quantum dot (QD). We herein focused on the integration of a disubstituted tetraphenylporphyrin (H_2(TPP)) and its metal complexes into a cGNR-H_2(TPP)-cGNR heterostructure. Electronic characterization of the resulting metalloporphyrin-cGNR hybrid materials by UV-Vis absorption and fluorescence emission spectroscopy shows strong electronic communication between the porphyrin and cGNR segments. We further demonstrate that reversible binding of primary amine ligands to the axial coordination site of the metalloporphyrin core can serve as a tool to direct the assembly of cGNR-Zn(TPP)-cGNR heterostructures on photolithographically patterned substrates.

(5) *Orbitally Matched Edge-Doping in Graphene Nanoribbons*[9] Herein, we report the bottom-up synthesis of a series of atomically precise nitrogen-, oxygen-, and sulfur-doped cGNRs. The placement of trigonal planar heteroatom dopants at defined positions along the convex protrusion lining the edges of cGNRs ensures the overlap of the heteroatom lone-pairs with the extended π-system. N-, O-, and S-dopant atoms were selected in this series for their varying degrees of electronegativity. Samples of edge-doped cGNRs were prepared in ultra-high vacuum (UHV) on a Au(111) surface. Scanning tunneling microscopy (STM) as well as non-contact atomic force microscopy (nc-AFM) confirms the precise dopant incorporation along the GNR edges. Scanning tunneling spectroscopy (STS) reveals a narrowing of the band gap by ~0.2–0.3 eV per dopant atom per monomer unit when compared to unsubstituted cGNRs. A correlation of the electronic band structures of N-, O-, and S-doped cGNRs establishes rational and predictable structure-function relationships that are corroborated by density functional theory (DFT) calculations.

(6) *Hierarchical On-Surface Synthesis of Graphene Nanoribbon Heterojunctions*[5,10] We describe a hierarchical fabrication strategy that allows the growth of bottom-up GNRs that preferentially exhibit a single heterojunction interface rather than a random statistical sequence of junctions along the ribbon. Such heterojunctions provide a viable platform that could be directly used in functional GNR-based device applications at the molecular scale. Our hierarchical GNR fabrication strategy is based on differences in the dissociation energies of C–Br and C–I bonds that allow control over the growth sequence of the block-copolymers from which GNRs are formed, and consequently yields a significantly higher proportion of single-junction GNR heterostructures. Scanning tunneling spectroscopy and density functional theory calculations confirm that hierarchically-grown heterojunctions between chevron GNR (cGNR) and binaphthyl-cGNR segments exhibit straddling Type I band alignment in structures that are only one atomic layer thick and 3 nm in width.

(7) *Topological Band Engineering of Graphene Nanoribbons*[13] Interfaces between topologically distinct GNRs characterized by different $\mathbb{Z}_2$ are predicted to support half-filled in-gap localized electronic states which can, in principle, be utilized as a tool for material engineering. Here we present the rational design and experimental realization of a topologically-engineered GNR superlattice that hosts a 1D array of such states, thus generating otherwise inaccessible electronic structure. Atomically-precise topological GNR superlattices were synthesized from molecular precursors on a Au(111) surface under ultra-high vacuum (UHV) conditions and characterized by low temperature scanning tunneling microscopy (STM) and spectroscopy (STS). Our experimental results and first-principles calculations reveal that the frontier band structure of these GNR superlattices is defined purely by the coupling between adjacent topological interface states. This novel manifestation of 1D topological phases presents an entirely new route to band engineering in 1D materials based on precise control of their electronic topology, and is a promising new platform for future studies of 1D quantum spin physics.

Future Plans

Continuing work beyond the sunset of this DOE Early Career Award will focus on the integration and the structural control of highly localized electron spins in bottom-up synthesized GNRs as functional materials for high temperature quantum computing, the development of metallic GNRs for low energy switching electronic devices, and the exploration of solution synthesized GNRs as functional supports for catalysis and energy storage.

Publications

(1) Marangoni, T.; Haberer, D.; Rizzo, D. J.; Cloke, R. R.; Fischer, F. R. *Chem. Eur. J.* **2016**, *37*, 13037-13040.
(2) Senkovskiy, B. V.; Fedorov, A. V.; Haberer, D.; Farjam, M.; Simonov, K. A.; Preobrajenski, A. B.; Marternsson, N.; Atodiresei, N.; Caciuc, V.; Blugel, S.; Rosch, A.; Verbitskiy, N. I.; Hell, M.; Evutushinsky, D. V. ; German, R.; Marangoni, T.; van Loosdrecht, P. H. M.; Fischer, F. R.; Grüneis, A. *Adv. Electron. Mater.* **2017**, 1600490.
(3) Rogers, C; Perkins, W. S.; Veber, G.; Williams, T. E.; Cloke, R. R.; Fischer, F. R. *J. Am. Chem. Soc.* **2017**, 139, 4052-4061.
(4) Nguyen, G. D.; Tsai, H.-Z.; Omrani, A. A.; Marangoni, T.; Wu, M.; Rizzo, D. J.; Rodgers, G.; Cloke, R.R.; Durr, R.A.; Sakai, Y.; Liou, F.; Aikawa, A. S.; Chelikowsky, J. R.; Louie, S. G.; Fischer, F. R.; Crommie, M. F. *Nature Nanotechnology* **2017**, *12*, 1077-1082.
(5) Bronner, C.; Marangoni, T.; Rizzo, D. J.; Durr, R.; Jorgensen, J.; Fischer, F. R.; Crommie, M. F. *J. Phys. Chem. C* **2017**, *121*, 18490-18495.
(6) Senkovskiy, B. V.; Pfeiffer, M.; Alavi, S. K.; Bliesener, A.; Zhu, J.; Michel, S.; Fedorov, A. V.; German, R.; Hertel, D.; Haberer, D.; Petaccia, L.;Fischer, F. R.; Meerholz, K.; van Loosdrecht, P. H. M.; Lindfors, K.; Grüneis, A. *Nano Lett.* **2017**, *17*, 4029-4037.
(7) Senkovskiy, B. V.; Haberer, D.; Usachov, D. Y.; Fedorov, A. V.; Ehlen, N.; Hell, M.; Petaccia, L.; Di Santo, G.; Durr, R. A.; Fischer, F. R.; Grüneis, A. *Phys. Status Solidi RRL* **2017**, 1700157.
(8) Perkins, W.; Fischer, F. R. *Chem. Eur. J.* **2017**, *23*, 17687-17691.
(9) Durr, R. A.; Haberer, D.; Lee, Y.-L.; Blackwell, R.; Kalayjian, A. M.; Marangoni, T.; Ihm, J.; Louie, S. G.; Fischer, F. R. *J. Am. Chem. Soc.* **2018**, *140*, 807–813.
(10) Bronner. C.; Durr, R. A.; Rizzo, D. J.; Lee, Y.-L.; Marangoni, T.; Kalayjian, A. M.; Rodriguez, H.; Zhao, W.; Louie, S. G.; Fischer, F. R.; Crommie, M. F. *ACS Nano* **2018**, *12*, 2193-2200.
(11) Passi, V.; Gahoi, A.; Senkovskiy, B. V.; Haberer, D.; Fischer, F. R., Grüneis, A.; Lemme, M. C. *ACS Appl. Mater. Interfaces* **2018**, *10*, 9900-9903.
(12) Senkovskiy, B. V.; Usachov, D. U.; Fedorov, A. V.; Haberer, D.; Ehlen, N.; Fischer, F. R., Grüneis, A. *2D Mater.* **2018**, *5*, 035007.
(13) Rizzo, D. J.; Veber, G.; Cao, T.; Bronner, C.; Chen, T.; Zhao, F.; Rodriguez, H.; Louie, S. G.; Crommie, M. F.; Fischer, F. R. *Nature* **2018**, *accepted*, arXiv:1805.06470.
(14) Pedramrazi, Z.; Chen, C.; Zhao, F.; Cao, T.; Nguyen, G.; Omrani, A.; Tsai, H.-Z.; Cloke, R.; Marangoni, T.; Rizzo, D.; Joshi, T.; Bronner, C.; Choi, W.; Fischer, F. R.; Louie, S.; Crommie, M. F. *Nano Lett.* **2018**, *ASAP*, DOI: 10.1021/acs.nanolett.8b00651.

High Pressure Synthesis of New Magnets, Featuring Diamagnetic Sources of Anisotropy

Danna E. Freedman | Northwestern University

Program Scope

Permanent magnets are the functional component of electric motors and generators found in numerous renewable energy applications spanning from regenerative brakes to wind turbines. Magnets that generate higher magnetic flux per volume are central to improved energy generation in these applications. To develop a new class of permanent magnets while retaining the properties conferred by rare-earth elements, a fundamentally different approach is required. We hypothesize that by engendering a covalent interaction between two elements, it will be possible to interact the two components of a magnetic moment—spin and orbital angular momentum—from two separate atoms to form a complete magnetic moment. This seed project focuses on the scale up of the compound $FeBi_2$, which was initially synthesized in our laboratory. Scale up approaches include slow decompression, alternate synthetic routes, and using fabrication approaches to more intimately mix the precursor elements.

Recent Progress

In our initial experiments we decompressed $FeBi_2$ down to 2.9 GPa, demonstrating a kinetic stability to the phase that enabled it to be recovered to an order of magnitude lower pressure than that needed to synthesize it (30 GPa). Our goal is to recover this exciting material to ambient pressures so that we can isolate samples for detailed physical properties measurements. We have undertaken three distinct approaches toward that goal, which we summarize below. Our two most notable results are the formation of a quenchable phase through antimony doping of $FeBi_2$, and the development of a new approach to preparing samples for diamond anvil cell syntheses.

Slow cryogenic decompression. We hypothesized that the two primary impediments to full decompression of $FeBi_2$ are the sudden stepwise reduction of pressure inherent to the release of cell pressure using bolts to adjust the load, and the relatively high thermal energy present at room temperature. To ameliorate decompression we designed and performed *in situ* XRD decompression experiments at the HPCAT beamlines of the Advanced Photon Source. We used a gas membrane apparatus to slowly and smoothly reduce the pressure in the cell over the course of a few hours while holding the entire cell at cryogenic temperatures (80 K) with liquid nitrogen. These experiments validate our hypothesis of an expanded stability field with slow decompression, but the low synthesis yield of the product in our initial experiments makes the data difficult to confidently interpret, due to peak broadening and diminishment. We have plans to revisit the cryogenic decompression in future experiments where the reaction yield has been significantly boosted (see next section).

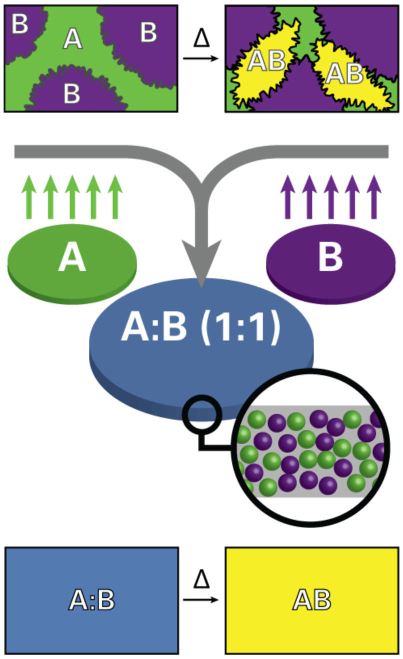

Figure 1. Schematic illustrating the issue of incomplete atomic mixing on the scale of laser heating.

Co-sputtering of elements for atomically-mixed precursors. Reaction yields in our DAC syntheses are typically on the order of 30–50 % at the small laser heated spot, and even then the product exists only within a very localized region of the sample. Thus, although we are able to obtain high quality structural data during synthesis, the overall yields of the novel phases are on the order of micrograms and can be difficult or impossible to locate in subsequent experiments where the sample must be found and then centered within a very narrow beam of radiation (FWHM on the order of microns). Our hypothesis for why synthesis only occurs on a very localized scale is that the atomic mixing is poor in our pressed powders, and is exacerbated by slow atomic diffusion under high pressures (Figure 1, top). A novel approach we are pursuing is to prepare co-sputtered films as the precursor material, rather than using pressed flakes of ball-milled powders. In this way, we anticipate a much higher conversion of our starting material, leading to a much greater yield, and thus opening the door to subsequent beamline experiments on the synthesized samples. We are currently preparing various precursor films using the NUFAB facility at Northwestern. We foresee this approach being transformative for other systems where atomically mixed precursors cannot be prepared by standard methods. We believe this approach can become the standard approach for diamond anvil cell based synthesis, and hope to validate this approach for widespread use.

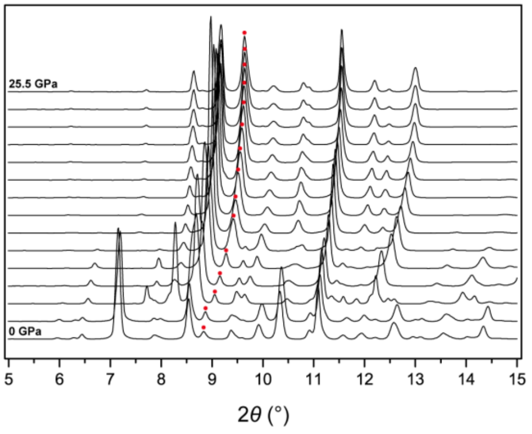

Figure 2. PXRD collected during decompression of Fe(Bi,Sb)$_2$, showing the retention of the most intense peak (red spot) down to ambient pressure.

Stabilization of unquenchable phases using doping. Another route we are pursuing toward the goal of recovering FeBi$_2$ to ambient pressures is the use of a chemical dopant as a stabilizing influence. A close structural analogue of FeBi$_2$ is FeSb$_2$, which adopts the same tetragonal structure above 14 GPa, and exists as an orthorhombic phase under ambient conditions. We proposed isolating a doped compound, Fe(Bi$_{1-x}$Sb$_x$), where the presence of antimony atoms extends the stability field of the FeBi$_2$ parent structure. Towards that end, we performed experiments at beamline 16-ID-B at the Advanced Photon Source at Argonne National

Laboratory using a BiSb 1:1 alloy we synthesized as one of our precursors. Fortunately, Bi–Sb forms a solid solution enabling us to tune the percent mixing of Bi–Sb precursors. We are able to detect the formation of the tetragonal structure at 30 GPa and with heating to 1400 K (the same conditions required for pure $FeBi_2$). The structure refinement reveals smaller cell dimensions in accord with the smaller Sb atoms. The intensity of the peaks drops over the decompression, but the major peak appears to remain after decompression to ambient pressure (Figure 2), demonstrating quenchability of this phase. We are pursuing scale-up reactions to obtain pellets of the quenchable $Fe(Bi_{1-x}Sb_x)$ phase to investigate its electronic and magnetic properties.

Future Plans

Within the remaining timeframe of the proposal, we will pursue these two promising results. Within the first goal of scaling up pure $FeBi_2$, we will combine the two approaches described above of slow decompression and sputtering to demonstrate quenchability. We will subject our co-sputtered films of 1:2 Fe:Bi to laser heating to 1400 K under pressures of 30 GPa to assess the impact of atomic mixing on the yield of $FeBi_2$. To enable full conversion of the sample we will use a wide beam (large FWHM) flat-top heating profile to raise the temperature of the entire flake at the same time, to minimize any effects from thermal diffusion gradients, which may also be causing problems in our standard laser heating approach using small heating spots. Decompression experiments will then be performed on the synthesized product to determine if the higher conversion leads to detection of the phase at lower pressures. If the sample can be detected under ambient pressures, we will be able to move forward with scale-up reactions using a multi-anvil press, allowing us to prepare large pellets of the $FeBi_2$ for characterization.

Further experiments in the antimony doping reactions will involve a variation of stoichiometry. This will allow us to determine the minimum amount of antimony required to stabilize the tetragonal structure to ambient pressures. It will also allow us to assess the impact of antimony sites on the crystal lattice, which could lead to interesting bulk properties through tuning of electronic bands (this direction will be supported by theory). Although bismuth and antimony are known to form Vegard alloys, we will likely adopt the co-sputtering technique to maximize the mixing between Fe and (Bi,Sb), leading to a higher yield and therefore a greater ability to assess any structural distortions during decompression (the subtle tetragonal→orthorhombic transition is more confidently detected or ruled out with a higher number of diffraction peaks). Sputtering methods also allow for an excellent control over stoichiometry, which will be crucial when trying to correlate crystal structure with atomic composition. Crucially, we will seek to scale up each of these compounds and acquire magnetometry data, resistivity data, and heat capacity data. The aggregate of these data will enable us to determine whether we synthesized a permanent magnet and to understand its properties.

References

Clarke, S. M.; Walsh, J. P. S.; Amsler, M.; Malliakas, C. D.; Yu, T.; Goedecker, S.; Wang, Y.; Wolverton, C.; Freedman, D. E. Discovery of a Superconducting Cu–Bi Intermetallic Compound by High-Pressure Synthesis. *Angew. Chem. Int. Ed.* **2016**, *55*, 13446–13449.

Clarke, S. M.; Amsler, M.; Walsh, J. P. S.; Yu, T.; Wang, Y.; Meng, Y.; Jacobsen, S. D.; Wolverton, C.; Freedman, D. E. Creating Binary Cu–Bi Compounds via High-Pressure Synthesis: A Combined Experimental and Theoretical Study. *Chem. Mater.* **2017**, *29*, 5276–5285.

Walsh, J. P. S.; Clarke, S. M.; Meng, Y.; Jacobsen, S. D.; Freedman, D. E. Discovery of $FeBi_2$. *ACS Cent. Sci.* **2016**, *2*, 867–871.

Powderly, K. M.; Clarke, S. M.; Amsler, M.; Wolverton C.; Malliakas, C. D.; Meng, Y.; Jacobsen, S. D.; Freedman, D. E. High-Pressure Discovery of β-NiBi *Chem. Commun.* **2017**, *53*, 11241–11244.

Walsh, J. P. S.; Freedman, D. E. High-Pressure Synthesis: A New Frontier in the Search for Next-Generation Intermetallic Compounds. *Acc. Chem. Res.* **2018**. DOI: 10.1021/acs.accounts.8b00143

Publications

None yet

Compositional Control of Fundamental Electronic and Magnetic Properties of Ordered Layered Multi-elemental MXenes

PI: Yury Gogotsi, Co-PIs: Steven May, Babak Anasori

A.J. Drexel Nanomaterials Institute and Department of Materials Science and Engineering, Drexel University, Philadelphia, PA 19104, USA

Program Scope

Research on two-dimensional (2D) materials have been rapidly growing in the past decade owing to their unique properties different from their bulk counterparts. Electronically, the quantum confinement effect present in 2D materials results in their distinct electronic structures. For example, charge carriers in graphene sheets can be described as massless Dirac fermions with high mobility exceeding 10,000 V cm^{-2} s^{-1}.(*1*) Transition metal dichalcogenides transform from in-direct to direct bandgap semiconductors with spin-valley coupling in the monolayer state.(*2*)

In 2011, another family of 2D transition metal carbides and nitrides, so called MXenes, was discovered at Drexel University.(*3*) MXenes have been shown to exhibit a unique combination of properties, including metallic conductivity, hydrophilicity, and the ability of intercalating ions, making them excellent candidates for applications ranging from energy storage devices to electromagnetic interference shielding.(*4-6*) To date, close to 30 MXenes have been experimentally synthesized and a dozen more were studied theoretically. Among them are ordered multi-elemental MXenes, in which one or two layers of a transition metal (e.g., titanium) are sandwiched between two layers of another transition metal (e.g., molybdenum) in a 2D carbide structure.(*7*) This discovery not only significantly expands the MXene family, but also provides new means to control their physical properties.

This research project focuses on how the different arrangement of transitions metal atoms, surface terminations, and intercalated species can be used to control the electronic and magnetic properties of the ordered multi-element MXenes. Guided by computational calculations, synthesis efforts will target stabilizing new multi-elemental MXenes, where transition metals chemistry is systematically varied in both the surface and middle layers. We will then investigate how to control MXene properties through surface chemistry and intercalation by using solution or high temperature gas-solid reactions.

Recent Progress

Effects of intercalation and surface terminations on MXenes' electronic properties were studied using *in situ* vacuum-annealing, electrical biasing, and spectroscopic analysis within the transmission electron microscope. We showed that MXenes' electronic properties are governed by both intra- and inter-flake electron hopping processes, as summarized in Figure 1. The former and the latter processes are affected by intercalated species and surface termination, respectively.

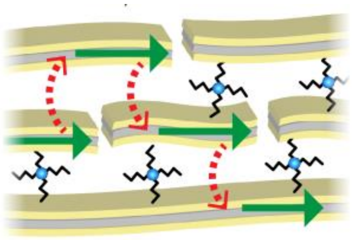

Figure 1. Intra- (green arrow) and inter-flake (red arrow) electron hopping processes in MXene film

Via vacuum-annealing, we demonstrated that the electronic conductivity of the three MXenes, $Ti_3C_2T_x$, Ti_3CNT_x, and $Mo_2TiC_2T_x$ studied can largely be improved. At low annealing temperature (<500 °C), the increase in electronic conductivity is attributed to removal of intercalated species such as water molecules and tetrabutylammonium ions, whereas the partial removal of -F or -O termination is responsible for further increase in conductivity after high temperature annealing, as shown in Figure 2. We also pointed out that the initially semiconductor-like behavior observed in Ti_3CNT_x and $Mo_2TiC_2T_x$ MXenes is attributed to the thermally-activated inter-flake electron hopping processes, where the samples exhibit metallic behavior after removal of the intercalated species.

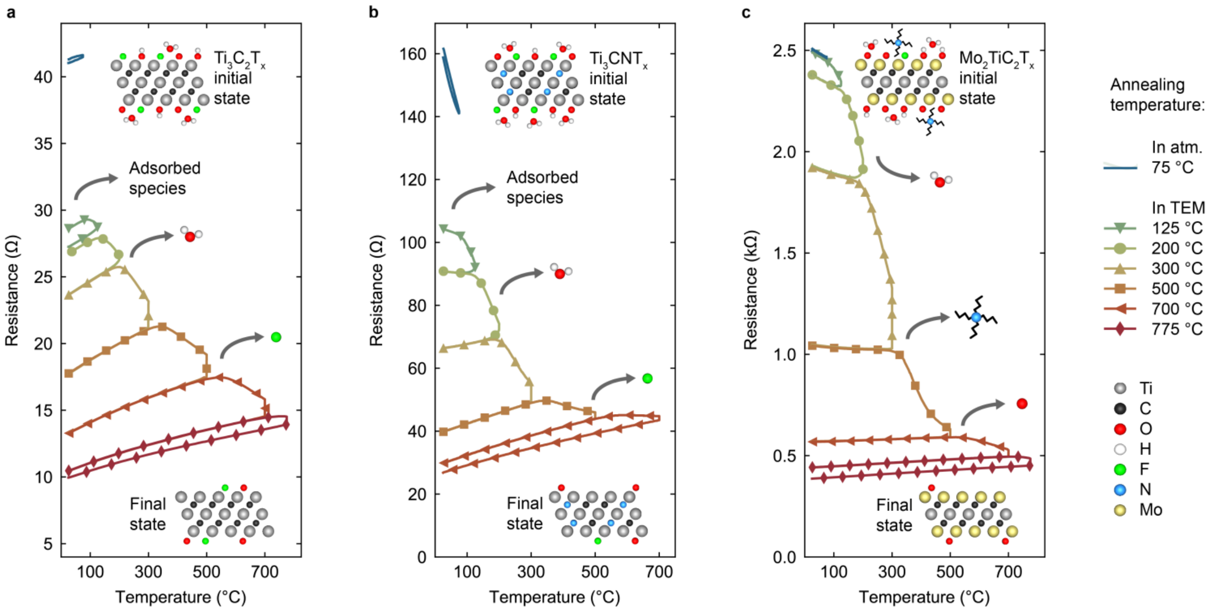

Figure 2. Evolution of MXenes' resistance upon vacuum annealing. a) $Ti_3C_2T_x$, b) Ti_3CNT_x, and c) $Mo_2TiC_2T_x$

Finally, we correlated our finding with theoretical prediction concluding that removing surface terminations (-F for $Ti_3C_2T_x$ and -O for $Mo_2TiC_2T_x$) results in higher electronic conductivity due to increase in carrier concentration close to the Fermi level, as shown in Figure 3. *In situ* electron energy loss spectra (EELS) shown in Figure 3a and d show a clear reduction of -F and O- terminations of $Ti_3C_2T_x$ and $Mo_2TiC_2T_x$ after annealing at 775 °C, respectively. Figure 3b and e show a clear correlation between reduction of surface termination and increase in MXenes' electronic conductivity. Figure 3c summarizes the change in electronic structure upon surface de-functionalization.

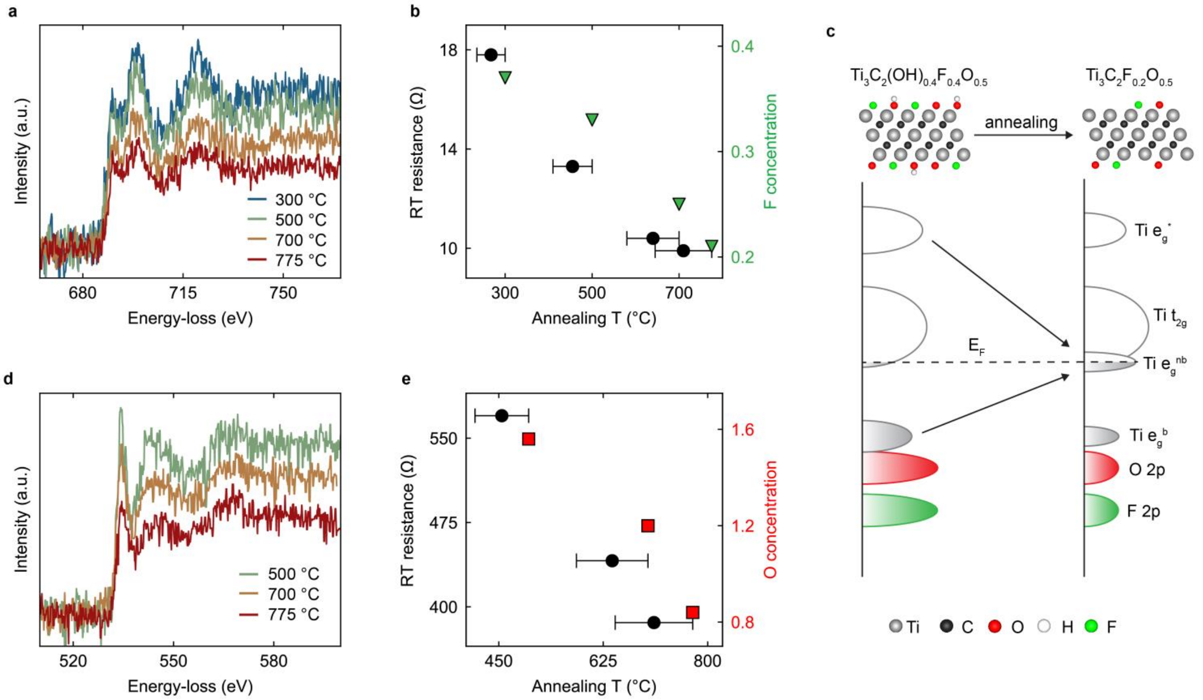

Figure 3. Correlation of MXene surface termination and conductivity. a) *in situ* EELS spectra of the fluorine K-edge of $Ti_3C_2T_x$. b) Comparison of the post-anneal room temperature resistance (black circles) and –F concentration (green triangles). c) Schematic showing the general effect of de-functionalization on the electronic structure of $Ti_3C_2T_x$. d) *in situ* EELS measurements spectra of the oxygen K-edge of $Mo_2TiC_2T_x$. e) Comparison of the post-anneal room temperature resistance (black circles) with the concentration of –O (red squares)

Future Plans

Our experimental approach is to systematically synthesize ordered $(M_2M')AlC_2$ (312) and $(M_2M'_2)AlC_3$ (413) MAX phases and convert them to $(M_2M')C_2$ (32) and $(M_2M'_2)C_3$ (43) MXenes, such as Mo_2TiC_2, Cr_2TiC_2, Cr_2VC_2, $Nb_2Ti_2C_3$, etc. Our approach to controlling MXene properties through surface chemistry and intercalation is to manipulate surface terminations and intercalants, by using solution or high temperature gas-solid reactions. Electronic and magnetic properties of these films will be fully characterized, and the results will be compared with predictions of various theoretical models in order to develop a deeper understanding of the effects of terminations and intercalants on properties. The focus will also be put on characterization of MXene single-flake devices to study their intrinsic transport properties. We will also use soft X-ray absorption spectroscopy (XAS) to probe the conduction band states derived from the M-site transition metals as a function of the terminations and intercalants species. In addition, we will continue to explore the magnetic properties of MXenes with the center largely on Mn and Cr-containing MXenes, which have been predicted to be ferromagnetic.(*8*-*9*)

References

1. K. S. Novoselov *et al.*, Electric field effect in atomically thin carbon films. *Science* **306**, 666-669 (2004).
2. Q. H. Wang, K. Kalantar-Zadeh, A. Kis, J. N. Coleman, M. S. Strano, Electronics and optoelectronics of two-dimensional transition metal dichalcogenides. *Nat. Nanotechnol.* **7**, 699-712 (2012).
3. M. Naguib *et al.*, Two-dimensional nanocrystals produced by exfoliation of Ti_3AlC_2. *Adv. Mater.* **23**, 4248-4253 (2011).
4. M. R. Lukatskaya *et al.*, Cation intercalation and high volumetric capacitance of two-dimensional titanium carbide. *Science* **341**, 1502-1505 (2013).
5. M. R. Lukatskaya *et al.*, Ultra-high-rate pseudocapacitive energy storage in two-dimensional transition metal carbides. *Nature Energy* **6**, 17105 (2017).
6. F. Shahzad *et al.*, Electromagnetic interference shielding with 2D transition metal carbides (MXenes). *Science* **353**, 1137-1140 (2016).
7. B. Anasori *et al.*, Two-Dimensional, Ordered, Double Transition Metals Carbides (MXenes). *ACS Nano* **9**, 9507-9516 (2015).
8. M. Khazaei *et al.*, Novel Electronic and Magnetic Properties of Two-Dimensional Transition Metal Carbides and Nitrides. *Adv. Funct. Mater.* **23**, 2185-2192 (2013).
9. N. Frey *et al.*, Tuning Noncollinear Spin Structure and Anisotropy in Ferromagnetic Nitride MXenes. *ACS Nano,* **Just Accepted Manuscript**, DOI: 10.1021/acsnano.8b03472

Publications

1. James L. Hart, Kanit Hantanasirisakul, Andrew C. Lang, Babak Anasori, David Pinto, Yevheniy Pivak, J. Tijn van Omme, Steven J. May, Yury Gogotsi, Mitra L. Taheri. Control of MXenes' Electronic Properties Through Termination and Intercalation, *submitted*.

Materials and Interfacial Chemistry for Next-Generation Electrical Energy Storage

John Goodenough and Arumugam Manthiram, Materials Science and Engineering Program, University of Texas at Austin, Austin, TX 78712

1. Program Scope

The major goal of the project is to develop materials and alternative strategies that will enable the next generation of safe, low-cost, rechargeable batteries. The project focuses on the fundamental structural, chemical, surface, and interfacial aspects of the major materials components of the next generation of rechargeable batteries: cathodes, anodes, electrolytes, and the interfaces associated with them. The project research has evolved into two different strategies for realization of rechargeable batteries that can meet the specifications for storage of electric power from renewable sources and for powering electric vehicles: one strategy uses a conventional organic liquid electrolyte and the other uses a solid electrolyte. With solid electrolytes, the work is focused on alkali-metal plating/stripping on solid electrolytes, cells with a mediator-ion solid electrolyte, and efficient electrocatalysts for oxygen reduction and evolution reactions in mediator-ion cells employing air as a cathode. With liquid electrolytes, the work is focused on polyvalent-metal – sulfur cells, cells based on sulfur and selenium, and novel alloy anode framework. The work has led to 74 journal articles published, 7 articles in press, and 4 articles submitted during the past 2 years. We present below briefly the recent progress on the two strategies, *i.e.*, cells based on solid electrolytes and liquid electrolytes, along with future plans.

2. Recent Progress

2.1. Cells Based on Solid Electrolytes

Alkali-metal plating/stripping on solid electrolytes: An advantage of a solid electrolyte is a large electronic energy gap $E_g = E_c - E_v$, where E_c and E_v are, respectively, the energies of the bottom of the conduction band and the top of the valence band. Long-term stability and cycle life of a cell depend on locating the anode and cathode electrochemical potentials μ_A and μ_C, respectively, within the electrolyte E_g. With the conventional organic-liquid electrolytes, this is not possible where μ_A is less than 1.3 eV below the Fermi level of metallic lithium; formation of a passivating solid-electrolyte interphase (SEI) is needed on the anode and also on a large-voltage cathode to enable an acceptably large open-circuit voltage $V_{oc} = (\mu_A - \mu_C)/e$ where e is the electron charge. Breakdown and reformation of the SEI with a liquid electrolyte introduces capacity fade. With a stable SEI at an anode/electrolyte solid-solid interface, we have achieved long cycle life with solid electrolytes. We have demonstrated that the key to plating/stripping dendrite-free anodes is the ability of the electrolyte to wet the surface of a solid electrolyte or the separator of a liquid electrolyte where the pore size of the porous electrolyte separator is smaller than a critical diameter. Simply blocking dendrites with a solid electrolyte is not adequate; dendrite growth opens the anode/electrolyte interface. However, anode dendrites do not form and grow during charge where the surface of a solid electrolyte is wet by the anode. Wetting occurs where the bonding of the alkali-metal anode to the solid electrolyte or se parator is stronger than the bonding of the alkali metal to itself. A liquid electrolyte that wets a solid electrolyte does not grow dendrites. We showed that Na-K alloy that is liquid at room temperature can act as a sodium or a potassium anode depending on whether the cathode insertion oxide accepts Na^+ versus K^+ guest ions at lower energies.[1] In addition, we have demonstrated low-impedance plating/stripping over a long cycle life of a metallic lithium anode where a stable solid SEI wets the solid electrolyte and is wet by the alkali-metal anode. The SEI may be formed by a reaction between the anode and the electrolyte or by a coating of the electrolyte surfaces with a thin polymer film. The strong wetting bond constrains the anode volume change during cycling to be perpendicular to the interface, and this 1D volume change can be accommodated in a cell. Another problem we addressed was the fabrication of a thin, flexible solid-electrolyte membrane with a polymer-solid-electrolyte composite that can be handled for cell fabrication, and we are exploring how to maintain a high ionic conductivity in those membranes.[2] Moreover, we have provided a comprehensive account of the electrode-electrolyte interfaces involved with various types of electrolytes and anode or cathode, including sulfur cathodes.

Cells with a mediator-ion solid electrolyte: We have broadened the mediator-ion battery concept with a NASICON-based sodium-ion solid electrolyte (Na-SSE) and lithium-ion solid electrolyte (Li-SSE) to a number of cathode redox couples with a zinc or iron anode in aqueous solutions.[3] The redox couples pursued include air, bromine, ceric ion, ferrocyanide, quinone, and polysulfide. The working principle of a "mediator-ion" battery is given in **Figure 1a** with the Zn(LiOH) ‖ Li-SSE ‖ Br_2(LiBr) cell as an example. During the discharge process, the zinc-metal anode is first oxidized to zinc ions (Zn^{2+}), which subsequently integrate with the negatively charged hydroxide ions (OH^-) to produce zincate ions $[Zn(OH)_4]^{2-}$. At the cathode, the reduction of liquid bromine forms negatively charged bromide ions. To balance the ionic charge between the anolyte and catholyte, the lithium ions in the anolyte migrate through the solid electrolyte from the anode to the cathode. During charge, the opposite processes occur. **Figure 1b** and **c** present the electrochemical cycling performances of two representative low-cost battery systems, a Zn (alkaline) ‖ Na-SSM ‖ polysulfide (alkaline) battery and a Fe(LiOH) ‖ Li-SSE ‖ $K_3Fe(CN)_6$(NaOH) battery. The mediator-ion strategy allows the use of active electrode (anode and cathode) materials in any physical form (solid, liquid, or gas), eliminates the crossover of chemicals between the two electrodes, and circumvents the dendrite problem with metal-anodes.

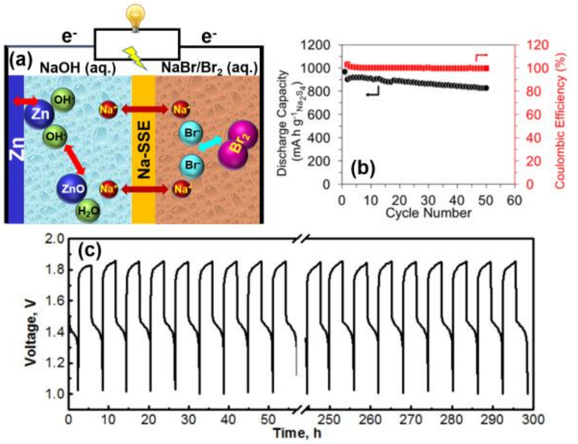

Figure 1. (a) Schematic of a Zn(LiOH) ‖ Li-SSE ‖ Br_2(LiBr) mediator-ion cell. (b) Discharge capacity and Coulombic efficiency versus cycle number of a Zn (alkaline) ‖ Na-SSM ‖ polysulfide (alkaline) cell. (c) Charge-discharge profiles of a Fe(LiOH) ‖ Li-SSE ‖ $K_3Fe(CN)_6$(NaOH) cell operated with an alkaline Fe anode and a liquid $K_3Fe(CN)_6$ catholyte.

Efficient electrocatalysts for oxygen reduction and oxygen evolution reactions: To use air as a cathode in the above strategy, we have explored new electrocatalysts. A one-dimensional (1D) hybrid catalyst composed of ultra-small cobalt phosphide nanoparticles supported by nitrogen-, sulfur-, phosphorus-doped carbon matrix, which was produced from a metal-organic framework, shows remarkable bifunctional activity (ORR and OER activities) close to that of precious-metal catalysts along with excellent durability in rechargeable zinc-air batteries; the *in-situ* conversion of the cobalt phosphide nanoparticles to cobalt oxide during OER and/or ORR contributes to the stability of the carbon material.[4] Also, a ternary nickel-cobalt phosphide catalyst produced with a bimetallic zeolitic imidazolate framework shows excellent bi-functional catalytic activity and durability toward both OER and hydrogen evolution reaction (HER).

2.1. Cells Based on Liquid Electrolytes

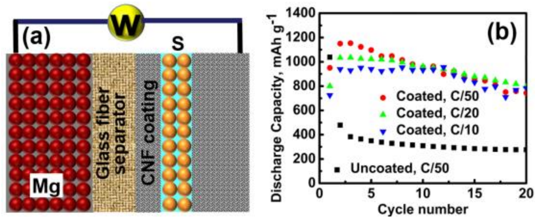

Figure 2. (a) Schematic of a Mg-S cell with an activated-CNF coated separator. (b) Cyclability of the Mg ‖ GF ‖ S and the Mg ‖ CNF-GF ‖ S cells at different C-rates.

Polyvalent metal – sulfur cells: Analogous to the Li-S system, we have explored cells with polyvalent metal ions, such as Mg^{2+} and Al^{3+}, and sulfur cathodes.[5] We have demonstrated a Mg-S cell with a cathode comprising a pre-activated carbon nanofiber (CNF) electrode matrix filled with elemental sulfur active material and a CNF coated separator, delivering an initial capacity of ~ 1,200 mAh g^{-1} (**Figure 2**). The conductive CNF coating on the separator traps the diffusing magnesium polysulfides and facilitates their reuse. For the Al-S system, we have demonstrated a highly reversible cell with a Li^+-ion mediated ionic liquid electrolyte. The cycle life of the Al-S batteries was significantly enhanced by the addition of a Li-salt ($LiCF_3SO_3$) to an Al[EMI]Cl_4 ionic liquid. The electrochemical mechanism of the Al-S battery has been investigated with electrochemical and spectroscopic techniques, as well as density functional theory (DFT) calculations. Presence of Li^+-ion in the Al[EMI]Cl_4 ionic liquid promotes the formation of soluble polysulfide intermediates, which lowers the electrochemical kinetic barrier for the reduction or oxidation of Al polysulfides. The results obtained with x-ray photoelectron spectroscopy analyses and DFT calculations suggest that the presence of Li^+-ion in the electrolyte promotes the reactivation of sulfide species through a suppression of the formation of Al=S double bonds upon full discharge of the sulfur cathode.

Cells based on sulfur and selenium: In collaboration with Dr. Gabriel Veith at the Oak Ridge National Laboratory, the Li_2S films produced established the unique electrochemistry associated with the charge-discharge process of solid-state Li_2S and the influence of film thickness on the charge-discharge process.[6] To reduce the polysulfide or polyselenide shuttling in lithium-sulfur and sodium-selenium cells, we have pursued a few strategies: (i) we have rationally designed a yolk-shelled carbon@Fe_3O_4 (YSC@Fe_3O_4) nanobox as a highly efficient sulfur host, which not only immobilizes the polysulfide through physical and chemical interactions, but also ensures fast electron/ion transfer due to the highly conductive carbon shell and Fe_3O_4 core; (ii) we were able to control the polysulfide diffusion with a novel polymer with intrinsic nanoporosity (PIN) with a pore size of < 1.0 nm; (iii) we have developed an integrated strategy based on a gel sulfur cathode, a solid electrolyte, and a protective anolyte composed of highly-concentrated salt electrolyte containing mixed additives, which blocks polysulfide diffusion and minimizes the electrolyte amount; and (iv) we have coupled a binder-free, self-interwoven carbon nanofiber–selenium cathode with a light-weight carbon-coated bifunctional separator to obtain good cycle life and shelf-life in sodium-selenium cells with a high selenium loading of 4.4 mg cm^{-2}.

Novel alloy anode framework: We have designed a novel interdigitated eutectic alloy (IdEA) anode framework, in which an electrochemically active material (*e.g.*, tin) is nanosized and dispersed throughout an electrically conductive matrix (*e.g.*, aluminum) by anisotropic cold rolling of a binary eutectic alloy.[7] With this ideal anode geometry, lithium reversibly alloys with tin nanodomains, and the electronically conductive scaffold accommodates the significant volume changes associated with alloying. The Al-Sn IdEA foils increase the anode gravimetric energy density by 60% compared to graphite anode. However, irreversible exfoliation of the foil resulted in a diminished performance. To characterize the realized volumetric energy density of IdEA anodes, foils were cycled in an optically transparent electrochemical cell and the electrode expansion was measured with microscopy. With this *in-situ* technique, the Zn-Sn eutectic system was identified as a promising alternative to the Al-Sn foils.

3. Future Plans

Building on the above results, our future efforts are focused on the following:

- Comparison of solid electrolytes with and without the presence of electric dipoles
- Comparison of solid electrolytes that are in a crystalline versus an amorphous state
- Comparison of different strategies for solving the cathode problem
- Broadening the mediator-ion battery concept to new liquid-phase, redox-active organic and inorganic materials
- Exploration of low-cost, efficient electrocatalysts for aqueous polysulfides and metal-air cells
- Development of catalysts and redox mediators for lithium - carbon dioxide batteries
- Investigation of room-temperature calcium-sulfur batteries with a focus on the electrolyte
- Investigation and mitigation of the interdigitated eutectic alloy anode degradation mechanisms
- Pairing the interdigitated eutectic alloy anodes with layered oxide cathodes and understanding the role of chemical crossover from cathode to anode in such systems

References

1. L. G. Xue, H.C. Gao, Y. T. Li, and J. B. Goodenough, "Cathode Dependence of Liquid-Alloy Na-K Anodes", *Journal of the American Chemical Society* **140**, 3292-3298, (2018).
2. Y. Li, B. Xu, H. Xu, H. Duan, X. Lu, S. Xin, W. Zhou, L. Xue, G. Fu, A. Manthiram, and J. B. Goodenough, "Hydrid Polymer/Garnet Electrolyte with a Small Interfacial Resistance for Lithium-Ion Batteries" *Angewandte Chemie* **56**, 753-756, (2017).
3. X. Yu, M. Gross, S. Wang, and A. Manthiram, "Aqueous Electrochemical Energy Storage with a Mediator-ion Solid Electrolyte," *Advanced Energy Materials* **7**, 1602454: 1-8 (2017).
4. S.-H. Ahn and A. Manthiram, "Cobalt Phosphide Coupled with Heteroatom-doped Nanocarbon Hybrid Electroctalysts for Efficient, Long-life Rechargeable Zinc-air Batteries," *Small* **13**, 1702068: 1-11 (2017).
5. X. Yu and A. Manthiram, "Ambient-temperature Energy Storage with Polyvalent Metal-Sulfur Chemistries," *Small Methods* **1**, 1700217: 1-11 (2017).
6. M. Klein, G. Veith, and A. Manthiram, "Chemistry of Sputter-deposited Lithium Sulfide Films," *Journal of the American Chemical Society* **139,** 10669–10676 (2017).
7. K. Kreder, B. Heligman, A. Manthiram, "Interdigitated Eutectic Alloy Foil Anodes for Rechargeable Batteries," *ACS Energy Letters* **2,** 2422–2423 (2017).

LIST OF PUBLICATIONS DURING THE PAST 2 YEARS

Articles Already in Print

1. S. O. Kim and A. Manthiram, “Facile Synthesis and Enhanced Sodium-storage Performance of Chemically Bonded CuP_2/C Hybrid Anode,” *Chemical Communications* **52,** 4337-4340 (2016).
2. Z. Jiang, Z.-J. Jiang, T. Maiyalagan, and A. Manthiram, “Cobalt Oxide-coated N- and B-doped Graphene Hollow Spheres as a Bifunctional Electrocayalyst for Oxygen Reduction and Oxygen Evolution Reactions,” *Journal of Materials Chemistry A* **4,** 5877-5889 (2016).
3. C. Zu, L. Li, J. Guo, S. Wang, D. Fan, and A. Manthiram, “Understanding the Redox Obstacles in High Sulfur-loading Li-S Batteries and Design of an Advanced Gel Cathode,” *Journal of Physical Chemistry Letters* **7,** 1392-1399 (2016).
4. K. A. Jarvis, C.-C. Wang, J. C. Knight, L. Rabenberg, A. Manthiram, and P. J. Ferreira, “Formation and Effect of Orientation Domains in Layered Oxide Cathodes of Lithium-ion Batteries,” *Acta Materialia* **108,** 264-270 (2016).
5. Y. Li, M. Parans Paranthaman, K. Akato, A. K. Naskar, A. M. Levine, R. J. Lee, S. O. Kim, J. Zhang, S. Dai, and A. Manthiram, “Tire-derived Carbon Composite Anodes for Sodium-ion Batteries,” *Journal of Power Sources* **316,** 232-238 (2016).
6. X. Yu and A. Manthiram, “Performance Enhancement and Mechanistic Studies of Magnesium-Sulfur (Mg-S) Cells with an Advanced Cathode Structure,” *ACS Energy Letters* **1,** 431-437 (2016).
7. S.-O. Kim and A. Manthiram, “High-performance Red P-based P-TiP_2-C Nanocomposite Anode for Lithium-ion and Sodium-ion Storage,” *Chemistry of Materials* **28,** 5935-5942 (2016).
8. M. J. Klein, K. Goossens, C. W. Bielawski, and A. Manthiram, “Elucidating the Electrochemical Activity of Electrolyte-insoluble Polysulfide Species in Lithium-sulfur Batteries,” *Journal of the Electrochemical Society* **163**, A2109-A2116 (2016).
9. A. Manthiram, “Electrical Energy Storage: Materials Challenges and Prospects,” *MRS Bulletin* **41**, 624-630 (2016).
10. L. Qie and A. Manthiram, “Uniform Li_2S Precipitation on N, O-Codoped Porous Hollow Carbon Fibers for High-energy-density Lithium-sulfur Batteries with Superior Stability,” *Chemical Communications* **52**, 10964-10967 (2016).
11. T.-T. Shan, S. Xin, Y. You, H.-P. Cong, S.-H. Yu, and A. Manthiram, “Combining Nitrogen-doped Graphene Sheets and MoS_2: A Unique “Film-foam-film” Structure for Enhanced Lithium Storage,” *Angewandte Chemie Int. Ed.* **55**, 12783-12788 (2016).
12. J. Liu, A. Huq, Z. Moorhead-Rosenberg, A. Manthiram, and K. Page, “Nanoscale Ni/Mn Ordering in the High Voltage Spinel Cathode $LiNi_{0.5}Mn_{1.5}O_4$,” *Chemistry of Materials* **28**, 6817-6821 (2016).
13. G.-P. Kim, H.-H. Sun, and A. Manthiram, “Design of a Sectionalized MnO_2-Co_3O_4 Electrode via Selective Electrodeposition of Metal Ions in Hydrogel for Enhanced Electrocatalytic Activity in Metal-air Batteries,” *Nano Energy* **30**, 130-137 (2016).
14. W. Kaveevivitchai and A. Manthiram, “High-capacity Zinc-ion Storage in an Open-tunnel Oxide for Aqueous and Nonaqueous Zn-ion Batteries,” *Journal of Materials Chemistry A* **4**, 18737-18741 (2016).

15. J.-S. Lee, W. Kim, J. Jang, and A. Manthiram, “Sulfur-Embedded Activated Multichannel Carbon Nanofiber Composites for Long-life, High-rate Lithium-sulfur Batteries,” *Advanced Energy Materials* **7**, 1-8 (2016).
16. S.-O. Kim and A. Manthiram, “Low-cost Carbon-coated Si-Cu_3Si-Al_2O_3 Nanocomposite Anodes for High-performance Lithium-ion Batteries,” *Journal of Power Sources* **332**, 222-229 (2016).
17. Y. You, S.-O. Kim, and A. Manthiram, “A Honeycomb Layered Oxide Cathode for Sodium-Ion Batteries with Suppressed P3-O1 Phase Transition,” *Advanced Energy Materials* **1601698**, 1-7 (2016).
18. S.-H. Ahn, M. Klein, and A. Manthiram, “One-dimensional Co- and N-doped Hierarchically Porous Carbon Nanotubes Derived from Bimetallic Metal Organic Framework for Efficient Oxygen and Tri-iodide Reduction Reactions,” *Advanced Energy Materials* **1601979**, 1-9 (2016).
19. K. Kreder and A. Manthiram, “Metal Nanofoams via a Facile Microwave-assisted Solvothermal Process,” *Chemical Communications* **53**, 865-868 (2016).
20. W. Kaveevivitchai, A. Huq, and A. Manthiram, “Microwave-assisted Chemical Insertion: A Rapid Technique for Screening Cathodes for Mg-ion Batteries,” *Journal of Materials Chemistry A* **5**, 2309-2318 (2016).
21. S.-M. Oh, P. Oh, S.-O. Kim, and A. Manthiram, “A High-performance Sodium-ion Full Cell with a Layered Oxide Cathode and a Phosphorous-based Composite Anode,” *Journal of Electrochemical Society* **164**, A321-A326 (2016).
22. H. Gao, W. Zhou, J. Jang, and J.B. Goodenough, “Cross-Linked Chitosan as a Polymer Network Binder for an Antimony Anode in Sodium-Ion Batteries” *Advanced Energy Materials* **6**, 1502130, (2016).
23. K. Park, B.-C. Yu, and J.B. Goodenough, “Li_3N As a Cathode Additive for High-Energy Density Lithium-Ion Batteries” *Advanced Energy Materials* **6**, 150234, (2016).
24. W. Zhou, S. Wang, Y.T. Li, S. Xin, A. Manthiram, and J.B. Goodenough, “Plating a Dendrite-Free Lithium Anode with a Polymer/Ceramic/Polymer Sandwich Electrolyte” *Journal of the American Chemical Society* **138**, 9385-9388, (2016).
25. Z. Cui, C.X. Zu, W. Zhou, A. Manthiram, and J.B. Goodenough, “Mesoporous Titanium Nitride-Enabled Highly Stable Lithium-Sulfur Batteries” *Advanced Materials* **28**, 6926-6931, (2016).
26. B.C. Yu, K.-S. Park, J.-H. Jang, and Goodenough, J.B. “Cellulose-Based Porous Membrane for Suppressing Li Dendrite Formation in Lithium-Sulfur Battery” *ACS Energy Letters* **1**, 633-637, (2016).
27. H. Gao, W. Zhou, K.-S., Park, and J.B. Goodenough, “A Sodium-Ion Battery with a Low-Cost Cross-Linked Gel-Polymer Electrolyte”, *Advanced Energy Materials* **6**, 1600467-1600473, (2016).
28. H. Gao, Y. Li, and J.B. Goodenough, “Sodium Extraction from NASICON-Structured $Na_3MnTi(PO_4)_3$ Through Mn(III/Mn(II) and Mn(IV)/Mn(III) Redox Couples” *Chemistry of Materials* **28**, 6553-6559 (2016).
29. G. Fu, Y.F. Chen, Z. Cui, Y. Li, W. Zhou, S. Xing, Y. Tang, and J.B. Goodenough, “Novel Hydrogel-Derived Bifunctional Oxygen Electrocatalyst for Rechargeable Air Cathodes” *Nano Letters*, **16**, 6516-6522 (2016).
30. H. Gao and J.B. Goodenough, “An Aqueous Symmetric Sodium-Ion Battery with NASICON-Structured $Na_3MnTi(PO_4)_3$” *Angewandte Chemie* **55**, 1-6 (2016).

31. S.-H. Ahn and A. Manthiram, “Self-templated Synthesis of Co- and N-doped Carbon Microtubes Composed of Hollow Nanospheres and Nanotubes for Efficient Oxygen Reduction Reaction,” *Small* **13**, 1603437 (2017).
32. J.-S. Lee, J. Jun, J. Jang, and A. Manthiram, “Sulfur-Immobilized, Activated Porous Carbon Nanotube Composite-based Cathodes for Lithium-sulfur Batteries,” *Small* **12**, 1602984 (2017).
33. S.-H. Ahn and A. Manthiram, “Direct Growth of Ternary Ni-Fe-P Porous Nanorods onto a Nickel Foam as a Highly Active, Robust Bifunctional Electrocatalyst for Overall Water Splitting,” *Journal of Materials Chemistry A* **5**, 2496-2503 (2017).
34. A. Manthiram, X. Yu, and S. Wang, “Lithium Battery Chemistries Enabled by Solid-state Electrolytes,” *Nature Reviews Materials* **2**, 1-16 (2017).
35. J.-S. Lee and A. Manthiram, “Hydroxylated N-doped Carbon Nanotube-sulfur Composites as Cathodes for High-performance Lithium-sulfur Batteries,” *Journal of Power Sources* **343**, 54-59 (2017).
36. C.-H. Chang, S.-H. Chung, and A. Manthiram, “Transforming Waste Newspapers into Nitrogen-doped Conducting Interlayers for Advanced Li-S Batteries,” *Sustainable Energy & Fuels* **1**, 444-449 (2017).
37. K. Kreder and A. Manthiram, “Vanadium-substituted LiCoPO$_4$ core with a monolithic LiFePO$_4$ shell for high-voltage lithium-ion batteries,” *ACS Energy Letters* **2**, 64-69 (2017).
38. S.-H. Ahn and A. Manthiram, “Wiring” Fe-N$_x$-embedded Porous Carbon Frameworks onto One-dimensional Nanotubes for Efficient Oxygen Reduction Reaction in Alkaline and Acidic Media,” *Advanced Materials* **1606534**, 1-10 (2017).
39. S.-O. Kim and A. Manthiram, “Phosphorus-rich CuP$_2$ Embedded in Carbon Matrix as a High-performance Anode for Lithium-ion Batteries,” *ACS Applied Materials & Interfaces* (2017).
40. Y. Li, B. Xu, H. Xu, H. Duan, X. Lu, S. Xin, W. Zhou, L. Xue, G. Fu, A. Manthiram, and J. B. Goodenough, “Hydrid Polymer/Garnet Electrolyte with a Small Interfacial Resistance for Lithium-Ion Batteries” *Angewandte Chemie* **56**, 753-756, (2017).
41. G. Fu, Z. Cui, Y. Chen, Y.T. Li, Y.W. Tang, and J.B. Goodenough, “Ni$_3$Fe-N Doped Carbon Sheets as a Bifunctional Electrocatalyst for Air Cathodes” *Advanced Energy Materials* **7**, 1601172 (2017).
42. Xue, L.G., Y.T. Li, H. Gao, W. Zhou, X. Lu, W. Kaveevivitchai, A. Manthiram, and J.B. Goodenough, “Low-Cost High-Energy Potassium Cathode” *Journal of the American Chemical Society* **139**, 2164-2167 (2017).
43. X. Yu and A. Manthiram, “Electrochemical Energy Storage with a Reversible Nonaqueous Room-temperature Aluminum-sulfur Chemistry,” *Advanced Energy Materials* **7**, 1700561: 1-9 (2017).
44. M. J. Klein, A. Dolocan, C. Zu, and A. Manthiram, “An Effective Lithium Sulfide Encapsulation Strategy for Stable Lithium-sulfur Batteries,” *Advanced Energy Materials* **7**, 1701122: 1-9 (2017).
45. X. Yu and A. Manthiram, “A Voltage-enhanced, Low-cost Aqueous Iron-air Battery Enabled with a Mediator-ion Solid Electrolyte,” *ACS Energy Letters* **2**, 1050-1055 (2017).
46. W. Kaveevivitchai, A. Huq, S. Wang, M. J. Park, and A. Manthiram, “Rechargeable Aluminum-ion Batteries Based on an Open Tunnel Framework,” *Small* **13**, 1701296: 1-10 (2017).

47. K. Jarvis, C.-C. Wang, M. Varela, R. Unocic, A. Manthiram, and P. Ferreira, "Surface Reconstruction in Li-rich Layered Oxides of Li-ion Batteries," *Chemistry of Materials* **29**, 7668-7674 (2017).
48. M. Klein, G. Veith, and A. Manthiram, "Chemistry of Sputter-deposited Lithium Sulfide Films," *Journal of the American Chemical Society* **139,** 10669–10676 (2017).
49. M. Klein, G. Veith, and A. Manthiram, "Rational Design of Lithium-sulfur Battery Cathodes Based on Experimentally Determined Maximum Active Material Thickness," *Journal of the American Chemical Society* **139**, 9229-9237 (2017).
50. S.-H. Ahn and A. Manthiram, "Cobalt Phosphide Coupled with Heteroatom-doped Nanocarbon Hybrid Electroctalysts for Efficient, Long-life Rechargeable Zinc-air Batteries," *Small* **13**, 1702068: 1-11 (2017).
51. Y. Li, B. Xu, H. Xu, H. Duan, X. Lü, S. Xin, W. Zhou, L. Xue, Q. Jia, A. Manthiram, and J. B. Goodenough, "Hybrid Polymer/Garnet Electrolyte with a Small Interfacial Resistance for Lithium-Ion Batteries," *Angewandte Chemie* **56**, 753-756 (2017).
52. X. Yu, M. M. Gross, S. Wang, and A. Manthiram, "Aqueous Electrochemical Energy Storage with a Mediator-ion Solid Electrolyte," *Advanced Energy Materials* **7**, 1602454, 1-8 (2017).
53. J.-S. Lee, J. Jun, J. Jang, and A. Manthiram, "Sulfur-Immobilized, Activated Porous Carbon Nanotube Composite Based Cathodes for Lithium-sulfur Batteries," *Small* **13**, 1602984: 1-7 (2017).
54. J. He, L. Luo, Y. Chen and A. Manthiram, "Yolk-Shelled C@Fe_3O_4 Nanoboxes as Efficient Sulfur Hosts for High-Performance Lithium–Sulfur Batteries," *Advanced Materials* **29**, 1702707: 1-5 (2017).
55. X. Yu and A. Manthiram, "A Zinc-Cerium Cell for Energy Storage Using a Sodium-ion Exchange Membrane," *Advanced Sustainable Systems* **1**, 1700082: 1-6 (2017).
56. X. Yu and A. Manthiram, "Ambient-temperature Energy Storage with Polyvalent Metal-Sulfur Chemistries," *Small Methods* **1**, 1700217: 1-11 (2017).
57. Y. You and A Manthiram, "Progress in High-voltage Cathode Materials for Rechargeable Sodium-ion Batteries," *Advanced Energy Materials* **8**, 1701785: 1-11 (2017).
58. A. Manthiram, "An Outlook on Lithium Ion Battery Technology," *ACS Central Science* **3**, 1063-1069 (2017).
59. K. Kreder, B. Heligman, A. Manthiram, "Interdigitated Eutectic Alloy Foil Anodes for Rechargeable Batteries," *ACS Energy Letters* **2,** 2422–2423 (2017).
60. X. Yu and A. Manthiram, "Electrochemical Energy Storage with Mediator-ion Solid Electrolytes," *Joule* **1**, 453-462 (2017).
61. X. Yu and A. Manthiram, "Electrode-Electrolyte Interfaces in Lithium-Sulfur Batteries with Liquid or Inorganic Solid Electrolytes," *Accounts of Chemical Research* **50**, 2653-2660 (2017).
62. H.C. Gao, L.G. Xue, S. Xin, K. Park, and J.B. Goodenough, "A Plastic-Crystal Electrolyte Interphase for All-Solid-State Sodium Batteries" *Angewandte Chemie International Edition* **56**, 5541-5545 (2017).
63. Z.M. Cui, G.T. Fu, Y.T. Li, and J.B. Goodenough, "Ni_3FeN-Supported Fe_3Pt Intermetallic Nanoalloy as a High-Performance Bifunctional Catalyst for Metal-Air Batteries" *Angewandte Chemie International Edition* **56**, 9901-9905, (2017).

64. G.T. Fu, Z. Cui, Y.F. Chen, L. Xu, Y.W. Tang and J.B. Goodenough, "Hierarchically Mesoporous Nickel-Iron Nitride as a Cost-Efficient and Highly Durable Electrocatalyst for Zn-air Battery" *Nano Energy*, **39**, 77-85, (2017).
65. Z. Cui, Y. Li, G.T. Fu, X. Li, and J.B. Goodenough, "Robust Fe_3Mo_3C Supported IrMn Clusters as Highly Efficient Bifunctional Air Electrode for Metal-Air Battery" *Advanced Materials* **29**, 1702385, (2017).
66. H. Wang, Y. Jiang, and A. Manthiram, "Long Cycle Life, Low Self-discharge Sodium-selenium Batteries with High Selenium Loading and Suppressed Polyselenide Shuttling," *Advanced Energy Materials* **8**, 1701953 (1-8) (2018).
67. X. Yu, M. Broyer, G. Hwang, and A. Manthiram, "Room-temperature Aluminum-sulfur Batteries with a Lithium-ion-mediated Ionic Liquid Electrolyte," *Chem* **4**, 586-598 (2018).
68. X. Yu, S. Feng, M. Boyer, M. Lee, R. Ferrier, N. Lynd, G. Hwang, G. Wang, S. Swinnea, and A. Manthiram, "Controlling the Polysulfide Diffusion in Lithium-Sulfur Batteries with a Polymer Membrane with Intrinsic Nanoporosity," *Materials Today Energy* **7**, 98-104 (2018).
69. X. Yu and A. Manthiram, "Electrode-Electrolyte Interfaces in Lithium-based Batteries," *Energy and Environmental Science* **11**, 527-543 (2018).
70. M. Gross and A. Manthiram, "A Rechargeable Zinc-Aqueous Polysulfide Battery with a Mediator-ion Solid Electrolyte," *ACS Applied Materials and Interfaces* **10**, 10612-10617 (2018).
71. X. Yu and A. Manthiram, "Electrochemical Energy Storage with an Aqueous Zinc-Quinone Chemistry Enabled by a Mediator-ion Solid Electrolyte," *ACS Applied Energy Materials* **1**, 273-277 (2018).
72. L.G. Xue, H.C. Gao, Y.T. Li, and J.B. Goodenough, "Cathode Dependence of Liquid-Alloy Na-K Anodes", *Journal of the American Chemical Society* **140**, 3292-3298, (2018).
73. H.C. Gao, L.G. Xue, S. Xin, and J.B. Goodenough, "A High-Energy-Density Potassium Battery with a Polymer-Gel Electrolyte and a Polyaniline Cathode" *Angewandte Chemie International Edition* **57**, 5449-5453, (2018).
74. H.C. Gao, S. Xin, L.G. Xue, and J.B. Goodenough, "Stabilizing a High-Energy-Density Rechargeable Sodium Battery with a Solid Electrolyte" *Chem* **4**, 833-834, (2018).

Articles in Press

75. X. Yu and A. Manthiram, "Electrochemical Energy Storage with an Aqueous Quinone-Air Chemistry," *ACS Applied Energy Materials* (in press).
76. H. Xu, S. Wang, and A. Manthiram, "Hybrid Lithium–sulfur Batteries with an Advanced Gel Cathode and Stabilized Lithium-metal Anode," *Advanced Energy Materials* (in press).
77. J. He, Y. Chen, and A. Manthiram, "MOF-derived Cobalt Sulfide Grown on 3D Graphene Foam as an Efficient Sulfur Host for Long-life Lithium-Sulfur Batteries," *iScience* (in press).
78. Y. You, S. Xin, Y. Asl, W. Li, P.-F. Wang, Y.-G. Guo, and A. Manthiram, "Insights into the Improved High-voltage Performance of Li-incorporated Layered Oxide Cathodes for Sodium-ion Batteries," *Chem* (in press).

79. G. Gnana kumar, S.-H. Chung, T. Raj kumar, and A. Manthiram, "A 3D Graphene-CNT-Ni Hierarchical Architecture as a Polysulfide trap for Lithium-Sulfur Batteries," *ACS Applied Materials & Interfaces* (in press).
80. X. Yu and A. Manthiram, "A Strategically Managed Rechargeable Battery System with a Neutral Methyl Viologen Anolyte and an Acidic Air-Cathode Enabled by a Mediator-ion Solid Electrolyte," *Sustainable Energy and Fuel* (in press).
81. N. Grundish, C.D. Amos, and J.B. Goodenough, "Characterization of $LiAlCl_4 \cdot xSO_2$ Inorganic Liquid Li^+ Electrolyte" *Journal of the Electrochemical Society* (in press).

Articles Submitted

82. X. Yu and A. Manthiram, "A Reversible Nonaqueous Room-temperature Potassium-sulfur Chemistry for Electrochemical Energy Storage," *Energy Storage Materials* (submitted).
83. H. Wang, Y. Jiang, and A. Manthiram, "N-doped Fe_3C@C as an Efficient Polyselenide Reservoir for High-performance Sodium-selenium Batteries," *Energy Storage Materials* (submitted)
84. J. He, Y. Chen, and A. Manthiram, "Vertical Co_9S_8 Hollow Nanowall Arrays Grown on Celgard Separator as a Multifunctional Polysulfide Barrier for High-performance Li-S Batteries," *Energy and Environmental Science* (submitted).
85. S.H. Ahn and A. Manthiram, "Highly Robust Tri-functional Electrocatalysts from a Single Bimetallic Zeolitic Imidazolate Framework with a Hierarchical Structure," *Advanced Materials* (submitted).

Surface ligand effects on energetics, charge transfer, and stability at interfaces between metal halide perovskites and organic semiconductors

Kenneth R. Graham, University of Kentucky

Program Scope

Organometal and metal halide perovskites (O)MHPs have emerged as a promising class of inexpensive and solution processed semiconductors for optoelectronic devices. The objectives of this project are centered upon understanding the surface chemistry of (O)MHPs and how surface ligands influence optoelectronic properties, charge transfer processes, and stability of (O)MHPs. Understanding and using surface ligands appropriately will help improve the stability and optoelectronic properties of these (O)MHP materials and the devices they are used in. The project starts from the more fundamental standpoint of identifying the most promising surface ligand binding groups based on binding affinity and influence of the binding group on optical and electronic properties; followed by determining how the ligand tail affects interfacial charge transfer processes, material stability, and photovoltaic device performance and stability; and concludes with developing novel surface ligands based on mixtures of extended π-conjugated and non-conjugated surface ligands to systematically investigate and control interfacial charge transfer processes and material and device stability. Much of the research takes advantage of the photoelectron spectroscopy capabilities developed in my laboratory specifically for investigating more damage prone materials, which includes X-ray, ultraviolet, and inverse photoelectron spectroscopy (XPS, UPS, and IPES, respectively). The project is currently in its first year and the results that will be presented focus primarily on (O)MHP energetics, surface ligand binding, and surface ligand effects on optical properties.

Recent Progress

The start of this project has centered on synthesizing high-quality perovskite thin films ($MAPbI_3$ and $FASnI_xBr_{3-x}$, where MA is methylammonium and FA is formamidinium) and nanoparticles ($CsPbBr_xCl_{3-x}$), investigating the energetics and optical properties of these materials, and investigating how surface ligands influence the surface chemistry and optical properties. Organometal halide perovskites can be processed in a variety of ways with different precursors, all of which should ideally produce the same material. We investigated multiple deposition strategies and found that they do not all produce the same materials. For example, as shown by the UPS spectra in

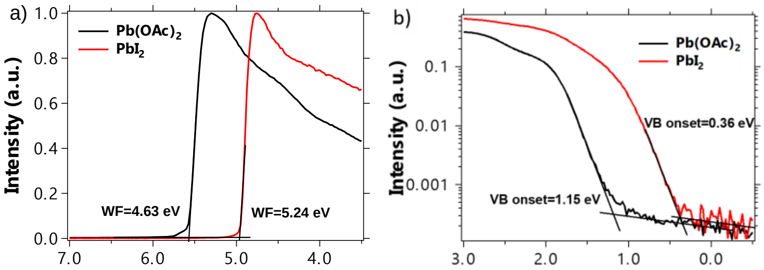

Figure 1 UPS spectra of $MAPbI_3$ showing the secondary electron cut-off region (a) and the valence band onset region (b) for $MAPbI_3$ films processed from $Pb(OAc)_2$ and PbI_2.

Figure 1, the work functions and ionization energies (IEs) vary by approximately 0.6 and 0.25 eV, respectively, depending on whether $MAPbI_3$ is produced with $Pb(OAc)_2$ or PbI_2 as the Pb source. The difference in materials formed from the precursors is not apparent in X-ray diffraction, UV-Vis absorbance, or photoluminescence spectra. We incorporated $MAPbI_3$ made from $Pb(OAc)_2$ and PbI_2 into solar cells with varying hole transport layers, including a new series of triarylaminoethynylsilanes. Through investigating a series of hole transport layers (HTLs) spanning over a 1 eV range in IE, we find that the PV devices are relatively insensitive to the HTL IE over a range of more than 0.5 eV; however, the optimal IE range for the HTL depends strongly on the processing method. We find that PV devices show high open-circuit voltages and relatively high performance for HTLs with IEs as low as 4.8 eV, which is nearly 1 eV lower than the IE of $MAPbI_3$ (5.5 to 5.9 eV).[1]

Surface binding affinity and the influence of surface ligand binding group on $MAPbI_3$ surface chemistry was investigated for a series of monofunctional ligands. Based on the XPS spectra of $MAPbI_3$ treated with different surface ligands, phosphonic acid and trichlorosilane show significant adsorption on the perovskite surface, whereas thiophenol, benzoic acid, and aniline derivatives do not. We suspect that the reason the phosphonic acid binds and the carboxylic acid does not, is due to the lower pKa of the phosphonic acid relative to the carboxylic acid. Binding of the trichlorosilane occurs through conversion of the trichlorosilane into siloxane, as evidenced by the appearance of oxygen and the absence of Cl in XPS spectra.

Procedures for fabricating both $MASnI_3$ and $FASnI_xBr_{3-x}$ were developed to yield morphologically homogeneous films with appropriate Sn:I stoichiometries and large Sn^{2+}:Sn^{4+} ratios based on XPS analysis. With the discrepancy in the literature reported valence and conduction band energies of organometal tin perovskites, we used our UPS and IPES systems to probe the energetics as a function of halide composition for $MASnBr_{3-x}I_x$, as shown in **Figure 2**. Our UPS results show that the IE is similar regardless of halide composition, varying from 4.68 to 4.82 eV for all compositions between x=0 and 3. On the other hand, our IPES measurements show that the electron affinity (EA) varies more widely, with the EA decreasing from 3.5 eV for $MASnI_3$ to 2.6 eV for $MASnBr_3$. Compared with $MAPbI_3$, the IE of $MASnI_3$ is *ca.* 1 eV lower, which is slightly more than the 0.7 eV predicted with theoretical calculations.[2] Currently, we are working on the surface modification of this series of tin perovskites and investigating binding group effects on energetics, optical properties, degree of tin oxidation to Sn^{4+}, and stability.

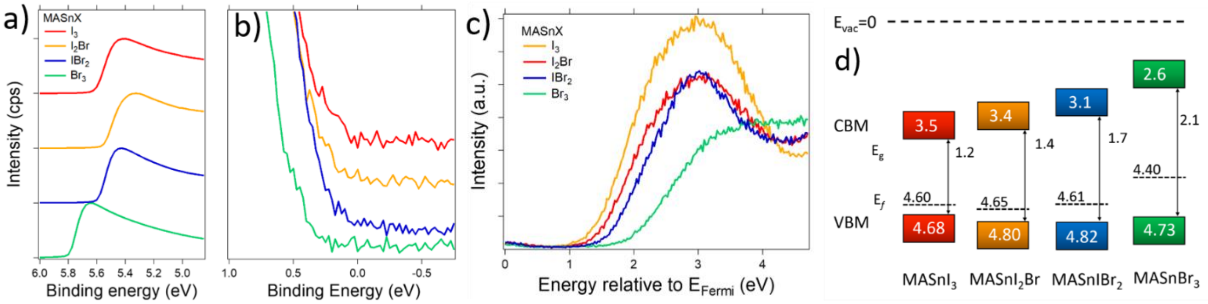

Figure 2. UPS spectra of the secondary electron cut-off (a) and valence band onset regions (b), IPES spectra (c), and extracted values for the conduction and valence band minima and maxima (d) for $MASnI_3Br_{3-x}$.

The large surface-to-volume ratio of nanocrystals (NCs) makes them natural amplifiers of surface chemistry changes. Surface ligands are essential for increasing the PLQYs and improving the stability of (O)MHP NCs. The most widely investigated (O)MHP NCs are $CsPbBr_3$ NCs, which are easily synthesized and show bright green emission with high PLQYs. We optimized our synthetic conditions to produce $CsPbBr_3$ NCs with PLQYs of 60-75%, long PL lifetimes of 9.4 ns, and nanocubes with edge lengths of 11.3 ± 1.7 nm. During our investigation into the synthesis of $CsPbBr_3$ NCs, we found that the initial PLQY as well as the NC stability were sensitive to the Cs:Pb ratio used in the synthesis (**Figure 3**). The $CsPbBr_3$ NC synthesis involves the reaction of Cs oleate with $PbBr_2$, with the balanced chemical reaction including a 2:3 molar ratio of Cs oleate to $PbBr_2$. However, a large excess of lead (e.g., 1:4 Cs:Pb molar ratio) is typically used to produce high-quality NCs. When the molar excess of lead is higher (1:5), the $CsPbBr_3$ nanoparticles are more stable and show relatively high PLQYs. As the molar excess of lead decreases, the stability also decreases, as shown in Figure 3. However, surface modification with dodecanethiol (DDT) results in higher and more stable PLQYs over a wide range of Cs:Pb ratios.

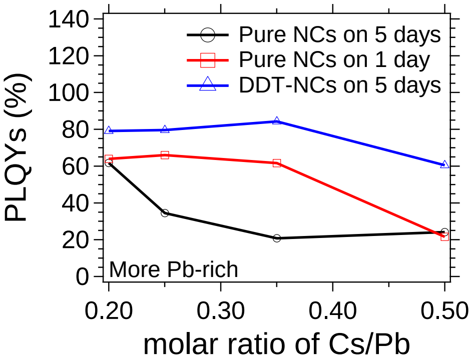

Figure 3. PLQY of $CsPbBr_3$ NCs recorded on the same day they were synthesized (red) and 5 days after synthesis without any additional surface ligands (black) and with DDT**.**

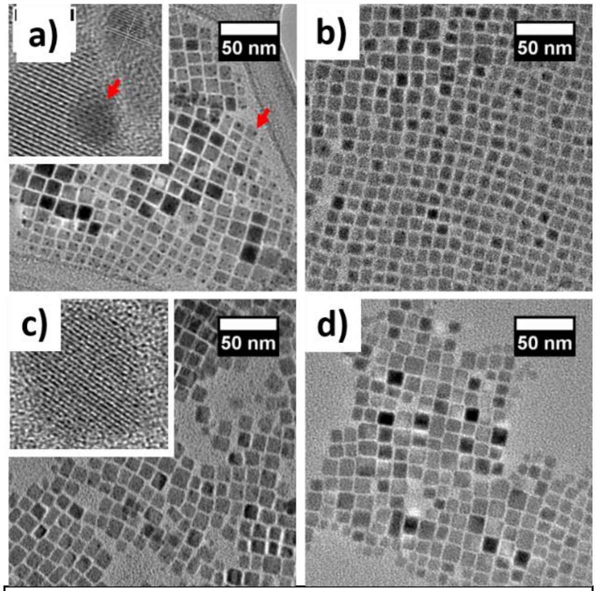

Figure 4. TEM images of $CsPbBr_3$ nanocrystals produced with a Cs:Pb ratio of 0.2 (a,c) and 0.25 (b,d) before (a,b) and after (c,d) DDT surface ligand modification.

An interesting observation is that with a Cs:Pb ratio of 1:5, small metallic lead particles (as confirmed by TEM lattice spacings) appear on the surface of the $CsPbBr_3$ particles, as shown in **Figure 4**. With thiol treatment these pure Pb particles dissolve and the PLQY of the nanocrystals increases. Interestingly, we find that ammonium and sodium thiocyanate (NH_4SCN and NaSCN), which were previously reported to yield nanocrystals with nearly 100% PLQY, only lead to increases in the PLQY when these pure Pb particles are present. On the other hand, alkylthiols lead to increases in PLQY regardless of the presence of pure Pb particles and Cs:Pb ratio.

In applying a host of surface ligands to $CsPbBr_3$ we discovered that alkyltrichlorosilanes lead to halide exchange reactions, with Cl^- from the trichlorosilane molecules being exchanged for Br^- from the $CsPbBr_3$ nanocrystal. As shown in **Figure 5**, as $CsPbBr_3$ nanocrystals are exposed to dodecyltrichlorosilane (DTS) in solution, the emission spectra shift from being characteristic of $CsPbBr_3$ NCs with a PL maximum at 512 to more characteristic of $CsPbCl_3$ NCs with a PL maximum at 413 nm. In addition to acting as a Cl^- source for anion exchange, the trichlorosilanes react to form siloxane shells around the nanoparticles. This siloxane shell leads to stable $CsPbCl_3$ NCs, with the PLQY remaining near record levels of 10% after storage in ambient conditions for one month. By contrast, the PLQY of $CsPbCl_3$ NCs produced through anion exchange with $PbCl_2$ as the Cl^- source decreases to 0.1% after one month storage in ambient conditions. Additionally, $CsPbCl_3$ NCs produced with DTS as the Cl^- source show a factor of two increase in the PL intensity upon water exposure; whereas, the PL intensity of $CsPbCl_3$ NCs produced with $PbCl_2$ decrease by 90% upon water exposure. Investigation of the $CsPbCl_3$ particles produced through DTS exposure with IR absorbance and Raman scattering shows that DTS reacts to form siloxane and displaces ammonium groups from the NC surface.

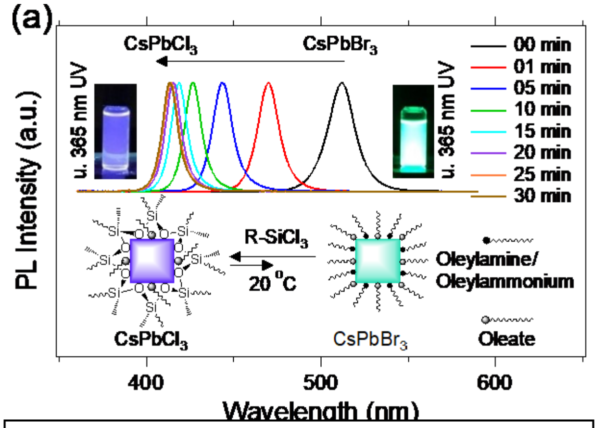

Figure 5. Change in the emission wavelength of $CsPbBr_3$ NCs upon addition of DTS to the NC solution. The schematic shows the simultaneous halide exchange and siloxane surface modification.

Future Plans

The plan for the next year is primarily centered on investigating the influence of the surface ligand binding group on energetics, optical properties, stability, and interfacial charge transfer processes as a function of (O)MHP composition. Relative binding affinities of the surface modifiers to (O)MHP thin films will be investigated through XPS. Surface ligand binding to $CsPbI_xBr_{3-x}$ and $MAPbI_xBr_{3-x}$ NCs will be investigated with NMR spectroscopy, and the effect of binding group on optical properties will be investigated. Electron transfer from the perovskite film to organic transport layer will be investigated through PL lifetime measurements with varying surface modifiers, including the zwitterionic surface ligands. Photovoltaic devices containing surface modifiers of varying binding groups will be fabricated and bimolecular recombination probed with transient photovoltage to further investigate how the modifier binding group influences charge transfer and recombination processes.

References

(1) Park, S. M.; Mazza, S. M.; Liang, Z.; Abtahi, A.; Boehm, A. M.; Parkin, S. R.; Anthony, J. E.; Graham, K. R. *ACS Appl. Mater. Interfaces* **2018**, *10* (18), 15548.
(2) Umari, P.; Mosconi, E.; De Angelis, F. *Sci. Rep.* **2015**, *4* (1), 4467.

Publications

(1) Park, S. M.; Mazza, S. M.; Liang, Z.; Abtahi, A.; Boehm, A. M.; Parkin, S. R.; Anthony, J. E.; Graham, K. R. Processing Dependent Influence of the Hole Transport Layer Ionization Energy on Methylammonium Lead Iodide Perovskite Photovoltaics. *ACS Appl. Mater. Interfaces* **2018**, *10*, 15548–15557.

(2) Uddin, M. A.; Calabro, R. L.; Kim, D.-Y.; Graham, K. R. *Under review.* “Halide Exchange and Surface Modification of Metal Halide Perovskite Nanocrystals with Alkyltrichlorosilanes”

Ordered Phases of Chiral Block Copolymers: Mesochiral, Periodic Nanostructures via Self-Assembly

Gregory M. Grason, Dept. of Polymer Science Engineering, University of Massachusetts Amherst; Edwin L. Thomas, Dept. of Materials Science and NanoEngineering, Rice University

Program Scope

Motivated by the observation of chirality transfer from polymer backbone to the *mesohelical* shape of nanophase-separated domains [R1], this project aims to understand mechanisms and structural implications of the physical coupling between 3D morphology of nanostructure block copolymer (BCP) domains and orientational order of segments. The project integrates orientational self-consistent field (oSCF) theory methods [R2], with multi-scale experimental 3D imaging of polymer nanostructures, with the aims:

1) *Develop and study the physics of intradomain orientational order model of diblock melts.* The projects develops and applies theoretical methods to model the relationship between 3D microdomain shape in BCPs and orientational order of segments, at the sub-domain scale.

2) *Image/quantify patterns of intra-domain segment/chain twist in mesochiral assemblies.* The project explores novel high-resolution electron microscopy methods for directly imaging of block- and segment-orientations within self-assembled BCP domains and multiscale characterization of 3D morphologies.

3) *Model effects of intra-segment orientational interactions on diblock assembly; and experimentally observe and characterize new mesochiral diblock morphologies.* Theory explores the physical effects of orientational segment interactions on BCP domain shape and guides experimental characterization of sub-domain chain structure and mesochiral architectures in 3D block copolymer assembly.

Recent Progress

Intra-domain textures in diblock copolymer assemblies. While liquid-crystallinity is a well-studied effect in the context of rigid-chain BCPs, the nature of orientational order of segments in *flexible-chain* BCP assemblies has, until now, been overlooked. We have developed a new approach to predict patterns of intra-domain segment orientation, or *textures*, from the self-consistent field (SCF) theory of flexible chains, and applied this to model the nature of intra-domain segments in the simplest and most common flexible-chain, Flory-Huggins BCP mode [P1]. The study shows the surprising result that all BCP assemblies have liquid-crystalline-like features in terms of segmental order, even the most simple models that *lack explicit (intra- or inter-chain) orientational interactions*. In any microphase separated domain, there exists a characteristic *multi-zone* pattern: deep within the “brush-like" domain core, segments are *normal* to the inter-domain surface, while at that inter-domain surface, segments are strongly aligned *parallel*. Perhaps most surprising, we show that anisotropic curvature of inter-domain surfaces (i.e., different principal curvatures), drives biaxial nematic order, with the alignment dependent not only on principle curvature directions, but also on block location. For example, segments at the interface of cylinder-forming BCP orient axial *or* coaxially, depending on whether they are from the core versus coronal blocks (Fig. 1B). The generic, yet previously unrecognized, features of the segmental textures casts a new light on the morphological features of BCP assemblies that exist and vary spatially at the subdomain scale, such as the highly complex pattern of topological defects threaded through the tubular domains of gyroid network phases (Fig. 1C).

Intra-domain phase transitions in self-aligning flexible BCPs. The omnipresent liquid-crystalline order in BCP assemblies raises a basic and previously unstudied question about the susceptibility of the intra-domain textures to the presence of specifically designed anisotropic interactions between segments. We have developed a new approach to model of fully-flexible (intra-chain) BCP melts that incorporate anisotropic orientational interactions, arguably the simplest generalization of the scalar Flory-Huggins interactional model. A novel SCFT approach was developed that generalizes the so-called pseudo-spectral approaches to incorporate the effects of *self-consistent torque* fields [P4]. The study explores the structure and thermodynamics of lamellar mesophases of diblocks with "polar" segments as functions of scalar inter-block repulsion (e.g. χN) and enthalpy of alignment of the polar segments. This model exhibits a range of previously unknown phenomena, including "intra-domain phase transitions" marked by coexistence of different states of orientational symmetry breaking *within a single lamellar mesodomain* as well a new regime of anomalous dependence of domain spacing on inter-block repulsion (i.e., spacing *decreases* with χN near the ODT).

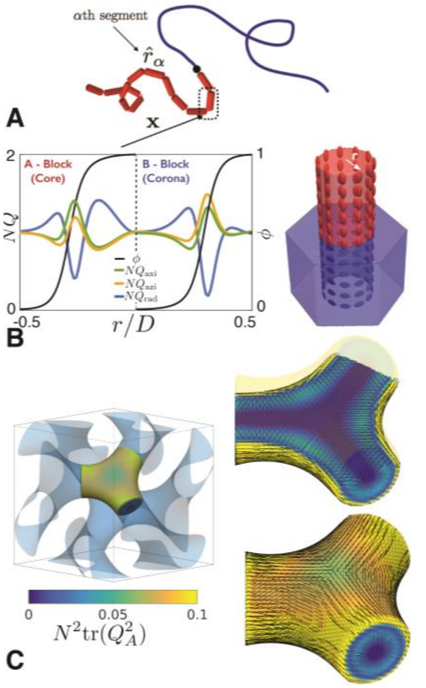

Fig. 1 – In (A), orientation of flexible-chain BCP segments. In (B), the intradomain nematic order profile in cylinder forming BCPs and in (B), the normal core vs. tangential segment alignment in double gyroid phases.

Mesogeometric anatomy of triply-periodic networks phases. We have developed a new method to analyze the mesoscale geometry of network phases of BCPs based on experimentally observed 3D electron tomography reconstructions of their compositions [P3]. Motivating this effort is the fact that until now there are no methods to directly quantify the chirality of networks domains formed in experimental BCP systems, which may possess variable symmetry, topology and degree of order. For example, the double-gyroid (DG) is composed of two enantiomeric single-gyroid (SG) networks. Our approach is to analyze the chirality in terms of the dihedral geometry of the *skeletal graph* that threads through the center of tubular domains. To apply this method to experimental data, we developed a method to numerically fit the skeletal graph to the domains based on (greyscale) 3D intensity data, high-resolution TEM 3D reconstructions of a DG-forming polystyrene-*b*-polyisoprene-*b*-polystyrene triblock previously obtained by H. Jinnai et al. [R3]. Significantly, we show that we can quantitatively distinguish between the "handedness" of each of the self-assembled networks of the DG phase based on the mean value of the a newly defined *network chirality order parameter*, which provides a direct quantitative measure of chirality from experimental BCP networks of arbitrary symmetry (see Fig. 2E-G). Beyond the application to network chirality, this analysis also developed and analyzed new measures to quantify the inhomogeneous thickness of tubular domains in BCP, to our knowledge, the first direct experimental measurement of so-called "packing frustration" of chain extensions within BCP networks.

Slice-and-view SEM (SVSEM) tomography for multi-scale characterization of BCP networks. We have succeeded to make high fidelity 3D tomographic reconstructions of complex 3D BCP domains employing SVSEM [P5]. This technique can be significantly superior to TEM 3D reconstruction for a variety of reasons: SVSEM does not require microtoming of a thin section (typically ~ 100nm, severely limiting the ability to image the structure normal to the section) with the accompanying undesirable plastic deformation of the lattice, since the ion beam sequentially molecularly mills away an ultrathin slice (~ 3nm) of the sample without deformation. A near-surface signal is obtained for each newly cut surface by using a very low incident electron beam (~ 1 KeV instead of the usual 5-30 KeV). Hence, there is no deleterious loss of information from the "missing wedge" of data from the TEMT approach. Moreover, the extreme electron dose imparted to the thin sample in TEM during the typical 121 images (+/- 60° tilt) needed for the 3D reconstruction is avoided since each image is of a freshly ion milled sample surface and the complex influence of the objective lens contrast transfer function of the TEM on the contrast of each of the 100+ images is also avoided. The net result is a vast improvement in the fidelity of the reconstruction and along with a huge gain in the size of the reconstruction, enables heretofore unobtainable visualization and statistical sampling of the detailed nature of the block polymer morphology spanning lengths scales of ~1 nm to 10s of microns along the orthogonal viewing directions.

The sample initially investigated with SVSEM is a PS-PDMS diblock with a PS block having MW of 43.5 kg/mol and a PDMS block with 29 kg/mol, leading to two 20 vol % PDMS networks separated by the majority PS block (see Figure 2). The unit cell lattice parameter is 132 nm and the strut diameter is 30nm. 3nm thin slices were made using the Ga+ beam of a Helios NanoLab 660 Dual Beam tool, operating the ion beam at 30 KeV and the electron imaging beam at 1 KeV. A 45 degree specimen stub was used in conjunction with stage tilt so to be able to image the near surface region with secondary electrons with the incident electron beam perpendicular to the specimen after each slice. The typical field

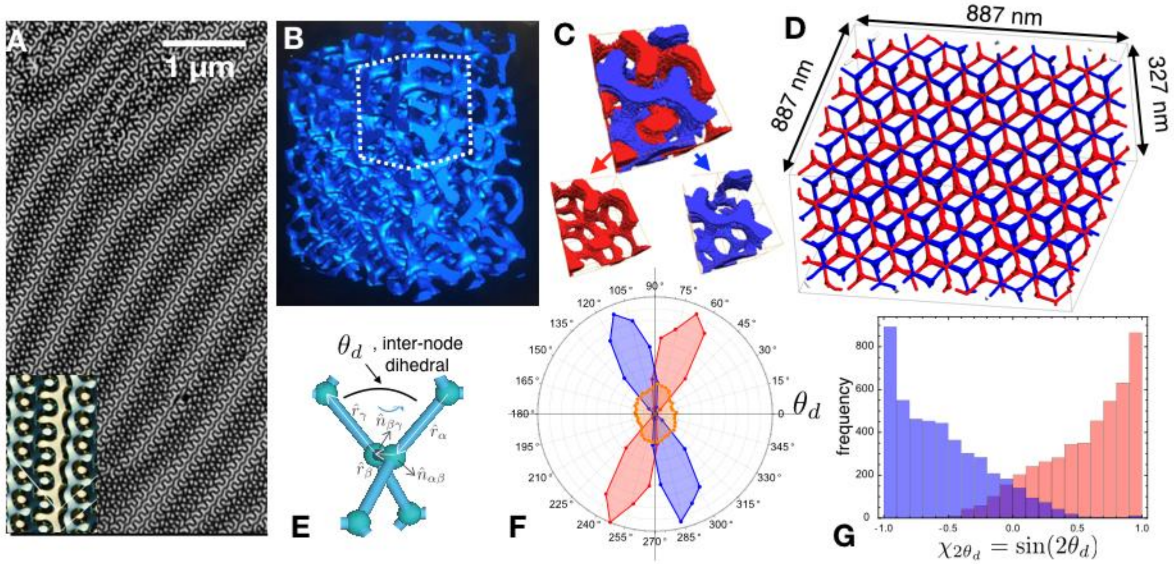

Fig. 2 – (A), A 3.11 µm x 6.14 µm excerpt from a single 2D slice SEM image (from the 3D image stack) of PS-PDMS. The bright regions are the PDMS domains due to the stronger secondary electron emission from the Si containing block. Inset: a simulated slice image for DG normal to the (123) plane with good correspondence to the image features in (A). In (B) 3D reconstruction of a large volume of a PS-PDMS DG. (C). Magnified view of the small boxed region in (B) showing the two interpenetrating, left (blue) and right (red) handed gyroid networks. (D) Skeletal graphs of the DG structure (each of which is SG) computed from reconstrution. (F) A polar plot quantifying the preference and fluctuation of the red and blue networks for opposite sense of rotation dihedral angles, with geometry defined in (E). For comparison, the inner orange plot shows the same analysis applied to a TEMT data set, where the various imaging problems of TEM degrade the ability to distinguish the two enantiomeric SG networks. (G) shows the histogram of the "node chirality" for the opposite chirality networks.

of view is 2.1 microns x 1.4 microns and sampled at 100-200 x 3 nm slices, so that the volume imaged contains 400-800 unit cells. This is dramatically larger (~ 10^2 x 10^3 times by volume) than TEM tilt tomographic data (widely in use in the field) and enables direct and meaningful statistical analysis of key 3D network geometrical and topological parameters (e.g. chirality, defects), opening up new avenues for inquiry into the 3D block copolymer morphologies over an unprecedented range of length scales. A unit cell of the double gyroid contains 2 networks with eight 3-strut nodes in each network, so analysis of 400 unit cells gives 6400 data points for the dihedral analysis. The image contrast in each slice varies from the maximum brightness of the PDMS (Si and O atoms produce more secondary electrons in the PDMS domains than the C, H in the PS domains) to the lowest brightness of the PS domains, so normalization of the images is straightforward. We drill a micron deep, 5nm diameter hole using the Ga+ beam in the region of interest and this allows correct registration of the entire series of slices. The segmentation of the two PDMS network regions from the PS matrix is straightforward based on the excellent contrast between the domains. Our method gives a volume fraction of the networks quite consistent with the known fraction. The ability to image such large regions with high fidelity provides an unprecedented opportunity to measure the subunit cell morphological features (both the high-resolution mean structure and its spatial variation from point to point in the sample) such as the node to node distances, the dihedral angles, the skeletal to interface distances and especially the mean and Gaussian interface curvatures, which together will enable critical comparison of the experimental morphology to detailed sub-domain and super-domain predictions available via SCFT. The SVSEM technique holds particular promise for experimental identification of new BCP morphologies whose symmetries and domain topologies are not known a priori, particular those with large, complex spatial periodicities (such as Frank Kasper or quasi-crystalline phases).

Future Plans

Based on our successes to date, we plan to explore the role of *elastic asymmetry* in multiblock architectures in the formation of novel triply-periodic network (TPN) assemblies of block copolymers, as routes to novel functional nanostructured architectures. Specifically, the aim is to understand how tailoring of specially designed branched polymer architectures control the relative stiffness of channel and inter-channel forming domains, how this stiffness controls the fraction of channel to inter-channel domains (i.e. minority vs. majority channel fractions), and how this sub-unit cell morphology effects the formation of non-canonical TPN symmetries (i.e., beyond gyroid networks with variable junction topology (e.g. networks having an ordered mixture of 3 and 4 junction nodes). Theory will map the "molecule to network" fingerprint of a new class of architecturally tailored, *inverse-bowtie triblocks,* onto equilibrium network symmetry. Synthesis, assembly and characterization of multi-scale structure of IBTs will be carried out, to explore the role of channel vs. inter-channel chain frustration on TPN assembly. New TPN symmetries and sub-domain distributions of chains within heterogeneous channels will be characterized by SVSEM as well as 3D STEM imaging of high atomic number -labeled chain positions.

References

R1. R.-M. Ho, E. L. Thomas, *et al., J. Am. Chem. Soc.* **134**, 10974 (2012), DOI: /10.1021/ja303513f.

R2. G. M. Grason, *ACS MacroLett.* **4**, 526 (2015), DOI: /10.1021/acsmacrolett.5b00131.

R3. H. Jinnai *et al., Phys. Rev. Lett.* **84**, 518 (2000), DOI:1 0.1103/PhysRevLett.84.518.

Publications

P1. I. Prasad, Y. Seo, L. M. Hall and G. M. Grason, "Intradomain textures in Block Copolymers: Multizone Alignment and Biaxiality", *Physical Review Letters* **118,** 247801 (2017), DOI: 10.1103/PhysRevLett.118.247801 .

P2. E. L. Thomas, “Nanoscale 3D ordered polymer networks”, *Science China Chemistry* **61**, 25-32 (2018), DOI: 10.1007/s11426-017-9138-5.

P3. I. Prasad, H. Jinnai, R.-M. Ho, E. L. Thomas and G. M. Grason, "Anatomy of triply-periodic network assemblies: Characterizing skeletal and inter-domain surface geometry of block copolymer gyroids", *Soft Matter* **14,** 3612-3623 (2018), DOI: 10.1039/C8SM00078F .

P4. C. J. Burke and G. M. Grason, "Intradomain phase transitions in flexible block copolymers with self-aligning segments", *Journal of Chemical Physics* **148**, 174905 (2018), DOI: 10.1063/1.5025809 .

P5. H. Gua, M. Zhou, C. J. Burke, I. Prasad, A. Avgeropoulos, R.-M. Ho, G. M. Grason and E. L. Thomas, “High Fidelity, Multiscale 3D Imaging of Block Polymer Morphologies“ *to be submitted* in July 2018.

Late-Metal Phosphorescent Lumophores

Thomas G. Gray, Department of Chemistry, Case Western Reserve University

Program Scope

Work done under BES auspices focuses on the syntheses and characterization of late, heavy-metal organometallics. Complexes of iridium, silver, and gold have been emphasized. The new organometallics are triplet-state lumophores; they have been characterized by multinuclear NMR experiments, absorption and emission spectroscopies (including time-resolved emission), and X-ray diffraction crystallography.

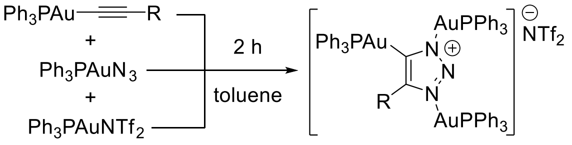

R = Ph, **1**
R = 1-naphthyl, **2**

Scheme 1. Synthesis of triazolides.

Recent Progress

A. Tri-Gold(I) Triazolides with Long-Lived Phosphorescence. The Gray group invented the concept of *gold-click chemistry* where *C*-bound triazolyls form in reactions of organic azides with gold alkynyls. Gray and co-workers have published gold triazolides having phosphorescence lifetimes as long as 19 μs at 77 K. In pursuit of lumophores suitable for OLEDs, we have investigated *tri*-gold triazolides and characterized their luminescence. These complexes are long-lived emitters at 298 K, despite having three gold centers per molecule. Absorption and emission spectra appear in Figure 1. Tri-gold complexes self-assemble in one-pot reactions, as shown in Scheme 1. Emission lifetimes are 4.7 μs (**1**) and 10.3 μs (**2**) at 298 K. Density-functional theory calculations suggest that these complexes become planar in the emitting excited state.

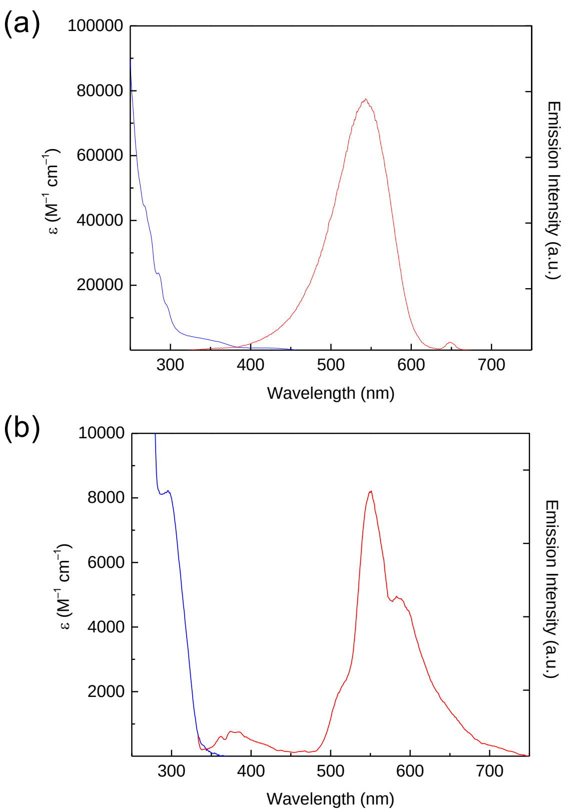

Figure 1. Absorption (blue) and emission (red) spectra (298 K) in 2-methyltetrahydrofuran solution: (a) **1**, and (b) **2**.

B. Regiospecific Arylation of Gold(III). Mixed-ligand cyclometalates bearing aryl and halide ligands are expected to be triplet-state lumophores and also precursors to other organometallics. The Gray research group has developed facile syntheses of singly arylated gold(III) cyclometalates. A leading objective has been to isolate monoaryls by halting the reaction after the first ligand substitution. The general reaction appears as Scheme 2, and representative crystal structures are shown in Figure 2. The incoming aryl group binds *trans* to the nitrogen of the capping ligand. This stereochemistry is consistent with the expected thermodynamic *trans* influence: the strongly *trans* directing aryl ligand binds across from nitrogen, and the (hypothetical) isomer with two mutually *trans* carbon ligands is avoided.

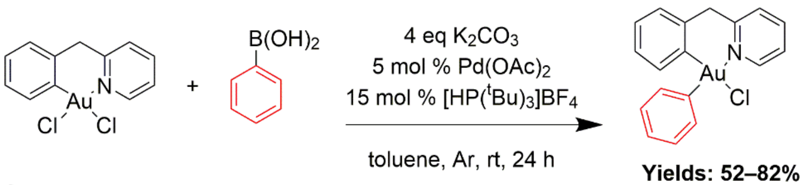

Scheme 2. Single-arylation reactions.

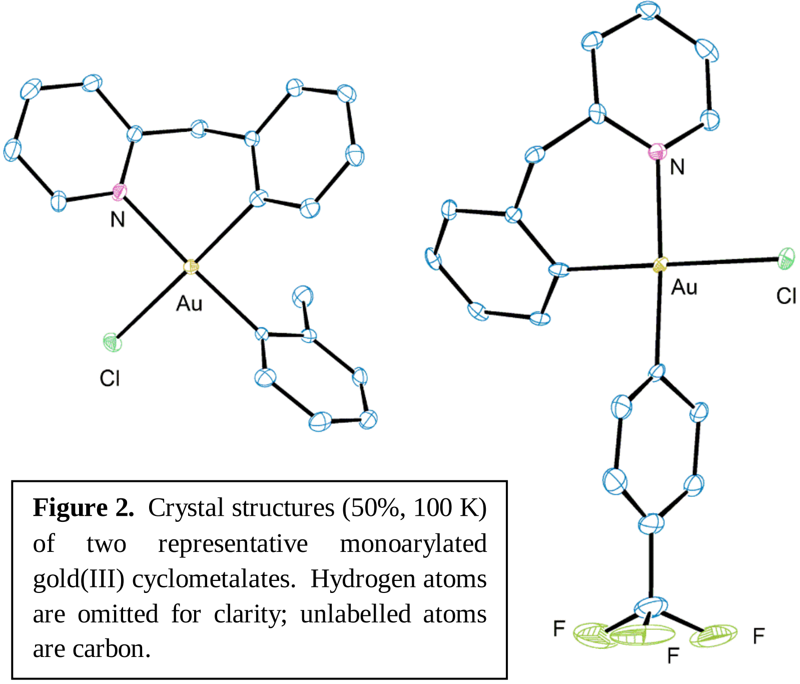

Figure 2. Crystal structures (50%, 100 K) of two representative monoarylated gold(III) cyclometalates. Hydrogen atoms are omitted for clarity; unlabelled atoms are carbon.

Cyclic voltammograms of singly arylated products indicate that the new gold(III) aryls are redox stable from –1.4 to +0.8 V. This stability is favorable for embedding in devices such as OLEDs and luminescent solar collectors.

C. Gold Complexes of Polarizable, Strong-Field Ligands. We have undertaken the synthesis of gold(I) complexes of the conjugated benzothiazyl-fluorenyl ligand BTF, both as triplet lumophores in their own right, and as synthons for gold(III) complexes. BTF has been investigated for third-order nonlinear optical properties that come about, in part, from the long (μs) triplet excited states of its platinum(II) alkynyl complexes.[2] We hypothesize that gold complexes of the BTF ligand system will possess the strong ligand fields that afford useful performance in electroluminescent devices.

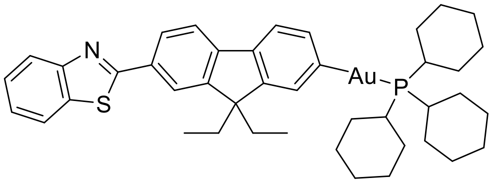

3

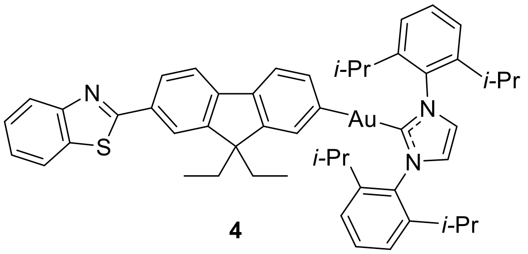

4

Complexes **3** and **4** were synthesized; their crystal structures appear as Figure 3. The complexes exhibit dual emission at room temperature in both fluid toluene solution and rigid poly(methyl methcrylate) (PMMA) films. Triplet-state emission was found for both complexes. The fluorescence lifetimes in both toluene and PMMA were on the order of hundreds of picoseconds. The emission spectra are characterized by dual fluorescence and phosphorescence. The observed fluorescence and phosphorescence from both complexes is structured. The dual emission signals indicate that fluorescence competes with intersystem crossing, despite the presence of a heavy gold atom (*Z* = 79). Luminescence decay profiles were obtained by 375-nm excitation with detection at 420 nm. Compound **4** gave a single exponential fit with a lifetime of 238 ps, but **3** was double exponential with lifetimes of 81 and 460 ps. Emission lifetimes in the hundreds of ps range and the knowledge that intersystem crossing competes with fluorescence suggest that both rate constants are on the order of 10^9 – 10^{10} s^{-1}.

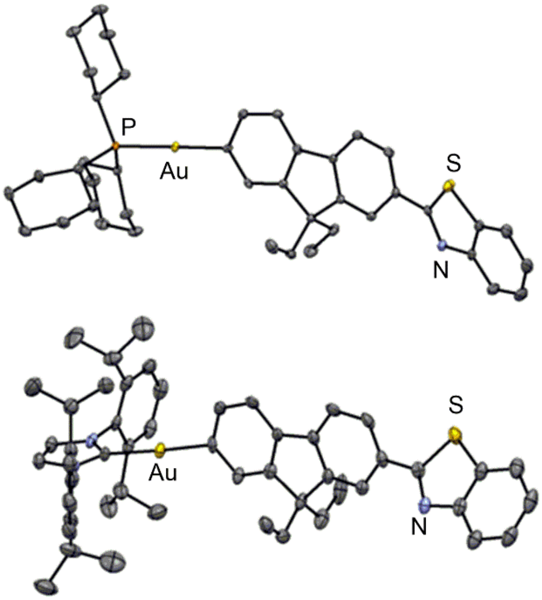

Figure 3. Crystal structures of gold(I) complexes of the aryl BTF fragment (100 K, 50%). A partial atom labelling scheme is indicated. Unlabeled atoms are carbon; hydrogen atoms are omitted for clarity. (a) Tricyclohexylphosphine complex **3**. (b) *N*-heterocyclic carbene complex **4**.

D. Dual Emission from Silver(I) Complexes of Tris-Carbene Borate Ligands. Tri-silver complexes of tetradentate *N*-heterocyclic carbene complexes have been discovered to be luminescent. The metal centers have all-carbon ligand spheres. The excited-state properties of **5** are under investigation. The crystal structure of this tri-silver product appears as Figure 4. Its most notable feature is the conformation of the tris(carbene)borate ligand, with the central B–H bond pointing *inward*. To the best of our knowledge, this binding mode of a scorpionate ligand is unprecedented.

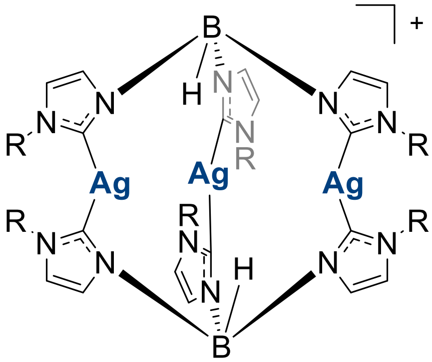

Cation of **5**

Complex **5** shows wavelength-dependent luminescence in solution. Combined absorption and emission spectra in 2-methyltetrahydrofuran appear in Figure 5. Broad, unstructured luminescence appears on excitation at 355 nm, with an emission maximum at 415 nm. A shoulder at *ca*. 575 nm is also evident. Exciting at 450 nm elicits a different emission that maximizes at 575 nm, and which is also unstructured.

Future Plans:

(1) Synthetic and photophysical investigations of platinum cyclometalates.

(2) Synthesis of a family of gold(III) complexes having strong-field ligands that are expected to be triplet-state lumophores.

(3) Characterization of new luminescent complexes by static and time-resolved emission spectroscopy and electrochemical measurements.

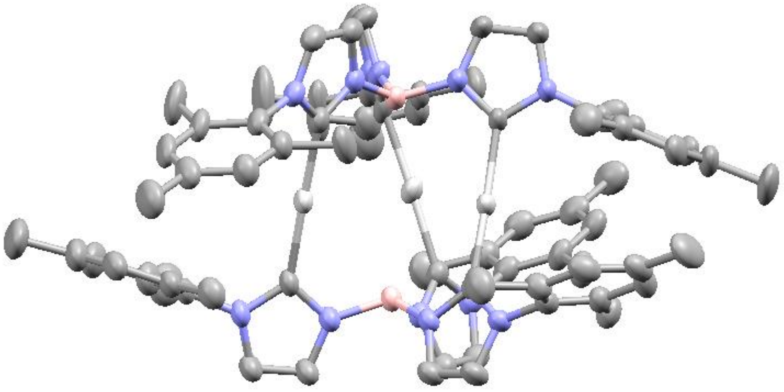

Figure 4. Crystal structure of a tri-silver(I) bis(bis(carbene borate)) complex **5** (50% probability). H atoms are omitted for clarity. Color scheme: silver, light grey; nitrogen, blue; carbon, gray; boron, pink.

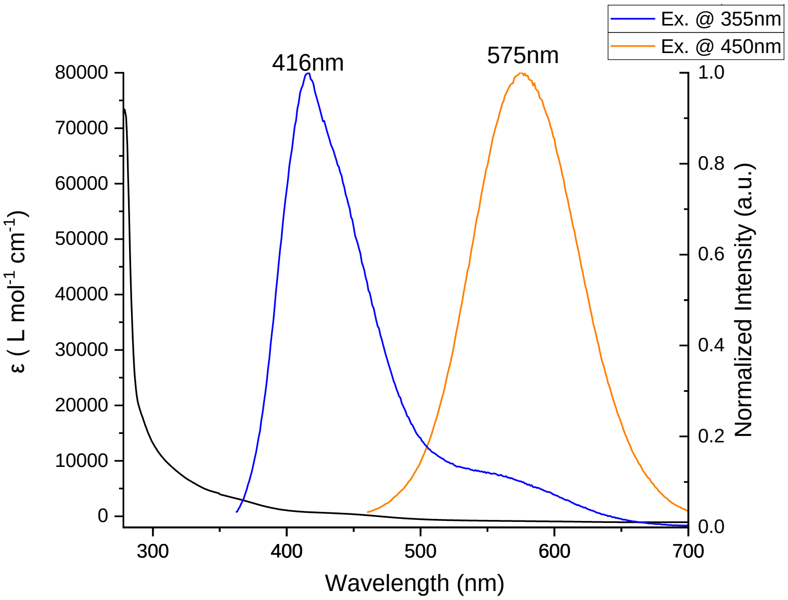

Figure 5. Absorption and emission of **5** in 2-methyltetrahydrofuran solution at 298 K.

References:

1. Partyka, D. V.; Gao, L.; Teets, T. S.; Updegraff, J. B. III; Deligonul, N.; Gray, T. G. Copper-Catalyzed Huisgen [3 + 2] Cycloaddition of Gold(I) Alkynyls with Benzyl Azide. Syntheses, Structures, and Optical Properties. *Organometallics* **2009**, *28*, 6171–6182.

2. Rogers, J. E.; Slagle, J. E.; Krein, D. M.; Burke, A. R.; Hall, B. C.; Fratini, A.; McLean, D. G.; Fleitz, P. A.; Cooper, T. M.; Drobizhev, M.; et al. Platinum Acetylide Two-Photon Chromophores. *Inorg. Chem.* **2007**, *46* (16), 6483–6494.

Publications

1. “Bonding and Reactivity of a Dicopper(I) μ-Boryl Cation.” Wyss, C. M.; Bitting, J.; Bacsa, J.; Gray, T. G.; Sadighi, J. P. *Organometallics* **2016**, *35*, 71–74.10.1021/acs.organomet.5b00961
2. “Cyclometalated Gold(III) Trioxadiborrin Complexes: Studies of the Bonding and Excited States,” Ayoub, N. A.; Browne, A. R.; Anderson, B. L.; Gray, T. G. *Dalton Trans.* **2016**, *45*, 3820-3830. 10.1039/C5DT04732C
3. “A tri-gold triazolide with long-lived luminescence,” Heckler, J. E.; Anderson, B. L.; Gray, T. G. *J. Organomet. Chem. 2016*, *818*, 68–81. 10.1016/j.jorganchem.2016.05.020

Project title: Targeted design of co-continuous nanostructures in randomly end-linked copolymer networks

PI: Ryan C. Hayward

Department of Polymer Science and Engineering, University of Massachusetts Amherst

Program Scope

This program seeks to understand and exploit the formation of disordered co-continuous nanostructures by randomly end-linked copolymer networks (RECNs). Such highly-interconnected 3D nanostructures offer opportunities to synergistically combine properties of the constituent materials in a wide variety of contexts, including as separation membranes, electrodes or separators, catalyst supports, insulation, and lightweight structural materials. Through systematic studies on how the breadth and location of the thermodynamic 'window' for co-continuous nanostructures depend on networks parameters, our work has established that RECNs provide a simple, robust and general pathway to achieve simultaneous percolation of two polymer microphases. We have also elucidated the mechanism by which these materials undergo strain-induced orientation, resulting in co-continuous materials with tunable anisotropy.

Recent Progress

Our recent efforts have focused on: (i) establishing a morphological phase diagram for RECNs, (ii) understanding how the parameters of the network strands - in particular, segregation strength, asymmetry and dispersity of strand molecular weight - control the breadth and location of the co-continuous window, and (iii) characterizing the process by which RECN nanostructures orient under strain, as well as the resulting improvements in mechanical properties of the micro-phase separated materials along the orientation direction.

In Figure 1, a phase diagram is shown for a model RECN system consisting of polystyrene (PS) and polylactic acid (PLA) with symmetric strand molecular weights. Above a critical segregation strength of $\chi N \approx 10$, where χ is the

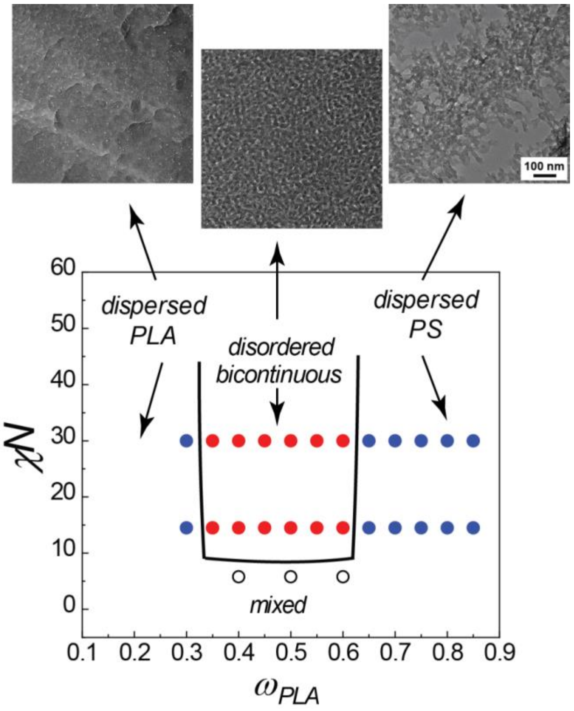

Figure 1. Phase diagram of binary PS/PLA RECNs with TEM images (top).

PS/PLA interaction parameter and *N* the combined degree of polymerization of the two strands, RECNs show disordered co-continuous morphology over a wide range (30 vol%) of composition near the middle of phase diagram, while morphologies with dispersed domains of one phase in a matrix of the other are located to either side. Surprisingly, we find that introducing an asymmetry in molecular weight between the two components has almost no effect on the location or width of the bicontinuous window. However, increasing the molecular weight dispersity of the PLA strands is found to both widen the co-continuous window and shift it towards larger PLA fraction. These findings are consistent with our expectations based on the behavior of block copolymers, where greater dispersity has been found to both promote formation of disordered co-continuous structures and also favor the location of the high dispersity block on the inward side of curved interfaces, due to the tendency for increased dispersity to relieve packing frustration.

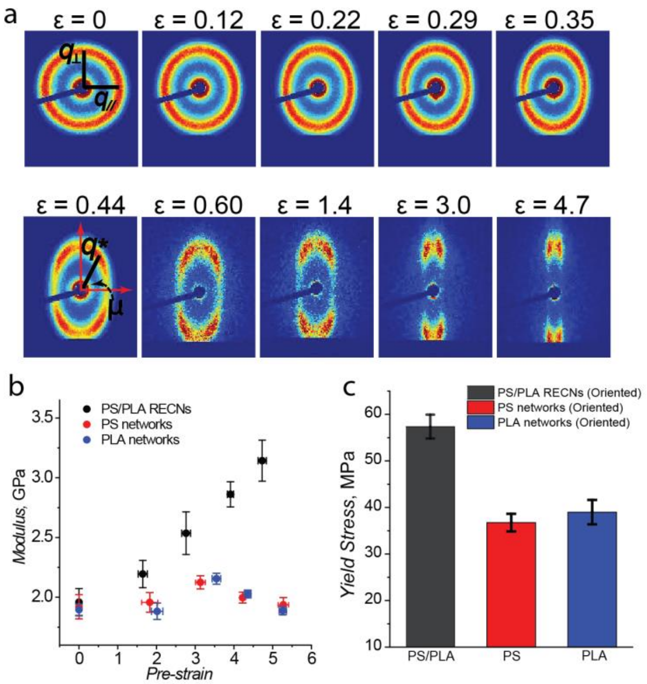

Figure 2. (a) 2D SAXS patterns of PS/PLA RECNs under different strain. (b) Comparison of yield stress among pre-oriented PS/PLA RECNs, PS networks and PLA. (c) Elastic modulus of PS/PLA RECNs, PS networks and PLA under different amounts of pre-orientation.

Pre-stretching PS/PLA RECNs at 130 ^{o}C, followed by quenching to room temperature provides a simple method to fabricate highly oriented and co-continuous morphologies. As shown in Figure 2a, quantitative analysis of small angle X-ray scattering patterns as a function of pre-strain demonstrates a two-step domain orientation process in which domains initially undergo non-affine stretching at low strain, followed by domain rotation towards the stretching direction, yielding a “soft elastic” response and providing a high degree of orientation. Remarkably, the highly oriented PS/PLA nanostructures provide a dramatic increase in toughness (> 600-fold) compared to non-oriented PS/PLA, while also providing high stiffness and yield strength along the stretching direction. Surprisingly, both the modulus and yield stress of oriented PS/PLA RECNs are greater than those of pre-stretched networks of either PS and PLA alone. We speculate that this reflects a higher degree of molecular scale orientation in the aligned nanostructured RECNs compared to that in homogenous networks of PS or PLA alone.

Future Plans

In the future, we will fill in the phase diagram at higher segregation strength by preparing symmetric PS/PLA RECNs with higher strand lengths, as well as exploring in greater detail the behavior at low segregation strength. We will study the effect of junction functionality by generating higher average junction functionalities. We will also study how the behavior of

RECNs compares to linear multi-block copolymers formed using difunctional chain extenders and trifunctional crosslinkers to understand to what extent block length dispersity, chain branching, and crosslinking each influence the formation of co-continuous morphologies. Finally, we intend to vary the polymer chemistries used, for example to yield more mechanically robust porous membranes, or to provide porous materials whose pore walls are coated with hydrophilic polymers.

Publications

1. Zeng, D., Ribbe, A. & Hayward, R. C. Anisotropic and Interconnected Nanoporous Materials from Randomly End-Linked Copolymer Networks. *Macromolecules* **2017**, 50, 4668–4676.

2. Zeng, D., Ribbe, A. & Hayward, R. C. Stress-induced Orientation of Co-continuous Nanostructures within Randomly End-linked Copolymer Networks. **2018**, Submitted.

***Project Title*: New instrumentation and tools to study dynamic (non-equilibrium) physico-chemical interfacial processes across large length, rates, and time scales** (DOE Award number: DE-FG02-87ER45331)

PI: Jacob Israelachvili, Dept Chemical Engineering, Materials Dept, and Materials Research Laboratory (MRL), University of California (UCSB), Santa Barbara, CA93106.
Presenter: Kai Kristiansen, Dept Chemical Engineering, UCSB, Santa Barbara, CA93106.

Program Scope

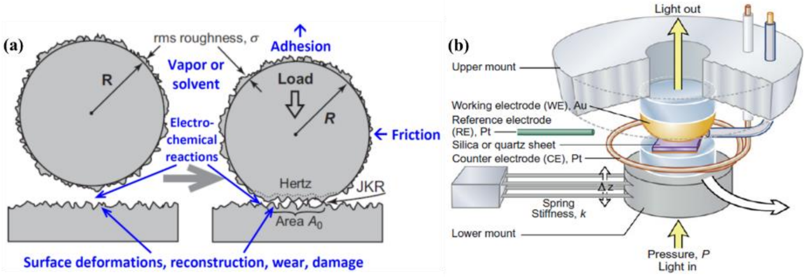

Fig. 1. (a) Adhesion and friction forces between "real" (rough and textured) surfaces are being measured over 7 orders of magnitude of length and time (rate)scales. **(b)** EC-SFA for simultaneous visualization, control and measurement of electro-chemical reactions.

***1.* Measure and characterize complex dynamic molecular interactions** by continuing to apply and develop new experimental techniques to gain fundamental understanding of the adhesion, friction, lubrication and particularly the initiation of damage (wear) to surfaces of engineering interest and investigate the dynamics, i.e., the roles of rate and time, on these often non-equilibrium interactions [1-4]. ***2.* Correlate chemistry with physical interaction forces** by further developing and applying new experimental techniques [5] for measuring the complex dynamic interaction (see above) while simultaneously measuring and controlling the voltages and currents between or flowing through the solid-liquid interfaces to establish the (electro)chemical reactions going on at each surface [6-8].

Recent Progress

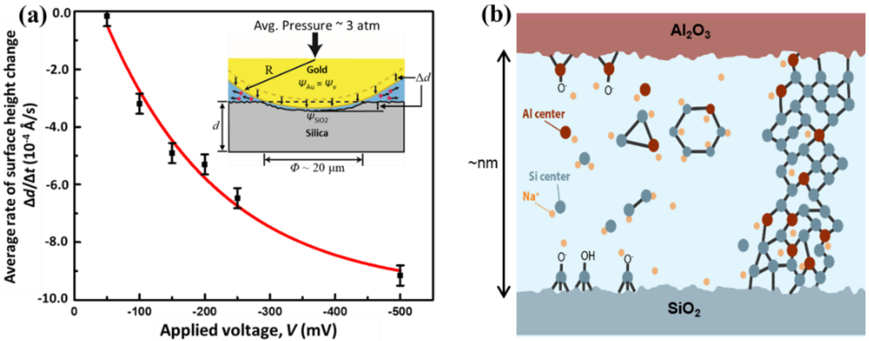

Fig. 2. (a) Dissolution of silica measured using an electrochemical pressure cell where a gold electrode with controllable surface potential is in contact with a silica surface in 0.1 mM NaOH (pH 10) solution. **(b)** Complex and coupled transient processes and network formation of aluminosilica cements.

The electrochemical SFA (EC-SFA): dissolution/corrosion and network formation [6]: A Surface Forces Apparatus (SFA) with an electrochemical attachment was used to directly visualize electrochemical reactions, dissolution and pitting on surfaces when confined in nano-scale gaps (or 'crevices') in *real time*. The results provide unique insights into how two closely apposed surfaces (e.g., alumina, silica, nickel, aluminum) degrade (i.e., dissolve) under confinement (Fig. 2a), which is different from degradation of surfaces exposed to bulk solution. Degradation usually proceeds via local nucleation of 'pits' at the periphery or center of the 'contact area' that rapidly grow outwards (in radius) and, more slowly, in depth, until the pits converge and the whole area has become one large pit. These results support a general concept for dissolution enhancement based solely upon the variation of surface electrochemical properties and solution conditions to manipulate dissolution rates by several orders of magnitude compared to bulk. Our findings high-light the importance of the electrostatic properties of asymmetric solid-liquid-solid interface and suggest new methods for understanding and manipulating dissolution processes in a variety of technological applications.

Inorganic polymer binders (IPBs) are attractive as low-CO_2 alternatives to conventional cementitious structural materials and consist of networked (alumino)silica particles which partially dissolve and crosslink under alkaline conditions. Solution phase species condense, gel, and reprecipitate, forming aluminosilica networks at and between particle surfaces that yield macroscopic strength, which evolves over time (Fig. 2b). Recently developed solid-state NMR techniques and advances in the surfaces forces apparatus (SFA) enable detection and correlation of atomic bonding and hydration environments in aluminosilica networks formed at different reaction times (hours to weeks) as well as the nanoscopic interparticle adhesion energies and strength properties. Complementary *in-situ* surfaces forces measurements between alumina and silica surfaces under analogous reaction conditions (in progress) track the surface morphologies, interparticle layer thicknesses, and adhesion forces and energies of aluminosilica networks.

Ultra-smooth, chemically functional silica surfaces for surface interaction measurements and optical/interferometry-based techniques [5]: We have developed a method for fabricating reflective, deformable composite layers that expose an ultra-smooth silica (SiO_2) surface (RMS roughness <0.4 nm) with interferometric applications. The robust design allows for cleaning and reusing the same surfaces for over a week of continuous experimentation without degradation. The electric double-layer forces measured using the composite surfaces are within 10% of the theoretically predicted values. We have demonstrated that standard chemisorption and physisorption procedures on silica can be applied to chemically modify the surfaces (Fig. 3). Studying intermolecular forces and processes of interfaces at the sub-nano scale has proven difficult due to limitations in surface preparation methods. These composite surfaces provide a basis for the preparation of a variety of new surfaces and should be particularly beneficial for the SFA and colloidal probe methods that

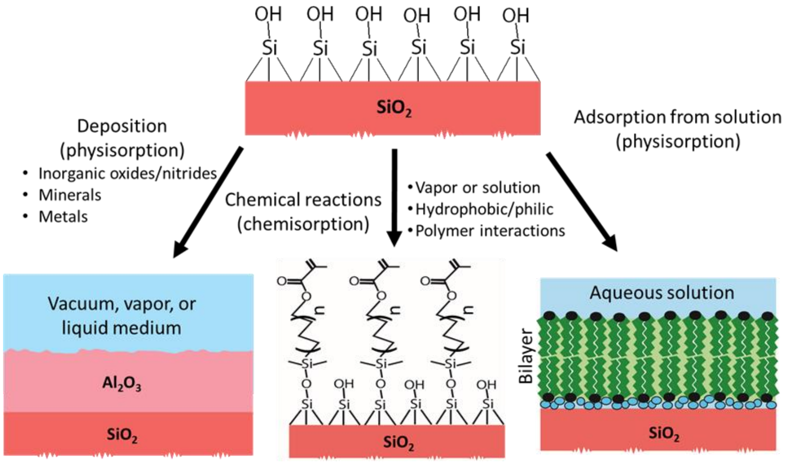

Fig. 3. Different ways through which the silica fabricated disks can be modified via chemical reaction (i.e., chemisorption), deposition (i.e., physisorption), adsorption from solution, etc. to produce novel inorganic/organic surfaces for surface and interface analysis in a variety of environments.

employ optical/interferometric and electrochemical techniques, enabling characterization of previously unattainable surface and interfacial phenomena, including friction/wear and ion-transport in batteries.

Future Plans

Simultaneous imaging and force measurements during AC response of room temperature ionic liquids: We have developed a unique experimental setup using the SFA which enables the characterization of the influence of DC and AC electric fields in solid-ionic liquid-solid confined interfaces. The electric field is applied between the two silica surfaces and allows for simultaneous imaging and force measurements important to understanding how these systems respond under dynamic charging environments, as occurs in electrochemical battery or capacitor applications. The current setup is possible using a modified version of the recently finished composite surfaces designed for the SFA [5] where a gold electrode is covered with a 600 nm silica dielectric to apply an AC or DC field without fully screening the applied electric field. We anticipate these studies will lead to new frameworks for understanding and tuning the *dynamic electric* (and interaction) properties of ionic liquids and other battery electrolytes, such as conductivity and charge transport.

Chemical mechanical polishing: We will carry out simultaneous measurements of dynamic surface forces between moving (i.e., shearing) surfaces and electrochemical reactions and processes.

Vibration-induced hydrodynamic repulsion and wear for confined-lubricant environments: We have performed high-frequency vibration force measurements on fluids commonly used as lubricants, such as glycerol, and materials currently being investigated for use as lubricants, such as ionic liquids, to explore the impact of hydrodynamic forces and mechanical resonances on vibrational-induced wear and cavitation. Unexpected long-range, frequency-dependent repulsions in confined mica-lubricant-mica systems can lead to surface damage/wear when the frequency response is large enough to induce cavitation within the lubricant. A critical parameter for the design of lubricated mechanical systems will be the propensity of the lubricant to cavitate as apposed to typical fluid properties, such as viscosity. Current experiments are being performed to image the exact cavitation event under high-frequency vibrations to understand the origin of the damage. Our findings demonstrate the importance of mechanical vibrations on lubrication and wear relevant to a wide range of mechanical applications and suggest new parameters to be observed when selecting appropriate lubricants.

Instrument developments: New spectroscopic attachments for the multi-modal micro-SFA enable measurement of dynamics, molecular and surface structures, chemical compositions, and reaction/adsorption properties with simultaneous *in-situ* surface forces measurements. The new SPR-SFA attachment (Fig. 4) will measure surface forces between apposing gold and mica surfaces with complementary *in-situ* time-resolved SPR spectroscopy, to provide detailed insights into dynamic adsorption, desorption, and reaction properties of proteins, thin films, organic molecules, or inorganic species between the surfaces. The development and application of

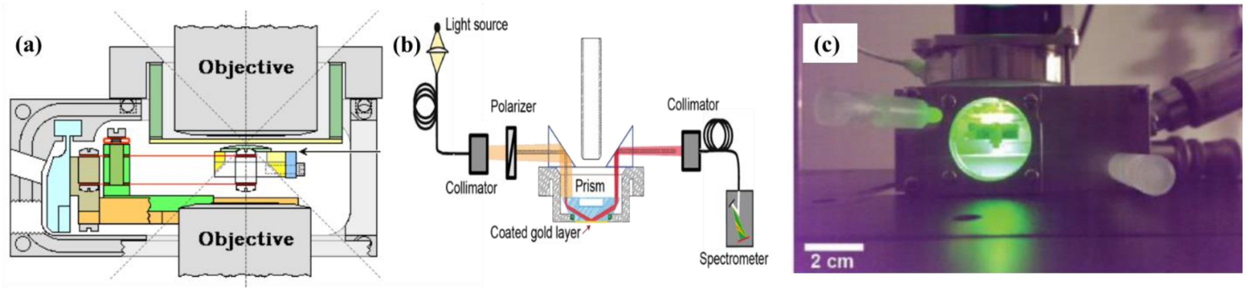

Fig. 4. Proposed multi-modal µSFA. (a) Schematic of the main chamber showing microscope objectives, including wide confocal objectives for both top and inverted imaging, and both grazing incidence and wide-angle x-ray scattering (dashed cones). (b) Schematic of the light path of the SPR-SFA. (c) Photo of the µSFA on the stage of a fluorescence microscope.

additional spectroscopic attachments is in progress, including infrared spectroscopy and fluorescence imaging and spectroscopy, which will each substantially broaden the range of accessible physicochemical and dynamic information accessible. Implemented with the SFA, the combined spectroscopic and surface forces techniques will provide new means of developing fundamental physicochemical understanding of complex interactions at interfaces, with implications for the study of biomolecules, lipid bilayers, adhesives, lubricants, and energy-storage devices.

References / Publications (2 years: mid 2016 – mid 2018)

1. **Adhesion and detachment mechanisms between polymer and solid substrate surfaces: using polystyrene-mica as a model system.** Zeng H, Huang J, Tian Y, Li L, Tirrell M, Israelachvili J. *Macromolecules* **49** (2016) 5223-5231.
2. **Influence of humidity on grip and release adhesion mechanisms for gecko-inspired microfibrillar surfaces.** Cadirov N, Booth JA, Turner KL, Israelachvili J. *ACS Appl. Mater. Interfaces* **9** (2017) 14497-14505.
3. **Toughening elastomer using mussel-inspired iron-catechol complexes.** Filippidi E, Cristiani TR, Eisenback CD, Waite JH, Israelachvili JN, Ahn BK, Valentine MT. *Science* **358** (2017) 502-505.
4. **Duplicating dynamic strain-stiffening behavior and nanomechanics of biological tissues in a synthetic self-healing flexible network hydrogel.** Yan B, Huang J, Han L, Gong L, Li L, Israelachvili J, Zeng H. *ACS Nano* **11** (2017) 11074-11081.
5. **Ultra-smooth, chemically functional silica surfaces for surface interaction measurements and optical/interferometry-based techniques.** Dobbs H, Kaufman Y, Scott J, Kristiansen K, Schrader A, Chen S-Y, Duda P, Israelachvili J. *Advanced Engineering Materials* (2017) 1700630.
6. **In situ nano- to microscopic imaging and growth mechanism of electrochemical dissolution (e.g., corrosion) of a confined metal surface.** Merola C, Cheng H-W, Schwenzfeier K, Kristiansen K, Chen Y-J, Dobbs H, Israelachvili, and Valtiner M. *PNAS* **114** (2017) 9541-9546.

7. **Long range electrostatic forces in ionic liquids.** Gebbie M, Smith AM, Dobbs H, Lee AA, Warr GG, Banquy X, Valtiner M, Rutland M, Israelachvili J, Perkin S, Atkin R. *Chem. Commun.* **53** (2017) 1214-1224.
8. **Effect of salinity on oil recovery (the 'dilution effect'): Experiments and theoretical studies of crude oil/water/calcite surface restructuring and associated physico-chemical interactions.** Chen S-Y, Kaufman Y, Kristiansen K, Seo DJ, Schrader AM, Alotaibi MB, Dobbs HA, Cadirov NA, Boles JR, Ayirala SC, Israelachvili JN, Yousef AA. *Energy Fuels* **31** (2017) 8925-8941.

Predictive coarse-grained modeling of morphologies in polymer nanocomposites with specific and directional intermolecular interactions

PI: Arthi Jayaraman, University of Delaware, Newark

Program Scope: The overarching goal of the project is to develop predictive coarse-grained (CG) models for investigating structure and dynamics in soft materials with chemistries that have specific and directional molecular interactions. The successful development of qualitatively, and *in some cases* quantitatively, accurate CG models is enabled by synergistic feedback from experiments via synthesis and structural characterization of these materials using x-ray scattering, neutron scattering and microscopy. Although past computational studies have been tremendously useful in understanding molecular phenomena and guiding synthesis of new macromolecular soft materials for a wide variety of applications, the inability to capture small scale specific and directional interactions alongside macromolecular length and time scales represents a key limitation of most studies to date. Our work in this project addresses this grand challenge in computational materials chemistry, i.e., to be able to model the anisotropic, directional and specific interactions that govern the behavior of many macromolecular soft matter systems of interest, thus, greatly expanding the predictive potential of simulations.

The specific aims of the proposed work are as follows: **Aim 1:** *To develop new coarse-grained (CG) models for polymers with hydrogen (H-) bonding, specifically for PNCs composed of polymer grafted nanoparticles in a polymer matrix, with donors and acceptors in the graft and matrix polymers.* (**Figure 1**). During this model development stage, large scale CG molecular simulations will be used to predict how varying sequences and stoichiometry of the H-bonding donors and acceptors in the graft and matrix chains impact mixing/interpenetration of graft and matrix chains, and in turn, dispersed and aggregated particle morphologies. Through comparison of chain conformations and composite morphology with experiments (Aim 2), these CG models will be refined and validated. ***Aim 2:*** *To validate and refine the CG model developed in Aim 1 through synthesis and characterization of PNCs comprised of poly(styrene-r-2-vinylpyridine) grafted gold nanoparticles in poly(styrene-r-4-vinyl phenol) matrix, for varying sequences and stoichiometry of the H-bonding donors and acceptors in the graft and matrix chains.* Alongside the model development in Aim 1, PNCs will be synthesized and characterized using a combination of small angle x-ray scattering (SAXS) to determine PNC morphology, and small angle neutron scattering (SANS) on partially-deuterated samples to elucidate the matrix and grafted polymer conformations. **Aim 3:** *To use the validated CG model and computationally explore a large materials design space to establish the effects of*

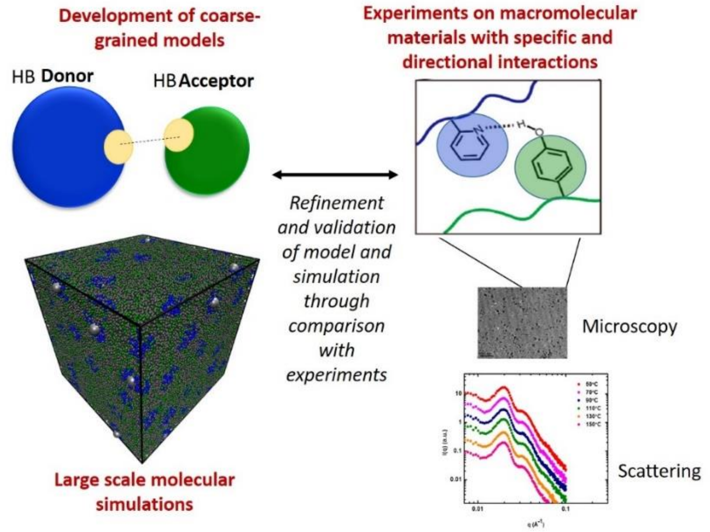

Figure 1: Proposed work with coarse-grained model development (PI Jayaraman) refined and validated through experiments (collaborators Butler at NIST, Hayward at UMass)

placement, valency, stoichiometry (or composition) and strength of the specific and directional bonds in the graft and matrix monomers on the PNC structure and thermodynamics. "

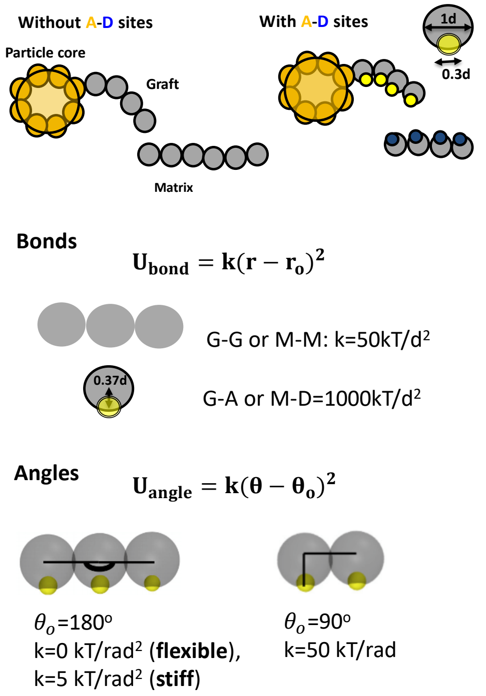

Figure 2: The developed CG model for capturing the directional and specific H-bond interaction between the graft and matrix monomers. We only show one graft chain on the particle for clarity; we vary the grafting density on the particle. We also show the two types of bonded interactions besides the non-bonded interactions described in the text.

Recent Progress: In <u>this first year of this project</u> we have accomplished the initial tasks set forth within Aim 1 (theory and simulations) and Aim 2 (experiments). In PI Jayaraman's lab, a team comprised of one undergraduate student, one graduate student and a postdoc (partial effort), has been working on developing a CG model that captures the large length and time scales of PNCs while mimicking the small-scale H-bond type directional and specific interaction.

In the newly developed CG model, the graft (G) and matrix (M) polymers are represented as chains of CG beads where the beads are either non-H-bonding monomers (e.g., polystyrene in the experiments) or H-bonding monomers (e.g., poly 2-vinyl pyridine and poly 4-vinyl phenol). Each graft or matrix CG bead is of diameter *d* that represents approximately two monomers in the experimental chemistries. The flexibility of the graft and matrix polymer chains can be altered using angle potentials as shown in **Figure 2**. The major new model development pertains to the H-bonding interaction between H-bond donor and acceptor monomer chemistries. To achieve directional and specific H-bond, we have introduced an electrostatically-neutral H-bonding donor (D) site or acceptor (A) site on each of those graft or matrix beads (**Figure 2**). The A-D sites interact with a cut and shifted Lennard-Jones (LJ) potential such that the value of the well depth can be varied to correspond to 5kT (say a weak H-bond) to 15 kT (strong H-bond). Next, the directionality and specificity of the H-bonds is captured by designing the relative size of graft or matrix bead (*d*) and the A or D beads (*0.3d*), relative placement of the two (*0.37d*) (**Figure 2**) and also by defining a repulsive interaction that is only effective between HB sites of the same type (D-D or A-A), similar to previous work by PI Jayaraman's group for DNA systems [1-2].This purely repulsive interaction is captured through a Weeks-Chandler-Andersen (WCA) potential. The graft (G) and matrix (M) bead interactions are modeled using WCA or LJ potentials depending on whether we intend to mimic athermal G-M interactions or attractive G-M interactions, respectively. The nanoparticle is represented using a spherical rigid-body of smaller beads to achieve the desired particle size (D). All G and M bead interactions with the nanoparticle (P) beads are maintained athermal via the WCA potential. Using the above CG model, we perform molecular dynamics (MD) simulations using LAMMPS package[3]. So far, we have focused on a single polymer grafted nanoparticle with particle size D=5d, grafted chains of length N_G = 10 or 20 and grafting density 0.32 chains/d^2 and 0.65 chains/d^2 placed in a matrix of chains of length N_M =10, 20 or 60. For every simulation, an initial configuration is created using one polymer grafted particle placed in the center of the simulation box, that is surrounded by matrix chains with the total PNC occupied volume fraction of 0.376 (melt-like density). The system is equilibrated in NVT ensemble to generate production configurations that are used for calculating grafted layer structure, graft-matrix chain concentration profiles, radii of gyration and end-end distances. Figure 3 shows an example of preliminary wetting-dewetting data using this newly developed model.

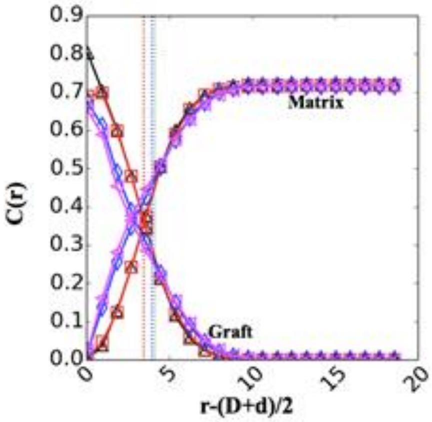

Figure 3. Graft and matrix monomer concentration profiles for a single polymer grafted nanoparticle with particle size D=5d, grafting density= 0.65 chains/d^2, flexible stiff graft chains of length N_G=20 and matrix chains of length N_M =60. Symbol legend described in the text. The grafted brush heights are shown as vertical dotted lines.

In Figure 3 we show for one PNC design, four cases: (i) where the H-bond sites are absent in the graft and matrix chains with athermal graft-matrix interaction (black), (ii) where H-bond sites are present but interact through athermal repulsive-only interactions and graft-matrix interactions are athermal (red), (iii) where H-bond sites are present, directional and attractive through LJ potential of strength $\varepsilon_{AD}=10kT$ and graft-matrix interactions are athermal (blue), and (iv) where there are athermal H-bond sites on grafts and matrix chains with isotropically attractive graft-matrix interaction of LJ attraction strength ε_{GM}~$0.6kT$ (pink). We see that the presence of athermal H-bond sites in athermal G-M PNC (red squares) gives the same wetting behavior as the case where the H-bond sites are absent in athermal G-M PNC (black triangles). This means that the new H-bond CG model features – bonded interactions and repulsive A-A, A-D and D-D interactions – capture the same behavior as in a purely entropically driven PNC. When A and D H-bond sites are attractive with 10kT strength (blue diamonds), wetting in the PNC increases drastically compared to the purely entropic case (black or red), due to the directional attractive H-bond related enthalpic driving forces that favor graft-matrix wetting. This means that in experiments you would see improved particle dispersion at temperatures when H-bond attraction is dominant. Interestingly, we see that to achieve the same extent of wetting as an anisotropic/directional H-bond attraction of 10kT, we would only need an isotropic G-M attraction strength of 0.6kT. In other words, the directional and specific attraction between G and M, accomplished through the A and D sites, has to be really strong to overcome the entropically preferred wetting/dewetting, while the isotropic attraction between G and M can be much weaker to break away from the entropically driven structure. In experiments, the direct way to characterize the extent of wetting and dewetting is via small angle X-ray and neutron scattering measurements[4]. An indirect way to quantify wetting and dewetting is through microscopy (TEM) images; as the nanoparticle aggregation increases essentially the grafted layer wetting decreases.

In our experimental **collaborator Prof. Ryan Hayward's lab at UMass Amherst**, one graduate student supported by the NDSEG fellowship has been synthesizing PNCs comprised of 3-5nm gold nanoparticles grafted with 2-vinylpyridine-containing polysytrene grafts placed in 4-vinylphenol-containing polystyrene copolymer matrices. These chemistries exhibit H-bonding between the 2-vinyl pyridine and 4-vinyl phenol monomers and serve as a specific case to check the validity of the generic CG models developed in PI Jayaraman's group. The PS monomer in the graft and matrix chains are the graft and matrix beads that do not contain the H-bond site, while the 2VP and 4VPh monomers are the graft and matrix beads with A and D sites. As the PNC temperature increases, we expect the anisotropic attraction due to H-bond to diminish, and either purely entropic driving forces or mostly entropic driving forces with some attractive G-M interactions to dominate. Therefore, the high temperature experimental results should mimic the athermal PNC simulation results. The results at room temperature or slightly higher than room temperature, where H-bonds are still existent, are analogous to the attractive results in simulations.

In Figure 4, TEM images show that with increasing H-bond donors in the matrix, the PNCs are more dispersed and higher annealing temperatures are needed for aggregation to start to occur. This is in qualitative agreement with the simulations that show increased wetting in the presence of attractive H-bond interactions as compared to athermal interactions. In the simulations, the PNC systems studied so far all have an acceptor (on graft) or donor (on matrix) H-bond site *on every* (graft or matrix) bead. We are now varying the fraction of the beads in the graft and matrix that have A and D sites to see at what composition we essentially do not see same behavior as the athermal system.

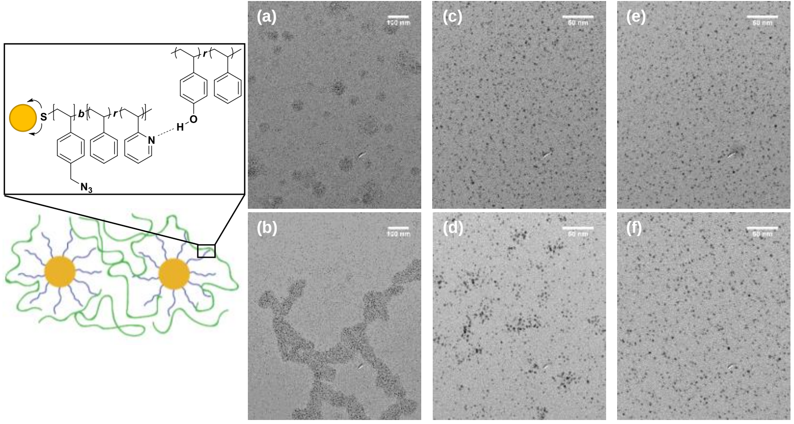

Figure 4: TEM images of spin-coated films of Au NP/P[(S-N_3)-*b*-(S-*r*-2VP)] in matrices of P(S-*r*-4VPh) with varying 4VPh contents; (a) and (b) polystyrene matrix; (c) and (d) P(S-*r*-4VPh) with 1.9 mol% vinylphenol; (e) and (f) P(S-*r*-4VPh) with 3.6 mol% vinylphenol; images are of samples at room temperature and annealed at 180 ˚C for 24h, respectively.

Future Plans: Moving forward, based on the experimentally synthesized materials we will vary the composition of the graft and matrix chains (e.g. number of beads along the graft chain with an acceptor site/ N_G) as well as the ratio of the total number of acceptors to total number of donors in the PNC as described in the plan of work for the next reporting period. Lastly, the materials by Zhao and Hayward will also be characterized by scattering measurements. Zhao is attended neutron scattering school at NIST this summer to be trained to do these measurements.

References

1. Ghobadi, A. F.; Jayaraman, A., Effect of backbone chemistry on hybridization thermodynamics of oligonucleic acids: a coarse-grained molecular dynamics simulation study. *Soft Matter* **2016,** *12* (8), 2276-2287.
2. Ghobadi, A. F.; Jayaraman, A., Effects of Polymer Conjugation on Hybridization Thermodynamics of Oligonucleic Acids. *J. Phys. Chem. B* **2016,** *120* (36), 9788-9799.
3. LAMMPS Package. http://lammps.sandia.gov/.
4. Martin, T. B.; Mongcopa, K. I. S.; Ashkar, R.; Butler, P.; Krishnamoorti, R.; Jayaraman, A., Wetting–Dewetting and Dispersion–Aggregation Transitions Are Distinct for Polymer Grafted Nanoparticles in Chemically Dissimilar Polymer Matrix. *J. Am. Chem. Soc.* **2015,** *137* (33), 10624-10631.

Publications: No publications to report from the first year of this DOE grant support from BES.

Fundamental Studies of Charge Transfer in Nanoscale Heterostructures of Earth-Abundant Semiconductors for Solar Energy Conversion

Song Jin, John C. Wright, and Robert J. Hamers
Department of Chemistry, University of Wisconsin-Madison, Madison, Wisconsin 53706
(jin@chem.wisc.edu, wright@chem.wisc.edu, rjhamers@wisc.edu)

Program Scope

We create new earth-abundant semiconductor nanostructures of two families of materials, layered metal chalcogenides (MX_2) and lead halide perovskites, and their heterojunctions with well-defined chemistry and develop new coherent multidimensional spectroscopies (CMDS) and atomic force microscopy integrated with ultrafast spectroscopy that probe charge transport at the quantum mechanical level in nanoscale heterostructures. They provide the fundamental understanding required to enable transformative solar energy nanotechnologies. In this abstract, we will focus on the ongoing work of perovskite nanostructure synthesis and the CMDS studies of MX_2 materials.

Recent Progress

Solution growth of single-crystal lead halide perovskite nanostructures for fundamental studies and optoelectronic applications

Amidst the exciting progresses in solar cells based on lead halide perovskites, better control of the crystal growth of these materials and improved fundamental understanding of their photophysical properties could further boost their performance. We found that the formation of halide perovskites can involve different pathways of either a conversion reaction at low precursor concentration or dissolution-recrystallization at high precursor concentration (Fig. 1a). We discovered a simple solution growth of single-crystal nanowires (NWs) and nanoplates of $MAPbI_3$ *via* the dissolution-recrystallization pathway by carefully tuning the supersaturation of crystal growth. We have further expanded the family of NWs to formamidinium lead halides ($FAPbX_3$) and all-inorganic cesium lead halides ($CsPbX_3$) (Fig. 1b). We have further expanded nanostructure growth chemistry into 2D layered perovskite materials, using 2-phenylethylammonium ($C_6H_5CH_2CH_2NH_3^+$, PEA) lead halides [$(PEA)_2PbX_4$] (X = Br, I) as the first examples. The natural quantum confinement of 2D layered perovskite $(PEA)_2PbX_4$ allows for PL of shorter wavelength and a larger exciton binding energy than its 3D counterpart. We developed a facile solution growth of single-crystal $(PEA)_2PbX_4$ with a well-defined rectangular nanoplate geometry (Fig. 1c) with typical size of tens of micrometers and thickness of hundreds of nanometers using an improved solution-phase transport growth process. Through halide alloying, the PL emission of $(PEA)_2Pb(Br,I)_4$ nanoplates with narrow peak bandwidth could be readily tuned across from violet (~410 nm) to green (~530 nm) color (Fig. 1d).

The facile solution growth of single-crystal nanostructures of diverse families of perovskite materials with different cations, anions, and dimensionality and different properties have provided and will continue to provide model systems for the fundamental studies discussed in this project. They have also enabled high performance optoelectronic applications, especially lasing. The same amazing physical properties that make halide perovskites highly efficient solar materials are also ideal for semiconductor lasers and other photonic applications. In collaboration with Prof. Xiaoyang Zhu at Columbia University, we demonstrated wavelength tunable room temperature lasing from these single-crystal lead halide perovskite NWs (Fig. 1e) with low lasing thresholds, and high lasing quality factors, and near unity quantum yield. The use of all-inorganic perovskites $CsPbX_3$ greatly enhanced the robustness of the lasing and expanded the tunable lasing wavelength from 420 nm to 824 nm (Fig. 1f). Recently, they have also shown continuous wave (cw) lasing from the $CsPbBr_3$ nanowires with uneven mode spacing, which may suggest strong light-matter interactions. The high lasing performance, coupled with facile solution growth of single-crystal nanowires and broad tunability of emission color using different perovskite stoichiometry, makes lead halide perovskites ideal materials for the development of nano-photonics and optoelectronic devices.

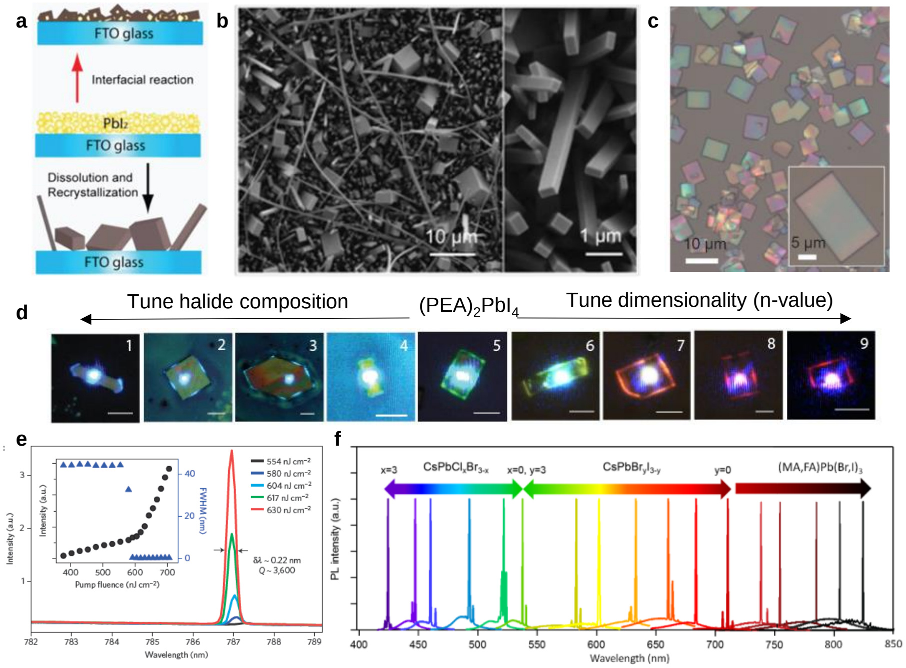

Fig. 1. Solution growth of nanostructures of diverse 3D and 2D lead halide perovskite materials and their tunable optical and lasing properties. (a) Two growth pathways for halide perovskite formation in solutions. (b) SEM images of single-crystal CsPbBr3 NWs. (c) Optical images of nanoplates of 2D perovskite PEA_2PbI_4. (d) Optical images of a series of individual microplates of $(PEA)_2(MA)_nPb_nI_{3n+1}$ with different halide compositions and *n*-values under laser excitation that show tunable emission color. (e) Emission spectra of $MAPbI_3$ NWs photoexcited by increasing power demonstrating stimulated light emission (lasing), (f) Broad wavelength-tunable lasing from a variety of single-crystal lead halide perovskite NWs we have synthesized.

Stabilization of Metastable Halide Perovskite Phases in Nanostructures and Thin Films

We have further developed the nanomaterials chemistry of halide perovskites that might be thermodynamically unstable or metastable at ambient conditions. Due to the mismatch of ionic radii as reflected by the Goldsmidt structural tolerance factor, the perovskite structures of $FAPbI_3$ and $CsPbI_3$ are metastable at room temperature; however, they hold great promises in solar and light-emitting applications. Using the smaller cations of MA (in comparison with FA) and smaller anions of Br^- (in comparison with I^- ions), MABr-stabilized $FAPbI_3$ or $FA_{1-x}MA_xPbI_3$ NWs that are stabilized in the perovskite structure can be directly synthesized from solutions. For the Cs-perovskite family, starting from the directly solution grown single-crystal NWs of $CsPbX_3$ (X = Br, Cl), we have developed a low-temperature vapor-phase halide exchange method to convert $CsPbBr_3$ NWs into perovskite phase $CsPb(Br,I)_3$ alloys and metastable $CsPbI_3$ with well-preserved perovskite crystal lattice and NW morphology.

We have further developed a new chemical strategy based on surface ligand functionalization during direct solution growth to stabilize the metastable *pure* lead iodide perovskite nanostructures and thin films. The surface functionalization can reduce the surface energy and promote the crystal growth of metastable perovskite phase both thermodynamically and kinetically. Moreover, thin films of two different metastable $CsPbI_3$ perovskite polymorphs in the cubic (α-$CsPbI_3$) and the less common orthorhombic (β-$CsPbI_3$) structures can be directly synthesized in a one-step spin coating film deposition by using oleylammonium or phenylethylammonium additives, respectively, and both phases are stable at room temperature for months. These discoveries have not only enabled the practical optoelectronic applications of metastable perovskites, but also provide new insights on the control of metastable structural polymorphs and manipulating the thermodynamic phase stability of solid state materials in general.

Vapor Phase Epitaxial Growth of Halide Perovskite Nanowires and Thin Films.

We have developed the vapor phase epitaxial growth of high-quality crystalline inorganic halide perovskites $CsPbX_3$ (X = Cl, Br, I) with controllable morphologies and growth directions. Horizontal single-crystal $CsPbX_3$ NWs and microwires (MWs) with controlled crystallographic orientations on the (001) plane of phlogopite and muscovite mica can be grown via CVD due to an incommensurate heteroepitaxial lattice match between the $CsPbBr_3$ and mica crystal structures and the asymmetric lattice mismatch. High-quality halide perovskite single crystals have low defect densities and excellent photophysical properties, yet thin films are the most sought-after material geometry for optoelectronic devices. We further developed the facile vapor-phase epitaxial growth of continuous SCTFs of $CsPbBr_3$ with controllable micrometer thickness, as well as nanoplate arrays, on traditional oxide perovskite $SrTiO_3$(100) substrates. Heteroepitaxial single-crystal growth is enabled by the serendipitous incommensurate lattice match between these two perovskites (Fig. 2), and overcoming the limitation of island-forming Volmer–Weber crystal growth is critical for growing large-area continuous thin films. Time-resolved PL, transient reflection spectroscopy, and electrical transport measurements show that the $CsPbBr_3$ epitaxial thin film has a slow charge carrier recombination rate, low surface recombination velocity (10^4 cm s^{-1}), and low defect density of 10^{12} cm^{-3}, which are comparable to those of $CsPbBr_3$ single crystals. This work suggests a general approach using oxide perovskites as

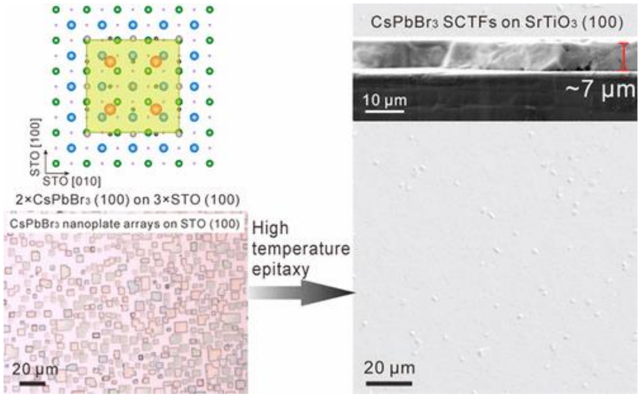

Fig. 2. Heteroepitaxial growth of single-crystal thin films of $CsPbBr_3$ as well as nanoplate arrays on $SrTiO_3$ (001) substrate. The upper left scheme illustrates the serendipitous incommensurate lattice match between $CsPbBr_3$ and $SrTiO_3$.

substrates for heteroepitaxial growth of halide perovskites. The high-quality halide perovskite SCTFs epitaxially integrated with multifunctional oxide perovskites could open up opportunities for optoelectronics devices and are the material foundations for several heterostructures in our proposed future work. We have also developed a solution growth method for making vertically stacked double heterostructures and complex multilayer heterostructures of 2D lead iodide perovskites $[(PEA)_{2}(MA)_{n-1}Pb_{n}I_{3n+1}]$ via van der Waals epitaxy, because ion migration is suppressed along both in-plane and out-of-plane directions in 2D RP perovskites.

CDMS Studies of MX_2 and Perovskite Materials.

Our previous work on the QD systems demonstrated how we could use different CMDS methods to obtain the complementary information required to understand the exciton and free carrier dynamics. The shortcomings and limitations of our first published work on CMDS studies of MoS_2 films used a transient grating geometry in reflection mode, namely the need for flat and smooth samples, narrower tuning range and short delay time, provided the impetus for implementing other CMDS methodologies. MoS_2, WS_2, and the MoS_2-WS_2 heterostructures have been used as our model systems to develop these new methodologies. We have complemented this work with TA and TG pathways whenever possible in order to provide comparisons with the spectroscopy normally used in the field. These methods are also being applied to halide perovskite nanostructures or thin films discussed above.

Future Plans

We will develop new synthetic and characterization methods for creating novel, high quality, monolithically integrated heterostructures of 2D or 3D halide perovskites with sharp, atomic scale interfaces and rigorous characterization. We will explore new ideas for controlling moisture sensitivity, ionic diffusion and phase stability that are central to maintaining pristine interfaces between perovskites. In addition to often-used characterization methods, we will use time-resolved microwave conductivity and surface photovoltage to measure bulk and near-surface free charge carriers, respectively, and global analysis methods of charge carrier dynamics based on the dependence of photoluminescence and transient absorption on transient and steady state charge carrier concentrations. Our high quality 2D heterostructure samples of both MX_2 and 2D perovskites also form the basis for our continued development of novel pump-CMDS probe methods that provide additional ultrafast capabilities for resolving charge transfer dynamics on femtosecond time scales with single quantum state resolution. The latter will also directly address the quantum mechanical coherences that recent theories employ for understanding how charge separation can occur in 2D heterostructures where the large binding energies of quantum confined excitons, the lack of a built-in potential, and weak interlayer coupling oppose charge carrier separation. These, combined with surface photovoltage Kelvin probe force microscopy would allow us to spatially and temporally resolve charge carrier dynamics and reveal charge transfer mechanism(s) across the heterostructures.

References (see the next section)

Two Year List of Publications

1. Samad, L.; Bladow, S. M.; Ding, Q.; Zhuo, J.; Jacobberger, R. M.; Arnold, M. S.; Jin, S.; Layer-Controlled Chemical Vapor Deposition Growth of MoS_2 Vertical Heterostructures via van der Waals Epitaxy. *ACS Nano* **2016**, *10,* 7039-7046. DOI: 10.1021/acsnano.6b03112.
2. Liang, D.;† Peng, Y.;† Fu, Y.; Shearer, M. J.; Zhang, J.; Zhai, J.; Zhang, Y.; Andrew, T. L.; Jin, S. Color-Pure Violet Light-Emitting Diodes Based on Layered Lead Halide Perovskite Nanoplates, *ACS Nano* **2016**, *10,* 6897-6904. DOI: 10.1021/acsnano.6b02683.
3. Fu, Y.; Zhu, H.; Stoumpos, C. C.; Ding, Q.; Wang, J.; Kanatzidis, M. G.; Zhu, X.; Jin, S.; Broad Wavelength Tunable Robust Lasing from Single-Crystal Nanowires of Cesium Lead Halide Perovskites ($CsPbX_3$, X = Cl, Br, I). *ACS Nano* **2016**, *10,* 7963–7972. DOI: 10.1021/acsnano.6b03916.
4. Zhu, H.; Miyata, K.; Fu, Y.; Wang, J.; Joshi, P. P.; Niesner, D.; Williams, K. W.; Jin, S.; Zhu, X.-Y.; Screening in crystalline liquids protects energetic carriers in hybrid perovskites, *Science* **2016**, *353*, 1409-1413. DOI: 10.1126/science.aaf9570.
5. Zhu, H.; Trinh, M. T.; Wang, J.; Fu, Y.; Joshi, P. P.; Miyata, K.; Jin, S.; Zhu, X. Y. Organic Cations Might Not Be Essential to the Remarkable Properties of Band Edge Carriers in Lead Halide Perovskites. *Adv. Mater.* **2017**, 1603072. DOI: 10.1002/adma.201603072.
6. Xiao, R.; Hou, Y.; Fu, Y.; Peng, X.; Wang, Q.; Gonzalez, E.; Jin, S.; Yu, D. Photocurrent Mapping in Single-Crystal Methylammonium Lead Iodide Perovskite Nanostructures. *Nano Letters* **2016**, *16*, 7710. **DOI:** 10.1021/acs.nanolett.6b03782.
7. Dai, J.; Fu, Y.; Manger, L. H.; Rea, M. T.; Hwang, L.; Goldsmith, R. H.; Jin, S. Carrier Decay Properties of Mixed Cation Formamidinium–Methylammonium Lead Iodide Perovskite $[HC(NH_2)_2]_{1-x}[CH_3NH_3]_xPbI_3$ Nanorods. *The Journal of Physical Chemistry Letters* **2016**, *7*, 5036. DOI:10.1021/acs.jpclett.6b01958.
8. Ding, Q.; Song, B.; Xu, P.; Jin, S.; Efficient Electrocatalytic and Photoelectrochemical Hydrogen Generation Using MoS_2 and Related Compounds, *Chem* **2016**, *1*, 699-726. DOI: http://dx.doi.org/10.1016/j.chempr.2016.10.007. (Invited Feature Review)
9. Manger, L. H.; Rowley, M. B.; Fu, Y.; Foote, A. K.; Rea, M. T.; Wood, S. L.; Jin, S.; Wright, J. C.; Goldsmith, R. H. Global Analysis of Perovskite Photophysics Reveals Importance of Geminate Pathways. *The Journal of Physical Chemistry C* **2017**, *121*, 1062. DOI: 10.1021/acs.jpcc.6b11547.
10. Chen, J.; Fu, Y.; Samad, L.; Dang, L.; Zhao, Y.; Shen, S.; Guo, L.; Jin, S.; Vapor-Phase Epitaxial Growth of Aligned Nanowire Networks of Cesium Lead Halide Perovskites ($CsPbX_3$, X = Cl, Br, I), *Nano Letters* **2017**, *17*, 460-466. **DOI:** 10.1021/acs.nanolett.6b04450.
11. Ding, Q.; Czech, K. J.; Zhao, Y.; Zhai, J.; Hamers, R. J.; Wright, J. C.; Jin, S.; Basal Plane Ligand Functionalization on Semiconducting 2H-MoS_2 Monolayers. *ACS Appl. Mater. Interface* **2017**, *9*, 12734–12742. **DOI:** 10.1021/acsami.7b01262.
12. Shearer, M. J.; Samad, L.; Zhang, Y.; Zhao, Y.; Puretzky, A. A.; Eliceiri, K. W.; Wright, J. C.; Hamers, R. J.; Jin, S., Complex and Noncentrosymmetric Stacking of Layered Metal Dichalcogenide Materials Created by Screw Dislocations. *J. Am. Chem. Soc.* **2017**, *139*, 3496–3504. **DOI:** 10.1021/jacs.6b12559.

13. Fu, Y.; Wu, T.; Wang, J.; Zhai, J.; Shearer, M. J.; Zhao, Y.; Hamers, R. J.; Kan, E.; Deng, K.; Zhu, X.; Jin, S.; Stabilization of the Metastable Lead Iodide Perovskite Phase via Surface Functionalization, *Nano Letters* **2017,** *17,* 4405-4414. DOI: 10.1021/acs.nanolett.7b01500.

14. Fu, Y.; Rea, M. T.; Chen, J.; Morrow, D.; Hautzinger, M. P.; Zhao, Y.; Pan, D.; Manger, L. H.; Wright, J. C.; Goldsmith, R. H.; Jin, S.; Selective Stabilization and Photophysical Properties of Metastable Perovskite Polymorphs of $CsPbI_3$ in Thin Films. *Chem. Mater.* **2017**, *29*, 8385–8394. DOI: 10.1021/acs.chemmater.7b02948.

15. Chen, J.; Morrow, D. J.; Fu, Y.; Zheng, W.; Zhao, Y.; Dang, L.; Stolt, M. J.; Kohler, D. D.; Wang, X.; Czech, K. J.; Hautzinger, M. P.; Shen, S.; Guo, L.; Pan, A.; Wright, J. C.; Jin, S.; Single-Crystal Thin Films of Cesium Lead Bromide Perovskite Epitaxially Grown on Metal Oxide Perovskite ($SrTiO_3$). *J. Am. Chem. Soc.* **2017**, *139*, 13525–13532. DOI: 10.1021/jacs.7b07506.

16. Hautzinger, M. P.; Dai, J.; Ji, Y.; Fu, Y.; Chen, J.; Guzei, I. A.; Wright, J. C.; Li, Y.; Jin, S.; Two-Dimensional Lead Halide Perovskites Templated by a Conjugated Asymmetric Diammonium. *Inorg. Chem.* **2017**, 56, 14991–14998. DOI:10.1021/acs.inorgchem.7b02285.

17. Daniel D. Kohler, Blaise J. Thompson, and John C. Wright, Frequency-domain coherent multidimensional spectroscopy when dephasing rivals pulse width: Disentangling material and instrument response, *The Journal of Chemical Physics* ***2017****, 147,* 084202-1-17. DOI: 10.1063/1.4986069.

18. Darien J. Morrow, Daniel D. Kohler, and John C. Wright, Group and phase velocity mismatch fringes in non-resonant triple sum-frequency spectroscopy. *Physical Review A* **2017,** *96,* 063835. DOI: 10.1103/PhysRevA.96.063835.

19. Evans, T. J. S.; Schlaus, A.; Fu, Y.; Zhong, X.; Atallah, T. L.; Spencer, M. S.; Brus, L. E.; Jin, S.; Zhu, X. Y.; Continuous-Wave Lasing in Cesium Lead Bromide Perovskite Nanowires. *Adv. Opt. Mater.* **2018**, *6*, 1700982. DOI: 10.1002/adom.201700982.

20. Pan, D.; Fu, Y.; Chen, J.; Czech, K. J.; Wright, J. C.; Jin, S.; Visualization and Studies of Ion Diffusion Kinetics in Cesium Lead Bromide Perovskite Nanowires. *Nano Letters* **2018**, *18*, 1807-1813. DOI: 10.1021/acs.nanolett.7b05023.

21. Fan, X.; Zhao, Y.; Zheng, W.; Li, H.; Wu, X.; Hu, X.; Zhang, X.; Zhu, X.; Zhang, Q.; Wang, X.; Yang, B.; Chen, J.; Jin, S.; Pan, A.; Controllable Growth and Formation Mechanisms of Dislocated WS_2 Spirals. *Nano Letters* **2018**, *18,* ASAP. **DOI:** 10.1021/acs.nanolett.8b01210.

22. Shearer, M. J.; Li, M.-Y.; Li, L.-J.; Jin, S.; Hamers, R. J.; Nanoscale Surface Photovoltage Mapping of 2D Materials and Heterostructures by Illuminated Kelvin Probe Force Microscopy. *J. Phys. Chem. C* **2018**, *8*, ASAP. DOI: 10.1021/acs.jpcc.7b12579.

23. Kohler, D. D.; Thompson, B. J.; Wright, J. C. Resonant Third-Order Susceptibility of PbSe Quantum Dots Determined by Standard Dilution and Transient Grating Spectroscopy. Accepted for publication, *J Phys Chem C.*

Statically Polarized Polymer Heterostructures for Charge Carrier Density Control in Energy-Relevant Semiconductors

Howard E. Katz, Principal Investigator

Daniel H. Reich, N. Peter Armitage, and Arthur Bragg, co-Principal Investigators

Johns Hopkins University, 3400 North Charles Street, Baltimore, MD 21218

Program Scope

The objectives as listed in the original proposal, in order of priority during the most recent project period, are as follows:

1. Design and synthesize new crosslinkable dielectric polymers with static charge-stabilizing functionality.
2. Prepare heterostructures of these polymers and determine their interfacial morphologies and electronic charge storage properties.
3. Prepare and evaluate capabilities of these heterostructures to control and stabilize desired charge carrier densities in adjacent semiconductors, starting with organic transistor (OFET) semiconductors but also including some used in thermoelectrics and as topological insulators.
4. Prepare dielectric polymers with mechanical compliance greater than for typical glassy polymers, such as polystyrenes, to determine the required rigidity for heterostructure integrity and stable charge localization, and conduct electromechanical characterization.
5. Attach charge-stabilizing functionality to polymers that also have substrate surface-bonding functional groups.
6. Evaluate heterostructure morphologies of the surface-attaching polymers.
7. Evaluate charge density-controlling surface-attached polymers on semiconductors.

Recent Progress

Dielectric polymer synthesis: We synthesized and characterized PS2a-c and crosslinked PS3 (Figure 1). These are new polystyrenes, crosslinkable with no fragmentation, with charge storage-promoting subunits that form curable spincoated films with smooth topographies and stability to subsequent solution coating steps.

Dielectric polymer heterostructures as gate dielectrics: PS2b was placed in the top or bottom positions with plain polystyrene in the converse positions in bilayer gate dielectric OFETs, and in the middle position of a trilayer dielectric device. Neutron reflectivity and scanning electron microscopy (SEM) verified the multilayer morphology.

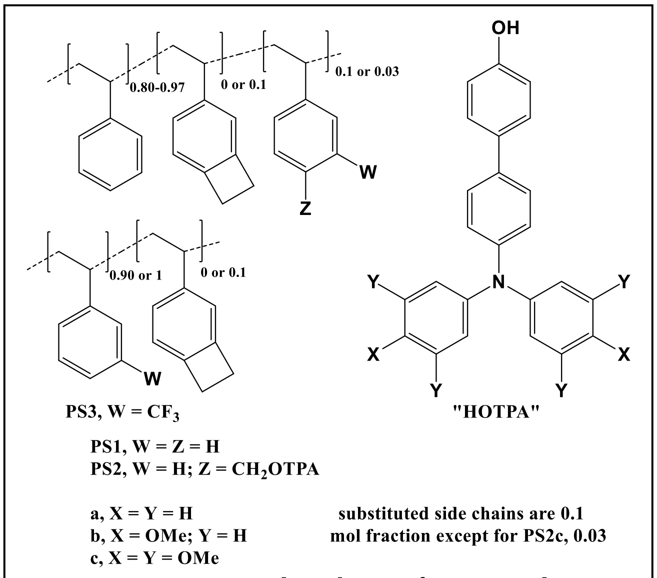

Figure 1. Structures and syntheses of styrene polymers.

The mean interfacial roughness at the XLPS-TPAOMe / d8-PS interface was 4.86 nm ± 0.02 nm. This was 5.5% of the total layer thickness, demonstrating the integrity of the copolymer during cross-linking. However, the significant increase in interfacial roughness when compared to the value of ~2.5 nm found previously for TPA-substituted polystyrenes is consistent with the effects of an increase in free volume and steric hinderance of the TPAOMe functional group compared with the smaller TPA moiety.

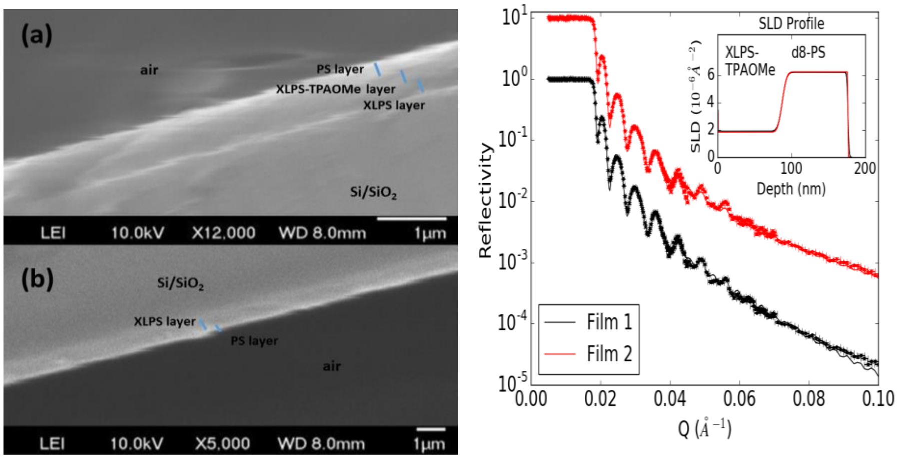

Figure 2. (left) Cross-section SEM of a) XLPS/XLPS-TPAOMe/PS trilayer and (b) XLPS/PS bilayer. (right) Measured neutron reflectivity for XLPS-TPAOMe/d8-PS.

We compared V_{th} shift before and after charging stacks in OFETs by applying ±100V across 0.5-1 μm total thicknesses. Bias stress dominated in bilayers with PS2b contacting pentacene. With no PS2b contacting pentacene, when charging with -100V on top of the source and drain electrodes, electron injection from pentacene to dielectric was the major charging mechanism, again consistent with bias stress. When charging with +100V, bilayer devices without PS2b showed little change in V_{th}, suggesting there was no bias stress effect or charge injection in these devices for this charging polarity. For the bilayer devices with the PS2b layer in the bottom, and the trilayer devices with PS2b in the middle, when +100V was applied, the V_{th} shifts were opposite those expected from bias stress. For the trilayer structure (PS1-PS2b-PS1), large negative threshold voltage shifts, which made the devices much easier to turn on, were observed when *both signs of voltages were applied*. The situation was different from the unsubstituted bilayer structure because V_{chg} = +100 V resulted in large V_{th} shifts in the same direction as that resulting from V_{chg} = -100 V, while there was no obvious V_{th} shift in the unsubstituted bilayer structures in the case of V_{chg} = +100 V (Figure 3). Dipole formation or partial ionization of chargeable groups at the interface between the dielectric layers are likely polarization mechanisms in the cases where charging is opposite to what would be expected from bias stress. This work provides examples of both stabilization and shifting of V_{th},

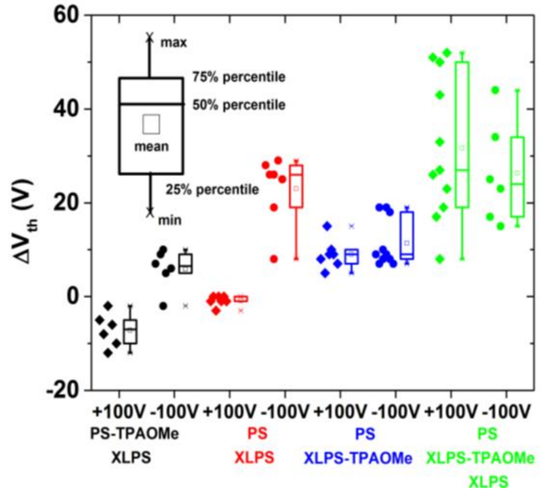

Figure 3. Boxplot of the threshold voltage shifts ΔV_{th} as a result charging with $V_{chg} = \pm 100$ V. We denote negative shift as an increase in the magnitude of the V_{th}, indicating devices were harder to turn on and a positive shift as a decrease in the magnitude of the V_{th}. From left to right: V_{th} shift for XLPS/PS, XLPS/PS-TPAOMe, XLPS/XLPS-TPAOMe/PS and XLPS-TPAOMe.

and therefore controlling charge carrier density, in semiconductors overlying the dielectric multilayers. We prepared PS2c to determine the effects of a more strongly donating side chain. A single layer of this polymer had excessive conductivity to serve as an insulator between gate and semiconductor in OFETs. There was a marginal improvement when PS2c was spincoated over crosslinked PS1. However, with only 3% incorporation of the side chain, PS2c spincoated over crosslinked PS1 showed consistent, stable 20-V shifts in the direction of bias stress with V_{chg} = +100 V, consistent with PS2b when at the semiconductor interface but obtained with much lower active side chain concentration. This controllable chargeability with such a dilute side chain provides guidance and encouragement as we embark on studies of more electroactive polymers.

We synthesized crosslinked PS3, and characterized PS1, PS3; PS1-PS3 bilayers with either PS3 on top or PS3 on the bottom; and a control bilayer with PS1 in both positions. All bottom layers are crosslinked. Pentacene-polystyrene transistors were tested as-prepared, after charging, after operating, and then after intentionally discharging. PS3 shows both greater V_{th} shifts on charging either as a monolayer, or in either position of a bilayer, compared to the other three configurations with comparable total thicknesses. The single PS3 layer additionally shows greater stability against discharging. The PS3-pentacene interface provides a less negative initial V_{th} than the PS1-pentacene interface. Thus, this polymer has superior charge retention properties compared to PS1.

Surface-assembled chargeable dielectrics. We prepared a self-assembling polystyrene with a surface attaching group at one end and a chargeable group at the other, which would be located on average at a radius-of-gyration distance from the surface. The polymer was synthesized in three stages: design and preparation of a donor-functionalized initiator, atom transfer radical polymerization, and terminal group modification with a reactive silane.

Crosslinked PS polymer charging to modulate semiconducting polymer thermoelectrics. A static gate dielectric is a means of controlling the conductivity-Seebeck coefficient tradeoff in thermoelectric materials. The static gate changes doping level without changing the semiconductor polymer morphology. We developed a device structure that allows for charging the dielectric polystyrenes and addressing the semiconductors for conductance and Seebeck coefficient measurements. We employed the gold-gated OFET structure on glass substrates instread of Si to avoid interference in measurements from Si. We used crosslinked PS1 layers several times thicker than used for gate dielectrics and dried the films under vacuum at 60 °C. Poly(3-hexylthiophene) P3HT doped with tetrafluorotetracyanoquinodimethane (F4TCNQ), used as the thermoelectric polymer, was dropcast within an area bounded by Novec fluorinated polymer. A +100 V charging (lower electric field than similar OFET charging) caused conductivity increases by approximately a factor of 2; Seebeck coefficient decreases by ca. 20%. The simultaneous opposite changes in the two parameters are as expected from their mutual tradeoff. The directions of the changes indicate volume dielectric polarization, as observed in OFETs with PS2b in the middle of a trilayer dielectric.

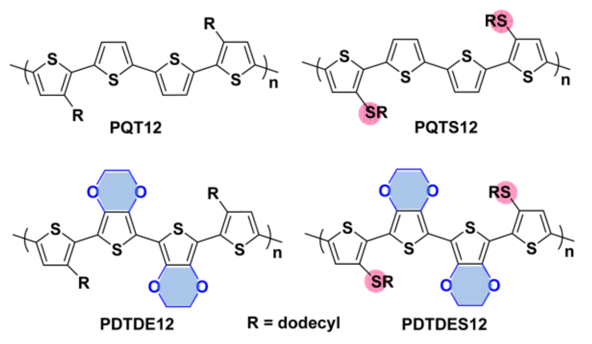

Figure 4. New EDOT and alkylthio copolymers.

Conjugated polymers for charge-tuned thermoelectrics. We studied higher-conductivity thermoelectrics on which higher power factors (Seebeck coefficient squared times conductivity) could be obtained from charge carrier densities optimized with static gates. We synthesized two new thiophene-ethylenedioxythiophene copolymers intending to combine the high dopability of PEDOT (the most widely used conducting polymer) with the hydrophobicity and ion density control of PQT12 (Figure 4), reaching conductivity of 100 S/cm doping with F4TCNQ. We also studied PQT12S and used $NOBF_4$ to dope it to a conductivity up to 350 S/cm, the highest nonionic polymer conductivity yet reported. UV-vis spectroscopy verified the doping-induced radical cation formation. Grazing incidence x-ray scattering (GIXRS) and field-effect transistor measurements showed a rarely observed increased ordering and hole mobility from the doped form of PQT12S. The mobility of doped PQTS12 ($0.045 \pm 0.2\times10^{-2}$ cm^2 V^{-1} s^{-1}) and doped PDTDE12 ($0.011 \pm 0.2\times10^{-2}$ cm^2 V^{-1} s^{-1}) is about five times higher than that of the corresponding pure polymer. If half of the repeat units of PQTS12 are assumed to be doped (molar ratio is 0.5) in the film of PQTS12/NOBF4 (the weight of the mixture is 1 g), the carrier concentration could reach 4.2×10^{20} cm^{-3}. The carrier concentration could reach 5.5×10^{20} cm^{-3} in the film of PDTDE12/F4TCNQ (molar ratio is 1:1) if all repeat units are assumed to be doped. Mobility is up to 5.2 cm^2 V^{-1} s^{-1} for doped PQTS12 and 1.6 cm^2 V^{-1} s^{-1} for doped PDTDE12, respectively. This further means that *the high conductivity of PQTS12/NOBF4 can be partly ascribed to an increase of the charge carrier mobility accompanying the doping.* The Seebeck coefficient (S) and power factor agreed with predictions of both the Chabinyc and Snyder models for high-performing, all-electronic thermoelectric polymers the high doped-form mobilities drive the materials into the preferred region of the S-σ plot. A related study of n-type polymers was completed and published.

Future Plans

Our plans for the third project year include the synthesis and characterization of the most electron donating but stable side chain copolymers (more donating than PS2c) for charge stabilization, stronger connection of thermoelectric and transistor behavior of the device architecture designed for the thermoelectric measurements, determination of the minimum T_g needed for stable charging and piezoelectric behavior in polystyrene electrets, and comparison of the semiconductor charge-controlling capabilities of spincoated and surface-attached polystyrenes adjacent to transistor and thermoelectric semiconductors.

Publications supported by this project, past two years

Note: all published work described above appears in the following publications:

Ireland, R.M.; Wu, L.; Salehi, M.; Oh, S.; Armitage, N.P.; Katz, H.E.
"Nonvolatile Solid-State Charged-Polymer Gating of Topological Insulators into the Topological Insulating Regime" Phys. Rev. Appl. 9, 044003 DOI:https://doi.org/10.1103/PhysRevApplied.9.04400 2018

Zheng, Y.; Shi, W.; Katz, H.E.; Taylor, A.D. "A Cytop insulating tunneling layer for efficient perovskite solar cells" Small Methods 1 1700244 DOI 10.1002/smtd.201700244 2017

Li, H.; DeCoster, M.E.; Ireland, R.M.; Song, J.; Hopkins, P.E.; Katz, H.E.
"Modification of the Poly(bisdodecylquaterthiophene) (PQT12) Structure for High and Predominantly Nonionic Conductivity with Matched Dopants" J. Am Chem. Soc.
DOI: 10.1021/jacs.7b05300 139 11149-11157 2017

Shi, W.; Zheng, Y.; Taylor, A.D.; Yu, J.; Katz, H.E.
"Increased mobility and on/off ratio in organic field-effect transistors using low-cost guanine-pentacene multilayers" Applied Physics Letters 111 043301 DOI: 10.1063/1.4995251 2017

Zhao, X.; Madan, D.; Cheng, Y.; Zhou, J.; Li, H.; Thon, S.M.; Bragg, A.E.; DeCoster, M.E.; Hopkins, P.E.; Katz, H.E. "High Conductivity and Electron Transfer Validation in an n-Type Fluoride Anion Doped Polymer for Thermoelectrics in Air" Adv. Mater. 29 https://doi.org/10.1002/adma.201606928 1606928 2017

Li, H.; Dailey, J.; Kale, T.; Besar, K; Koehler, K.; Katz, H.E.
"Sensitive and Selective NO_2 Sensing Based on Alkyl- and Alkylthio-thiophene Polymer Conductance and Conductance Ratio Changes from Differential Chemical Doping"
ACS Applied Materials and Interfaces, 9, 20501-20507 10.1021/acsami.7b02721 2017

Ireland, R.M.; Jones, T.; Li, H.; Jang, H.-J.; West. J.E.; Katz, H.E.
"Statically Charged Electret Polymers as Solid, Nonvolatile Gates Encapsulating and Tuning Polymer Thermoelectric Parameters" ACS Energy Letters 1 612-617
DOI: 10.1021/acsenergylett.6b00269 2016

Alley, O.J.; Plunkett, E.; Kale, T.S.; Guo, X.; McClintock, G.; Bhupathiraju, M.; Kirby, B.J.; Reich, D.H,; Katz, H.E. "Synthesis, Fabrication, and Heterostructure of Charged, Substituted Polystyrene Multilayer Dielectrics and Their Effects in Pentacene Transistors"
Macromolecules 10.1021/acs.macromol.6b00253 49, 3478-3489 2016

Zhang, Q.; Kale, T.; Plunkett, E.; Shi, W.; Kirby, B.J.; Reich, D.H.; Katz, H., Highly Contrasting Static Charging and Bias Stress Effects in Pentacene Transistors with Polystyrene Heterostructures Incorporating Oxidizable N,N'-bis(4-Methoxyphenyl)aniline Side Chains as Gate Dielectrics, under revision, 2018

Mesoscale Fragments of Crystalline Silicon by Chemical Synthesis

Rebekka S. Klausen, PI, Johns Hopkins University, Baltimore, MD 21218

Program Scope

Silicon is the dominant semiconductor for both electronics and solar cells, suggesting opportunities for molecular and polymeric silicon in optoelectronic device applications. Such materials could combine the practical advantages of organic electronics, including solution processing, with the performance of inorganic semiconductors. The aim of this program is to develop an innovative synthetic approach towards silicon architectures based on novel cyclic precursors inspired by fragments of the crystalline silicon lattice. The design and synthesis of chair-like cyclohexasilane monomers site-specifically labeled with functional groups for silane polymerization is described. Controlled polymerization and incorporation of organic and inorganic substituents is envisioned to control the properties of the polymer.

Recent Progress

This program focuses on the design and synthesis of novel cyclic precursors to complex, functional silicon-based polymers called poly(cyclosilane)s. Rational synthesis, the strategic choice of a sequence of chemical reactions that leads to a desired chemical target, is enormously powerful for the construction of complex chemical architectures. The application of rational synthesis to organic materials chemistry leads to the isolation of innovative and well-defined materials inaccessible by top-down methods. The smaller synthetic toolkit available to the silicon chemist limits the role of strategic synthesis in the design and preparation of silicon nanomaterials for optoelectronic and biomedical applications. Yet increased structural complexity in polysilanes has great potential to lead to novel properties.

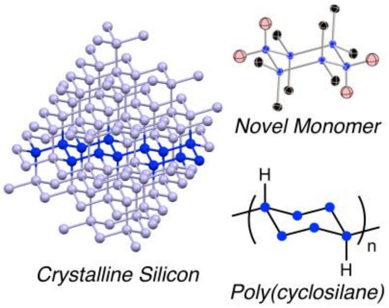

Figure 1. Poly(cyclosilane) and crystalline silicon.

We identified a synthetic approach to increasing the complexity of the silicon framework itself. Embedded within the crystalline silicon lattice is a chair cyclohexasilane.[1] Inspired by this structure, we target the synthesis of a class of polymers we have named poly(cyclosilane)s which contain repeating cyclosilane subunits (Figure 1). Our synthesis of novel monomer **1,4Si$_6$** proceeds via the salt metathesis reaction of dianion **1** and Cl(SiMe$_2$)$_2$Cl (Figure 2). Polymerization is initiated by a molecular zirconocene transition metal dehydrocoupling catalyst.

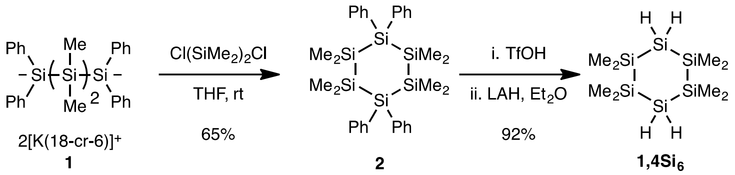

Figure 2. Synthesis of **1,4Si$_6$**.

Proof of linear structure is obtained from extensive ^{1}H and ^{29}Si NMR spectroscopy. A linear polymer is expected to have both secondary silane end groups as well as internal tertiary silanes (Figure 3). ^{29}Si {^{1}H} DEPT NMR spectroscopy reveals signals at chemical shifts consistent with different degrees of proton substitution. Further support for the spectroscopic assignments arises from considering the ^{1}H-^{29}Si coupling (not shown). The signals assigned to the end group appears as the expected triplet structure, while the internal silanes appear as a family of doublets. ^{1}H-^{29}Si HSQC NMR spectroscopy confirms correlation to SiH groups.

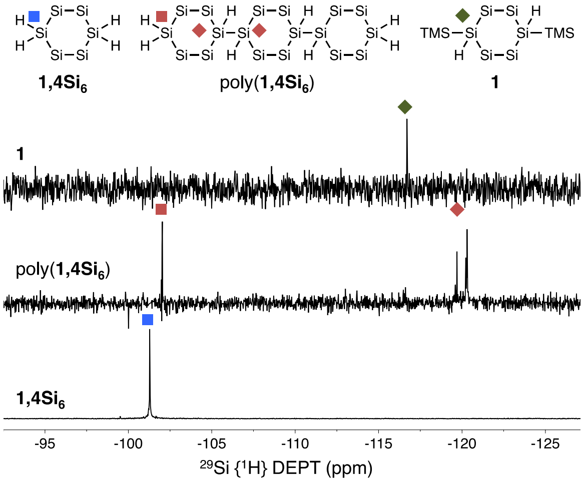

Figure 3. ^{29}Si DEPT NMR spectra showing linear poly(cyclosilane structure.

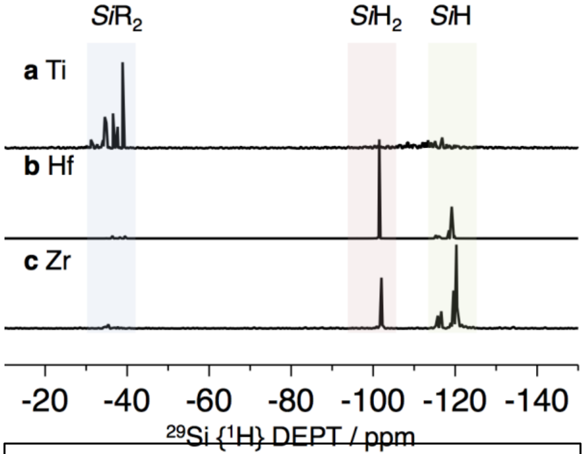

Figure 4. Variation in ^{29}Si NMR DEPT spectra with initiator.

A systematic investigation of the influence of the metallocene catalyst on poly(**1,4Si$_6$**) was carried out.[2] The Cp_2ZrCl_2/*n*-BuLi system provided the highest molecular weight polymer (M_n 2.67 kDa, Đ = 1.34) and all monomer is consumed within the 24-hour reaction period. Cp_2HfCl_2/*n*-BuLi is slower than Cp_2ZrCl_2/*n*-BuLi and somewhat lower poly(**1,4Si$_6$**) molecular weight is obtained (M_n = 2.15 kDa, Đ = 1.36). Cp_2TiCl_2/*n*-BuLi provides low molecular weigh material that is more disperse than both the Zr- and Hf-derived samples (M_n = 1.92 kDa, Đ = 1.85).

NMR spectroscopy reveals that significant structural rearrangement accounts for the lower molecular weights and high dispersities observed with Cp_2TiCl_2/*n*-BuLi. Figure 4 shows the ^{29}Si {^{1}H} DEPT NMR spectra of poly(**1,4Si$_6$)** prepared with different metallocene initiators. Both Zr and Hf provide polymers with the signature resonances of a linear poly(cyclosilane), including a δ −102 resonance assigned to the end groups (labeled SiH_2) and the δ −120 resonances assigned to internal silanes (SiH). Both polymer samples also feature δ −35 resonances assigned to backbone $SiMe_2$, which appear less intense than SiH resonances due to weaker two-bond ^{1}H-^{29}Si polarization transfer. Poly(**1,4Si$_6$**) arising from Ti-catalysis has a very different structure. A cluster of resonances between δ −35 and –45 are consistent with backbone $SiMe_2$ while the signature end group and backbone SiH_2 and SiH resonances diminish in intensity. We suggest that Ti-catalyzed alkyl scrambling in the **1,4Si$_6$** monomer introduces significant amounts of cyclosilanes that can act as chain capping agents or branching points. UV-vis spectroscopy supports the hypothesis that Ti-catalysis provides a unique poly(**1,4Si$_6$**) structure. All poly(**1,4Si6**) samples are red-shifted relative to monomer, which strongly absorbs ca. 210 nm ultraviolet light, however Ti-derived poly(**1,4Si$_6$**) has a broader and less well-defined absorption profile compared to Zr- and Hf-derived samples.

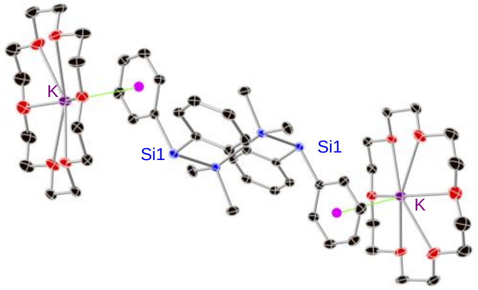

Figure 5. X-ray crystal structure of **1**.

In the course of our studies on the synthesis of cyclosilane building blocks, we identified dianion **1** as a versatile intermediate in the synthesis of novel cyclosilanes.[3] We obtained a crystal structure of **1** and were surprised to observe an unexpected interaction: instead of a Si-K bond (typically ~3.5 Å), the K^+ cation is engaged in a cation-pi interaction with an adjacent phenyl ring (Figure 5). The lack of contact ion-pairing is rationalized with hard-soft acid-base theory. Based on these insights, we optimized synthetic conditions to ensure the best match of hard and soft character between nucleophile and electrophile.

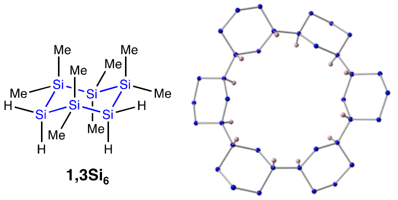

Figure 6. Design of **1,3Si$_6$**, a monomer for Si macrocycles.

1,3Si$_6$ is a new cyclosilane building block isomeric to **1,4Si$_6$** that templates an entirely different architecture.[4] Achieving a scalable, selective, and high-yielding synthesis of 1,3Si6 depended on the insights into disilanide nucleophilicity described above as only a magnesium countercation provided useful yields of the target structure.

Dehydrocoupling polymerization of **1,3Si$_6$** was initiated with Cp_2ZrCl_2/*n*-BuLi, which resulted in a highly soluble material (M_n = 3260 Da, $Đ$ = 1.47). Extensive spectroscopic characterization (IR and ^{1}H & ^{29}Si NMR spectroscopy) supports assignment to an ensemble of macrocycles with between 5-15 repeat units. Key evidence for a

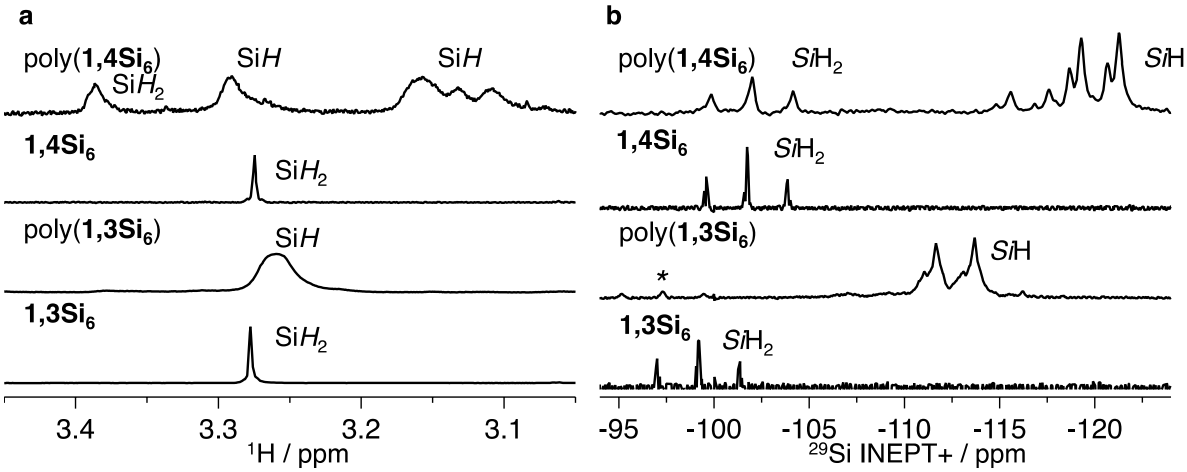

Figure 7. Structural characterization of poly(**1,3Si$_6$**) supporting a macrocyclic structure.

cyclic structure includes a ^{1}H NMR spectrum indicating high symmetry (Figure 7a), ^{29}Si NMR spectra showing a lack of end group resonances (Figure 7b), and excellent agreement between an experimentally determined IR spectrum and the calculated IR spectrum of a macrocylic hexamer (data not shown).

Macrocycles are excellent ionophores and quantum chemical calculations indicate that poly(**1,3Si₆**) can bind Li^+ via the hydridic SiH bonds. An electrostatic potential map of a cyclic hexamer indicates a porous structure lined with electron rich hydridic groups (Figure 8). Strong gas phase Li^+ binding is predicted (enthalpy of binding: −53.5 kcal mol^{-1}) between a simplified model compound and Li^+. We suggest these observations are relevant to understanding Li^+ binding in porous silicon materials that find wide application in lithium-ion batteries. We expect that these unique properties may result in poly(**1,3Si₆**) finding application as well-defined model system for understanding surface effects in silicon-based anodes through our ability to control structure via h ydrosilation.

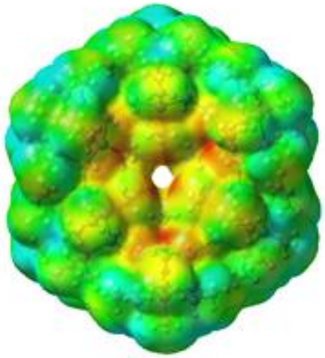

Figure 8. ESP map of a cyclic poly(cyclosilane).

Future Plans

Future work will continue to expand the scope of cyclosilane building blocks and novel silicon frameworks.

References

1 E. M. Press, E. A. Marro, S. K. Surampudi, M. A. Siegler, J. A. Tang and R. S. Klausen, *Angew. Chemie Int. Ed.*, 2017, **56**, 568–572.

2 J. Zhou, C. P. Folster, S. K. Surampudi, D. Jimenez, R. S. Klausen and A. E. Bragg, *Dalt. Trans.*, 2017, **46**, 8716–8726.

3 E. A. Marro, E. M. Press, T. K. Purkait, D. Jimenez, M. A. Siegler and R. S. Klausen, *Chem. - A Eur. J.*, 2017, **23**, 15633–15637.

4 E. A. Marro, E. M. Press, M. A. Siegler and R. S. Klausen, *J. Am. Chem. Soc.*, 2018, **140**, 5976–5986.

Publications

(1) Press, E. M.; Marro, E. A.; Surampudi, S. K.; Siegler, M. A.; Tang, J. A.; Klausen, R. S. Synthesis of a Fragment of Crystalline Silicon: Poly(Cyclosilane). *Angew. Chem. Int. Ed.* **2017**, *56*, (2), 568–572.

(2) Zhou, J.; Folster, C. P.; Surampudi, S. K.; Jimenez, D.; Klausen, R. S.; Bragg, A. E Asymmetric Charge Separation and Recombination in Symmetrically Functionalized sigma,pi-Hybrid Oligosilanes. *Dalt. Trans.* **2017**, *46*, 8716–8726.

(3) Marro, E. A.; Press, E. M.; Purkait, T. K.; Jimenez, D.; Siegler, M. A.; Klausen, R. S. Cooperative Noncovalent Interactions Induce Ion Pair Separation in Diphenylsilanides. *Chem. – Eur. J.* **2017**, *23* (62), 15633–15637.

(4) Folster, C. P.; Klausen, R. S. Metallocene Influence of Poly(Cyclosilane) Structure and Properties. *Polym. Chem.* **2018**, *9*, 1938–1941.

(5) Marro, E. A.; Press, E. M.; Siegler, M. A.; Klausen, R. S. Directional Building Blocks Determine Linear and Cyclic Silicon Architectures. *J. Am. Chem. Soc.* **2018**, *140* (8), 5976–5986.

Synthesis and Single Crystals of Refractory Oxides of Lanthanides and Thorium DE-SC0014271

Joseph W Kolis Department of Chemistry Clemson University

Program Scope

This project focuses on the use of high temperature hydrothermal fluids to induce chemical reactivity and crystal growth of otherwise intractable materials. In earlier work we developed technology that enables reaction conditions at 700˚C and 200MPa. We found that in the presence of suitable mineralizers we can solubilize many refractory materials to make new compounds and to grow large high quality single crystals. We can employ these conditions both as a synthetic route to do exploratory reaction chemistry, and also to grow single crystals of materials that were previously only accessible as powders. This second part is particularly significant as it can provide high quality single crystals of important systems that were only previously prepared as powders using high temperature ceramic methods or extremely high temperature melt techniques. These techniques inevitably lead to defects, disorder and/or lattice impurities. Thus the technology being developed in this project enables detailed single crystal studies using both x-ray and neutron diffraction, as well as other physical property measurements best performed on single crystals (i.e. oriented magnetic measurements, conductivity etc.)

This project focuses in particular on the oxides of the rare earth metals, especially the lanthanides and to a lesser extent the actinides. The lanthanide oxides are important for a wide variety of potential applications of interest to the DOE but at the same time are among the most refractory oxides known. Even the simplest binary oxides RE_2O_3 have not been prepared as high quality single crystals in the traditional literature. In our preliminary work we demonstrated that such rare earth sesquioxides could be solubilized and crystallized as high quality materials.[1] This enables and doping for potential high power laser applications as well as other physical property measurements. For this project our goal was to build on this progress to examine reactions of the rare earth oxides with other refractory oxides to gain access to important classes of compounds that have important potential applications but are not otherwise well understood. The focus is both on exploratory synthesis to make new phases and to also obtain detailed understanding of structures and properties.

The specific current focus of the program is on the reactions of rare earth oxides with refractory tetravalent oxides (Ge^{4+}, Sn^{4+}, Zr^{4+}, Hf^{4+}, Ce^{4+}, Th^{4+}, U^{4+} etc.). These all have undertake interesting chemistry with the lanthanides and the resultant products have many applications of interest to the DoE. The chemistry and structures of these materials are often not well understood however, because of the refractory nature of the oxides. This demands extremely high temperatures for classical ceramic preparation, leads to defects and site disorder, which in turn precludes the detailed understanding required for such complex studies. One goal of our program is to explore phase space for some exotic materials and make new materials. The second goal is to employ the hydrothermal method as a relatively low temperature route to single crystals that have minimal site disorder and low oxide defect density. This will hopefully provide much better structural data from single crystal x-ray diffraction as well as improved magnetic data from single crystal neutron diffraction.

Recent Progress

One class of rare earth metal oxides garnering considerable current attention is the pyrochlore cubic structure type $RE_2M_2O_7$.[2] The primary interest in these materials is their extremely complex magnetic behavior which is the result of their three-dimensional spin frustration, leading to formation of spin ices, spin liquids and perhaps even quantum materials such as quantum spin liquids (QSL). Such materials are tremendously exciting within the physics community because they would represent new forms of matter. Several rare earth stannates such as $Yb_2Sn_2O_7$ and $Dy_2Sn_2O_7$ display magnetic frustration and complex magnetic structures such as spin ice behavior at low temperature.[3] The corresponding $Yb_2Ge_2O_7$ is particularly interesting because it orders antiferromagnetically and may provide entrée to quantum spin liquids. [4,5]

Despite their interest, the pyrochlores are a classical example of materials with significant site disorder when prepared at using traditional high temperature methods. Furthermore there are fundamental stability issues also. For example previous attempts to access cubic $Yb_2Ge_2O_7$ using traditional high temperature synthetic approaches lead to a non-cubic phase, and extreme high-pressure methods were required to access the cubic pyrochlore of $Yb_2Ge_2O_7$.[6] We recently found that the hydrothermal approach could address all of these issues and we systematically grew single crystals of the entire series of lanthanide stannate cubic pyrochlores. We found that there was little if any site disorder and no oxide defects. The $Yb_2Sn_2O_7$ crystals are currently undergoing single crystal neutron diffraction measurements with our collaborator Professor Kate Ross at Colorado St. Most exciting is the fact we found that $Yb_2Ge_2O_7$ can be grown as high quality single crystals *in the cubic pyrochlore phase*. This is the subject of an ongoing magnetic and neutron diffraction investigations in collaboration with Professor Ross.

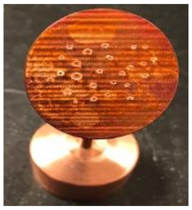

Figure 1. View of Yb2Ge2O7 single crystals mounted for single crystal

One interesting result from this work was the synthesis of high quality single crystals of $Ce_2Sn_2O_7$. These are prepared cleanly in hydrothermal fluids and show no site disorder or lattice defects in either the oxide or metal sites. It was postulated that they would display QSL behavior as well,[7] so initial measurements will be undertaken shortly. Other rare earth stannates such as $Pr_2Sn_2O_7$ have also been grown as large, site-ordered single crystals and are currently under investigation via neutron diffraction and low temperature magnetic measurements. We are also performing a systematic examination of the reaction chemistry of the lanthanide stannates and germanates, and find that the products are sensitive to reactions conditions, including stoichiometry and mineralizer. This leads to a wide range of interesting new materials. For example the reaction of GeO_2 with Tb_4O_7 led to the isolation of two new materials, $Tb^{(III)}_{13}(GeO_4)_6O_7(OH)$ and $K_2Tb^{(IV)}Ge_2O_7$. The latter compound contains a stable, well-characterized Tb^{4+} ion, examples of which are extremely rare. A range of new rare earth germanates and stannates will be discussed in this talk.

Figure 2 Single crystals of $Ce_2Sn_2O_7$

As an extension of this chemistry to more exotic building blocks we recently initiated examination of tetravalent building blocks containing open-shell electrons. These include Re^{4+}, Ru^{4+}, Mo^{4+} and W^{4+}. The focus is on the heavy d-block materials because they provide an interesting confluence of strong ligand field splitting as well as strong spin orbit splitting.[8] We have not yet isolated any cubic pyrochlores, but have isolated a wide range of exotic and interesting new compounds (see below). This chemistry obviously very different than that of the tetravalent building blocks with empty orbitals, and fuller investigation of the chemistry and physical properties of these novel materials is underway and will be discussed here.

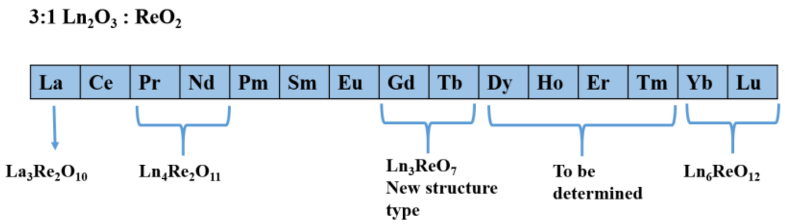

Figure 3a) Example of some reactions of rare earth rhenates.

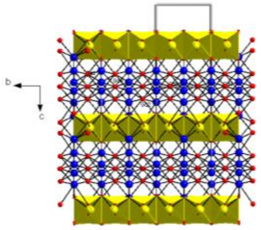

b) View of new phase of Gd_3ReO7

Future Plans

The pyrochlores remain a source of extremely fruitful collaborative investigation and we will continue to examine their chemistry and magnetism in detail. For example the Yb germanates display antiferromagnetic ordering at low temperatures while the stannates order ferromagnetically. As such it will be of interest to grow the $Yb_2Ge_{2-x}Sn_xO_7$ phase (x = ca. 0.10) to hopefully trap the quantum spin liquid phase as a single crystal. Also to obtain high quality magnetic and ESR date on the Yb system we will grow $Lu_2Ge_2O_7$ crystals doped with 0.5% Yb^{3+}. It will be of great interest to continue to examine the stannates since they are the only empty shell tetravalent ions that form cubic pyrochlore for all 14 lanthanides. Thus we can fully explore the effects of doping on the various sites to affect the magnetic behavior. For example we are unable to prepare germanate cubic pyrochlores of any rare earth larger than Yb^{3+} but we surmise the cubic stability field cannot be too far away for many. Thus we will examine the effects of doping on other Kramers doublet ions such as $Er_2Ge_{2-x}Sn_xO_7$ to see if small amounts of tin will stabilize the cubic structure and make that material available for neuron diffraction and magnetic measurements. Other tetravalent ions will be examined in the pyrochlore phase, particularly the larger ions such as Zr^{4+}, Hf^{4+} and Th^{4+}. The larger lanthanides display stability of the cubic phase along with promising magnetic behavior. Since these oxides are extraordinarily refractory, the access to site ordered defect free single crystals at a temperature as low as 700˚C provides an important pathway to new high quality materials.

The ability to cleanly prepare Ce^{3+} refractory oxides opens up an entirely new area of study. The Ce^{3+} ion is of interest since it is an f^1 ion with possible QSL behavior. Its investigation is badly neglected however, due to its tendency to oxidize to Ce^{4+} at the rigorous conditions normally employed by classical ceramic synthesis. Having demonstrated that we can grow a range of Ce^{3+} oxides straightforwardly, we will pursue systematic investigation of a range of the f^1 ions starting with cubic pyrochlores $Ce_2M_2O_7$, (M = Zr, Hf, Th). We already demonstrated that the titanates lead to a different phase with a new structure $Ce_2Ti_4O_{11}$ since the Ti^{4+} ion is too small to stabilize the cubic structure. Subsequent work will examine the synthesis of new perovskites phases with smaller trivalent ions such as $CeScO_3$, $CeInO_3$, $CeLuO_3$.

Having developed the chemistry necessary to gain access to these refractories, we are beginning to examine other phases of in this field of oxides including δ-$RE_4M_3O_{12}$ and the defect fluorite

$RE_2M_2O_{8-x}$ phases.[9] We recently did a careful structural study of large single crystals of the δ-$Sc_4Zr_3O_{12}$ trigonal phase. We analyzed the disordering on the metal sites, and also found the oxide defect sites to be fully ordered. This category of oxides is of great interest to the DoE for its radiation stability. Since it is postulated that the radiation stability of the oxides is a function of disorder of the metal ions and oxide defects, it is critical to understand the initial structure of the parent compounds.[10] In many cases however, even the most basic structural details are not understood well. We will examine the synthesis and single crystal structures of many of these phases with particular emphasis on those that are postulated to be radiation stable, such as the $Dy_2Zr_2O_{8-x}$ disordered fluorite phase. We anticipate some well ordered initial structures from the single crystals as well as several new phases. This will lead to a fuller understanding of these compounds, and assist in the design of new radiation stable materials.

References

(1) McMillen, C.; Thompson, D.; Tritt, T.; Kolis, J. Hydrothermal Single-Crystal Growth of Lu_2O_3 and Lanthanide-Doped Lu_2O_3. *Cryst. Growth Des.* **2011**, *11* (10), 4386–4391.

(2) Gardner, J. S.; Gingras, M. J. P.; Greedan, J. E. Magnetic Pyrochlore Oxides. *Rev. Mod. Phys.* **2010**, *82* (1), 53–107.

(3) Bramwell, S. T. Spin Ice State in Frustrated Magnetic Pyrochlore Materials. *Science* **2001**, *294* (5546), 1495–1501.

(4) Dun, Z. L.; Li, X.; Freitas, R. S.; Arrighi, E.; Dela Cruz, C. R.; Lee, M.; Choi, E. S.; Cao, H. B.; Silverstein, H. J.; Wiebe, C. R. Antiferromagnetic Order in the Pyrochlores $R_2Ge_2O_7$ (R = Er , Yb). *Phys. Rev. B* **2015**, *92* (14), 140407.

(5) Ross, K. A.; Savary, L.; Gaulin, B. D.; Balents, L. Quantum Excitations in Quantum Spin Ice. *Phys. Rev. X* **2011**, *1* (2). 021002

(6) Wiebe, C. R.; Hallas, A. M. Frustration under Pressure: Exotic Magnetism in New Pyrochlore Oxides. *APL Mater.* **2015**, *3* (4) 041519.

(7) Sibille, R.; Lhotel, E.; Pomjakushin, V.; Baines, C.; Fennell, T.; Kenzelmann, M. Candidate Quantum Spin Liquid in the Ce^{3+} Pyrochlore Stannate $Ce_2Sn_2O_7$. *Phys. Rev. Lett.* **2015**, *115* (9).

(8) Cava, R. J. Schizophrenic Electrons in Ruthenium-Based Oxides. *Dalton Trans.* **2004**, 19, 2979.

(9) Stanek, C. R.; Jiang, C.; Uberuaga, B. P.; Sickafus, K. E.; Cleave, A. R.; Grimes, R. W. Predicted Structure and Stability of $A_4B_3O_{12}$ δ-Phase Compositions. *Phys. Rev. B* **2009**, *80* (17), 174101.

(10) Sickafus, K. E.; Grimes, R. W.; Valdez, J. A.; Cleave, A.; Tang, M.; Ishimaru, M.; Corish, S. M.; Stanek, C. R.; Uberuaga, B. P. Radiation-Induced Amorphization Resistance and Radiation Tolerance in Structurally Related Oxides. *Nat. Mater.* **2007**, *6* (3), 217–223.

Publications

L. D. Sanjeewa, K. A. Ross, C. L. Sarkis, H. S. Nair, C. D. McMillen, J. W. Kolis "Single Crystals of Cubic Rare Earth Pyrochlore Germanates: $RE_2Ge_2O_7$ (*RE* = Yb and Lu) Grown by a High Temperature Hydrothermal Technique" Inorg Chem. 2018 submitted.

Fulle, K.; Sanjeewa, L.D.; McMillen, C.D.; Kolis, J.W. Hydrothermal Crystal Growth of 2-D and 3-D Barium Rare Earth Germanates: $BaREGeO_4(OH)$ and $BaRE_{10}(GeO_4)_4O_8$ (RE=Ho,Er)" *J Alloys Compd.* 2018 in press.

K.F. Fulle, L.D. Sanjeewa, C.D. McMillen, J.W. Kolis "High Temperature Hydrothermal Synthesis of Rare-Earth Titanates: Synthesis and Structure of $RE_5Ti_4O_{15}(OH)$ (RE = La, Er), $Sm_3TiO_5(OH)_3$, $RE_5Ti_2O_{11}(OH)$ (RE = Tm-Lu) and $Ce_2Ti_4O_{11}$" J. Chem. Soc. Dalton Transactions 2018, 47, 6754-6762. 10.1039/C7DT04810F

K.F. Fulle, L.D. Sanjeewa, C.D. McMillen, Y. Wen, G. Chumanov, J.W. Kolis "One Pot Hydrothermal Synthesis of $Tb^{(III)}_{13}(GeO_4)_6O_7(OH)$ and $K_2Tb^{(IV)}Ge_2O_7$: Preparation of a Stable Tb^{4+} Complex" Inorg. Chem 2017 56, 6044-6047. 10.1021/acs.inorgchem.7b00821

K. Fulle, L.D. Sanjeewa, C.D. McMillen, J.W Kolis "Crystal Chemistry of the Discrete Tetrasilicate Units with Rare Earth Dimers: $Ba_2RE_2Si_4O_{12}F_2$ (RE = Er-Lu) and $Ba_2Re_2SiO_{13}$ (RE = Pr-Sm) Acta Crystallographica B 2017 B73, 907-91510.1107/S2052520617009544

Structure-properties relationship in transition metal-phosphorus clathrate thermoelectrics

Kirill Kovnir

Iowa State University, Ames, Iowa 50011

Program Scope

Thermoelectrics (TEs) convert heat into electrical energy and vice versa. The development of novel materials where charge and heat transport are partially de-coupled is a key factor for the next generation of TEs. This project seeks to develop a new class of bulk TE materials based on transition metal-phosphorus clathrates with a three-dimensional framework containing oversized cages that encapsulate guest cations. The rattling of guest cations provides an effective scattering of heat carrying phonons while the host framework is responsible for transporting charge carriers. The tunability of the chemical bonding in the metal-phosphorus framework was used as a tool to significantly enhance the thermoelectric performance of the clathrates materials.

Recent Progress

$Ba_8Cu_{14}Ge_6P_{26}$: Bridging the gap between tetrel-based and tetrel-free clathrates

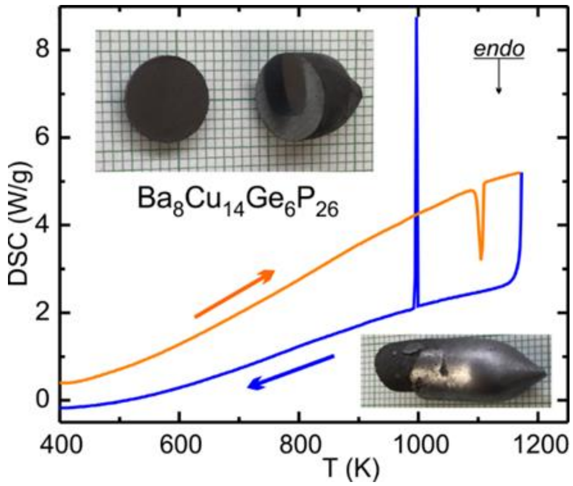

Figure 1. DSC results for $Ba_8Cu_{14}Ge_6P_{26}$. The insets are photographs of Bridgman growth crystal and slices of such crystals with mirror-like surfaces.

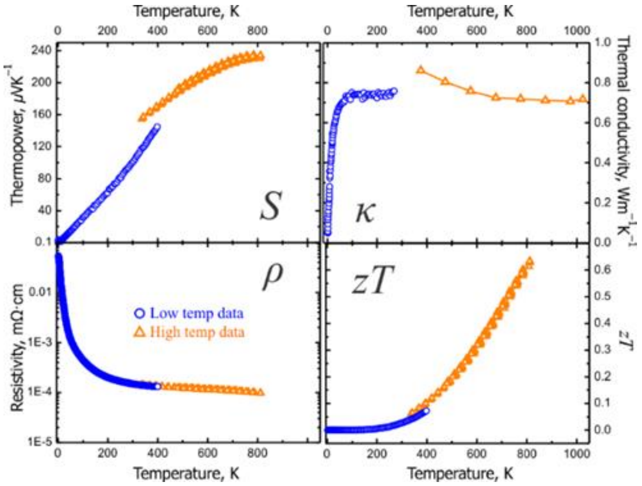

Figure 2. Low- (blue) and high-temperature (orange) transport properties on a slice of the Bridgman growth crystal of $Ba_8Cu_{14}Ge_6P_{26}$.

A new type-I clathrate, $Ba_8Cu_{14}Ge_6P_{26}$, was synthesized by solid-state methods as polycrystalline powder and grown as a cm-sized single crystal via vertical Bridgman method. Single-crystal and powder X-ray diffraction show that $Ba_8Cu_{14}Ge_6P_{26}$ crystallizes in the cubic space group $Pm\bar{3}n$ (No. 223). $Ba_8Cu_{14}Ge_6P_{26}$ is the first representative of anionic clathrates whose framework is composed of three atom types of very different chemical natures: a transition metal, tetrel element, and pnicogen. Uniform distribution of the Cu, Ge, and P atoms over framework sites and the absence of any superstructural or local ordering in $Ba_8Cu_{14}Ge_6P_{26}$ were confirmed by synchrotron X-ray diffraction, electron diffraction and high angle annular dark field scanning-transmission electron microscopy, and neutron and X-ray pair distribution function analyses. Characterizations of the transport properties demonstrate that $Ba_8Cu_{14}Ge_6P_{26}$ is a *p*-type semiconductor with an intrinsically low thermal conductivity of 0.72 $Wm^{-1}K^{-1}$ at 812 K. The thermoelectric figure of merit, *ZT*, for a slice of the Bridgman-grown crystal of $Ba_8Cu_{14}Ge_6P_{26}$ approaches 0.63 at 812 K due to high power factor of 5.62 $\mu Wcm^{-1}K^{-2}$. The thermoelectric efficiency of $Ba_8Cu_{14}Ge_6P_{26}$ is on par with the best optimized *p*-type Ge-based clathrates and it outperforms the majority of clathrates in the 700-850 K temperature region. $Ba_8Cu_{14}Ge_6P_{26}$ expands clathrate chemistry by bridging conventional tetrel-based and tetrel-free clathrates. Advanced transport properties, in combination with earth-abundant framework elements and congruent melting make $Ba_8Cu_{14}Ge_6P_{26}$ a strong candidate as a novel and efficient thermoelectric material.

Controlling Superstructural Ordering in the Clathrate-I $Ba_8M_{16}P_{30}$ (M= Cu, Zn)

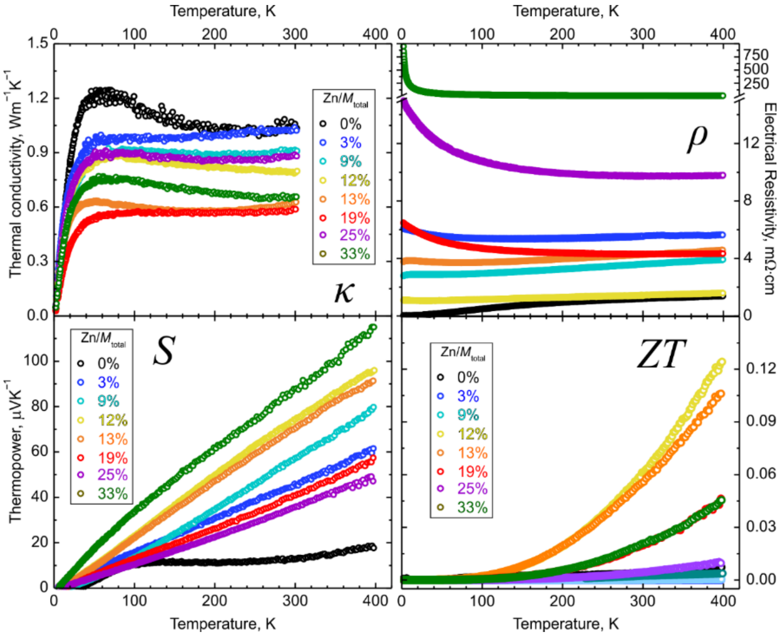

Figure 3. Low-temperature thermoelectric properties for selected samples of $Ba_8M_{16+y}P_{30-y}$, *M* = Cu, Zn.

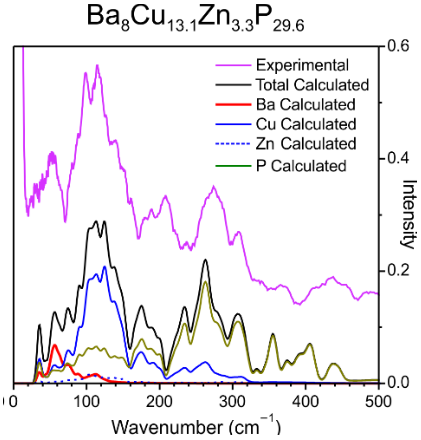

Figure 4. Experimental (T = 5 K) and calculated inelastic neutron scattering (INS) spectra for $Ba_8Cu_{13}Zn_3P_{30}$.

Order-disorder-order phase transitions in the clathrate-I $Ba_8Cu_{16}P_{30}$ were induced and controlled by aliovalent substitutions of Zn into the framework. Unaltered $Ba_8Cu_{16}P_{30}$ crystallizes in an ordered orthorhombic (*Pbcn*) clathrate-I superstructure that maintains complete segregation of metal and phosphorus atoms over 23 different crystallographic positions in the clathrate framework. The driving force for the formation of this *Pbcn* superstructure is the avoidance of Cu-Cu bonds. This superstructure is preserved upon aliovalent substitution of Zn for Cu in $Ba_8Cu_{16-x}Zn_xP_{30}$ with $0 < x < 1.6$ but vanishes at greater substitution concentrations. Higher Zn concentrations resulted in the additional substitution of Zn for P in $Ba_8M_{16+y}P_{30-y}$ (M = Cu,Zn) with $0 \leq y \leq 1$. This causes the formation of Cu-Zn bonds in the framework, leading to a collapse of the orthorhombic superstructure into cubic subcell of clathrate-I (*Pm*-3*n*). Detailed structural characterizations of the Ba-Cu-Zn-P clathrates-I via single crystal X-ray diffraction, joint synchrotron X-ray and neutron powder diffractions and PDF STEM, and NMR indicate that local ordering is present in the cubic clathrate framework, suggesting the evolution of Cu-Zn bonds. The overall thermoelectric figure-of-merit, *ZT*, of $Ba_8Cu_{14}Zn_2P_{30}$ is 0.62 at 800 K which is 9 times higher than the thermoelectric performance of the ternary parent phase $Ba_8Cu_{16}P_{30}$. A combination of inelastic neutron scattering and single crystal X-ray diffraction experiments at 10 K revealed low-energy rattling of the Ba guest atoms located inside the large tetrakaidecahedral cages to be responsible for the observed low thermal conductivities of the studied clathrates.

Breaking the Tetra-Coordinated Framework Rule: New Clathrate $Ba_8Cu_{13}Zn_{11}P_{30}$

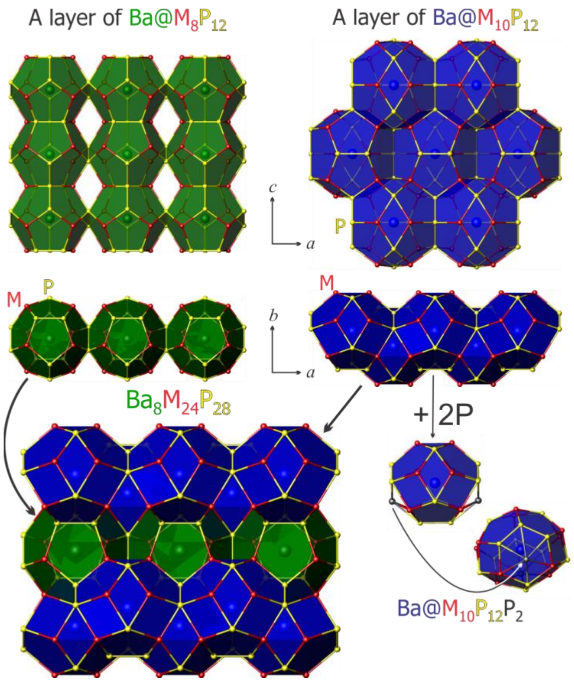

Figure 5. Polyhedral representation of the crystal structure of $Ba_8M_{24}P_{28+\delta}$.

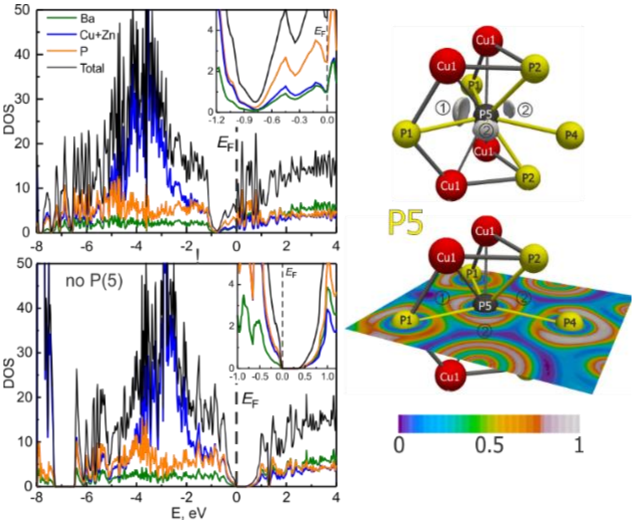

Figure 6. Left: DOS for (top) $Ba_8Cu_{12}Zn_{12}P_{32}$ and (bottom) $Ba_8Cu_{12}Zn_{12}P_{28}$. Right: 3D isosurfaces (η = 0.77) and slice of ELF for the P(5) local coordination.

A new clathrate type has been discovered in the Ba-Cu-Zn-P system. The crystal structure of the $Ba_8Cu_{13}Zn_{11}P_{30}$ clathrate is composed of the pentagonal dodecahedra common to clathrates along with a unique 22-vertex polyhedron with two hexagonal faces capped by additional partially-occupied phosphorus sites. This is the first example of a clathrate compound where the framework atoms are not in tetrahedral or trigonal-pyramidal coordination. In $Ba_8M_{24}P_{28+\delta}$ a majority of the framework atoms are 5- and 6-coordinated, a feature more common to electron-rich intermetallics. The crystal structure of this new clathrate was determined by a combination of X-ray and neutron diffraction and was confirmed with solid state ^{31}P NMR spectroscopy. Based on chemical bonding analysis, the driving force for the formation of this new clathrate is the excess of electrons generated by a high concentration of Zn atoms in the framework.

Hosting trivalent rare-earth guests in Cu-P clathrate cages

The most striking difference between the trivalent rare-earth cations and their alkali and alkaline-earth peers is the presence of localized 4*f*-electrons. A long sought-after yet undiscovered material is a semiconducting compound where rare-earth cations are situated inside the oversized polyhedral cages of a three-dimensional framework. In this work we present a synthesis of unconventional clathrates, $Ba_{8-x}R_xCu_{16}P_{30}$, with the smallest pentagonal dodecahedral cages encapsulating La^{3+} and Ce^{3+}. Their composition and crystal structure were unambiguously determined by a combination of synchrotron and neutron powder diffraction, STEM and EELS. Our calculations and experimental characterizations show that the incorporation of the rare-earth cations significantly enhances the hole mobility and reduces the hole concentration, resulting in a drastic (700%) increase in the thermoelectric performance.

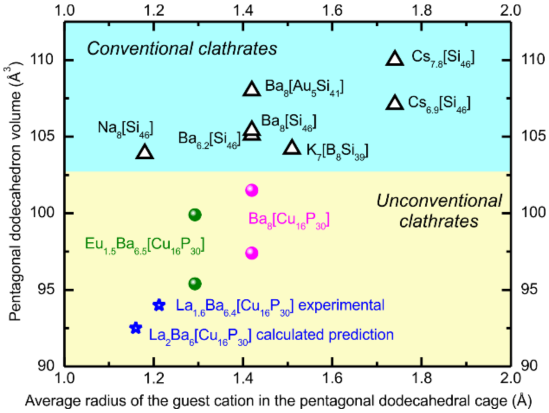

Figure 7. Volumes of the pentagonal dodecahedron cages for tetrel-based and transition metal-pnicogen-based clathrates-I.

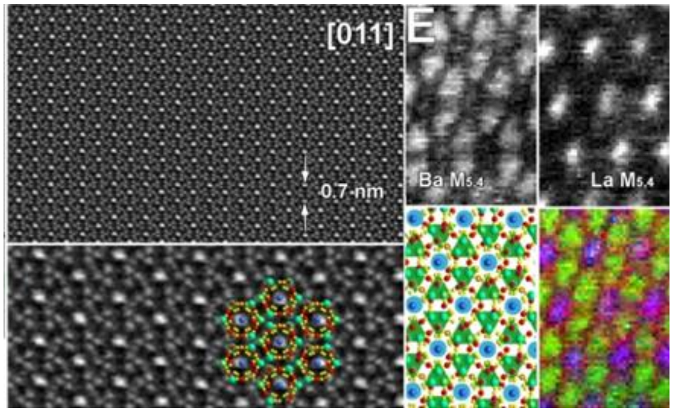

Figure 8. STEM high resolution HAADF images for the [011] zone of $Ba_{6.4}La_{1.6}Cu_{16}P_{30}$ together with (E) atomic resolution EELS elemental mapping.

Future Plans

Over the previous years of this project we have shown that transition metal-phosphorus clathrates can be tuned by aliovalent substitution in both the transition metal sites in framework and guest cation sites. On the model system, the clathrate $Ba_8Cu_{16}P_{30}$, we have shown that framework or guest sublattice substitutions guided by Zintl electron count and band structure calculations strongly affect the transport properties of clathrate materials resulting in an order of the magnitude enhancement of the thermoelectric performance. Our next goal is to expand the clathrate chemistry to heavier than phosphorus pnicogen, arsenic. We hypothesized that the presence of 4s and 4p orbitals will improve the framework orbital overlap resulting in the enhancement of the mobility while the overall increase of the volume of clathrate polyhedral cages will provide more space for the guest cations rattling. This will lead to the further enhancement of the thermoelectric efficiency.

Publications

1. Wang, J.; He, Y.; Mordvinova, N. E.; Lebedev, O. I.; Kovnir, K.
The smaller the better: hosting trivalent rare-earth guests in Cu-P clathrate cages.
Chem, **2018,** *DOI: https://doi.org/10.1016/j.chempr.2018.04.001*.

2. Dolyniuk, J.; Wang. J.; Marple, M.; Sen, S.; Cheng, Y.; Ramirez-Cuesta, A. J.; Kovnir, K. Chemical bonding and transport properties in clathrates-I with Cu-Zn-P frameworks.
Chem. Mater. **2018,** *DOI: 10.1021/acs.chemmater.8b00966*.

3. Zevalkink, A.; Smiadak, D.; Martin, D.; Chabinyc, M.; Delaire, O.; Blackburn, J.; Ferguson, A.; Wang, J.; Kovnir, K.; Schelhas, L.; Kang, S. D.; Dylla, M. T.; Snyder, G. J.; Ortiz, B.; Toberer, E. A practical field guide to thermoelectrics: fundamentals, synthesis, and characterization.
Appl. Phys. Rev. **2018,** *accepted*.

4. Dolyniuk, J.; Lee, S.; Tran, N.; Wang. J.; Kovnir, K. Eu_2P_7X and Ba_2As_7X (X = Br, I): Chiral Double-Zintl Salts Containing Heptapnictortricyclane Clusters.
J. Solid State Chem. **2018,** *doi.org/10.1016/j.jssc.2018.04.026*.

5. Wang, J.; Wang, L.-L.; Kovnir, K. Phonon Glass Behavior Beyond Traditional Cage Structures: Synthesis, Crystal and Electronic Structure, and Properties of KMg_4Sb_3.
J. Mater. Chem. A **2018,** *6,* 4759-4767.

6. Wang, J.; Dolyniuk, J.; Kovnir, K.
Unconventional Clathrates with Transition Metal-Phosphorus Frameworks.
Acc. Chem. Res. **2018,** *51,* 31-39.

7. Wang, J.; Lebedev, O.I.; Lee, K.; Dolyniuk, J.; Klavins, P.; Bux, S.; Kovnir, K.
A high-efficiency thermoelectric $Ba_8Cu_{14}Ge_6P_{26}$: Bridging the gap between tetrel-based and tetrel-free clathrates.
Chem. Sci. **2017,** *8,* 8030-8038.

8. Owens-Baird, B.; Lee, S.; Kovnir, K. Two-Dimensional Metal $NaCu_{6.3}Sb_3$ and Solid-State Transformations of Sodium Copper Antimonides.
Dalton Trans. **2017,** *46,* 12438-12445. **Inside Cover Figure.**

9. Wang, J.; Greenfield, J.; Kovnir, K. Synthesis, Crystal Structure, and Magnetic Properties of $R_2Mg_3SiPn_6$ (R = La, Ce; Pn = P, As).
Inorg. Chem. **2017,** *56,* 8348-8354.

10. Dolyniuk, J.; Whitfield, P.S.; Lee, K.; Lebedev, O.I.; Kovnir, K.
Controlling Superstructural Ordering in the Clathrate-I $Ba_8Cu_{16}P_{30}$ (M= Cu, Zn) through the Formation of Metal-Metal Bonds.
Chem. Sci. **2017,** *8,* 3650-3659.

11. Wang, J.; Mazzetti, J.; Kovnir, K. Synthesis, crystal and electronic structure, and physical properties of a new quaternary phosphide $Ba_4Mg_{2+\delta}Cu_{12-\delta}P_{10}$ ($0 < \delta < 2$).
    Inorg. Chem. Front. **2017,** *4,* 801-808.

12. Owens-Baird, B.; Heinrich, S.; Kovnir, K. Thermoelectric Materials.
    Encyclop. Inorg. Bioinorg. Chem. **2017**, 1-35.

13. Dolyniuk, J.; Zaikina, J.V.; Kaseman, D.C.; Sen, S.; Kovnir, K. Breaking the Tetra-Coordinated Framework Rule: New Clathrate $Ba_8M_{24}P_{28+\delta}$ (M = Cu/Zn).
    Angew. Chem. Int. Ed. **2017,** *56,* 2418-2422. **Cover Figure; Very Important Paper.**

14. Wang, J.; Lee, K.; Kovnir, K.
    Synthesis, Crystal Structure, and Properties of $La_4Zn_7P_{10}$ and $La_4Mg_{1.5}Zn_{8.5}P_{12}$.
    Inorg. Chem. **2017,** *56,* 783-790.

15. Dolyniuk, J.; Owens-Baird, B.; Wang, J.; Zaikina, J.V.; Kovnir, K.
    Clathrate Thermoelectrics.
    Mater. Sci. Engin. R. **2016,** *108,* 1-46.

16. Dolyniuk, J.; Kovnir, K. High Pressure Properties of a Ba-Cu-Zn-P Clathrate-I.
    Materials. **2016,** *9,* 692.

17. Wang, J.; Marple, M.; Lee, K.; Sen, S.; Kovnir, K. Synthesis, crystal structure, and advanced NMR characterization of a low temperature polymorph of $SiSe_2$.
    J. Mater. Chem. A **2016,** *4,* 11276-11283. **HOT Paper.**

Anionic porous organic frameworks as advanced functional adsorbents for CO_2 and organic micropollutants in water

Kai Landskron, Department of Chemistry, Lehigh University, 6 East Packer Ave, Bethlehem, PA 18015

Program Scope

The objective of the work is to produce nanoporous, weakly coordinating, anionic frameworks (P-WCAs), and determine their structures, and properties. Similarly to the molecular WCAs, there are no strong coordination sites for the cations, but with the difference that the cations are located inside of nanopores. To produce the materials logical and feasible synthetic strategies are developed. They identify reactions that will interconnect tetrahedral boron(III) as well as octahedral phosphorus(V) by organic bridging ligands to form porous structures. A range of interesting, energy-relevant properties for P-WCAs is expected from this new structural feature. The weak coordination of metal ions in the nanopores suggests that the ions can be exchanged. The facile exchange is expected to coincide with high ion mobility and high ion conductivity suggesting potential utility of P-WCAs as solid state electrolytes. The weakly coordinated metal cations in the nanopores of P-WCAs are expected to be highly electrophilic adsorption sites for gas molecules that enter the nanopores, which is relevant for gas separation and storage. In addition, the cation exchange properties and the organic pore walls suggest that the materials will be able to remove both toxic heavy metal ions as well as organic micropollutants from water. These energy-relevant properties are broadly investigated within the project period.

Recent Progress

New anionic porous organic frameworks with phosphate groups are synthesized through Yamamoto coupling reactions. These materials have excellent adsorption properties towards CO_2 compared to other porous organic frameworks. In addition, the materials have high adsorption capacity and exceptional adsorption kinetics towards bisphenol A (BPA) in water, a wide-spread organic pollutant and a known endocrine disruptor (Fig. 1). The maximum adsorption capacity of BPA at equilibrium is found to be as high as 3366 mg g^{-1} according to the Langmuir adsorption model, which is more than 10 times greater than those of peer materials. The polymer also rapidly removes various other organic micropollutants with more than 90% removal efficiencies. In addition, the PA-POF material can be regenerated at least five times by mild washing using methanol without significant loss in removal efficiency.

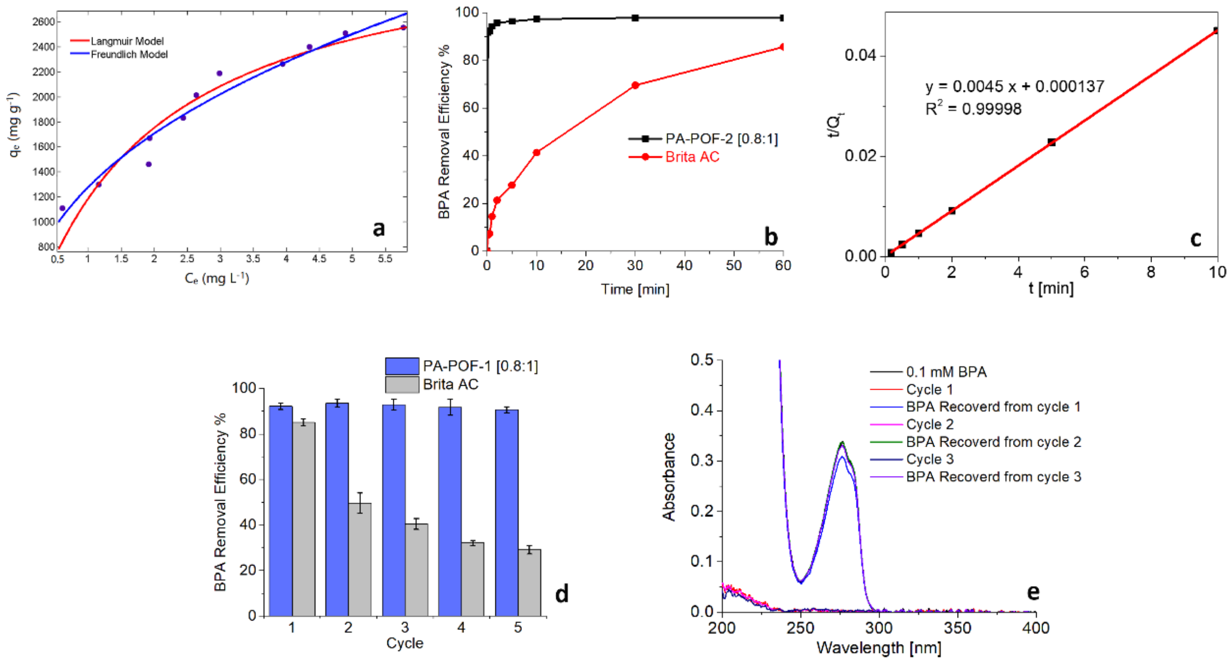

a) Langmuir (red) and Freundlich (blue) adsorption isotherms of BPA by PA-POF-2 [0.8 : 1]. (b) Effect of contact time on the adsorption of 10 mL mg_1 BPA by PA-POF-2 [0.8 : 1] and Brita AC. (c) Pseudo-second-order plot of the PA-POF-2 [0.8 : 1] kinetic study (q_e = 222 mg g^{-1}, k_{obs} = 0.15 g mg^{-1} min^{-1}). (d) The average percentage BPA removal efficiency by PA-POF-2 [0.8 : 1] and Brita AC after regeneration cycles. (e) The UV-vis spectra of the filtrate after adsorption and the redissolved BPA solution recovered by extraction with MeOH. UV-vis absorbance of BPA recovered from MeOH in each cycle equals the absorbance of the stock BPA solution which proves that all the BPA adsorbed by adsorbents can be extracted with MeOH.

Future Plans

The future emphasis is on the synthesis of crystalline, weakly coordinating porous organic frameworks via kinetically reversible reactions. Our current focus is on condensation reactions between aromatic alcohols and P(V) sources. Another research focus will be on the incorporation of perfluorinated organic bridging groups into the frameworks. Due to the electron-withdrawing character of the fluorine atoms these groups should lead to extremely weakly coordinating anionic, porous organic frameworks.

Publications

Liu, Y.; Landskron, K. Anionic porous organic frameworks as advanced functional adsorbents for CO_2 and organic micropollutants in water. *Journal of Materials Chemistry a* **2017,** *5*, 23523.

Directed Synthesis of New Actinide Containing Oxides, Fluorides and Chalcogenides

Hans-Conrad zur Loye
Department of Chemistry and Biochemistry
University of South Carolina

Program Scope

Our research continues to focus on advancing the crystal chemistry of complex actinide (uranium and thorium) containing solid state materials by exploring three classes of materials: oxides (including phosphates, silicates and borates), fluorides, and chalcogenides, and to investigate the magnetic properties of the new structures and compositions we expect to synthesize. Our program is based on the concept of materials discovery via crystal growth where we propose to apply two complementary crystal growth routes 1) mild hydrothermal and 2) high temperature solutions, to create new Th(IV), U(IV), U(V), and U(VI) containing materials in order to study their physical properties. A continuing long-term endeavor is to advance our understanding of uranium and thorium crystal chemistry to allow us to progress beyond “serendipitous materials discovery” and achieve the “directed synthesis” of new uranium and thorium containing materials.

Recent Progress

We have concentrated on expanding the crystal chemistry of uranium and thorium containing solid-state materials, focusing primarily on oxides and fluorides where we investigated several material classes including porous U(VI) containing salt inclusion phase silicates, non-porous U(IV) and U(VI) containing silicates, non-uranium silicates, uranium fluorides, thorium fluorides, non-uranium fluorides, U(IV) and U(VI) containing phosphates, U(V) containing borates and complex uranium oxides. In addition, we started successfully to apply our flux synthesis approach to the crystal growth of uranium containing phosphates and chalcogenides. The latter is tightly coupled to our working hypothesis that the development and application of new synthetic approaches and the use of existing synthetic approaches to new systems is most likely to result in the discovery of new actinide containing compositions exhibiting complex structures and, potentially, new or enhanced properties. Moreover, the ability to prepare these new materials as high quality single crystals is extremely desirable for crystal and magnetic structure determinations.

Synthetic Strategies for the Synthesis of Ternary Uranium(IV) and Thorium(IV) Fluorides

A series of new U(IV) and Th(IV) fluorides, $Na_7U_6F_{31}$ (**1**) (Figure 1), $NaUF_5$ (**2**), NaU_2F_9 (**3**) (Figure 2), KTh_2F_9 (**4**), $NaTh_2F_9$ (**5**) (Figure 3), $(H_3O)Th_3F_{13}$ (**6**), and $(H_3O)U_3F_{13}$ (**7**), was obtained using hydrothermal and low temperature flux methods. Mild hydrothermal reactions with uranyl acetate as a precursor yielded **1**, **7**, and the monoclinic polymorph of NaU_2F_9, whereas direct reactions between UF_4 and NaF led to the formation of **2**, and orthorhombic NaU_2F_9 (**3**). This highlights an unexpected difference in reaction products when different starting uranium sources are used. All seven compounds were characterized by single crystal X-ray diffraction and their structures are compared on the basis of cation topology, revealing a close topological resemblance between fluorides based on the layers observed in $NaUF_5(H_2O)$. Phase pure samples of **1**, **2**, and both polymorphs of NaU_2F_9 were obtained, and their spectroscopic and magnetic properties were measured. The UV-vis data is dominated by the presence of U^{4+} cations and agree well with its electronic transitions. Effective magnetic moments of the studied compounds were found to range from 3.08–3.59 μ_B.

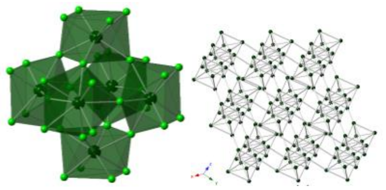

Figure 1. An octahedral cluster in $Na_7U_6F_{31}$ (**1**) (left); the arrangement of the octahedral clusters (right)

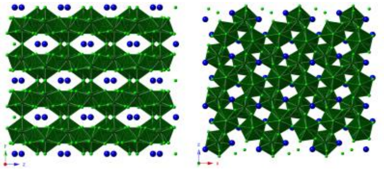

Figure 2. Structure of orthorhombic NaU_2F_9 (**3**) along the *a* and *b* axes. The uranium, fluorine, and sodium atoms are shown in dark green, light green, and blue, respectively.

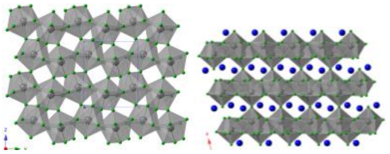

Figure 3. A view of a pseudo-layer (left) and the connectivity between the layers in the structure of $NaTh_2F_9$ (**5**) (right).

We have shown previously that utilizing uranyl acetate $UO_2(CH_3CO_2)\cdot 2H_2O$ as a precursor serves as a convenient way of obtaining new uranium(IV) fluorides, since both the uranium and the reducing agent are simultaneously present in a single precursor.[1] This technique employs an *in situ* reduction step and often produces phase pure samples in excellent yields; however, it often requires the use of a copper salt that acts as a catalyst for the formation of complex fluorides, which severely hinders the synthesis of new complex fluoride phases containing sodium due to the preferential formation of the $Na_4CuU_6F_{30}$ phase.[2]

Similar synthetic considerations can be applied to thorium(IV) fluorides, which have been more intensively investigated than their U(VI) counterparts. To date, there are >80 ternary and 9 quaternary thorium fluoride crystal structures deposited in the ICSD, although many of them are structure redeterminations, or a series of structure determinations under high pressure. The primary difference between thorium and uranium is the absence of a higher than +4 oxidation state for thorium, which prevents *in situ* reduction as a possible strategy for obtaining thorium fluorides; on the other hand, it makes it possible to use oxidative fluxes for thorium crystal growth. In this paper, we report on the synthesis and properties of new uranium(IV) fluorides as well as on the development of hydrothermal and high-temperature synthetic routes leading to thorium(IV) fluorides. We demonstrate that sodium uranium fluorides can be successfully grown under mild hydrothermal conditions, starting with either UF_4 or uranyl acetate. Notably, the application of the mild hydrothermal method and of nitrate flux crystal growth were both highly successful for producing thorium fluorides.

Quaternary thorium fluorides

Recently, we reported a series of quaternary uranium(IV) fluorides with a general formula $Na_nMU_6F_{30}$, where M is a di- or trivalent cation in an octahedral fluorine environment. The uranium quaternary fluoride series encompasses a wide range of M cation sizes, reaching a maximum size at about 0.745 Å corresponding to Sc^{3+} cation. The size limit lies slightly below the size of the smallest cation in the lanthanide series, lutetium, 0.861 Å, and therefore can be expanded in order to accommodate cations as large as lanthanides (Figure 4). To achieve this goal, we substituted U^{4+} cations in this structure type by slightly larger Th^{4+} cations. This minor increase in the actinide site size, 1.05 for U^{4+} vs. 1.09 Å for Th^{4+}, is on one hand is small enough for thorium to adapt the same structure type, while on the other it drastically changes the M site size because of the large number of the actinide atoms per formula unit. This subtle change of the actinide atom size allowed us to obtain a large family of new quaternary thorium fluorides, which can host at least 19 elements in either +2 or +3 oxidation states on the M site. Apart from the elements which were previously shown to fit well on the M site in the uranium series we managed to introduce larger cations, such as late lanthanides, in this structure type. It is noteworthy however that the size increase in the lanthanide series is accompanied by a decrease of the M site occupancy, whereas the raising due to this charge discrepancy is compensated by partial occupancy of the sodium sites.

$Cs_2MU_3F_{16}$ (M = Mg^{2+}, Mn^{2+}, Co^{2+}, Ni^{2+}, or Zn^{2+})

Another fluoride series with interesting magnetic properties was obtained via hydrothermal route involving an *in situ* reduction step. We have shown that this approach involving uranyl acetate as a precursor for obtaining U(IV) compounds can be successfully extended to the fluorides. Albrecht-Schmitt has reported $Ni_2(H_2O)_6U_3F_{16}\cdot 3H_2O$, which is based on hexagonal $[U_3F_{16}]^{4-}$ layers decorated with hydrated nickel(II) cations on each side. In order to explore the magnetic properties of uranium fluorides based on these layers, which can possibly show frustrated magnetism on uranium atoms due to their kagome-like cation topology (Figure 5), we synthesized a series of novel quaternary uranium fluorides $Cs_2MU_3F_{16}$, where M is Mg^{2+}, Mn^{2+}, Co^{2+}, Ni^{2+}, or Zn^{2+}. The main difference between these five compounds and the previously reported uranium nickel fluoride is that the $[U_3F_{16}]^{4-}$ layers are no longer isolated but assemble into a 3D entity through the M atoms (Figure 5). This structure assembly allows the M atoms to build their preferred octahedral coordination environment, whereas the charge balance is achieved by introducing the Cs atoms into the interlayer space. Such atom arrangement allows magnetic interactions within the layers, which also mediates magnetic exchange between interlayer M atoms. Hydrothermal conditions for these reactions were optimized to obtain phase pure samples and their magnetic data were collected using a SQUID magnetometer. The Mn-, Co-, and Ni-containing compounds exhibit a clear indication of a transition at low temperatures in their molar susceptibility vs. temperature plots (Figure 6), accompanied by a significant growth of susceptibility with decreasing temperature.

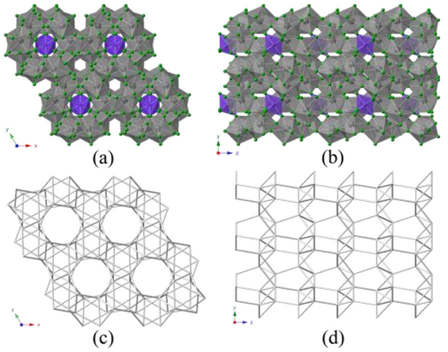

Figure 4. (a and b) A view on the structure of $Na_4ZnTh_6F_{30}$ and (c and d) the simplified net of the $[Th_6F_{30}]^{6-}$ framework with **wmo** topology.

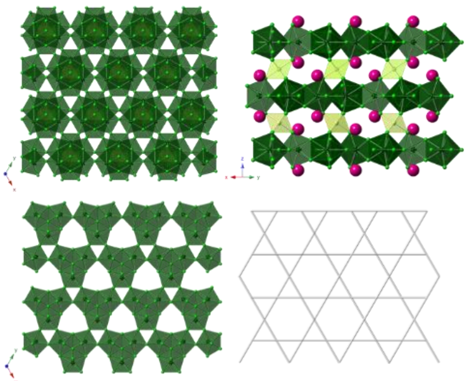

Figure 5. (top left and right) View on the structure of $Cs_2NiU_3F_{16}$. Yellow NiF_6 octahedra connect uranium $[U_3F_{16}]^{4-}$ layers (shown in green). (bottom left and right) View of a single uranium layer and its cation topology.

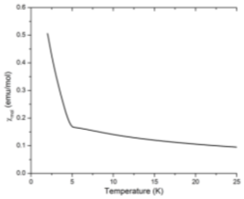

Magnetic susceptibility vs. temperature plot

Figure 6. A ferromagnetic-like transition is observed for $Cs_2NiU_3F_{16}$ at a temperature of ~5 K.

Uranium sulfides

The flux crystal growth method using halide fluxes was found to be extremely helpful in not only obtaining new uranium thiophosphates in the form of single crystals which are suitable for single crystal X-ray diffraction, a condition which is not easily achievable for usually extremely moisture sensitive thiophosphates, but also allowed us to obtain phase pure samples of several materials in this underexplored, as compared to oxysalts, class of compounds. Despite difficulties in their syntheses, uranium thiosalts offer a convenient scaffold to probe uranium behavior in highly reducing sulfide-rich conditions, as well as studying electronic and magnetic properties of reduced uranium compounds with soft Lewis bases. We found that the uranium thiophosphate formation is favored at a temperature range below 700–750°C, which falls outside of the typical temperature range for chloride fluxes but works well for iodide fluxes and their eutectic mixtures. Employing CsI-NaI and RbI-NaI eutectic fluxes, we obtained a series of uranium thiophosphates based on a complex non-centrosymmetric $[U(PS_4)_2]^{2-}$ bilayer. The bilayers consist of crisscross chains running parallel on different levels and connected through a uranium thiophosphate groups located in between them. The bilayers are stacked in a zip lock fashion, and severely disordered cesium, rubidium, sodium, and iodide ions are located between them, resulting in the compositions $Rb_{1.35}Na_{0.93}I_{0.28}[U(PS_4)_2]$, $Cs_{1.033}Na_{1.343}I_{0.376}[U(PS_4)_2]$, and $Cs_{1.70}Na_{0.50}I_{0.20}[U(PS_4)_2]$. We obtained the latter compound as a phase pure sample and measured its magnetic properties. This compound exhibits paramagnetic behavior and follows Curie-Weiss law in a range about 100–300 K. The obtained effective magnetic moment per one uranium atom is 3.11 μ_B.

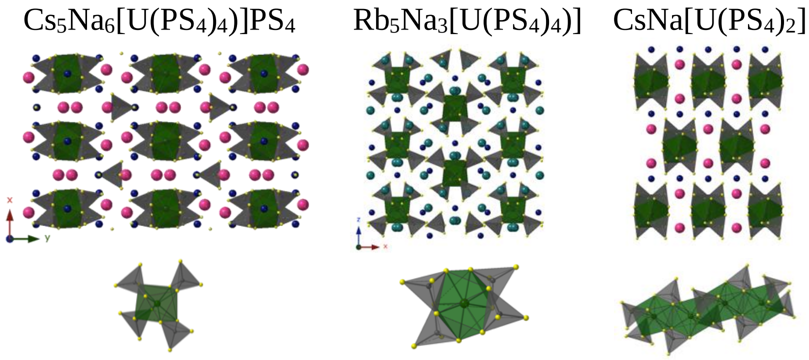
$Cs_5Na_6[U(PS_4)_4)]PS_4$ $Rb_5Na_3[U(PS_4)_4)]$ $CsNa[U(PS_4)_2]$

Figure 7. View on the crystal structures of $Cs_5Na_6[U(PS_4)_4)]PS_4$, $Rb_5Na_3[U(PS_4)_4)]$, and $CsNa[U(PS_4)_2]$.

Another group of thiophosphate compounds obtained from iodide fluxes are $Cs_5Na_6[U(PS_4)_4)]PS_4$, $Rb_5Na_3[U(PS_4)_4)]$, and $CsNa[U(PS_4)_2]$ (Figure 7). This series allowed us to explore the influence of the U:P ratio on the uranium thiophosphate structural features. The lowest ratio observed, 1:5, in $Cs_5Na_6[U(PS_4)_4)]PS_4$, leads to the formation of $[U(PS_4)_4]^{8-}$ complexes and isolated PS_4^{3-} units surrounded exclusively by the alkali cations. Separation of the uranium(IV) atom from the fifth thiophosphate group allows us to suggest that the coordination capacity of U(IV) can virtually be saturated by four thiophosphate groups. Indeed, the structure of $Rb_5Na_3[U(PS_4)_4)]$ exhibits similar $[U(PS_4)_4]^{8-}$ complexes. Further increase of the U:P ratio to 1:2 results in the compound $CsNa[U(PS_4)_2]$. The uranium complexes in the structure of this compound share two thiophosphate groups with each of two neighboring uranium atoms, condensing the uranium units into chains. The magnetic measurements on a sample of the latter compound revealed two paramagnetic reagions over the temperature ranges of 100–200 and 240–375 K, with a gradual transition between them. The effective moments for both regions are close to each other and equal to 4.19 and 4.13 μ_B, respectively.

References

[1] Yeon, J.; Smith, M. D.; Tapp, J.; Möller, A.; zur Loye, H.-C. Application of a Mild Hydrothermal Approach Containing an in Situ Reduction Step to the Growth of Single Crystals of the Quaternary U(IV)-Containing Fluorides $Na_4MU_6F_{30}$ (M = Mn^{2+}, Co^{2+}, Ni^{2+}, Cu^{2+}, and Zn^{2+}) Crystal Growth, Structures, and Magnetic Properties. *J. Am. Chem. Soc.* **2014**, *136* (10), 3955–3963.

[2] Yeon, J.; Smith, M. D.; Tapp, J.; Möller, A.; zur Loye, H.-C. Mild Hydrothermal Crystal Growth, Structure, and Magnetic Properties of Ternary U(IV) Containing Fluorides: $LiUF_5$, KU_2F_9, $K_7U_6F_{31}$, $RbUF_5$, RbU_2F_9, and RbU_3F_{13}. *Inorg. Chem.* **2014**, *53* (12), 6289–6298.

Publications

Felder, J. B., Calder, S., zur Loye, H.-C., "Retention of a Paramagnetic Ground State at Low Temperatures in a Family of Structurally Related U^{IV} Phosphates", Inorg. Chem., **2018**, submitted.

Felder, J. B., Smith, M. D., zur Loye, H.-C., "Breaking a Paradigm: Observation of Magnetic Order in the Purple U(IV) Phosphite: $U(HPO_3)_2$", Inorg. Chem., **2018**, submitted.

Felder, J. B., Smith, M. D., zur Loye, H.-C., "Utilizing an *in situ* Reduction in the Synthesis of $BaMoOF_5$", J. Chem. Cryst., **2018**, submitted.

Usman, M., Felder, J., Morrison, G., zur Loye, H.-C., "A Family of Rare Earth Uranium Oxides, RE_6UO_{12}, (RE = Rare Earth). Synthesis, Structure and Magnetic Behavior", J. Solid State Chem., **2018**, submitted.

Felder, J. B., Smith, M. D., Sefat, A. S., zur Loye, H.-C., "Magnetic and Thermal Behavior of a Family of Compositionally Related Zero-Dimensional Fluorides", DOI:org/10.1016/j.solidstatesciences.2018.04.014. Solid State Sci., **2018**, *81*, 19-25.

Klepov, V. V., Felder, J. B., zur Loye, H.-C., "New Synthetic Strategies for the Synthesis of Ternary Uranium(IV) and Thorium(IV) Fluorides", DOI:10.1021/acs.inorgchem.8b00570. Inorg. Chem., **2018**, *57*, 5597-5606.

Felder, J. B., Smith, M. D., zur Loye, H.-C., "$[Co(H_2O)_6]_3[U_2O_4F_7]_2$: A Model System for Understanding the Formation of Dimensionally Reduced Materials", DOI:10.1021/acs.cgd.7b01780. Cryst. Growth Des., **2018**, *18*, 1236-1244.

Felder, J., M. D. Smith, and H.-C. zur Loye. "Supercritical Synthesis and Topological Analysis of $K_5U_5O_{17}(OH)$", *CrystEngComm,* **2017**, *19*, 3499-3505. DOI:10.1039/C7CE00746A.

Yeon, J., and H.-C. zur Loye. "Hydrothermal Synthesis and Crystal Structure of Hexafluorogallate, Na_3GaF_6", *J. Chem. Crystallogr.,* **2017**, *47,* 129-132. DOI:10.1007/s10870-017-0687-x.

Morrison, G., M. D. Smith, and H.-C. zur Loye. "Flux versus Hydrothermal Growth: Polymorphism of $A_2(UO_2)Si_2O_6$ (A = Rb, Cs)", *Inorg. Chem.,* **2017**, *56*, 1053-1056. DOI:10.1021/acs.inorgchem.6b02931.

Felder, J., J. Yeon, M. D. Smith, and H.-C. zur Loye. "Application of a Mild Hydrothermal Method to the Synthesis of Mixed Transition-Metal(II)/Uranium(IV) Fluorides", *Inorg. Chem. Front,* **2017**, *4*, 368-377. DOI:10.1039/C6QI00491A.

Morrison, G., M. D. Smith, and H.-C. zur Loye. "Understanding the Formation of Salt-Inclusion Phases: An Enhanced Flux Growth Method for the Targeted Synthesis of Salt-Inclusion Cesium Halide Uranyl Silicates", *J. Am. Chem. Soc.,* **2016**, *138,* 7121-7129. DOI:10.1021/jacs.6b03205.

The Nature of Charge Storage in Nitroxide Radical Polymers

Jodie L. Lutkenhaus, Artie McFerrin Department of Chemical Engineering, Department of Materials Science & Engineering, Texas A&M University

Program Scope

Organic radical polymers for batteries represent some of the fastest charging electroactive materials available. Organic radical polymers are electrochemically active owing to the reversible reduction-oxidation (redox) reaction of pendant radical groups and offer a vast synthetic landscape for customization, which can yield theoretical capacities >100 mAh/g. Also, the singly occupied molecular orbitals in the radical groups result in fast electron transfer and consequently rapid charge and discharge (as high as 50 C, where 1 C is the current required to discharge a battery in one hour) and good cycling behavior. Despite these benefits, there remains a poor understanding of the redox mechanism itself, even for the most well-studied organic radical polymer poly(2,2,6,6-tetramethylpiperidinyloxy-4-yl) (PTMA). Also, PTMA requires large amounts of carbon in the electrode to facilitate electron transfer, which points to PTMA's low electronic conductivity. *Therefore, the scope of this project is to probe the nature of electron and ion transport in the organic radical polymer PTMA and to examine possible conductivity enhancements using conjugated backbone platforms.*

Recent Progress

First, we discuss the progress made toward understanding the mechanism of electron transport in organic radical polymers. This is not well understood, as researchers have applied various models such as diffusive hopping among frozen sites, ion transport limited, suppressed movement due to electrostatic interactions, and elevated reorganization energy models, but they failed to fully capture experimental observations. By considering segmental mobility in addition to diffusive hopping, Lutkenhaus, Nishide, and Oyaizu developed a model that suitably captured the charge transport behavior of organic radical polymers and other non-conjugated redox-active polymers.[1] *The main finding was that both homogeneous and heterogeneous charge transport is regulated by the physical diffusion of redox active sites.*

To describe the theory in more detail, the radical polymer is considered to transport electrons homogeneous and heterogeneously, Figure 1a. Homogeneous charge transfer occurs by apparent self-exchange with neighboring radical sites, described by $k_{ex,app}$. Heterogeneous charge transfer describes the transfer of an electron from the organic radical polymer to the current collector as k^o. Notably, both $k_{ex,app}$ and k^o were found to be dependent on D_{phys}, the main finding of this work (Figure 1b and 1c).

In a broader sense, these results explain why organic radical polymers have not displayed the same kinetics of charge transport as their small molecule radical analogs. Importantly, they also connect to the disagreement in literature on whether organic radical polymers are electronically conductive in the solid state. In the solid state, the organic radical polymer (usually PTMA) is glassy and D_{phys} is expected to be very low, which is consistent with the observation that PTMA is insulating.[2] On the other hand, adding a small molecule plasticizer would increase D_{phys}, consistent with the observation that conductivity increases for small molecule TEMPO added to PTMA.[1, 3]

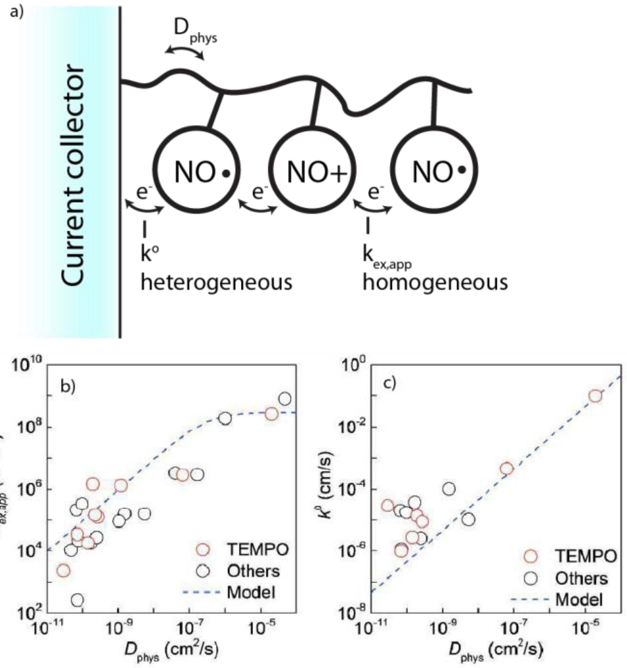

Figure 1. a) Schematic of homogeneous self-exchange and heterogeneous charge transfer and charge transport modes in organic radical polymers. **b)** $k_{ex,app}$ and **c)** k^o values found from experiment for various radical polymers (including TEMPO-based polymers) *vs.* D_{phys} and compared against the model described in ref. 1. (Lutkenhaus, Nishide, Oyaizu).

We next discuss progress made toward understanding the transport of ions in PTMA. Using electrochemical quartz crystal microbalance with dissipation monitoring (EQCMD), electron and ion transport processes were separated as a function of potential and of ion type ($LiCF_3SO_3$. $LiClO_4$, and $LiBF_4$ in propylene carbonate). *The main findings were that ion transport occurs both internally (electrolyte already imbibed into the swollen polymer) and externally (electrolyte in the bulk solution), and that external transport is favored at higher scan rates.*

With the support of this project, the Lutkenhaus lab has developed the unique capability of monitoring ion and electron transport *in situ* using EQCMD.[4] Standard electrochemical measurements (cyclic voltammetry, galvanostatic cycling) were conducted while monitoring changes in the organic radical polymer-coated crystal's frequency and dissipation. Using viscoelastic modeling, changes in the mass and the shear modulus of the electroactive material are obtained throughout the electrochemical measurement. This system is specially designed to handle both aqueous and non-aqueous media, the latter of which includes battery electrolyte. With this approach, an overall mass balance was performed, and, by examining the minutiae of this response, it was concluded that ion transport occurred in two modes: "externally" and "internally".[4b] Figure 2a shows an example of "internal" ion transport, in which an anion already within the swollen polymer dopes the positively charged PTMA; to maintain charge neutrality a lithium cation is expelled from the electrode, resulting in a theoretical mass decrease on the order of -0.072 mg/C. Figure 2b shows an example of external ion transport, in which the dopant anion ($CF_3SO_3^-$) is provided by the external electrolyte solution, resulting in a theoretical mass increase of 1.545 mg/C. If the experimental value is between the two, then it can be assumed that mixed transport occurs and the two can be separated. Figure 3 below shows an extreme case (low electrolyte concentration) when the two modes could be clearly separated.

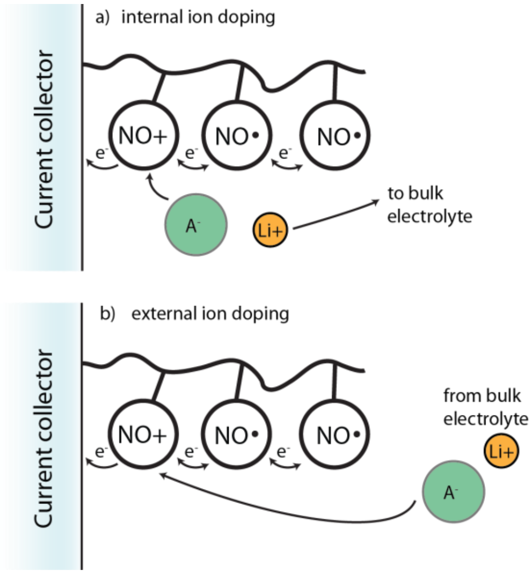

Figure 2. a) Internal ion doping, in which an anion (A^-) already imbibed in the polymer dopes PTMA, expelling a lithium cation. **b)** External ion doping, in which an anion from the bulk electrolyte dopes PTMA. Adapted from ref. 4b. (Lutkenhaus).

We finally discuss the influence of a conjugated backbone on the activity of an organic radical polymer was investigated. Lutkenhaus synthesized[5] and studied[6] a series conjugated radical polymers (CRPs) to assess the origin of the low capacity and conductivity of CRPs to-date, Figure 4. These consisted of polythiophenes with pendant radical groups separated by alkyl tethers of varying length. *The main finding was that electron transfer between the radical and the polythiophene backbone caused dedoping of the polythiophene backbone, essentially quenching the anticipated performance.* For that case, it was found that the alkyl tether length had only a small effect, so it was concluded that the relative redox potentials of the radical group and the conjugated backbone were the dominating factor.

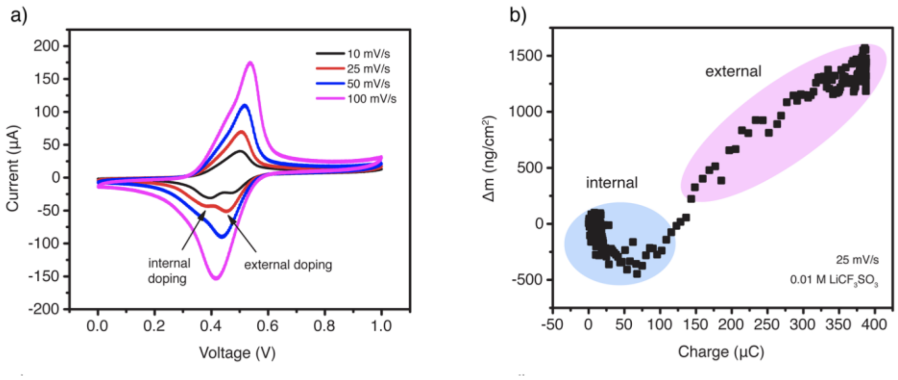

Figure 3. a) Cyclic voltammetry of PTMA at the low electrolyte concentration of 0.01 M $LiCF_3SO_3$ in propylene carbonate, showing peaks attributed to internal and external ion doping. **b)** Change in electrode mass vs. charge passed during PTMA oxidation at 25 mV/s via EQCMD. The blue region highlights internal ion doping and the pink region highlights external doping. Adapted from ref 4b. (Lutkenhaus).

The origin of this behavior stems from the different redox potentials of the TEMPO radical functional group and the polythiophene backbone (3.6 and 3.8 V *vs.* Li/Li^+, respectively). TEMPO, having very fast kinetics relative to polythiophene, easily oxidizes, but polythiophene is more sluggish. During charging or oxidation, TEMPO and polythiophene units oxidize and become doped, but not completely. Upon removal of the potential, the system rapidly relaxes (on the order of 10s of seconds) such that TEMPO gives an electron to the polythiophene backbone, and, in the process, de-dopes it. Now, with the mechanism of charge storage loss identified,[6] new CRPs may be designed that are both conductive and active.

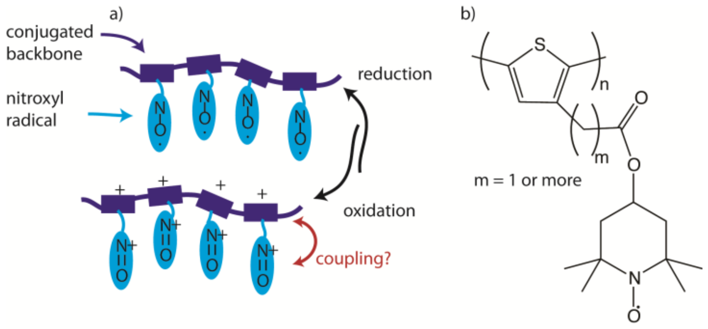

Figure 4. a) Schematic of a nitroxide radical-modified conjugated polymer undergoing a redox reaction. **b)** TEMPO-modified polythiophenes.

Future Plans

Our future plans are to verify, refine, and harness the diffusive hopping with segmental mobility model to design high rate organic radical polymers; to quantify internal and external ion transport in organic radical polymers beyond PTMA; and to orchestrate and understand internal electron transfer in conjugated radical polymers. We are also synthesizing crosslinkable PTMA and assessing PTMA-solvent interactions using polymer solution theory.

References

[1] K. Sato, R. Ichinoi, R. Mizukami, T. Serikawa, Y. Sasaki, J. L. Lutkenhaus, H. Nishide, K. Oyaizu, *Journal of the American Chemical Society* **2017**.

[2] Y. Zhang, A. Park, A. Cintora, S. R. McMillan, N. J. Harmon, A. Moehle, M. E. Flatte, G. D. Fuchs, C. K. Ober, *Journal of Materials Chemistry C* **2018**, *6*, 111-118.

[3] (a) Y. Sasada, R. Ichinoi, K. Oyaizu, H. Nishide, *Chemistry of Materials* **2017**, *29*, 5942-5947; (b) E. P. Tomlinson, M. J. Willmore, X. Zhu, S. W. A. Hilsmier, B. W. Boudouris, *ACS Applied Materials & Interfaces* **2015**, *7*, 18195-18200.

[4] (a) F. Li, Y. Zou, S. Wang, L. Fang, J. L. Lutkenhaus, *Macromolecular Rapid Communications* **2017**, 1700067; (b) S. Wang, A. D. Easley, J. L. Lutkenhaus, *In Revision at Nature Materials*.

[5] F. Li, Y. Zhang, S. R. Kwon, J. L. Lutkenhaus, *ACS Macro Letters* **2016**, *5*, 337-341.

[6] F. Li, D. N. Gore, S. Wang, J. L. Lutkenhaus, *Angewandte Chemie International Edition* **2017**, *56*, 9856-9859.

Publications

1 Sato, K., Ichinoi, R., Mizukami, R., Serikawa, T., Sasaki, Y., Lutkenhaus, J.L., Nishide, H., & Oyaizu, K., Diffusion-cooperative Model for Charge Transport by Redox-active Non-conjugated Polymers. *Journal of the American Chemical Society* (2017).

2 Morris, M.A., An, H., Lutkenhaus, J.L., & Epps, T.H., Harnessing the Power of Plastics: Nanostructured Polymer Systems in Lithium-Ion Batteries. *ACS Energy Letters* 2 (8), 1919-1936 (2017).

3 Li, F., Gore, D.N., Wang, S., & Lutkenhaus, J.L., Unusual Internal Electron Transfer in Conjugated Radical Polymers. *Angewandte Chemie International Edition* 56 (33), 9856-9859 (2017).

4 Li, F., Zou, Y., Wang, S., Fang, L., & Lutkenhaus, J.L., Scalable Synthesis and Multi-Electron Transfer of Aniline/Fluorene Copolymer for Solution-Processable Battery Cathodes. *Macromolecular Rapid Communications*, 1700067 (2017).

5 Wang, S., Easley, A.D., & Lutkenhaus, J.L., Real-time insight into the doping mechanism of redox-active organic radical polymers. *In Revision at Nature Materials*.

6 Li, F., Wang, S., Zhang, Y., & Lutkenhaus, J.L., Electrochemical Energy Storage in Poly(dithieno[3,2-b:2',3'-d]pyrrole) Bearing Pendant Nitroxide Radicals. *In Revision at Chemistry of Materials*.

Dynamic Properties of Nanostructured Porous Materials

Principal Investigator: Adam J. Matzger; Co-Investigator: Antek G. Wong-Foy
Department of Chemistry and the Macromolecular Science and Engineering Program
University of Michigan, Ann Arbor, MI 48109-1055

Program Scope

The ultimate purpose of the research program is to understand the influence of dynamic phenomena in microporous coordination polymers (MCPs) on their properties, and to leverage this understanding to improve their syntheses. MCPs have the potential for myriad applications, including separations, gas storage, and catalysis, but further development of methods to control their syntheses are necessary. The research program is split into three facets: understanding and controlling MCP linker exchange rates to beget previously inaccessible complex structures, determining the causes and nature of MCP collapse during activation, and controlling MCP properties by interfacing these structures with soft polymeric material.

Recent Progress

Creating core-shell MCP architectures by controlled linker diffusion via PSE

Direct syntheses of many desirable MCP architectures are not always possible. An alternate route to many of these structures is post-synthetic ligand exchange (PSE). Despite its utility, the process of ligand diffusion and exchange into the MCP scaffold is not understood. To probe this process, we performed PSE on MOF-5, a prototypical Zn-based MCP, to exchange its BDC linkers for their perdeuterated analogue, d_4-BDC, which should be effectively identical from both steric and electronic standpoints. The products of this exchange were characterized with mapping Raman microscopy to determine spatial differences in the resulting crystals. We observed surprisingly slow exchange in the center of the crystals, as evidenced by the formation of core-shell structures. (Figure 1) This PSE experiment was repeated with UMCM-8 and UiO-66, and the same behavior was observed in both cases.

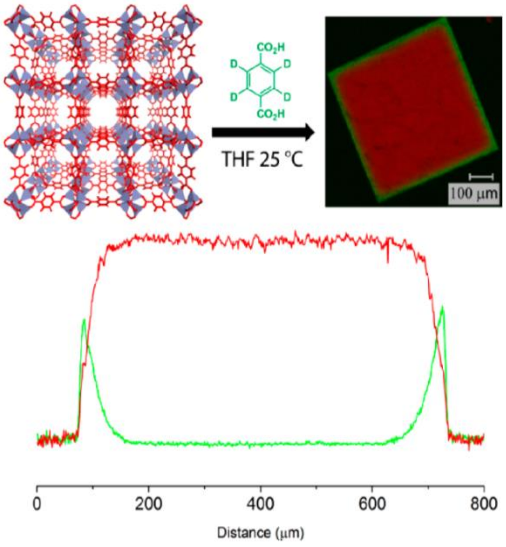

Figure 1. (top) Reaction scheme for PSE of MOF-5 with H_2BDC-d_4 yielding a core−shell structure (BDC-d_4, green; BDC, red). (bottom) Line graph from edge to edge showing BDC-d_4 concentrated on the outer edges of the crystal and decreasing towards the center.

The underlying cause of the formation of core-shell structures of BDC ligands throughout MCPs was then probed. MOF-5 pores are not expected to be small enough to block BDC via size exclusion. To ensure that slow BDC diffusion through MOF-5 pores was responsible for the observed behavior, we monitored the MCP core environment alone during PSE using confocal Raman microscopy. When MOF-5 was incubated in a saturated solution of d_4-BDC, the presence of d_4-BDC was not observed within the MCP core until after an hour of exposure, consistent with slow diffusion into the MCP. In contrast, the dimethyl ester of BDC was able to diffuse throughout the MCP in less than 10 minutes. This suggests that free carboxylate groups rather than steric bulk are responsible for slow linker diffusion. This was further verified by comparing diffusion rates for benzoic acid and methyl benzoate, with the same trends being observed. For all of the MCPs that were tested, incorporation of the deuterated linker began first at the surface, followed by eventual migration towards the center. This process allows for creation of more uniform core-shell MCP crystals than can be created via epitaxial overgrowth, without competition from the growth of new pure phases. Additionally, this method has the potential to concentrate catalytic sites on the surface of MCPs and to selectively control guest access to MCP pore sites.

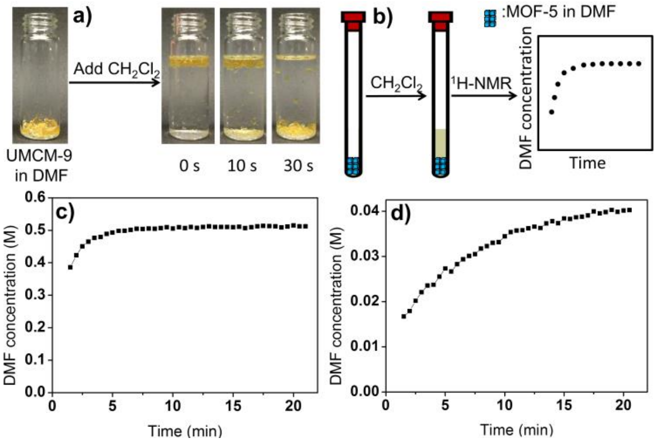

Figure 2. (a) Images of UMCM-9 in DMF exchanged into CH_2Cl_2. Crystals were found to float (0s) and then sink back to the bottom (10s) completely (30s). (b) ^{1}H-NMR spectroscopy monitoring of the amount of DMF diffusing into CH_2Cl_2 during the (c) first and (d) second solvent exchange process of MOF-5.

Optimizing MCP activation by use of ultra-low surface tension solvents

MCP activation generally involves solvent exchange from the synthesis solvent to a high vapor pressure solvent, followed by the removal of this solvent by some combination of low pressure and high temperature treatment. MCP activation often leads to products with broadened PXRD peaks and lower surface area than predicted, through a process often referred to as collapse. Usually solvent exchange is performed over several days. Visually, we observed that solvent exchange seems to occur within seconds, as an example, UMCM-9 crystals sink over the course of ~30 seconds when transferred from DMF to higher-density CH_2Cl_2. (Figure 2) Using ^{1}H-NMR, we determined that the DMF to CH_2Cl_2 exchange process in MOF-5 undergoes full equilibration during the first 5-10 minutes for the first wash, while the second wash is complete within ~20 minutes. To test the importance of multiple washes, we performed multiple washes of MOF-5 from DMF to CH_2Cl_2, each lasting 20 minutes, and characterized the products by measuring their surface area and quantifying residual DMF via ^{1}H-NMR after digestion. The first, second, and third washes gave products which contained 0.78, 0.12, and 0.014 DMF molecules per unit cell, respectively, with increasing surface area of 2650, 3410, and 3640 m^2/g, relative to the theoretical surface area of 3527 m^2/g.

Finally, we tested the effect of ultra-low surface tension solvents on the activation of fragile MCPs. Prior to these studies, the successful activation of UMCM-9 had only been accomplished via $scCO_2$ activation. Activation of UMCM-9 from CH_2Cl_2 gave a Brunauer–Emmett–Teller (BET) surface area of 1330 m^2/g versus 4970 m^2/g from $scCO_2$ (theoretical surface area is 4900 m^2/g). n-hexane was chosen as a trial activation solvent due to its low surface tension (17.9 mN/m vs 27.1 mN/m for CH_2Cl_2). From n-hexane, we obtained a surface area of 4980 m^2/g, with PXRD confirming a product with good crystallinity. (Figure 3) Following this experiment, an even more fragile MCP, FJI-1, was also tested with several activation solvents. Like UMCM-9, it had previously only been reported to demonstrate full surface area following $scCO_2$ treatment. However, FJI-1 activated from n-hexane showed poor surface area, prompting us to utilize even lower surface tensions solvents . When perfluoropentane was used as the activation solvent, a product with surface area equivalent to that resulting from flowing $scCO_2$ treatment was obtained, consistent with our predictions. This demonstrates that in situations where standard activation procedures fail, switching to an ultra-low surface tension solvent has the potential to reveal the full surface area inherent to the material.

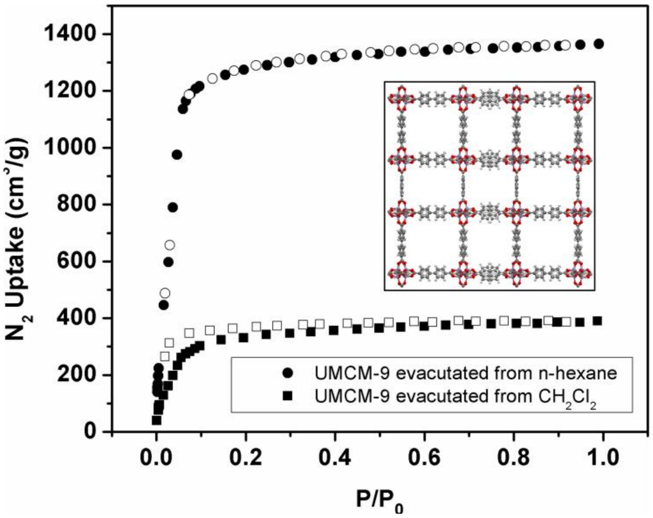

Figure 3. N_2 isotherm plots of UMCM-9 activated from n-hexane and CH_2Cl_2 exchanged materials. Inset: Structure of UMCM-9 (Zn_4O(naphthalene-2,6-dicarboxylate)$_{1.5}$ (biphenyl-4,4'-dicarboxylate)$_{1.5}$).

Probing nature of MCP activation-induced collapse

It is generally stated in MCP literature that longer, more flexible linkers make MCPs more liable to collapse than shorter, rigid linkers. Similarly, solvents with higher surface-tension are more destructive during activation relative to low surface-tension solvents. Despite these general guidelines, the process of collapse is still poorly understood. To probe the structural changes occurring during collapse, a series of MCP activations were monitored *in-situ* using two-dimensional powder X-ray diffraction (2D-PXRD). This technique allows for characterization of crystalline samples in a more nuanced fashion than does standard PXRD by the addition of a second axis (the β-axis) which separates diffracted X-rays according to crystallite orientation. Three different solvents with varying properties were chosen for this study: CH_2Cl_2, tetrahydrofuran (THF), and n-hexane. We studied a series of Zn_4O-based MCPs with varying linker flexibilities: MOF-5 (1,4-benzenedicarboxylic acid), UMCM-9 (2,6-napthalenedicarboxylic acid and 4,4'-biphenyldicarboxylic acid), and SNU-70 (4-(2-carboxyvinyl)benzoic acid). While previous reports indicate that CH_2Cl_2 is suitable for MOF-5 activation and UMCM-9 can be successfully activated from hexane, activated SNU-70 has successfully achieved its calculated surface area only by supercritical CO_2 treatment.

Four of the nine MCP/solvent combinations (all MOF-5 combinations, and UMCM-9/hexane) underwent no observable crystallographic changes during activation. These activations also yielded products with full predicted surface area, consistent with a completely successful activation. Similarly, three of the pairs gave fully unsuccessful activations (UMCM-9/THF, SNU-70/THF, SNU-70/CH_2Cl_2), with negligible surface area and near complete loss of all PXRD signal. However, two of the pairs demonstrated intermediate activation efficacy. UMCM-9/CH_2Cl_2 gave a product with approximately a quarter of the predicted surface area, and which produced 2D-PXRD patterns with significant 2θ-axis peak broadening as well as partial but incomplete broadening along the β-axis, indicating that the product contains crystalline domains separated by amorphous regions. The relatively high degree of β-axis broadening implies that the crystalline domains are generally shifted relative to their original orientations, but that some degree of orientation is preserved. SNU-70/hexane gave a product with full surface area, but again with 2θ- and β-axis peak broadening, albeit to a lesser degree than in UMCM-9/CH_2Cl_2. The full retention of surface area suggests that the product has little to no amorphous character, but the 2D-PXRD peak broadening indicates that the crystallites lose a small degree of orientational coherence. This is interpreted as resulting from the formation of cracks within the MCP during the activation process, which effectively lead to the formation of many smaller crystallites, along with some degree of strain, accounting for the 2θ-axis peak broadening. From all of these observations, a generalized scale describing MCP activation efficacy was developed (Figure 4), onto which each set of activation conditions was placed. This represents the first step towards a structural understanding of the basis and products of activation-induced MCP collapse.

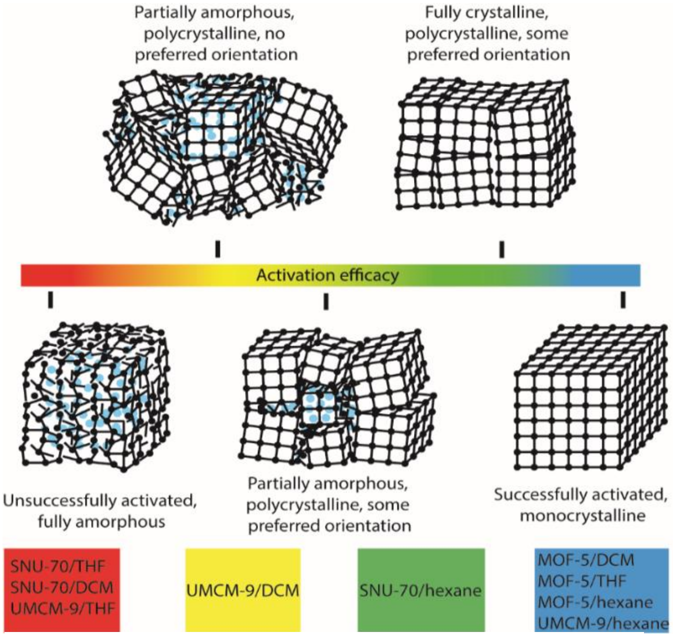

Figure 4. Ranked MOF activation efficacies with illustrations of each product.

Future Plans

The microstructure of MCPs produced by PSE will be explored for broader classes of materials and ligand types to define the scope of this core-shell production approach. Similarly we plan to examine additional MCP activation strategies with *in situ* tools to identify where structure collapse occurs so that protocols can be adjusted to maintain porosity.

References

1. Boissonnault, J. A.; Wong-Foy, A. G.; Matzger, A. J. Core–Shell Structures Arise Naturally During Ligand Exchange in Metal–Organic Frameworks. *J. Am. Chem. Soc.*, **2017**, *139*, 14841-14844.

2. Ma, J.; Kalenak, A. P.; Wong-Foy, A. G.; Matzger, A. J. Rapid Guest Exchange and Ultra-Low Surface Tension Solvents Optimize Metal–Organic Framework Activation. *Angew. Chemie Int. Ed.*, **2017**, *56*, 14618-14621.

Publications

Damron, J.; Ma, J.; Kurz, R.; Saalwaechter, K.; Matzger, A. J.; Ramamoorthy, A. The Influence of Chemical Modification on Linker Rotational Dynamics in Metal Organic Frameworks. *Angew. Chemie Int. Ed.*, **2018**, accepted.

Seth, S.; Matzger, A. J. Metal–Organic Frameworks: Examples, Counterexamples, and an Actionable Definition. *Crystal Growth & Design*, **2017,** *17*, 4043-4048.

Boissonnault, J. A.; Wong-Foy, A. G.; Matzger, A. J. Purification of Chloromethane by Selective Adsorption of Dimethyl Ether on Microporous Coordination Polymers. *Langmuir*, **2016**, *32*, 9743–9747.

Gamage, N.-D. H.; McDonald, K. A.; Matzger, A. J. MOF-5-Polystyrene: Direct Production from Monomer, Improved Hydrolytic Stability, and Unique Guest Adsorption. *Angew. Chemie Int. Ed.*, **2016**, *55*, 12099-12103.

DE-SC0018074: High Rate Sodium Storage Mechanisms in Non-Graphitic Carbons

David Mitlin, Principal Investigator, Eunsu Paek, Co-Investigator, Clarkson University, Potsdam, NY, 13699

Program Scope:

A wide survey of existing scientific literature shows minimal discussion regarding any transitions in dominant charge storage or capacity loss mechanisms as the charging rate is increased for a range of Na storage materials, ranging from anode carbons and anode Na metal, to cathode selenium (Se) compounds. Moreover, while there is a wide variability in the Coulombic efficiency and cycling lifetime values reported for these materials, the origin of either is not understood. This combined experimental – simulation proposal seeks to provide new fundamental insight into these unexplored aspects of Na charge storage in a wide range of anode/cathode structure and chemistries. We will employ a range of electrochemical, analytical and modeling techniques to establish fundamental structure – property relations at charge rates that are far beyond what has been studied for sodium battery applications to date. We will partner with Oak Ridge National Laboratory to perform detailed Neutron Diffraction (ND) analysis on Na charged materials. We will also partner with Brookhaven National Laboratory to explore the surface structure/chemistry aspects in these materials, employing techniques such as X-ray Photoelectron Spectroscopy (XPS). Our modeling effort will combine various state-of-the-art theoretical methods, with a particular emphasis on the role of heteroatom chemistry in charge storage. With the successful execution of this research, it is expected that many of the existing "battery-inherited" paradigms regarding high rate Na storage would be disrupted.

Recent Progress

Fundamental Science of Multi-rate Sodium Storage in Selenium - Sodium Metal Batteries

Summary - Energy density (energy per volume) is a key consideration for portable, automotive and stationary battery applications. We created selenium (Se) lithium and sodium metal cathodes that are monolithic and free-standing, and with record Se loading of 70 wt%. The carbon host is derived from nanocellulose, an abundant and sustainable forestry product. The composite is extremely dense (2.37 g cm^{-3}), enabling theoretical volumetric capacity of 1120 mAh cm^{-3}. Such architecture is fully distinct from previous Se – carbon nano or micropowders, intrinsically offering up to 2X higher energy density. For Li storage, the cathode delivered reversible capacity of 1028 mAh cm^{-3} (620 mAh g^{-1}) and 82% retention over 300 cycles. For Na storage 848 mAh cm^{-3} (511 mAh g^{-1}) was obtained with 98% retention after 150 cycles. The electrodes yield superb volumetric energy densities, being 1727 Wh L^{-1} for Li-Se and 980 Wh L^{-1} for Na-Se normalized by total composite mass and volume. Despite the low surface area, over 60% capacity is maintained as the current density is increased from 0.1 to 2 C (30 min charge) with Li or Na. Remarkably, the electrochemical kinetics with Li and Na are comparable, including the transition from interfacial to diffusional control.

Introduction - While lithium ion batteries (LIBs) are a ubiquitous commercial technology, sodium ion batteries (NIBs) are receiving increasing scientific attention due to the much wider distributed reserves of Na precursors and the cost savings associated with an aluminum versus a copper anode current collector. For both LIBs and NIBs, the gravimetric capacity of the cathode is lower than that of the anode. Lithium rich and nickel rich layered oxides and other emerging cathodes are being explored. Researchers are actively pursuing Group 16 element based cathodes, e.g. Li-O_2, Li-S batteries. There is the documented low reactivity between solid sulfur and sodium at room temperature. Although major advances in room temperature Na-S systems have been recently mademost sodium-sulfur batteries rely on molten salt and operate above 300°C. Selenium possesses similar chemical and electrochemical properties to sulfur, but orders of magnitude higher electrical conductivity. Selenium with an equilibrium trigonal structure has an electrical conductivity on the order of 10^{-3} S m^{-1}, while amorphous Se has a conductivity on the order of 10^{-11} S m^{-1}.[25][26] For comparison sulfur is at 10^{-27} S m^{-1}. Selenium is a reasonably priced element, being around $ 32/kg when purchased in industrial quantities. When reacted with Li or Na, selenium has only a slightly lower energy density as compared with sulfur ($LiSe_2$, $NaSe_2$, 3254 mAh cm^{-1} vs. 3467 mAh cm^{-1}). It has been recently demonstrated that selenium electrochemically reacts with both Li and Na in standard carbonate based electrolytes. Despite the heavy focus on specific capacity (energy per weight) in scientific literature, it is the energy density (energy per volume) that is the primary consideration for most portable, stationary and even automotive applications. Our approach here is fundamentally different from that of previous studies. Rather than seeking to create a nanostructured high – surface area electrode based on Se and a nano – carbon, we achieve the opposite by creating a low surface area monolithic electrode-grade film. On a per volume basis, a dense electrode is twice as energetic as the same electrode when it is fabricated into a micro or a nano powder.

Results and Discussion NanoCellulose derived Mesoporous Carbon film (NCMC) was prepared by a sacrificial-template method, followed by carbonization. In summary, Tetraethylorthosilicate (TEOS) was hydrolyzed in an aqueous system forming a silica sol, which self-assembled with the nanocellulose colloids during stirring. After the water has fully evaporated, the resultant opalescent colored cellulose-silica thin film was pyrolyzed in an argon atmosphere at 1000°C, yielding carbon-silica composite films. Next, ordered mesoporosity was obtained by removing the silica through HF etching.

Figure 1a illustrates the dense macroscopic flakes of monolithic Se-NCMC, showing a plan view image of a fractured film. As will be demonstrated by the N_2 adsorption data in the next set of figures, Se-NCMC does not display any remaining open porosity, although some closed porosity undetectable by BET may still be present. Per the energy dispersive X-ray (EDX) spectroscopy maps of Se shown in **Figure 1**b, the Se distribution is completely uniform within the resolution of the analysis. A thin Se layer also likely coats the carbon film surface. **Figure 1**c shows a SEM image of a cross-section Se-NCMC flake along with a corresponding Se element map of the same region. The selenium signal is uniform through the flake thickness, which proves full penetration of selenium into the pores throughout. **Figure 1**d shows a bright TEM micrograph of a small fragment Se-NCMC and the corresponding diffraction pattern. The pattern did not show any Bragg reflections, only an amorphous halo. Therefore, the composite is amorphous with only short-range near neighbor ordering for both the Se and the carbon host.

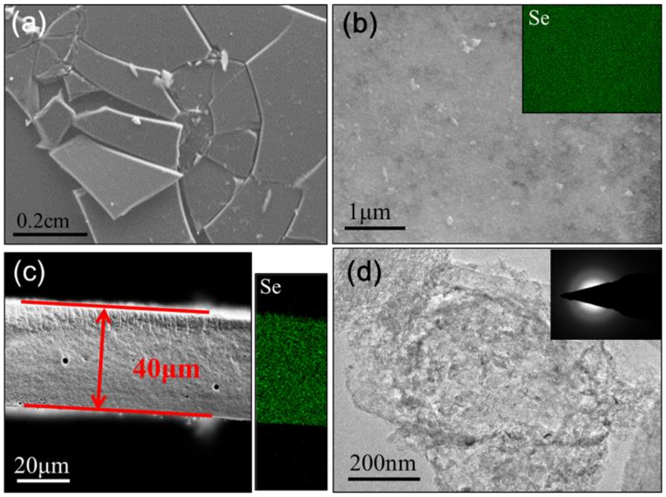

The electrochemical functionality of Se-NCMC was investigated, employing lithium and sodium metal as anodes. Depending on whether the target application is lithium/sodium ion batteries (LIBs, NIBs) or lithium/sodium metal batteries (LMBs, NMBs), this configuration may be considered as "half-cell" or as "full cell". Here the envisioned system is based on a metal rather than on a graphite anode, making LMBs and NMBs the targeted application. We employed a standard organic carbonate-based (EC/DMC) electrolyte with $NaClO_4$ salt, without any additives, and sodium metal as the anode. **Figure 2**a shows the CV curve of the Se-NCMC against sodium, tested between 0.5-3V at 0.1 mVs^{-1}. Compared to the Li-Se system, the cathodic/anode peaks for the Na-Se are much broader. As shown in **Figure 2**b, the galvanostatic discharge/charge profiles for Na-Se are also more sloped in shape with less pronounced plateaus. For the Na-Se system, the observed broad redox peak and sloped voltage profile reveal that the reaction is more complex than just a direct transformation between Se and Na_2Se. Likely there are one or a series of intermediate Na-Se phases involved (e.g. Na_2Se_2), and/or the terminal phase changes in structure/chemistry during sodiation (e.g. $Na_{2-\delta}Se$). Per **Figure 2**c, the discharge process exhibits gravimetric energy of over 400 Wh kg^{-1} and volumetric energy of over 900 Wh L^{-1}. **Figure 2**d shows the capacity of Se-NCMC cathode against sodium, at 0.1C – 4C (0.068 Ag^{-1} - 2.7 Ag^{-1}). Reversible capacities by active mass(electrode mass) were 301(210), 265(186), 198(139) $mAhg^{-1}$, obtained at 1C – 4C respectively. The corresponding volumetric capacities are 500, 441 and 328 mAh cm^{-3}. As will be further discussed, this performance is fairly comparable to the Li system in terms of capacity retention with increasing rate, although the low rate baseline capacity is lower with Na. The cyclability of Se-NCMC cathode in Na cell was tested at the same current as with

Li, i.e. 0.2C (135 mAg^{-1}). As shown in **Figure 2**e, although the electrode delivered a lower initial capacity value than with Li, it was overall quite stable during cycling.

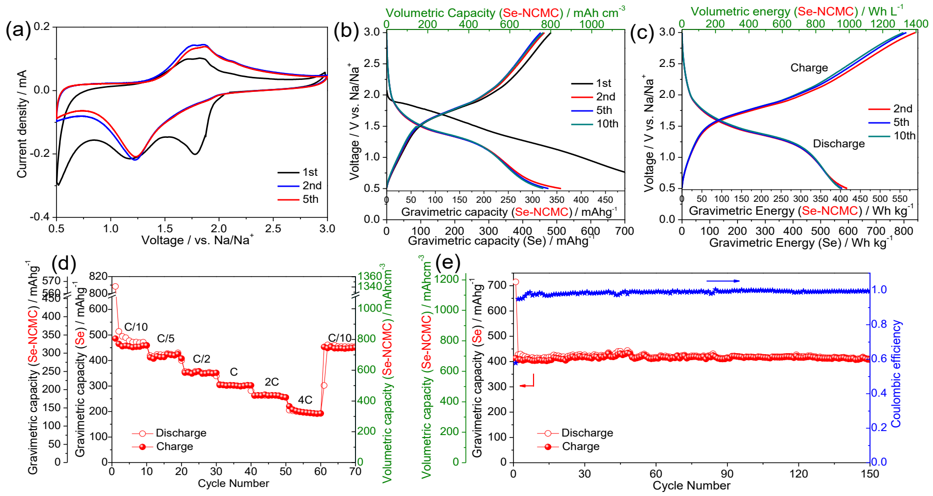

To further elaborate the electrochemical kinetics of Se-NCMC with lithium and sodium, we investigated its current response behavior at scan rates of 0.1 - 5 mVs^{-1} These results are shown in **Figures 3**a-b, for Li and Na systems, respectively.

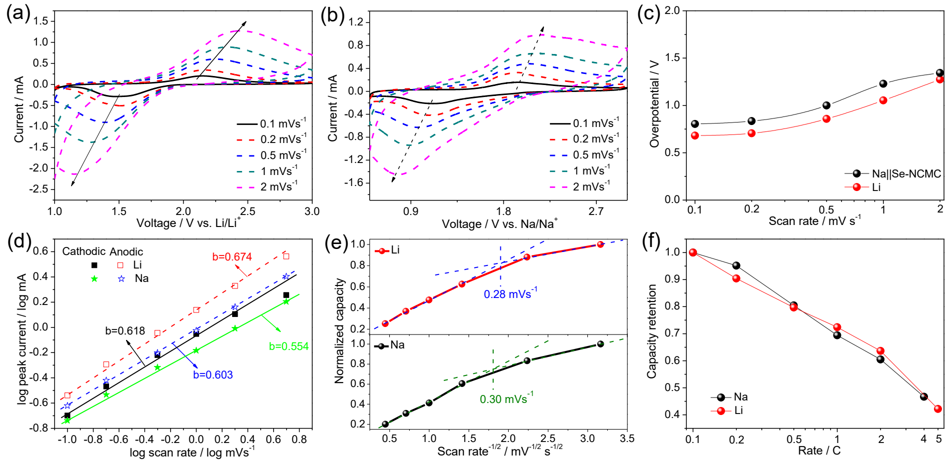

Future Plans: In the next reporting period we will be simultaneously pursuing collaborative fundamental research in multi-rate rate Na storage mechanisms/phenomena in anode carbons with various structure/chemistry, Se and Se-S cathodes for sodium metal batteries, and Na metal anodes.

Publications:

J. Ding, H. Zhou, H. Zhang, L. Tong, D. Mitlin, Selenium impregnated monolithic carbons as cathodes for high volumetric energy lithium and sodium metal batteries. ***Advanced Energy Materials***, 2017, 1701918.

Programming Function via Soft Materials: Dynamic Polymer Networks

Jeff Moore, Paul Braun, Randy Ewoldt, Ralph Nuzzo, Ken Schweizer, Frederick Seitz Materials Research Laboratory, University of Illinois at Urbana-Champaign, Urbana, IL 61801

Program Scope

The cluster has established a unique enabling vision for materials that embraces the dynamically reconfigurable 3-dimensional organization of building blocks into architectures that facilitate ion and electron transport, provide unique mechanical responsivities, and underpin advanced energy harvesting and storage concepts as well as other applications. This presentation will focus on an effort within Thrust 1: Reconfigurable and Dynamic Assemblies entitled *Dynamic Polymer Networks*

Recent Progress

Understanding the Force-Modified Potential Energy Surface: Work in the past year involving **Braun** and **Moore** has focused on both gaining a better fundamental understanding of mechanochemical activation as well as developing novel mechanoresponsive materials. One of the prevailing, unsolved challenges in the field of mechanochemistry is the heuristic approach that is used to design and discover new mechanophores. A main outcome of this project is to develop rational mechanophore design principles by deepening our fundamental understanding of mechanochemical transduction across the multiple length scale. Our approach combines materials theory and simulation together with synthesis and testing.

The naphthopyran mechanophore is a promising new family of mechanochromic switches that is central to the studies described here. Research on the naphthopyran has yielded important advances illustrating its role as a molecular platform for advancing basic science principles in mechanophore design (Fig. 1). One gap in knowledge that is central to the field is to understand the force-to-chemical energy transduction process. From a practical standpoint, this information is relevant to mechanophore design (e.g., how do various modes of mechanophore coupling to macromolecules or polymer networks alter its force-modified potential energy surface). We

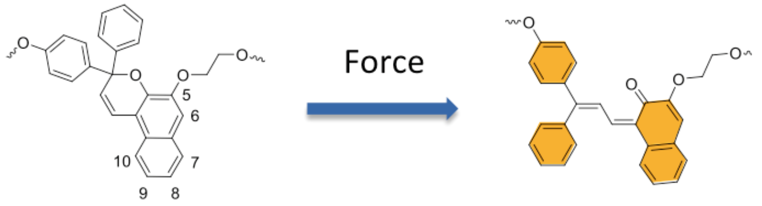

Fig. 1. When the NP5, NP6 , and NP7 regioisomers are incorporated into a crosslinked PDMS matrix and subjected to mechanical force they undergo a 6π electrocyclic ring opening reaction to form the orange colored merocyanine species.

tested this question by studying the previously reported NP5 mechanophore and two additional regioisomers. CoGEF (Constrained Geometries Simulate External Force) calculations predict that NP5 is activated at a lower F_{max} than NP6 and that NP7 is not expected to exhibit mechanochromism. A comparison of the F_{max} values of the unpublished regioisomers is shown in Fig. 2. Experimental mechanical testing, showed that both NP6 and NP7 are mechanochromic and that the maximum absorbance at different true stress values differed between the three mechanophores when normalized to remove the effect of differing extinction coefficients. The maximum absorbance of NP5, the previously published mechanochromic regioisomer, increased the most with increasing true stress followed by NP6 and then NP7. Thus, we have shown that the color switching properties of naphthopyran depend on the regiochemistry of attachment. This is important in our pursuit of rationally designed mechanophores as it provides fundamental insight into the relationship between structure and mechanochemical activation by systematically changing how the mechanical field couples to the mechanophore's force-modified potential energy surface. Recent computational findings from the Moore and Braun groups have shown that electronic effects alter the force-modified potential energy surfaces to enable an additional level of tunability. These findings open the way to our ongoing and future systematic studies.

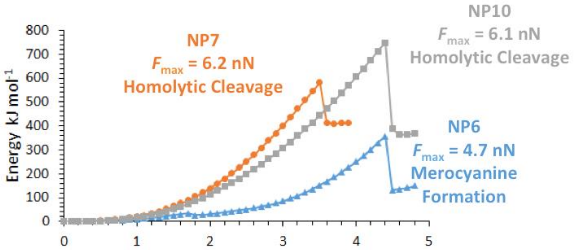

Fig. 2. DFT (CoGEF) calculations at the B3LYP/6-31G* level of theory show that the value of F_{max} for NP6 is higher than that of NP5, which has an F_{max} value of 4.1 nN, but lower than those of NP7 and NP10. Experimentally we found that both NP6 and NP7 exhibit mechanochromism.

Dynamic Polymer Networks: **Ewoldt** and **Schweizer**, working with Braun and Moore, have synthesized, characterized and analyzed spiropyran-containing polymers in the liquid state that form light and temperature triggerable non-covalent reversible crosslinks [1]. The pendant spiropyran can be triggered to transform reversibly between an uncharged (ring-closed) and a zwitterionic (ring-open) state (Fig. 3). In the ring-open state it can form coordination complexes with metal cations which dissociate upon ring-closure, enabling reversible crosslinking. Viscoelastic data suggest ~15% of spiropyrans participate in crosslinks. Guided by computational studies, progress has also been made (Moore, Braun, Ewoldt and **Nuzzo**) in the search for new molecular switches. A new system based on naphthopyran and its regioisomers has been identified, attached to polydimethysiloxane polymer chains. In parallel with the experimental efforts, an equilibrium statistical mechanical theory (Schweizer) has been constructed for the liquid structure of associating polymers. Predictions for the intermolecular pair correlation functions between all species have been made as a function of experimentally-controllable variables. Fig. 4 shows how the effective crosslink functionality or physical bond number of a simple copolymer model depends on the strength and spatial range of interchain attractions.

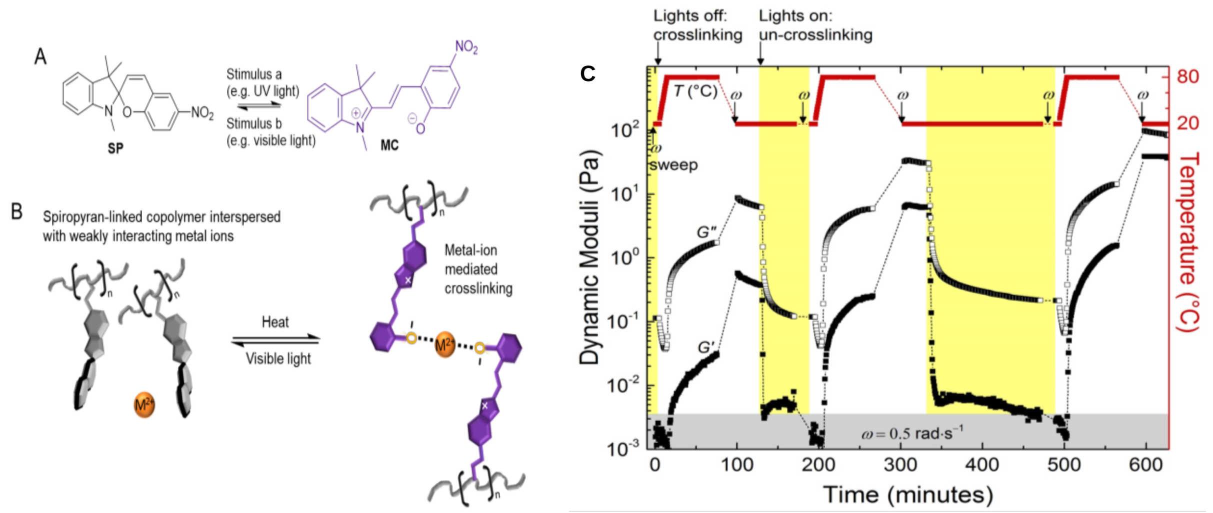

Fig. 3. (A, B) Spiropyran (SP) as a multifunctional molecular switch which heat triggers polymer crosslinking and uncrosslinking via light. (C) Rheological measurements for 24.5 wt% poly(di(ethylene glycol) methyl ether methacrylate – spiropyran containing methacrylate) in propylene carbonate with 2:1 SP:$Co(NTf_2)_2$ that establish the stated functional response.

In a complementary effort, Ewoldt and Schweizer have more deeply tested our model formulated last year [2] for weakly nonlinear viscoelastic properties as probed in medium-amplitude oscillatory shear in new parameter regimes [3] for strain-stiffening reversible hydrogel networks of poly(vinyl alcohol) (PVA) transiently-crosslinked by sodium tetraborate (Borax). For all eleven compositions studied the model accounts very well for our third-harmonic data. Schweizer and Ewoldt have also developed a microscopic statistical mechanical theory for understanding the key physical mechanism driving the intrinsic nonlinearity of these associating polymer networks -- deformation-induced change of local polymer packing due to polymer orientation and stretching. This is predicted to result in an increase of the transient crosslink density due to an enhancement of the interchain correlation function near contact [4]. The theory is in remarkable agreement with our observations on PVA-borax, and is also relevant to dynamic polymer networks based on mechanophores and other material systems.

Future Plans

We aim to understand how to increase the degree of transient crosslinking and optimize the design of reversible, stimuli-responsive polymers based on triggerable mechanophores. Systematic experimental studies (Braun, Ewoldt, Moore, Nuzzo) will explore how chemically-distinct spiropyrans and other mechanophores respond to a wider range of external stimuli including heat, light, pH and mechanical force. The role of flow-induced chain orientation as a strategy to improve mechanochemical transduction will be studied, and strategies for extending these responsive network materials to function in aqueous environments which is a major challenge. Our theories (Schweizer) of the structure of associating polymers, and of deformation-induced increases of transient crosslink density (Ewoldt, Schweizer), will provide a foundation to

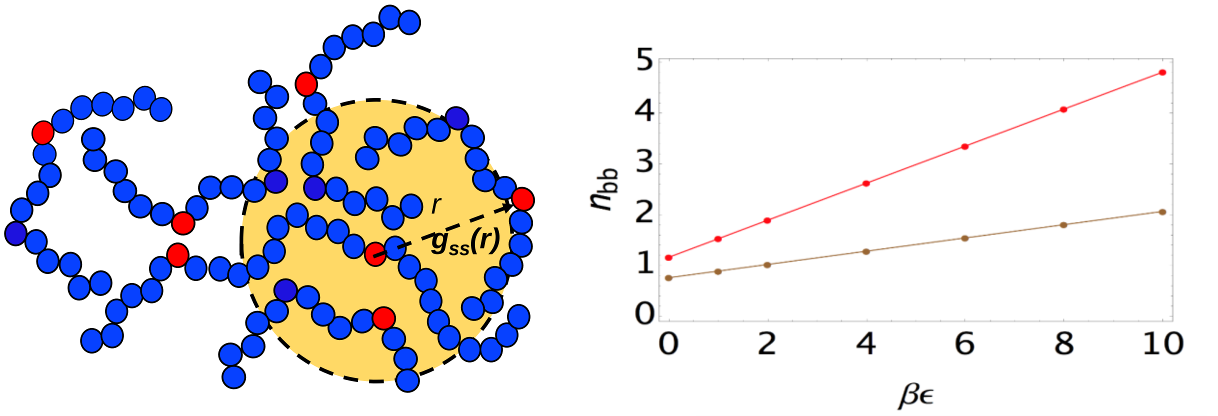

Fig 4. (left) Schematic of statistical mechanical theory for intermolecular structure of polymers with associating groups that can form reversible crosslinks. (right) Predicted mean number of monomers forming a transient crosslink is shown as a function of physical bonding energy (in units of thermal energy) for a very short (red) and longer (brown) range attractive interaction.

create predictive force-level theories for the dynamics of these physical network forming polymer liquids.

References

(1) Epstein, E. S.; Martinetti, L.; Carey-De La Torre, O.; Moore, J. S.; Ewoldt, R. H.; Braun, P. V., Modulating non-covalent crosslinks with molecular switches, Under review.
(2) Bharadwaj, N. A.; Schweizer, K. S.; Ewoldt, R. H., A strain stiffening theory for transient polymer networks under asymptotically nonlinear oscillatory shear, *Journal of Rheology* **2017**, *61*, 643-665.
(3) Carey-De La Torre, O.; Ewoldt, R. H., First-harmonic nonlinearities can predict unseen third-harmonics in medium-amplitude oscillatory shear (MAOS), *Korea-Australia Rheology Journal* **2018**, *30*, 1-10.
(4) Carey-De La Torre, O.; Martinetti, L.; Schweizer, K. S.; Ewoldt, R. H., Inferring the strain-stiffening mechanism in an associating polymer network by medium-amplitude oscillatory shear (MAOS), *Macromolecules*, Under review.

Publications (this sub-task only)

(1) Epstein, E. S.; Martinetti, L.; Carey-De La Torre, O.; Moore, J. S.; Ewoldt, R. H.; Braun, P. V., Modulating non-covalent crosslinks with molecular switches, Under review.
(2) Bharadwaj, N. A.; Schweizer, K. S.; Ewoldt, R. H., A strain stiffening theory for transient polymer networks under asymptotically nonlinear oscillatory shear, *Journal of Rheology* **2017**, *61*, 643-665.
(3) Carey-De La Torre, O.; Ewoldt, R. H., First-harmonic nonlinearities can predict unseen third-harmonics in medium-amplitude oscillatory shear (MAOS), *Korea-Australia Rheology Journal* **2018**, *30*, 1-10.
(4) Carey-De La Torre, O.; Martinetti, L.; Schweizer, K. S.; Ewoldt, R. H., Inferring the strain-stiffening mechanism in an associating polymer network by medium-amplitude oscillatory shear (MAOS), *Macromolecules*, Under review.

Informed Materials Design Principles From Local Structures and Dynamics In Hybrid Inorganic-Organic Perovskite Halides [DE-SC001608]

James R Neilson
Department of Chemistry
Colorado State University

Program Scope

Hybrid inorganic-organic perovskite halides have the potential to shift the paradigm by which we use functional semiconducting materials for energy-conversion technologies, as the structure/ property relationships of hybrid perovskites seem to follow a distinct set of rules in which the lattice and molecular dynamics play a large role. In this project, we elucidate the materials design principles behind if and how dynamic organic dipoles and disorder correlate with the paradigm-shifting electronic properties in hybrid inorganic-organic perovskite halides. The potential for transformative properties of these materials (*e.g.*, high photovoltaic energy conversion efficiencies, radiation detectors, and thermoelectrics) suggests that new materials design principles are needed to produce materials with tailored properties that will enable the next-generation of energy-relevant technologies.

Recent Progress

Orientational Glass formation in substituted hybrid perovskites

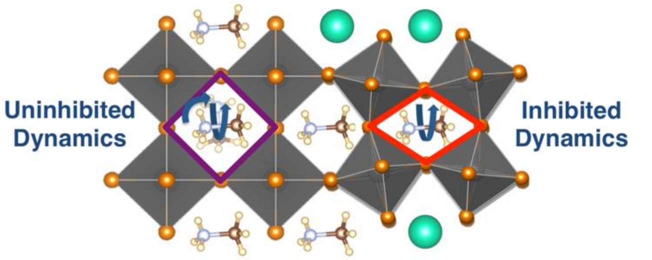

Figure 1: Substitution of Cs^+ for $CH_3NH_3^+$ in $(CH_3NH_3)_{1-x}(Cs)_xPbBr_3$ leads to inhibited dynamics of the organic dipole and formation of an orientational glass [1].

The organic cations found in hybrid perovskites form a plastic crystalline sublattice: the positions of the molecules have transitional order; however, their orientations are dynamically disordered. The orientations and displacements of these molecules are thought to play a role in mediating electronic carrier thermalization and relaxation. Our work shows that these dynamics are significantly hindered upon substitution of the organic molecule by the spherical cation, Cs^+ [1]. We synthesized various members of the solid solution, $(CH_3NH_3)_{1-x}(Cs)_xPbBr_3$, x = 0.0, 0.1, 0.2, 0.3, and 0.4 (values x > 0.4 phase separate). Neutron spectroscopy (particularly quasielastic and inelastic neutron scattering performed at Oak Ridge National Laboratory) revealed that partial substitution leads to inhibition of the orientational dynamics of methylammonium with increasing cesium substitution. The size mismatch and different octahedral tilting preferences between methylammonium and Cs yields rich temperature-dependent crystallographic behavior across the solid solution (Figure 1), including a rare re-entrant phase transition. These results point toward a theoretical framework to describe the complex dynamics in these materials. The primary impact of this finding lies in the inhibited motion of organic cations upon chemical substitution: substitution appears to be important for long-term device stability and performance, yet organic dynamics are implicated in long-lived excited states.

Anharmonicity and inorganic-organic coupling in hybrid perovskites:

Vacancy-ordered double perovskite halides provide a crystalline framework for understanding the coupling between octahedral subunits and dynamic organic cations. While Cs_2SnI_6 is a semiconductor with moderately high electron mobility, replacement of Cs^+ with the larger and dipolar organic methylammonium or formamidinium cations reduces the carrier mobility despite having nearly identical crystalline and electronic structures. This strongly implicates the essential role of lattice dynamics in deciding the macroscopic, functional properties. We observe distortions in the local coordination environment of $(CH_3NH_3)_2SnI_6$ and $(CH(NH_2)_2)_2SnI_6$ from pair distribution function analysis of synchrotron X-ray total scattering, but not in Cs_2SnI_6. Our analysis reveals that these distortions are a manifestation of an anharmonic potential brought about by coupling of the organic molecules to octahedral rotations (Figure 2) [2]. Our combined experimental and computational study correlates the reduced carrier mobility with the presence of soft, anharmonic lattice dynamics; these dyanmics enable the formation of polarons that increase the mass of carries while extending their lifetime.

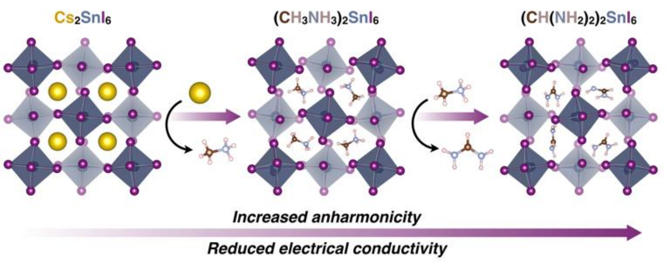

Figure 2: Coupling of dynamics between organic and inorganic sublattices lead to strong anharmonicity [2].

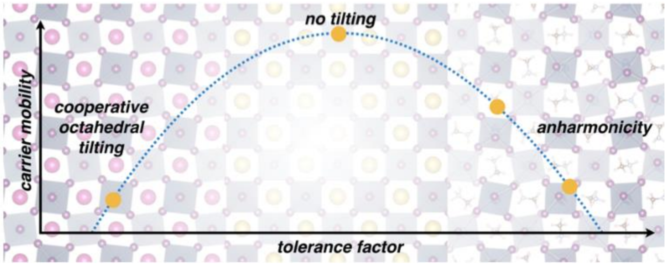

Figure 3: Electronic properties of vacancy-ordered perovskite halides follow the perovskite tolerance factor as well [3].

In the case that Cs^+ is replaced with a smaller cation, as in Rb_2SnI_6, the octahedral dynamics freeze out with long range order of octahedral tilting. We synthesized Rb_2SnI_6 and characterized this phase behavior with temperature-dependent neutron total scattering. Analysis of the octahedral tilting in the crystal structure, local structure, and properties of Rb_2SnI_6 revealed that the standard Goldschmidt tolerance factor provides a simple descriptor of the materials design principle for electronic transport properties in vacancy-ordered double perovskites (Figure 3) [3]. Together, our work provides evidence of organic-inorganic coupling and the atomistic origin and impact of anharmonic lattice dynamics on the charge transport properties of hybrid perovskite halide semiconductors.

Future Plans

Our group continues to elucidate how compositional substitution and structural modification influences the dynamics and phase behavior of hybrid perovskites. We will continue our use of neutron crystallography and spectroscopy to provide a molecular-level understanding of what enables and influences the dynamics, while also digging into the properties that result from these dynamics.

Publications

1. E. M. Mozur, A. E. Maughan, Y. Cheng, A. Huq, N. Jalarvo, L. L. Daemen, and J. R. Neilson, Orientational Glass Formation in Substituted Hybrid Perovskites. *Chem. Mater*. (2017), 29(23), 10168-10177.

2. A. E. Maughan, A. M. Ganose, A. M. Candia, J. T. Granger, D. O. Scanlon, and J. R. Neilson. Anharmonicity and octahedral tilting in defect-ordered hybrid perovskites. *Chem. Mater.*, 30(2), 472-483, 2018.

3. A. E. Maughan, A. M. Ganose, M. Almaker, D. O. Scanlon, and J. R. Neilson. Tolerance Factor and Cooperative Tilting Effects in Vacancy-Ordered Double Perovskite Halides. *Chem. Mater.* (2018). *ASAP*.

Understanding Novel Lewis Acid Doping Mechanisms in Organic Semiconductors

Thuc-Quyen Nguyen[a], Guillermo C. Bazan[a], Sergei Tretiak[b]
a) University of California, Santa Barbara b) Los Alamos National Laboratory

Program Scope

The objective of this study program is to combine synthesis, theory, optical characterization, chemical characterization, and electrical characterization of soft semiconductors with the goal of understanding emerging approaches to electrically dope soft semiconductors through the use of Lewis acids (LAs). The current understanding of this doping phenomenon suggests that energy level matching between the semiconductor and dopant is not a requirement, but the precise doping mechanism remains elusive. The currently proposed doping mechanism is shown in Figure 1. Successful completion of the program will provide a fundamental understanding of Lewis acid doping mechanisms in organic semiconducting materials, as well as guidelines for the design and synthesis of semiconductors that can best utilize the nonstandard approach of doping *via* LAs.

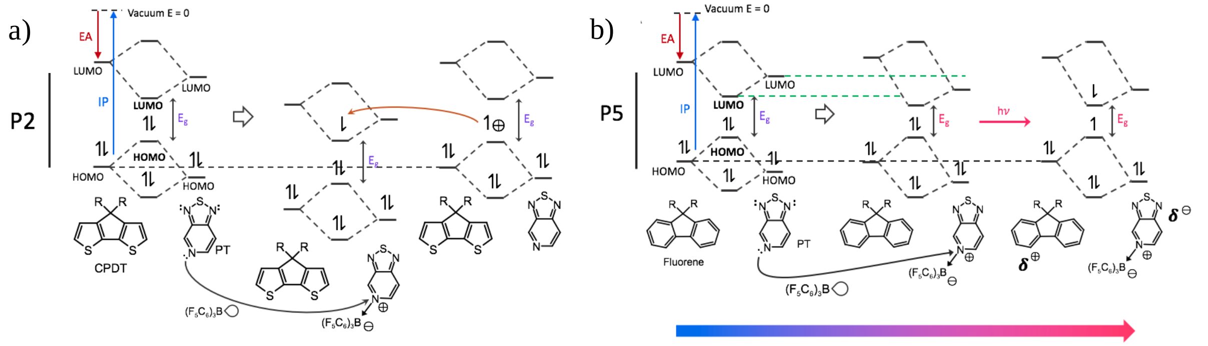

Figure 1. a) The proposed hypothesis for the formation of free charge carriers seen in P2 upon coordination with tris(pentafluorophenyl)borane (BCF). b) The proposed hypothesis for the changes of the optical band gap seen in P5 upon coordination with a LA, in this specific case BCF.

Recent Progress

Our initial efforts at studying the doping mechanism of Lewis acids with Lewis basic organic semiconductors has focused primarily on the characterization and analysis of polymers P2 and P5 (chemical structures shown in Figure 2). The only structural difference in these two polymers is the choice of the electron donating unit: P2 contains the electron-rich cyclopentadithiophene (CPDT) donor monomer, whereas P5 contains fluorene as the donor moiety, which is a less electron rich unit than CPDT. The change in relative electron-donating strength is apparent in the absorption spectra of the polymers (Figure 2): P2 has a much smaller optical bandgap than P5, indicating greater donor-acceptor interaction between the two subunits. Film absorption spectra of pristine P2 and P5 polymers are the same as in solution.

The redshift of the low-energy absorption peaks upon addition of BCF (in solution) indicates the formation of a Lewis acid adduct. The stoichiometry of these complexes is believed to be 1:1 Lewis acid:monomer repeat unit, which is consistent with the saturation of absorption upon increasing the concentration of Lewis acid. By applying a 1:1 binding isotherm model to the solution absorption data with BCF, we were able to determine the change in free energy upon formation of the Lewis acid adduct: -0.28 eV for P2 and -0.26 eV for P5.

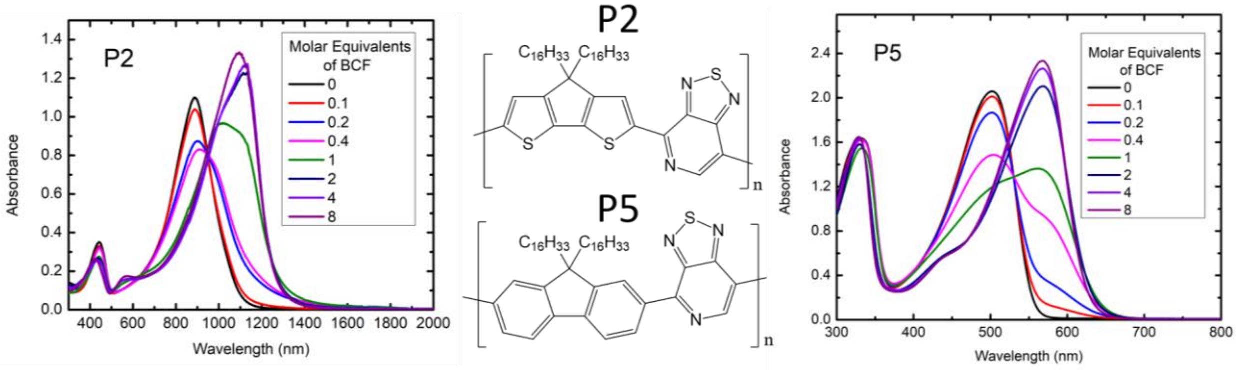

Figure 2. UV-vis-nIR spectra of P2 and P5 in solution before and after addition of BCF.

High-resolution XPS analysis supports the formation of the polymer-LA complexes *via* an increase in the area of peaks at higher binding energy. In addition, the particular peaks that are changing are consistent with Lewis acid binding to the pyridyl nitrogen in both P2 and P5. This result is also supported by ^{11}B nuclear magnetic resonance (NMR) spectroscopy analysis of benzo-1,2,5-thiadiazole with BCF and pyridyl-1,2,5-thiadiazole with BCF. Only the latter pairing shows a shift in the ^{11}B NMR spectrum, which is further evidence that the BCF preferentially binds to the pyridyl nitrogen.

EPR measurements in solution and in the solid state of P2 and P5 with BCF show the presence of an unpaired electron for only P2. Thus, while P5 seems capable of forming Lewis acid adducts in solution, it is incapable of generating unpaired electrons after adduct formation. The small signal in solid state EPR of the pristine P2 polymer is attributed to minor impurities leading to trap states in the polymer band gap allowing for formation of a small amount of free charge carriers without BCF (Figure 3).

The electrical conductance of pristine P2 significantly increases upon addition of 0.01 and 0.05 eq. of BCF. In addition, temperature dependent measurements show that a decrease in activation energy at high temperatures, which indicates a shift of the Fermi level position towards the HOMO level. This observation is supported by kelvin probe measurements which show a gradual increase in the work function of P2 films with increasing BCF concentration. The measured increase of the work function directly represents a shift of the Fermi level closer to the HOMO level, which is further evidence for electrical doping of P2 by BCF. For P5 however, we see that the pristine P5 and P5 with 0.05 eq. of BCF have very low electrical conductance even at elevated temperatures, presumably due to the relatively large band gap (~2.3 eV), which supports our EPR measurements (Figure 3). From a combination of X-ray Reflectivity measurements and temperature-dependent electrical measurements, we were able to estimate the doping efficiency of BCF with respect to P2. Having considered the high temperature activation energies to be equal to the depth of the Fermi level location with respect to the HOMO level EF - EHOMO we estimated the concentration of holes in the P2 films doped with 0.01 and 0.05 eq. of BCF to be 3.81 × 10^{17} cm^{-3} and 3.83 × 10^{18} cm^{-3}, respectively. The ratio (p/nBCF)×100% gives us the estimated doping efficiency of P2 by BCF, which increases from 4.5 to 9.1 % with an increase of the BCF content from 0.01 monomeric eq. to 0.05 monomeric eq.

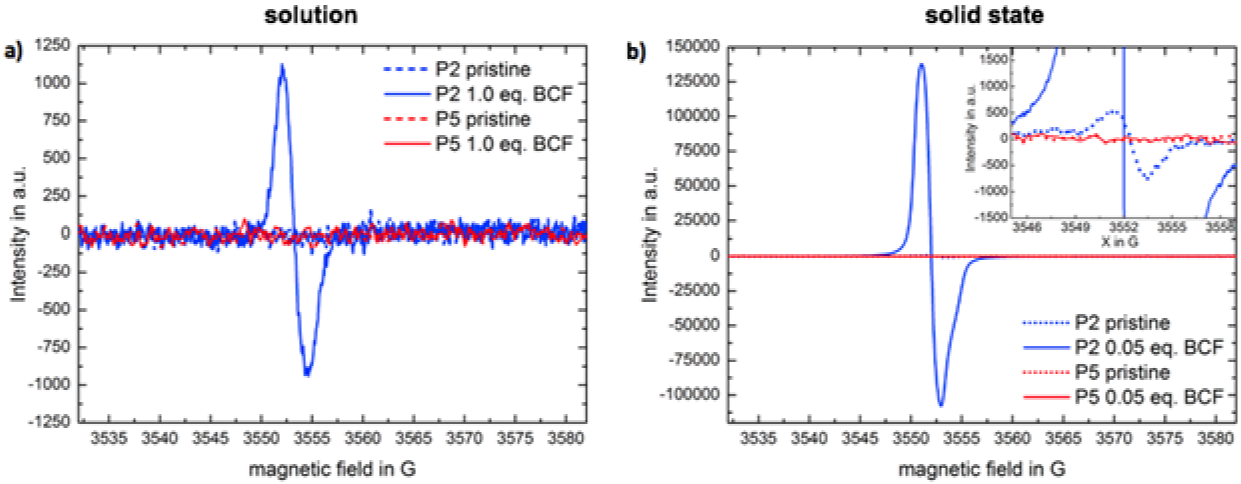

Figure 3. EPR measurements in solution (a) and solid state (b) of the polymers P2 and P5 with and without BCF.

In addition to experimental data, we are also currently pursuing computational approaches for gaining insight into the optical and electrical properties of known Lewis acid-conjugated (LA-CM) adducts to enable the prediction of new Lewis acid-polymer pairings in the future. We started with a small molecule for which there is already experimental data and structural characterization in order to develop our computational methodologies. These studies showed that increasing LA strength correlates with an increasing red-shift of the maximum absorption wavelength (λ_{max}), in agreement with spectroscopic studies. We have also investigated various functionals (B3LYP, CAM-B3LYP, WB97XD) with and without added empirical dispersion functions (GD3 and GD3BJ), and found that the combination of CAM-B3LYP and GD3BJ gives the most consistent results.[1,2]

In summary, we have demonstrated the impact of polymer chemical structure for doping by the Lewis acid BCF. The difference between the two polymers lies in the donor unit, with P2 containing the stronger electron-donating unit CPDT and P5 containing the weaker electron-donating unit fluorene. In both polymers, there is binding of the Lewis acid to the same nitrogen on the acceptor unit, but only P2 gives free charge carriers as seen via EPR and electrical measurements. However, given recent reports in the literature, more experiments need to be run with different polymers to further elucidate the precise doping mechanism.[3,4] In addition, theoretical studies have demonstrated the ability to reproduce the same UV-vis-nIR trends seen experimentally, but more work needs to be done in order to obtain the same experimental λ_{max} *via* DFT.

Future Plans

We plan to continue studying the effects of chemical structure on doping by Lewis acids by further modifications to either the donor or acceptor subunit of the polymer structure. These additional polymers have already been synthesized in small quantities, allowing us to begin our characterization of these materials while simultaneously investigating the doping mechanism. Systemically changing the polymer structure will allow us to determine the structural subunits that lead to favorable doping by Lewis acids. We will continue using the techniques described above to gain further mechanistic and electrical insight into the formation of Lewis acid adducts with semiconducting polymers. In addition, we will pursue further NMR (^{1}H, ^{19}F, ^{11}B, ^{13}C) characterization experiments to gain insights into the formation of Lewis acid adducts with semiconducting polymers, and additional electrical measurements with hole-only diodes and metal-insulator-semiconductor devices to better understand the doping efficiency in these organic semiconductor-Lewis acid adducts.

References

1. Zhugayevych, A. *et al.* Ab Initio Study of a Molecular Crystal for Photovoltaics: Light Absorption, Exciton and Charge Carrier Transport. *J. Phys. Chem. C* **117,** 4920–4930 (2013).
2. Coughlin, J. E., Zhugayevych, A., Wang, M., Bazan, G. C. & Tretiak, S. Charge delocalization characteristics of regioregular high mobility polymers. *Chem. Sci.* **8,** 1146–1151 (2017).
3. Pingel, P. *et al.* p-Type Doping of Poly(3-hexylthiophene) with the Strong Lewis Acid Tris(pentafluorophenyl)borane. *Adv. Electron. Mater.* 1600204 (2016). doi:10.1002/aelm.201600204
4. Lee, J. *et al.* A Planar Cyclopentadithiophene − Benzothiadiazole-Based Copolymer with sp 2 - Hybridized Bis (alkylsulfanyl) methylene Substituents for Organic Thermoelectric Devices. *Macromolecules* **51,** 3360–3368 (2018).

Publications

This project started in September 2017 so there is no publication yet.

Counterions for controlled dissolution, precipitation and stabilization of molecular clusters and extended lattices

May Nyman, Department of Chemistry, Oregon State University, Corvallis, OR 97331 USA
Carles Bo, Departament de Química Física i Inorgànica, Universitat Rovira i Virgili
Av. dels Països Catalans, 16, 43007 Tarragona (Spain)

Program Scope

Metal-oxo clusters from across the periodic table are like molecular (soluble and discrete) metal oxides. They both provide function in energy applications (i.e. oxygen evolution, hydrogen evolution, organic catalysts, sequestration of radionuclides, energy storage) and serve as models to understand growth, function and interfacial chemistry of related metal oxides. In some cases, the arrangement of metal-oxo polyhedra is similar to the related metal oxides; and in other cases they differ dramatically. In the case of the latter, one grand challenge is to convert the metal-oxo clusters to extended lattice materials while preserving the kinetically stabilized cluster forms, engendering new materials with unique properties. In addition to this grand challenge, we are seeking to understand the role of counter-ions and co-ions on stabilization and growth of metal-oxo clusters, as well as controlling solubility of clusters and their related metal oxide lattices. Current and future main research foci discussed below include: 1) Alkali-counterion promoted disassembly and reassembly of niobium-oxo clusters. 2) Defining and evaluating descriptors that predict solubility trends between polyoxometalates (POMs) and alkali counterions. 3) Defining the role of clusters in growth of first-row transition metal oxides, and pathways to clusters vs. pathways to metal oxides: how are they the same, how do they differ? 4) Corroborating molecular dynamics of alkali-POMs with experiment (X-ray and neutron scattering). Highlights and/or work in progress of these foci are described below.

Recent Progress

Alkali-counterion promoted disassembly and reassembly of niobium-oxo clusters. POMs are anionic metal oxo clusters of V, Nb, Ta, Mo, & W. The role of alkalis in templating self-assembly of POMs; precipitating, crystallizing and dissolving POMs; and even facilitating electron transfer to POMs is well-documented in multiple examples. On the other hand, there has never been documentation of these 'spectator' ions serving a deeper role of actually driving change in speciation. In a recently submitted study,[1] we describe how alkalis drive the conversion of decaniobate $[Nb_{10}O_{28}]^{6-}$ **{Nb_{10}}** to a large aggregates of $[(H_xNb_{24}O_{72})^{(24-x)-}]_y$ (y=2,4), **{Nb_{24}}**.The **{Nb_{10}}** POM has only been isolated with tetramethylammonium (TMA) counterions, and it is stable indefinitely at neutral pH (self-buffering pH) as a TMA salt. When we add alkali chloride salts to TMA-**{Nb_{10}}** solutions, conversion of **{Nb_{10}}** to **{Nb_{24}}** is documented by Raman spectroscopy (**figure 1**) and small-angle X-ray scattering (SAXS; **figure 1**). Both increased alkali concentration and increased alkali radius promotes a faster reaction, providing ample evidence that the alkalis are driving the reaction. The pH increase from 7 to 9 during this transition can be buffered, and the reaction still occurs via the same pathway, albeit more slowly. We can write a generalized balanced equation, showing it is possible for the proposed reaction to occur without added acid or base:

$$3[Nb_{10}O_{28}]^{6-} + (14+x)H_2O \rightarrow [Nb_{24}O_{72}H_8]^{16-} + 1.07[Nb_3O_6(OH)_3(H_2O)_4]^{2+} + 0.93[Nb_3O_6(OH)_5(H_2O)_2]^{2-} + xOH^- \qquad (2)$$

The experimentally obtained pH of 9 is computed with x=0.14. Cationic species must be considered in the exercise (unusual for POM chemistry), and these small trimer species were indeed detected by electrospray ionization mass spectrometry. Via computational studies (**figure 1**), we propose an energetically favorable reaction pathway in which alkalis distort **{Nb$_{10}$}**, opening up the cluster to a metastable intermediate, which is then accessible to reactivity with water. The computed reaction proceeds at neutral pH, only in the presence of alkalis. In essence, we are growing metal oxide networks using only ‘water and salt’, where these reactions usually requires harsher conditions of acid or base.

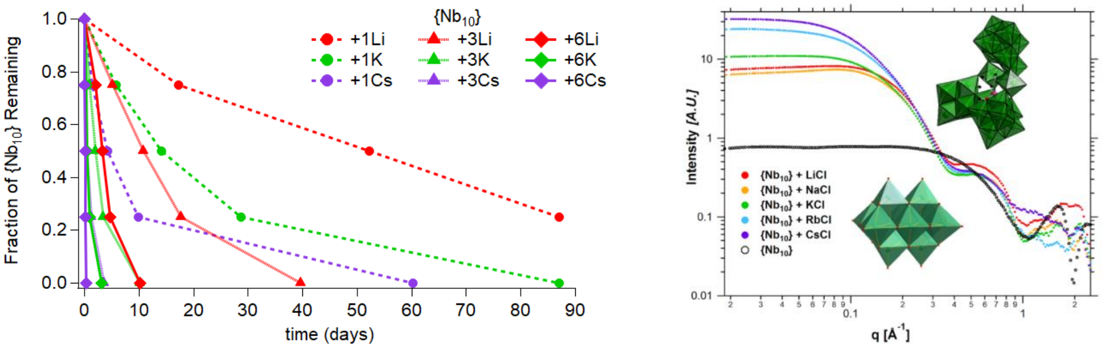

Figure 1. (***up left)*** Monitoring the conversion of **{Nb$_{10}$}** to **{Nb$_{24}$}** via diminution of the **{Nb$_{10}$}** Raman peak as a function of time, alkali, and alkali concentration. (***up right***) SAXS spectra of TMA-**{Nb$_{10}$}**, and TMA-**{Nb$_{10}$}** with added alkali chloride, promoting conversion to **{Nb$_{24}$}** assemblies. Increasing size (Cs>Rb>K>Na>Li) is noted by shift of the Guinier region to lower-q; and increasing I_0 (scattering intensity as q approaches 0 Å^{-1}). Inset shows **{Nb$_{10}$}** plus a computed dimer; **{Nb$_{24}$}$_2$**, which dominates the scattering solutions with added LiCl or NaCl to TMA-**{Nb$_{10}$}.**
Figure 2.(**right**) Energetic profile of the first steps of alkali-promoted conversion of **{Nb$_{10}$}** to **{Nb$_{24}$}**, the conversion of {Nb$_{10}$}-to-{Nb$_3$} plus {Nb$_7$ }, two fragments of **{Nb$_{10}$}** that are also identified by mass spectrometry.

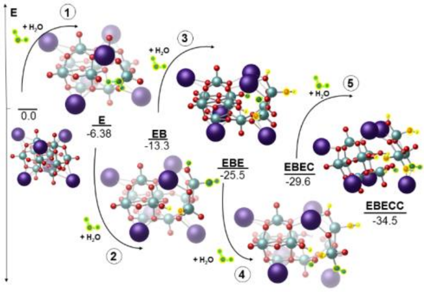

Another notable effect of the alkalis is linking together the **{Nb$_{24}$}** units, in which the larger alkalis correlate with larger aggregates of **{Nb$_{24}$}** building blocks. This was surmised from SAXS characterization, in conjunction with simulated SAXS from computational models. For example, computed structures suggests dimers **{Nb$_{24}$}$_2$**, dominate the solutions with LiCl and

NaCl as the added salt; while tetramers **Nb$_{24}$}$_4$** are assembled in the presence of CsCl, and we observe an intermediate mixture with KCl or RbCl. Although the solutions of TMA-**{Nb$_{10}$}** plus added alkali chloride appear monodisperse via the SAXS analysis; surprisingly their crystallization was not achieved by standard methods. Rather, the solutions, upon evaporation to dryness, yield transparent gels. The high solubility of these large aggregates (~2 molar Nb) near neutral pH coupled with their gelation behavior are extraordinary conditions for solution deposition of thin film materials or monoliths. The reaction is also readily driven by ammonium, if alkalis are not desired in the final material form. Moreover, heterometallic dopants can be introduced and incorporated into the niobium oxide lattice in the **{Nb$_{10}$}**-to-**{Nb$_{24}$}** alteration process.

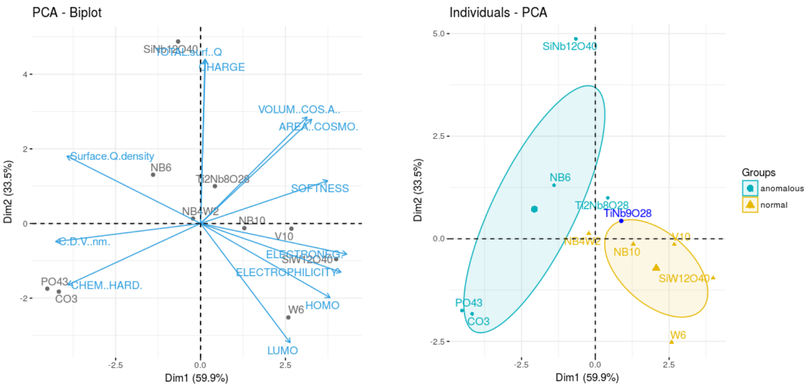

Figure 2 (***left***). PCA biplot of POM characteristics and individual clusters. Juxtaposition of variable and cluster means a high corresponding value. (***right***) Ellipse confidence of anomalous and normal solubility POMs, based on evaluated characteristics. Position of TiNb9O28 (in blue) is predicted based on characteristics. POMs that lie between the ellipsoids have transitional solubility behavior and warrant detailed study.

Defining and evaluating descriptors that predict solubility trends of POMs. Briefly, alkalis salts of POMs exhibit opposite solubility trends. Niobate POMs are generally very soluble as Cs salts, and insoluble as Li salts. Tungstate POMs are soluble as Li salts, and insoluble as Cs salts. As a first estimate this is related to charge density, and is consistent with simple oxoanions (carbonate, phosphate) solubility. Here, we are performing a principle component analysis (PCA) of characteristics of POMs to determine which property or combination of properties can be used to predict solubility of not only alkali POMs, but any oxoanion specie. Preliminary results are summarized in **figure 2**.

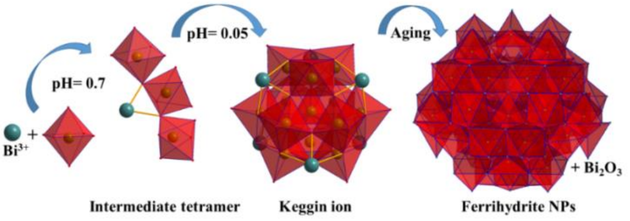

Figure 3. Schematic showing role of bismuth in promoting hydrolysis reactions in very acidic conditions, forming polynuclear heterometallic species. All reaction steps are controlled by Bi, opposing the effect of pH.

Role of clusters in growth of first-row transition metal oxides. Cluster building block motifs are recognized in compositionally similar metal oxides, and large polynuclear species are observed in solution prior to precipitation of metal oxides. Therefore researchers hypothesize that cluster building blocks are kinetic intermediates that influence the phase, composition and long range order of metal oxides grown from water. As mentioned briefly in the niobate study, pH is usually the main parameter that influences cluster and metal oxide formation in water. Generally, first row transition metals such as iron oxyhydroxides are formed by increasing the pH of a metal salt solution. We have recently shown[2,3] that Bi^{3+} can promote growth of metal-oxo clusters of Ti and Fe, in lieu of pH.

Bi^{3+} is one of the most insoluble metal oxides, even in acidic conditions. Therefore, in heterometallic mixtures of Bi^{3+} plus transition metals, hydrolysis reactions to form heteropolynuclear fragments (leading to metal oxides) occurs in high acid conditions. The role of strong acid is to disaggregate any poly-homonuclear Bi clusters that normally would form, so the poly-heteronuclear species can form. We have isolated a small tetramer, $BiFe_3$ at higher pH, which converts to a larger aggregate (Bi_6Fe_{13}) at lower pH (**figure 3** schematic), which is the opposite that we expect in the absence of bismuth. On the other hand, if Bi is removed from the solution, the preassembled iron-oxo fragments undergo rapid conversion to iron oxyhydroxides. Contrarily, since Bi-O-M (M=first row transition metal such as Ti and Fe) linkages form in highly acidic conditions, it follows that heterometallic Bi-M oxides should be extremely *insoluble* in acid. Therefore they could be exploited, for example, as a water oxidation catalyst in polymer electrolyte membrane fuel cells.

Future Plans

Niobate studies**.** In our continued attempt to crystallize the large aggregates of $\mathbf{\{Nb_{24}\}_y}$ (for absolute identification and to further understand the high solubility), we will add heterometals that we hypothesize will stabilize the aggregates in key positions, in addition to peroxoanions of these heterometals. These activities will also further develop Nb-POM chemisty and provides a segue into more extensive Ta-POM chemistry. We will explore formation of niobate, alkali niobate, and doped niobate coatings from these neutral, high-Nb concentration solutions and (with collaboration) test properties including ferroelectric response, acid stability and supercapacitance.

Defining descriptors for oxoanion and POM solubility trends. We will explore other descriptors to better understand the POMs that do not lie in the predicted solubility trend ellipsoids (including $[Nb_4W_2O_{19}]^{6-}$ $[Ti_2Nb_8O_{28}]^{8-}$and $[TiNb_9O_{28}]^{7-}$). Since these are all of mixed metal composition, we will investigate acid-base behavior and electronegatively of specific oxygen sites. We will also investigate kosmotropic effects in conjunction with molecular dynamics. From the experimental side, we will study the solution chemistry of these outliers (in addition to POMs with better-understood solubility behavior), using SAXS and neutron scattering. By combining neutron and X-ray scattering we can simulate scattering data of not just the POM, but the solution as a whole, developing a means to utilize the high-q solvent scattering region of spectra. These spectra will be compared to those generated from molecular dynamics.

First row transition-metal clusters & Bi. We will study Ti-sulfate solutions by X-ray absorption spectroscopy (collaboration), SAXS and neutron scattering to determine speciation, their evolution to TiO_2 in the industrial process, and determine if structural motifs are preserved in the transition. We will produce acid stable matrices (i.e. transition metal-Bi oxides) containing redox active POMs and assess the stability and activity for water oxidation (collaboration) in PEM fuel cells. We will investigate the transition of Zn-Cr nitrate solutions to polynuclear species, and to oxyhydroxide precipitates. We will investigate the cluster-to-oxyhydroxide pathway of iron-oxo clusters. The combined results of these two studies will help develop a general framework to understand if clusters lie on the same or different reaction pathway between monomers and metal oxide lattices.

Publications

1. Sures, Dylan, Centellas, Mireia Segado, Bo, Carles, Nyman, May. “Alkali-driven disassembly and reassembly of molecular niobium oxide in water”. In review, *Journal of the American Chemical Society* (2018)
2. Sadeghi, Omid, Mehran Amiri, Eric W. Reinheimer, and May Nyman. "The Role of Bi^{3+} in Promoting and Stabilizing Iron Oxo Clusters in Strong Acid." *Angewandte Chemie* 130, no. 21 (2018): 6355-6358.
3. Molina, P. I., Kozma, K., Santala, M., Falaise, C., & Nyman, M. (2017). Aqueous Bismuth Titanium-Oxo Sulfate Cluster Speciation and Crystallization. *Angewandte Chemie (International ed. in English)*, *56*(51), 16277.
4. Nyman, M. (2017). Small-angle X-ray scattering to determine solution speciation of metal-oxo clusters. *Coordination Chemistry Reviews*, *352*, 461-472.
5. Sures, Dylan, & Nyman, May. (**2017**). Anomalous Cesium Ion Behavior in Aqueous Polyoxometalate Solutions, *Cesium: Properties, Production and Applications* (119-148). Nova Science Pub Inc (book chapter).
6. Fullmer, L. B., and M. Nyman. "Probing Crystallization Pathways in Group V Polyoxometalate Solutions." *Journal of Cluster Science* 28, no. 2 (2017): 813-823.
7. Bandeira, N.A., Sadeghi, O., Woods, T.J., Zhang, Y.Z., Schnack, J., Dunbar, K., Nyman, M. and Bo, C., 2017. Magneto-Structural Analysis of Iron (III) Keggin Polyoxometalates. *The Journal of Physical Chemistry A*, *121*(6), pp.1310-1318.
8. Sures, Dylan J., Stefano A. Serapian, Károly Kozma, Pedro I. Molina, Carles Bo, and May Nyman. "Electronic and relativistic contributions to ion-pairing in polyoxometalate model systems." *Physical Chemistry Chemical Physics* 19, no. 13 (2017): 8715-8725.
9. Sadeghi, Omid, Clément Falaise, Pedro I. Molina, Ryan Hufschmid, Charles F. Campana, Bruce C. Noll, Nigel D. Browning, and May Nyman. "Chemical stabilization and electrochemical destabilization of the iron Keggin ion in water." *Inorganic chemistry* 55, no. 21 (2016): 11078-11088.
10. Sures, D.J., Sahu, S.K., Molina, P.I., Navrotsky, A. and Nyman, M., 2016. Distinctive Interactions of Cesium and Hexaniobate in Water. *ChemistrySelect*, *1*(9), pp.1858-1862.
11. Sures, D. J., Molina, P. I., Miró, P., Zakharov, L. N., & Nyman, M. (2016). Cesium salts of niobo-tungstate isopolyanions with intermediate group V–group VI character. *New Journal of Chemistry*, *40*(2), 928-936.

Engineering transport in confined environments of self-assembled stable radical polymers

Christopher Ober (PI), MS&E, Cornell University; Michael Flatté (Co-PI), P&A, ECE, U Iowa; Greg Fuchs (Co-PI), A&EP, Cornell University

Program Scope

We are focused on polymer-based stable radicals with a focus on the charge and spin transport behavior of these materials. Specific questions that are being addressed by this interdisciplinary research project include:

1. What are the fundamental mechanisms of electronic transport involving stable radical polymer materials?
2. How do stable radicals influence conductivity and charge storage in solid polymer films?
3. Can we control the conductivity of stable radical polymers by introducing conjugation to the polymer backbone?
4. What is the role of electron spin in the electronic transport through these materials?
5. Can we use confinement and orientation imposed through block co-polymer self-assembly to influence the conductivity and charge storage?

To address these questions, our research project brings together: i) synthesis and processing of stable radical polymers and copolymers combined with ii) the characterization of these new materials including electronic transport and electron paramagnetic resonance measurements. Finally, iii) theoretical and computational studies will play a key role in understanding the conduction process in the solid-state. This combination of approaches is aimed at establishing a fundamental and quantitative picture of electronic transport in these materials.

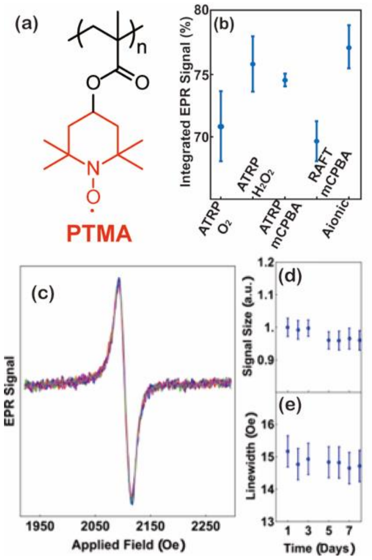

Figure l. (a) Chemical Structure of PTMA. (b) Radical yield for PTMA synthesized with different methods is between 70-80% but similar for each method. (c-e) On-chip EPR measured for over a week shows minimal variation in amplitude and linewidth, indicating the stability of a radical over the course of time.

Recent Progress

Radical Polymer Poly(TEMPO Methacrylate), PTMA

To understand the discrepancies between prior reports and our experimental findings, we prepared well-controlled PTMA using three of the available living synthesis methods: anionic, ATRP and RAFT polymerizations. Subsequent chemical treatments generate TEMPO radicals efficiently, and overoxidation species formed in earlier reports can be avoided using anionic polymerization or $H_2O_2/NaWO_4$ oxidation, which can provide PTMA more suitable for electrical measurements.

From quantitative EPR of solution state PTMA, we show that radical yield is relatively high for all synthetic methods and does not vary significantly depending on the specific approach (Fig. 1b). Using on-chip EPR, we also show that stable radicals in the PTMA solid film state do not oxidize or degrade over long times even in an ambient environment (Fig. 1c-e).

Our preliminary work suggests the solid-state conductivity of a radical polymer is very low, in agreement with some reports and not others. With a focus on the validity of the electrical measurement, and taking advantage of the opportunity to measure the conductivity for all synthetic preparations of PTMA, we designed a special electrical setup that is optimized to measure very low conductivity samples. We obtain conductivity in the 10^{-11} S/cm range for PTMA synthesized by anionic, ATRP and RAFT methods. Theoretical modeling with a variable range hopping (VRH) picture shows that for high radical yield PTMA, the fraction of TEMPO contributing to the solid-state conductivity is very small, rendering the material insulating.

Table 1. Conductivity of PTMA under various synthesis and oxidation conditions

Sample	Polymerization	Oxidation	Conductivity (S/cm)
PTMA-Anionic	Anionic	—	$1.09 \pm 0.76 \times 10^{-11}$
PTMA-H_2O_2	ATRP	H_2O_2	$5.59 \pm 0.78 \times 10^{-11}$
PTMA-RAFT	RAFT	*m*CPBA	$2.54 \pm 0.31 \times 10^{-11}$

Conjugated Radical Polymer – P3HT-TEMPO

Considering the insulating nature of PTMA, we next considered a π-conjugated radical polymer material system as an alternate approach for achieving electron transport in a single stable radical polymer using an alternate mechanism. We synthesized a series of conjugated polythiophenes with pendent TEMPO radical groups using Grignard metathesis polymerization (GRIM) and azide-click reactions, affording the resultant polymer with a regioregular backbone (~92% Head-Tail fraction), controlled molecular weight (6~9 kDa) and low dispersity (~ 1.10). We systematically varied the TEMPO radical attachment on the polythiophene backbone, and the resultant P3HT-TEMPO-X (X = 25, 50, 75 and 100%) are soluble in organic solvents, which simplified the subsequent structure characterization and film preparation.

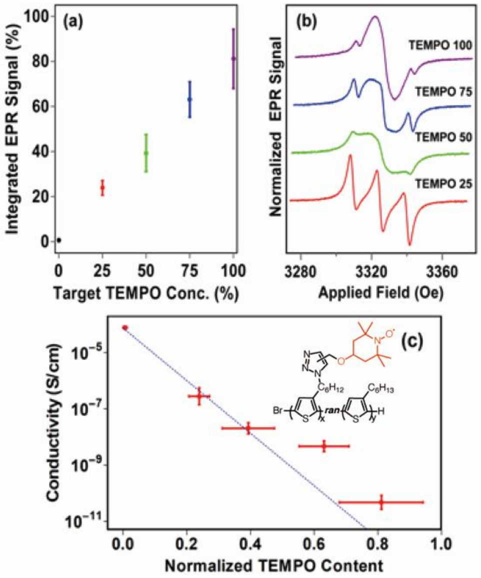

Figure 2. (a) Solution state EPR of P3HT-TEMPO with respect to target TEMPO concentration shows linear trend. (b) Individual lineshape for each species of P3HT-TEMPO samples synthesized. (c) Conductivity of P3HT-TEMPO with respect to TEMPO content. Dashed line shows a fit to exponential trend.

As shown in Fig. 2, quantitative solution state EPR of P3HT-TEMPO confirms that the fraction of attached TEMPO is well controlled. This conclusion is also supported by spectral lineshape. In particular, TEMPO groups with nearby neighbors contribute spectral weight to the singlet lineshape because the spin-spin interactions quench the triplet hyperfine splitting. As we increase the fraction of TEMPO, we observe that the singlet line contribution grows relative to the triplet as expected for a strong TEMPO synthetic yield.

Our incorporation of a conjugated backbone increases the conductivity compared to that of a radical polymer without a conjugated backbone; however, there is a trade-off between pendent TEMPO incorporation and order in the solid films which leads to an exponential relationship between conductivity and

TEMPO fraction (Fig. 2c). Theoretical modeling shows that this behavior can be explained by the disorder induced by the bulky pendent groups. This conclusion is supported by analysis of Raman spectroscopy and atomic force microscopy (AFM) data (Fig. 3). Upon an increase of TEMPO radical substituents, the intermolecular stacking in P3HT is impeded and amorphous aggregates form as the TEMPO content exceeds 50%. The intrachain electron transfer is further impeded as TEMPO content increases, as the symmetric P3HT C_α-C_β stretching peak at 1447 cm^{-1} increases to 1465 cm^{-1} in P3HT-TEMPO-100.

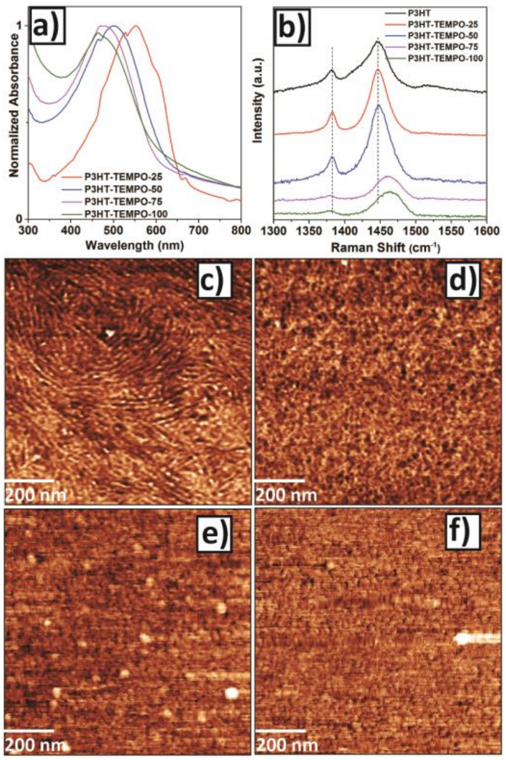

Figure 3. (a) UV-vis absorption of drop-cast P3HT-TEMPO-X film on glass substrate. (b) Raman spectra of drop-cast P3HT and P3HT-TEMPO-X films on Si substrate. AFM phase images of (c) P3HT, (d) P3HT-TEMPO-25, (e)P3HT-TEMPO-50, (f) P3HT-TEMPO-75 after spin-coating from chlorobenzene solution and annealing in THF.

The increase in disorder in the conjugated polymer introduces steric effects to polaron spin and charge transport in these materials, which prompted a fundamental theoretical investigation of the effect of confinement and steric hindrance on transport of charge and spin within polymers with radical side chains. The spin correlations in hopping are calculated by considering the spin-orbit effects in the side chains, which serve to preferentially orient the spins parallel to the orbital degrees of freedom in a ring, shown schematically in Fig. 4. As a result, we find that the hopping that involves spin flip is inversely correlated with the hopping that does not involve spin flip (when the rings are aligned the spin flip rates are weak and the non-spin-flip rates are fast, and when they are perpendicular the spin flip rates are large and the non-spin-flip rates smaller). We are now proceeding to constrain the relative orientation of the two rings, and expect that the effects on spin and charge transport will be dramatic.

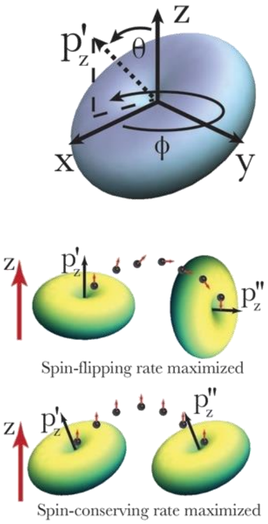

Figure 4. Depiction of primed local basis and un-primed global basis (top) and relative orientations leading to extrema in hopping rates.

P3HT-TEMPO doping

Another advantage of using a conjugated backbone is that we can charge-dope the system using iodine or 2,3,5,6-tetrafluoro-7,7,8,8-tetracyanoquinodimethane (F4-TCNQ). Although stable radical containing conjugated polymers lack conductivity in the neutral state, introduction of dopants can generate more charge carriers to further improve conductivity. With the presence of nitroxide radicals in P3HT-TEMPO species, this material system can help us to better understand the interplay of charge carriers (such as polarons) and the pendent radical group. In preliminary measurements we find that the EPR lineshape of F4-TCNQ doped P3HT-TEMPO-25 differs from undoped P3HT-TEMPO-25. We expect that a systematic

EPR study with different dopants and TEMPO concentration will reveal more information about the interaction between electron transporting polarons and the localized radical sites. Preliminary electrical transport measurements show strongly increased conductivity as expected. Whether the steric disruption caused by pendent radical groups persists in the doped polymer requires further investigation.

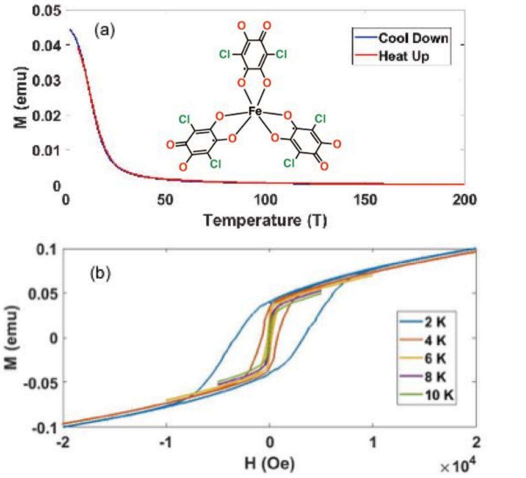

Figure 5. (a) Temperature- and (b) field-dependent magnetic measurement of iron-quinoid films showing ferromagnetic ordering at T=10.8 K.

Returning to the fundamental questions that we proposed as part of our program scope, the work performed under this project to date leads us to conclude that although spin is a valuable tool for understanding the properties of radical polymer materials, radical-mediated solid-state transport can be well-understood by variable-range hoping, and that there is no significant interplay between spin and charge transport in non-conjugated radical polymers. As a means of better understanding spin-charge interactions (question #4 above), we have begun the synthesis of hybrid metal-organic iron-quinoid materials [3] in which spin interactions are strong enough to create ferromagnetic order at accessible temperatures and the spins are located in well-defined, 2D periodic sites not possible in organic materials. Here the unpaired spin comes from a metal atom bonded into the molecular structure and the precise location and spacing will enable us to better understand spin-charge transport interactions. These materials are a model system, complimentary to radical polymer materials, to study spin-charge interactions in organic materials both above and below the ordering temperature. Figure 5 shows the magnetization of an iron-quinoid film we have made and measured as a function of temperature and magnetic field. We see an ordering temperature of T = 10.8 K and corresponding hysteresis.

Future Plans

We plan to focus our effort on understanding spin-charge interplay in organic materials, both in doped conjugated-backbone radical polymer systems as we have already described, and in hybrid-organic materials in which spin-charge interactions will be even stronger. The goal of our effort remains to obtain fundamental understanding in these materials leading to new functionality that can find applications including flexible electronics, sensing, and charge storage. We will do this synthesizing organic stable radicals coupled to conjugated materials and new compounds (like iron-quinoid materials) that have spin-charge combinations in organized and self-assembling systems.

References

1. Y. Zhang, A. Park, A. Cintora, S. R. McMillan, N. J. Harmon, A. Moehle, M. E. Flatté, G. D. Fuchs and C. K. Ober, "Impact of the Synthesis Method on the Solid-State Charge Transport of Radical Polymers." *J. Mater. Chem. C* **6**, 111 - 118 (2018)
2. Y. Zhang, A. Park, S. R. McMillan, N. J. Harmon, M. E. Flatté, G. D. Fuchs and C. K. Ober, "Charge Transport in Conjugated Polymers with Pendent Stable Radical Groups." *Chem. of Mat.*, submitted.
3. Ie-Rang Jeon, Bogdan Negru, Richard P. Van Duyne, and T. David Harris, "A 2D Semiquinone Radical-Containing Microporous Magnet with Solvent-Induced Switching from Tc = 26 to 80 K." *J. Amer. Chem. Soc.* **137**, 15699−15702 (2015)

Publications

1. Y. Zhang, A. Park, A. Cintora, S. R. McMillan, N. J. Harmon, A. Moehle, M. E. Flatté, G. D. Fuchs and C. K. Ober, “Impact of the Synthesis Method on the Solid-State Charge Transport of Radical Polymers.” *J. Mater. Chem. C* **6**, 111 - 118 (2018)
2. Y. Zhang, A. Park, S. R. McMillan, N. J. Harmon, M. E. Flatté, G. D. Fuchs and C. K. Ober, “Charge Transport in Conjugated Polymers with Pendent Stable Radical Groups.” Chem. of Mat., submitted.
3. S. R. McMillan, N. J. Harmon, and M. E. Flatté, “Steric Effects on Spin Dynamics in Organic Semiconductors.” *Phys. Rev. Lett.*, submitted.

Elucidating the Structural and Chemical Factors Influencing Alkali Ionic Conductivity

Shyue Ping Ong, University of California, San Diego

Program Scope

The aim of this project is to conduct fundamental investigations into the structural and chemical factors that affect ionic conductivity in oxide and sulfide structural frameworks using a combination of automated first principles calculations and topological analysis. This project comprises two complementary thrusts:

- Thrust 1: Detailed investigations will be conducted into several prototypical structure types / chemistries of significant interest in energy storage, where we will attempt to answer some of the most pressing questions regarding alkali conductivity in these structure types / chemistries.
- Thrust 2: A broader study encompassing all structures and chemistries under investigation will be undertaken. This broader study will data mine the results from the detailed investigations in Thrust 1 for insights into the relationships between structure, chemistry, and alkali ionic conductivity.

Recent Progress

Effect of Transition Metal Mixing on P2 $NaMO_2$ cathodes

The layered P2 sodium transition metal (TM) oxides are promising cathode materials for rechargeable sodium-ion batteries. While there have been extensive efforts to improve the performance of these materials via TM mixing strategies, there is currently a lack of understanding on the relationship between TM mixing and kinetics.

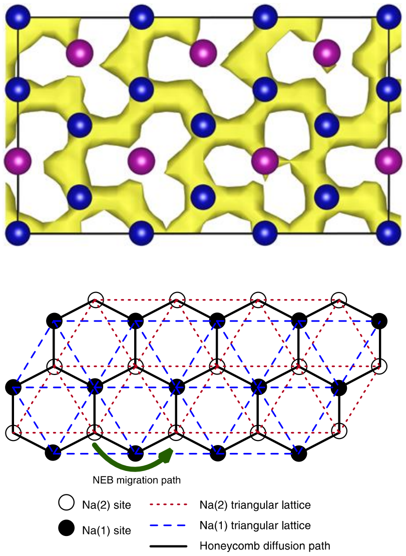

Figure 1: (Top) AIMD trajectories showing relative site preference in $Na_{0.5}Mn_{0.33}Co_{0.67}O_2$. (Bottom) Overlapping triangular lattices in P2 structure.

Using P2 $Na_xCo_{1-y}Mn_yO_2$ as a model system, we have developed a universal framework to guide TM mixing efforts in the layered P2 oxides.[1] Using AIMD simulations and CI-NEB calculations, we demonstrate that the TM coordination has a pronounced effect on the relative energy for Na to occupy the Na(1) site, which shares faces with two MO_6 octahedra. For instance, the presence of Mn is found to lead to a significant increase in the Na(1) site, while Fe decreases its energy. By employing a site percolation model, we derive theoretical upper and lower bounds on the concentration of TM species in the P2 layered oxides based on their effects on Na migration barriers.

Role of defects in superionic conductors

We conducted a detailed first principles study into the role of defects in promoting ionic conductivity in the argyrodite[2] Li_6PS_5Cl superionic conductor.[3] We show that Li^+ excess, charge-balanced by changes to the S^{2-}:Cl^- anion ratio, is crucial to enhancing the conductivity of Li_6PS_5Cl by increasing the occupancy of interstitial sites that promote long-range diffusion between cage-like frameworks (Figure 2). The predicted room-temperature conductivities and activation barriers are in reasonably good agreement with experimental values. We will also demonstrate that similar principles of defect control apply in other Li and Na superionic conductors, including the Na_3PS_4 family[4,5], and highlight analytical approaches (e.g., van Hove correlation functions) to characterize short and long-range diffusive processes in these materials.

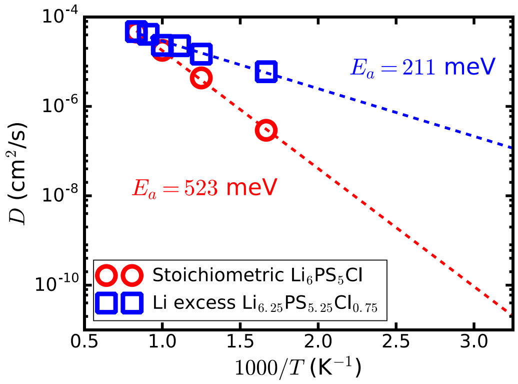

Figure 2: Arrhenius plot showing orders of magnitude differences in the ionic conductivity of stoichiometric vs Li-excess Li_6PS_5Cl.

Novel thiophosphate superionic conductors

Thiophosphate lithium superionic conductors, such as the $Li_{10}GeP_2S_{12}$ family[6,7] and the $Li_7P_3S_{11}$ glass-ceramic[8], have emerged as one of the leading contenders for solid electrolytes in all solid-state lithium-ion batteries, with ionic conductivities exceeding 10 mS/cm, on par or even exceeding that of organic solvent electrolytes. Many of these lithium thiophosphates bear significant structural similarities with Ag thiophosphates, e.g., $Li_7P_3S_{11}$ is similar to $Ag_7P_3S_{11}$,[9] and the Li argyrodite superionic conductors Li_6PS_5X (where X is a halide)[2] derive their name from the mineral argyrodite Ag_6GeS_8.

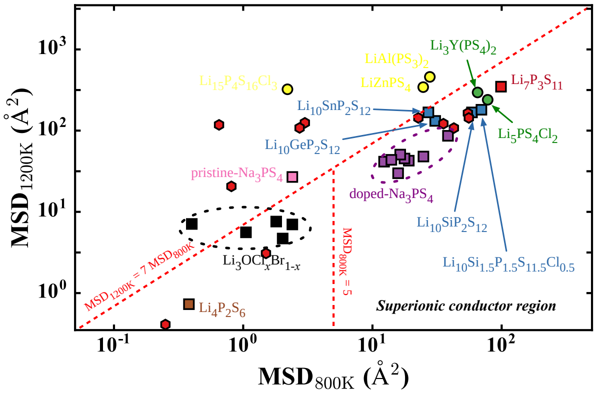

Figure 3. Plot of mean square displacement at 1200 K (MSD_{1200K}) versus MSD_{800K} for a wide range of known alkali conductors, predicted superionic conductors $Li_3Y(PS_4)_2$ and $Li_5PS_4Cl_2$, and new compositions (red hexagons, anonymized) studied in our follow-up A-M-M'-S screening work.

Driven by our hypothesis is that the larger Ag^+ ion can create topologies with larger channels for alkali diffusion, we have performed a comprehensive screening of the Li-P-S, Li-M-P-S, Na-P-S, Na-M-P-S chemical spaces (M is non-redox-active element) for novel alkali superionic conductors[10], including candidates obtained by replacing Ag with Li/Na in Ag-P-S and Ag-M-P-S compounds. We have developed an efficient tiered screening strategy that combines rapid topological evaluation with a short AIMD screening (see Figure 3) to rapidly exclude candidates unlikely to satisfy the stringent conductivity requirements using a minimum amount of computational resources. The screening results in several highly promising candidates that are predicted to satisfy the necessary combination of excellent phase and electrochemical stability, high Li+ conductivity, and low electronic conductivity. We will discuss in detail two highly related compounds – $Li_3Y(PS_4)_2$ (LYPS) and $Na_3Y(PS_4)_2$ (NYPS) – providing insights into the diffusion mechanisms and pathways in these materials. Utilizing insights on defect tuning from prior work, we further show that the Li$^+$ conductivity of LYPS can be enhanced from 2.16 mS/cm to 7.14 and 5.25 mS/cm via doping of Y^{3+} with Ca^{2+} and Zr^{4+}, with the concomitant creation of Li interstitials and vacancies, respectively.

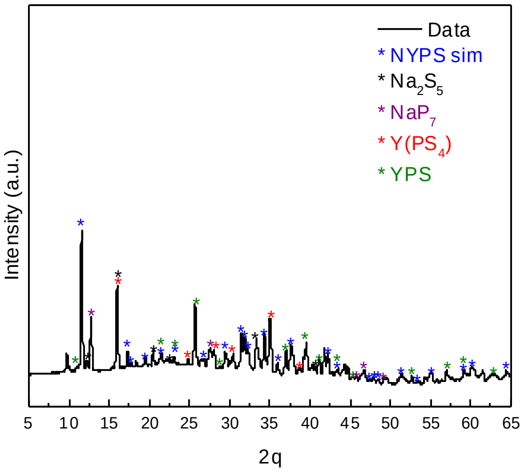

Figure 4. Preliminary XRD confirming formation of $Na_3Y(PS_4)_2$.

We have also performed a detailed assessment of the sodium analog, $Na_3Y(PS_4)_2$ for potential sodium solid electrolyte applications. From our density functional theory (DFT) total energy calculations along with ab initio molecular dynamics (AIMD) simulations, we predict that this material exhibits excellent phase stability, and 3D pathways for Na$^+$ diffusion with an estimated room-temperature Na$^+$ conductivity of exceeding 10 mS/cm, which is significantly higher than that of existing Na superionic conductors. Our collaborators in the Meng group at UCSD has successfully synthesized $Na_3Y(PS_4)_2$ (see Figure 4) and are currently conducting further optimizations on the synthesis conditions as well as characterizing its conductivity.

A provisional patent has been filed on the screening approach and all novel compositions identified.

Future Plans

Going forward, our plan is to go beyond extend the general insights we have obtained from our studies on alkali conductors to other ionic conduction phenomenon in energy-related systems. For instance, the techniques we have developed to study defect tuning and its consequences on macroscopic diffusivity (e.g., through the application of percolation models) can be applied to topologically similar systems such as halide diffusivity in hybrid organic-inorganic perovskites, a critical issue of interest for solar applications. We are also applying the principles of cation mixing to tune the structure, defects and phase stability of other families of superionic conductors to achieve maximum conductivity.

We are also in the process of distilling the insights of these prior works into a coherent set of design rules based on structural and chemical factors for identifying fast ion conductors.

References

(1) Zheng, C.; Radhakrishnan, B.; Chu, I.-H.; Wang, Z.; Ong, S. P. Effects of Transition-Metal Mixing on Na Ordering and Kinetics in Layered P2 Oxides. Phys. Rev. Appl. 2017, 7 (6), 064003 DOI: 10.1103/PhysRevApplied.7.064003.

(2) Deng, Z.; Zhu, Z.; Chu, I.-H.; Ong, S. P. Data-Driven First-Principles Methods for the Study and Design of Alkali Superionic Conductors. Chem. Mater. 2017, 29 (1), 281–288 DOI: 10.1021/acs.chemmater.6b02648.

(3) Deiseroth, H.-J.; Kong, S.-T.; Eckert, H.; Vannahme, J.; Reiner, C.; Zaiß, T.; Schlosser, M. Li6PS5X: A class of crystalline Li-rich solids with an unusually high Li+ mobility, Angew. Chemie Int. Ed., 2008, 47, 755–758, doi:10.1002/anie.200703900.

(4) Chu, I.-H.; Kompella, C. S.; Nguyen, H.; Zhu, Z.; Hy, S.; Deng, Z.; Meng, Y. S.; Ong, S. P. Room-Temperature All-solid-state Rechargeable Sodium-ion Batteries with a Cl-doped Na3PS4 Superionic Conductor. Sci. Rep. 2016, 6 (1), 33733 DOI: 10.1038/srep33733.

(5) Zhu, Z.; Chu, I.-H.; Deng, Z.; Ong, S. P. Role of Na+ Interstitials and Dopants in Enhancing the Na+ Conductivity of the Cubic Na3PS4 Superionic Conductor. Chem. Mater. 2015, 27 (24), 8318–8325 DOI: 10.1021/acs.chemmater.5b03656.

(6) Kamaya, N.; Homma, K.; Yamakawa, Y.; Hirayama, M.; Kanno, R.; Yonemura, M.; Kamiyama, T.; Kato, Y.; Hama, S.; Kawamoto, K.; et al. A lithium superionic conductor. Nat. Mater. 2011, 10 (9), 682–686 DOI: 10.1038/nmat3066.

(7) Bron, P.; Johansson, S.; Zick, K.; Schmedt auf der Günne, J.; Dehnen, S.; Roling, B. Li10SnP2S12: an affordable lithium superionic conductor. J. Am. Chem. Soc. 2013, 135 (42), 15694–15697 DOI: 10.1021/ja407393y.

(8) Seino, Y.; Ota, T.; Takada, K.; Hayashi, A.; Tatsumisago, M. A sulphide lithium super ion conductor is superior to liquid ion conductors for use in rechargeable batteries, Energy Environ. Sci., 2014, 7, 627–631, doi:10.1039/C3EE41655K.

(9) Yamane, H.; Shibata, M.; Shimane, Y.; Junke, T.; SEINO, Y.; Adams, S.; Minami, K.; Hayashi, A.; Tatsumisago, M. Crystal structure of a superionic conductor, Li7P3S11, Solid State Ionics, 2007, 178, 1163–1167, doi:10.1016/j.ssi.2007.05.020.

(10) Zhu, Z.; Chu, I.-H.; Ong, S. P. $Li_3Y(PS_4)_2$ and $Li_5PS_4Cl_2$: New Lithium Superionic Conductors Predicted from Silver Thiophosphates using Efficiently Tiered Ab Initio Molecular Dynamics Simulations. Chem. Mater. 2017, 29 (6), 2474–2484 DOI: 10.1021/acs.chemmater.6b04049.

Publications

(1) Li, H.; Tang, H.; Ma, C.; Bai, Y.; Alvarado, J.; Radhakrishnan, B.; Ong, S. P.; Wua, F.; Meng, Y. S.; Wu, C. Understanding the Electrochemical Mechanisms Induced by Gradient Mg2+ Distribution of Na-Rich $Na_{3+x}V_{2-x}Mg_x(PO_4)_3$/C for Sodium Ion Batteries. Chem. Mater. 2018, acs.chemmater.7b03903 DOI: 10.1021/acs.chemmater.7b03903.

(2) Shi, Y.; Tang, H.; Jiang, S.; Kayser, L. V.; Li, M.; Liu, F.; Ji, F.; Lipomi, D. J.; Ong, S. P.; Chen, Z. Understanding the Electrochemical Properties of Naphthalene Diimide: Implication for Stable and High-Rate Lithium-Ion Battery Electrodes. Chem. Mater. 2018, acs.chemmater.8b01304 DOI: 10.1021/acs.chemmater.8b01304.

(3) Luo, Y.; Khoram, P.; Brittman, S.; Zhu, Z.; Lai, B.; Ong, S. P.; Garnett, E. C.; Fenning, D. P. Direct Observation of Halide Migration and its Effect on the Photoluminescence of Methylammonium Lead Bromide Perovskite Single Crystals. Adv. Mater. 2017, 29 (43), 1703451 DOI: 10.1002/adma.201703451.

(4) Zheng, C.; Radhakrishnan, B.; Chu, I.-H.; Wang, Z.; Ong, S. P. Effects of Transition-Metal Mixing on Na Ordering and Kinetics in Layered P2 Oxides. Phys. Rev. Appl. 2017, 7 (6), 064003 DOI: 10.1103/PhysRevApplied.7.064003.

(5) Deng, Z.; Zhu, Z.; Chu, I.-H.; Ong, S. P. Data-Driven First-Principles Methods for the Study and Design of Alkali Superionic Conductors. Chem. Mater. 2017, 29 (1), 281–288 DOI: 10.1021/acs.chemmater.6b02648.

(6) Zhu, Z.; Chu, I.-H.; Ong, S. P. $Li_3Y(PS_4)_2$ and $Li_5PS_4Cl_2$: New Lithium Superionic Conductors Predicted from Silver Thiophosphates using Efficiently Tiered Ab Initio Molecular Dynamics Simulations. Chem. Mater. 2017, 29 (6), 2474–2484 DOI: 10.1021/acs.chemmater.6b04049.

(7) Chu, I.-H.; Nguyen, H.; Hy, S.; Lin, Y.-C.; Wang, Z.; Xu, Z.; Deng, Z.; Meng, Y. S.; Ong, S. P. Insights into the Performance Limits of the $Li_7P_3S_{11}$ Superionic Conductor: A Combined First-Principles and Experimental Study. ACS Appl. Mater. Interfaces 2016, 8 (12), 7843–7853 DOI: 10.1021/acsami.6b00833.

(8) Deng, Z.; Mo, Y.; Ong, S. P. Computational studies of solid-state alkali conduction in rechargeable alkali-ion batteries. NPG Asia Mater. 2016, 8 (3), e254 DOI: 10.1038/am.2016.7.

Activation of Hydrogen under Ambient Conditions by Main Group Molecules

PI: Philip P. Power, Department of Chemistry, University of California, Davis, California 95616.

Program Scope

The major objective of the project is to understand the reactions of open-shell or multiple bonded derivatives of the heavier main group elements with important small molecules such as hydrogen olefins, ammonia or carbon monoxide under mild conditions. A detailed mechanistic picture of these reactions is essential for the design of catalysts based on inexpensive elements such as aluminum or silicon. We have demonstrated that many of the reactions that constitute the individual steps in catalytic cycles can be effected with main group compounds[1] at ambient temperatures. The focus now is to determine the factors that enables reversibility in these reactions which is essential for their use in catalysis.

Recent Progress

In the past year we have demonstrated that a main group compound, the distannyne $Ar^{Pr^i}{}_4SnSnAr^{Pr^i}{}_4$ ($Ar^{Pr^i}{}_4 = C_6H_3\text{-}2,6(C_6H_3\text{-}2,6\text{-}Pr^i{}_2)_2$), which is a tin analog of an alkyne, reversibly binds hydrogen in toluene solution at 80°C.[2] The chemistry is shown in Scheme 1.

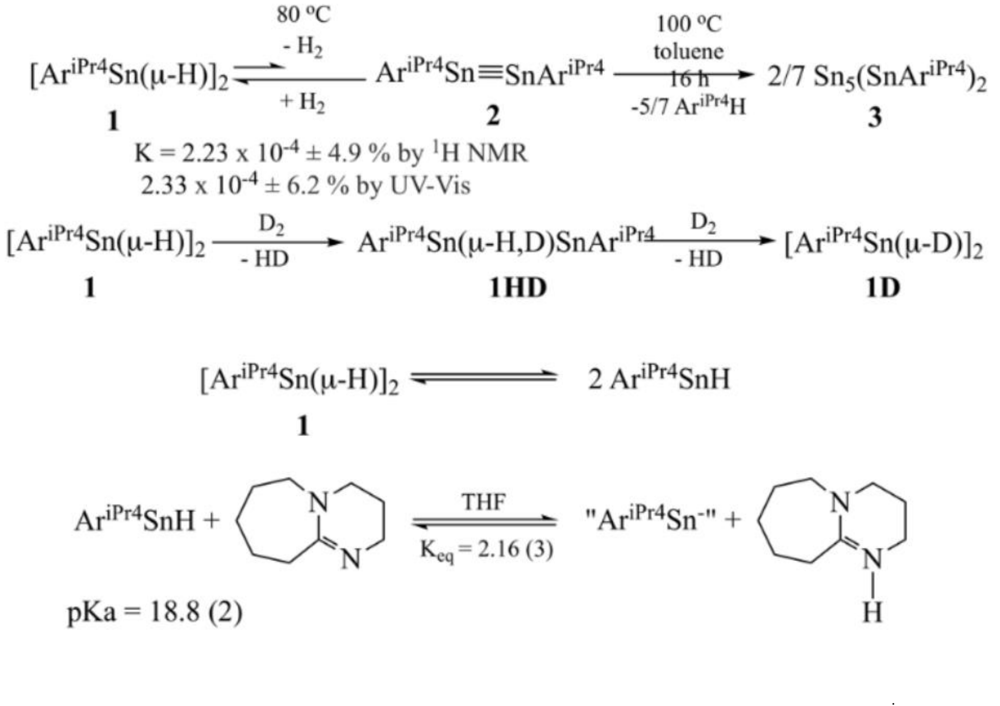

Scheme 1. Summary of the recent work establishing the equilibrium of the Sn(II) hydride $[Ar^{Pr^i}{}_4Sn(\mu\text{-}H)]_2$ (**1**) with $Ar^{Pr^i}{}_4SnSnAr^{Pr^i}{}_4$ (**2**) and H_2. Heating **1** or **2** to higher temperature gives the cluster $Sn_5(Ar^{Pr^i}{}_4)_2$ **(3)**.[2]

The equilibrium constant for the dissociation of H_2 from $[Ar^{Pr^i_4}Sn(\mu\text{-}H)]_2$ is 2.23 x 10^{-4} $\underline{+}$ 4.9% (by ^{1}H NMR spectroscopy) or 2.33 x 10^{-4} (by UV-vis spectroscopy) with a Gibbs free energy for the reaction near 5.9 kcal mol^{-1} showing that the hydride is strongly favored. The bond dissociation energy of the Sn–H bond was estimated to be near 51 kcal mol^{-1} on the basis of pK_a and reduction potential measurements. Ready exchange of the reaction with D_2 was also shown. The above measurements along with our earlier reports on the equilibria of ethylene[3], isocyanides[4], with $Ar^{Pr^i_4}SnSnAr^{Pr^i_4}$ establish a pattern of reversible equilibria involving a unimolecular main group species.

Other recent work has shown that a related compound the diaryl stannylene $:Sn(Ar^{Pr^i_4})_2$ undergoes C–H metathesis with toluene, m-xylene or mesitylene in these solvents at 80°C to afford the dimerized stannylene $:Sn(CH_2Ar)Ar^{Pr^i_4}$ (Ar = C_6H_5, C_6H_4-3-Me or C_6H_3-3,5-Me_2) as well as $Ar^{Pr^i_4}H$ as shown in Scheme 2.

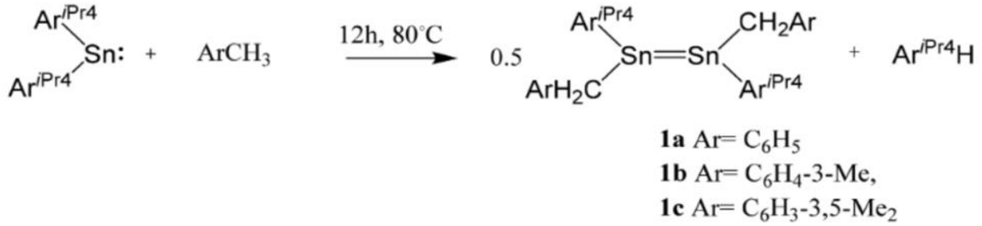

Scheme 2. Reaction of $:Sn(Ar^{iPr_4})_2$ with Arenes

Further studies of this reaction by EPR spectroscopy indicated the presence of a new type of one-coordinate group 14 radical $:SnAr^{Pr^i_4}$ that results from Sn–C bond cleavage in $:Sn(Ar^{Pr^i_4})_2$. The radical is persistent[5] at room temperature which should greatly facilitate planned mechanistic investigations of its reactions.

Future Plans

Over the past year the research supported by DOE has established the reversibility of hydrogen coordination as well as the existence of C–H metathesis by a main group compound under mild conditions. These reactions represent fundamental steps in many organometallic catalytic cycles and along with other important steps established by us for main group species should allow us to develop a complete catalytic cycle using the open-shell group 14 compounds.

The simplest such cycle would involve the hydrogenation of olefins under ambient conditions. We will investigate the effectiveness of several compounds in such a cycle as well as continuing to uncover new main group species that are capable of catalytic behavior.

References

1. P. P. Power, Main Group Elements as Transition Metals, *Nature,* **2010**, *463*, 1.71-177.
2. S. Wang, T. J. Sherbow, L. A. Berben, and P. P. Power. Reversible Coordination of H_2 by a Distannyne. *Journal of the American Chemical Society.* **2018**, *140*, 590-593. DOI: 10.1021/jacs.7b11798
3. Peng, Y.; Wang, X.; Fettinger, J. C.; Power, P. P. Reversible Complexation of Isocyanides by the Distannyne Ar′SnSnAr′ (Ar′ = C_6H_3-2, 6 (C_6H_3-2, 6-$^iPr_2)_2$), *Chemical Communications,* **2010,** 943-945.
4. T. Y. Lai, J. C. Fettinger and P. P. Power. Facile C-H Bond Metathesis Mediated by a Stannylene. *Journal of the American Chemical Society*. In press. DOI: 10.1021/jacs.8b01878
5. P. P. Power. Persistent and Stable Radicals of the Heavier Main Group Elements and Related Species. *Chemical Reviews*, **2003**, *103*,789-809.

Publications Supported by BES

1. N. Y. Tashkandi, L. C. Pavelka, P. D. Boyle, P. P. Power, and K. M. Baines. Probing the mechanism of the addition of alkynes to digermynes. *Dalton Transactions*. **2016**, *45*, 7226-7230. DOI: 10.1039/C6DT01015F
2. J. D. Erickson, R. D. Riparetti, J. C. Fettinger, and P. P. Power. Molecular Zinc Species with Ge-Zn and Sn-Zn Bonds: A Reversible Insertion of a Stannylene into a Zinc-Carbon Bond. *Organometallics*. **2016**, *35*, 2124-2128. DOI: 10.1021/acs.organomet.6b00344
3. M. L. McCrea-Hendrick, C. A. Caputo, J. Linnera, C. M. Weinstein, J. C. Fettinger, H. M. Tuononen, and P. P. Power. Cleavage of Ge-Ge and Sn-Sn Triple Bonds in Heavy Group 14 Element Alkyne Analogues $(EAr^{iPr4})_2$ (E = Ge, Sn; Ar^{iPr4} = C_6H_3-2,6(C_6H_3-2,6-$^iPr_2)_2$) by Reaction with Group 6 Carbonyls. *Organometallics*. **2016**, *35*, 2759-2767. DOI: 10.1021/acs.organomet.6b00519
4. J. D. Erickson, T. Y. Lai, D. J. Liptrot, and P. P. Power. Catalytic Dehydrocoupling of Amines and Boranes by an Incipient Tin(II) Hydride. *Chemical Communications*. **2016**, *52*, 13656-13659. DOI: 10.1039/C6CC06963K
5. S. Wang, M. L. McCrea-Hendrick, C. M. Weinstein, C. A. Caputo, E. Hoppe, J. C. Fettinger, M. M. Olmstead, and P. P. Power. Dynamic Behavior and Isomerization Equilibria of Distannenes Synthesized by Tin Hydride/Olefin Insertions: Characterization of the Elusive Mono-Hydrido Bridged Isomer. *Journal of the American Chemical Society*. **2017**, *39*, 6586-6595 DOI: 10.1021/jacs.7b02269

6. S. Wang, M. L. McCrea-Hendrick, C. M. Weinstein, C. A. Caputo, E. Hoppe, J. C. Fettinger, M. M. Olmstead, and P. P. Power. Tin(II) Hydrides as Intermediates in Rearrangements of Tin(II) Alkyl Derivatives. *Journal of the American Chemical Society*. **2017**, *139*, 6596-6604. DOI: 10.1021/jacs.7b02271
7. C. M. E. Graham, P. P. Power, Z. D. Brown, and P. J. Ragogna. Transition Metal Functionalization of P_4 using a Diarylgermylene Anchor. *Inorganic Chemistry*. **2017**, *56*, 9111-9119. DOI: 10.1021/acs.inorgchem.7b01138
8. M. McCrea-Hendrick, S. Wang, K. L. Gullett, J. C. Fettinger, and P. P. Power. The Reactions of Aryl Tin(II) Hydrides $\{\mathrm{Ar}^{i\mathrm{Pr}6}\mathrm{Sn}(\mu\text{-H})\}_2$ ($\mathrm{Ar}^{i\mathrm{Pr}6} = \mathrm{C_6H_3}$-2,6-($\mathrm{C_6H_2}$-2,4,6-$^{i}\mathrm{Pr}_3)_2$) and $\{\mathrm{Ar}^{i\mathrm{Pr}4}\mathrm{Sn}(\mu\text{ -H})\}_2$ ($\mathrm{Ar}^{i\mathrm{Pr}4} = \mathrm{C_6H_3}$-2,6-($\mathrm{C_6H_3}$-2,6-$^{i}\mathrm{Pr}_2)_2$) with Aryl Alkynes: Substituent-Dependent Structural Isomers. *Organometallics.* **2017**, *36*, 3799-3785. DOI: 10.1021/acs.organomet.7b00570
9. S. Wang, T. J. Sherbow, L. A. Berben, and P. P. Power. Reversible Coordination of H_2 by a Distannyne. *Journal of the American Chemical Society.* **2018**, *140,* 590-593. DOI: 10.1021/jacs.7b11798
10. T. Y. Lai, J. C. Fettinger and P. P. Power. Facile C-H Bond Metathesis Mediated by a Stannylene. *Journal of the American Chemical Society*. **2018**, *140*, 5674-5677. DOI: 10.1021/jacs.8b01878

Materials Characterization With Sensitivity-Enhanced Solid-State NMR Spectroscopy

Aaron J. Rossini, Marek Pruski, LinLin Wang, Wenyu Huang, Frederic A. Perras
Division of Materials Science and Engineering
US DOE Ames Laboratory, Ames, Iowa, USA

Program Scope

The properties, activity, and performance of many energy relevant materials are governed by the structure of their surface, subsurface and interfacial regions which are often difficult to probe with existing analytical techniques. Additionally, many materials are amorphous or only partially ordered and are also difficult to precisely characterize. SSNMR spectroscopy is a powerful tool for the study of the complex materials, except that the Achilles' heel of NMR spectroscopy – a fundamental lack of sensitivity – limits its applications to bulk phases, large surface area materials, and materials with sufficient concentrations of receptive nuclei. To overcome these limitations, we exploit and develop high-field dynamic nuclear polarization (DNP) and/or ultrafast magic-angle spinning (UFMAS) to enhance the sensitivity of SSNMR experiments by orders of magnitude. We then apply these advanced SSNMR experiments to precisely measure the atomic-level structural details of semiconductor nanoparticles (NPs), metal-organic frameworks (MOFs), lead halide perovskites, inorganic glasses and low-surface-area materials, amongst other energy relevant materials.

Recent Progress

Development of UFMAS SSNMR. UFMAS at frequencies above 50 kHz opens up many perspective avenues for SSNMR spectroscopy. UFMAS improves the resolution of ^{1}H SSNMR spectra by averaging homonuclear ^{1}H dipolar couplings. This enables efficient ^{1}H detection schemes that can provide order of magnitude gains in sensitivity. For example, we have recently demonstrated how fast MAS and proton detection can be applied to accelerate or enable SSNMR experiments with unreceptive low-frequency spin-1/2 nuclei (Figure 1),[1] nuclei such as ^{195}Pt and ^{71}Ga, that give rise to wideline SSNMR spectra[2,3] and half-integer quadrupolar nuclei such as ^{17}O, ^{27}Al and ^{71}Ga.[4] We have subsequently applied these ^{1}H detected UFMAS methods to obtain 2D HETCOR NMR spectra of unreceptive nuclei in materials.

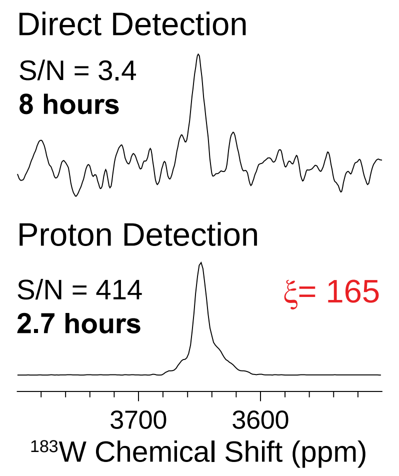

Figure 1. Comparison of direct detected and proton detected ^{183}W SSNMR spectra of ammonium thiotungstate. Proton detection improves sensitivity by a factor 165.

Materials Characterization. Below we describe applications of DNP and/or proton detected fast MAS SSNMR spectroscopy to characterize state-of-the-art energy-relevant materials.

Silicon nanocrystals (Si NCs) have a variety of potential applications including photovoltaics, batteries, biosensors and catalysts. We have recently shown that proton detected ^{29}Si SSNMR experiments can be used to characterize the surface of hydride passivated, as-synthesized Si NCs and alkyl functionalized Si NCs.[5] Notably, we demonstrated that scalar-coupling ^{1}H-^{29}Si correlation methods (INEPT) can detect and quantify the population of different hydride groups on the Si NC surface (Figure 2). NMR experiments on functionalized Si NCs provide direct insight into the mechanism of attachment and location of alkyl ligands on the Si NC surface.

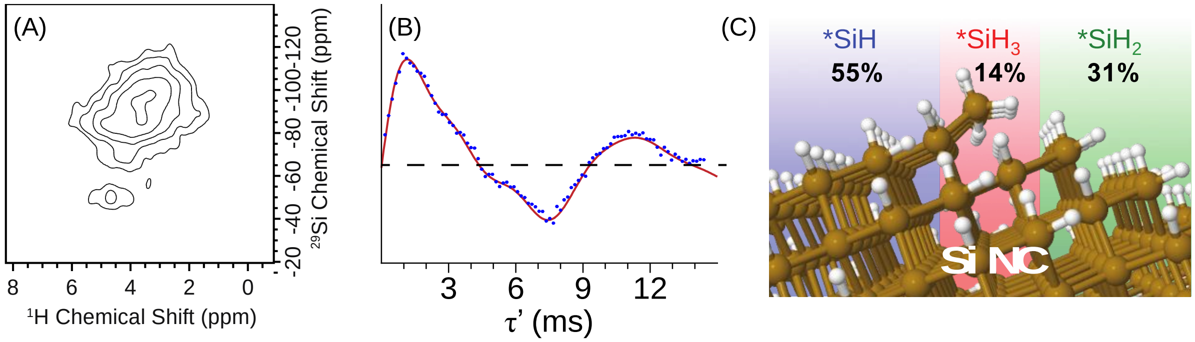

Figure 2. (A) ^{1}H detected ^{1}H{^{29}Si} scalar-INEPT 2D HETCOR spectrum of hydride passivated Si NCs. (B) A plot showing the evolution of the ^{29}Si INEPT NMR signal due to scalar coupling to ^{1}H spins. (C) The populations of the different hydride groups on the surface of the Si NCs were quantified by fitting the INEPT curve.

Methylammonium lead halide perovskites have attracted considerable interest as materials for next-generation photovoltaics (PV) and optoelectronics. The most promising lead perovskite materials usually contain mixed halide anions. ^{207}Pb SSNMR spectroscopy is a powerful probe of the local lead coordination environment and can provide insight into the mixing and phase segregation of cations and anions.[6,7] However, ^{207}Pb SSNMR experiments on mixed halide perovskites are often challenging due to the breadth of the ^{207}Pb SSNMR spectra and unfavorable relaxation characteristics.[6,7] We have recently demonstrated how both DNP and UFMAS can be applied to boost the sensitivity of ^{207}Pb SSNMR experiments on mixed halide perovskites and obtain order of magnitude reductions in experiment time.[8] Using 100 K SSNMR experiments it was possible to obtain the ^{207}Pb SSNMR spectrum of a methylammonium lead iodide model thin film (Figure 3). This result shows it is feasible to use SSNMR for characterization of perovskite thin films.

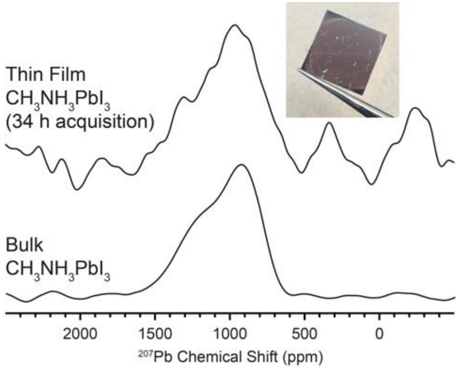

Figure 3. Static, 100 K ^{207}Pb SSNMR spectra of bulk $CH_3NH_3PbI_3$ and a 500 nm thick thin film deposited on a glass cover slip.

Theoretical Models of DNP. We have developed theoretical quantum mechanical models to delineate the elementary mechanisms by which electron spin polarization is transferred to and spreads amongst the nuclear spins. In order to improve biradical DNP polarizing agents we have performed 3-spin quantum mechanical calculations to determine the optimal relative orientation of the tethered nitroxide units.[9] Recently, we have developed a new software program that takes advantage of numerical approximations and enables fully quantum mechanical calculations of spin dynamics and DNP enhancements for up to 70 nuclear spins.[10] With this program we can obtain direct insight into how experimental parameters such as the deuteration of the radical[11] and the MAS frequency affect the achievable DNP enhancements (Figure 4).

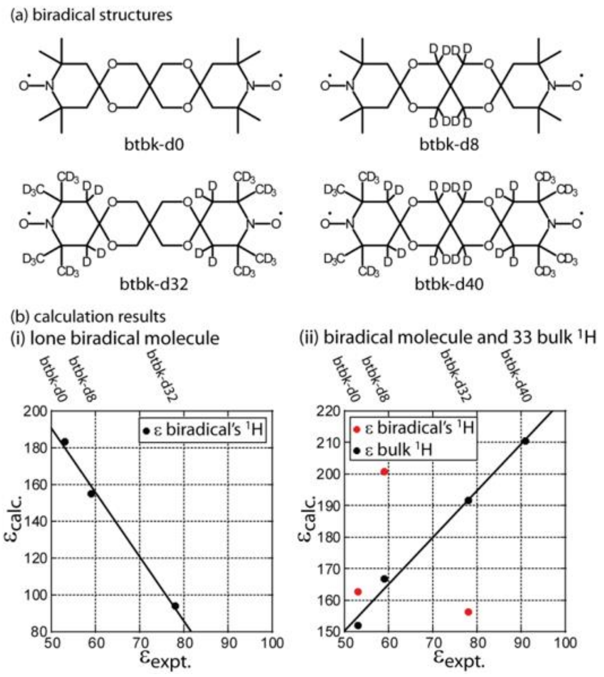

Figure 4. Results of spin dynamic calculations on deuterated biradicals showing the predicted variation of DNP enhancement for ^1H spins on the biradical and ^1H spins that are distant from the biradical.

Future Plans

Extending DNP-Enhanced SSNMR to Inorganic Oxides and Glasses. SSNMR spectroscopy is often applied for the characterization of mixed oxides and amorphous inorganic materials. However, only basic 1D NMR experiments are feasible on many inorganic materials because unfavorable relaxation properties often reduce sensitivity. We have obtained promising preliminary data showing that there are two general approaches to extend DNP to inorganic glasses and oxides: (i) Introduction of paramagnetic metal ions provides unpaired electrons that can be used to hyperpolarize bulk nuclei in the glass. (ii) Ionizing radiation can introduce stable radical defects with favorable properties for DNP.

DNP-Enhanced SSNMR Spectroscopy of Nanomaterials. It has previously been shown that DNP-enhanced SSNMR can be performed on colloidal NPs by trapping them in mesoporous silica with the polarizing agent.[12] DNP-enhancements above 100 can be routinely obtained with this approach, however, the DNP sensitivity gains are partially offset by dilution of the NPs, which has lead us to pursue alternative sample formulations. We found that DNP can be easily applied to alkyl functionalized Si NCs by impregnating the powdered NCs with a biradical solution. This has enabled acquisition of 2D ^{29}Si-^{29}Si homonuclear and ^{29}Si-^{13}C heteronuclear correlation spectra of the Si NC surface. Colloidal semiconductor NPs can also be precipitated onto boron nitride (BN) to obtain high DNP enhancements with minimal dilution. We are currently applying this technique to study the surface structure of semiconductor NPs.

DNP-Enhanced SSNMR Spectroscopy of MOFs. MOFs are a versatile and tunable class of crystalline porous materials. For instance, they can be used for gas absorption and separation and for the selective capture of heavy metals or molecular contaminants. We are applying SSNMR spectroscopy to detect structural defects that are likely responsible for the MOF's activity, but which are difficult or impossible to detect with other techniques. We are using DNP-enabled natural-abundance ^{13}C-^{14}N distance measurements to study the distribution of linkers in mixed-linker MOFs, ^{13}C-^{13}C correlation experiments to locate amino acid species coordinating to the MOF's cornerstones, ^{15}N SSNMR to detect the absorption and complexation of Pd ions and ^{89}Y SSNMR in order to study the absorption of various Lewis bases, including potential neurotoxins.

UFMAS SSNMR Spectroscopy. In early 2019 we will receive a state of the art probe capable of achieving MAS frequencies above 100 kHz. This new technology will greatly improve the resolution of ^{1}H solid-state NMR and provide access to novel structural constraints. We will use the probe to detect long range ^{1}H-^{1}H correlations by multiple-quantum spectroscopy, and gain insights into the spatial distributions of different species. For instance, the improved ^{1}H resolution will allow us to determine the distribution of linkers in mixed-linker MOFs, which otherwise requires the use of heteronuclear NMR experiments that are far less sensitive to crystal packing. We are also developing new low power recoupling schemes that will enable precise homonuclear and heteronuclear distance measurements at UFMAS frequencies.

References

(1) Venkatesh, A.; Ryan, M. J.; Biswas, A.; Boteju, K. C.; Sadow, A. D.; Rossini, A. J. *The Journal of Physical Chemistry A* **2018**, *DOI:10.1021/acs.jpca.8b05107*.
(2) Rossini, A. J.; Hanrahan, M. P.; Thuo, M. *Phys. Chem. Chem. Phys.* **2016**, *18*, 25284-25295.
(3) Perras, F. A.; Venkatesh, A.; Hanrahan, M. P.; Goh, T. W.; Huang, W.; Rossini, A. J.; Pruski, M. *J. Magn. Reson.* **2017**, *276*, 95-102.
(4) Venkatesh, A.; Hanrahan, M. P.; Rossini, A. J. *Solid State Nucl. Magn. Reson.* **2017**, *84*, 171-181.
(5) Hanrahan, M. P.; Fought, E. L.; Windus, T. L.; Wheeler, L. M.; Anderson, N. C.; Neale, N. R.; Rossini, A. J. *Chem. Mater.* **2017**, *29*, 10339-10351.
(6) Rosales, B. A.; Men, L.; Cady, S. D.; Hanrahan, M. P.; Rossini, A. J.; Vela, J. *Chem. Mater.* **2016**, *28*, 6848−6859.
(7) Rosales, B. A.; Hanrahan, M. P.; Boote, B. W.; Rossini, A. J.; Smith, E. A.; Vela, J. *ACS Energy Letters* **2017**, *2*, 906-914.
(8) Hanrahan, M. P.; Men, L.; Rosales, B. A.; Vela, J.; Rossini, A. J. *Submitted for Publication* **2018**.
(9) Perras, F. A.; Ivanov, K. L.; Sadow, A. D.; Pruski, M. *ChemPhysChem* **2017**, *18*, 2279-2287.
(10) Perras, F. A.; Pruski, M. *Submitted for Publication* **2018**.
(11) Perras, F. A.; Reinig, R. R.; Slowing, I. I.; Sadow, A. D.; Pruski, M. *Phys. Chem. Chem. Phys.* **2016**, *18*, 65-69.
(12) Piveteau, L.; Ong, T. C.; Rossini, A. J.; Emsley, L.; Coperet, C.; Kovalenko, M. V. *J. Am. Chem. Soc.* **2015**, *137*, 13964-13971.

Publications (Since October 2017)

1.) Hanrahan M.P., Fought E.L., Windus T.L., Wheeler L.M., Anderson N.C., Neale N.R., Rossini A.J. Characterization of Silicon Nanocrystal Surfaces by Multidimensional Solid-State NMR Spectroscopy, *Chem. Mater.*, **2017**, *29*, 10339–10351.
2.) Venkatesh A., Ryan M.J., Biswas A., Boteju K.C., Sadow A.D., Rossini A.J. Accelerating Solid-State NMR Experiments on Low-Gyromagnetic Ratio Nuclei with Fast MAS and Proton Detection, *J. Phys. Chem. A*, **2018**, *DOI:10.1021/acs.jpca.8b05107*.
3.) Hanrahan M.P., Men L., Rosales B.A., Vela J., Rossini A.J. Sensitivity-Enhanced ^{207}Pb Solid-State NMR Spectroscopy for the Rapid, Non-Destructive Characterization of Organolead Halide Perovskites, *Submitted for Publication*.
4.) Chang B.S., Chen J., Tevis I., Çınar S., Oyola-Reynoso S., Li A., Gong J., Rossini A.J., Thuo M. Self-Assembled Coordination Polymer as Intermediates in Synthesis of 2D Porous Oxide Photo-catalysts from Bulk Metal, *Submitted for Publication*.
5.) Love A.M., Thomas B., Specht S.E., Hanrahan M.P., Venegas J.M., Burt S.P, Grant J.T., Cendejas M.C., McDermott W.P., Rossini A.J., Hermans I. Probing the Active Phase of Boron Nitride Based Catalysts for the Oxidative Dehyrdrogenation of Propane, *Submitted for Publication*.
6.) Rossini A.J. Materials Characterization by Dynamic Nuclear Polarization Enhanced Solid-State NMR Spectroscopy, *Submitted for Publication*.
7.) Perras, F. A.; Pruski, M. Large-scale ab initio simulations of MAS DNP enhancements using a Monte Carlo optimization strategy, *Submitted for Publication*

DE-SC0017620: Molecular Design and Vapor Phase Synthesis of Hybrid Ion-Conducting Materials Based on Crown Ethers

Gary W. Rubloff, University of Maryland (Principal Investigator)

Sang Bok Lee, University of Maryland (Co- Investigator)

Keith Gregorczyk, University of Maryland (Co-Investigator)

Program Scope

The overall goal of this work is to develop and demonstrate an expanded methodology for synthesis of tailored and functional materials using surface mediated vapor phase chemistry. Specifically, we seek to exploit the chemical selectivity of molecular layer deposition (MLD) and/or atomic layer deposition (ALD) to control growth of thin films, achieving versatile materials design with bonding configurations which translate into desired material properties. By employing the selectivity of MLD/ALD in concert with the diversity of homo and hetero bi-functional organic and hybrid-organic precursors available, we seek to mimic the way organic synthesis enlists known reaction and ligand exchange mechanisms in the liquid phase but now applied to synthesis of solid thin films.

As a concrete example, we seek to incorporate crown ethers (CEs) as a functional "**host**" for their ability to recognize (e.g., capture, retain, and release) mobile ions, thus providing a basis for a material with high ion conductivity, while the variety of CE molecules available offers tunability of the material and its ion-conducting properties (i.e, different CEs for Li, Na, Mg). The intent is to link the CE molecules through "**linke**r" molecules delivered through MLD (or ALD) precursor dose sequences, where small organic or organometallic molecules are chosen as linkers for their anticipated reaction with the CEs and potentially additional linkers. A variety of linkers have been previously studies in MLD processes, such as malonyl chloride, ethylene glycol, di-ethyl zinc, tri-methyl aluminum, etc [1,2]. Using the substantial knowledge base of organic and organometallic chemistry to choose linkers and MLD precursor dose sequences, we believe we can substantially expand the materials synthesis capability of self-limiting MLD/ALD processes to a broad variety of hybrid organic/inorganic and related "**hybrid**" host-linker(s) material combinations.

The goal of this **seed project** is to demonstrate synthesis of solid thin films from MLD hosts and MLD/ALD linkers, where (1) the growth exhibits layer-by-layer control characteristic of MLD and ALD processes, and (2) the composition of the resulting hybrid material is that expected chemically for the chosen host and linker. We are pursuing a twofold strategy. First, we are combining a crown ether (15C5) host with an organic linker (malonyl chloride, MC) to form a hybrid thin film material with potential as a selective ion conductor. Second, we are using a Li-containing host (Li test-butoxide, LiO^tB) in combination with organic linkers (propanediol, PPD, and glycerol, GL). As the scope of the seed project is to demonstrate MLD synthesis of hybrid host-linker solid thin films, the extensive real-time and in-situ characterization available in the ALD Nanostructures Lab and elsewhere at UMD will be used primarily to verify the behavior of the synthesis process.

Recent Progress

Crown-ether-based MLD hybrid thin films. We first evaluated candidate CE's 15C5 and 18C6 by DSC and TGA to confirm suitability in terms of thermal stability and volatility. Malonyl chloride was chosen as a linker molecule with suitable vapor pressure and the possibility to employ the Cl content as indicator of MLD growth. A number of hybrid MLD process recipes were explored, leading to film growth, accompanied by real-time in-situ spectroscopic ellipsometry. Initial experimental conditions produced a low growth rate and films <10nm thick. As seen in Fig. 1, chemical analysis by in-situ XPS - i.e., without intervening air exposure - shows the presence of all expected elements (and the Si substrate underlying the thin MLD layer). Importantly, the relative intensities of the primary XPS peaks match what is expected for the proposed reaction scheme. The low growth rate could be an indicator of steric hindrance effects to be further explored; this has stimulated ideas to alter CE ligands with other linkers. The presence of the C-N bond may suggest preservation of part/all of the CE ring structure. The weak Cl signal indicates reaction and incorporation of the MC into the film.

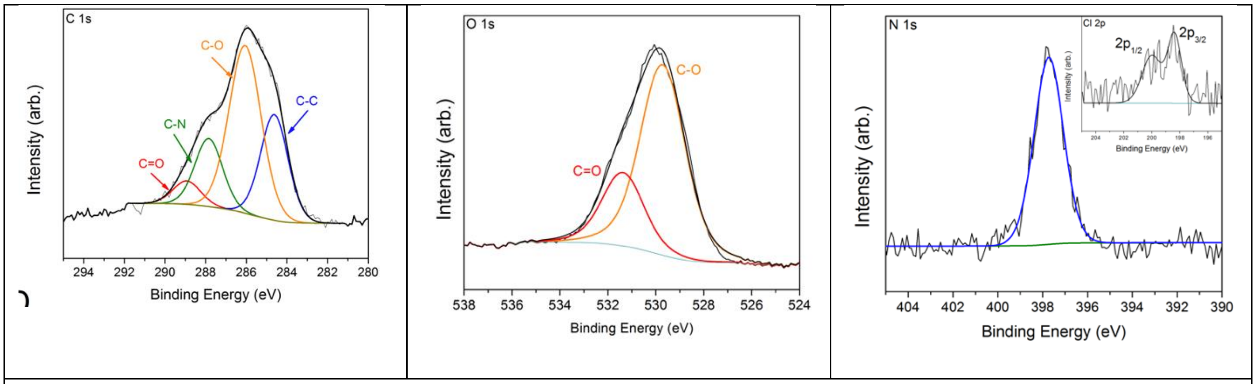

Figure 1. XPS core level spectra for hybrid MLD film synthesized from 15C5 crown ether and malonyl chloride precursors.

<u>Li-based MLD hybrid thin films</u>. We have also chosen to exploit our experience with Li precursors (e.g., ALD LiPON) as another avenue to demonstrate the hybrid MLD synthesis [4,5,6]. We have used Li-*tert*-butoxide (LiO^{t}B) in combination with linkers propanediol (PPD) or glycerol (GL) to form hybrid thin films [7,8]. Propanediol (PPD) is a homo-bifunctional precursor has a C-C-C chain with an –OH end groups, while glycerol (GL) is chosen due to its similar backbone structure, a C-C-C chain, but an extra –OH group linked to the center C atom [10]. Precursor dose and temperature parameters were explored to identify MLD-like regimes of parameters. For LiO^{t}B +PPD, the temperature window is between ~115-165^{o}C, and beyond 165 ^{o}C, the growth rate dropped drastically as the organic molecules decompose or desorbed from the surface. In comparison, the LiO^{t}B + GL reaction exhibited an MLD temperature window at a higher range: ~195-245^{o}C.

As seen in Fig. 2, linear growth behavior for both chemistries (LiOtB + PPD, and LiOtB + GL) are observed for both systems as monitored by real-time in-situ spectroscopic ellipsometry, showing growth rates per cycle (GPC) of 0.4 A/cycle and 0.5 A/cycle respectively for PPD at 110oC and GL at 240oC.

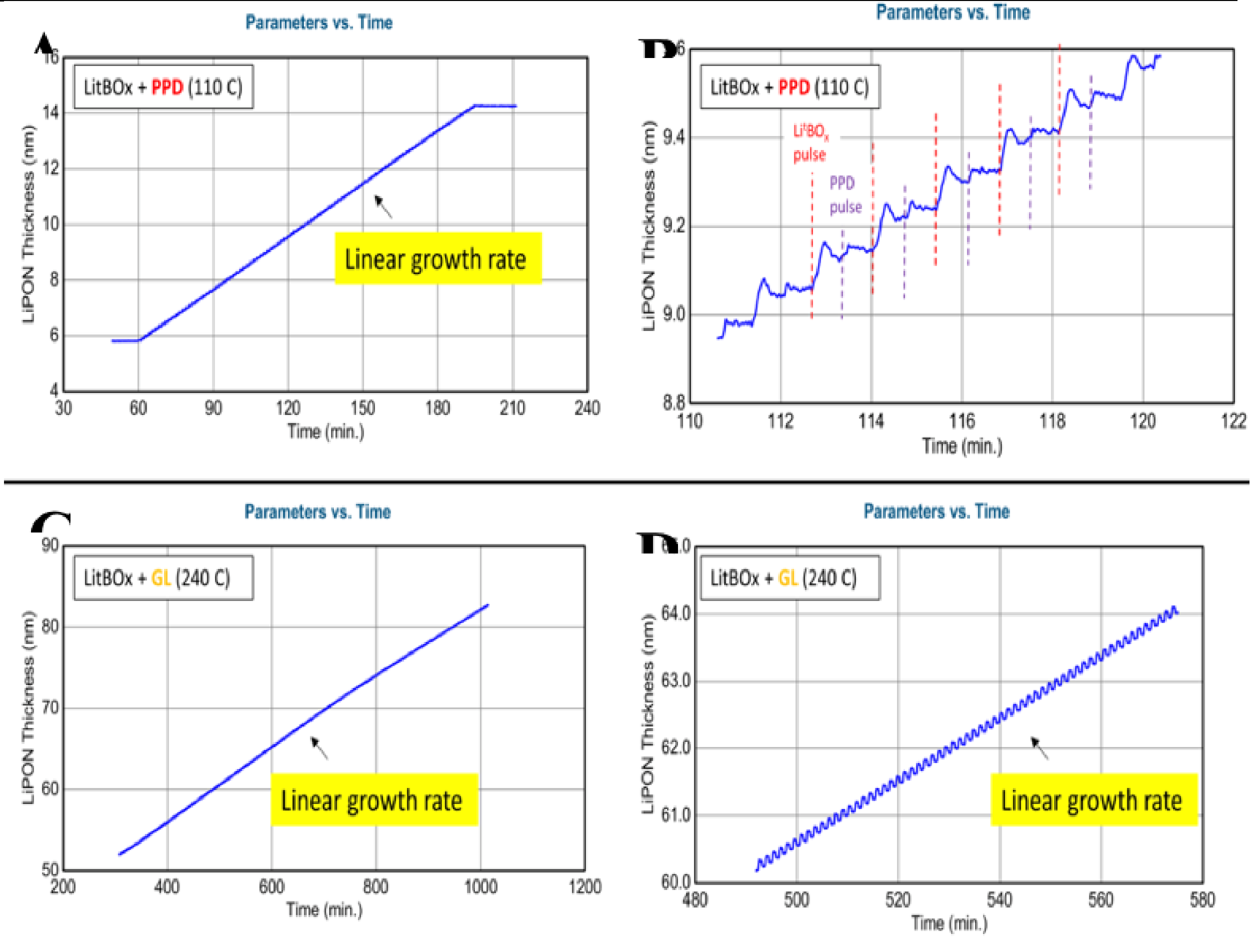

Figure 2. Linear growth of LiO^{t}B-based MLD films with propanediol (top) or glycerol (bottom), monitored by real-time in-situ spectroscopic ellipsometry. Expanded view revealing dose-by-dose behavior on right.

Future Plans

Both the crown-ether-based and Li-based hybrids give credence toward our overall goal in highly controlled vapor phase synthesis of hybrid thin solid films. In the near term we will continue these two hybrid synthesis directions described above to more fully describe the MLD reaction parameter space, establish ellipsometry models, and composition/chemical bonding of the hybrid materials producted. We will also add observations that further characterize and validate the process mechanisms (e.g., real-time downstream mass spectrometry to identify volatile MLD reaction products).

Given the promising results to date with both CE and LiO^{t}B based hybrids, we have begun to assemble a full proposal for submission well in advance of the 10/31/18 end of this seed project.

This progress has also stimulated new ideas to program the assembly of materials, particularly with respect to extending chemical reaction sequences to more complex systems. For example, linking the 15C5 CE and the LiO^{t}B hybrids may provide a new hybrid which incorporates metal ions into a solid CE-based electrolyte whose ion conduction can be tailored to the metal ion species. More expansively, multiple linkers may be considered to impart additional functionality to the MLD hybrid films, building on the extensive chemistry knowledge base and recognizing new levels of detail in understanding the correlation of selective precursor-surface reaction with morphological materials growth consequences [11].

References

(1) George, S. M.; Yoon, B.; Dameron, A. A. Surface Chemistry for Molecular Layer Deposition of Organic and Hybrid Organic-Inorganic Polymers. *Acc. Chem. Res.* **2009**, *42* (4), 498–508.

(2) Mikkulainen, V.; Leskela, M.; Ritala, M.; Puurnen, R. L. Crystallinity of Inorganic Films Grown by Atomic Layer Deposition: Overview and General Trends. *J. Appl. Phys.* **2013**, *113* (21301).

(3) Chen, C.; Li, P.; Wang, G.; Yu, Y.; Duan, F.; Chen, C.; Song, W.; Qin, Y.; Knez, M. Nanoporous Nitrogen-Doped Titanium Dioxide with Excellent Photocatalytic Activity under Visible Light Irradiation Produced by Molecular Layer Deposition. *Angew Chem Int Ed Engl* **2013**.

(4) Kozen, A. C.; Pearse, A. J.; Lin, C.-F.; Noked, M.; Rubloff, G. W. Atomic Layer Deposition of the Solid Electrolyte LiPON. *Chem. Mater.* **2015**, 150709110756002.

(5) Kozen, A. C.; Pearse, A. J.; Lin, C.-F.; Schroeder, M. A.; Noked, M.; Lee, S. B.; Rubloff, G. W. Atomic Layer Deposition and in Situ Characterization of Ultraclean Lithium Oxide and Lithium Hydroxide. *J. Phys. Chem. C* **2014**, *118* (48), 27749–27753.

(6) Pearse, A. J.; Schmitt, T. E.; Fuller, E. J.; El-Gabaly, F.; Lin, C. F.; Gerasopoulos, K.; Kozen, A. C.; Talin, A. A.; Rubloff, G.; Gregorczyk, K. E. Nanoscale Solid State Batteries Enabled by Thermal Atomic Layer Deposition of a Lithium Polyphosphazene Solid State Electrolyte. *Chem. Mater.* **2017**, *29* (8), 3740–3753.

(7) Gregorczyk, K.; Knez, M. Hybrid Nanomaterials through Molecular and Atomic Layer Deposition: Top Down, Bottom Up, and in-between Approaches to New Materials. *Prog. Mater. Sci.* **2016**, *75*, 1–37.

(8) George, S. M.; Lee, B. H.; Yoon, B.; Abdulagatov, A. I.; Hall, R. A. Metalcones: Hybrid Organic–Inorganic Films Fabricated Using Atomic and Molecular Layer Deposition Techniques. *J. Nanosci. Nanotechnol.* **2011**, *11* (9), 7948–7955.

(9) Knez, M.; Nielsch, K.; Niinistö, L. Synthesis and Surface Engineering of Complex Nanostructures by Atomic Layer Deposition. *Adv. Mater.* **2007**, *19* (21), 3425–3438.

(10) Sundberg, P.; Karppinen, M. Organic and Inorganic-Organic Thin Film Structures by Molecular Layer Deposition: A Review. *Beilstein J Nanotechnol* **2014**, *5*, 1104–1136.

(11) Zhengning, G., Wu, F., Myung, Y., Fei, R., Kanjolia, K.,Yang, Li., Banerjee, P. Stand and sitting adlayers in atomic layer deposition of ZnO. J. Vacuum Sci. & Tech. A., **2016**, 34, 01A143.

Publications

No publications yet, ~11 months into a new seed program

Energy Flow in Polymers with Mixed Conduction Pathways: New Routes to Improving Thermopower and Thermoelectric Power Factor

Rachel Segalman, Department of Chemical Engineering, UC Santa Barbara
Michael Chabinyc, Materials Department, UC Santa Barbara

Program Scope

Mixed ion/electron conducting materials are essential for all electrochemical devices, including batteries and fuel cells, and have potential applications in thermoelectrics, bioelectronics and neuromorphic computing. Ionic conductivity can play an important role in the properties of organic semiconductors. In doped organic semiconductors, ionic moieties serve as the counter charges to electronic charge carriers and have a significant effect on energetic structure. Ionic effects are especially important in organic thermoelectric materials, where the ions can drift in a temperature gradient and contribute to the Seebeck coefficient (thermopower, S). Our goal is to understand the physical nature of ion-carrier interactions and mixed ion/electron transport in organic materials by using both electrical and thermoelectric measurements to study electronic structure. Ultimately, this knowledge will be used to develop design rules for organic thermoelectric materials with mixed ion/electron functionality as well as mixed conducting materials for other applications.

One of our main goals is to understand how ionic interactions in mixed conducting systems can be used to improve thermoelectric transport. In previous work, we have found that ionic conductivity plays an essential role in the thermoelectric properties of the high performing organic thermoelectric material PEDOT:PSS, a blend of the electron conducting polymer poly(ethylenedioxythiophene) and the ionic polymer poly(styrenesulfonate).[1,2] In the current study, we implement controlled modulation of ionic interactions in PEDOT:PSS through the addition of ionic moieties with differing structure and ionic character. By measuring the transport properties that result from these modulations in the ionic environment in PEDOT:PSS, we gained insight into the role of ion-electron interactions in electronic structure and thermoelectric performance.

To further understand these interactions, it is crucial to ascertain how carrier mobility, carrier concentration, and thermoelectric properties are affected at the interface between an ion conductor and an electron conductor. By assembling bilayers of ion conducting polymers and semiconducting polymers, we formed well-defined macroscopic ion-electron interfaces for gated conductivity measurements (**Figure 2a**). A gate voltage is used to control the number of electronic carriers in the presence of a temperature gradient, allowing us to controllably study electronic and thermoelectric properties in-situ.

In conjunction with the development of these characterization techniques, we seek to design and synthesize processable mixed conducting systems that have independently defined ion and electron components and highly tunable morphologies. The fundamental design rules for such systems are completely opaque at this point including simple concepts such as whether phase separated or phase mixed ion/electron conducting components are desired to optimize mixed conduction. As we synthesize the two components, their material properties will be characterized independently as well as in blends such as polymer composites or block copolymers to understand the role of mesoscale structure on complex ion/electron conductivity.

Recent Progress

One of our first goals is to develop an understanding of the interactions that play a role in the exceptional thermoelectric properties of mixed conducting materials. We studied how the addition of ionic liquids to solutions of PEDOT:PSS could control both morphological and electronic properties. By modifying the ratio of cation to anion in an ionic liquid, we enhance the thermoelectric power factor ($S^2\sigma$) of PEDOT:PSS by over two orders of magnitude relative to films cast without the additive. Blending I. L. additives with a 1:1 stoichiometry between cationic imidazolium (Im+) and anionic bis(trifluoromethane)sulfonamide (TFSI-) groups into PEDOT:PSS dispersions restructure the film morphology to increase the carrier mobility, resulting in a film conductivity of ~1000 S/cm but no change in the Seebeck coefficient. Blending I. L. additives with an excess of cation (4:1 stoichiometry between Im+ and TFSI- groups) raises the conductivity in a similar manner, but also enhances the Seebeck coefficient by over a factor of two, leading to an overall increase in power factor ($S^2\sigma$) by two orders of magnitude (**Figure 1**). The ability to decouple and tailor the thermoelectric properties of PEDOT:PSS with minor changes in ionic liquid additives is completely unprecedented in the literature. (Mazaheripour et. al.)

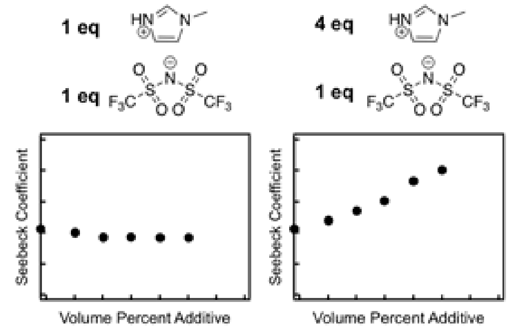

Figure 1: Plot of the Seebeck coefficient of the I. L. blended PEDOT:PSS films vs. % volume of I.L. in the solid film for stoichiometric (left) and non-stoichiometric (right) I.L.s

To further investigate the role of ionic-electronic interfaces on the electronic and thermoelectric properties of mixed conductors, we have developed a model bilayer between a single ion conductor and an electron conductor that allows us to introduce carriers by electrochemical doping (**Figure 2a**). Due to the energetic disorder of polymers, the thermopower is a complex function of carrier density, which makes it difficult to assess structure-property relationships for the thermoelectric power factor. Using gated thermopower measurements, we demonstrated that while doping a semiconducting polymer increases the carrier concentration and thermoelectric power factor, the presence of charged counterions broadens its electronic density-of-states (DOS). Because the DOS broadens upon doping, there exists a balance between a well-defined electronic structure and high conductivity necessary for mixed conduction in thermoelectrics. As carrier density increases, so does the concentration of associated counterions, leading to a greater degree of energetic disorder within the semiconductor. Dopant-induced disorder at high carrier density justifies a widely observed power law trend in thermopower and conductivity, indicating that routes to increase power factor in organic thermoelectrics likely arise from minimizing energetic disorder at high doping levels. (Thomas, Popere et. al.)

Further investigation of this system using *operando* grazing incidence X-ray scattering has revealed that the distribution of ions in a semicrystalline semiconductor is not homogeneous and the structural changes that ion infiltration induces has a large impact on charge carrier mobility. An electrochemical transistor with the semiconductor poly(3-hexylthiophene) (P3HT) at a free interface (Popere et. al.) allows us for the first time to connect the structural changes that occur in a semiconductor with the optoelectronic and electrical properties as the device is operated (**Figure 2b**). Negatively-charged ions from the dielectric first infiltrate the amorphous regions of the semiconductor, and penetrate the crystalline regions at a critical carrier density of 4 × 10^{20} cm^{-3}. The stark change in crystal structure of P3HT correlates with a sharp increase in the effective carrier mobility, indicating that more effective mixing between the electronic and ionic components of a mixed conductor is beneficial to carrier transport. UV-visible spectroscopy reveals that holes induced in P3HT first reside in the crystalline regions of the polymer, which verifies that a charge carrier need not be in the same physical domain as its associated counterion. The dopant-induced morphological changes of P3HT rationalize the dependence of mobility on carrier concentration and suggests that a doped polymer is a fundamentally different material than its pristine counterpart. (Thomas, Brady et. al.)

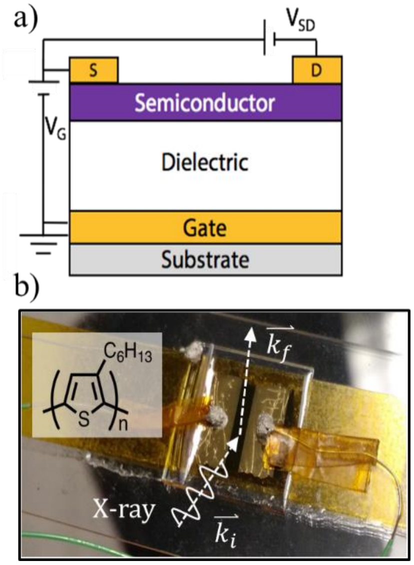

Figure 2: a) Schematic of an organic electrochemical transistor. The dielectric used here consists of a single-ion conducting polymer that controls ion diffusion to one species. b) Photograph of organic electrochemical transistor with illustrated schematic of *operando* grazing incidence x-ray scattering

To extend the findings from our model interfaces to that of a bulk mixed conductor, we have synthesized a novel PEG substituted PEDOT-type semiconductor that can withstand high doping and ion concentrations without losing stability. We have found that the counterion that stabilizes the charge carrier plays a direct role in the thermoelectric properties. Although PEDOT:PSS is the most successful mixed conducting thermoelectric material, it comes as a complex, insoluble dispersion involving these two components, and is difficult to study as such. We therefore designed and synthesized an analogue to PEDOT that can be processed and studied in a variety of solvents with and without the presence of various ions. In preliminary work, we have solution doped this polymer to high concentrations with a sulfonate-type anion (similar to PSS) or a TFSI-type anion. While the TFSI-type anion favors bipolaron charge carriers, the sulfonate-type anion favors polaronic charge carriers. We have already shown that the Seebeck coefficient and conductivity is sensitive to the polaron/bipolaron ratio in these materials, so this demonstrates the significant role of ionic character on the transport properties and thermoelectric performance of the electron-conducting component in polymeric mixed conductors.

Future Plans

We have devised a system by which carrier concentration, an independent variable in thermoelectric charge transport, can be controlled in the polymeric semiconductor. From this work, the stark difference in the distribution of holes and counterions suggests that crystallinity and morphology play an important role in how the semiconductor is doped. It is likely that a balance exists between the amount of amorphous and crystalline regions to maximize electronic performance in the semiconductor without sacrificing mobility. We plan to explore the role of crystallinity in electrochemically doped polymers with the goal of achieving insight into an optimal morphology for high-performance organic thermoelectrics. Percent crystallinity can be altered synthetically through side chain engineering or through processing conditions, such as quenching or polymer blending. We plan to vary the crystalline fraction from mostly crystalline to completely amorphous to study the impact of ion infiltration and morphology on thermoelectric charge transport.

Through successfully switching the polarity of the tethered ion in PILs, we can control the mode of operation in a PIL-gated transistor between inducing charges electrochemically or through electrostatics. The impact of the mode of operation on the thermoelectric properties of the semiconductor is a future direction we are currently pursuing. By inducing charge in the semiconductor and preventing ion infiltration, a true macroscopic ion/electron interface is established, which opens a new route for higher power factor in polymeric semiconductors.

We have synthesized our ion-conducting PIL components and have shown that they can control ion infiltration into the electron conducting domain. We have also shown that our electron conducting ProDOT component is amenable to large ion concentrations. One of our ultimate goals is to understand the transport properties and ionic-electronic interactions in mixed conducting materials with more complex geometries. This will be accomplished by synthesizing a block copolymer that consists of our ion conducting PIL and our electron conducting ProDOT as the two components. Controlled variation of the volume fraction of ProDOT or the PIL will then be used to systematically vary the interfacial area between the ionic and electronic domains. By measuring the electronic and thermoelectric properties as a function of domain size, the effect of the ionic-electronic interfacial interactions on the bulk properties can be elucidated. In conjunction with the OFET measurements, these studies will lead to comprehensive design rules for the optimization of mixed conducting thermoelectric materials.

References

1. Chang, W. B.; Fang, H.; Liu, J.; Evans, C. M.; Russ, B.; Popere, B. C.; Patel, S. N.; Chabinyc, M. L.; Segalman, R. A. Electrochemical Effects in Thermoelectric Polymers. ACS Macro Letters 2016, 5 (4), 455–459.
2. Yee, S. K.; Coates, N. E.; Majumdar, A.; Urban, J. J.; Segalman, R. A. Thermoelectric Power Factor Optimization in PEDOT:PSS Tellurium Nanowire Hybrid Composites. Phys. Chem. Chem. Phys. 2013, 15, 4024–4029.

Publications

Published

Role of Disorder Induced by Doping on the Thermoelectric Properties of Semiconducting Polymers

Elayne M. Thomas, Bhooshan C. Popere, Haiyu Fang, Michael L. Chabinyc*, and Rachel A. Segalman*

Chemistry of Materials **2018** *30* (9), 2965-2972

DOI: 10.1021/acs.chemmater.8b00394

> "The authors gratefully acknowledge support from the Department of Energy Office of Basic Energy Sciences under Grant No. DE-SC0016390. E.M.T. kindly acknowledges a National Science Foundation Graduate Research Fellowship under Award No. 1650114. Synthesis of the PIL was supported by the Air Force Office of Scientific Research through the Multidisciplinary University Research Initiative on Controlling Thermal and Electrical Transport in Organic and Hybrid Materials, Grant No. AFOSR FA95501210002, and measurements under shared facilities were supported through the MRSEC Program of the National Science Foundation under Award DMR-1720256."

Submitted

Tailoring the Seebeck Coefficient of PEDOT:PSS by Controlling Ion Stoichiometry in Ionic Liquid Additives

Amir Mazaheripour, Shubhaditya Majumdar, Dakota Hanemann-Rawlings, Elayne M. Thomas, Christine McGuiness, Lauriane d'Alencon, Michael L. Chabinyc, and Rachel A. Segalman.

Chemistry of Materials. Submitted.

> "The authors gratefully acknowledge a grant from Solvay Chemical for device fabrication and the Department of Energy Office of Basic Energy Sciences (Grant No. DE-SC0016390) for materials characterization and analysis. We also gratefully thank UCSB Materials Research Laboratory Shared Experimental Facilities, supported by the MRSEC Program of the NSF under Award No. DMR 1720256; a member of the NSF-funded Materials Research Facilities Network (www.mrfn.org). Use of the Stanford Synchrotron Radiation Light Source, SLAC National Accelerator Laboratory, is supported by the U.S. Department of Energy, Office of Science, Office of Basic Energy Sciences under Contract No. DE-AC02-76SF00515. The authors thank Bhooshan C. Popere for insightful discussions and Hidenori Nakayama for assistance with processing of the GIWAXS data."

Implications of Charge Distribution on the Morphology and Charge Transport Properties in Doped Polymeric Semiconductors

Elayne M. Thomas, Michael A. Brady, Hidenori Nakayama, Bhooshan C. Popere, Rachel A. Segalman, and Michael L. Chabinyc. *Adv. Func. Mater*. Submitted.

> "The authors acknowledge funding support from the Department of Energy Office of Basic Energy Sciences under grant no. DE-SC0016390 for all device fabrication, device characterization, and analysis. Synthesis of the anthracene-

> functionalized PIL made use of shared facilities of the UCSB MRSEC (NSF DMR 1720256), a member of the Materials Research Facilities Network (www.mrfn.org). E.M.T. gratefully acknowledges support from the NSF Graduate Fellowship (DGE-1650114). This research used resources of the Advanced Light Source, which is a U.S. Department of Energy Office of Science User Facility under contract no. DE-AC02-05CH11231."

Photocrosslinkable Polymeric Ionic Liquids *via* [4π + 4π] Cycloaddition Reaction of Anthracene: Decoupling Mechanics and Ionic Conductivity to Facilitate Processing

Bhooshan C. Popere, Gabriel E. Sanoja, Elayne M. Thomas, Seamus D. Jones, Nicole S. Schauser, Joshua M. Bartels, Matthew E. Helgeson, Michael L. Chabinyc, and Rachel A. Segalman. *Journal of Materials Chemistry C.* Submitted.

> "We gratefully acknowledge the MRSEC Program of the National Science Foundation under Award DMR-1720256 for the synthesis of the PIL. We also gratefully acknowledge support from the Department of Energy Office of Basic Energy Sciences under Grant No. DE-SC0016390 for all the device and structural characterization. E.M.T. acknowledges the National Science Foundation Graduate Research Fellowship Program Award No. 1650114 for financial support. Any opinions, findings, and conclusions or recommendations expressed in this material are those of the author(s) and do not necessarily reflect the views of the National Science Foundation. The authors also thank Costantino Creton and Mehdi Vahdati for helpful discussions."

To Be Submitted By End of Fiscal Year (July 2018)

Controlling the Doping Mechanism in Polymeric Thermoelectrics Through Polymeric Ionic Liquid-gated Transistors

Dakota R. Rawlings, Elayne M. Thomas, Michael L. Chabinyc, Rachel A. Segalman.

Electrical Consequences of High Chemical Doping Levels in Soluble PEDOT Analogues

Amir Mazaheripour, Rachel A. Segalman, Michael L. Chabinyc.

Coacervation of a Conjugated Polyelectrolyte for Mixed Conductive Complex Fluids

Scott P. O. Danielson, Thuc-Quyen Nguyen, Glenn H. Fredrickson, Rachel A. Segalman.

DE-SC-0012541: Hybrid Metal Halides: Advancing Optoelectronic Materials

Ram Seshadri, (Lead PI, University of California, Santa Barbara)
Michael Chabinyc, (Co-PI, University of California, Santa Barbara)
Mercouri Kanatzidis (Co-PI, Northwestern University)

Program Scope

Main-group halide compounds with the perovskite crystal structure, particularly hybrid organic-inorganic lead halides, have recently attracted immense attention for their remarkable optoelectronic properties, ease of preparation, and abundant constituent elements. Such compounds — of which methylammonium lead iodide $(CH_3NH_3)PbI_3$ has been the most extensively studied — are strong optical absorbers, display reasonable charge-carrier mobilities and long exciton diffusion lengths and lifetimes, all of which contribute to impressive photovoltaic performance. Like their well-studied oxide analogues, halide perovskites exhibit great chemical flexibility, leading to diverse structure and function. Since the first application of hybrid lead iodides in PV devices in 2009, the scope has broadened substantially to include the pursuit of lead-free materials, bromides, and mixed halides for light emission and detection applications. However, key aspects regarding the origins of the remarkable functionality of these materials remain enigmatic. There has also been a great need for the advancement of new materials and new chemistries beyond the simple perovskites to expand this class of materials.

This project has a strong focus on the creation of new materials, as well as developing fundamental understanding of the materials science of these hybrid metal halides, both perovskites and beyond. Some of the questions driving the research in this project include: *How does the interaction between the organic species and the inorganic sub-lattice influence structural transitions and lattice dynamics in halide perovskites*? *What is the impact of the lone pair of electrons on the central, divalent main-group cation on key properties*? *What is the manner in which halide ion migration and segregation takes place in solid-solution halide perovskites? Can we expand the domain of known functional hybrid metal halides through the creation of novel materials? What is the nature of film growth and the impact of structural defects on electronic properties, and how does structure and chemistry influence charge carriers?*

We address these questions by employing sophisticated probes of the structure (including *local* structure) and dynamics of these hybrid halide materials as a function of temperature and chemistry, and we examine the influence of dynamic lone pair stereochemical activity on the carrier behavior of halide perovskites through studying compositionally controlled materials. We study site mixing of both the organic cations and halide anions, which has implications for halide ion migration and segregation in solid-solution materials, ultimately impacting the physical properties. A new and expanded portfolio of materials being developed, including those displaying the greater stability of 2D metal halides with the desired electronic performance of 3D perovskites. We are advancing an understanding of the growth processes and resulting performance in thin film architectures, and capitalizing on unique infrastructure to understand charge carriers in these materials towards the goal of improved optoelectronic performance. Select aspects of the research from the past two years are described in the rest of this extended abstract.

Recent Progress

Tunable dynamic distortions and cation dynamics in the halide perovskites: Expanding upon the prior, detailed study of perovskite $CsSnBr_3$, X-ray total scattering studies and pair distribution function (PDF) analysis demonstrate local, dynamic distortions of the lead or tin coordination environments across the entire hybrid perovskites materials class as a consequence of lone-pair stereochemical activity. Further, the strength of these distortions is shown to controllable by chemical substitution on all sites of the crystal, with a lighter carbon-group cation, a more electronegative halide anion, and a larger *A*-site counter-cation all leading to greater distortions (Figure 1). These dynamic, polar distortions are proposed to enhance lattice polarizability, screening charge carriers from one another and from charged defect complexes, leading to the low trapping and recombination rates (and modest mobilities) observed in experiment. Since the publications which reveal the chemical origins and tunability of this phenomenon, several other groups have reported observations that reflect these intrinsic instability.

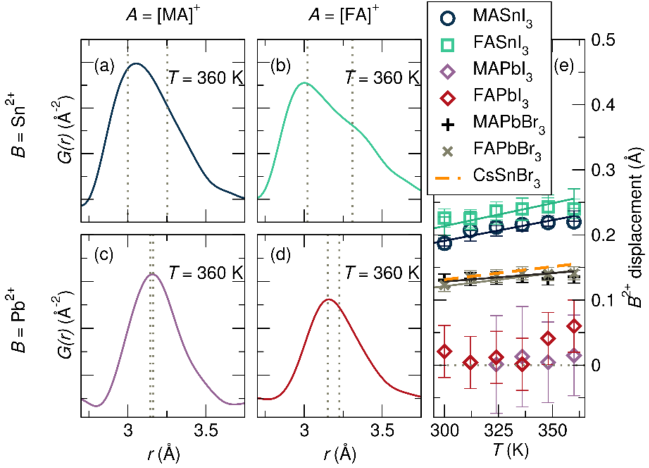

Figure 1: (a-d) X-ray pair distribution functions of hybrid tin and lead iodide perovskites reveal locally distorted main-group cation coordination, with the degree of distortion enhanced for a lighter group 14 cation or a larger molecular counter-cation. (e) Comparison of the temperature-dependence of distorted local structure models additionally demonstrates increased distortion arising from the greater electronegativity of the bromide anion.

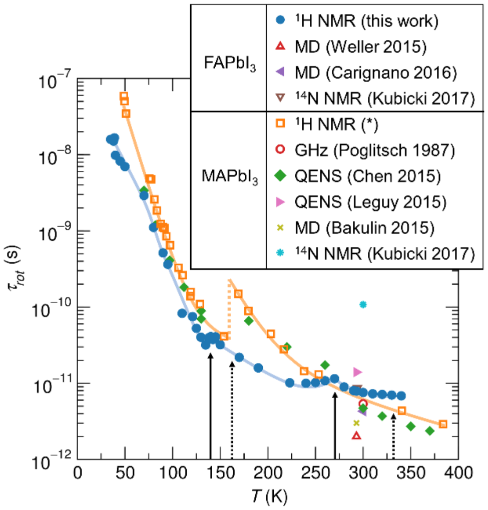

Figure 2: Temperature-dependence of the molecular reorientation time (τ_{rot}) in $FAPbI_3$ and $MAPbI_3$ modeled from ^{1}H T_1. Phase transition temperatures are indicated by solid ($FAPbI_3$) and dashed ($MAPbI_3$) arrows. Colored lines are to guide the eye only. Reported reorientation times from GHz spectroscopy, quasi-elastic neutron scattering (QENS), ab initio molecular dynamics (MD), and ^{14}N NMR are presented for comparison.

The importance (or lack thereof) for properties and performance of the molecular cations in the hybrid perovskites has been a key matter of debate within the field. Critical evaluation of hypotheses regarding the impacts of the molecules has been hampered by a lack of comprehensive study of the crystallographic and local structures of these compounds, quantitative information on the dynamics of molecular motion, and omission of the significant differences in dipole moment between methyl ammonium and formamidinium in many analyses. Building on our prior work on the molecule–framework interaction in the hybrid lead iodides, solid state nuclear magnetic resonance (NMR) spectroscopy, dielectric spectroscopy, calorimetry, neutron total scattering, and *ab initio* studies were employed to establish the dynamics of molecular motion and the nature of hydrogen-bonding in the high-performance absorber, formamidinium (FA) lead iodide ($FAPbI_3$). Additionally, existing data on methylammonium (MA) lead iodide ($MAPbI_3$) and $FAPbI_3$ were reanalyzed in the context of the current literature, revealing strikingly similar dynamics at room temperature for the two compounds, despite significant differences in other regimes. This study provides essential information for future scrutiny of several of the prevailing hypotheses about the origins of slow recombination in these materials.

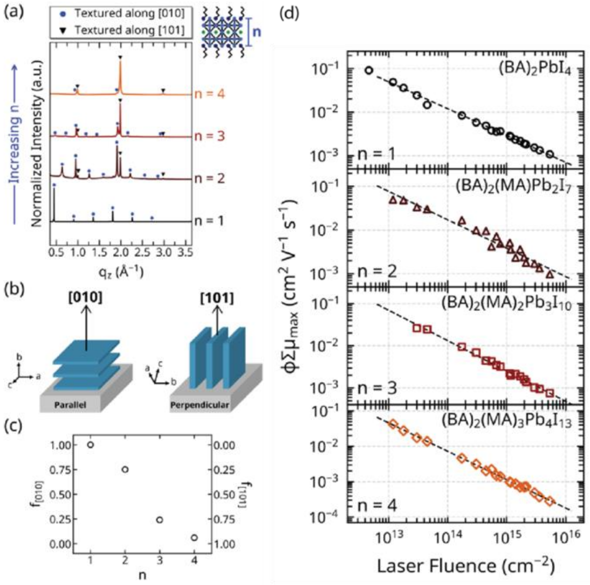

Figure 3. (a) Specular XRD spectra of $(BA)_2(MA)_{n-1}PbnI_{3n+1}$ for $n = 1$ to 4, illustrating an increase in the fraction of crystals textured along [101] with increasing *n*. (b) Schematic of parallel and perpendicular texturing of lead iodide sheets (blue layers) along with their respective crystallographic axes and (c) fraction of [010] and [101] textured domains for each of the four phases. (d) Maximum values of TRMC figure-of-merit ϕΣμ over a range of incident laser fluences, with dashed lines indicating power law fits to the data.

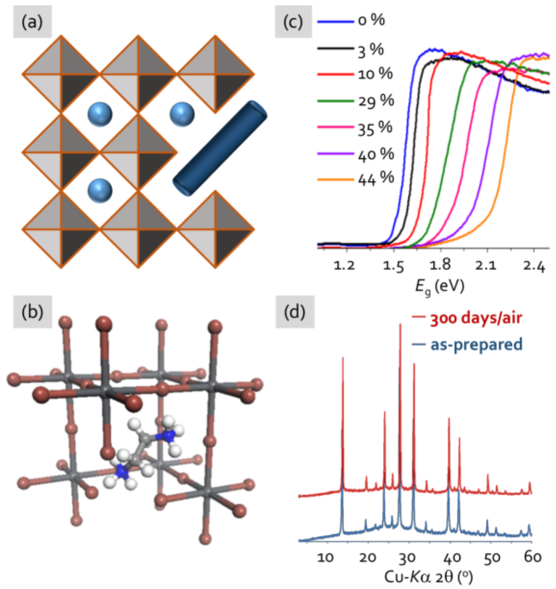

Figure 4. (a) and (b) Schematic illustrations of the “hollowing” of the 3D perovskite through the introduction of ethylenediamine (*en*). (c) Optical absorption spectra of compounds $(MA)_{1-x}(en)_x(Pb)_{1-0.7x}I_{3-0.4x}$, with increasing amount of *en* in the stating composition showing the tunability of properties. (d) Experimental powder X-ray diffraction (PXRD) patterns of the freshly prepared compound $(FA)_{0.61}(en)_{0.39}Pb_{0.727}I_{2.844}$ and after exposure to air for 300 days, attesting to the stability.

Structure–property control in films of Ruddlesden-Popper compounds: The presence of spacer cations such as butylammonium can direct the growth of layered Ruddlesden-Popper perovskite phases with systematic effects on grain texturing in thin film devices. These layered phases show similar optoelectronic properties to the three-dimensional hybrid perovskites, but with improvements in stability and a versatile range of compositions to tune material behavior. By examining thin films of a series of Ruddlesden-Popper phases utilizing a butylammonium spacer cation with the structure $(C_4H_9NH_3)_2(CH_3NH_3)_{n-1}Pb_nI_{3n+1}$ it was found that changes in crystallographic texture with the value of *n* (thickness of Pb–I sheet layer). The crystallites in the films orient in two different crystallographic directions, [010] and [101] [Figure 3 (a)]. As the value of *n* increases, the amount of crystallites along [101] increases, equivalent to perpendicular stacking of lead iodide domains on the substrate, the ideal geometry for a vertical optoelectronic device. To relate the structure to electronic properties, we utilized time-resolved microwave conductivity (TRMC) to measure the carrier mobilities and lifetimes for each composition. The results of the TRMC measurements are shown in Figure 3 (d) and suggest that there is substantial higher-order recombination in all of the layered compounds, illustrated by the monotonic decrease in the value of $\phi\Sigma\mu$ as the laser power increases. However, it appears that there are no enhanced carrier lifetimes as seen in three dimensional methylammonium lead iodide even with $n = 3$ or 4.

3D "Hollow" hybrid halide perovskites: A new family of 3D perovskites, known as "hollow" perovskites, have been developed that exhibit admirable environmental stability as well as tunable electronic properties (Figure 4). Hollow perovskites derive from three-dimensional (3D) AMX_3 perovskites (A = MA, FA; M = Sn, Pb; X = Cl, Br, I) where small molecules such as ethylenediammonium cations (*en*) can be incorporated as the dication without altering the structure dimensionality (Figure 4). However, their incorporation in the 3D perovskite structure leads to massive M and X vacancies in the 3D $[MX_3]$ framework, thus the term "hollow". Through a combination of physical and spectroscopic methods (XRD, gas pycnometry, ^{1}H-NMR, TGA, SEM/EDX), we assigned the general formula $(A)_{1-x}(en)_x(M)_{1-0.7x}(X)_{3-0.4x}$, to the hollow perovskites. The resulting materials are semiconductors with significantly blue-shifted direct band gaps from 1.25 eV to 1.51 eV for Sn-based perovskites and from 1.53 eV to 2.1 eV for the Pb-based analogues. The increased structural disorder and hollow nature were validated by single crystal X-ray diffraction analysis as well as pair distribution function (PDF) analysis. Density functional theory (DFT) calculations support the experimental trends and suggest that the observed widening of the band gap is attributed to the massive M and X vacancies which create a less connected 3D hollow structure. The resulting hollow materials have superior air stability, where in the case of Sn-based hollow perovskites it exceeds two orders of temporal magnitude compared to the conventional full perovskites of $MASnI_3$ and $FASnI_3$.

Future Plans

The major goal in the next months is to carry out a systematic examination of *local structure* within the cubic regimes of AMX_3 compounds, where A = Rb and Cs, M = Ge, Sn, Pb, and X = Cl, Br, I, via total scattering techniques. The stereochemical behavior of the main group metal ns^2 "lone pair" as temperature is varied across this series will be studied, with the goal of describing the potential ubiquity of the phenomenon dubbed "*emphanisis*". Currently, many of these halide perovskite family members (particularly the Ge containing compounds) are understudied in their cubic phases, but based on our prior work regarding related members of this series ($CsSnBr_3$, hybrid Sn and Pb halides, it is believed that this "hidden" lone pair phenomenon will be present. This work is of great interest to the scientific community, as lone-pair behavior in main group metal containing compounds has substantial impact on material physics. The growth kinetics of Ruddlesden-Popper thin films will be studied to understand how such phases arise. Initial work using grazing incidence X-ray scattering shows defective structures in thin films of compounds with $n > 2$ where multiple phases are present with complex disorder. It is of great interest to understand the electronic structure of these polycrystalline films and whether there is strong interaction between the phases.

Publications from two prior years acknowledging DE-SC-0012541 (reverse chronology)

1. I. Spanopoulos, W. Ke, C. Stoumpos, E. C. Schueller, O. Kontsevoi, R. Seshadri, and M. Kanatzidis, Unraveling the chemical nature of the 3D “hollow” hybrid halide perovskites, *J. Am. Chem. Soc.* **140** (2018) 5728–5742. [DOI: 10.1021/jacs.8b01034]
2. A. Marronnier, G. Roma, S. Boyer-Richard, L. Pedesseau, J.-M. Jancu, Y. Bonnassieux, C. Katan, C. C. Stoumpos, M. G. Kanatzidis, and J. Even, Anharmonicity and disorder in the black phases of cesium lead iodide used for stable inorganic perovskite solar cells, *ACS Nano* **12** (2018) 3477–3486. [DOI: 10.1021/acsnano.8b00267]
3. S. Nah, B. M. Spokoyny, C. M. M. Soe, C. C. Stoumpos, M. G. Kanatzidis, and E. Harel, Ultrafast imaging of carrier cooling in metal halide perovskite thin films, *Nano Lett.* **18** (2018) 1044–1048 [DOI: 10.1021/acs.nanolett.7b04520]
4. N. R. Venkatesan, J. G. Labram, and M. L. Chabinyc, Charge-carrier dynamics and crystalline texture of layered Ruddlesden–Popper hybrid lead iodide perovskite thin films *ACS Energ. Lett.* **3** (2018) 380–386. [DOI: 10.1021/acsenergylett.7b01245]
5. G. C. B. Alexander, D. H. Fabini, R. Seshadri, and M. G. Kanatzidis, $AuPb_2I_7$: A narrow bandgap Au^{3+} iodide semiconductor, *Inorg. Chem.* **57** (2018) 804–810. [DOI: 10.1021/acs.inorgchem.7b02723]
6. S. Nah, B. Spokoyny, X. Jiang, C. Stoumpos, C. M. M. Soe, M. G. Kanatzidis, and E. Harel, Transient sub-bandgap states in halide perovskite thin films, *Nano Letters* **18** (2018) 827–831. [DOI: 10.1021/acs.nanolett.7b04078]
7. E. Schueller, G. Laurita, D. Fabini, C. Stoumpos, M. Kanatzidis, and R. Seshadri, Crystal structure evolution and notable thermal expansion in hybrid perovskites formamidinium tin iodide and formamidinium lead bromide, *Inorg. Chem.* 57 (2018) 695–701. [DOI: 10.1021/acs.inorgchem.7b02576]
8. D. Fabini, T. A. Siaw, C. Stoumpos, G. Laurita, D. Olds, K. Page, J. Hu, M. Kanatzidis, S. Han, and R. Seshadri, Universal dynamics of molecular reorientation in hybrid lead iodide perovskites, *J. Am. Chem. Soc.* **139** (2017) 16875–16884. [DOI: 10.1021/jacs.7b09536]
9. S. Soe, C. Stoumpos, M. Kepenekian, B. Traoré, H. Tsai, W. Nie, B. Wang, C. Katan, R. Seshadri, A. Mohite, J. Even, T. Marks, and M. Kanatzidis, New type of 2D perovskites with alternating cations in the interlayer space, $(C(NH_2)_3)(CH_3NH_3)_nPb_nI_{3n+1}$: Structure, properties and photovoltaic performance, *J. Am. Chem. Soc.* **39** (2017) 16297–16309. [DOI: 10.1021/jacs.7b09096]
10. H. A. Evans, E. C. Schueller, S. R. Smock, G. Wu, R. Seshadri, and F. Wudl, Perovskite-related hybrid noble metal iodides: Formamidinium platinum iodide $[(FA)_2Pt^{IV}I_6]$ and mixed-valence methylammonium gold iodide $[(MA)_2Au^{I}Au^{III}I_6]$, *Inorg. Chim. Acta* **68** (2017) 280–284. [DOI: 10.1016/j.ica.2017.04.060]
11. F. O. Saouma, C. C. Stoumpos, M. G. Kanatzidis, Y. S. Kim, and J. I. Jang, Multiphoton absorption order of $CsPbBr_3$ as determined by wavelength-dependent nonlinear optical spectroscopy, *J. Phys. Chem. Lett.* **8** (2017) 4912–4917. [DOI: 10.1021/acs.jpclett.7b02286]

12. P. Guo, Y. Xia, J. Gong, C. C. Stoumpos, K. M. McCall, G. C. B. Alexander, Z. Ma, H. Zhou, D. J. Gosztola, J. B. Ketterson, M. G. Kanatzidis, T. Xu, M. K. Y. Chan, and R. D. Schaller, Polar fluctuations in metal halide perovskites uncovered by acoustic phonon anomalies, *ACS Energy Lett.* **2** (2017) 2463–2469. DOI: 10.1021/acsenergylett.7b00790
13. G. M. Dalpian, Q. Liu, C. C. Stoumpos, A. P. Douvalis, M. Balasubramanian, M. G. Kanatzidis, and A. Zunger, Changes in charge density *vs* changes in formal oxidation states: The case of Sn halide perovskites and their ordered vacancy analogues, *Phys. Rev. Mater.* **1** (2017) 025401. [DOI: 10.1103/PhysRevMaterials.1.025401]
14. L. Mao, Y. Wu, C. C. Stoumpos, B. Traore, C. Katan, J. Even, M. R. Wasielewski, and M. G. Kanatzidis, Tunable white-light emission in single-cation-templated three-layered 2d perovskites $(CH_3CH_2NH_3)_4Pb_3Br_{10-x}Cl_x$, *J. Am. Chem. Soc.* 139 (2017) 11956–11963. [DOI: 10.1021/jacs.7b06143]
15. G. Laurita, D. H. Fabini, C. Stoumpos, M. G. Kanatzidis, and R. Seshadri, Chemical tuning of dynamic cation off-centering in the cubic phases of hybrid tin and lead halide perovskites. *Chem. Sci*. **8** (2017) 5628–5635. [DOI: 10.1039/C7SC01429E]
16. J. G. Labram, N. R. Venkatesan, C. J. Takacs, H. A. Evans, E. E. Perry, Fred Wudl, and M. L. Chabinyc, Charge transport in a two-dimensional hybrid metal halide thiocyanate compound, *J. Mater. Chem. C* 5 (2017) 5930–5938. [DOI: 10.1039/C7TC01161J]
17. A. Kaltzoglou, C. C. Stoumpos, A. G. Kontos, G. K. Manolis, K. Papadopoulos, K. G. Papadokostaki, V. Psycharis, C. C. Tang, Y.-K. Jung, A. Walsh, M. G. Kanatzidis, and P. Falaras, Trimethylsulfonium lead triiodide: an air-stable hybrid halide perovskite**,** *Inorg. Chem.* **56** (2017) 6302–6309. [DOI: 10.1021/acs.inorgchem.7b00395]
18. S. Nah, B. Spokoyny, C. Stoumpos, C. M. M. Soe, M. Kanatzidis, and E. Harel, Spatially segregated free-carrier and exciton populations in individual lead halide perovskite grains, *Nat. Photon.* **11** (2017) 285–288. [DOI: 10.1038/nphoton.2017.36]
19. Lingling Mao, Yilei Wu, Constantinos C. Stoumpos, Michael R. Wasielewski, and Mercouri G. Kanatzidis, White-light emission and structural distortion in new corrugated two-dimensional lead bromide perovskites, *J. Am. Chem. Soc.* **139** (2017) 5210–5215. [DOI: 10.1021/jacs.7b01312]
20. J.-C. Blancon, H. Tsai, W. Nie, C. C. Stoumpos, L. Pedesseau, C. Katan, M. Kepenekian, C. M. M. Soe, K. Appavoo, M. Y. Sfeir, S. Tretiak, P. M. Ajayan, M. G. Kanatzidis, J. Even, J. J. Crochet, and A. D. Mohite, Extremely efficient internal exciton dissociation through edge states in layered 2D perovskites, *Science* **355** (2017) 1288-1292. [DOI: 10.1126/science.aal4211]
21. C. C. Stoumpos, C. M. M. Soe, H. Tsai, W. Nie, J.-C. Blancon, D. H. Cao, F. Liu, B. Traoré, C. Katan, J. Even, A. D. Mohite, and M. G. Kanatzidis, High members of the 2D Ruddlesden-Popper halide perovskites: synthesis, optical properties, and solar cells of $(CH_3(CH_2)_3NH_3)_2(CH_3NH_3)_4Pb_5I_{16}$, *Chem* **2** (2017) 427–440. [DOI: 10.1016/j.chempr.2017.02.004]

22. P.-A. Mante, C. C. Stoumpos, M. G. Kanatzidis, A. Yartsev, Electron–acoustic phonon coupling in single crystal $CH_3NH_3PbI_3$ perovskites revealed by coherent acoustic phonons, *Nat. Commun*. **8** (2017) 14398. [DOI: 10.1038/ncomms14398]

Transition Metal Oxides Nanomaterials for Aqueous Electrochemical Energy Storage

Xiaowei Teng, Department of Chemical Engineering, University of New Hampshire

Program Scope

There is an essential priority of developing large-scale stationary electrochemical energy storage (EES) systems efficiently and economically storing energy generated from renewable sources (e.g., solar or wind) in order to withstand the gaps between the peak production and peak consumption. Rechargeable non-aqueous lithium-ion batteries (LIBs) have advanced rapidly in the past twenty years with much improved energy density, widely used from portable electronics to electrical vehicle. However, high cost and safety concerns make the current LIBs less appealing for large-scale stationary EES, where the cost, safety, and cycle life become important in addition to mere energy density. Rechargeable EES devices using aqueous electrolytes and earth abundant cations (e.g., Na and K) as the charge carrier show several advantages compared with non-aqueous LIBs. For example, using non-flammable and environmentally benign water-based electrolytes not only mitigates the safety issue of non-aqueous LIBs, but also significantly lowers the production cost by avoiding rigorous manufacturing conditions. Moreover, compared with Li-ions, hydrated Na- or K-ions possess the smaller Stokes radius, defined as the total radius of the ion and bound water molecules, and thus greater transport properties in aqueous electrolytes. The utilization of aqueous Na-ion storage could fulfill essential requirements of large-scale stationary EES, where low cost and environmental sustainability become imperative. However, the current aqueous EES needs further improvement in the energy density in order to rival the performance of the non-aqueous LIBs. The energy density of aqueous EES is limited to its narrow voltage window and low storage capacity. To tacking these technical bottlenecks, the overall goals of the project are:

(i) Discover new aqueous EES material chemistry that enables metal oxide nanomaterials to be operated at the potential window beyond 1.23 V. Aqueous EES devices usually operate at or below 1.23 V. Beyond this thermodynamically stable potential window the hydrogen evolution reaction (HER) and oxygen evolution reaction (OER) occur. However, a voltage window of 1.23 V is too narrow to achieve high energy density and power density. The primary goal of the project is to discover a new type of materials that are not only redox active for charge storage, but also inert to HER and OER (high overpotential) thus a kinetically stable potential window higher than 1.23 V can be achieved.

(ii) Develop new metal oxide structures that reversibly store alkali cations in aqueous electrolyte via various charge storage mechanisms (e.g., capacitive and diffusion-limited redox). Our approach is through the design of layered electrode materials, from which the interlayer distance can afford nearly reversible insertion/extraction of alkali without causing structural degradation.

Recent Progress

(i) The PI has discovered the formation of the hydroxylated interphase on the surface of Mn_5O_8 materials during the electrochemical cycling, which inhibits the HER/OER and thus enables a kinetically stable potential window of 2.5 V for aqueous Na-ion storage in half-cell (**Figure 1**).[1] This is the one of the most important achievements from PI's previous support. Monoclinic manganese oxide (Mn_5O_8, $Mn^{2+}_2Mn^{4+}_3O_8$) nanoparticles were synthesized using a wet chemistry method and discovered that this material forms a hydroxylated interphase upon the interaction with water during the electrochemical cycling. The theoretical calculations showed that the strong interaction between Mn^{2+} layer on the surface and water might account for the formation of such a hydroxylated interphase that increased the energy barrier for the consequent water decomposition processes. The hydroxylated Mn_5O_8 greatly suppressed gas evolution reactions (> 0.6 V overpotential towards HER and OER) and delivered a kinetically stable potential window of 2.5 V in a half-cell (**Figure 1a**). An aqueous symmetric full cell using such electrodes demonstrated a stable potential window of 3.0 V, and good energy and power performance. The results offer a new paradigm for developing electrode materials with hydroxylated interphase for aqueous EES with a high voltage window.

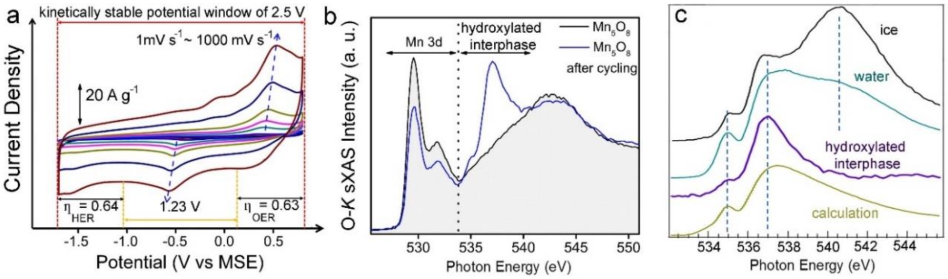

Figure 1. (a) Cyclic voltammetry (CV) of Mn_5O_8 materials in 0.1 M Na_2SO_4 solution between -1.7 to 0.8 V (vs MSE) in a half-cell. (b) Oxygen K-edge sXAS of Mn_5O_8 (pristine) and Mn_5O_8 after two CV cycles. The 535 and 537 eV peaks are fingerprints of the water. (c) A comparison of the oxygen K-edge features of the hydroxylated interphase with water, ice, and the reported calculation.

The PI conducted the oxygen K-edge soft X-ray Absorption Spectroscopy (sXAS) measurement on the pristine Mn_5O_8 and Mn_5O_8 after two cycles of CVs at beamline 8.0.1 at the Advanced Light Source (ALS) at Lawrence Berkeley National Lab (LBNL). Cycled Mn_5O_8 electrode displayed peaks at the 535 eV and 537 eV (**Figure 1b**), resembling the "pre-edge" and "main peak" fingerprints from water and indicating the formation of hydroxylated interphase on the surface of Mn_5O_8. **Figure 1c** shows the oxygen K-edge spectra after subtracting the Mn_5O_8 (pristine) signal. It is clear that the hydroxylated interphase layer is different from ice, by missing the high-energy hump from the saturated H-bonds in ice. It reproduces the "pre-peak" and "main peak" of liquid water, with the "main peak" at 537.5 eV dominating the spectrum. The enhancement of this main peak stems from a combination of an extended O-O distance and perfectly aligned H-bonds along the O-O direction.[2] DFT calculation was used to determine the activation energy of each intermediate reaction steps during the HER and OER on surfaces of hydroxylated Mn_5O_8, pure Mn_5O_8 and Mn_3O_4 (**Figure 2**). The activation energy of the rate determining step are all substantially high for OER, indicating that OER is intrinsically difficult. Particularly, activation energy of water dissociation ($H_2O^* \rightarrow H^* + OH^*$), the second catalytic step of gas evolutions, follows the order of hydroxylated Mn_5O_8 (1.41 eV) > Mn_5O_8 (0.45 eV) > Mn_3O_4 (~ 0 eV). Hydroxylated Mn_5O_8 shows about 1 eV higher in activation energy than that of Mn_5O_8, implying that the reaction rate at 300 K is at least

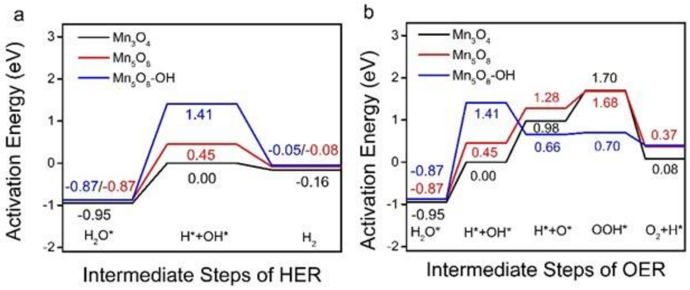

Figure 2. The activation energies of intermediate reaction steps of (a) HER and (b) OER on Mn_5O_8 with a hydroxylated interphase, Mn_5O_8 without interphase and Mn_3O_4 (the asterisk symbol denotes the adsorbed species on the surface).

17 orders of magnitude slower according to the Arrhenius equation. Therefore, the DFT calculation directly confirmed the inhibitive role of the hydroxylated interphase on the HER and OER.

(ii) The PI has studied the influences of the structural water on the stability and electrochemical performance of the disordered V_2O_5 nanostructures using neutron total scattering collected at Spallation Neutron Source (SNS) at Oak Ridge National Lab and pair distribution function (PDF) analysis as shown in **Figure 3a**.[3] The fully hydrated V_2O_5 material showed a much larger coherence length, the rearrangement of the local structure and larger occupancy of the water intercalated between the layers, compared with partially hydrated V_2O_5. These results indicated that disordered V_2O_5 could be stabilized via a strong interaction between O (from structural water) and V atoms. V_2O_5 engaged by structural water exhibited superior capacity (0.89 electrons transfer per vanadium atom) for aqueous K-ion storage in half-cell. *In situ* X-ray diffraction was conducted to examine the evolution of (001) diffraction peak upon the three cycles of cyclic voltammetry at 17-BM-B beamline at APS at Argonne National Lab. The results demonstrated that disordered V_2O_5 layered materials engaged with structural water showed more continuous expansion/contraction of (001) diffraction planes and a wider redox-active potential window during electrochemical cycling in a Contour plot (**Figure 3b**), compared with highly crystalline materials (**Figure 3c**). These results are important for designing a new type of disordered electrode materials stabilized by structural water for aqueous energy storage with a large storage capacity.

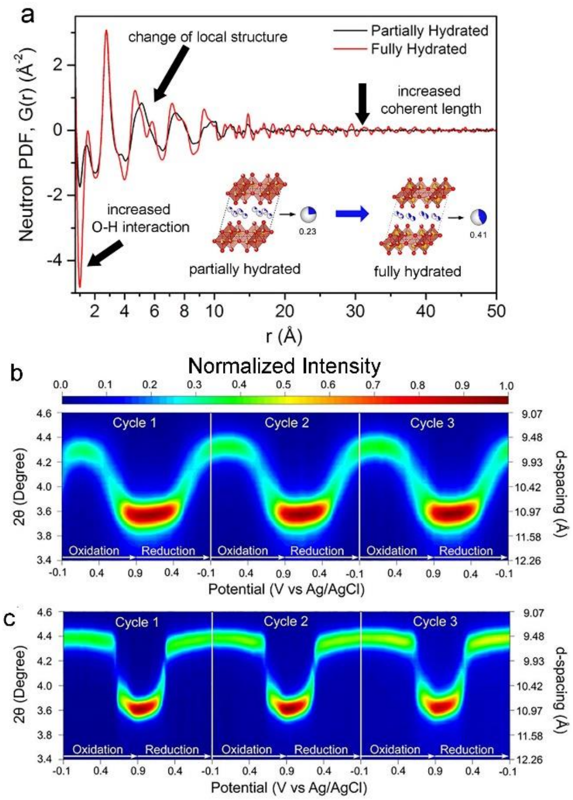

Figure 3. (a) Neutron PDFs of partially and fully hydrated disordered V_2O_5. The Contour plot of *in situ* XRD spectra of the (001) plane during CVs for (b) disordered V_2O_5 and (c) ordered V_2O_5 materials.

(iii) One of the research objectives is to understand the charge storage mechanism of transition metal oxides for aqueous EES with high storage capacity and long cycling life. By rational design of electrode materials with desired morphologies, sizes, compositions, storage capacity of electrode materials could be improved by enhancing both capacitive (including electrical double layer capacitance [EDLC] and pseudocapacitance) and diffusion-limited redox processes, while still sustained a plausible rate-performance. The PI developed a surfactant-free wet chemistry method to synthesize various metal oxide nanostructures.[4-7] Using this scalable method, the PI developed synthetic capability to prepare the multi-phase electrode materials with different morphologies. More importantly, with proper control of reaction conditions and post-synthesis thermal treatment, the local structures of the nanomaterials (e.g., cation/anion defect, disorder, bonding) can also been tuned. The PI reported the preparation of bi-phase Co-Mn-O nanostructures comprised of layered $MnO_2\cdot H_2O$ birnessite and tetragonal $Co_xMn_{3-x}O_4$ spinel $[(Co_{0.83}Mn_{0.13}Va_{0.04})_{tetra}(Co_{0.38}Mn_{1.62})_{octa}O_{3.72}$; tetra: tetrahedral sites; octa: octahedral sites; Va:

vacant site].[8] The layered MnO_2 phase significantly improved the capacitive charge storage process of Na-ions, while the Co-Mn-O spinel phase with predominant disorder in cation sites caused by cobalt insertion facilitated both storage capacity and ionic transport of Na-ion (**Figure 4**). Synergistic effect from layered and spinel bi-phase lead to the superior specific storage capacity for Na-ions (121 mAh g^{-1} in half-cell) and rate performance (81 mAh/g after 5000 cycles at 2 A/g in full-cell).

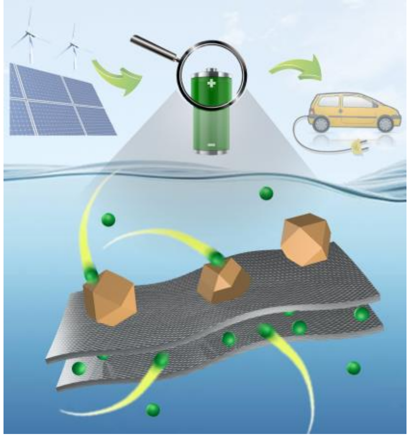

Figure 4. Bi-phase cobalt manganese oxide electrode materials comprised of layered MnO2 birnessite phase and $Co_{1.21}Mn_{1.75}O_{3.72}$ spinel phase

Future Plans

A new proposal titled "Understanding the Interplay between Nanostructured Electrode and Aqueous Electrolyte for Na-Ion Energy Storage" has been submitted to DOE-BES in Jan 2018, with an objective to understand the interplay between nanostructured metal oxides and aqueous electrolyte, and to discover how such interplay contributes to the interphases formation and how such interphases work for aqueous Na-ion storage.

Reference:

1. Shan, X. Q.; Charles, D. S.; Lei, Y. K.; Qiao, R. M.; Wang, G. F.; Yang, W. L.; Feygenson, M.; Su, D.; Teng, X. W., Bivalence Mn5O8 with hydroxylated interphase for high-voltage aqueous sodium-ion storage. *Nat. Commun.* **2016,** *7*, 8.
2. Wernet, P.; Nordlund, D.; Bergmann, U.; Cavalleri, M.; Odelius, M.; Ogasawara, H.; Naslund, L. A.; Hirsch, T. K.; Ojamae, L.; Glatzel, P.; Pettersson, L. G.; Nilsson, A., The structure of the first coordination shell in liquid water. *Science* **2004,** *304* (5673), 995-9.
3. Charles, D. S.; Teng, X., Vanadium Pentoxide (V2O5) Electrode for Aqueous Energy Storage: Understand Ionic Transport using Electrochemical, X-ray and Neutron Tools. In *Alkali-ion Batteries*, Yang, D., Ed. InTech: 2016.
4. Shan, X. Q.; Guo, F. H.; Xu, W. Q.; Teng, X. W., High purity Mn5O8 nanoparticles with a high overpotential to gas evolution reactions for high voltage aqueous sodium-ion electrochemical storage. *Front. Energy* **2017,** *11* (3), 383-400.
5. Yeager, M.; Du, W. X.; Si, R.; Su, D.; Marinkovic, N.; Teng, X. W., Highly Efficient K0.15MnO2 Birnessite Nanosheets for Stable Pseudocapacitive Cathodes. *J. Phys. Chem. C* **2012,** *116* (38), 20173-20181.
6. Yeager, M. P.; Du, W. X.; Bishop, B.; Sullivan, M.; Xu, W. Q.; Su, D.; Senanayake, S. D.; Hanson, J.; Teng, X. W., Storage of Potassium Ions in Layered Vanadium Pentoxide Nanofiber Electrodes for Aqueous Pseudocapacitors. *ChemSusChem* **2013,** *6* (12), 2231-2235.
7. Yeager, M. P.; Su, D.; Marinkovic, N. S.; Teng, X. W., Pseudocapacitive NiO Fine Nanoparticles for Supercapacitor Reactions. *J. Electrochem. Soc.* **2012,** *159* (10), A1598-A1603.
8. Shan, X.; Charles, D. S.; Xu, W.; Feygenson, M.; Su, D.; Teng, X. W., Bi-phase Cobalt-Manganese Oxide with High Capacity and Rate Performance for Aqueous Sodium-ion Electrochemical Energy Storage. *Advanced Functional Materials* **2017**, 1703266.

Publications (Past Two Years)

(i) A list of papers and book chapters published in which DOE support is acknowledged

1). Shan, X., Charles, D.S., Xu, W., Feygenson, M., Su, D., Teng, X.W. *Bi-phase Cobalt-Manganese Oxide with High Capacity and Rate Performance for Aqueous Sodium-ion Electrochemical Energy Storage*. **Advanced Functional Materials**, 2017, 1703266, DOI: 10.1002/adfm.201703266

2). (Invited Contribution) Shan, X., Guo, F., Xu, W., Teng, X.W., *High purity* Mn_5O_8 *nanoparticles with a high overpotential to gas evolution reactions for high voltage aqueous sodium-ion electrochemical storage*. **Frontiers in Energy**, 2017, DOI: 10.1007/s11708-017-0485-3

3). Charles, D.S., Feygenson, M., Page, K., Neuefeind,J., Teng, X.W. *Structural Water Engaged Disordered Vanadium Oxide Nanosheets for High Capacity Aqueous K-ion Storage*. **Nature Communications** 2017, 7, 15520

4). Shan, X., Charles, D.S., Lei, Y., Qiao, R., Wang, G., Yang, W., Feygenson, M., Su, D., Xu, W., Teng, X.W. *Bivalence* Mn_5O_8 *with hydroxylated interphase for high-voltage aqueous sodium-ion storage*. **Nature Communications** 2016, 7, 13370

5). (Book Chapter) Guo, F., Gupta, N., Teng, X.W. *Enhancing pseudocapacitive process for energy storage devices: analyzing the charge transport using electro-kinetic study and numerical modelling*, Chapter in "**Supercapacitors - Theoretical and Practical Solutions**", Intech, New York, (2017) Editor: Lionginas Liudvinavičius

(ii) A list of Patents filed in which DOE support is acknowledged

1) Teng, X.W., Shan, X., *Sodium-Rich Manganese Hydrate with Capacity for Aqueous Na-ion Electrochemical Energy Storage*, **U.S. Provisional Patent**, Application Number: 62/587,060 (2017)

2) Teng, X.W., Charles, D.S., *Preparation of Intercalative Metal Oxide/Conductive Polymer Composites as Electrode Materials for Rechargeable Batteries*, **U.S. Provisional Patent**, Application Number: 62/585,031, (2017)

3) Teng, X.W. *Manganese Oxide Compositions and their Use as Electrodes for Aqueous Phase Energy Storage Devices*, **U.S. Non-Provisional Patent**, Application Number: 14/737,823 (2016)

2D Electrically Functional Carbon-Chalcogenide Alloys by Design (2D-EFICACY)

PI: Mauricio Terrones[1,2,3,4]; Co-PI: Susan Sinnott[1,2, 4]

1. Department of Materials Science and Engineering, The Pennsylvania State University, University Park, PA 16802 USA
2. Center for Two Dimensional and Layered Materials, The Pennsylvania State University, University Park, PA 16802, USA
3. Department of Physics, The Pennsylvania State University, University Park, PA 16802 USA
4. Department of Chemistry, The Pennsylvania State University, University Park, PA 16802 USA

Program Scope

The current availability of layered materials “beyond graphene”, such as monolayered semiconducting transition metal dichalcogenides (TMDs) and two-dimensional transition metal carbides (2D TMC), has led to new fundamental challenges in the design of novel 2D alloys and hybrid hetero-interfaces with controllable electronic properties, ranging from semiconducting to metallic and superconducting. Such challenges are the focus of the synergistic computational-experimental project between the Terrones and Sinnott groups at Penn State University. While previous work considered the combination of two semiconducting TMD phases, many emerging opportunities remain unexplored. For instance, the formation of hybrid structures of 2D TMDs and TMCs is yet to be realized. We aim to examine the effect of alloying the dichalcogenides with carbon atoms so as to form novel compounds of the form $M_xM_{1-x}C_yS_2$ (M= W, Mo, Nb, Ta, and Re). In particular the focus is on the development of phase diagrams, determining the role of C doping, alloying TMCs with TMDs, examining the effect of defects on electronic structure, investigating the structure-property relationships of hybrid 2D materials heterointerfaces, and observing *in-situ* the dynamics and stability of these novel hybrids. A further objective is to predict the electronic, optical and vibrational properties of these phases as carbon is introduced and compare the predictions to experimental data.

Recent Progress

TMCs such as Mo_2C exhibit intriguing properties such as variable superconducting transition temperatures as a function of thickness[1] and electrochemical activity for hydrogen evolution reaction (HER) catalytic reactions[2]. By atmospheric pressure chemical vapor deposition (CVD) we have successfully grown 2D α-Mo_2C nanosheets directly onto molten Cu (Figure 1a-e). Moreover, we have achieved careful control of the thickness and domain size of these nanosheets. In addition to its metallic and superconducting properties, 2D α-Mo_2C features a low onset potential and Tafel slope in HER, which makes it an attractive alternative candidate to platinum catalysts for high efficiency energy conversion.[3] By *using 2D α-*Mo_2C *platelets as building blocks*, we have been able to grow TMC/TMD heterolayers (such as Mo_2C/MoS_2, $Mo_2C/MoSe_2$, $Mo_2C/W_xMo_{1-x}S_2$ and $Mo_2C/W_xMo_{1-x}Se_2$). Raman, photoluminescence spectroscopy (PL), fluorescence microscopy, high resolution transmission electron microscopy

(HRTEM), are among the techniques that we used to characterize the synthesized heterointerfaces (Figure 1f and g show the TEM characterization of hybrid $Mo_2C/MoSe_2$). We plan to additionally explore the HER performance of $Mo_2C/W_xMo_{1-x}S_2$, as it combines the high electrical conductivity of Mo_2C with the low proton absorption energy of the alloyed TMDs, which could exhibit a synergistic effect in HER. Future work also includes the exploration of their electrical properties. For instance, in a lateral heterostructure configuration, the metallic Mo_2C phases with low work function could serve as electrical contacts to the semiconducting TMDs.[4] In a vertically stacked geometry, the plasmonic mode generated from Mo_2C may be coupled to the excitonic emission of the TMDs for optoelectronic devices.[5] We envisage the observation of new physics may also emerge when superconducting Mo_2C phases merge with a semiconducting TMDs.

Density functional theory (DFT) calculations were further used to predict the relevant reaction energy barriers and intermediate states at the interface between MoS_2 and Mo_2C. Our DFT results provide interfacial energies, and electronic structures of these heterostructures as a function of the crystal orientation and the atomic alignment. For lateral heterostructures, the band structure calculations reveal a metallic contact and associated band bending, while for vertical heterostructures, the calculations indicate a superconducting behavior in the 2D Mo_2C. The new fundamental knowledge from this combined computational and experimental effort indicates how these materials may be used in future applications such as switches, sensors, and coatings.

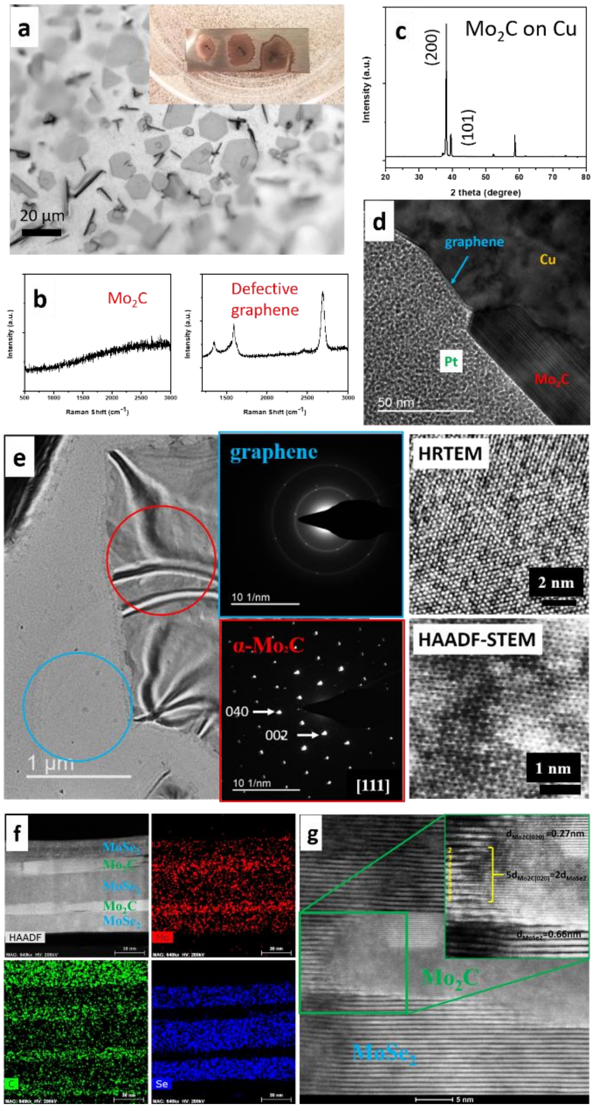

Figure 1. (a) Optical image of 2D Mo_2C domains on Cu. (b) Raman of the as-grown Mo_2C crystals embedded in defective graphene; (c) XRD show the as-grown Mo_2C is α-phase; (d) Cross-sectional TEM image of the Mo_2C; (e) Planar view TEM image and SAED of the Mo_2C (red) and graphene (blue), respectively; HRTEM image and HAADF-STEM image show the hexagonal arrangements of the Mo_2C crystals. (f) Cross-sectional STEM-EDS mapping of $Mo_2C/MoSe_2$ heterostructures; (g) Atomic resolution HAADF-STEM images of $Mo_2C/MoSe_2$

We have additionally explored the alternative route of building TMD/TMC hybrids by *covalently doping carbon of TMDs* (Figure 2). In this context, we have used a plasma-assisted strategy to “gently” incorporate carbon as an anion substitutional dopant within TMDs (e.g. WS_2). The C-doped WS_2 monolayers own tunable optical and electronic properties. First principles DFT calculations reveal the most energetically favorable chemical saturation of the carbon dopants and substitutional position in the lattice (CH@V_S), and the doped system exhibits a band gap decrease of 0.17 eV and functions as a p-type semiconductor with a direct band gap. Atomic resolution scanning (S)TEM and X-ray photoelectron spectroscopy (XPS) have been used to identify the presence of covalently bonded carbon atoms. Electrical tests indicate that carbon can act as an acceptor in WS_2, and effectively tune the work function of WS_2 to make it ambipolar. This work constitutes a significant step forward in the identification of novel structure-property correlations and compositional recipes for designing 2D TMC/TMD heterostructures for novel applications.

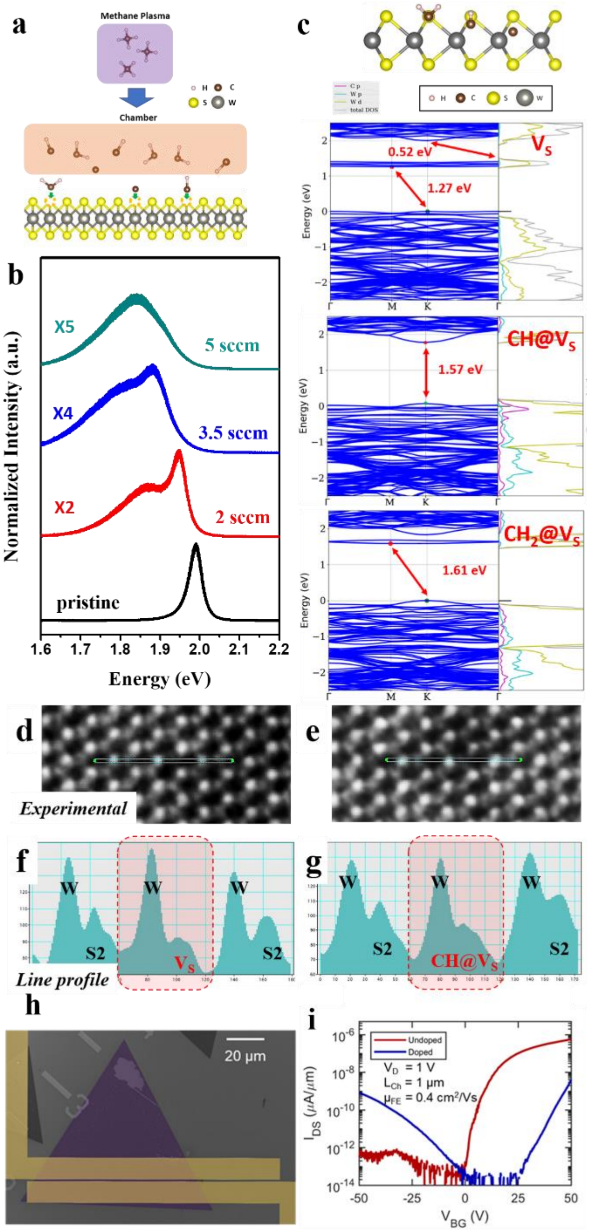

Figure 2. (a) Schematics of plasma doping in monolayer WS_2; (b) Calculated band structure and density of states of WS_2 with 2.67 at% single vacancies (V_S); CH-doped WS_2 with the dopant in the middle position (CH@V_S); and CH_2-doped WS_2 with the dopant at the surface position (CH_2@V_S); (c) PL spectrum of the pristine and carbon doped monolayer WS_2; (d-g) STEM proof of covalently bonded carbon atoms; (h) and (i) FET characteristics of undoped and carbon doped monolayer WS_2.

Future Plans

Thermodynamic stability and electronic properties of $(M_xM_{1-x})_2C_yS_2$ (M= W, Mo, Nb, Ta, and Re). The Sinnott group will investigate the viability of various alloyed materials in the $(M_xM_{1-x})_2C_yS_2$ compositional spaces using first principles calculations of their relative energies. Sinnott has previously used identical techniques to predict the stability of 2D TMCs with oxygen-terminated surfaces. These calculations are key to identifying the compositions that will have the greatest stability against decomposition, and similar calculations have already aided in the experimental synthesis of novel compounds. Additionally, the Sinnott group will calculate the electronic band structures of all stable materials to probe for any compositions with uniquely useful electronic properties. This will include a search for semiconducting compounds whose band edges envelop the stability range of water and are therefore possible candidates for photosynthesis. The Sinnott group will further create maps of band gap vs. composition in each system that can be used to design materials with tailored band gaps.

Josephson junctions Semiconductor-Superconductor interfaces Josephson junctions are created by putting two superconductors in close proximity, separated by some non-superconducting layer, either an insulator, semiconductor or a non-superconducting metal.[6] We expect to be able to design and construct Josephson junction using 2D layered superconductor Mo_2C is by creating vertical heterostructure that might display the Josephson effect. The planned method to fabricate the junction is direct synthesizing high quality planar thin film TMDs on top of Mo_2C flakes, followed by a deterministic transfer of another Mo_2C flake to sandwich the TMD thin layers. Such junctions are of interest as logic components in high-performance computers, or as superconducting quantum interference device (SQUID) circuits,[6] which can detect voltages as low as a few pV.

Direct growth of TMCs or graphene quantum dots (GQDs) on TMDs It has been found in our current carbon doping work that when methane (carbon gas source) increases at elevated temperature, it triggers the reaction between CH_4 and WS_2 to form graphene and TMC nanoparticles.[7] It is evident that the trion peak (X^-) shifts to neutral exciton peak (X^0) after PECVD treatment onto the WS_2, which confirms that electrons are transferred from WS_2 to GQDs at the interface[8]. The formation of WC or graphene quantum dots in which the plasmonic resonance interact with the excitonic modes in WS_2, such heterostructures may have potentials in HER catalysis properties[7] and plasmonic-based optoelectronics.[9, 10]

References

[1] Xu, C.; Wang, L. et al. *Nature materials* **2015,** *14* (11), 1135.
[2] Wan, C.; Regmi, Y. N. et al. *Angewandte Chemie* **2014,** *126* (25), 6525-6528.
[3] Geng, D.; Zhao, X. et al. *Advanced Materials* **2017,** *29* (35).
[4] Jeon, J.; Park, Y.et al. *ACS nano* **2018**, *12* (1).
[5] Lin, Y.-C.; Lu, N. et al. *ACS Nano* **2014,** *8* (4), 3715-3723.
[6] Albiez, M.; Gati, R. et al. *Physical review letters* **2005,** *95* (1), 010402.
[7] Wu, J.; Ma, L. et al. *Advanced Materials Interfaces* **2017,** *4* (4).
[8] Liu, P.; Zhu, X. et al. *Applied Physics Letters* **2017,** *111* (11), 111603.
[9] Wang, Z.; Dong, Z. et al. *Nature communications* **2016,** *7*, 11283.
[10] Najmaei, S.; Mlayah, A. et al. *ACS nano* **2014,** *8* (12), 12682-12689.

Publications

1. Journal paper: Plasma-assisted Carbon Doping of 2D Tungsten Disulfide. Fu Zhang*, Yanfu Lu*, Tianyi Zhang, Daniel Schulman, Kazunori Fujisawa, Zhong Lin, Saptarshi Das, Susan B. Sinnott and Mauricio Terrones. To be submitted to *Nano Letters*.

Controlling Solid-State Conjugated Materials with Aromatic Interactions of Side Chains

Samuel W. Thomas III, Tufts University, Department of Chemistry, 62 Talbot Avenue, Medford, MA 02155

Program Scope: This presentation will describe how interactions of discrete, specific interactions of arenes in the side chains of conjugated materials can control their solid-state packing and optical properties. Conjugated materials combine the favorable optoelectronic properties of inorganic materials, such as charge transport and luminescence, with structural tunability, processability, and flexibility. Therefore, these materials have a strong connection to many fundamental and applied problems in energy, including energy transport within materials, efficient conversion of photons to electricity, and energy-efficient solid-state electroluminescence. Despite their central role in energy-relevant problems, progress is limited by our collective inability to execute rational design of their solid-state packing.[1] New approaches to this problem are important to organic and polymer chemists, materials scientists, and solid-state physicists.

Most conjugated materials follow the same design paradigm, dividing structures into: i) conjugated “main chains”, which is largely responsible for the optoelectronic properties, and ii) solubilizing (usually alkyl) “side chain”, which are often required to yield good solubility and processability.[2] Instead, our group uses a different approach in which non-covalent interactions between these typically orthogonal substrcturs interact. Our molecular construct enables these side chain/main chain interactions to control the conformations and packing of conjugated materials – specifically phenylene-ethynylenes (PEs) functionalized with benzylic esters (Figure 1). Previous work from our lab[3] showed how this molecular test-bed harnesses non-covalent interactions of arenes to control electronic coupling of solids.

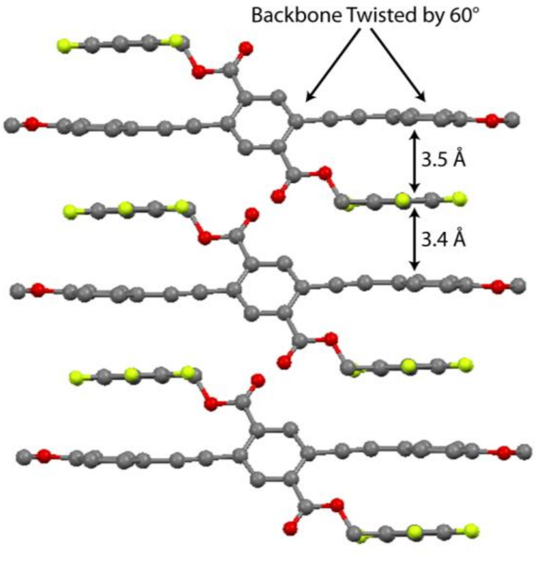

Figure 1. *Top:* Crystal structure of a 3-ring phenylene-ethynylene (PE) with ArF-ArH stacking interactions causing twisting of the PE backbones and preventing inter-PE aggregation.

Generally, PEs prefer to adopt coplanar conformations with maximum conjugation along backbone, and intermolecular cofacial stacking between molecules in the crystal lattice.[4] In our molecules, however, alternating cofacial stacking of heavily fluorinated ArF rings, which are part of the side chain, with non-fluorinated rings (ArH rings) within the conjugated main chains yields twisting of the PE backbone. This platform therefore controls intra- and intermolecular coupling with discrete non-covalent interactions involving aromatic rings within side-chains. The first objective of our program is to use this platform as a molecular test bed for understanding how the chemical structure, and the resulting strengths of non-covalent interactions, influences the conformations and packing of these molecules in the crystalline lattice, with the eventual goal of rational design of solid-state optoelectronic properties.

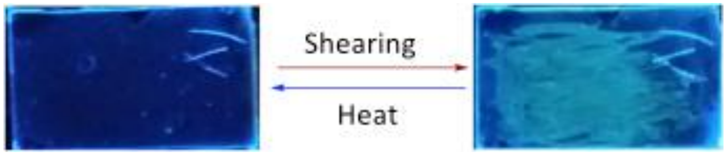

Figure 2: Mechanofluorochromism of a solid, twisted PE under UV light.

These solids comprising twisted PE backbones that avoid intermolecular aggregation are also stimuli-responsive through increases of electronic coupling through planarization or aggregation cause bathochromic shifts of optical spectra. For example, mechanical shear force yields this shifting reversibly (mechanofluorochromism, MF). MF is attracting increasing interest due to the implications for a variety of prospective applications as well as improved fundamental understanding of how conjugated materials respond to force.[5] Nevertheless, the empirical nature of the vast majority of published MF studies prevents rational design and tuning of force-sensitive optical materials. Therefore, a second objective of our program is to develop clear structure-property relationships for MF materials, with the eventual goal of their rational design.

Although the test-bed described above is useful for understanding how non-covalent interactions dictate conformation and optical properties, it remains limited in terms of the breadth of structures and properties that can be accessed. In addition, the reliance upon highly crystalline MF materials poses challenge with their poor mechanical toughness and difficulty in preparing uniform coatings. Therefore, a third objective of our program is to determine the extent to which fluorinated benzylic esters can serve as reliable structural features for programmed twisting and mechanically sensitive conjugated materials.

Recent Progress: ***1. Controlling Packing Using Electronic Substituent Effects*****:** In this study published in *JACS*, we hypothesized that electronic substituent effects on ArH rings would dictate whether the ArF- ArH stacking, and result ant twisting of PE backbone, would occur in the crystalline lattice of a series of three-ring PEs. As shown in Figure 3, we showed two structural factors that determine whether the ArF–ArH interactions, and the resulting twisted, unaggregated chromophores, occur in these solids: (i) the electron-releasing characteristic of substituents on ArH, with more electron-releasing character favoring ArF–ArH interactions, and (ii) the fluorination pattern of the ArF ring, with 2,3,4,5,6-pentafluorophenyl favoring ArF–ArH interactions over 2,4,6-trifluorophenyl. Studies of the X-ray crystal structures and optical spectra of these materials as solids support our hypothesis, indicating that considerations of electrostatic complementarity, whether through a polar–π or substituent–substituent mechanism, can serve as an effective design principle in controlling the interaction strengths, and therefore the optoelectronic properties, of these molecules as solids.

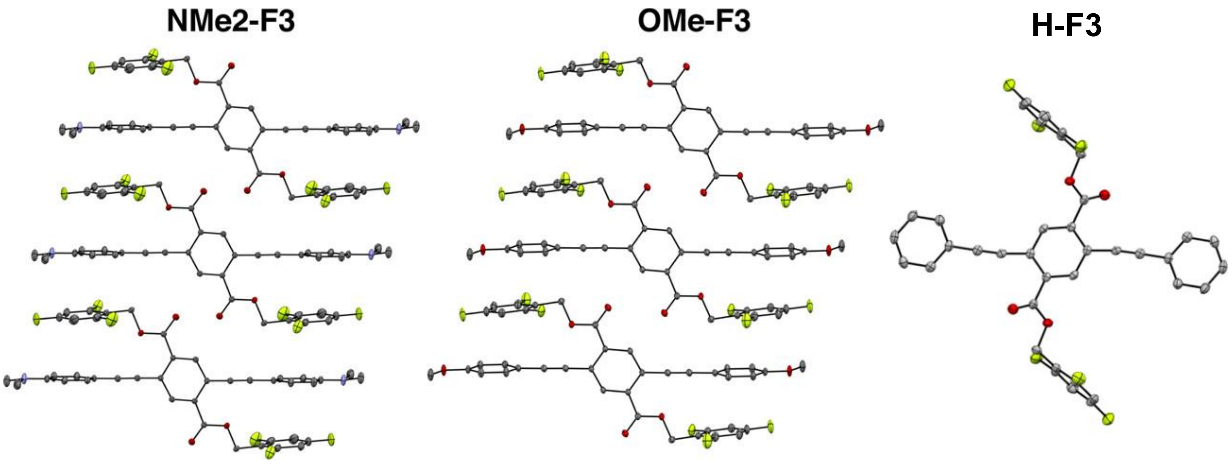

Figure 3: Controlling molecular geometry in the crystal lattice through electronic substituent effects. When three fluorine atoms are present in the ArF rings, electron-donating amines or ethers are required on the ArH rings to observe ArF-ArH stacking and PE twisting. When the ArH ring is unsubstituted, ArF-ArH stacking does not occur, and the PE chromophores are both coplanar and intermolecularly aggregated.

2. Controlling MF Reversion with Alkyl Chain Lengths: In this study recently accepted for publication in *Chemical Science,* we demonstrated that lengths of alkyl substituents correlated with the MF properties of a range of aniline-functionalized three-ring PEs. The crystalline phases of these materials are twisted due to perfluoroarene-arene (ArF-ArH) interactions involving perfluorophenyl pendants and the terminal aniline rings of the PE chromophores. Shearing yielded transitions from green-emitting crystalline phases to orange-emitting amorphous phases as established by DSC and X-ray diffraction. Molecules with shorter alkyl chain lengths required higher temperatures to recover the hypsochromically shifted crystalline phases after grinding, while the recovery with chain lengths longer than butyl occurred at room temperature. Related structure-property relationship studies currently ongoing include: 1) Comparing benzoate esters with varying alkyl chain lengths. Here, we discovered widespread polymorphism, which we attribute to the weakness of the ArF-ArH interaction with the electron-withdrawing ester groups. This includes a thermally induced crystal-to-crystal transition and bathochromically shifting MF behavior 2) We have discovered that even slight changes in the regiochemistry of fluorine substituents on the ArF ring, which is not formally conjugated to the PE backbones of these materials, can have strong influence over their crystal packing, optical properties, and MF behavior.

Future Plans 1. *Extension to polymers.* We have already shown that doping these PEs into poly(methacrylate) matrices at high (20%) loading preserves MF behavior, and that the temperature at which reversion occurs depends on local mobility of polymer chains (Tg values). We are

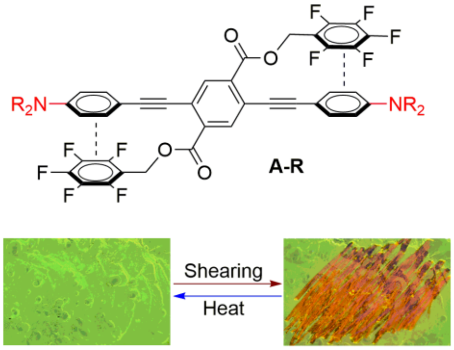

A-R	R
A-1	Me
A-2	Et
A-3	*n*-Pr
A-4	*n*-Bu
A-6	*n*-Hex
A-8	*n*-Oct
A-18	*n*-Octadec

Figure 4: Chemical structure and example mechanofluorochromic response of aniline terminated three-ring phenylene-ethynylenes.

currently preparing polyurethanes with twisted PE cores as one of the monomer units (Figure 5). We also are pursuing polymers in which the MF units are pendants, modeled on side-chain liquid crystal polymers.

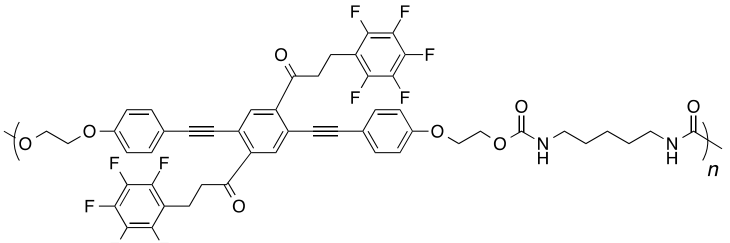

Figure 5: Example target polyurethane currently under investigation. This polymer retains MF properties similar to those of the crystals described earlier.

2. ***Extension to longer conjugated systems and a broader array of interactions.*** We have preliminary data showing that the motif of perfluorinated benzylic esters can be integrated into other arylene-ethynylenes and reliably yield twisting about conjugated backbone (see Figure 6). In this crystal structure, the ArF-ArH interactions in a four-ring PE yield programmed twisting about two alkynes, improving the structural breadth over which the "twistigen" concept can be employed. We will continue to test the limits of this concept with longer PE oligomers and polymers. We will also be broadening the scope of this type of programmed control over electron coupling to molecules without alkynes in the backbone, as well as harnessing other direction non-covalent interactions of aromatic rings within the side chains, such as n-π* between the lone pairs on nitrogen-containing heterocycles and the face of the ArF rings. We expect the different geometries of these interactions (edge-to-face instead of cofacial) to yield programmed coplanar backbone geometries.

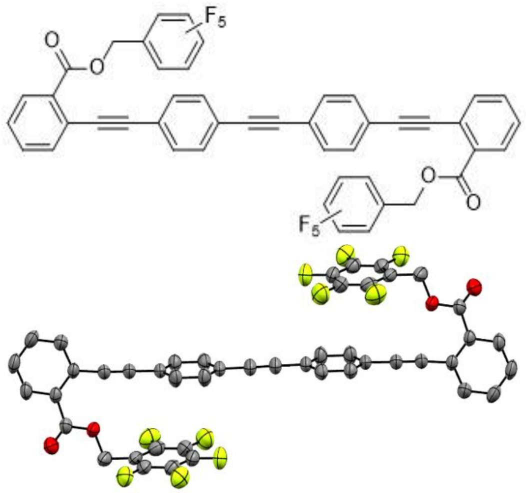

Figure 6. Programmed twisting about a four-ring PE backbone using ArF-ArH interactions.

References

1. Henson, Z. B.; Mullen, K.; Bazan, G. C. Design Strategies for Organic Semiconductors Beyond the Molecular Formula. *Nature Chemistry* **2012,** *4,* 699-704.
2. Mei, J. G.; Bao, Z. N. Side Chain Engineering in Solution-Processable Conjugated Polymers. *Chemistry of Materials* **2014,** *26,* 604-615.
3. Pawle, R. H.; Haas, T. E.; Muller, P.; Thomas, S. W. Twisting and Piezochromism of Phenylene-Ethynylenes with Aromatic Interactions between Side Chains and Main Chains. *Chemical Science* **2014,** *5,* 4184-4188.
4. Bunz, U. H. F.; Imhof, J. M.; Bly, R. K.; Bangcuyo, C. G.; Rozanski, L.; Bout, D. A. V. Photophysics of Poly [p-(2,5-Didodecylphenylene)ethynylene] in Thin Films. *Macromolecules* **2005,** *38,* 5892-5896.
5. Huang, X.; Qian, L.; Zhou, Y.; Liu, M.; Cheng, Y.; Wu, H. Effective Structural Modification of Traditional Fluorophores to Obtain Organic Mechanofluorochromic Molecules. *Journal of Materials Chemistry C* **2018,** *6,* 5075-5096.

Publications

1. Sharber, S.; Baral, R. N.; Frausto, F.; Haas, T. E.; Müller, P.; Thomas, S. W. Substituent Effects that Control Conjugated Oligomer Conformation through Non-Covalent Interactions. *J. Am. Chem. Soc.* **2017**, *139*, 5164-5174. DOI: 10.1021/jacs.7b00878

2. Sharber, S.; Shih, K. C.; Mann, A.; Frausto, F.; Haas, T. E.; Nieh, M. P.; Thomas, S. W. Reversible Mechanofluorochromism of Aniline-Terminated Phenylene Ethynylenes. *Chem. Sci.* **2018**, *In Press*.

3. Sharber, S.; Thomas, S. W. Regiochemical Effects on Fluorescence and Mechanochromism of Phenylene-Ethynylenes *Manuscript in Preparation*

4. Sharber, S.; Mann, A.; Shih, K. C.; Nieh, M. P.; Thomas, S. W. Reversible Mechanofluorochromsim of Ester Terminated Phenylene Ethynylenes. *Manuscript in Preparation.*

Using Nanoporous and Nanostructured Materials to Understand and Optimize Pseudocapacitive Charge Storage

Sarah H. Tolbert, UCLA, Depts. of Chem. & Biochem. and Materials Sci. & Engineering

Program Scope

The primary goal of this program is to understanding the fundamental nature of intercalation pseudocapacitance. Pseudocapacitors can combine many of the favorable aspects of batteries and double layer capacitors by relying on surface or near-surface Faradaic redox reactions, so that high power density can be combined with reasonably high energy density. Historically, these reactions have been divided into two categories: When ions are electrochemically adsorbed onto redox sites at the solid-electrolyte interface of the material, the process is termed redox or surface pseudocapacitance, and this is standardly what is thought of a pseudocapacitive charge storage. Alternatively, when ions intercalate into the channels or layers of the redox-active material in a non-diffusion controlled manner without inducing a phase transition, the process is called intercalation pseudocapacitance. The stipulation of no phase transition arises because large scale structural changes, like those observed in most batteries, are unfavorable for fast charging systems because the nucleation and growth of these new phases can be slow, and can impede rapid battery cycling. The major goal of this project is to understand the relationship between suppression of phase transitions in nanostructured materials and the extent of intercalation pseudocapacitance. To this end, both cathode and anode materials have been synthesize in nanoporous form and studied using a combination of electrochemical and *operando* diffraction methods. Our fundamental goal is to explore the role of nanoscale architecture, domain size, and intercalant ion on phase transition suppression and on the ability of these materials to show intercalation pseudocapacitance.

Additional work funded under this project was aimed at understanding how porous structures can accommodate the deleterious large volume changes in high capacity alloying anodes. While porosity is clearly good for electrodes with large volume changes, some critical questions remained unanswered, in particular, the relationship between structural stability and the microstructure of these porous materials. We address this question using dealloyed nanoporous metals. Using nanoporous tin (NP-Sn) and various Sn containing allows (particularly nanoporous antimony tin, NP-SbSn), we aim to tailor size and composition of the nanoscale ligaments to best accommodate volume change. We further aim to use X-ray imaging to directly understand how porous materials can accommodate large volume changes in alloy type anode materials.

Recent Progress

To date, we have explored intercalation kinetics and structural change upon ion intercalation in a range of materials, including MoO_{3-x}, Nb_2O_5/Nb_4N_5, $LiMn_2O_4$, and MoS_2. For space reasons, we will only highlight result from $LiMn_2O_4$ and MoS_2 here. Nanoporous MoS_2 powders were made by thermal sulfurization of solvothermally synthesized MoO_2 nanocrystals, followed by network assembly. MoS_2 was chosen because the more polarizable soft sulfur anion should enhance solid-state ion diffusion rates and a porous network was created to provide short metal ion diffusion distances, combined with easy electrolyte access to all nanoscale domains. These optimized atomic and nanoscale architectures were then combined with ideal electronic properties. MoS_2 as synthesized is a semiconductor, but it can be irreversibly converted to a metallic 1T phase upon cycling with Li^+ or Na^+, and all kinetics studies were done on metallic phase materials, so that porosity, surface area, solid-state diffusion distances, solid-state diffusion rate, and electrical conductivity were all optimized. Slurry electrodes made form nanoporous

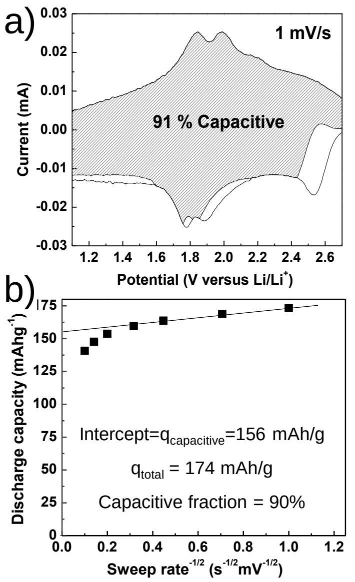

Fig. 1: Kinetic analyses for porous MoS_2 cycled with Li^+ using Eq. 1 (a) and the Trasatti method (b). Both give very similar results.

MoS_2 showed high capacity, good capacity retention at high rate, and very stable long term cycling.

To quantify the fraction of stored charge in these electrodes that is capacitive and to distinguish that from traditional diffusion controlled reactions like those occurring in standard lithium-ion battery materials, we use multiple related kinetic analysis techniques, all based on sweep voltammetry. For a redox reaction limited by semi-infinite diffusion, the peak current response varies with the square root of the sweep rate ($v^{1/2}$); for a capacitive process, it varies linearly with v. With this analysis, it is straightforward to distinguish between a typical battery material and a pseudocapacitive material. The slope of log current vs. log sweep rate gives a value between 0.5 and 1, with 0.5 corresponding to pure battery-like kinetics, and a slope approaching 1 corresponds to pure pseudocapacitance. More generally, $i(v) = k_1 v^{1/2} + k_2 v$ (Eq. 1). Solving for the values of k_1 and k_2 at each potential allows for the separation of the diffusion and capacitive currents. Alternatively, we can use the Trasatti analysis, which stipulates that as $\nu \Rightarrow \infty$, access to the more diffusion controlled redox sites are excluded so extrapolation of capacity versus $v^{-1/2}$ gives the capacitive charge storage ($q_{capacitive}$). As $\nu \Rightarrow 0$, access to diffusion limited redox sites can occur and so extrapolation of the inverse capacity versus $v^{1/2}$ gives the extrapolated total charge (q_{total}). Using these two values, we can again calculate the capacitive fraction for a material. Fig. 1 shows results for nanoporous MoS_2 cycled with Li^+ indicating that these nanoscale materials are fully ($\geq$ 90%) capacitive (i.e. they show intercalation pseudocapacitance), and that all analysis methods give similar results.

Using *operando* X-ray diffraction studies at the Stanford Synchrotron Radiation Lightsource (SSRL), we then went on to study suppression of ion intercalation induced phase transitions. Using these methods, we observe suppression of Li^+ intercalation induced phase transitions, consistent with the highly capactive behavior shown in figure 1.We then turned to sodium, which is a more stringent test because of the large size of Na^+. Here again we observed highly capacitive behavior with almost 100 mAh/g capacity charged in just under 40 sec. Bulk MoS_2 shows significant structural change upon Na^+ intercalation in a process called staging, where multiple different phase transitions take place. In stark contrast to the phase transitions observed in bulk MoS_2 during charge and discharge with Na^+ (Fig. 2a), nanoparticle based MoS_2 does not undergo any significant structural changes, as shown in Fig. 2b. In bulk

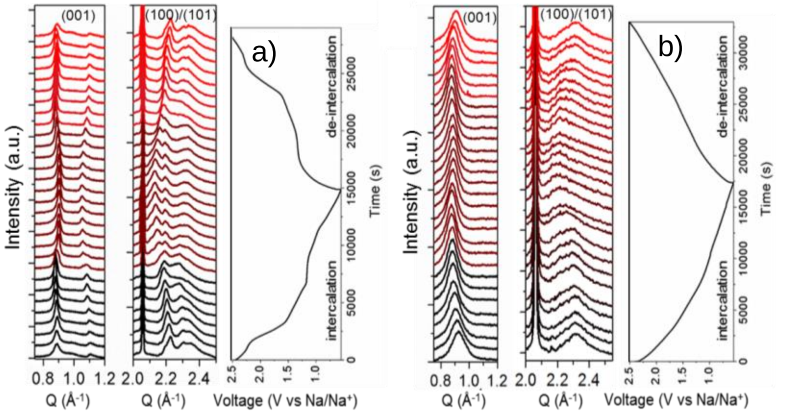

Fig. 2: *Operando* X-ray diffraction data for bulk (a) and nanocrystal based MoS_2 (b) during sodium intercalation. Staging is seen in the bulk MoS_2, but no phase transitions are observed in the nano-MoS_2.

MoS_2, a first-order phase transition from the 1T to $NaMoS_2$ (triclinic) is observed in figure 2a (see the triclinic peak increase at 1.1 Å^{-1}). The splitting of the diffraction peak near 2.2 Å^{-1} is then indicative of the second phase. These results thus demonstrate that dramatic suppression of phase transitions can be observed in nanostructured materials, and that this suppression is associated with increased charge/discharge kinetics without capacity loss through intercalation pseudocapacitance.

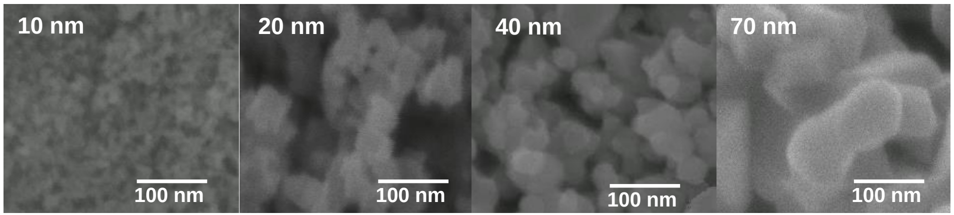

Fig. 3: Nanoporous LMO with different average domain sizes made using solution phase templating, combined with thermal coarsening from 600-900 °C.

To determine if suppression of phase transitions is a general phenomenon to many nanostructured electrode materials, *operando* X-ray diffraction was also performed on a very different material system. The layered MoS_2 discussed above is an anode material, so we turned instead to a spinel structured cathode material: $LiMn_2O_4$ (LMO). Here we made nanoporous $LiMn_2O_4$ using both nanocrystal templating and sol-gel methods. To make materials with larger crystalline domains, we simply coarsened the nanoporous networks by heating at higher temperatures (600-900 ºC) for a short amount of time, as shown in Fig. 3. Average domain sizes up to 100 nm could be made in this way, albeit with significant size polydispersity. Samples with domain sizes up to 40 nm show fast kinetic with good capacity retention at 20C. However, we found a significant drop in rate capability for nanoporous materials with crystallite sizes greater than 40 nm. We hypothesized that phase transitions might not be suppressed in larger nanocrystals and that there could be a critical size where phase transitions become energetically accessible. Since we hypothesize that phase transitions can dominate the kinetics of the intercalation reactions, even in systems with short solid-state diffusion lengths, this critical phase transition size would correlate with a critical size for pseudocapacitive behavior.

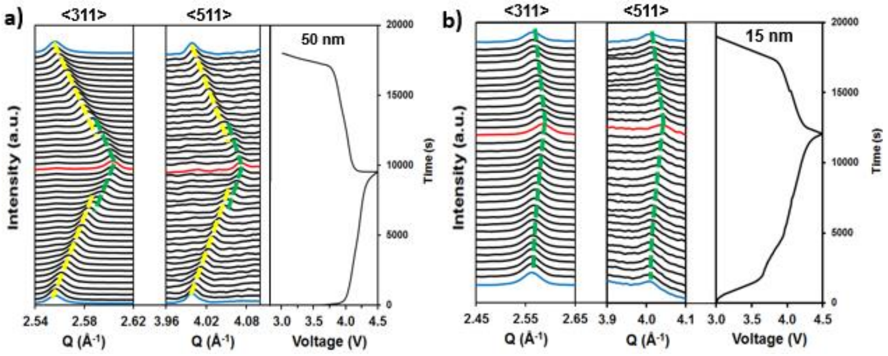

Fig. 4: *Operando* diffraction showing 50 nm nanoporous LMO with a phase transition (a) and 15nm nanoporous LMO with no phase transition (b).

In agreement with this idea, *operando* X-ray studies show that 15 nm $LiMn_2O_4$ does not exhibit a phase transition (Fig. 4b), while 50 nm $LiMn_2O_4$ shows a discontinuity in both the (311) and (511) diffraction peaks (Fig. 4a), indicating the occurrence of a phase transition in nanoporous $LiMn_2O_4$ with the larger domain size, but not the smaller domain material. This suggests that a critical size for the onset of pseudocapacitive behavior in $LiMn_2O_4$ may lie somewhere between 15-50 nm. Moreover, the observation of phase transition suppression in another material system at small size helps prove the hypothesis that phase transition suppression is at the core of fast charging in nanostructured pseudocapacitors.

In a final project are, only partly related to the work described above, we explore the role of porosity in stabilizing high volume expansion anode materials such as group IV alloy anodes.

A common failure mechanism in alloy-type anodes arises from the interfacial strain within a particle due to the volume mismatch resulting from limited Li^+ diffusion kinetics. Typically, a core-shell structure with lithium-rich and lithium-deficient phases is generated as lithiation begins at the outer-most surface of a particle. Nanoporous structures have the potential to solve these problems because the pores within the structure can accommodate the expansion and reduce the overall strain, while simultaneously maintaining good electrical contact and allowing electrolyte access to all parts of the material for more even lithiation.

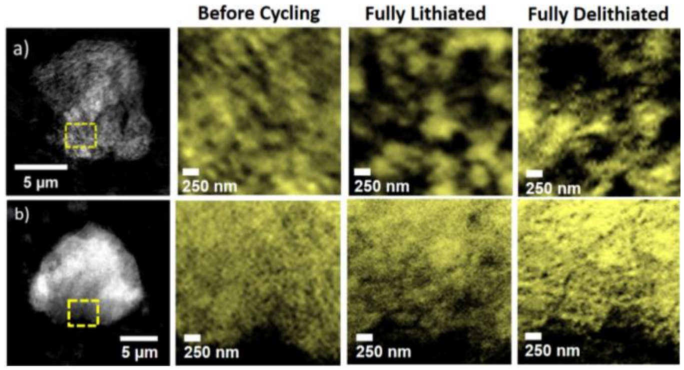

Fig. 5: Low magnification TXM images of 3D nanoporous (a) Sn and (b) SbSn. High magnification TXM images at different stages of cycling are shown in column two to four (top row for Sn and bottom row for SbSn). SbSn show a more stable pore structure and volume expansion into the pore space.

With DOE support, we have demonstrated capabilities to synthesize 3D nanoporous network of both Sn and SbSn (NP-Sn, NP-SbSn). Both materials are made using facile one-step selective dealloying methods and both materials show good cycling stability as alloy anodes. To study the dynamic evolution of the 3D architecture upon cycling, *operando* transmission X-ray microscopy (TXM) was performed in addition to the electrochemical measurements. Interestingly, although NP-Sn showed reasonable cycling capabilities, 2D TXM shows that the porous structure is highly disrupted upon lithiation and delithiation (Fig. 5a). We then moved to NP-SbSn, which has two active components that alloy at different potentials. Here there should always be an inactive component stabilizing the pore, and indeed we find the pores of NP-SbSn are well preserved upon cycling (Fig. 5b). Optimizing both atomic composition and nanoscale architecture in nanoporous metals is thus an effective way to stabilize alloy anode materials with large volume changes.

Future Plans

In our future work, we aim to understand the origins of phase transition suppression in pseudocapacitors so that fast kinetics can be designed into future generations of materials. We begin with a goal of determining the critical size for suppression of phase transitions in a number of known pseudocapacitive systems – that critical size marks the cross-over from battery-like to pseudocapacitive behavior. We also propose to explore how nanocrystal shape and surface faceting affect the critical size. With that knowledge in hand, we then propose to undertake a series of experiments aimed at determining if phase transition suppression in finite size pseudocapacitors is primarily a thermodynamic or a kinetic effect. This knowledge is key to designing the next generation of fast charging pseudocapacitive materials.

In parallel with these fundamental studies, we propose to broaden the palette of available pseudocapacitive materials. Currently we have a number of very fast charging systems that are appropriate for use as pseudocapacitive anode materials, but many fewer choices for fast charging cathodes. As a result, we propose methods to synthesize nanoporous versions of two known cathode materials that show exciting potential for fast kinetics when synthesized in nanoscale form. These materials are $LiNi_{0.80}Co_{0.15}Al_{0.05}O_2$ (NCA) and $LiVPO_4F$ (LVPF). Both materials show high capacity in bulk form and show promise for fast charging in nanoporous form.

Publications

E. Detsi, X. Petrissans, Y. Yan, J.B. Cook, Y.-L. Liang, B. Dunn, S.H. Tolbert, “Tunable Ligament Shape in Dealloyed Nanoporous Tin and Impact of Nanoscale Morphology on its Performance as High Capacity Anode Material for Na-ion Battery.” Phys. Rev. Mater. 2, 055404 (2018); DOI: 10.1103/PhysRevMaterials.2.055404.

C.-H. Lai, D.S. Ashby, T.C. Lin, J. Lau, A. Dawson, S.H. Tolbert, B, Dunn, “Application of Poly(3-hexylthiophene-2,5-diyl) as a Protective Coating for High Rate Cathode Materials.” *Chem. Mater.*, **30**, 2589–2599 (2018); DOI: 10.1021/acs.chemmater.7b05116.

B.K. Lesel, J.B. Cook, Y. Yan, T.C. Lin, S.H. Tolbert, “Using Nanoscale Domain Size To Control Charge Storage Kinetics in Pseudocapacitive Nanoporous $LiMn_2O_4$ Powders.” *ACS Energy Lett.* **2**, 2293-2298, (2017); DOI: 10.1021/acsenergylett.7b00634.

J.B. Cook, E. Detsi, Y. Liu, Y.-L. Liang, H.-S. Kim, X. Petrissans, B. Dunn, S.H. Tolbert, “Nanoporous Tin with a Granular Hierarchical Ligament Morphology as a Highly Stable Li-Ion Battery Anode.” *ACS Appl. Mater. Interfaces*, **9**, 293−303, (2017); DOI: 10.1021/acsami.6b09014.

J.B. Cook, H.-S. Kim, T.C. Lin, S. Robbennolt, E. Detsi, B. Dunn, S.H. Tolbert, “Tuning Porosity and Surface Area in Mesoporous Silicon for Application in Li-ion Battery Electrodes.” *ACS Appl. Mater. Interfaces*, **9**, 19063, (2017); DOI: 10.1021/acsami. 6b16447

J.B. Cook, T.C. Lin, E. Detsi, J. Nelson Weker, S.H. Tolbert “Using X-ray Microscopy To Understand How Nanoporous Materials Can Be Used To Reduce The Large Volume Change In Alloy Anodes.” *Nano Lett.*, **17**, 870−877 (2017); DOI: 10.1021/acs.nanolett.6b04181.

H.-S. Kim, J.B. Cook, H. Lin, J.S. Ko, Sarah H. Tolbert, V. Ozolins, B. Dunn “Oxygen Vacancies Enhance Pseudocapacitive Charge Storage Properties of MoO_{3-x}.” *Nature Mater.* **16**, 454-460 (2017); DOI:10.1038/nmat4810.

J.B. Cook, H.-S. Kim, T.C. Lin, C.-H. Lai, B. Dunn, S.H. Tolbert, “Pseudocapacitive Charge Storage in Thick Composite MoS_2 Nanocrystal Based Electrodes. *Adv. Energy Mater.* 1601283 (2016). DOI: 10.1002/aenm.201601283.

B.K. Lesel, J.S. Ko, B. Dunn, S.H. Tolbert, “Mesoporous $Li_xMn_2O_4$ Thin Film Cathodes for Lithium-Ion Pseudocapacitors.” *ACS Nano* **10**, 7572−7581 (2016). DOI: 10.1021/acsnano.6b02608.

E. Detsi, J.B. Cook, B.K. Lesel, C.L. Turner, Y.-L. Liang**,** S. Robbennolt, S.H. Tolbert “Mesoporous $Ni_{60}Fe_{30}Mn_{10}$-Alloy Based Metal/Metal Oxide Composite Thick Films As Highly Active and Robust Oxygen Evolution Catalysts.” *Energy Environ. Sci.* **9,** 540-549 (2016). DOI: 10.1039/C5EE02509E.

J.B. Cook, H.-S. Kim, Y. Yan, J.S. Ko, S. Robbennolt, B. Dunn, S.H. Tolbert, “Mesoporous MoS_2 as a Transition Metal Dichalcogenide Exhibiting Pseudocapacitive Li and Na-Ion Charge Storage.” *Adv. Energy Mater.* **6**, 1501937 (2016); DOI: 10.1002/aenm.201501937.

Functional Nanomaterials with Tunable Plasmonic and Emittive Properties

Award Number: DE-SC0002232

Mostafa El-Sayed
Julius Brown Chair and Regents Professor
School of Chemistry and Biochemistry, Georgia Institute of Technology
770 State Street, Atlanta, GA 30332
Phone: 404-894-0292; fax: 404-894-0294
http://www.chemistry.gatech.edu/faculty/elsayed/el-sayed.html

Vladimir V. Tsukruk
Dean's Professor of Engineering and Regents Professor
School of Materials Science and Engineering, Georgia Institute of Technology,
771 Ferst Dr., NW. Atlanta, GA 30332
Phone: 404-894-6081; fax: 404-894-9140
vladimir@mse.gatech.edu; http://polysurf.mse.gatech.edu/

Program Scope

The goal of the project is ***on understanding the principles*** of non-covalent assembling of tunable functional materials with various inorganic nanocrystals in order to control light-matter interactions by changing localized interfacial refractive properties, coupling parameters, or the ionic environment of surrounding media. We will explore *novel soft functional matrices* with controlled physical properties via the application of light, mechanical stresses, ionic environment, and electrical potential. These ***functional soft matrices and shells*** will be used in conjunction with novel anisotropic inorganic nanostructures such as noble metal/metal alloy anisotropic nanostructures with complex optical properties (multiple LSPR modes)[1] and quantum dots with light-emissive or absorbing properties in a broad spectral range from the UV to the near IR.[2]

Select Results and Recent Progress

We studied dual-responsive plasmonic core/shell nanostructures composed of gold nanorod (AuNR) cores and polyaniline (PANI) shells with plasmonic mode reversible modulated through orthogonal stimuli (i.e. electrical potential and pH change) (**Figure 1a, b**). In this system, the chemical structure of PANI shells can be reversibly changed between emeraldine salt (ES), emeraldine base (EB), and leucoemeraldine base (LB) depending on the chemical environments, thus providing three different complex refractive indices. To rationally design dual-responsive core/shell nanostructures, the refractive indices of the three different forms of the PANI shell were obtained using ellipsometry, revealing that the local pH change could give the highest refractive index change of the PANI shells. Hence, the highest localized surface plasmonic resonance (LSPR) shift of the Au nanorod cores above 100 nm (**Figure 1c, d**).

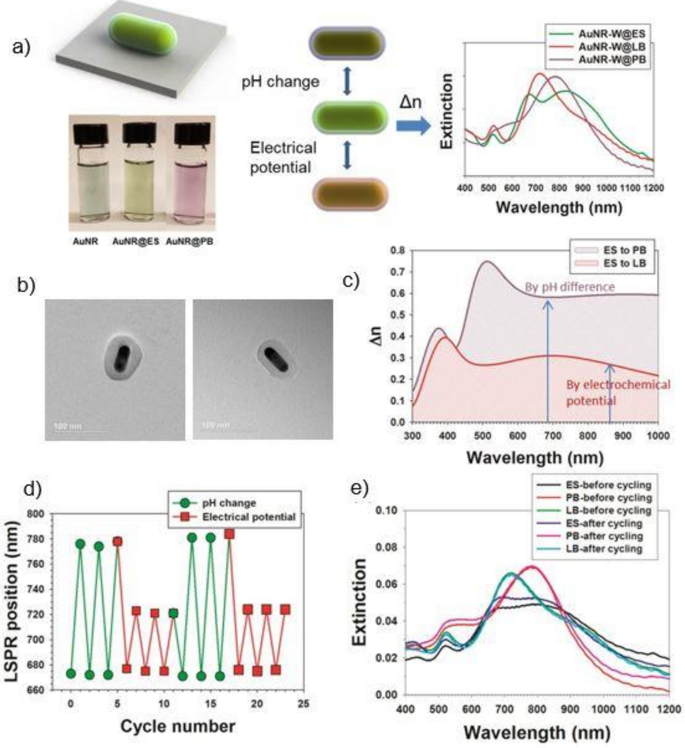

Figure 1. a) AuNR@PANI core/shell nanostructures. b) TEM images c) Real refractive index d) LSPR peak position during cycling. e) UV-vis spectra of AuNR-W@PANI core/shell nanostructures with different PANI shells.

Notably, a significant plasmon band shift by 107 nm was realized with only 8 nm thick PANI shells due to the large refractive index change at the gold-polymer interface. A maximum shift of the longitudinal plasmon mode of 149 nm is obtained by applying a modest electrical potential (below ± 1 V). The anisotropic core/shell nanostructures exhibit very stable and reversible dual-responsive LSPR behavior over 100 cycles without detectable degradation (**Figure 1e**). This hybrid AuNR@PANI core/shell structure with the capability of a high degree of modulation can be used for various applications including photovoltaics, dynamic optics, nanophotonics, and optoelectronics.

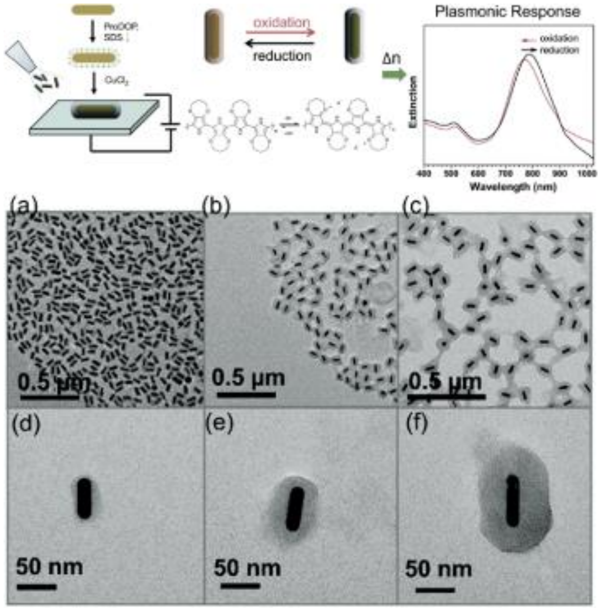

Figure 2. The electrochemically tunable PProDOP@AuNR core–shell nanoparticles and the corresponding spectral shifts and TEM images

We studied the electrochemically tunable hybrid nanostructures composed of gold nanorods encapsulated within directly polymerized poly[(3,4-propylenedioxy)pyrrole] (PProDOP) nanoshells with controlled nanoscale thicknesses. This system displays narrow visible-near infrared absorption bands upon applying a variable electric potential due to the remarkable transmissivity of PProDOP at various oxidation states (**Figure 2**). The stable reversible modulation of the observed plasmonic response of the gold nanorods was caused by the variation of the refractive index of PProDOP shells at different oxidation states as shown by spectroscopic ellipsometry and confirmed by finite-difference time-domain (FDTD) simulations. A surface plasmon resonance (LSPR) band of gold nanorods at 800 nm was shifted reversibly by 24 nm by multiple cycling of the electric potential. Overall, these core–shell structures with electrochemical plasmonic tunability in the near-infrared region allow for tailoring of the optical and electrochemical properties of pre-programmed plasmon responses for active control of colorimetric appearance not just across the visible range but also toward the near-infrared.

We have previously shown that resonant excitation of AuNR by femtosecond (fs) laser pulses induces reshaping with an incident energy threshold 2 orders of magnitude lower than when nanosecond laser pulses are used, as cooling processes are more competitive on slower time scales. As the nanorods "melt", shorter but wider nanorods form, eventually reshaping into nanospheres, with a broad distribution of particle sizes. Recently, we have been able to guide the fs laser-induced reshaping by changing the chemical environment around the AuNRs. The addition of a small excess of the surfactant cetyltrimethylammonium bromide (CTAB), used in the synthesis of the AuNRs themselves, modifies the nanorod product distribution to produce a significantly narrower and more intense longitudinal LSPR band with little change in the transverse LSPR band (**Figure 3a**).

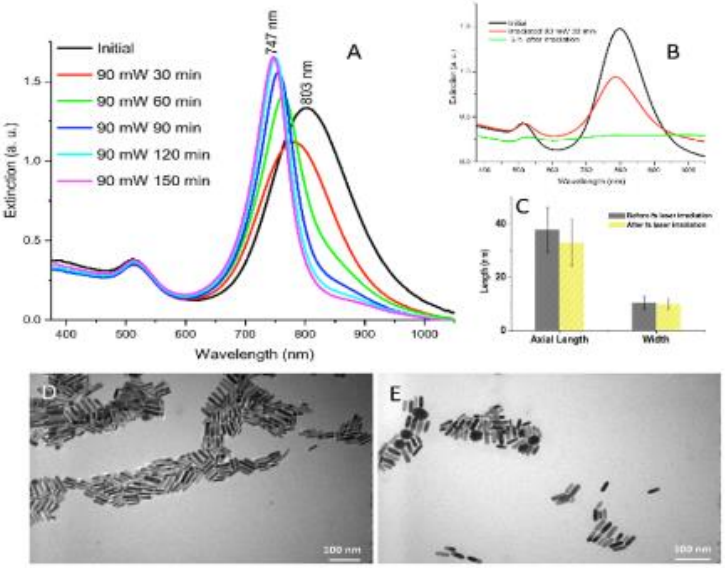

Figure 3. (a) Extinction spectra of AuNRs collected as a function of time during the irradiation with fs laser. (b) Irradiation of AuNRs without excess CTAB causes broadening of the spectrum (c) Plot showing the length/diameter changes of AuNRs. TEM images before (d) and after (e) laser irradiation

This is consistent with a narrower distribution of nanorod aspect ratios post-irradiation with almost no reshaping into nanospheres. The resulting AuNRs are significantly blue-shifted from both the original LSPR wavelength and the laser wavelength, thereby self-limiting the extent of reshaping possible. Without CTAB addition, a broad distribution of NPs results in agreement with our previous work (**Figure 3b**). Additionally, slight decrease in the axial length of the nanorods, while preserving their width nearly unchanged, was also observed from statistical analysis from transmission electron microscopy results (**Figure 3c-e**). Furthermore, through ablation of Pd coated AuNCs in a liquid with fs pulse lasers (150 mW, 519 nm), branched star-shaped NPs have been synthesized with no need of stabilizing ligands. However, pulsed laser ablation of parent AuNCs resulted in their transformation to spherical nanoparticles. The applicability of pulsed coherent light has been further extended toward the direct manipulation of the length of the alloyed Au/Pd NRs.

We demonstrate that cellulose nanofibers (CNF) with high transparency and mechanical robustness can be combined with gold nanorods to form a multifunctional porous membrane for dual-mode surface-enhanced Raman scattering (SERS) detection of both small molecules and cells. The nanoporous nature of the nanofiber membranes allows for effective pre-concentration of the analytes, further boosting the SERS performance. Specifically, because of the low fluorescence and Raman background of the CNF matrix, extremely low loading density of gold nanorods can be used (**Figure 4**). The nanorod assemblies within the CNF network can be resonantly driven by a 532 nm laser (transverse mode) and near resonantly driven at by a 785 nm laser (longitudinal mode), facilitating dual operation (**Figure 4**). The shorter wavelength excitation mode yields high Raman scattering efficiency and detecting R6G down to picomolar concentration. On the other hand, the longer wavelength excitation mode provides autofluorescence suppression for the better detection of microorganisms such as *Escherichia coli*.

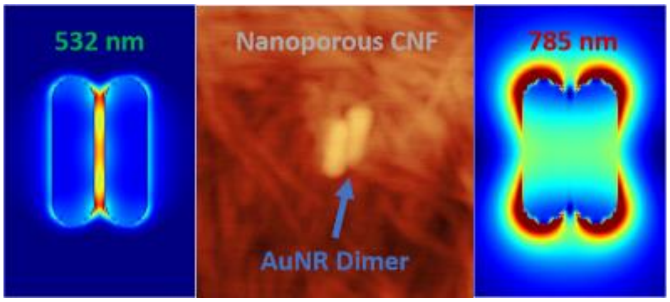

Figure 4. AFM image of AuNR dimer unit on nanoporous CNF substrate (center) and its dual plasmonic responses under two different laser excitation wavelengths (left, right).

Future Research Plans

- Synthesis of hybrid nanostructures composed of hollow gold nanocrystals and assemble them with electroactive conjugated polymers for the study of their electrochemically tunable plasmonic behavior under resonant and coupled-resonant conditions.
- *In situ* single individual and coupled nanoparticles study of energy transfer process between Au or Ag nanocrystals and electroactive-conjugated polymers and quantum dots under illuminating conditions accompanied by FDTD simulations.
- Possibilities for the use of novel bionanocomposites from nanofibrillar porous membranes with gold nanorods for sensing applications including SERS sensing.
- Fabrication of plasmonic nanohole arrays on evaporated metal substrates for electroactive conjugated polymers based electrically actuated active light absorption control.
- Mechanistic understanding of femtosecond laser-induced reshaping of AuPdNCs, AuPtNCs, AuPdNRs, AuPtNRs, and their trimetallic analogs.

References

1. Gramotnev, D. K.; Bozhevolnyi, S. I., Plasmonics beyond the diffraction limit. *Nat. Photon.*, **2010**, *4*, 83-91.
2. Biju, V.; Itoh, T.; Anas, A.; Sujith, A.; Ishikawa, M., Semiconductor quantum dots and metal nanoparticles: syntheses, optical properties, and biological applications. *Anal. Bioanal. Chem.*, **2008**, *391*, 2469.

Project Publications, 2016-2018

1. Zhang, S.; Geryak, R.; Geldmeier, J.; Kim, S.; Tsukruk, V. V. Synthesis, Assembly, and Applications of Hybrid Nanostructures for Biosensing. *Chem. Rev.* **2017,** *117*, 12942-13038, *Invited Review*
2. Xiong, R.; Grant, A. M.; Ma, R.; Zhang, S.; Tsukruk, V. V. Naturally-derived biopolymer nanocomposites: Interfacial design, properties and emerging applications. *Mater. Sci. Eng. R Rep.* **2018,** *125*, 1-41, *Invited Review*
3. Zhang, S.; Xiong, R.; Mahmoud, M. A.; Quigley, E. N.; Chang, H.; El-Sayed, M.; Tsukruk, V. V. Dual-Excitation Nanocellulose Plasmonic Membranes for Molecular and Cellular SERS Detection. *ACS Appl. Mater. Interfaces,* **2018**, *in print*
4. Nazemi, M.; Panikkanvalappil, S. R.; El-Sayed, M. A. Enhancing the rate of electrochemical nitrogen reduction reaction for ammonia synthesis under ambient conditions using hollow gold nanocages. *Nano Energy* **2018,** *49*, 316-323.
5. Xiong, R.; Kim, H. S.; Zhang, S.; Kim, S.; Korolovych, V. F.; Ma, R.; Yingling, Y. G.; Lu, C.; Tsukruk, V. V. Template-Guided Assembly of Silk Fibroin on Cellulose Nanofibers for Robust Nanostructures with Ultrafast Water Transport. *ACS Nano* **2017,** *11*, 12008-12019.
6. Zhou, J.; Jeon, J.-W.; Ponder, J. F.; Geldmeier, J. A.; Mahmoud, M. A.; El-Sayed, M.; Reynolds, J. R.; Tsukruk, V. V. Electrochromic tuning of transparent gold nanorods with poly [(3, 4-propylenedioxy) pyrrole] shells in the near-infrared region. *J. Mater. Chem. C* **2017**, *5*, 12571-12584.
7. Geldmeier, J.; Rile, L.; Yoon, Y. J.; Jung, J.; Lin, Z.; Tsukruk, V. V. Dewetting-Induced Photoluminescent Enhancement of Poly(lauryl methacrylate)/Quantum Dot Thin Films. *Langmuir* **2017**, *33*, 14325-14331.
8. Zhang, S.; Kim, S.; Tsukruk, V. V. Ligand-Exchange Dynamics on Gold Nanocrystals: Direct Monitoring of Nanoscale Polyvinylpyrrolidone–Thiol Domain Surface Morphology. *Langmuir* **2017,** *33*, 3576-3587.
9. Jeon, J.-W.; Zhou, J.; Geldmeier, J. A.; Ponder Jr, J. F.; Mahmoud, M. A.; El-Sayed, M.; Reynolds, J. R.; Tsukruk, V. V. Dual-Responsive Reversible Plasmonic Behavior of Core–Shell Nanostructures with pH-Sensitive and Electroactive Polymer Shells. *Chem. Mater.* **2016,** *28*, 7551-7563.
10. Ledin, P. A.; Jeon, J.-W.; Geldmeier, J. A.; Ponder, J. F.; Mahmoud, M. A.; El-Sayed, M.; Reynolds, J. R.; Tsukruk, V. V. Design of Hybrid Electrochromic Materials with Large Electrical Modulation of Plasmonic Resonances. *ACS Appl. Mater. Interfaces* **2016,** *8*, 13064-13075.
11. Geldmeier, J. A.; Mahmoud, M. A.; El-Sayed, M. A.; Jeon, J. W.; El-Sayed, M. A.; Tsukruk V. V., The effect of plasmon resonance coupling in P3HT-coated silver nanodisk monolayers on their optical sensitivity. *J. Mater. Chem. C* **2016**, *4*, 9813-9822.
12. Tian, L.; Liu, K.-K.; Fei, M.; Tadepalli, S.; Cao, S.; Geldmeier, J. A.; Tsukruk, V. V.; Singamaneni, S. Plasmonic Nanogels for Unclonable Optical Tagging. *ACS Appl. Mater. Interfaces* **2016,** *8,* 4031-4041.
13. Mahmoud M. A., Tunable Plasmonic Neutral Density Filters and Chromatic Polarizers: Highly Packed 2D Arrays of Plasmonic Nanoparticle on Elastomer Substrate. *J. Phys. Chem. C* **2016**, *119*, 18249.
14. Jeon, J.-W.; Ledin, P. A.; Geldmeier, J. A.; Ponder, J. F.; Mahmoud, M. A.; El-Sayed, M.; Reynolds, J. R.; Tsukruk, V. V. Electrically Controlled Plasmonic Behavior of Gold Nanocube@Polyaniline Nanostructures: Transparent Plasmonic Aggregates. *Chem. Mater.* **2016,** *28*, 2868-2881.
15. Mahmoud M. A., Overgrowth of Silver Nanodisks on a Substrate into Vertically Aligned Nanopillars for Chromatic Light Polarization. *ACS Appl. Mater. Inter.* **2016**, *8*, 23827–23836.
16. Mahmoud M. A., Silver Nanodisk Monolayers with Surface Coverage Gradients for Use as Optical Rulers and Protractors. *Langmuir* **2016**, *32*, 11631–11638.

Click Synthesis of Metallopolymers and Highly Emissive Materials

PI: Adam S. Veige, University of Florida

Co-PI: Kirk S. Schanze, University of Texas San Antonio

Students: Christopher C. Beto, James. D. Bullock, Yajing Yang, Ethan D. Holt, Charles J. Zeman IV, Xi Yang

Senior Scientist: Ion Ghiviriga, University of Florida

Program Scope

iClick is a synthetic technique that links metal ions through a triazolate bridge. Originally, inorganic click (iClick) was defined as the cycloaddition reaction between a metal-azide and metal-alkyne (Eq. 1). iClick now includes the cycloaddition of a metal-azide and an organic alkyne or a metal-acetylide and an organic azide. This presentation further expands iClick to include heterometallic complexes, self-assembled clusters, and metallopolymers. The research focuses on exploiting aurophilic interactions to produce white light emitting materials.

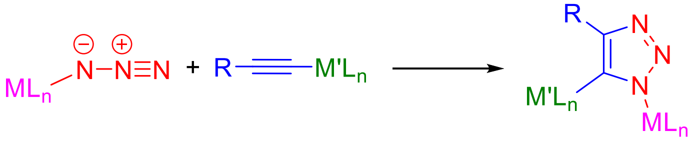

(1)

Recent Progress

iClick was employed to link two or four Au(I) metal ions through a triazolate bridge. Depending on the choice of phosphine ligand, (PEt_3 or PPh_3) dinuclear $[PPh_3Au]_2(\mu\text{-}N_3C_2)$-9,9-dioctyl-9*H*-fluorene or tetranuclear $[PEt_3Au]_4[(\mu\text{-}N_3C_2)$-9,9-dioctyl-9*H*-fluorene$]_2$ complexes can be controllably synthesized according to Figure 1.

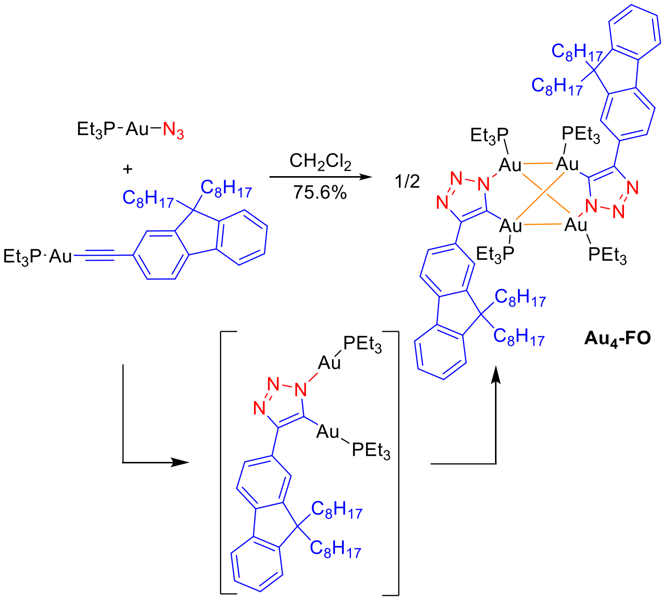

Figure 1. iClick synthesis of the tetragold complex **Au$_4$-FO**.

The iClick products are characterized by MS and multinuclear NMR, TOCSY 1D, ^{1}H-^{13}C gHMBC, and ^{1}H-^{13}C gHSQC. In addition, the photophysical properties of the dimer and tetramers were examined. Designing molecules that can access or increase aurophilic interactions in the excited state provides another tool for fine-tuning the emission profiles of gold complexes.

Another application of iclick to be presented includes the first example of an in-chain metallo-poly(triazolate) (MPTA) synthesized by copper-catalyzed azide-alkyne cycloaddition (CuAAC). Azido–platinum–acetylide (A–M–B) monomers *trans*-$(PBu_3)_2(N_3CH_2C_6H_4)Pt(C\equiv CC_6H_4X$ (X = F and NO_2) are catalytically polymerized with copper(I) acetate to yield 1,2,3-triazolate linked Pt(II) units, poly(*trans*-$(PBu_3)_2Pt(\mu\text{-}CH_2C_6H_4N_3C_2C_6H_4X)$ (X = F and NO_2) according to Figure 2. The metallopolymers are characterized by multinuclear NMR, IR, UV/Vis, GPC, and MS.

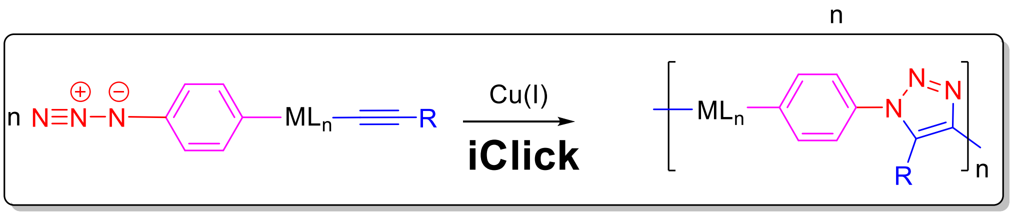

Figure 2. iClick synthesis of the tetragold complex **Au$_4$-FO**.

Future Plans

The major goal for the next year is to realize a solution-based preparation of a dynamically tunable light emitting material. By exploiting the reversible tetra-gold Au-Au bond forming reaction we aim to link π-conjugated chromophores with different bandgaps that can be titrated as needed to alter the color of light emission according to Figure 3.

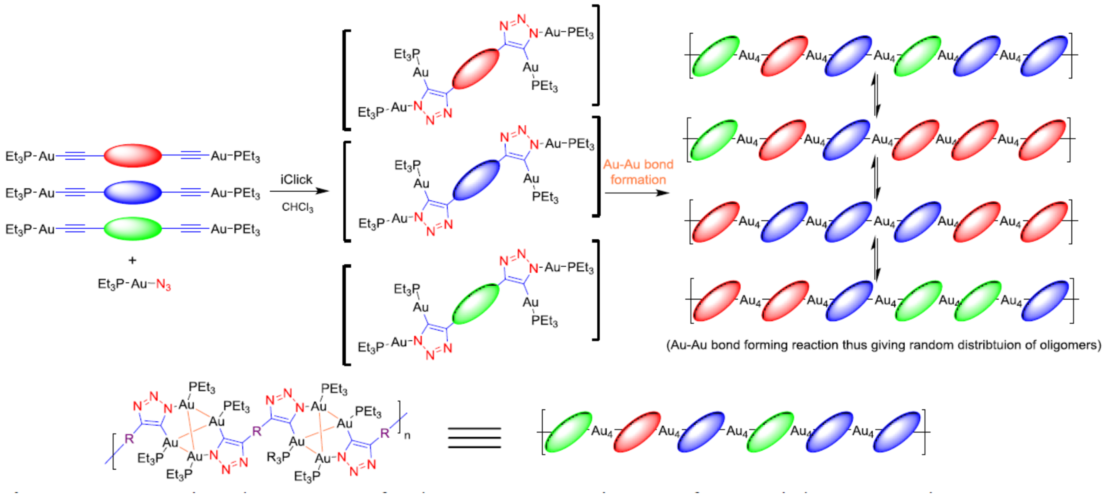

Figure 3. iClick synthesis oligomeric gold complexes featuring dynamically tunable light emission. Colored units represent π-conjugated chromophores with different bandgaps.

Another future direction involves expanding the synthesis of metallopolymers according to Figure 4. An important variation to the synthetic scheme will be to replace the PBu_3 with Nheterocyclic carbene ligands. In our labs we have demonstrated efficient triplet emission from Pt-NHC complexes.

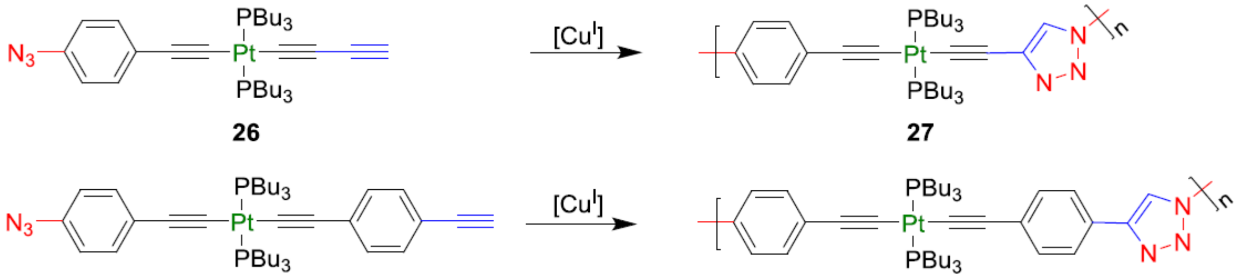

26 **27**

Figure 4. Future iCick synthesis of metallopolymers

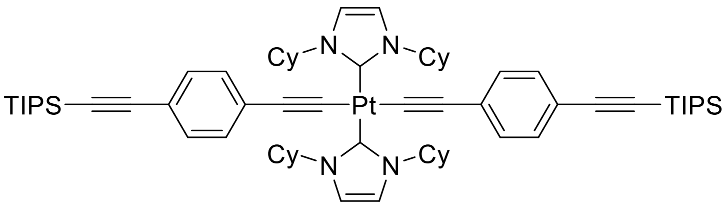

Figure 5. Proposed replacement of PR_3 with an NHC.

Publications

1. Midas Touch Imparts White Light: A Novel Application Exploiting Aurophilic Interactions and iClick to Produce White Light Emitting Materials. C. C. Beto, J. D. Bullock, Y. Yang, E. D. Holt, C. J. Zeman IV, X. Yang, I. Ghiviriga, K. S. Schanze, and A. S. Veige, *Inorg. Chem.* **2018**, *submitted*.

2. A New Synthetic Route to In-Chain Metallopolymers via Copper(I) Catalyzed Azide-Platinum-Acetylide iClick. C. C. Beto, E. D. Holt, Y. Yang, I. Ghiviriga,K. S. Schanze, and A. S. Veige. *Chem. Commun.*, 2017,**53**, 9934-9937.

3. Single versus double Cu(I) catalyzed [3+2] azide/platinum diacetylide cycloaddition reactions. X. Yang, S. VenkatRamani, C. C. Beto, T. Del Castillo, I. Ghiviriga, K. A. Abboud, A. S. Veige, *Organometallics*, **2017**, 36 (7), pp 1352–1357.

Linearly- and Cross-Conjugated Porphyrin Oligomers

Hong Wang, Associate Professor, Department of Chemistry, University of North Texas

Francis D'Souza, Professor, Department of Chemistry, University of North Texas

Program Scope

Largely pi-extended structures represent one most interesting yet challenging frontiers in chemistry and materials science due to their potential applications in various areas, particularly in organic electronics. Acenes is one attractive class of pi-extended materials, consisting of linearly fused benzene rings.[1-3] Acenes have shown to posses exceptionally high charge mobility, and have thus been of intense research interest. Longer acenes fused to another chromophores, such as porphyrins have never been reported. The fusion of an acene with two or more chromophores will greatly extend the pi-conjugation, and will likely produce electronically highly interactive multiporphyrinic systems. Given the rich photophysical and optoelectronic properties of porphyrins, and the unique set of electronic properties of acenes, such nano-sized fused *pi*-systems are enticing, promising new opportunities for organic electronics.

The Wang group has been engaged in developing new synthetic methodologies for *pi*-extended porphyrins. We have developed a number of concise and versatile synthetic methods in the past several years.[4-6] The availability of these methods makes it possible to design and synthesize novel pi-extended porphyrins such as pentacene-fused, and pentaquinone-fused porphyrins. The purpose of this project are: First, new synthetic methods will be developed to further extend the porphyrin □*i*-system. Second, using methods developed to design and synthesize cross- and linearly conjugated porphyrin oligomers incorporating acenes. Third, the electronic and photophysical properties of these compounds will be investigated using UV-Vis, steady state and life time fluorescence, and transient spectroscopies, along with DFT calculations.

Recent Progress

We have developed several new synthetic methods for the extension of the *pi*-system of porphyrins in the past two years. Using these methods, we have designed and prepared a number of novel □*i*-extended porphyrin systems, including cross- and linearly-conjugated porphyrin dimers, linearly push-pull dibenzoporphyrins, and A2B2 push-pull tetrabenzoporphyrins. Our studies have demonstrated significant push-pull and substituent effects of these porphyrins. In particular**,** the pentacene-fused porphyrins show unexpected stability as compared with their corresponding pentacene derivatives. The unusual stability of these pentacene-fused porphyrins has been investigated both experimentally and theoretically.

Figure 1. Pentacene-fused porphyrin dimer.

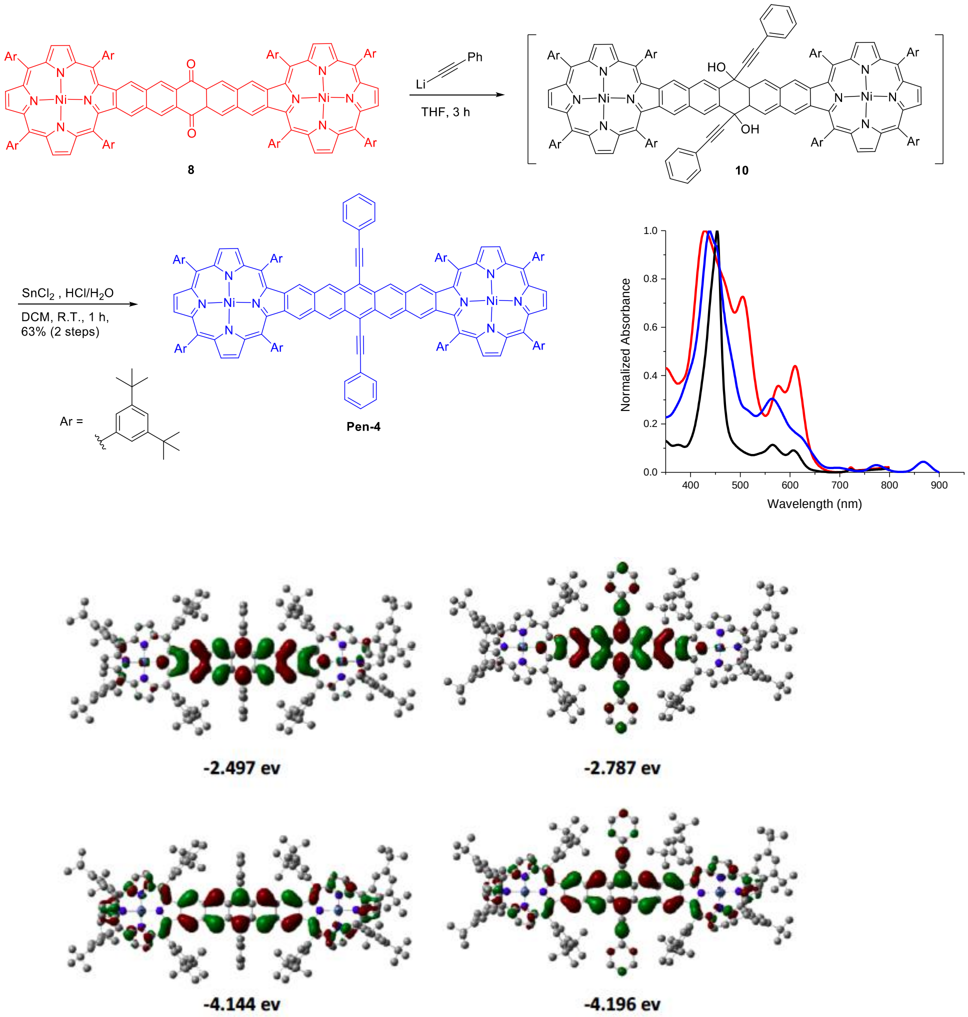

Future Plans

1. We will continue to work on methodology development to further extend the □*i*-conjugation of porphyrin systems, including tetracenoporphyrins and hexacenoporphyrins.

2. We will design and synthesize new oligomeric porphyrins fused with symmetrically and unsymmetrically fused with acenes. We will study the electronic and photophysical properties of these compounds using UV-Vis spectroscopy, time-resolved and steady state fluorescence spectroscopy, transient spectroscopy, cyclic voltammetry and DFT calculations.

3. We will investigate the possibility of these acene-fused porphyrins to release singlet fission.

References

1. Q. Ye, C. Chi, *Chem. Mater.*, 2014, **26** (14), 4046–4056.
2. S. S. Zade, M. Bendikov., *J. Phys. Org. Chem.*, 2012, **25** (6), 452-461.

3. J. E. Anthony, *Angew. Chem. Int. Ed.,* 2008, **47** (3), 452-483.
4. R. Deshpande, L. Jiang, G. Schmidt, J. Rakovan, X. P. Wang, K. Wheeler, H. Wang, *Org. lett* 2009, **11**, 4251-4253
5. L. Jiang, R. A. Zaenglein, J. T. Engle, C. Mittal, C. S. Hartley, C. J. Ziegler, H. Wang, *Chem. Commun.* 2012, **48**, 6927-6929
6. L. Jiang, J. T. Engle, L. Sirk, C. S. Hartley, C. J. Ziegler, H. Wang, *Org. Lett*., 2011, **13**, 3020-3023.

Publications

1. R. G. Waruna Jinadasa, Bihong Li, Benjamin Schmitz, Siddhartha Kumar, Yi Hu, Lei Kerr, and Hong Wang*, “Monobenzoporphyrins as Sensitizers for Dye-Sensitized Solar Cells: Observation of Significant Spacer-Group Effect”, *ChemSusChem,* **2016**, *9,* 2239-2249.

2. Benjamin Schmitz, Bihong Li, R. G. Waruna Jinadasa, Shashi B. Lalvani, Lei L. kerr, Hong Wang* “Benzoporphyrins bearing pyridine or pyridine-N-oxide anchoring groups as sensitizers for dye-sensitized solar cell”, J. Porphyrins and Phthalocyanines., **2016**, 20, 1-14.

3. C. Frigerio, J. P. G. Santos, P. Quaresma, S. L. H. Rebelo, A. Gomes, P. Eaton, E. Pereira, P. A. Carvalho, J. A. Shelnutt, L. Jiang, H. Wang, and Craig J. Medforth, “Ionic Self-Assembly Reactions of a Porphyrin Octacation”, *Tetrahedron*, **2016**, 72, 6988-6995.

4. Yi Hu, Michael B. Thomas, R. G. Waruna Jinadasa, Hong Wang* and Francis D’Souza*, “Competitive Energy and Electron Transfer in β-Functionalized Free-Base Porphyrin-Zinc Porphyrin Dimer Axially Coordinated to C$_{60}$: Synthesis, Supramolecular Formation and Excited State Processes”, Chem. Eur. J., Chem. Eur.J. **2017**, 23,12805 –12814. **Highlighted** in **Cover page**.

5. Y. Hu, S. Yellappa, M. B. Thomas, R. G. W. Jinadasa, A. Matus, M. Shulman, F. D’Souza*, Hong Wang*, “β-Functionalized push-pull opp-dibenzoporphyrins as sensitizers for dye-sensitized solar cells”, *Chem. Asian J.*, **2017**. 2749-2762.

6. R. G. Waruna Jinadasa, Michael B. Thomas, Yi Hu, Francis D’Souza* and Hong Wang*, “Investigation of the push-pull effects on β-functionalized benzoporphyrins bearing ethynylphenyl bridge”, *Phys. Chem. Chem. Phys.,* **2017**, **19**, 13182-13188.

7. M. B. Thomas, R. G. W. Jinadasa, Y. Hu, B. Schmitz. H. Wang* and F. D’Souza*, “β-functionalized zinc porphyrin coordinated to C60 donor-acceptor conjugates”, *Can. J. Chem.*, **2018**, in press.

8. Siddhartha Kumar, Xiaoqin Jiang, Wenqian Shan, R. G. Waruna Jinadasa, Karl M. Kadish and Hong Wang*, "β-Functionalized Trans-A2B2 Push-Pull Tetrabenzoporphyrins", *Chem. Commun.*, **2018**, 54, 5303. **Highlighted in back Cover page**.

An Integrated Theoretical and Experimental Approach to Achieve Highly Polarizable Relaxor Ferroelectric Liquid Crystalline Polymers

Lei Zhu and Philip Taylor, Case Western Reserve University, Cleveland, Ohio 44106-7202

Bin Zhao, University of Tennessee, Knoxville, Tennessee 37996

Program Scope

This project aims to rationally design novel mesogen (i.e., connected phenyl rings)-free ferroelectric liquid crystalline polymers (FE LCPs) based on sulfonyl-containing side-chain chiral polymers. Unlike conventional FE LCPs [1], the driving force for the liquid crystal formation is the strong dipolar interactions among highly dipolar sulfonyl groups directly connected to the polymer main chain. The chiral center can be placed on the main chain or the side chains in order to induce the chiral smectic C (SmC*) phase. Because of the large dipole moment (4.5 D) of the small-sized sulfonyl groups [2], high spontaneous polarization is expected for these FE LCPs. In the next step, copolymerization will be used to break up large FE domains into nanosized domains (nanodomains) to achieve the relaxor ferroelectric (RFE) behavior. Given the expected high dielectric constant of these FE LCPs, potential applications could be envisioned. For example, if the Curie transition could be significantly altered by an external electric field, the electrocaloric effect is expected [3]. The advantage of FE LCPs lies in the fact that the driving electric field for FE switching is significantly lower than that for FE crystalline polymers such as poly(vinylidene fluoride-*co*-trifluoroethylene) [P(VDF-TrFE)]. In addition, these FE LCPs could also be a good candidate for electroactive liquid crystalline elastomers if their glass transition temperature is relatively low.

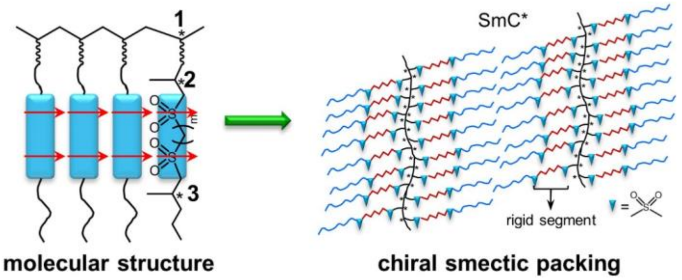

Molecular design of sulfonyl-containing ferroelectric liquid crystalline chiral polymers.

Recent Progress

In the first year, we have achieved the following progresses for the project. First, high molecular weight isotactic polyepichlorohydrin (PECH) has been synthesized using methylaluminoxane (MAO)-based catalyst. Both monosulfonyl and disulfonyl side groups having long alkyl tails are successfully grafted to both isotactic and achiral PECHs. Second, these side-chain sulfonyl polymers have been characterized by differential scanning calorimetry (DSC) and synchrotron X-ray diffraction (XRD). Liquid crystalline structures have been identified for non-oriented samples.

Future Plans

In the next year, we plan the following research activities. First, structure characterization on uniaxially stretched samples will be carried out to determine the SmC* phase. Second, dielectric and FE characterizations will be carried out to determine their electrical properties. Third, preliminary electrocaloric characterization will be performed to prove the viability of these FE LCPs for electrocaloric cooling application.

References

1. Scherowsky, G., Ferroelectric liquid crystal (FLC) polymers. In *Ferroelectric Polymers: Chemistry, Physics, and Applications*; Nalwa, H. S., Ed.; Marcel Dekker, Inc.: New York, 1995; Chapter 10, pp. 435-537.
2. Zhang, Z.; Wang, D. H.; Litt, M. H.; Tan, L.-S.; Zhu, L. High temperature and high energy density dipolar glass polymers based on sulfonylated poly(2,6-dimethyl-1,4-phenylene oxide). *Angew. Chem. Int. Ed.* **2018**, *57*, 1528-1531.
3. Qian, X. S.; Lu, S. G.; Li, X. Y.; Gu, H. M.; Chien, L. C.; Zhang, Q. M., Large electrocaloric effect in a dielectric liquid possessing a large dielectric anisotropy near the isotropic-nematic transition. *Adv. Funct. Mater.* **2013**, *23*, 2894-2898.

Publications

1. Seymour, B. T.; Zhang, Z.; Kwok, M.-H.; Zhao, B.; Zhu, L. Synthesis and ferroelectric liquid crystalline structures in sulfonyl-containing side-chain isotactic liquid crystalline polymers. 2018, in preparation.

Charge carrier dynamics in hybrid organic-inorganic semiconductors

Xiaoyang Zhu, Department of Chemistry, Columbia University, New York, NY 10027

Program Scope

During this funding period, the PI has made major advances in understanding charge carrier dynamics in lead halide perovskites. The PI's proposal on large polaron formation and dielectric screening has gained wide acceptance and is becoming part of the "standard" model to explain why hybrid organic-inorganic lead halide perovskites (HOIPs) work so well in solar cells and light-emitting devices. Highlights of the research achievements include: 1) the discovery of long-lived hot carriers and its correlation to crystal-liquid duality of the HOIPs; 2) the direct time-domain view of large-polaron formation dynamics in an HOIP and its all-inorganic counterpart, $MAPbBr_3$ and $CsPbBr_3$; and 3) the finding of the polariton nature of lasing from $CsPbBr_3$ nanowires. Achievements 1 & 2 are detailed below.

Recent Progress

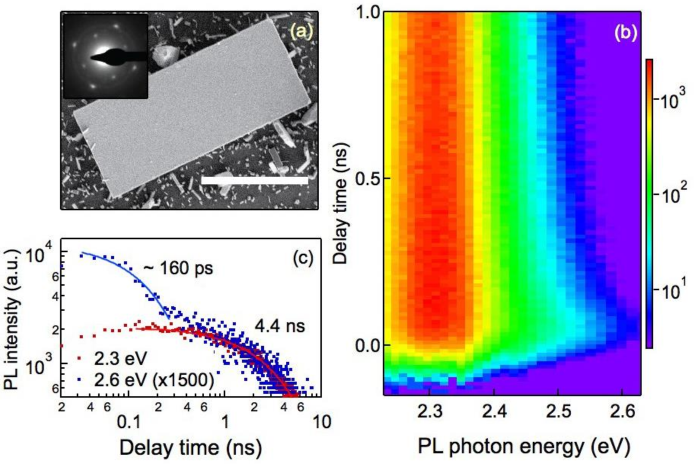

Fig. 1 Time-dependent PL revealing long-lived hot carriers in $MAPbBr_3$. (a) SEM image of a single crystal $MAPbBr_3$ micro-plate. Scale bar = 10 µm. (b) Pseudo-color plot of TR-PL spectra at room temperature under 3.08 eV excitation and excitation density of 1.7 µJ cm^{-2}. (b) PL intensity decay kinetics at 2.3 eV (red) and 2.6 eV (blue) and single exponential fits (solid). Ref. [1]

One of the most striking observations in HOIPs is long-lived energetic carriers at low excitation densities [1,2]. In a conventional polar semiconductor, excess electronic energy above the LO-phonon energy is lost on ultrafast time scales of 100s fs due to the ubiquitous Coulomb potential which governs the scattering of electrons with polar LO-phonons [3,4]. In GaAs, the electronic cooling rate $\langle dE/dt \rangle$ is of the order of 1 eV/ps for hot electrons with mean energy $\langle dE^* \rangle$ higher than the LO phonon energy (E_{LO}); the cooling is slowed down by 3-4 orders of magnitude when $\langle dE^* \rangle$ falls below E_{LO} and scattering with acoustic phonons becomes dominant [3,4]. Using time-resolved PL (Fig. 1) and time-resolved two-photon photoemission, the PI's group discovered long-lived hot carriers in HOIPs at room temperature [1,2]. The excess electronic energy of the order of 100 meV, which is much higher than

E_{LO}, cools down at rates typical of acoustic phonon scattering, as shown in Fig. 7 [1,2]. A comparison of HOIP single crystals with their all-inorganic counterpart at room temperature showed long-lived hot PL in $MAPbBr_3$ and $FAPbBr_3$, but not in $CsPbBr_3$ [1]. This correlates well with the more liquid-like responses in $MAPbBr_3$ and $FAPbBr_3$ than that in $CsPbBr_3$, as observed in TR-OKE measurements. While large polarons form in both $MAPbBr_3$ and $CsPbBr_3$,[5] the rate of formation is not competitive with phonon cooling in the latter. The presence of long-lived energetic carriers has also been observed by Guo et. al in $MAPbI_3$ thin films using transient absorption (TA) microscopy [6] and by Monahan et al. in 2D electronic spectroscopy of $MAPbI_3$ [7]. The transfer of phonon energy from the subset of optical phonons that are in quasi-equilibrium with the hot carrier to the acoustic phonon bath is slowed down due to the low thermal conductivity, a result of the phonon glass character [8,9]. The slowed cooling of energetic carriers due to large polaron formation is mechanistically different from the conventional phonon bottleneck effect observed in $MAPbI_3$ thin films at high excitation densities ($\geq 10^{18}/cm^3$) [10–12]. As pointed out by Frost et al., the transition density of ~ $10^{18}/cm^3$ is essentially the Mott density when the large polarons overlap spatially and are destabilized [9].

The PI's group also succeeded in providing a direct time-domain view of large polaron formation in single-crystal lead bromide perovskites: $CH_3NH_3PbBr_3$ and $CsPbBr_3$. Using time-resolved optical Kerr effect spectroscopy (TR-OKE) and transient reflectance spectroscopy, the PI's group found large polaron forms predominantly from the deformation of the $PbBr_3^-$ frameworks, irrespective of the cation type. First principles calculation confirms large polaron formation, identifies the Pb-Br-Pb deformation modes as responsible, and explains quantitatively the rate difference between $CH_3NH_3PbBr_3$ and $CsPbBr_3$. The findings reveal the general advantage of the soft $[PbX_3]^-$ sub-lattice in charge carrier protection and suggest that there is likely no mechanistic limitations in using all inorganic or mixed cation lead halide perovskites to overcome instability problems and to tune the balance between charge carrier protection and mobility.

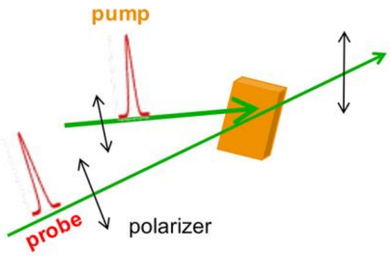

Fig. 2. Schematic illustration of a TR-OKE measurement.

In a TR-OKE experiment, Fig. 2, a linearly polarized pump laser pulse induces polarization and thus anisotropy in the refractive index; polarization rotation (Kerr effect) of a linearly polarized probe pulse is used to detect the decay in this polarization. Fig. 3 shows TR-OKE responses and Fourier transforms in $MAPbBr_3$ as pump hν is varied from non-resonant (1.85 – 2.03 eV), to pre-resonant (2.10 – 2.18 eV), and charge injection (2.3 eV) regimes. We see the broad and featureless nuclear response characteristic of liquids [13,14]. The absence of oscillatory features suggests that we detect predominantly over-damped phonon modes that can be attributed to strong anharmonicity and dynamic disorder [15,16]. As hν moves closer (2.03→ 2.18 eV) to E_g, we find enhanced slow responses (≥ 1 ps) attributed to the resonant Raman mechanism where nuclear motions are coupled to electronic transitions. These motions are mainly Pb-Br-Pb stretching and bending motions, as shown by calculations in the inset in Fig. 3B. By tuning hν to 2.30 eV (≥ E_g) we directly probe the OKE response upon charge injection. We observe qualitatively different structural dynamics with a fast component with time constant of $\tau_1 = 0.29 \pm 0.04$ ps and longer-lived anisotropy decay with $\tau_2 = 3.4 \pm 0.5$ ps. These features are associated with the dynamic response of nuclei to the photo-injection of carriers, i.e. formation and movement, respectively, of the large polarons.

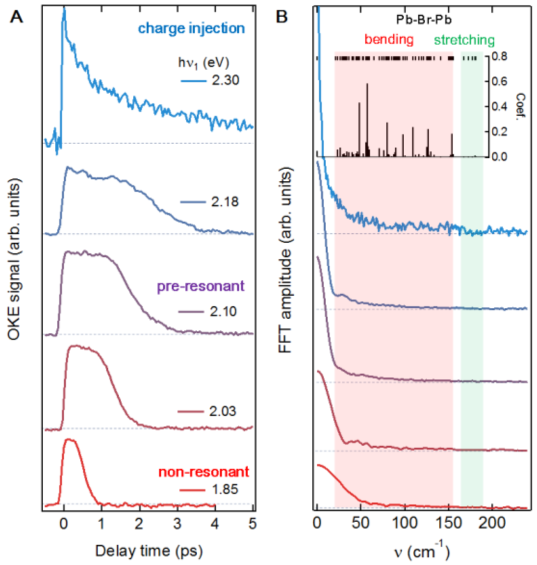

Fig. 3. TR-OKE reveals phonon dynamics and large polaron formation in $MAPbBr_3$. (A) TR-OKE and (B) Fourier transforms as a function of pump energy (hν = 1.85 – 2.30 eV). The inset in (B) shows calculated normal modes and sticks are projections onto the normal modes of the displacement vector upon polaron formation. Ref. [5].

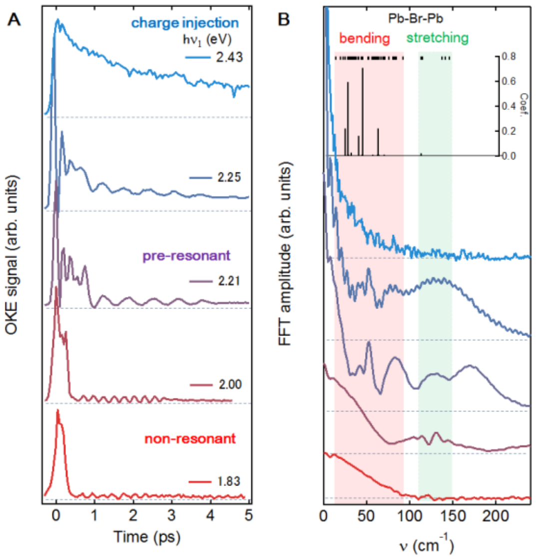

Fig. 4. TR-OKE reveals phonon dynamics and large polaron formation in $CsPbBr_3$. (A) TR-OKE transients and (B) Fourier transforms as a function of pump energy (hν = 1.85 – 2.43 eV). The inset in (B) shows calculated normal modes and sticks are projections onto the normal modes of the displacement vector upon polaron formation. Ref. [5].

As comparison, we show OKE responses for $CsPbBr_3$ single crystal, Fig. 4. When hν (= 1.83 or 2.00 eV) is far below E_g, the OKE signal consists of two responses: a broad feature within ≤0.5 ps and an oscillatory response distributed over a few ps (Fig. 2A); the former is liquid-like [13,14] while the latter are Raman active vibrations typical of solids [17]. Thus, in addition to the liquid-like phonon dynamics which dominates $MAPbBr_3$, $CsPbBr_3$ shows partial phonon characteristics of typical crystalline solids. As we increase hν to the pre-resonant regime (2.21-2.25 eV), we again see the resonance-enhancement of slower responses attributed to the Pb-Br-Pb stretching and bending motions. When hν (= 2.43 eV) exceeds E_g, the TR-OKE response changes completely. Instead of oscillations, we see a sub-ps component with a time constant of $\tau_1 = 0.7 \pm 0.1$ ps and longer-lived anisotropy that decays with $\tau_2 = 6.5 \pm 0.3$ ps, again attributed to large polaron formation and movement, respectively.

The difference in polaron formation time, which in $MAPbBr_3$ (0.3 ps) is less than half of that in $CsPbBr_3$ (0.7 ps), makes the former, more competitive with hot carrier cooling. While there is more liquid-like disorder in the cubic $MAPbBr_3$ than that in the orthorhombic $CsPbBr_3$, at room temperature, the intrinsic softness and polarizability of the PbX_3^- framework structure enables easy formation of large polarons upon charge injection in both HOIPs and their all-inorganic counterparts. Indeed, HOIPs and their all-inorganic counterparts show similarly exceptional charge carrier properties for band edge carriers and solar cell performances [18–23].

Future Plans

During the next funding period, the PI aims to develop the ferroelectric large polaron mechanism for defect tolerance in lead-halide perovskite materials and develop design principles for the mixed cation/anion lead halide perovskites for optimal performance in solar cells and light emitting devices. This research takes the large polaron proposal one step further and is based on the hypothesis that polarons in LHPs are *ferroelectric large polarons*. This hypothesis came from the realization that the dielectric function of a hybrid LHP possesses combined characteristics of a polar liquid and a ferroelectric material, but not that of a conventional polar semiconductor. In particular, the ferroelectric-like response in the THz region may lead to dynamic and local ordering of polar nano regions (PNRs) by an extra electron or hole, resulting a quasiparticle which can be called a *ferroelectric large polaron*. Compared to a conventional large polaron, the collective nature of polarization in a ferroelectric large polaron may give rise to order(s)-of-magnitude larger reduction in the Coulomb potential and introduce potential barriers to charge carrier scattering. One of the most successful strategies in the development of ferroelectric materials is to tune its properties by mixed/alloyed composition, which introduces local disorder/heterogeneity and, thus, the size, energetics, and dipole moments of PNRs. The PI will establish ferroelectric large polarons in mixed cation/anion hybrid LHPs systems, e.g, $[(FAPbI_3)_{1-x}(MAPbBr_3)_x]$, that are being actively explored in different contexts, i.e., for improved chemical stability and solar cell efficiencies.

References

1. Zhu, H. *et al.* Screening in Crystalline Liquids Protects Energetic Carriers in Hybrid Perovskites. *Science* **353,** 1409–1413 (2016).
2. Niesner, D. *et al.* Persistent Energetic Electrons in Methylammonium Lead Iodide Perovskite Thin Films. *J. Am. Chem. Soc.* **138,** 15717–15726 (2016).
3. Balkan, N. *Hot Electrons in Semiconductors*. (Oxford University Press, 1998).
4. Shah, J. & Leheny, R. F. in *Semiconductors Probed by Ultrafast Laser Spectroscopy (Academic Press, Orlando)* 45 (Academic, 1984).
5. Miyata, K. *et al.* Large Polarons in Lead Halide Perovskites. *Sci. Adv.* **3,** e1701217 (2017).
6. Guo, Z. *et al.* Long-range hot-carrier transport in hybrid perovskites visualized by ultrafast microscopy. *Science* **356,** 59–62 (2017).

7. Monahan, D. M. *et al.* A Room Temperature Coherent Optical Phonon in 2D Electronic Spectra of CH3NH3PbI3 Perovskite is a Possible Cooling Bottleneck. *J. Phys. Chem. Lett.* **8,** 3211–3215 (2017).
8. Yang, J. *et al.* Acoustic-optical phonon up-conversion and hot-phonon bottleneck in lead-halide perovskites. *Nat. Commun.* **8,** 14120 (2017).
9. Frost, J. M., Whalley, L. D. & Walsh, A. Slow cooling of hot polarons in halide perovskite solar cells. *ACS Energy Lett.* **2,** 2647–2652 (2017).
10. Yang, Y. *et al.* Observation of a hot-phonon bottleneck in lead-iodide perovskites. *Nat. Photonics* **10,** 53–59 (2016).
11. Price, M. *et al.* Hot Carrier Cooling and Photo-induced Refractive Index Changes in Organic-Inorganic Lead Halide Perovskites. *Nat. Commun.* **6,** 8420 (2015).
12. Chen, K., Barker, A. J., Morgan, F. L. C., Halpert, J. E. & Hodgkiss, J. M. Effect of Carrier Thermalization Dynamics on Light Emission and Amplification in Organometal Halide Perovskites. *J. Phys. Chem. Lett.* **6,** 153–158 (2015).
13. Righini, R. Ultrafast Optical Kerr Effect in Liquids and Solids. *Science* **262,** 1386–1390 (1993).
14. McMorrow, D., Lotshaw, W. T. & Kenney-Wallace, G. a. Femtosecond Optical Kerr Studies on the Origin of the Nonlinear Responses in Simple Liquids. *IEEE J. Quantum Electron.* **24,** 443–454 (1988).
15. Ivanovska, T. *et al.* Vibrational Response of Methylammonium Lead Iodide: From Cation Dynamics to Phonon-Phonon Interactions. *ChemSusChem* 1–12 (2016). doi:10.1002/cssc.201600932
16. Yaffe, O. *et al.* Local Polar Fluctuations in Lead Halide Perovskite Crystals. *Phys. Rev. Lett.* **118,** 136001 (2017).
17. Polok, K., Ratajska-Gadomska, B., Konarska, J. & Gadomski, W. Coherent optical phonons in pure and Pr3+ doped YAG crystal studied by Optical Kerr Effect spectroscopy: Temperature and concentration dependence. *Chem. Phys.* **442,** 119–127 (2014).
18. Kulbak, M., Cahen, D. & Hodes, G. How Important Is the Organic Part of Lead Halide Perovskite Photovoltaic Cells? Efficient CsPbBr3 Cells. *J. Phys. Chem. Lett.* **6,** 2452–2456 (2015).
19. Zhu, H. *et al.* Organic Cations Might Not Be Essential to the Remarkable Properties of Band Edge Carriers in Lead Halide Perovskites. *Adv. Mater.* **29,** 1603072 (2017).
20. Frolova, L. A. *et al.* Highly Efficient All-Inorganic Planar Heterojunction Perovskite Solar Cells Produced by Thermal Coevaporation of CsI and PbI 2. *J. Phys. Chem. Lett.* **8,** 67–72 (2017).
21. Berdiyorov, G. R., Kachmar, A., El-mellouhi, F., Carignano, M. A. & Madjet, M. E.-A. Role of Cations on the Electronic Transport and Optical Properties of Lead-iodide Perovskites. *J. Phys. Chem. C* **120,** 16259–16270 (2016).
22. Saliba, M. *et al.* Cesium-containing Triple Cation Perovskite Solar Cells: Improved

Stability, Reproducibility and High Efficiency. *Energy Environ. Sci.* **9,** 1989–1997. (2016).

23. McMeekin, D. P. *et al.* A mixed-cation lead mixed-halide perovskite absorber for tandem solar cells. *Science* **351,** 151–155 (2016).

Publications

- H. Zhu, K. Miyata, Y. Fu, J. Wang, P. P. Joshi, D. Niesner, K. W. Williams, S. Jin, X.-Y. Zhu, "Screening in crystalline liquids protects energetic carriers in hybrid perovskites," *Science*, **2016**, *353*, 1409-1413.
- D. Niesner, H. Zhu, K. Miyata, P. Joshi, T. J. Evans, B. J. Kudisch, M. T. Trinh, M. Marks, X.-Y. Zhu, "Persistent energetic electrons in methylammonium lead iodide perovskite thin films," *J. Am. Chem. Soc*. **2016**, *138*, 15717−15726.
- Y. Fu, H. Zhu, A. Schrader, D. Liang, Q. Ding, L. Hwang, X-Y. Zhu, Song Jin, "Nanowire lasers of formamidinium lead halide perovskites and their stabilized alloys with improved stability," *Nano Lett.* **2016**, *16*, 1000-1008.
- Z. Guo, X. Wu, T. Zhu, X.-Y. Zhu, L. Huang, "Electron-phonon scattering in atomically thin 2D perovskites," *ACS Nano,* **2016**, *10,* 9992-9998.
- X.-Y. Zhu, "The perovskite fever and beyond," *Acct. Chem. Res.* **2016**, *49*, 355-356.
- H. T. Yi, X. Wu, X.-Y. Zhu, V. Podzorov, "Intrinsic charge transport across phase transitions in hybrid organo-inorganic perovskites," *Adv. Mater.* **2016**, *28,* 6509-6514.
- Y. Chen, H.-T. Yi, X. Wu, R. Haroldson, Y. Gartstein, Y. I. Rodionov, K. S. Tikhonov, A. Zakhidov, X.-Y. Zhu, V. Podzorov, "Extended carrier lifetimes and diffusion lengths in hybrid perovskites revealed by steady-state Hall effect and photoconductivity measurements," *Nature Commun*. **2016** *7,* 12253.
- Y. Fu, H. Zhu, C. C. Stoumpos, Q. Ding, J. Wang, M. G. Kanatzidis, X-Y. Zhu, S. Jin, "Broad wavelength tunable robust lasing from single-crystal nanowires of cesium lead halide perovskites ($CsPbX_3$, X=Cl, Br, I)," *ACS Nano,* **2016**, *10, 7963-7972.*
- K. Miyata, D. Meggiolaro, M. T. Trinh, P. P. Joshi, E. Mosconi, S. Jones, F. De Angelis, X.-Y. Zhu, "Large polarons in lead halide perovskites," *Science Adv.* **2017**, *3,* e1701217.
- K. Miyata, T. L. Atallah, X.-Y. Zhu, "Lead halide perovskites: crystal-liquid duality, phonon glass electron crystal, and large polaron formation," *Science Adv.* **2017**, *3,* e1701469.
- M. Bonn, K. Miyata, E. Hendry, X.-Y. Zhu, "On the Role of Dielectric Drag in Polaron Mobility in Lead Halide Perovskite," *ACS Energy Lett.* **2017**, *2*, 2555-2562.
- H. Zhu, M. T. Trinh, Y. Fu, J. Wang, P. P. Joshi, L. Miyata, S. Jin, X.-Y. Zhu, "Organic cations might not be essential for the exceptional properties of bandedge carriers in lead halide perovskites," *Adv. Mater.* **2017**, *29,*1603072.
- Y. Fu, T. Wu, J. Wang, J. Zhai, M. J. Shear, Y. Zhao, R. J Hamers, E. Kan, K. Deng, X-Y. Zhu, S. Jin, "Stabilization of the metastable perovskite phase of formamidinium lead triiodide ($FAPbI_3$) *via* surface functionalization," *Nano Lett.* **2017**, *17,* 4405-4414.

- X. Wu, L. Tan, K. Miyata, T. Hu, M. T. Trinh, S. Liu, D. Egger, R. Li, R. Coffee, I. Makasyuk, A. Fry, X. Wang, L. Kronik, A. Rappe, X.-Y. Zhu, A. Lindenberg, "Light-induced picosecond rotational disordering of the inorganic sublattice in hybrid perovskites," *Science Adv.* **2017**, *3*, e1602388.
- Tyler J. Evans, A. Schlaus, Yongping Fu, Xinjue Zhong, Timothy Atallah, Michael S. Spencer, Louis Brus, Song Jin, X.-Y. Zhu, "Continuous-wave lasing in cesium lead bromide perovskite nanowires," *Adv. Opt. Mat.* **2018**, *5*, 1700982.

DE-SC0018021: Understanding and Controlling Aggregation Processes in Mixed-Molecular Solids

Jeramy D. Zimmerman, Colorado School of Mines.

Program Scope

Over the last two decades an immense improvement in our understanding of the underlying mechanisms governing organic photovoltaics has been enabled, in large part, by the development of advanced scattering techniques (e.g. X-ray and transmission electron microscopy based). However, many materials, such as those for organic light emitting diodes (OLEDs), are difficult to probe with these tools because of the poor contrast between different molecules and the weak chemical discrimination capabilities, making correlations to morphology unfeasible.

We have developed atom probe tomography (APT) techniques to extend its applicability to include organic molecular solids. APT provides an unparalleled spatial resolution of < 1 nm and mass-to-charge resolution of <1 Da, providing the ability to probe morphology previously unattainable, enabling the development of new structure-property relationships for solid-state blends of molecules. These mixed-molecular solids are important for a wide variety of materials, including those used in devices such as organic light emitting diodes (OLEDs), high resolution photoresists, charge carrier doping of organic electronics, and organic photovoltaics (OPVs). This project uses primarily OLED materials to test and validate our conclusions because there are a wide variety of materials commercially available and the lessons learned will improve efficiency of OLED lighting and displays reducing energy consumption in homes and mobile devices.

Material morphology of these organic molecular materials is characterized from 100 nm-scales down to molecular-dimer scale using APT. Spatial statistics provides quantitative analysis of the APT generated point cloud data to aid in understanding clustering. The morphology of the mixed molecular solids will be compared against molecular cohesive forces such as Hansen solubility parameters to understand why the materials phase segregate and to learn how to prevent segregation by creating a thermodynamically stable solid-solutions of molecules. The morphology will then be correlated to physical properties of the material blends, such as the emission efficiency, transport properties, and types of energy loss mechanisms that dominate the materials.

Recent Progress

In the first year of this project we have focused on completing the development of atom probe tomography (APT) for molecular organic materials. APT combines point projection microscopy with time-of-flight mass spectrometry in a technique that we have now shown to have a mass resolution of < 1 Da, a spatial resolution of ~0.3 nm in z and ~1 nm in x-y, and an analytic sensitivity of ~50 ppm, which is more than adequate to characterize the morphology of small-molecule organic semiconducting systems. We have also been developing a suite of spatial statistical analysis tools and simulations to help understand the significance of the data provided by APT. Our APT system is able to identify mass-charge states for about 60% of the molecules in the film, spatial statistics is critical because it allows us to interpretation of the incomplete data set. The APT technique has been used to improve our understanding of materials for both OLED and OPV active layers, demonstrating the presence of chemical reactions at heterointerfaces in acene/fullerene bilayers and phase segregation in archetypal OLED blends.

When applying this new APT technique, it is important to understand the quality of data it provides. For APT, there are three major concerns: (1) species discrimination, (2) molecular fragmentation, and (3) spatial resolution. We address each of these to validate APT for organic molecular materials. Finally (4), spatial statistics techniques are used to analyze and understand the point cloud data provided by APT.

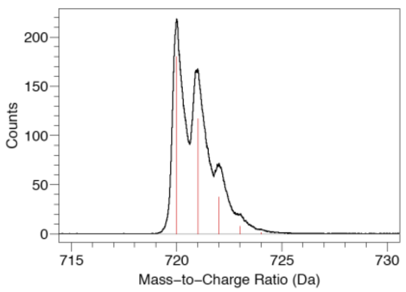

Figure 1. Mass spectrum of C_{60}^+ showing isotopic peaks; the red lines are the expected isotopic distribution. This spectrum has a mass resolving power ($m/\Delta m$) of about 1000.

1. Species discrimination: APT is inherently a mass spectrometer. In APT mass resolution is commonly characterized by the mass resolving power of $MRP = \frac{m}{\Delta m}$, where Δm is the full-width at half-maximum of the peak at mass m. We have demonstrated MRPs of >1000; Figure 1 shows a mass spectrum collected on a sample of C60 in which the isotopic peaks are resolved and compared to the expected isotopic distribution. This high MRP allows identification of the molecular constituents of a sample by comparing to the expected isotope distribution.

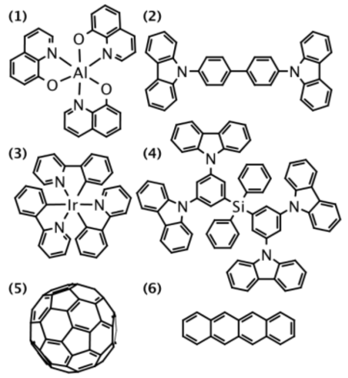

Figure 2. Example molecules successfully analyzed with atom probe: (1) *tris- (8-hydroxy-quinoline) aluminum* (Alq_3), (2) *4,4'-bis(N-carbazolyl)-1,1'-biphenyl* (CBP), (3) *tris[2- phenylpyridinato-C2,N]iridium(III)* ($Ir(ppy)_3$), (4) *bis[3,5-di(9H-carbazol-9-yl) phenyl] diphenyl-silane* (SimCP2), (5) C_{60}, (6) tetracene.

2. Organic molecular materials span a wide range of bonding types, shapes and sizes. We have successfully analyzed a number of materials systems with APT that represent a cross-section of common organic electronic molecular classes; some of these structures are shown in Figure 2. In each of these materials, the main mass peaks observed are for the expected masses and evidence of fragmentation is not observed (either through mass analysis of other lower-mass peaks and time of flight deviations). Thus far, we have focused on thermally evaporable molecules, but this is not a known limitation of the technique; in fact, we have observed C_{60} dimers and trimers evaporate, which are both insoluble and cannot be sublimed. The limits for applicability of APT to organic and other materials systems are not yet fully known.

3. Spatial Resolution: In APT, the sample is the primary ion optic. We use an unconventional tip geometry and sample preparation relative to most APT work; therefore, it is critical to understand the spatial resolution for our implementation. To evaluate our spatial resolution, we prepared APT specimens of C_{60} on diindenoperylene (DIP), which templates C_{60}

with the (111) plane parallel to the substrate and enhances crystallinity. The crystalline structure provides an internal measure of the spatial resolution. A projection of the APT 3D point cloud (Figure 3a) shows layers of higher density (i.e. lattice planes). Figure 3b shows a spatial distribution map (SDM), which quantifies the distribution of z-axis components of the vectors between points. Fitting the SDM to a model of evenly spaced Gaussian functions with equal standard deviations returns a peak spacing of 0.817(2)nm, which corresponds to 0.817 nm for C_{60} (111). The width of the peaks (e.g. one standard deviation) indicates the spatial resolution of 0.313(3) nm in the z-direction. The field of view for this sample is ~760 nm; as there are about 800 pixels across the detector, our x-y resolution is limited to about 1 nm. These resolutions are not a physical limit of the technique, but what was achieved for this particular sample geometry and test conditions.

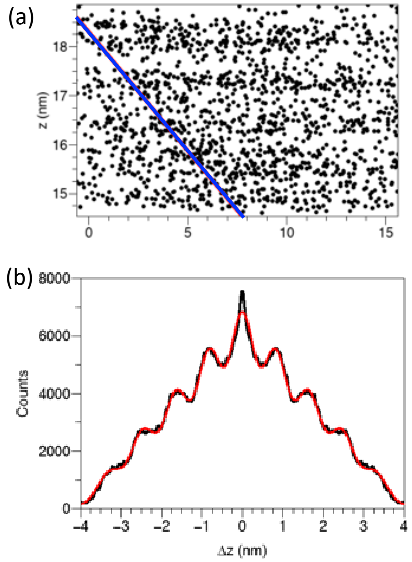

Figure 3. (a) A real-space projection of molecular centroids of C_{60} templated on (DIP) showing crystal planes. The blue line marks a grain boundary. (b) Spatial distribution map (SDM) in the z-direction. A fit to data is in red.

4. Spatial Statistics: The heavily-studied, archetypal phosphorescent OLED system of CBP:Ir(ppy)$_3$ is suspected of emitter aggregation, increasing self-quenching, exciton-exciton and exciton-polaron interaction, and expediting device degradation. To study aggregation, we deposited a blended film of 6% (vol. %) Ir(ppy)$_3$ in CBP and performed APT. To characterize clustering of Ir(ppy)$_3$, we use a variety of spatial statistics techniques. One primary clustering metric, K-function (K_3) measures the number of other like molecules contained within a sphere of radius *r* centered about each molecule, normalized by the bulk concentration. Acceptance interval (AI) envelopes are generated by randomly relabeling the molecular identities of the point cloud and calculating K_3 50,000 times. We use the square root of the K-function to stabilize the variance of the envelopes and subtract the median value of the envelope center the plot about zero. From the K_3 anomaly and envelopes shown in Figure 4, we observe deviation outside a 99.9% acceptance interval, indicating clustering of the Ir(ppy)$_3$ over the range of about 5 nm to 12 nm.

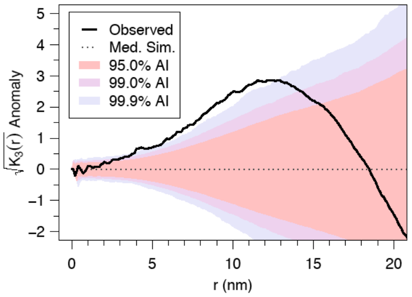

Figure 4. K-function anomaly for Ir(ppy)$_3$ in CBP. The excursion of the observed K-function above the 99.9 AI envelopes indicates significant non-random clustering of the Ir(ppy)$_3$ in the range of 5 nm to 12 nm.

Future Plans

Now that we have verified the quality of our APT data and have observed clustering, we can move on towards the scientific goals of the project—correlating morphology to materials properties. Our current work is focused on extension of spatial statistics and correlations to materials properties.

First, we have outlined a detailed set of computational experiments to formally develop and test the spatial statistics used in this program with a Senior Design student that will then complete a Master's Degree in Applied Statistics at Mines. This statistical analysis work uses the high-performance computing (HPC) node to perform numerous statistical tests on generated data sets with known clustering behavior. We also have a summer undergraduate student through the Citrine Informatics NextGen Fellowship data analytics and machine learning program that will analyze data sets with the goal of simplifying and guiding the necessary spatial statistics.

Second, we are focusing on extending our work on OLED systems with differing degrees of dopant segregation so that results can be compared against spatial data. This involves significant work we have done in this year to allow expand the conditions (e.g. temperatures) at which films can be deposited. We have been and will continue to expand our efforts to characterize fundamental materials parameters such as mobility and time-resolved photoluminescence of emissive-layer molecular blends and correlate these to transport and decay models. A student that performed his senior design work last year will be working on his MS degree this year, continuing his work on understanding Hansen Solubility parameters and their influence on spatial data.

With the fundamental platforms we have developed in the first year and expanded forays into deeper understanding of statistical tests we have planned, we expect to be well positioned to address the fundamental question in this proposal of how spatial distributions of molecules affect materials properties in mixed molecular blends.

Publications

We have been invited to submit a topical review in Applied Physics Reviews which will be submitted in June of 2018: A.P. Proudian, M.B. Jaskot, D.R. Diercks, B.P. Gorman, and J.D. Zimmerman, "Atom Probe Tomography of Organic Molecular Materials"

Conference presentations:

1. MB Jaskot, AP Proudian, D Diercks, BP Gorman, JD Zimmerman, "Unraveling the Effects of OLED Active Layer Morphology on Degradation Using Atom Probe Tomography" OSA Light, Energy and the Environment Congress, Boulder CO, Nov. 6-9, 2017. *Oral*
2. A Proudian, M Jaskot, D Dierks, B Gorman, J Zimmerman "Atom Probe Tomography of Small-Molecule Organic Electronic Systems" 2017 MRS Fall Meeting, Boston MA, Nov.26-Dec1, 2017. *Oral*
3. M Jaskot, A Proudian, HN Fujishin, G Vincent, D Diercks, B Gorman, J Zimmerman, "Spatial Statistics as a Quantitative Tool to Study Morphology in Organic Light-Emitting Diodes" Atom Probe Tomography & Microscopy 2018, Washington, DC, June 10-15, 2018. *Oral*
4. M Jaskot, A Proudian, D Diercks, B Gorman, J Zimmerman "Reconstruction Solution Envelopes for Improved Morphological Confidence" Atom Probe Tomography & Microscopy 2018, Washington, DC, June 10-15, 2018. *Poster*
5. M Jaskot, A Proudian, HN Fujishin, G Vincent, D Diercks, B Gorman, J Zimmerman "Atom Probe Tomography of Molecular Organic Electronic Materials" Atom Probe Tomography & Microscopy 2018, Washington, DC, June 10-15, 2018. *Oral*

POSTER SESSIONS

LIST OF POSTER PRESENTATIONS
ODD numbers on Day 1 and EVEN numbers on Day 2

	PI Name	Institution	Title
1	**Alivisatos**	**LBNL**	**Physical Chemistry of Inorganic Nanostructures**
2	**Bo**	**Institut Catalan**	**Counterions for Controlled Dissolution, Precipitation and Stabilization of Molecular Clusters and Extended Lattices**
3	**Bobev**	**U. Delaware**	**Novel Pnictides with d- and f-Metals as Prospective Materials for Thermal Energy Conversion**
4	**Braun**	**U. Illinois, Urbana-Champaign**	**Programming Function via Soft Materials**
5	**Brutchey**	**U. Southern California**	**Quantifying the Phase Behavior and Surface Chemistry of $CsPbBr_3$ Quantum Dots**
6	**Chabal**	**U. Texas, Dallas**	**Synthesizing New Metal Organic Frameworks with Tailored Physical and Chemical Properties**
7	**Cohen**	**U.C. San Diego**	**Transforming Metal-Organic Frameworks into Polymer Hybrids and Biomimetic MetalloMOFzymes**
8	**Dai**	**ORNL**	**Materials and Interfacial Chemistry for Next Generation Electrical Energy Storage**
9	**de Pablo**	**ANL**	**Precision Synthesis and Assembly of Ionic and Liquid Crystalline Polymers**
10	**Miller**	**AMES**	**Complex Magnetic Interactions in Novel Rare Earth-Rich Polar Intermetallic Systems**
11	**Epps/Hall**	**U. Delaware/Ohio State U.**	**Nanostructured Polymer Electrolytes: Tuning Interfaces to Manipulate Transport**
12	**Feng**	**U.C. Riverside**	**Pore Space Engineering and Functionalization in Porous Metal-Organic Framework Materials**
13	**Fischer**	**U.C. Berkeley**	**Atomically Defined Doping of Graphene Nanoribbons for Mesoscale Electronics**
14	**Grason**	**U. Mass. Amherst**	**Ordered Phases of Chiral Block Copolymers: Mesochiral, Periodic Nanostructures via Self-Assembly**
15	**Israelachvili**	**U.C. Santa Barbara**	**New Instrumentation and Tools to Study Dynamic (Non-equilibrium) Physico-chemical Interfacial Processes across Large Length, Rates, and Time Scales**
16	**Jayaraman**	**U. Delaware**	**Predictive Coarse-Grained Modeling of Morphologies in Polymer Nanocomposites with Specific and Directional Intermolecular Interactions**
17	**Jin**	**U. Wisconsin, Madison**	**Fundamental Studies of Charge Transfer in Quantum Confined Nanostructure Heterojunctions and Applications to Solar Energy Conversion**
18	**Kanatzidis**	**ANL**	**Rational Synthesis of Superconductors**
19	**Katz**	**Johns Hopkins U.**	**Statically Polarized Polymer Heterostructures for Charge Carrier Density Control in Energy-Relevant Semiconductors**
20	**Klausen**	**Johns Hopkins U.**	**Mesoscale Fragments of Crystalline Silicon by Chemical Synthesis**
21	**Kolis**	**Clemson U.**	**Synthesis and Single Crystals of Refractory Oxides of Lanthanides and Thorium**

22	**Manthiram**	**U. Texas, Austin**	**Materials and Interfacial Chemistry for Next-Generation Electrical Energy Storage**
23	**Moore**	**U. Illinois, Urbana-Champaign**	**Programming Function via Soft Materials: Dynamic Polymer Networks**
24	**Matzger**	**U. Michigan**	**Dynamic Properties of Nanostructured Porous Materials**
25	**Ober**	**Cornell U.**	**Engineering Transport in Confined Environments of Self-Assembled Stable Radical Polymers**
26	**Ong**	**U.C. San Diego**	**Elucidating the Determinants of Alkali Ionic Conductivity in Oxide and Sulfide Frameworks**
27	**Salmeron**	**LBNL**	**Structure and Dynamics of Materials Interfaces**
28	**Seshadri**	**U.C. Santa Barbara**	**Hybrid Metal Halides: Advancing Optoelectronic Materials**
29	**Tolbert**	**U.C. Los Angeles**	**Using Nanoporous Materials to Understand Kinetic Constraints in Pseudocapacitive Energy Storage**
30	**Tsukruk**	**Georgia Inst. Tech.**	**Functional Nanomaterials with Tunable Plasmonic and Emittive Properties**
31	**Xu**	**LBNL**	**Inorganic/Organic Nanocomposites**
32	**Zhu**	**Columbia U.**	**Charge Carrier Dynamics in Hybrid Organic-Inorganic Semiconductors**
33	**Lutkenhaus**	**Texas A&M U.**	**The Nature of Charge Storage in Nitroxide Radical Polymers**

AUTHOR INDEX

PARTICIPANT LIST

Name	**Organization**	**Email**
Baldo, Marc	Massachusetts Institute of Technology	baldo@mit.edu
Bazan, Guillermo	University of California, Santa Barbara	bazan@chem.ucsb.edu
Bo, Carles	Institute of Chemical Research of Catalonia	cbo@iciq.cat
Bobev, Svilen	University of Delaware	bobev@udel.edu
Bragg, Arthur	Johns Hopkins University	artbragg@jhu.edu
Braun, Paul	University of Illinois at Urbana-Champaign	pbraun@illinois.edu
Brutchey, Richard	University of Southern California	brutchey@usc.edu
Cava, Robert	Princeton University	rcava@princeton.edu
Chabinyc, Michael	University of California, Santa Barbara	mchabinyc@engineering.ucsb.edu
Clearfield, Abraham	Texas A&M University	clearfield@chem.tamu.edu
Cohen, Seth	University of California, San Diego	scohen@ucsd.edu
Cui, Yi	Stanford University and SLAC National Accelerator Laboratory	yicui@stanford.edu
Dadmun, Mark	Univ. of Tennessee/Oak Ridge National Laboratory	dad@utk.edu
Dai, Sheng	Oak Ridge National Laboratory	dais@ornl.gov
Das, Siddhartha	University of Maryland	sidd@umd.edu
Das, Swapan Kumar	Lehigh University	swd217@lehigh.edu
Dincă, Mircea	Massachusetts Institute of Technology	mdinca@mit.edu
Dravid, Vinayak	Northwestern University	v-dravid@northwestern.edu
El-Sayed, Mostafa	Georgia Institute of Technology	melsayed@gatech.edu
Epps, Thomas	University of Delaware	thepps@udel.edu
Feng, Pingyun	University of California, Riverside	pingyun.feng@ucr.edu

Fischer, Felix	University of California, Berkeley	ffischer@berkeley.edu
Flatte, Michael	University of Iowa	shyam-udas@uiowa.edu
Freedman, Danna	Northwestern University	danna.freedman@northwestern.edu
Fuchs, Gregory	Cornell University	gdf9@cornell.edu
Gersten, Bonnie	US Department of Energy	Bonnie.Gersten@science.doe.gov
Gogotsi, Yury	Drexel University	gogotsi@drexel.edu
Graham, Kenneth	University of Kentucky	kenneth.graham@uky.edu
Grason, Gregory	University of Massachusetts, Amherst	grason@mail.pse.umass.edu
Gray, Thomas	Case Western Reserve University	tgray@case.edu
Gregorczyk, Keith	University of Maryland	kgregorc@umd.edu
Hall, Lisa	The Ohio State University	hall.1004@osu.edu
Hayward, Ryan	University of Massachusetts, Amherst	rhayward@mail.pse.umass.edu
Jayaraman, Arthi	University of Delaware	arthij@udel.edu
Jin, Song	University of Wisconsin, Madison	jin@chem.wisc.edu
Kanatzidis, Mercouri	Argonne National Laboratory	m-kanatzidis@northwestern.edu
Katz, Howard	Johns Hopkins University	hekatz@jhu.edu
Klausen, Rebekka	Johns Hopkins University	klausen@jhu.edu
Kolis, Joseph	Clemson University	kjoseph@clemson.edu
Kovnir, Kirill	Iowa State University	kovnir@iastate.edu
Kristiansen, Kai	University of California, Santa Barbara	kai_kristiansen@ucsb.edu
Landskron, Kai	Lehigh University	kal205@lehigh.edu
Lee, Sang Bok	University of Maryland	slee@umd.edu

Li, Jing	Rutgers University	jingli@rutgers.edu
Lin, Qisheng	AMES Laboratory	qslin@ameslab.gov
Lu, Yanfu	Pennsylvania State University	yfl5133@psu.edu
Lutkenhaus, Jodie	Texas A&M University	jodie.lutkenhaus@tamu.edu
Manthiram, Arumugam	University of Texas at Austin	rmanth@mail.utexas.edu
Markowitz, Michael	US Department of Energy	mike.markowitz@science.doe.gov
Matzger, Adam	University of Michigan	matzger@umich.edu
May, Steven	Drexel University	smay@drexel.edu
Melosh, Nick	Stanford University and SLAC National Accelerator Laboratory	nmelosh@stanford.edu
Mitlin, David	Clarkson University	david.mitlin2@gmail.com
Moore, Jeff	University of Illinois at Urbana-Champaign	jsmoore@illinois.edu
Nealey, Paul	University of Chicago and Argonne National Laboratory	nealey@uchicago.edu
Neilson, James	Colorado State University	james.neilson@colostate.edu
Nguyen, Thuc-Quyen	University of California, Santa Barbara	quyen@chem.ucsb.edu
Nyman, May	Oregon State University	may.nyman@oregonstate.edu
Ober, Christopher	Cornell University	cko3@cornell.edu
Ong, Shyue Ping	University of California, San Diego	ongsp@eng.ucsd.edu
Paek, Eunsu	Clarkson University	epaek@clarkson.edu
Perras, Frederic	AMES Laboratory	fperras@ameslab.gov
Power, Philip	University of California, Davis	pppower@ucdavis.edu
Rabani, Eran	Univ. of California, Berkeley/Lawrence Berkeley National Laboratory	eran.rabani@berkeley.edu
Reich, Daniel	Johns Hopkins University	reich@jhu.edu

Rossini, Aaron	Iowa State University/AMES Laboratory	arossini@iastate.edu
Rubloff, Gary	University of Maryland	rubloff@isr.umd.edu
Salmeron, Miquel	Lawrence Berkeley National Laboratory	mbsalmeron@lbl.gov
Schanze, Kirk	University of Texas, San Antonio	Kirk.Schanze@utsa.edu
Segalman, Rachel	University of California, Santa Barbara	segalman@ucsb.edu
Seshadri, Ram	University of California, Santa Barbara	seshadri@mrl.ucsb.edu
Sinnott, Susan	Pennsylvania State University	sbs5563@psu.edu
Sokolov, Alexei	Oak Ridge National Laboratory	sokolov@utk.edu
Somorjai, Gabor A.	Lawrence Berkeley National Laboratory	somorjai@berkeley.edu
Stamenkovic, Vojislav	Argonne National Laboratory	vrstamenkovic@anl.gov
Tan, Kui	University of Texas, Dallas	kuitan@utdallas.edu
Teng, Xiaowei	University of New Hampshire	xw.teng@unh.edu
Terrones, Mauricio	Pennsylvania State University	mut11@psu.edu
Thiyagarajan, Thiyaga	US Department of Energy	p.thiyagarajan@science.doe.gov
Thomas, Samuel	Tufts University	sam.thomas@tufts.edu
Thomas, Edwin	Rice University	elt@rice.edu
Thonhauser, Timo	Wake Forest University	thonhauser@wfu.edu
Tirrell, Matthew	University of Chicago/Argonne National Laboratory	mtirrell@uchicago.edu
Tolbert, Sarah	University of California, Los Angeles	tolbert@chem.ucla.edu
Tsukruk, Vladimir	Georgia Institute of Technology	vladimir@mse.gatech.edu
Veige, Adam	University of Florida	veige@chem.ufl.edu
Wang, Hong	University of North Texas	hong.wang@unt.edu

Xu, Ting	University of California, Berkeley and Lawrence Berkeley National Laboratory	tingxu@berkeley.edu
Yan, Hao	Stanford University and SLAC National Accelerator Laboratory	yanhao@stanford.edu
Zhang, Fu	Pennsylvania State University	zhangfu1991@gmail.com
Zhao, Bin	University of Tennessee, Knoxville	bzhao@utk.edu
Zhu, Lei	Case Western Reserve University	lxz121@case.edu
Zhu, Xiaoyang	Columbia University	xyzhu@columbia.edu
Zimmerman, Jeramy	Colorado School of Mines	jdzimmer@mines.edu
Zur Loye, Hans-Conrad	University of South Carolina	zurloye@mailbox.sc.edu